THE UNIVERSITY *of* EDINBURGH

Elucidating Regulators and Biomarkers of Synaptic Stability During Neurodegeneration

Maica Llavero Hurtado

Thesis submitted for the degree of Doctor of Philosophy

University of Edinburgh

2017

Declaration

I declare that this thesis has been composed solely by myself and that it has not been submitted, in whole or in part, in any previous application for a degree. The work described in this thesis is my own, except where collaborative contributions were required. Any collaborations have been explicitly acknowledged in the text.

Maica Llavero Hurtado

Acknowledgments

I would like to thank everyone who has contributed in one way or another toward reaching this point.

First of all, I thank my supervisor, Tom Wishart, for trusting me since the beginning ever since I first started doing my master's project in the lab. I thank him for all the support during these past 5 years now and for teaching me everyday. He is a great scientist but also a great leader and able to inspire and challenge at the same time, building confidence. I always thought leaders aren't just brilliant at what they do but they also make you feel brilliant too!

Thanks to Laura Graham. She is more than a labmate. We started our PhD at the same time and went through all this together. Thanks for all the support (science and non-science!), for all the conversations, for all the trips...! It wouldn't have been the same without you.

Thanks to Sam Eaton. You were always there to help. Always caring with a comforting smile. You always made me feel better under stressful times. Thanks for that, but also for the nice chats and trips.

Thanks to Giusy Pennetta and Mario Sanhueza. The second year of my PhD was very special. Thanks for hosting me in your lab and introducing me to the wonderful *Drosophila* world. I have very fond memories of that year. I have missed a lot, the long conversations in the flylab and the afternoon espresso breaks. I heard once that either you hate or love *Drosophila*…well I have to say I 100% love them.

Thanks to Jon Cooper and his lab for hosting me for a month and teaching me immunohistochemistry techniques. Thanks a lot for all the discussions and inspiration regarding the NCL work as well as for donating the tissues I used in this thesis. I feel glad I had the opportunity to collaborate with you. Thanks, also to Hemanth Nelvagal for helping me with the thresholding methodology and for assisting in getting mice blood samples needed for my biomarker study.

Thanks to Tom Gillingwater for all the support given during my PhD. Your comments were incredibly helpful and inspiring for interpreting some of the data. Thanks to that I learnt the importance of zooming in and out of a specific question in order to get the whole picture.

Thanks to Heidi Fuller, Dougie Lamont, Amy Tavendale and Abdel Atrih for contributing with the proteomics experiments in this project. Thanks for always being there to answer all my questions. Specially thanks to Dougie and Amy for hosting me in their lab for a few days to learn the label free protocols used there.

Thanks to the Darwin Trust of Edinburgh for funding my PhD and for giving me this opportunity.

Thanks to George for your unconditional support, and for always cheering me up even from a distance. Thanks for inspiring me with your entropic mind and always giving me ideas. Thanks for having the patience to teach me “R” and “Python” and especially, thanks for proofreading this thesis. Now you know how important synapses are! I should probably thank this thesis itself because otherwise I wouldn’t have met you.

Thanks to my scientist friends, Ana and Kevin for your advice at the beginning of my PhD, especially when trying to decide whether to come to Edinburgh or not. You were absolutely right. Big thanks to Kevin for accompanying me in part of this journey: for the long evenings playing music and cooking new recipes while dancing. Edinburgh was never the same after you moved.

Thanks to my non-scientist and best friend Natalia, for trying to understand what I do and listening to my stories about proteins and flies. I am very thankful for all your visits to Edinburgh and you always being there, no matter which country you were in.

Thanks to my flatmate Andrés for all the random conversations about life, politics, science, and about how annoying people are (especially that)... etc. You are not as good of a dancer as Kevin, but who is?

Special thanks to Yasmina. You were the one who first thought of moving abroad to do research. You will never know that, but you made me aim high. You were never able to do that so I thought I had to try and do it for us both.

Thanks to my family for always trusting me. You never questioned my choices and always were there caring even from a distance. Thanks for feeding and pampering me every time I returned home and always refilling me with energy to achieve this!

Lastly, thanks to my other family here in Edinburgh. Some of you are not here anymore, but you will always be related to Edinburgh in my mind. You contributed to making Edinburgh my second home so there you are: Alberto, Lourdes, Irene, Rodrigo, Esther and Juanjo.

Abstract

Synapses are an early pathological target in a wide range of neurodegenerative conditions including adult-onset Alzheimer's and Parkinson's, and diseases of childhood such as spinal muscular atrophy and neuronal ceroid lipofuscinoses (NCLs). However, our understanding of the mechanisms regulating the stability of synapses and their exceptional vulnerability to neurodegenerative stimuli remains in its infancy.

To address this, we have used the NCLs to model the molecular alterations underpinning synaptic vulnerability. Our primary objective is to identify novel regulators of synaptic stability as well as highlight novel therapeutic targets which may prove effective across multiple neurodegenerative conditions where synapses are an early pathological target. The NCLs, are the most frequent autosomal-recessive disease of childhood. There are currently 14 individual genes whose mutations result in similar phenotypes including blindness, cognitive/motor deficits, seizures and premature death. This suggests that despite the difference in the initiating mutation and the degenerative processes across this collective group are likely to impact on overlapping pathways.

Focusing on two murine models of NCL; one with an infantile onset - CLN1 disease (*Ppt1*$^{-/-}$) and one with a juvenile onset - CLN3 disease (*Cln3*$^{-/-}$) we made use of the temporospatial synaptic vulnerability pattern in these mice to plan proteomic and in silico analyses. This pipeline was utilised to identify perturbed protein candidates and pathways correlating with differential regional synaptic vulnerability. This ultimately allowed the generation of a list of candidate proteins, some of which were relevant to human NCL as they were altered in post mortem brain samples. Interestingly, many of the correlative candidates also appear to show conserved alterations in both NCL forms examined and other neurodegenerative diseases.

Next, candidates were genetically and/or pharmacologically targeted to study their modulatory effects on neuronal stability in vivo. This was done using CLN3 Drosophila as a rapid screening assay and led to the successful characterisation of a subset of candidates as either enhancers or suppressors of the CLN3-induced phenotype in vivo.

As well as identifying regulators of neuronal stability, following a similar pipeline, we identified a set of putative biomarkers of disease progression in muscle and blood in the *Ppt1*$^{-/-}$ mice, a subset of which appeared conserved in *Cln3*$^{-/-}$ mice. One of these conserved candidates presented the same directionality of change in human post mortem brain samples, indicating its relevance to the human NCL.

Following this workflow from spatio-temporal profiling of murine synaptic populations, to in silico analyses and in vivo phenotypic assessment, we demonstrate that we can identify multiple protein candidates capable of modulating neuronal stability in vivo and identified putative biomarkers that tracked disease progression.

Lay summary

Neurons are connected through complex structures called synapses which are responsible for many essential processes happening in the brain such as cognition or movement. In many neurodegenerative diseases, such as Alzheimer's or Parkinson's, it has been shown that synaptic changes happen early on in disease progression contributing to the dysfunction of the nervous system. Yet, why synapses are so sensitive in a variety of diseases remain unclear. For this reason, this study aims to elucidate the biological factors regulating synaptic loss, which may help our understanding of the mechanisms underpinning neurodegeneration as well as highlight novel therapeutic targets.

To do so, genetically modified mice were used, which serve as models of a fatal childhood neurodegenerative disease called neuronal ceroid lipofucinosis (NCL). In this disease, synapses are an early pathological target. These mice reproduce various aspects of the human disease, such as blindness, motor and cognitive problems suggesting they may allow us to further understand how the disease works in humans.

The brain is divided into various regions which are affected differently depending on the disease. We used the structural patterns of synaptic vulnerability across different brain areas in these mice to characterise the changes at the molecular level (proteins). Using a combination of bioinformatic tools, we identified proteins and biological pathways that were perturbed in the mice models correlating to this synaptic vulnerability pattern. This suggests that these proteins are likely to regulate the process of synaptic loss during neurodegeneration and were identified as candidates for further characterization. Importantly, some of these candidates, were also found to be changed in NCL patient synapses and therefore were disease-relevant.

Next, to test if these proteins just correlate or can also affect neuronal stability, we studied them in the nervous system of fruit fly models of NCL. The nervous system of the fly has been very well characterized and, unlike mammals, allows a straight-forward and rapid screening, providing further understanding of disease-related pathways. Thus, by genetically and/or pharmacologically disrupting these proteins in NCL fruit fly models, we identified a sublist of the candidates which were actually able to improve or worsen the "disease" in the flies.

Following this workflow, which includes the examination of synaptic (neuronal connections) populations from mammalian models of diseases (mice) followed by bioinformatics analyses and studies using the fruit fly, we identified multiple proteins able to change neuronal stability (regulators) and inform on disease progression (biomarkers) in model systems.

Publications

Chapter 3 and part of Chapter 5 have been published in a peer reviewed journal:

> **Llavero Hurtado M,** Fuller HR, Wong AMS, Eaton SL, Gillingwater TH, Pennetta G, Cooper JD, Wishart TM**.** 2017. Proteomic mapping of differentially vulnerable pre-synaptic populations identifies regulators of neuronal stability in vivo. *Sci Rep.* 7(1):12412.

Chapter 6 is currently submitted for for publication:

> **Llavero Hurtado M**, Marchant TW, Eaton SL, Fuller HR, Lamont DJ, Gillingwater TH, Cooper JD, Wishart TM. Proteomic workflows for the discovery of peripherally accessible biomarkers - identification of NDUFS3 in Neuronal Ceroid Lipofuscinosis (NCL). Submitted

Chapter 4 and part of Chapter 5 is currently in preparation to submit for publication.

The workflows described here using proteomics, *in silico* tools and *in vivo* validation methods have been published here:

> Fuller HR, Graham LC, **Llavero Hurtado M,** Wishart TM. 2016. Understanding the molecular consequences of inherited muscular dystrophies: advancements through proteomic experimentation. *Expert Rev Proteomics.* 13(7):659-71.

Quantitative fluorescent western blotting methodology and normalisation approach has been published here:

> Eaton SL, **Llavero Hurtado M,** Oldknow KJ, Graham LC, Marchant TW, Gillingwater TH, Farquharson C, Wishart TM. 2014 A guide to modern quantitative fluorescent western blotting with troubleshooting strategies. *J Vis Exp*. 20;(93):e52099.

> Eaton SL, Roche SL, **Llavero Hurtado M,** Oldknow KJ, Farquharson C, Gillingwater TH, Wishart TM. 2013. Total protein analysis as a reliable loading control for quantitative fluorescent Western blotting. *PLoS One.* 8(8):e72457.

Other publications arising from collaborations during my PhD are outlined below. In these projects I carried out proteomic analyses and processing addressing a variety of experimental questions related to neuroscience topics such as:

- Molecular differences between mice and human neuromuscular junction:

  Jones RA, Harrison C, Eaton SL, **Llavero Hurtado M**, Graham LC, Alkhammash L, Oladiran OA, Gale A, Lamont DJ, Simpson H, Simmen MW, Soeller C, Wishart TM, Gillingwater TH. 2017. Cellular and molecular architecture of a human synapse. *Cell Rep.* 21(9):2348-2356.

- Elucidation of mechanistic pathways underlying axonal degeneration.

  Catenaccio A, **Llavero Hurtado M,** Diaz P, Lamont DJ, Wishart TM, Court FA. 2017. Molecular analysis of axonal-intrinsic and glial-associated co-regulation of axon degeneration. *Cell Death Dis*. 8(11):e3166.

- Characterisation of molecular perturbations in equine multiple system neuropathy.

  McGorum BC, Pirie RS, Eaton SL, Keen JA, Cumyn EM, Arnott DM, Chen W, Lamont DJ, Graham LC, **Llavero Hurtado M,** Pemberton A, Wishart TM. 2015. Proteomic Profiling of Cranial (Superior) Cervical Ganglia Reveals Beta-Amyloid and Ubiquitin Proteasome System Perturbations in an Equine Multiple System Neuropathy. *Mol Cell Proteomics.* 14(11):3072-86.

- Proteomic profile of SMA mice derived schwann cells.

  Aghamaleky Sarvestany A, Hunter G, Tavendale A, Lamont DJ, **Llavero Hurtado M,** Graham LC, Wishart TM, Gillingwater TH. 2014. Label-free quantitative proteomic profiling identifies disruption of ubiquitin homeostasis as a key driver of Schwann cell defects in spinal muscular atrophy. *J Proteome Res.* 13(11):4546-57

- Elucidating molecular perturbations in a Parkison's disease mouse model.

  Fuller HR, **Llavero Hurtado M,** Wishart TM, Gates MA. 2014. The rat striatum responds to nigro-striatal degeneration via the increased expression of proteins associated with growth and regeneration of neuronal circuitry. *Proteome Sci.* 12:20. doi: 10.1186/1477-5956-12-20. eCollection 2014.

Table of Contents

DECLARATION I

ACKNOWLEDGMENTS II

ABSTRACT IV

LAY SUMMARY V

PUBLICATIONS VI

TABLE OF CONTENTS VIII

LIST OF FIGURES XII

LIST OF TABLES XV

LIST OF ABBREVIATIONS XVI

CHAPTER 1. GENERAL INTRODUCTION 1

1.1 Socioeconomic impact of neurodegenerative diseases 1

1.2 Compartmentalised pathology in neurodegenerative diseases 2

1.3 The synapse 4

1.4 The synapse as an early pathological target in neurodegenerative disease 6

1.5 Mechanisms of synaptic vulnerability 8

1.5.1 "Synaptosis" 8

1.5.2 Mitochondrial homeostasis 8

1.5.3 Metabolic pathways 9

1.5.4 Protein homeostasis 11

1.6 The neuronal ceroid lipofuscinoses as a model of neurodegenerative disease 13

1.6.1 Genetics 14

1.6.2 Differential progressive regional/neuronal vulnerability pathology 15

1.6.3 Mechanisms of neurodegeneration in NCLs 16

1.6.4 CLN1/PPT1 disease 23

1.6.5 CLN3 disease 25

1.7 Drug target and biomarker discovery approaches 27

1.7.1 Proteomic technologies as a data-driven approach 27

1.7.2 Phenotypic assessment in drug discovery 30

1.7.3 Translational approaches 31

1.8 *Drosophila melanogaster* as a model system 33

1.8.1 *Drosophila* use in studies of neurodegenerative diseases 33

1.8.2 *Drosophila* nervous system 35

1.8.3 NCL *Drosophila* models 39

1.9 Experimental aims 41

CHAPTER 2. GENERAL MATERIALS AND METHODS 43

2.1 Animals and tissues 43

2.1.1 Mice 43

2.1.2 Humans 44
2.1.3 *Drosophila* 44
2.2 Antibodies 45
2.2.1 Primary antibodies 45
2.2.2 Secondary antibodies 46
2.3 Immunohistochemistry 46
2.3.1 Mouse brain 46
2.3.2 *Drosophila* larvae neuromuscular junctions 47
2.4 Synaptosome preparation 47
2.5 Protein extraction 48
2.6 Proteomics 49
2.6.1 ITRAQ 49
2.6.2 Label-free 51
2.7 Quantitative fluorescent western blotting (QWB) 53
2.8 Bioinformatics 53
2.8.1 *Progenesis* 53
2.8.2 *DAVID* 54
2.8.3 *BioLayout Express* 54
2.8.4 *Ingenuity Pathway Analysis (IPA)* 55
2.9 Imaging 56
2.10 Data collection and statistical analyses 57

CHAPTER 3. CHARACTERISATION OF DIFFERENTIALLY VULNERABLE SYNAPTIC POPULATIONS AT AN EARLY DISEASE STAGE USING *Cln3*$^{-/-}$ MICE AS A MODEL 58
3.1 Introduction 58
3.2 Materials and methods 60
3.2.1 Animals and tissue harvesting 60
3.2.2 Immunohictochemistry (IHC) 60
3.2.3 Synaptosome production 60
3.2.4 Protein extraction 60
3.2.5 iTRAQ proteomics 61
3.2.6 Quantitative fluorescent western blotting (QWB) 61
3.2.7 *In silico* analyses 61
3.3 Results 62
3.3.1 Quantitative immunohistochemistry identifies differential rates of synaptic pathology between brain regions in *Cln3*$^{-/-}$ mice 62
3.3.2 Comparative molecular profiling reveals proteomic perturbations that correlate with the extent of synaptic vulnerability 67
3.3.3 *In silico* analysis highlights alterations in valine catabolic and ROCK2 signalling cascades in vulnerable thalamic synapses 72
3.4 Discussion 83

CHAPTER 4. SPATIO-TEMPORAL ANALYSIS OF DIFFERENTIALLY VULNERABLE SYNAPTIC POPULATIONS IN *Ppt1*$^{-/-}$ MICE 85
4.1 Introduction 85
4.2 Materials and methods 88

4.2.1 Animals and tissue harvesting 88
4.2.2 Synaptosome preparation 88
4.2.3 Protein extraction 88
4.2.4 Label free proteomics 89
4.2.5 Quantitative fluorescent western blotting (QWB) 89
4.2.6 *In silico* proteomic analysis 89
4.3 Results 91
4.3.1 Processing and analysis of thalamic proteomic data 91
4.3.2 Processing and analysis of cortical proteomic data 99
4.3.3 Thalamus and cortex comparative analysis 103
4.3.4 *Ppt1*$^{-/-}$ and *Cln3*$^{-/-}$ comparative analysis 114
4.4 Discussion 117

CHAPTER 5. *IN VIVO* PHENOTYPIC ASSESSMENT OF PROTEIN CANDIDATES IN *DROSOPHILA MELANOGASTER* 121
5.1 Introduction 121
5.2 Materials and methods 124
5.2.1 *Drosophila* husbandry and maintenance 124
5.2.2 *DIOPT* 124
5.2.3 UAS/GAL4 system 128
5.2.4 *Drosophila* phenotypic assessment 128
5.3 Results 137
5.3.1 Characterization on CLN3 *Drosophila* models 137
5.3.2 Modifier screening in the eye 148
5.4 Discussion 164

CHAPTER 6. PROTEOMIC PROFILING OF PERIPHERALLY ACCESSIBLE TISSUES IDENTIFIES MOLECULAR PATHOLOGY AND PUTATIVE BIOMARKERS 172
6.1 Introduction 172
6.2 Materials and methods 175
6.2.1 Animals and tissue harvesting 175
6.2.2 Synaptosome preparation 175
6.2.3 Protein extraction 175
6.2.4 iTRAQ Proteomic processing 176
6.2.5 Label-free proteomic processing 176
6.2.6 Quantitative fluorescent western blotting (QWB) 176
6.2.7 *In silico* proteomic analysis 177
6.2.8 Data analysis and figure production 177
6.3 Results 178
6.3.1 iTRAQ proteomics identifies molecular pathology at early stages of *Cln3*$^{-/-}$ mice 178
6.3.2 Proteomic analyses of *Cln3*$^{-/-}$ mouse muscle correctly predicts disruption of ubiquitination-related pathway perturbations in patient post mortem brain 181
6.3.3 Label-free proteomics throughout the whole time-couse of disease identifies proteins whose expression profile correlates with progression 184
6.3.4 Ndufs3 and Calreticulin represent putative biomarkers for disease progression relevant to human NCL, and are detectable in muscle and blood samples in *Ppt1*$^{-/-}$ mice 189

6.4 Discussion 194

CHAPTER 7. GENERAL DISCUSSION 197
7.1 Overview of results 197
7.2 The importance of target and biomarker discovery 198
7.3 Conserved modulators of neurodegeneration across multiple conditions 199
7.4 The NCLs as model of neurodegeneration 202
7.5 Conclusions 203

REFERENCES 204

APPENDIX. DATA TABLES 229

List of figures

Fig. 1.1. Neuron schematic representation. **3**
Fig. 1.2. Schematic representation of a chemical synapse. **5**
Fig. 1.3. Mechanisms of neurodegeneration and therapies in the NCLs. **18**
Fig. 1.4. Time-course schematic in *Ppt1*$^{-/-}$ mice. **25**
Fig. 1.5. Strategies of drug target discovery based on omics. **32**
Fig. 1.6. Synaptic connections in the lamina. **38**
Fig. 2.1. Experiment design workflow of all the label-free proteomics datasets. **52**
Fig. 3.1. Brain region schematic. **64**
Fig. 3.2. Pre-synaptic immunostaining detects no pathological change at 6.5 months across brain regions in *Cln3*$^{-/-}$. **65**
Fig. 3.3. Spatio-temporal synaptic loss study in *Cln3*$^{-/-}$ detected differentially vulnerable synaptic populations across brain regions. **66**
Fig. 3.4. Experimental design workflow. **68**
Fig. 3.5. Molecular changes correlate with the synaptic vulnerability characterized across brain areas. **69**
Fig. 3.6. Representation of the valine degradation pathway in cortex, hippocampus and thalamus using *IPA*. **70**
Fig. 3.7. Differentially vulnerable synaptic population molecular profiling. **71**
Fig. 3.8. Synaptic thalamic proteome filtering and validation. **73**
Fig. 3.9. IPA analysis of the thalamic synaptic proteome. **75**
Fig. 3.10. HIBCH downregulation in thalamic synapses impacts in valine catabolism pathway. **77**
Fig. 3.11. QWB validation of fractionation of post mortem brain samples from JNCL patients and controls. **78**
Fig. 3.12. HIBCH QWB bands and quantification of cortical synaptosomes isolated from post mortem human JNCL patients and controls. **79**
Fig. 3.13. ROCK2 upregulation is a synaptic specific change conserved across a range of neurodegenerative conditions including NCL. **81**
Fig. 3.14. QWB bands and quantification of ROCK2 in synaptic fractions showing downregulation of this protein at end stages of the disease. **82**
Fig. 4.1. Synaptic pathology in thalamus and cortex throughout disease progression in *Ppt1*$^{-/-}$ mice. **87**
Fig. 4.2. Thalamus time-course quality control. **92**
Fig. 4.3. Data filtering of thalamic proteomic data. **95**
Fig. 4.4. Expression tracking of 3-month changed proteins throughout time-course of disease progression in thalamus. **96**
Fig. 4.5. QWB validation of thalamic proteomics. **97**
Fig. 4.6. Molecular profiling of protein changes through the time-course of disease progression in thalamic synaptosomes in *Ppt1*$^{-/-}$ mice. **98**
Fig. 4.7. Cortex time-course quality control. **99**
Fig. 4.8. Data filtering of cortical proteomic data. **100**
Fig. 4.9a. Molecular profiling of protein changes though the time-course of disease progression in cortical synaptosomes in *Ppt1*$^{-/-}$ mice. **102**

Fig. 4.9b. Molecular profiling of protein changes though the time-course of disease progression in cortical synaptosomes in *Ppt1*$^{-/-}$ mice. **103**
Fig. 4.10. Schematic and rationale used for comparative analysis of thalamic and cortical synaptic data. **104**
Fig. 4.11. Comparative analysis of biological functions perturbed in thalamic and cortical synapses at two equivalent stages. **105**
Fig. 4.12. Cell death-related protein networks generated in *IPA* in thalamus and cortex. **107**
Fig. 4.13. Comparative analysis of predicted upstream regulators perturbed in thalamus and cortex at two equivalent stages. **108**
Fig. 4.14. Regulatory networks generated in *IPA* in thalamic synaptosomes at 3 and 5 months. **109**
Fig. 4.15. Overlapping protein identifications between thalamic and cortical synaptosome proteomic data in *Ppt1*$^{-/-}$ mice. **110**
Fig. 4.16. Identified protein candidates with a "delayed up-down" profile between thalamus and cortex. **112**
Fig. 4.17. Identified protein candidates with a "delayed down-up" profile between thalamus and cortex. **112**
Fig. 4.18. Valine degradation cascade in the thalamus at 3 and 5 months. **113**
Fig. 4.19. Validation of proteomic data by QWB in mouse and human samples at end stage of the disease. **116**
Fig 5.1. Confocal imaging of NMJ in muscle 12/13 of WT *Drosophila* larvae fillet preparation stained with pre-synaptic (HRP) and post-synaptic markers (DLG). **130**
Fig. 5.2. Generation of *GMR-GAL4* and *UAS-CLN3* recombinant *Drosophila* line. **133**
Fig. 5.3. Genetic modifier screen mating scheme. **134**
Fig. 5.4. Fasudil therapeutic window concentration is between 1.4 and 5 mM. **136**
Fig. 5.5. CLN3-induced neurodegeneration in the eye is dose-dependent. **139**
Fig. 5.6. Overexpression of CLN3 driven to the motor-neuron causes a dose-dependent disruption of the NMJ architecture in the third instar *Drosophila* larvae and a decreased viability of adult flies. **141**
Fig. 5.7. Overexpression of CLN3 driven pan-neuronally causes a disruption of the NMJ architecture in the third instar Drosophila larvae and a dose-dependent decrease in viability of adult flies. **143**
Fig. 5.8. Overexpression of CLN3 driven post-synaptically caused disruption of the NMJ architecture in the third instar Drosophila larvae and a dose-dependent decrease in the viability of adult flies. **144**
Fig. 5.9. Knocking down CLN3 in the nervous system causes bouton loss in the NMJ of the third instar *Drosophila* larvae. **147**
Fig. 5.10. Quality control of the CLN3 recombinant fly as a tester line. **149**
Fig. 5.11. CLN3-induced degeneration is enhanced by the genetic downregulation of HIBCH and HADHA *in-vivo*. **151**
Fig. 5.12. CLN3-induced degeneration is suppressed by the downregulation of ROCK2 genetically and pharmacologically. **154**
Fig. 5.13. Fasudil inhibition of ROCK2 and other kinases might contribute in the suppression of CLN3 induced degeneration. **155**

Fig. 5.14. Downregulation of candidates does not give any phenotype in the eye of a WT fly. **157**
Fig. 5.15. Candidates identified in *Ppt1*$^{-/-}$ time-course dataset modulate eye morphology in CLN3-OE dependent manner. **159**
Fig. 5.16. Predicted upstream regulators modulate neurodegeneration in CLN3-OE and WT background. **161**
Fig. 5.17. Summary of candidate genetic screening in CLN3-induced degeneration in the eye. **166**
Fig. 5.18. Converging networks between candidates able to modulate neuronal stability in CLN3-induced neurodegeneration. **167**
Fig. 6.1. iTRAQ proteomics identified perturbations in muscle proteome from *Cln3*$^{-/-}$ mice compared to controls at 13 months. **178**
Fig. 6.2. *IPA* analysis reveals alterations in mitochondria-related pathways. **180**
Fig. 6.3. *Cln3*$^{-/-}$ mice muscle proteomics predicts perturbations in ubiquitin homeostasis confirmed by QWB in post mortem cortical extracts from INCL and JNCL patients. **183**
Fig. 6.4. Label-free proteomics reveals perturbations in muscle proteome throughout the time-course of disease progression in *Ppt1*$^{-/-}$ mice. **186**
Fig. 6.5. BioLayout clustering by protein expression trend allows the identification of 40 individual biomarker candidates whose expression correlates to disease progression in *Ppt1*$^{-/-}$ vs. WT. **187**
Fig. 6.6. Eight identified biomarker candidates from the *Ppt1*$^{-/-}$ analyses have a conserved change in the *Cln3*$^{-/-}$ mice at equivalent disease stage. **190**
Fig. 6.7. Calreticulin and Ndufs3 represent putative biomarkers of disease progression detectable in muscle and blood in *Ppt1*$^{-/-}$ mice. **191**
Fig. 6.8. Calreticulin and expression levels in SMA mice skin biopsies and NCL mice muscle extractions. **192**
Fig. 6.9. Ndufs3 changes detected in muscle and blood from mice models are relevant to infantile and juvenile NCL in humans. **193**

List of tables

Table 1.1. Genetic classification of NCL [adapted from (Nita et al., 2016)]. **15**
Table 2.1. Post mortem NCL and control patient sample details. **44**
Table 2.2. Primary antibodies. **45**
Table 2.3. Secondary antibodies. **46**
Table 3.1. *DAVID* analysis of proteomic data confirms synaptic protein enrichment. **67**
Table 4.1. *DAVID* enrichment analysis of unfiltered thalamic proteome. **93**
Table 4.2. Top canonical pathways identified in candidates with "delayed profile" between thalamic and cortical synaptosomes. **113**
Table 4.3. Conserved proteins in *Ppt1*$^{-/-}$ and *Cln3*$^{-/-}$ at equivalent disease stage. **115**
Table 5.1. *Drosophila* general stocks. **125**
Table 5.2a *Drosophila* candidate stocks. **126**
Table 5.2b *Drosophila* candidate stocks. **127**
Table 5.3. Summary of phenotypes observed in CLN3 OE driven in the synapse. **145**
Table 5.4. Summary of genetic modifier screen results. **163**
Table 6.1. Top Diseases and Disorders identified using *IPA* in *Cln3*$^{-/-}$ muscle extracts. **181**
Table 6.2. Proteins identified by label-free proteomics showing a steady up/downregulated profile throughout the time-course of disease progression in *Ppt1*$^{-/-}$/WT. **188**
Table A1. BioLayout analysis of cortical, hippocampal and thalamic samples in *Cln3*$^{-/-}$: Cluster 3 (Chapter 3). **229**
Table A2. BioLayout analysis of cortical, hippocampal and thalamic samples in *Cln3*$^{-/-}$: Cluster 4 (Chapter3). **231**
Table A3. BioLayout analysis of cortical, hippocampal and thalamic samples in *Cln3*$^{-/-}$: Cluster 6 (Chapter 3). **233**
Table A4. BioLayout analysis of cortical, hippocampal and thalamic samples in *Cln3*$^{-/-}$: Cluster 7 (Chapter 3). **234**
Table A5. *Cln3*$^{-/-}$ thalamic filtered proteins upregulated more than 20% (Chapter 3). **236**
Table A6. *Cln3*$^{-/-}$ thalamic filtered proteins downregulated more than 20% (Chapter 3). **241**
Table A7. Proteins identified by ≥ 2 peptide in *Ppt1*$^{-/-}$ thalamic synaptosomes (Chapter 4). **248**
Table A8. Proteins identified by ≥ 2 peptide in *Ppt1*$^{-/-}$ cortical synaptosomes (Chapter 4). **254**
Table A9 Proteins identified by ≥ 2 peptides and with a change >20% in *Cln3*$^{-/-}$ muscle (Chapter 6). **270**

List of abbreviations

-/-	Deficient
+/+	Control
AD	Alzheimer disease
AFU	Arbitrary fluorescent units
ALS	Amyotrophic lateral sclerosis
AMPA	α-amino-3-hydroxy-5-methyl-4-isoxazolepropionic acid
ANOVA	Analysis of variance
Anxa5	Annexin A5
APP	Amyloid precursor protein
Asah1	N-acylsphingosine amidohydrolase 1
ATP	Adenosine triphosphate
Atp1a2	ATPase Na+/K+ transporting subunit alpha 2
Atp5b	ATP synthase, H+ transporting, mitochondrial F1 complex, beta polypeptide
BCA	Bicinchoninic acid (assay)
BDSRC	Bloomington *Drosophila* stock center
BMP	Bis(monoacylglycerol)phosphate
Calr	Calreticulin
CathD	Cathepsin D
CFL1	Cofilin 1
CHCA	α-cyano-4-hydroxycinnamic acid
CLNx	Ceroid lipofuscinosis, neuronal x
CNS	Central nervous system
CS	Canton S
CS	Citrate synthase
CSF	Cerebrospinal Fluid
CSP-α	Cysteine-string protein α
Cy3	Indocarbocyanine
DAB	3, 3' diaminobenzidine tetrahydrochloride
DAVID	Database for Annotation, Visualization and Integrated Discovery
Dbn1	Drebrin 1
DIOPT	*DRSC* Integrative Ortholog Prediction Tool
DLG	Disks large homolog
DPI	Days post injury
Dpysl3	Dihydropyrimidinase-like 3
Dpysl4	Dihydropyrimidinase-like 4
DRSC	*Drosophila* RNAi screening centre
DTT	Dithiothreitol
EDTA	Ethylenediaminetetraacetic acid
Elav	Embryonic lethal abnormal vision
ER	Endoplasmatic reticulum
Esrra	Steroid hormone receptor ERR1
Ey	*Eyeless*
FASP	Filter Aided Sample Prep
FDR	False discovery rate

FTMS	Fourier Transform Mass Spectrometry
GABA	γ-aminobutyric acid
GAD65	Glutamic Acid Decarboxylase 65
GFP	Green fluorescent protein
GMR	Glass mutimer reporter
Gnb4	G protein subunit beta 4
GO	Gene ontology
GROD	Granular osmiophilic deposits
H2Ax	Histone H2AX
Hadha	Hydroxyacyl-CoA dehydrogenase/3-ketoacyl-CoA thiolase/enoyl-CoA hydratase (trifunctional protein), alpha subunit
Hba-a2	Hemoglobin, alpha 1
HD	Huntington disease
Hepacam	Hepatic and glial cell adhesion molecule
HET	Hetrerozygous
Hibadh	3-hydroxyisobutyrate dehydrogenase
Hibch	3-hydroxyisobutyryl-CoA hydrolase, mitochondrial
Hnf4a	Hepatocyte nuclear factor 4-alpha
HRP	Horseradish peroxidase
HSP	Heat shock protein
Igf1r	Insulin-like growth factor 1 receptor
IHC	Immunohistochemistry
INCL	Infantile Neuronal Ceroid Lipofuscinosis
InsR	Insulin receptor
IPA	Ingenuity Pathway Analysis
ITMS	Ion trap mass spectrometry
iTRAQ	Isobaric Tag for Relative and Absolute Quantitation
JNCL	Juvenile Neuronal Ceroid Lipofuscinosis
KD	Knock down
kDa	Kilodalton
KO	Knock out
L	Lobbe
LC	Liquid chromatography
LGNd	Dorsal lateral geniculate nucleus
LINCL	Late Infantile Neuronal Ceroid Lipofuscinosis
LSD	Lysosomal storage disorder
LTD	Long term depression
LTP	Long term potentiation
Map4k4	Mitogen-activated protein kinase 4
Mgea5	Mgea5 protein
Mitf	Microphthalmia-associated transcription factor
mM	Mili molar
MMTS	methylthio
MND	Motor neuron disease
MRI	Magnetic resonance imaging
MS	Mass spectrometry
NCL	Neuronal Ceroid Lipofuscinosis
NDUFS3	NADH dehydrogenase [ubiquinone] iron-sulfur protein 3, mitochondrial

Nfkb1	Nuclear factor NF-kappa-B p105 subunit
NGS	Normal goat serum
NIH	National institure of health
NMDA	N-methyl-D-aspartate
NMJ	Neuromuscular junction
Notch1	Neurogenic locus notch homolog protein 1
NSF	N-ethylmaleimide sensitive fusion
OE	Overexpression
Ogdhl	Oxoglutarate dehydrogenase-like
OMIM	On-line Mendelian Inheritance in Man
ORF	Open reading frame
OXFOS	Oxidative Phosphorylation
P	Pellet
P4HB	Protein disulfide-isomerase
PAGE	Polyacrylamide gel electrophoresis
PANTHER	Protein Analysis through evolutionary relationships
PBS	Phosphate buffered saline
PBT	Phosphate buffered saline + Triton X-100
PCA	Principal component analysis
PD	Parkinson disease
Pdx1	Pancreas/duodenum homeobox protein 1
PFA	Paraformaldehyde
PNS	Peripheral nervous system
PolyLC	Polysulfoethyl A column
Pparg	Peroxisome proliferator-activated receptor gamma
ppm	Parts per million
PPT1	Palmitoyl protein thioesterase 1
PSD-95	Post-synaptic density 95
Pten	Phosphatidylinositol 3,4,5-trisphosphate 3-phosphatase and dual-specificity protein phosphatase
PVDF	Polyvinylidene fluoride
QWB	Quantitative fluorescent western blotting
Rictor	Rapamycin-insensitive companion of mTOR
RIPA	Radio immunoprecipitation assay
RNA	Ribonucleic acid
RNAi	Ribonucleic acid interference
Rock2	Rho-associated, coiled-coil containing protein kinase 2
ROS	Reactive Oxygen Species
RT	Room temperature
S	Supernatant
S100A1	S100 calcium binding protein A1
S1BF	Primary somatosensory cortex
SCA	Spinocerebellar ataxia
SCX	Strong cation-exchange chromatography
Sdha	Succinate dehydrogenase complex flavoprotein subunit A
SDS	Sodium dodecyl sulfate
SEM	Standard error of the mean
Slc25a12	Solute carrier family 25 member 12

SMA	Spinal muscular atrophy
SNAP25	Synaptosomal-associated protein 25
SNARE	Soluble NSF attachment protein receptor
SNCA	α-synuclein
SOD	Superoxide dismutase
SPTBN2	Spectrin beta
SV2	Synaptic vesicle protein 2
SYN1	Synapsin 1
Syp	Synaptophysin
TBS	Tris buffered saline
TCA	Tricarboxylic acid cycle
TDP-43	TAR DNA-binding protein of 43 kDa
TEAB	Triethyl ammonium bicarbonate
TFA	Trifluoroacetic acid
Tkt	Transketolase
TRiP	Transgenic RNAi project
UAS	Upstream activator sequence
Ub	Ubiquitin
Uba1	Ubiquitin-like modifier-activating enzyme 1
UchL1	Ubiquitin carboxyl-terminal hydrolase isozyme L1
um	Micrometer
UPS	Ubiquitin Proteosome System
V1	Primary visual cortex
VAMP2	Vesicle-associated membrane protein 2
VDRC	Vienna Drosophila Resource Center
VPM/VPL	Ventral posterior medial/ventral posterior lateral thalamic nucleus
Wld^s	Wallerian degeneration slow
WT	Wild-type

Chapter 1

General introduction

1.1 Socioeconomic impact of neurodegenerative diseases

Neurodegenerative diseases are incapacitating conditions which are characterised by a progressive death of neurons. Since they are incurable, they place an enormous social, emotional and financial burden on affected individuals, care providers, health services and society at large. In the UK alone, there are around 850,000 people suffering from Alzheimer's disease (AD) and other dementias, which represents over 60-70% of the total cases of neurodegenerative diseases (https://www.mrc.ac.uk). Other more prevalent neurodegenerative diseases include: Parkinson's (Meek *et al.*, 1998), Amyotrophic lateral sclerosis, and multiple sclerosis (Gustavsson *et al.*, 2011).

In terms of economics, it is estimated that these diseases cost the UK economy £26 billion per year (https://www.mrc.ac.uk). Scaling that to a larger economy, it is predicted that the U.S spends around $259 billion in the management of Alzheimer's disease alone (http://www.alz.org/facts/overview.asp). Since, many neurodegenerative conditions are linked to aging, these numbers are expected to rise due to the increase in average human lifespan.

Despite large efforts of the research community, effective treatments for neurodegenerative conditions are still lacking. Therefore, there is an urgent requirement to understand the mechanisms underlying these conditions in order to elucidate molecular drug targets for the development of therapies that may halt or delay the progression of such diseases.

1.2 Compartmentalised pathology in neurodegenerative diseases

In order to understand the mechanisms regulating neurodegenerative processes, we need to consider the complexity of the nervous system, and neurons in particular. The high specialisation of intracellular communication of nerve cells translates into distinct morphological and biochemical properties which distinguishes neurons from other cell types. Broadly speaking, as represented in Fig. 1.1, (central) neurons can be divided into three main compartments: cell soma, axon and synapse. The **cell soma**, which contains the nucleus of the cell is characterized by its branching and arborisation of dendrites. Dendrites are the primary target for synaptic input coming from other neurons. They contain high numbers of ribosomes and have very organized cytoskeletal structures to receive and integrate information from other neurons. The **axon** is a unique extension from the cell body whose main function is signal conduction of the action potential to the synapse. Depending on the type of neuron and its location, axons can travel from a few micrometres to many centimetres in humans. It also contains an important cytoskeletal architecture which is key for axonal function. The **synapse** is made by contacts between the presynaptic cell, dendrites and the following neuron (post-synaptic side). It is responsible for the transmission of the action potential between neurons. Its main feature is the complex secretory apparatus by which synaptic transmission takes place in most of the neurons (Purves *et al.*, 2004).

It is therefore not surprising that the growing body of experimental evidence suggests that each of the neuronal compartments described above react differently to neurodegenerative stimuli (Gillingwater *et al.*, 2001, Coleman, 2005, Wishart *et al.*, 2012). Studies in "Wallerian degeneration slow" mice (*Wld^s*), a model of neuroprotection, showed that each one of these neuronal subcompartments is able to degenerate independently from the others (Gillingwater *et al.*, 2002, Gillingwater *et al.*, 2006, Parson *et al.*, 2004). The differential characteristics of neuronal cell death by apoptotic pathways and the "cytoplasmatic apoptosis" of axons suggests that different pathophysiological mechanisms may be orchestrating these processes (Gillingwater *et al.*, 2001). Among these three compartments, synapses have been reported to be especially vulnerable to a variety of neurodegenerative stimuli, preceding cell body alterations (Wishart *et al.*, 2006, Wishart *et al.*, 2012). Therefore, it is likely that distinct molecular mechanisms residing in the synapse confer this exceptional vulnerability. Gillingwater & Ribchester observed that in the *Wld^s* mice, where axonal

degeneration is delayed after axotomisation of the nerve, a novel form of synaptic-specific degeneration was unravelled (Gillingwater *et al.*, 2006, Parson *et al.*, 2004). They then proposed the term "synaptosis" to describe these specific mechanisms of synaptic degeneration (Gillingwater *et al.*, 2001).

For a few years, our group has been interested in the elucidation of these mechanisms underlying synaptic vulnerability. Importantly, Wishart *et al.* have recently showed that by targeting molecular changes happening in synapse, a beneficial effect can be seen beyond the synapse to the nervous system as a whole (Wishart *et al.*, 2014, Powis *et al.*, 2016). This has provided a proof of concept that through investigating differentially vulnerable synaptic compartments we can obtain a broad understanding of the whole process of neurodegeneration.

For this reason, the main focus of this thesis will be on investigating the molecular mechanisms regulating the exceptional vulnerability of synapses as it may be a source of drug targets for a wide range of neurodegenerative diseases.

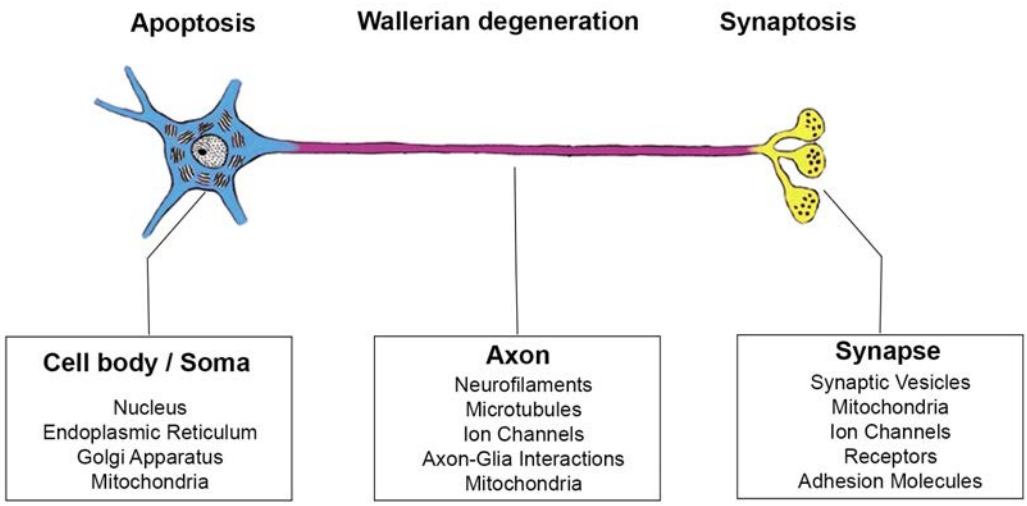

Fig. 1.1 Neuron schematic representation. A depiction of the three main functional and structural compartments of neurons: cell body/soma (in blue), where apoptosis is the main mechanisms of cell death. Axon (in pink), a specific "cytoplasmic apoptosis" (Wallerian degeneration) takes place. The synapse (in yellow) where a proposed mechanisms of specific degeneration in named "Synaptosis". Figure adapted from Fig. 4 in (Gillingwater *et al.*, 2001).

1.3 The synapse

As briefly described before, synapses are the connections between a pre-synaptic neuron and a post-synaptic cell, which is often another neuron. Synaptic junctions are responsible for transmitting action potential-encoded information from the presynaptic to the postsynaptic side (Sudhof, 2012). They can be divided into electrical and chemical, with the latter being the most abundant. In chemical synapses, there is a gap between pre- and post-synaptic cell (synaptic clefts) and the action potential is transmitted through neurotransmitters which are packed into synaptic vesicles. Synaptic vesicle exocytosis is triggered by the influx of Ca^{2+} through voltage-gated calcium channels, occurring when an action potential is reached. Vesicle exocytosis is restricted to a small area of the plasma membrane with electro-dense material, called an "active zone" (Couteaux *et al.*, 1970). Released chemical neurotransmitters then activate the post-synaptic receptors. After exocytosis, synaptic vesicles can be recycled through endocytosis and neurotransmitter refilling mechanisms (Sudhof, 2004).

It has been shown that synaptic terminals are not just secretory machines, but computational units where the relationship between action potential and neurotransmitter release changes continuously depending on intracellular messengers, extracellular modulators or repeated use of the synapse (Sudhof, 2004). The mammalian brain contains multiple types of synapse with particular sets of computational properties. These properties are defined by the differential neurotransmitter and/or post-synaptic receptor composition (Koester *et al.*, 2005).

Synaptic plasticity is believed to underlie the process of learning new skills, storing memories or responding to injury. Such plasticity is determined by changes in synaptic strength which depends on the patterns of synaptic activity. The long-lasting increase in synaptic strength is known as long-term potentiation (LTP), whereas long-lasting decrease is named long-term depression (LTD) (Citri *et al.*, 2007). A correct homeostasis of the synaptic compartments is therefore essential, for the maintenance of neuronal function. As stated before, defects in synaptic stability can trigger a series of events which will compromise the whole nervous system leading to neurodegenerative processes (Powis *et al.*, 2016, Wishart *et al.*, 2014, Wishart *et al.*, 2006, Wishart *et al.*, 2012). This concept will be further developed in following sections.

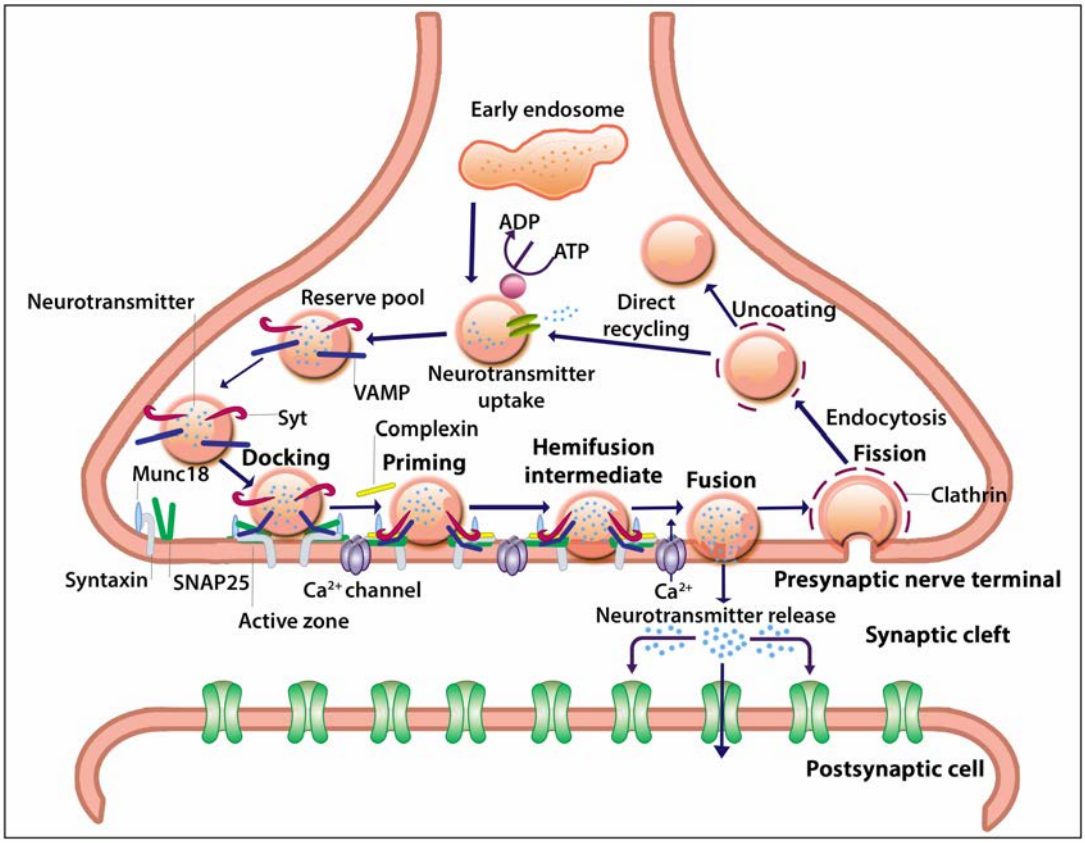

Fig. 1.2 Schematic representation of a chemical synapse and the synaptic vesicle cycle. Synaptic transmission occurs following a series of events. As indicated by the figure, the synaptic vesicle cycle is tightly regulated by multiple proteins some of which are represented here. The process is initiated when an action potential arrives to the pre-synaptic neuron. This changes the membrane potential and triggers the influx of calcium. As a consequence, synaptic vesicles containing a reserve pool of neurotransmitter bind to specialized sites of the membrane called active site (docking) and fuse in response to calcium influx (priming) releasing the contained neurotransmitters to the synaptic cleft. Next, neurotransmitters diffuse and bind to specific receptors of the post-synaptic cell. This causes the channels of the post-synaptic neuron to open/close, changing the flow of ions to go in and out of the post-synaptic neuron. This flow increase/decrease the probability of the neuron firing an action potential. The lumen of the synaptic vesicle exposed during neurotransmitter release is later internalized by endocytosis. After internalization the synaptic vesicle is refilled with neurotransmitter and a new cycle begins. Following these steps, information between neurons is transmitted. Syt=synaptotagmin. (Figure inspired by (Rossetto *et al.*, 2014), Box 2).

1.4 The synapse as an early pathological target in neurodegenerative disease

Traditionally, the most studied pathophysiological hallmarks of many neurodegenerative diseases were the aberrant protein accumulations preceding generalised neuronal loss, usually located in the cell soma (Soto, 2003, Moreno-Gonzalez I, 2011). These abnormal misfolded proteins were often detected in *post mortem* tissue of patients suffering from conditions such as Alzheimer's (Beta-amyloid and Tau) (Glenner, 1984, Grundke-Iqbal *et al.*, 1986), Parkinson's (α-synuclein) (Forno, 1996, Spillantini, 1997) and Huntington's (huntingtin) (DiFiglia *et al.*, 1997, Davies *et al.*, 1997). For this reason, researchers have focused their strategies on stopping cell death targeting such mechanisms primarily located in somatic compartments (Wishart *et al.*, 2006).

Nevertheless, as indicated in section 1.2 above, more recent reports have highlighted the importance of early events happening at distal neuronal compartments such as axons and synapses, often preceding the appearance of characteristic pathophysiological disease hallmarks in the soma and eventual neuronal loss (Coleman, 2005, Gillingwater *et al.*, 2001, Wishart *et al.*, 2006). In fact, synapses have been described as an early pathological target in a wide range of conditions including diseases associated with ageing and infantile onset diseases, some of which are briefly described below.

It is now known that synaptic loss is a major contributor of disease progression and that subtle synaptic dysfunction can be detected at pre-symptomatic stages in Alzheimer's disease (Selkoe, 2002, Coleman *et al.*, 2004). Moreover, synaptic loss is one of the more consistent pathological correlates of cognitive decline in Alzheimer's disease and other dementias (Terry *et al.*, 1991, Davies *et al.*, 1976, DeKosky *et al.*, 1990). Importantly, such cognitive alterations can be detected up to 10 years before the detection of clinical manifestations (Kawas *et al.*, 2003, Elias *et al.*, 2000), highlighting the importance of synaptic abnormalities early on during disease progression. As previously mentioned, synaptic disruption has also been detected in other dementias and may be also relevant to "normal healthy" aging-associated cognitive decline (Brown *et al.*, 1998, Zhou *et al.*, 1998, Lipton *et al.*, 2001, Uylings *et al.*, 2002).

For example, Parkinson's Disease (PD) (Meek *et al.*, 1998) targets specifically dopaminergic

neurons triggering high rates of degeneration in nigro-striatal brain areas. Synaptic alterations have also been described in striatum in early phases of experimental PD contributing to the clinical progression of the disease (Picconi *et al.*, 2012). Also, in Huntington's disease (HD) synaptic pathology correlates with the clinical manifestations of the disease in patients including the impairment of psychiatric, motor and cognitive functions (Li *et al.*, 2003). Dendritic spine loss was shown to precede neuronal loss in animal models as well as synaptic transmission defects in the peripheral and central nervous system (CNS) (Guidetti *et al.*, 2001, Kraemer *et al.*, 2010, Klapstein *et al.*, 2001).

Synapses in the peripheral nervous system (PNS) are also an early pathological target in some neurodegenerative conditions. This is the case in motor neurone diseases (MND). In Amyotrophic lateral sclerosis, synaptic loss occurs at the neuromuscular junctions (NMJ), lower motor neurons in the spinal cord ventral horn, as well as in cortical areas in both patients and animal models of ALS (Sasaki *et al.*, 1999, Sasaki *et al.*, 1994, Zang *et al.*, 2005, Maselli *et al.*, 1993). Similarly, in spinal muscular atrophy (SMA), a monogenetic and devastating infantile onset MND, evidence shows early functional and structural disruption of synaptic connectivity at the NMJ and in the spinal cord (Murray *et al.*, 2008, Kariya *et al.*, 2008, Ling *et al.*, 2010, Mentis *et al.*, 2011, Imlach *et al.*, 2012), as well as molecular pathological changes in hippocampal synapses (Wishart *et al.*, 2014).

Early synaptic loss is also a key event in another mono-genetic, neurodegenerative disease group: the neuronal ceroid lipofuscinoses (NCL or Batten disease) (Kielar *et al.*, 2009, Partanen *et al.*, 2008). The NCLs are a group of neurodegenerative diseases and form of dementia characterized by intellectual and neurological deterioration (Goebel, 1995). The main differences between each NCL form is the age of onset which can be infantile, juvenile and adult onset. Like many of the neurodegenerative diseases described here, no effective treatment is currently available which leads to premature death in patients suffering this devastating disease (Cooper, 2003, Cooper, 2010).

Since early synaptic loss seems to be a common event across multiple conditions regardless the initiating insult (whether genetic, infectious or injurious), it is highly likely that alterations in synaptic stability play an important role in the onset of neurodegeneration in multiple conditions. It has been suggested that these distinct, neurodegenerative stimuli may converge on a critical pathway which ultimately leads to synaptic degeneration (Wishart *et*

al., 2006).

Elucidating the molecular regulators of synaptic stability could therefore provide further understanding of potentially conserved mechanisms underlying a wide range of diseases and yeild a valuable source of drug targets for the development of therapeutic intervention.

1.5 Mechanisms of synaptic vulnerability

It is evident now that synapses play an important role on the onset of neurodegeneration in multiple conditions as indicated above. Yet, the molecular mechanisms underlying this exceptional vulnerability remains in its infancy. Nevertheless, the increasing development of animal models and the improvement of the sensitivity of experimental techniques, have provided some clues into the potential pathological pathways and/or regional subcellular organelles contributing to synaptic stability.

1.5.1 "Synaptosis"

As explained in section 1.2 and Fig. 1.1, "synaptosis" is the term proposed to name the specific molecular cascades underlying synaptic degeneration (Gillingwater *et al.*, 2001). Evidence indicates that apoptotic pathways can be initiated locally at the synapse after addition of proapoptotic components such as staurosporine, etoposide, and amyloid A peptide (Mattson *et al.*, 1998, Gilman *et al.*, 2003, Gylys *et al.*, 2004). However, the apoptotic pathways localised in the synapse may have a different nature from those in somatic compartments, since the global deletion of the apoptotic factor Bax, was able to rescue neuronal soma but not synapses (Chiesa *et al.*, 2005). Moreover, the endogenous biochemical transduction signalling residing in the synapse can stop the activation of apoptotic cascades. For instance, by means of neurotrophic factors exhibiting synaptoprotective effects via activation of anti-apoptotic cascades (Mattson, 2000).

1.5.2 Mitochondrial homeostasis

Mitochondria are the power-houses of cells generating [adenosine-triphosphate (ATP) production] through coupled, electron-transport chain and oxidative phosphorylation. Mitochondria also display key functions including (but not limited to), apoptosis, heme and steroid synthesis, thermogenesis and Ca^{2+} buffering (Scheibye-Knudsen *et al.*, 2015). Mitochondria are dynamic organelles constantly undergoing fission and fusion, and

exhibiting complex motility patterns (Sheng, 2014). They get produced in the cell body and are continuously trafficked through the axon to the distal synaptic compartments. Defects in the machinery regulating the complex antero/retrograde transport is thought to contribute to the pathogenesis of a number of neurodegenerative diseases (Chan, 2006, Itoh *et al.*, 2013).

Importantly, mitochondria can switch from being stationary to motile in response to synaptic function or metabolic changes (Sheng, 2014). It is believed that a population of mitochondria accumulate in the synapse displaying unique properties due to environmental adaptation (Gillingwater *et al.*, 2013, Ly *et al.*, 2006, Bertoni-Freddari *et al.*, 1993). These differential properties between non-synaptic and synaptic mitochondria includes different Ca^{2+} buffering capabilities which are essential for neurotransmission (Brown *et al.*, 2006), enzymatic activities (Lai *et al.*, 1977) and very different proteome composition (Graham *et al.*, 2017).

Mitochondrial deficiencies affect all of these functions and will therefore impact synaptic function and stability (DiMauro *et al.*, 2008). Furthermore, some authors suggested that these stationary mitochondria in synapses are older on average that those found in somatic compartments (Bertoni-Freddari *et al.*, 1993, Brown *et al.*, 2006) and consequently, this pool of "aged" mitochondria may be vulnerable to pathogenic insults (Bertoni-Freddari *et al.*, 1993). In fact, mitochondria have been implicated in the pathogenesis of many diseases where synapses are an early pathological target including Alzheimer's (Lee *et al.*, 2012), Parkinson's (Ferrer *et al.*, 2012), Huntington's (Reddy *et al.*, 2012) and the NCLs (Luiro *et al.*, 2006).

Altogether, it seems evident that mitochondria play an important role in synaptic stability as defects in its transport and/or function may contribute to the pathogenesis of multiple neurodegenerative diseases. Therefore, mitochondrial proteins represent attractive targets as potential modulators of synaptic stability.

1.5.3 Metabolic pathways

Accumulating evidence show a strong correlation between metabolism and neurodegeneration. The brain accounts for 20% of an individual's energy expenditure at rest and 70-80% is spent by neurons (Harris *et al.*, 2012).

This is not surprising taking into account the strong energetic requirements of brain cells needed to perform their complex cognitive functions. To maintain this constant biochemical milieu, membrane transporters, enzymatic pathways and regulatory networks work in a coordinated manner to maintain thermodynamic equilibrium and to avoid potentially toxic elevations of metabolite levels (Yudkoff, 2017).

Most brain energy is used on synaptic transmission, therefore an adequate supply of ATP must be provided to assure an optimal, synaptic function (Harris *et al.*, 2012). In addition to the production of ATP, glucose is also used for the generation of the metabolic intermediates required for the synthesis of fatty acids and other lipids needed for membrane and myelin synthesis (Jones *et al.*, 1975, Ramsey *et al.*, 1972). Importantly, neurons also require a correct balance of amino acids to ensure protein synthesis and neurotransmitter production (Vrba *et al.*, 1962). As well as this, it has recently been found that branched-chain amino acids play an important role in the synthesis of glutamate. The replacement of neuronal glutamate is essential to ensure correct neurotransmission in excitatory synapses (Yudkoff, 2017), and any defects in its metabolism may impair synaptic function.

Moreover, a growing number of reports are indicating that mid-life obesity is a risk factor for later-life development of dementia, Parkinson's (Abbott *et al.*, 2002), Alzheimer's disease and vascular dementia (Hassing *et al.*, 2009, Kivipelto *et al.*, 2005, Xu *et al.*, 2011). Evidence shows that decrease in glucose and oxygen metabolic rates of brain cells occur during normal aging (Hoyer, 1982b) and are more disrupted in diseases such as AD, ALS, PD and HD (Hoyer, 1982a). Furthermore, studies showed that ALS patients are hypercatabolic and have increased energy expenditure at rest. Additionally, glucose intolerance, insulin resistance and hyperlipidemia have all been identified in ALS patients (Camandola *et al.*, 2017).

Overall, it seems evident that bioenergetic pathways play an essential role in brain cells and especially in synaptic stability. Defects in any of these pathways may contribute to regulating synaptic vulnerability and for promoting pathogenesis in multiple, neurodegenerative diseases. Therefore, proteins regulating metabolic processes can also be considered as potential regulators of synaptic stability.

1.5.4 Protein homeostasis

A growing number of reports indicate the high sensitivity of synapses to proteostasis imbalance. Recent studies highlighted that different proteolytic pathways participate in the synaptic homeostatic maintenance including: autophagy, molecular chaperones, lysosomal degradation or the ubiquitin proteasome system (Rubin *et al.*, 2000, Wang *et al.*, 2017).

As indicated in the sections above, the synaptic terminals are relatively small, but are packed with an extremely dense combination of dynamic organelles and molecular machinery needed for synaptic function. The synaptic proteome requires highly coordinated regulation in order to fulfil its bioenergetic demands and/or vesicle/neurotransmitter release. This demanding activity has been associated with a high susceptibility to molecular damage (Ellis, 2001). The polarized nature of neurons has provided the synapse with mechanisms to develop its own local protein quality control pathways to regulate protein balance. Deregulation in these pathways has been associated with the pathogenesis of multiple neurodegenerative diseases (Neefjes *et al.*, 2014, Bayer, 2015).

Protein-protein interactions are essential for the correct functioning of molecular networks. Chaperones are a protein family whose core function is to assist the folding/unfolding and assembly/disassembly of macromolecular structures. They prevent or reverse incorrect interactions that may occur between macromolecular surfaces and the intracellular environment as a consequence of conformational changes. Therefore, chaperones assure that other protein complexes do not fail in carrying out an specific biological function (Ellis, 2006).

An example would be CSPα. This is a synaptic chaperone that forms a complex with heat shock cognate 70 – a small glutamine-rich tetratricopeptide repeat-containing protein (CSP-Hsc70-SGT). This complex's function is to maintain the correct functioning of the synaptic vesicle and exocytic machinery by refolding the SNARE complex into its competent state (Sharma *et al.*, 2011). CSPα deficiency results in presynaptic degeneration at both peripheral and central nervous system synapses (Fernández-Chacón *et al.*, 2004, Schmitz *et al.*, 2006). Moreover, mutations in *DNAJC5* (encoding CSPα) have been found to be the cause of autosomal-dominant, adult-onset, neuronal ceroid lipofuscinosis (CLN4 disease) (Nosková *et al.*, 2011).

The UPS is one of the major protein degradation pathways and targets misfolded or unwanted proteins to avoid cytotoxic effects (Hershko *et al.*, 1998). Whilst UPS may play an essential role in somatic compartments preventing protein aggregates linked to multiple

neurodegenerative diseases (Zheng *et al.*, 2016), it also plays a role in synapse formation and post-synaptic plasticity mechanisms (Haass *et al.*, 2007, Ehlers, 2003). Moreover, studies by our laboratories have reported that the disregulation of ubiquitination homeostasis promoted SMA and its pharmacological targeting rescued the synaptic phenotype in animal models (Wishart *et al.*, 2014).

The other main proteolytic pathway at the synapse is via lysosomal degradation. Lysosomal substrates include misfolded proteins, protein aggregates and dysfunctional organelles (Wang *et al.*, 2017). Importantly, macroautophagy is known to be required during synaptogenesis and participates in synaptic function (Shen *et al.*, 2015). Collectively, reports seem to indicate that lysosomal degradation is upregulated upon presynaptic activity.
Interestingly, recent findings indicate that lysosomes have more roles beyond their traditional degradation function. A growing body of evidence suggests that lysosomes serve as a Ca^{2+} storage organelle mediating various neuronal functions (Galione, 2015, Galione *et al.*, 2010). It has been recently revealed that lysosomes mediate activity-dependent Ca^{2+} signalling in dendrites where they play an important role in long-term maintenance of structural plasticity (Padamsey *et al.*, 2017).

Furthermore, the essential role of lysosomes in autophagic pathways relates these organelles to several cellular processes which are implicated in multiple neurodegenerative diseases (Settembre *et al.*, 2013). The lysosomal storage disorders (LSDs), are caused by genetic defects in specific lysosomal components that lead to the accumulation of undegraded material in the lysosomal lumen. This is followed by lysosomal dysfunction in several tissues that ultimately leads to neurodegeneration. However, the mechanisms by which the lysosomal storage material translates to neuronal loss is not understood. The NCLs are a group of LSD where synapses have been described to be an early pathological target, highlighting the connection between synaptic stability and lysosomal function in neurodegeneration pathogenesis (Cooper *et al.*, 2015, Wishart *et al.*, 2006). Lyosomal and autophagy dysfunction have also been implicated in the mechanisms underlying other synaptopathies previously mentioned here such as AD, PD and HD (Wong *et al.*, 2010).

Accumulating evidence suggests lysosomal signalling and autophagy are key to maintaining protein homeostasis in neurons. Moreover, lysosomes play significant regulatory roles at the synapse beyond its traditional, degradative function. Taking everything together, it all

indicates that proteins implicated in lysosomal function may be potential regulators of synaptic stability.

1.6 The neuronal ceroid lipofuscinoses as a model of neurodegenerative disease

In order to further investigate the critical pathways regulating synaptic stability and degeneration, animal models able to reproduce the human disease, are needed. The polygenic nature, and/or complex aetiologies (with potential implicated environmental components, not completely understood), of most prevalent neurodegenerative disease hampers the development of "good" animal models. This is the case for the more common/high profile neurodegenerative diseases such as Alzheimer's (Escott-Price *et al.*, 2015) and Parkinson's (La Cognata *et al.*, 2017) diseases as well as many psychiatric disorders (Gandal *et al.*, 2016).

For this reason, in this project, we turned to the neuronal ceroid lipofuscinoses, a group of mono-genetic neurodegenerative disease whose individual prevalences are comparatively low, but whose genetic cause is very well understood. This has facilitated the development of mutant animals which replicate many aspects of the human disease (Mitchison *et al.*, 1999, Pontikis *et al.*, 2004, Cotman *et al.*, 2002, Gupta *et al.*, 2001, Kielar *et al.*, 2007, Partanen *et al.*, 2008). The study of animal models has shed light on the pathogenesis of these diseases and have highlighted that synaptic pathology occurs very early in disease progression before neuronal loss takes place (Partanen *et al.*, 2008, Kielar *et al.*, 2009, Koch *et al.*, 2011, Cooper *et al.*, 2015). Thus, animal models of NCL could serve as a tool to understand the mechanisms underlying neurodegeneration in NCL but also in other conditions where synapses are an early pathological target (Llavero Hurtado *et al.*, 2017).

The NCLs or Batten disease, are the most frequent, autosomal-recessive neurodegenerative disease and form of dementia in childhood (Goebel, 1995). The term "NCL" currently encompasses up to 13 disease subtypes, which are grouped together due the lysosomal accumulation of autofluorescent storage material, distinct ultrastructural properties, broadly similar pathology and clinical features and a severe neurodegenerative phenotype (Cooper,

2003, Cooper, 2010). Incidence in the USA is estimated at 1.6-2.4/100,000 whereas in Scandinavian countries it is 2-7/100,000 (Uvebrant *et al.*, 1997, Mole *et al.*, 2011). As mentioned before, synaptic disruption is a key early event in NCL, accurately predicting the distribution of subsequent neuronal loss (Kielar *et al.*, 2009, Virmani *et al.*, 2005, Partanen *et al.*, 2008, Koch *et al.*, 2011, Cooper, 2010).

Although the NCL genes are ubiquitously expressed throughout the body, the most obviously affected tissues are neurological based. This feature is shared by other monogenetic, neurodegenerative conditions in which the causative mutations ubiquitously affect expressed proteins [e.g. the survival motor neuron (SMN) protein in spinal muscular atrophy (SMA) (Hamilton *et al.*, 2013)]. Yet, the reasons why neurons appear to be particularly vulnerable to defects in such broadly expressed proteins is not understood.

As mentioned above, the knowledge of the underlying genetic cause and/or storage material composition has provided a base for the basic understanding of the pathogenesis and their correlation to the clinical progression of the disease. Also, it has aided the design of gene replacement therapies and the development of animal models (Mole *et al.*, 2005, Cooper *et al.*, 2006, Bond *et al.*, 2013). However, the underpinning pathways and molecular cascades leading to neurodegeneration in NCL, as in many other neurodegenerative diseases, are still unknown.

1.6.1 Genetics

Mutations in the *CLN1/PPT1* and *CLN3* genes were the first ones to be discovered as the cause of infantile (INCL) and juvenile NCL (JNCL), respectively (The International Batten Disease Consortium, 1995, Vesa *et al.*, 1995). Other forms were later added to the list of NCLs: CLN2/TPP1(classical late-infantile NCL -LINCL) (D.E. Sleat, 1997), *CLN5* (Minna Savukoski *et al.*, 2008) and CLN6 (variant LINCL) (Wheeler *et al.*, 2002, Gao *et al.*, 2002), CLN7/MFSD8 (Siintola *et al.*, 2007), CLN8 (Susanna Ranta *et al.*, 1999), CLN10/CTSD (congenital NCL) (Siintola, 2006) and more recently 3 adult forms; CLN4/DNAJC5 (Nosková *et al.*, 2011), CLN11/GRN (K.R. Smith, 2012), CLN13/CTSF (Smith *et al.*, 2013), an infantile; CLN14/KCTD7 (Staropoli *et al.*, 2012) and a juvenile; CLN12/ATP13A2 (Bras *et al.*, 2012). For more information see the review (Kousi *et al.*, 2012) (Table 1.1).

Table 1.1 Genetic classification of NCL [adapted from (Nita et al., 2016)]

Locus Name	Gene symbol	Locus Protein	Protein Name	Phenotypic spectrum
CLN1	*PPT1*	1p34.2	Palmitoyl protein thioesterase 1	I, LI, J, A
CLN2	*TPP1*	11p15.4	Tripeptidyl peptidase 1	LI, J, P
CLN3	*CLN3*	16p11.2	CLN3	J, P
CLN4	*DNAJC5*	20q13.33	DnaJ homolog/CSPα	A (Parry disease) subfamily C member 5
CLN5	*CLN5*	13q22.3	CLN5	LI, J, P, A
CLN6	*CLN6*	15q23	CLN6	LI, P, A (Kufs type A)
CLN7	*MFSD8*	4q28.2	Major facilitator superfamily	LI, J domain-containing protein 8
CLN8	*CLN8*	8p23.3	CLN8	LI, P
CLN10	*CTSD*	11p15.5	Cathepsin D	C, LI, J, A
CLN11	*GRN*	17q21.31	Granulins	A
CLN12	*ATP13A2*	1p36.13	Probable cation-transporting	CLN12 J ATPase 13A2
CLN13	*CTSF*	11q13.2	Cathepsin F	A (Kufs type B)
CLN14	*KCTD7*	7q11.21	BTB/POZ domain-containing	I protein KCTD7

A: adult; C: congenital; I: infantile; J: juvenile; LI: late-infantile; P: protracted.

1.6.2 Differential progressive regional/neuronal vulnerability pathology

As mentioned above, the growing knowledge of the NCL genetic causes have facilitated the generation of animal models which serve as tools for understanding the disease pathogenesis and for investigations into novel therapeutic interventions (Bond *et al.*, 2013, Faller *et al.*, 2015, Shacka, 2012, Cooper *et al.*, 2006, Palmer *et al.*, 2013, Neverman *et al.*, 2015). Despite the limitations of these models, (ie. in mice, the level of degeneration is never as strong as in human, possibly due to the differences in ageing between species), they have provided insights regarding the progressive events occurring throughout the time-course of disease progression.

Although atrophy is widespread throughout the brain in terminal disease (Mitchison *et al.*,

1999, Kuhl *et al.*, 2013), differential vulnerability can be detected across brain regions and their respective resident cell types and associated pathways involved at early stages of the disease (Cooper *et al.*, 2015). This differential degenerative progression follows similar patterns in the vast majority of NCL murine models: during pre-symptomatic stages there is an early selectivity for relay neurons within the thalamic nuclei followed by the corresponding cortical areas (Pontikis *et al.*, 2005, Kielar *et al.*, 2007, Partanen *et al.*, 2008, Mitchison *et al.*, 1999, Kuhl *et al.*, 2013, Pontikis *et al.*, 2004, Kuronen *et al.*, 2012, Morgan *et al.*, 2013), as well as GABAergic hippocampal interneurons and Purkinje neurons (Mitchison *et al.*, 1999, Pontikis *et al.*, 2004). These reports in murine models regarding the vulnerability of the thalamus correlates with MRI studies in human patients showing alterations in thalamic areas at "pre-clinical" stages (Santavuori *et al.*, 2001, Autti *et al.*, 2007, Järvelä *et al.*, 1997). Interestingly, a recent report by Shyng *et al.*, denoted unexpected early and profound neuropathological changes taking place in all parts of the spinal cord of *Ppt1*$^{-/-}$ mice. Crucially, similar pathology was also present in human CLN1 spinal cord autopsy material (Shyng *et al.*, 2017).

Differential regional/neuronal vulnerability is a shared event in a great number of neurodegenerative diseases in which some brain regions seem affected earlier than others, such as in Alzheimer (Wang *et al.*, 2010, Khan *et al.*, 2014, Braak *et al.*, 1995), Parkinson (Surmeier *et al.*, 2017) or Huntington diseases (HD) (Lewandowski *et al.*, 2013, Sieradzan *et al.*, 2001).

Yet, our understanding of the mechanisms governing the differential vulnerability across brain areas/cell types in the NCLs, as well as many other neurodegenerative diseases is not completely understood. For this reason, in this project such differential vulnerability is taken into consideration in the experimental design, the analyses and interpretation of the data.

1.6.3 Mechanisms of neurodegeneration in NCLs

Even though the genetic cause of the distinct forms of NCLs has been well-characterized, little is known about the functions of each gene product [reviewed in (Carcel-Trullols *et al.*, 2015, Kollmann *et al.*, 2013)]. This has hampered the elucidation of the mechanisms underlying neurodegeneration in the NCLs.

Traditionally, researchers tended to focus on the most obvious pathological hallmarks of the NCLs, which is the auto-fluorescence storage material (AFSM) assuming it is toxic to

neurons. However, it is now accepted that there is no relationship between the storage material and the distribution of neuronal loss [reviewed in (Cooper, 2010, Cooper *et al.*, 2006, Palmer *et al.*, 2013)]. Nevertheless, AFSM is still used as biomarker for therapeutic efficacy of novel therapies (Sarkar *et al.*, 2013, Levin *et al.*, 2014), even though in some cases where storage material was cleared, no improvement of brain atrophy was confirmed (Levin *et al.*, 2014).

Since the genetic cause for the NCLs is known, it seems logical to put efforts into the development of enzyme replacement (Chang *et al.*, 2008b, Hu *et al.*, 2012, Lu *et al.*, 2015, Meng *et al.*, 2012) and gene therapies (Griffey *et al.*, 2004, Griffey *et al.*, 2006, Macauley *et al.*, 2012, Passini *et al.*, 2006, Shyng *et al.*, 2017) [reviewed in (Neverman *et al.*, 2015)]. However, it would also be valuable to investigate the downstream consequences of the NCL- deficient proteins that lead to disease. This will allow the development of mechanism-based therapies, especially important for transmembrane protein-deficiency NCLs (Cooper *et al.*, 2015) (Fig. 1.3). On the other hand, increased life-span following enzyme replacement or gene therapies, could lead to patients developing pathology in other organs, which, otherwise, would have been masked by the neuronal-based pathology. In this case, mechanistic-based therapies could act synergistically together with gene/enzyme therapies. It is therefore essential to define the disease mechanisms in order to find drug targets for therapeutic intervention. Animal models are key tools for this purpose. The study of their corresponding phenotypes (either morphologically or molecularly) presents many difficulties when investigating the downstream consequences of the genetic insults of any disease. It is very challenging to tell which phenotypes are a direct consequence of the genetic insult. This is because phenotypes may reflect underlying mechanisms or compensating for cell death, and/or alternatively, be a consequence of a secondary effects of the already ongoing neurodegeneration. These are the key questions required to address in order to envisage effective therapeutic strategies.

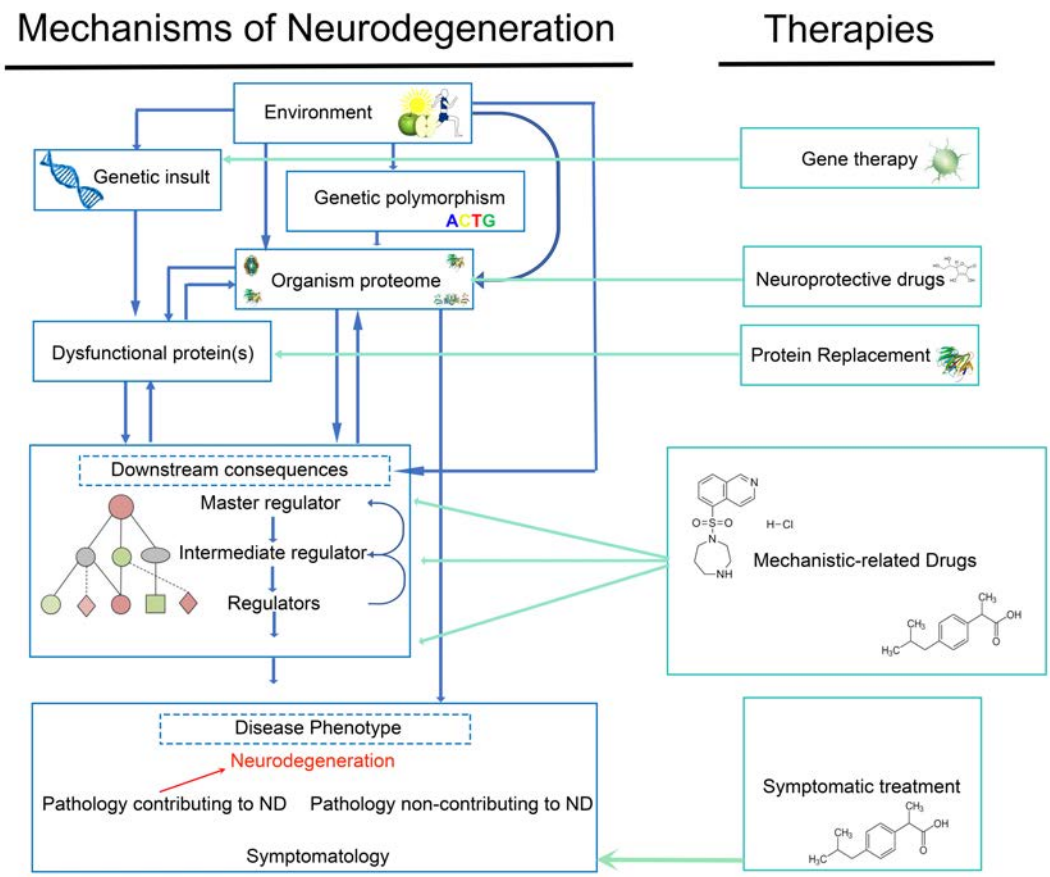

Fig. 1.3. Mechanisms of neurodegeneration and therapies in the NCLs. This schematic represents the cascades of events leading to neurodegeneration in the NCLs and the different therapeutic points where one could intervene. The NCLs are caused by monogenetic mutations. The loss of function of the protein product of that gene, will cause a series of molecular downstream consequences at the protein level. Some of these pathways will lead to neurodegeneration (ND). There will presumably be other molecular perturbations which are not directly related to neuronal cell death (ie. those leading to accumulation of storage material). In this context, the organism's proteome will also influence (and be influenced by) this cascade of events. Amongst all this we identify neuroprotective proteins, and modifiers of the disease which could be potential mechanistic targets for drug development.

The well characterised progressive spatio-temporal neuronal loss patterns of many animal (and particularly mouse) models of NCL offer key tools to address this issue. Differential vulnerability has been defined across brain areas and subcellular compartments (Kielar *et al.*, 2007, Kielar *et al.*, 2009, Partanen *et al.*, 2008, Kuronen *et al.*, 2012, Morgan *et al.*, 2013, Pontikis *et al.*, 2005). These pathological events can then be used to design experiments with the objective to define mechanistic pathways. This information will relate to results in Chapter 3 & 4 where we made use of the differential spatio-temporal vulnerability patterns

for experimental design and data analysis and interpretation.

Currently, there is/are no clear pathway/s relating the loss of function of the NCL-related genes and neuronal loss. However, some potential mechanisms have been proposed to be involved.

1.6.3.1 Synaptic vulnerability in NCL

We use the NCLs as a model of synaptic degeneration because as stated above, early synaptic pathology has been described in various NCLs forms. Thus, synaptic vulnerability has been proposed as one of the potential targetable factors underlying pathogenesis in the NCL (Cooper *et al.*, 2015).

Interestingly, although both *PPT1* and *CLN3* genes are expressed in the lysosome system (encoding a soluble and transmembrane protein respectively) in non-neuronal cells, they have also been shown to localise in the synaptic compartments of neurons (Luiro *et al.*, 2001, Kim *et al.*, 2008b). Somatic endocytosis and trafficking pathways have been shown to be disrupted in fibroblast cultures and mouse models (Luiro *et al.*, 2004, Fossale *et al.*, 2004, Ahtiainen *et al.*, 2006). Synaptic vesicle trafficking uses the same molecular machinery as the intracellular trafficking between ER and Golgi as well as endosome-lysosomal compartments, and therefore is also susceptible to perturbation. (Palmer *et al.*, 2013). Furthermore, synaptic vesicles contain large amounts of palmitoylated proteins which regulate endo/exocytosis machinery and are potential targets of PPT1 (Prescott *et al.*, 2009). Authors have reported a decrease in the synaptic vesicle pool and size in PPT1 disease (Virmani *et al.*, 2005, Kim *et al.*, 2006), suggesting that PPT1 may play a role in the modulation of endocytotic pathways at the synapse. Conversely, in Cathepsin D deficient mice brains, models of congenital NCL, there is an increase in the number of synaptic vesicles (Koch *et al.*, 2011).
Moreover, PPT1 deficiency has been reported to cause difficulties in the recycling of synaptic vesicle components leading to a progressive loss of releasable vesicles and defects in neurotransmission (Kim *et al.*, 2008b, Virmani *et al.*, 2005).

Studies in murine models of NCLs have revealed progressive, early synaptic loss starting in the thalamus and followed later in corresponding cortical areas in *Ppt1*$^{-/-}$, *Cln6*$^{-/-}$ or *CtsD*$^{-/-}$, models of CLN1/INCL, variant LINCL and CLN10/congenital NCL respectively (Partanen *et al.*, 2008, Kielar *et al.*, 2009, Koch *et al.*, 2011). Hippocampal structures seem to also be

affected early, although to a lesser extent than seen in the thalamus (Kuhl *et al.*, 2013). So far, synaptic vulnerability seems to mimic the regional-specific neuronal loss in many NCL forms (Pontikis *et al.*, 2005, Kielar *et al.*, 2007, Partanen *et al.*, 2008, Mitchison *et al.*, 1999, Kuhl *et al.*, 2013, Pontikis *et al.*, 2004, Kuronen *et al.*, 2012, Morgan *et al.*, 2013) (see section 1.3.2), highlighting again that synaptic pathology precedes neuronal loss.

Although, these synaptic phenotypes have not been systematically characterized across all forms of NCL, it is noticeable that synaptic pathology is an important event in multiple forms of NCLs. However, it would be necessary to have further studies to determine if synapses follow exactly the same patterns of vulnerability in all NCL forms.

1.6.3.2 Neuroinflammation

Synaptic changes are not the only early pathological event occurring in the NCLs. It is now evident that neuroinflammation plays a central role in many neurodegenerative diseases, including NCL [Reviewed in (Ransohoff, 2016, Palmer *et al.*, 2013)]. Glial activation has been reported to precede neurodegeneration in both sheep (Tammen *et al.*, 2006, Oswald *et al.*, 2005) and mouse models of NCL (Kielar *et al.*, 2007, Pontikis *et al.*, 2004, Pontikis *et al.*, 2005, Griffey *et al.*, 2006, Macauley *et al.*, 2011, Kuronen *et al.*, 2012). Therefore, glia could be contributing to mechanisms triggering neuronal loss. In fact, in Cln3 mouse models it was detected that there is an early low-level activation of astrocytes and microglia which appear to be attenuated as a result of a failure in the morphological transformation of these cells (Pontikis *et al.*, 2004, Pontikis *et al.*, 2005). Thus, it appears that glia are themselves dysfunctional *per se*, contributing to neuronal loss (Parviainen *et al.*, 2017).

Studies in Cln3 mutant mice have shown that immunosuppressive therapies are able to rescue motor performance (Seehafer *et al.*, 2011). These findings using animal models were translated into clinical trials using mycophenolate mofetil with CLN3 patients. It all indicates an important role in inflammation in the NCL pathogenesis. Nevertheless, inflammatory cascades are very complex and have multiple points of activation. Therefore, it would be necessary to have an in-depth characterisation of the specific steps where the inflammatory cascade is disrupted in the different forms of NCL. This will allow a strategic development of therapeutic interventions.

Whilst neuroinflammation pathways are very important, it all indicates that the dysfunction

in both glia and neurons have a role in the on-going pathological cascade of events contributing to exacerbate disease progression. The fact that both synaptic pathology and neuroinflammation happen at very similar times in the NCL mouse models points at a collaborative contribution to neurodegeneration. Therefore, therapeutic strategies will possibly have to be addressed at both glia and neurons. Cooper and colleagues have developed cell-type based experiments to study the contribution of each of these cell types to the NCL pathogenesis (Cooper *et al.*, 2016). The results from these experiments are starting to shed light into the mechanistic relationships between neurons and glia (Parviainen *et al.*, 2017).

1.6.3.3 Autophagy

As pointed out in section 1.5.4, autophagy is the mechanism by which macromolecules, organelles, toxic protein aggregates and intracellular pathogens get degraded via the lysosomal/vacuolar system of the cell (Mizushima *et al.*, 2008). Autophagy is also one of the three mechanisms by which cell death may take place (Yuan *et al.*, 2003). Abnormal autophagy has been described in *CtsD* (Mitchison *et al.*, 2004, Koike *et al.*, 2005), *Cln3* (Cao *et al.*, 2006) and *Cln6* (Thelen *et al.*, 2012, Cao *et al.*, 2011) mutant mice, contributing to disease pathogenesis. The lipidated autophagosomal marker microtubule-associated protein 1 light chain 3-II (LC3-II) is increased in *Cln3* and *Cln6* mutant mice (Cao *et al.*, 2006, Thelen *et al.*, 2012), suggesting a disruption in autophagic pathways in these mice. Some authors believe that the disruption of the autophagic vacuolar maturation leads to activation of autophagy as pro-survival response (Cao *et al.*, 2006). Others suggest that the defects in autophagy promotes neuronal cell death (Thelen *et al.*, 2012). More studies are needed to clarify the role of lysosomal/vacuolar system in the mechanisms of pathogenesis of NCL.

1.6.3.4 Mitochondrial dysfunction

There is a growing body of evidence suggesting that mitochondrial dysfunction and oxidative stress are related to NCL pathogenesis [reviewed in (Jolly *et al.*, 2002)].

Mitochondria started to be a focus of attention of the NCL community due to the fact that the main storage molecule detected in the AFSM in most NCL forms was identified as the subunit C of the ATP synthase (Palmer *et al.*, 2013). However, mitochondrial perturbances have now been identified in various NCL models as well as in patients suggesting that other mechanistic pathways are involved in mitochondrial malfunctioning which are independent

of the storage material composition (Jolly *et al.*, 2002)

Morphological studies have revealed the presence of enlarged mitochondria in GABAergic neurons of the neocortex, claustrum and basket cells of the cerebellum in the English setter dog model (*Cln8* mutant) (March *et al.*, 1995). Mitochondrial shape abnormalities have also been detected in cerebellar precursor cells carrying the $Cln3^{\Delta ex7/8}$ mutation (Fossale *et al.*, 2004). Studies in mouse models of different forms of NCL also found increased levels of reactive oxygen species (ROS) in $Cln3^{\Delta ex7/8}$ (Herrmann *et al.*, 2008), $Ppt1^{-/-}$ (Kim *et al.*, 2010) and *mnd/Cln8* mouse models (Guarneri *et al.*, 2004). The Cln3 protein has been recently found to localise in mitochondria in *Drosophila* (Mohammed *et al.*, 2017) where it seems to have a role in the response towards oxidative stress as indicated by experiments in Cln3-deficient *Drosophila* (Tuxworth *et al.*, 2011).

Molecular and omics studies also indicated perturbations in genes related to mitochondrial functions. In this case there are studies of gene expression in the eye of a Cln3 disease mouse model, where authors found a decrease in expression of multiple mitochondrial genes associated to energy production (Chattopadhyay *et al.*, 2004). Transcriptomic studies in Cln3 deficient embryonic primary cell cultures also indicated disturbances in mitochondrial-related pathways (Luiro *et al.*, 2006). Moreover, more recent proteomic studies in Ppt1-deficient mice also showed perturbations in mitochondrial-related cascades (Tikka *et al.*, 2016).

Functional assays regarding mitochondrial respiratory chain activities have also been studied in CLN1 patient fibroblasts, indicating a reduced activity (Das *et al.*, 1996). Later studies by Das *et al.* also detected perturbances in ATP synthase activity in CLN1, CLN2 and CLN3 cells (Das *et al.*, 1999).

Taken all together, mitochondrial dysfunction reported at morphological, molecular and functional level in both animal models and human patients seem to be potentially contributing to NCL pathogenesis. Nevertheless, the specific pathways mediating these perturbations remain to be elucidated.

1.6.4 CLN1/PPT1 disease

1.6.4.1 *PPT1* gene and protein

The *PPT1* gene codifies for Palmitoyl protein thioesterase 1 (PPT1), a soluble lysosomal enzyme whose main function is to remove palmitate residues from S-acylated proteins, as demonstrated *in vitro* (A.K.A depalmitoylation) (Vesa *et al.*, 1995, Camp *et al.*, 1993). However, the specific function of the PPT1 substrates is not completely understood. To date, 67 mutations have been described in CLN1 disease (http://www.ucl.ac.uk/ncl), causing a loss of function of PPT1 leading to infantile onset NCL (Vesa *et al.*, 1995).

PPT1 expression is ubiquitous (Ahtiainen *et al.*, 2003, Camp *et al.*, 1993) and is not enriched in any human tissue type (Chattopadhyay *et al.*, 2000). However, its expression increases in the human embryonic brain from the beginning of cortical neurogenesis through to cortical development. Therefore, it has relevant implications for neuronal development (Heinonen *et al.*, 2000). Besides its lysosomal localization, in neurons PPT1 is also present in axons (Ahtiainen *et al.*, 2003) and at the presynaptic level is especially enriched in synaptosomes and in synaptic vesicles where it has implications in the regulation of the synaptic vesicle machinery (Lehtovirta *et al.*, 2001, Kim *et al.*, 2008a). Moreover, palmitoylation has important implications in intracellular protein sorting and trafficking, cell signalling (Greaves *et al.*, 2007) and apoptotic pathways (Nita *et al.*, 2016). Overall, the reported localisation and function of PPT1 suggests it has a potential role in regulating synaptic neurotransmission.

1.6.4.2 PPT1 clinical progression

PPT1 deficiency leads to infantile NCL (INCL), the most common in Finland (Gupta *et al.*, 2001, Kielar *et al.*, 2007, Kielar *et al.*, 2009, Santavuori, 1998) and the U.S. population (Sleat *et al.*, 2016). The majority of patients follow the classic INCL clinical spectrum and start developing their first symptoms within the first two years of life. However, some individuals may have late-infantile, juvenile, and even adult-onset NCL (Ramadan *et al.*, 2007, Van Diggelen *et al.*, 2001). Classic INCL patients are born completely normal and start manifesting delays in development, irritability, deceleration of head growth, central hypotonia and defects in fine motor skills at the end of the first year of life. This is followed by myoclonic jerks and optic atrophy with subsequent vision loss (Mole *et al.*, 2005). Death usually occurs between 8 and 13 years old. Studies by brain magnetic resonance imaging

(MRI) showed low intensity signals early on in thalamic areas, whereas with T-weighted imaging there is a high intensity signal in white matter later on in disease progression (Vanhanen *et al.*, 2004).

Saposins A and D, also named sphingolipid activator protein, are the most abundant component of the storage autofluorescence material (Tyynelä *et al.*, 1993), with a hallmark ultrastructure of granular omiophilic deposits (GRODs) (Santavuori *et al.*, 1973).

1.6.4.3 Ppt1 mouse models

Two distinct mouse models targeting *PPT1* genes have been generated. The first one was produced by the insertion of a neomycin cassette into exon 9 (Gupta *et al.*, 2001), whereas the second one was generated by the deletion of exon 4 by means of Cre/lox technique (Jalanko *et al.*, 2005). Both approaches lead to the complete loss of PPT1 enzymatic activity and/or protein levels (Gupta *et al.*, 2001, Jalanko *et al.*, 2005).

For this study (Chapter 4&6), we utilised the first one generated by Gupta *et al.* 2001. Ppt1 null mice (*Ppt1*$^{-/-}$) exhibit various aspects of the human disease. It presents an abundant accumulation of autofluorescent storage material with GROD ultrastructure as well as increased levels of saposins A and D (Gupta *et al.*, 2001). Ppt1-deficient mice display progressive onset of seizure, decline of motor coordination, vision loss correlating with the marked decrease of brain mass and a premature death between 8-9 months (Gupta *et al.*, 2001, Bible *et al.*, 2004, Macauley *et al.*, 2009).

They exhibit a dramatic widespread neurodegeneration by terminal stage. However, as stated before, studies have indicated a specific spatio-temporal pattern of neuronal vulnerability. Thalamus, hippocampus and cortical areas are the areas which present more pronounced neuronal loss and marked reactive gliosis (Bible *et al.*, 2004, Kielar *et al.*, 2007, Kuhl *et al.*, 2013). There is also an early loss of Purkinje neuron population in the cerebellum followed by granular cell loss (Gupta *et al.*, 2001, Bible *et al.*, 2004, Macauley *et al.*, 2009). Crucially, for the purpose of this work the spatio-temporal synaptic loss profile of the *Ppt1*$^{-/-}$ mice have already been characterized (Kielar *et al.*, 2009). Kielar and colleagues showed that an early synaptic loss takes place in the thalamic nuclei (3 months) and only later in the cortex (5 months) preceding neuronal loss (Kielar *et al.*, 2007, Kielar *et al.*, 2009). The loss of thalamic relay neurons that innervate the cortex (S1BF and V1) may explain the visual defects detected in the disease. An enhancement of reactive gliosis as well as oxidative stress has also

been reported and may contribute to neuronal loss (Bible *et al.*, 2004, Kim *et al.*, 2006, Kielar *et al.*, 2007, Macauley *et al.*, 2009).

Overall, these studies highlight the progressive and differential vulnerability of synaptic populations across brain regions in this model (see also sections 1.6.2 & 1.6.3.1).

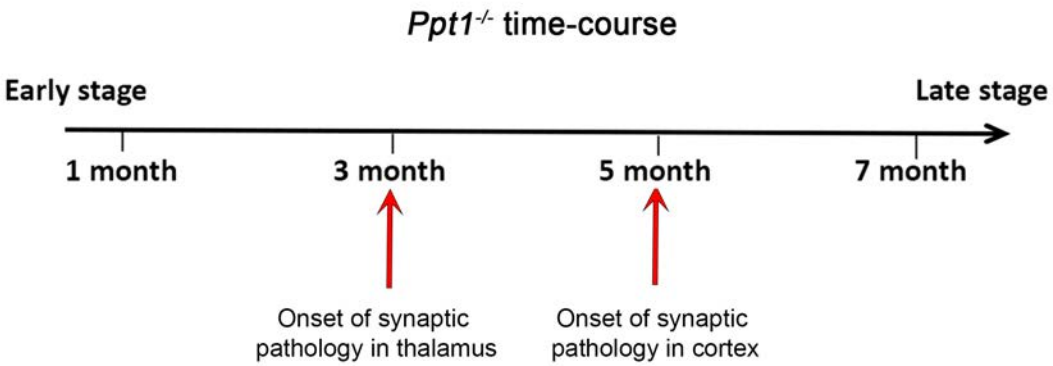

Fig.1.4. Time-course schematic in Ppt1$^{-/-}$ mice. Ppt1 null mouse present its first signs of synaptic pathology at 3 months in thalamus and 5 months in the cortex. These mice die prematurely between 8-9 months.

1.6.5 CLN3 disease

1.6.5.1 CLN3 gene and protein

Mutations in *CLN3* underlie a juvenile form of NCL, the most prevalent form worldwide (The International Batten Disease Consortium, 1995, Mitchison *et al.*, 1999, Pontikis *et al.*, 2004, Kuhl *et al.*, 2013). To date, there are 67 mutations described in CLN3 (http://www.ucl.ac.uk/ncl). The most common (85% of the patients) is a ~1kb deletion resulting in a truncated protein that retains partial activity (Phillips *et al.*, 2005, Kitzmuller *et al.*, 2008).

The *CLN3* gene encodes a very hydrophobic putative transmembrane protein whose function is not completely understood. Whilst traditionally, CLN3 protein was considered to be located mainly in the endosomal/lysosomal membrane (Järvelä I, 1998), more recent findings indicate that CLN3 is also located in synaptosomes (Luiro *et al.*, 2001), lipid rafts (Rakheja *et al.*, 2004, Persaud-Sawin *et al.*, 2004), Golgi (Persaud-Sawin *et al.*, 2004), mitochondria (Katz *et al.*, 1997), glia (Mohammed *et al.*, 2017) and endothelial cells (Phillips

et al., 2005, Katz *et al.*, 1997, Mohammed *et al.*, 2017, Tecedor *et al.*, 2013), where it may play other roles such as regulation of oxidative stress (Mohammed *et al.*, 2017, Tuxworth *et al.*, 2011), glial function (Pontikis *et al.*, 2004, Pontikis *et al.*, 2005) or blood-brain barrier homeostasis (Tecedor *et al.*, 2013). For more information regarding localization and function of CLN3 see this review (Phillips *et al.*, 2005).

The initial findings regarding the role of CLN3 protein has been found in experiments in yeast. *Btn1*, the *CLN3* ortholog in yeast, has been involved in the regulation of vacuolar pH (Pearce *et al.*, 1999) Also, *in vitro* experiments suggested the involvement of CLN3 in endocytic membrane trafficking (Luiro *et al.*, 2004). These results were later confirmed in human studies (Golabek *et al.*, 2000, Holopainen *et al.*, 2001). In mitochondria, it has been suggested that CLN3 assists the processing of mitochondrial membrane proteins (Margraf *et al.*, 1999). Interestingly, CLN3 has also been described to have an anti-apoptotic function via the C-terminus contributing in the modulation of the cell cycle (Puranam *et al.*, 1999). CLN3 has also been implicated in the biosynthesis of bismonoacylglycerol phosphate (BMP) (Hobert *et al.*, 2007).

1.6.5.2 CLN3 clinical progression

In humans, the onset of CLN3 disease typically occurs between 4-7 years of age, when loss of visual acuity is identified. Later, progressive dementia occurs with learning deficits and retardation. During adolescence, motor difficulties start with epilepsy and extrapyramidal/parkinsonian signs that include rigidity, hypokinesia and impaired balance. Motor deficits lead to complete immobility (Gardiner, 2002, Haltia, 2003, Nita *et al.*, 2016). Neuropsychiatric symptoms with anxiety and aggression are also frequently observed (Marshall *et al.*, 2005). As no effective treatment is currently available, premature death results at a mean age of 24 years old (Järvelä *et al.*, 1997). Its main pathological hallmark is the fingerprint shape profile of the autofluorescent lysosomal storage accumulations (Wisniewski et al., 1988) and the subunit C of the ATP-synthase protein is the main component (SCMAS) of these accumulations (Palmer *et al.*, 1989).

1.6.5.3 CLN3 mouse models

Four distinct Cln3-deficient mouse models of juvenile NCL have been generated. Two knock-out (KO) (Katz *et al.*, 1999, Mitchison *et al.*, 1999) and two knock-in mice (Cotman *et*

al., 2002, Eliason *et al.*, 2007). Whilst KO mice were generated by the targeted disruption of either exons 1-6 (Mitchison *et al.*, 1999) or 7-8 (Katz *et al.*, 1999) with a neomycin cassette, knock-in mice were produced using Cre/lox approach, mimicking the ~1kb deletion that human JNCL have (Cotman *et al.*, 2002).

For this study (Chapter 3), we also used the Cln3-null mouse generated by Mitchinson *et al.* (Mitchison *et al.*, 1999). Cln3 null mice (*Cln3*$^{-/-}$) reproduce various aspects of the human disorder (Mitchison *et al.*, 1999, Pontikis *et al.*, 2004). It exhibits the characteristic autofluorescent storage material with fingerprint profiles and its main component is the SCMAS (Mitchison *et al.*, 1999). *Cln3*$^{-/-}$ mice exhibit a delayed but progressive onset of neuronal loss which follows similar patterns as other NCL mouse models. During pre-symptomatic stages, there is an early vulnerability in relay neurons within the thalamic nuclei followed by other corresponding cortical areas (Mitchison *et al.*, 1999, Kuhl *et al.*, 2013, Pontikis *et al.*, 2004)(Weimer JM, 2006 #81), as well as GABAergic hippocampal interneurons and Purkinje neurons (Mitchison *et al.*, 1999, Pontikis *et al.*, 2004).

In *Cln3*$^{-/-}$ mice and in patients, an autoantibody against glutamic acid decarboxylase (GAD65) was detected. This autoantibody is able to inhibit GAD65 ability to transform glutamate into GABA which could contribute to excitotoxicity mechanisms (Chattopadhyay *et al.*, 2002) and to the vulnerability of GABAergic neurons in CLN3 disease. It is not clear, however, what the role of these auto-antibodies in the pathogenesis of the disease and suggests that more studies will be needed to clarify that.

In terms of synaptic pathology, no studies have been published yet. However, preliminary experiments by Cooper *et al.*, indicated early synaptic pathology happening in the *Cln3*$^{-/-}$ mice. In Chapter 3, experiments regarding the spatio-temporal synaptic pathology in these mice are addressed.

1.7 Drug target and biomarker discovery approaches

1.7.1 Proteomic technologies as a data-driven approach

Most of the current therapies for neurodegenerative diseases are based on symptomatic treatment which may be beneficial at early phases of the disease, but fail to succeed towards late stages of the disease (Zhang *et al.*, 2014). Moreover, some of the therapeutics cause large

side-effects affecting the daily life of the patient (Corbett *et al.*, 2012, Meissner *et al.*, 2011). The reasons why no effective drugs are available to prevent the progression of these diseases could be due to the high complexity of the pathogenesis, and the unknown aetiology of many of these conditions. Another reason contributing to this lack of successful therapies by both pharmaceutical industry and academia is believed to be the current reductionist approach taken, that has uniquely focused on preselected molecular targets (Prior *et al.*, 2014, Pangalos *et al.*, 2007).
For these reasons, drug discovery for neurodegenerative disease has been shifted to the identification of disease-modifying molecules that may halt or delay disease progression.

In the last few years, mass-spectrometry (MS) based proteomics has seen an exponential development and expansion in multiple research areas (Angel *et al.*, 2012). This includes, the use of proteomic technologies for drug target and biomarker discovery [reviewed in (Savino *et al.*, 2012, Yan *et al.*, 2015, Miller *et al.*, 2014)]. Great progress has been made in MS instrumentation, improving the sensitivity, quality and number of identifications in each experiment (Angel *et al.*, 2012, Aebersold *et al.*, 2016). MS approaches have become powerful tools to investigate the proteome compositional differences between multiple sample types. This includes the analysis of specific organelles such as synaptic vesicles, endoplasmic reticulum (ER) or Golgi apparatus (Au *et al.*, 2007) as well as its use in the generation of interaction maps in simple organisms such as yeast (Collins *et al.*, 2007). Importantly, proteomic approaches have become valuable tools for the investigation of disease animal models or clinical samples such as cell lysates, tissues or body fluids for the discovery of disease-specific drug targets and biomarkers (Savino *et al.*, 2012).

Moreover, MS technologies can also be utilised for the elucidation of the biological pathways and mechanistic networks providing insight into underlying disease processes. Such transduction pathways are key for the drug discovery pipeline (Kocher *et al.*, 2007, Tedford *et al.*, 2009). For instance, the use of proteomic technologies by our laboratory, followed by *in silico* analyses in murine models of SMA, allowed the identification of the ubiquitin homeostatic pathway deregulation (Wishart *et al.*, 2014). Targeting this pathway allowed the rescue of the neuromuscular system and the whole organism in animal models of the disease (Wishart *et al.*, 2014, Powis *et al.*, 2016).

Taken all together, it seems evident that there is potential in the using proteomic

technologies for elucidating mechanistic drugs to target neurodegenerative diseases. As indicated in Fig. 1.3, proteins as effector molecules in the cell, should not be considered as individual entities. Instead, we should take into account that each protein implies a series of interactions which lead to complex mechanistic pathways. In the words of Dr. Bruce Alberts *"Indeed, the entire cell can be viewed as a factory that contains an elaborate network of interlocking assembly lines, each of which is composed of a set of large protein machines"* (Alberts, 1998). Therefore, in the context of disease, genetic mutations will deregulate the whole cellular machinery (Fig. 1.3).

As mentioned before, proteomic technologies now provide large proteome coverage. To put this data into context, it is necessary to utilise *in silico* tools that allow filtering, data mining and interpretation of the MS data. All the omic approaches developed in the last few years have produced large amounts of data which has lead to the generation of multiple databases for bioinformatic analysis purposes such as: OMIM (Online Mendelian Inheritance in Man), TTD (Therapeutic Target Database) or DrugBank (Yan *et al.*, 2015). Based on these databases, bioinformatics gene ontology tools have also been elaborated such as the *Database for Annotation, Visualization and Integrated Discovery (DAVID*) (Huang *et al.*, 2009b, Huang *et al.*, 2009a) or *Gene Ontology enRIchment anaLysis and visuaLizAtion tool (GOrilla)* (Eden *et al.*, 2009), as well as network generator tools based on large set of functional association data; *GeneMANIA* (Warde-Farley *et al.*, 2010) or *Search Tool for the Retrieval of Interacting Genes/Proteins* (*STRING)* (Jensen *et al.*, 2009). Proteomic technologies are also able to provide quantitative expression data based on sample normalisation (Patel *et al.*, 2009, Wang *et al.*, 2012). Such expression data based on ratio or fold-change provides another layer of information regarding a specific biological question. Pattern recognition softwares such as *BioLayout*, allow a visualisation of the data based solely on the expression data input. It groups proteins/genes based on their expression trend across multiple samples (as well as between tissue types or time-points) (Theocharidis *et al.*, 2009). Other commercial softwares such as *Ingenuity Pathway Analysis* (*IPA*) allow the combination of both expression and functional data to generate knowledge-based interaction networks. It also allows the prediction of upstream regulators and its activation/inhibition state (Savli *et al.*, 2008).

Certainly, these tools offer great insight into specific biological questions. However, they also imply a number of caveats we should take into consideration when interpreting results. For

instance, knowledge-based interaction networks may bias the data generated towards current volumes of research which focus on popular pathways/diseases such as cancer signalling pathways. Overall, the combination of these bioinformatics tools provides a powerful analysis uncovering the significance of omics data and help improve the understanding and identification of candidate targets and/or biomarkers within the context of biological system/disease.

1.7.2 Phenotypic assessment in drug discovery

Following good quality proteomic and *in silico* analysis from animal models or clinical samples, we obtained a potential list of promising proteins and pathways. These candidates which are perturbed in relation to control samples are potentially involved in the mechanisms of neurodegeneration. In order to validate these results and identify potential drug targets, further validation is required. To do so, target-based and phenotypic screens are a broad approach used in drug discovery (Zhang *et al.*, 2014, Cooper *et al.*, 2017, Dawson *et al.*, 2014, Prior *et al.*, 2014).

Both screening strategies have contributed 45 first-in-class new small-molecule entities (NME) approved by the U.S. Food and Drug Administration (FDA) between 1999 and 2008 (Swinney *et al.*, 2011). Target-based screening via pharmacological or genetic targeting in specific disease models platforms can be used to establish if the modulation of a specific candidate has any beneficial therapeutic effect. Such disease platforms can be based on cell cultures (Cooper *et al.*, 2017, Vargas-Caballero *et al.*, 2016, Khurana *et al.*, 2015), or simple organisms such as yeast (Outeiro *et al.*, 2006), zebrafish (Prusothman *et al.*, 2017) or *Drosophila* (Konsolaki, 2013, Nichols, 2006).

Whilst all of the early drugs were discovered by phenotypic screening, in the past years there has been an increasing rise of new technologies for making large chemical libraries (combinatorial chemistry) and high throughput screening (HTS) (robotics) that have since dominated the pharmaceutical industry (Prior *et al.*, 2014). However, it has been proposed that such new technologies present many caveats for drug discovery in neurodegenerative diseases, as it cannot be assumed that the activity of a single molecule is responsible for the condition or that a single target drug can halt the entire process of neurodegeneration (Prior *et al.*, 2014).

Instead, many benefits of using phenotypic assessment for drug/target discovery approaches

over high-throughput screening (HTS) are highlighted here. 1. It Avoids the incompatibilities with the robotic equipment. For instance, most drugs targeting the brain are hydrophobic, which have the risk to bind to the equipment; 2. Derived-natural products are a promising family of lead compound for neurodegeneration (Rishton, 2008). However, they are often discarded based on erroneous pharmacological assumptions as they interfere with some of the assays used (promiscuous binders). 3. By doing phenotypic assessments a readout is obtained regarding the bioavailability of the compound as well as toxicity effects that can possibly be caused to a living organism. In HTS, such assays will have to be taken afterwards and many compounds could be lost later in the pipeline. More information regarding phenotypic assessment benefits can be found in (Prior *et al.*, 2014).

1.7.3 Translational approaches

Nevertheless, following the outlined pipeline above (see Fig. 1.5) does not guarantee the translatability of the targets or compounds found to the clinic. It is estimated that only 10% of the agents entering clinical trials phase 1 result in a clinically used drug (Hay *et al.*, 2014, Marchetti *et al.*, 2007). Therefore, there is a requirement for the establishment of bridges to translate the findings in bench research to clinical practice. Ways to do this include:

1. Improvement of animal models that better reflect human disease,
2. Careful planned experimental design to reduce noise of the experimental observations (ie..tissue vulnerability status or time-points are key for interpretation of results);
3. Instrumentation used will depend on the experimental design (ie. some proteomic techniques are better than others depending on the quantity and sample nature);
4. Use of human samples as a validation of the findings based on animal models. This last one may be controversial. First of all, most samples used in pre-clinical research are *post mortem* samples. In the context of neurodegenerative disease, these samples will be likely at the end stage of the disease. This indicates that the molecular changes detectable at the end stage might not be that informative regarding the pathological molecular mechanisms of neurodegeneration. Moreover, the collection protocol of the samples often varies between hospitals/laboratories making it more difficult to establish direct comparisons between samples from different sources. Furthermore, unlike animal models, human disease is intrinsically highly heterogeneous between each individual which hampers the statistical power of human studies. Ways to overcome these caveats are the use of tissue dissected from neurosurgical procedures, this tissue can remain electrophysiological active for up to 24 hours (Verhoog *et al.*, 2013). Because such resected tissue is very limited, the development of

public databases has become very valuable in this context. An example of a resource is *CARMEN* (*Code Analysis, Repository & Modelling for e-Neuroscience*. Available from: http://www.carmen.org.uk/), which allows data-sharing across laboratories using human tissue providing strict standardised reporting requirements (Vargas-Caballero *et al.*, 2016).

In this project, the main objective is to elucidate molecular regulators of synaptic stability in neurodegenerative disease that could serve as drug targets for the development of therapeutic approaches. As explained above, we are using murine models of the infantile NCL (*Ppt1*$^{-/-}$) and the juvenile NCL (*Cln3*$^{-/-}$). In the NCLs, there has been a growing number of gene therapy and enzyme replacement trials that are generating promising results (Neverman *et al.*, 2015). However, as further developed in section 1.6.3, mechanistic-based therapies could act synergically together with gene/enzyme therapies (Cooper *et al.*, 2015). To do so, we have taken into consideration some of the information contained in this section, summarised in Fig. 1.5. We combine proteomic technologies and some of the bioinformatic tools described in this section to further characterise the molecular changes occurring in these mice. Ultimately, we generated a list of protein candidates which were tested using *Drosophila in vivo* phenotypic assessment for target validation. The use of *Drosophila* as a model system is further developed in the following sections.

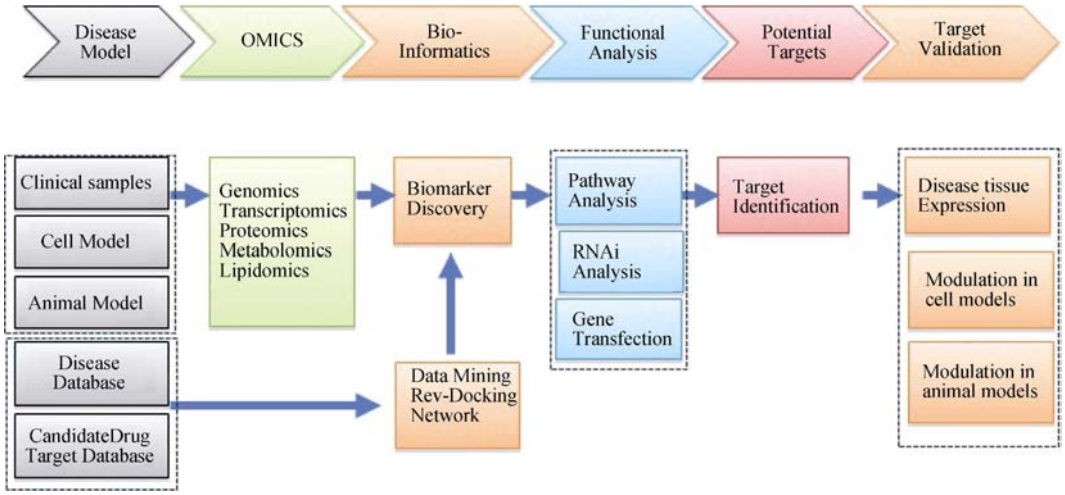

Fig. 1.5. Strategies of drug target discovery based on omics. Pipeline for the discovery of targets and biomarkers based on omic approaches, including proteomics. After target identification, a validation step to assess the modulatory effects of candidates is taken. In this project we propose *in vi*vo phenotypic assessment using *Drosophila* as a model organism. Figure adapted from Fig. 3 in (Yan *et al.*, 2015).

1.8 *Drosophila melanogaster* as a model system

Drosophila melanogaster, commonly known as fruit fly, has become one of the most studied organisms for geneticists since 1908 when Thomas Hunt Morgan started working using the model during his studies on chromosomal inheritance (Kohler, 1994). The growing sophistication of the technology surrounding fly genetics has led to multiple studies regarding organism development, the molecular mechanisms underlying biological processes as well as physiology and behavior (Martinez-Arias, 2008, Green, 2010, O'Kane, 2003, Mehregan *et al.*, 2016). Classical genetic studies in *Drosophila* helped in finding the functional role of many genes due to the availability of a broad range of tools and techniques for its genetic manipulation, short generation time, large number of progeny, and relatively well known phenotypes (St Johnston, 2002, Venken *et al.*, 2005).

Furthermore, half of the *Drosophila* genes show a significant homology to human genes and it is estimated that 77% of genes associated with human diseases have an ortholog in the fruit fly (Reiter *et al.*, 2001). Additionally, in spite of the evolutionary distance, comparative genomic studies between human and *Drosophila* have indicated a high conservation in fundamental biological pathways (Rubin *et al.*, 2000). Thus, the balance between similarities to human biology and simplicity has made the fruit fly an excellent model organism for the study of the molecular and cellular pathology of human diseases, including neurodegenerative conditions.

1.8.1 *Drosophila* use in studies of neurodegenerative diseases

Drosophila has been used as a model for the study of many relevant neurodegenerative conditions where synapses are an early pathological target, including but not limited to polyglutamine diseases (SCA and HD), PD, MND (including ALS and SMA) and also the NCLs (Bilen *et al.*, 2005, Vanhauwaert *et al.*, 2015, Hirth, 2010, Bond *et al.*, 2013). Different approaches are utilised (alone or in combination) with *Drosophila,* in order to elucidate pathogenic pathways underlying neurodegeneration. Some of the approaches include: 1. Misexpression of a human disease gene (WT or mutant): 2. Loss (LOF) and gain of function (GOF) of the *Drosophila* homolog of a human disease gene; and 3. Genetic/pharmacological screen to identify modifiers (enhancers or suppressors) of the disease phenotype induced by 1 or 2 (Hirth, 2010).

Some examples of *Drosophila* models of the most common neurodegenerative disease are outlined here.

The insertion of *SCA1* human gene led to the generation of a *Drosophila* model that helped develop the understanding of the pathogenesis of Spinocerebelalar ataxia type 1 (Fernandez-Funez *et al.*, 2000). Later studies proved the relevance of the fly model compared to mammalian systems by showing conserved perturbations in the RAS–MAPK–MSK1 pathway in both *Drosophila* and mice models of SCA1 (Park *et al.*, 2013).

Likewise, Jackson *et al.* generated the first *Drosophila* model of HD, another polyglutamine disease. In a similar way to the human condition, the pathogenicity was proportional to the length of polyQ repeats (Jackson *et al.*, 1998). Later models generated targeting HTT in different ways also demonstrated the disruption of the release of neurotransmitter (Rozas *et al.*, 2011), transcriptional deregulation (Steffan *et al.*, 2001) and fast-axonal transport (Lee *et al.*, 2004).

Like mammals, developing and adult *Drosophila* have dopaminergic neurons that are also involved in locomotion control (Monastirioti, 1999, Lima *et al.*, 2005). Targeting specific gene orthologs related to human PD, such as *SNCA*, *PINK*, *PRKN* and *LRRK2* triggers the loss of a specific subset of dopaminergic neurons leading to parkinsonian-like phenotype in the flies (Vanhauwaert *et al.*, 2015). These investigations have provided insights into the pathomechanisms regulating neuronal loss in PD including the involvement of abnormal protein aggregation, vesicle trafficking defects, oxidative stress and mitochondrial dysfunction (Vanhauwaert *et al.*, 2015, Hirth, 2010). Furthermore, studies by Tuffi *et al.* demonstrated that it was possible to target mitochondrial impairment genetically and pharmacologically rescuing the phenotypes observed in *Pink1* mutant flies (Tufi *et al.*, 2014).

Motor neurone diseases such as ALS and SMA also have disease models in *Drosophila*. Most cases of ALS are sporadic and of unknown aetiology and therefore, difficult to model. However, 5-10 % of ALS are familial cases for which some disease-related genes have been identified. These include *SOD1*, *TDP43*, *C9orf72, VAPB* or *TARDBP* (Robberecht *et al.*, 2013), some of which have orthologs in *Drosophila* (Chai *et al.*, 2015). The motor neuron specific expression of either WT or mutant *SOD1* produced progressive climbing defects, impaired neuronal circuit and stress response in glial cells (Watson *et al.*, 2008).

Furthermore, targeting TDP-43 showed a decrease in lifespan, locomotion defects and alterations in NMJ synaptic number (Feiguin *et al.*, 2009, Lu *et al.*, 2009) as well as larvae lethality (Fiesel *et al.*, 2010).

Drosophila VAPB mutants have also been generated modeling a rare late onset ALS.
DVAP-P58S fruit fly recapitulates the major features of the human disease including aggregate formation, neurodegeneration, locomotion defects and decreased life-span (Chai *et al.*, 2015, Forrest *et al.*, 2013). Adult flies present progressive motor phenotype and disruption of the neuromuscular junction (NMJ) in the larvae when driven paneuronally (Sanhueza *et al.*, 2015). Other *Drosophila* mutants such as *DVAP-V260I*, a gain of function mutation, cause a muscle phenotype when driven postsynaptically (Sanhueza *et al.*, 2014).
Moreover, loss-of-function of dSMN, a homolog of *SMN* in flies, results in recessive larval lethality, NMJ defects as well as muscle atrophy (Rajendra *et al.*, 2007, Chan *et al.*, 2003).

As pointed above, *Drosophila* models of neurodegenerative disease have provided valuable tools for genetic and pharmacological screens for the identification of modifiers of the disease phenotype (Chang *et al.*, 2008a, Sanhueza *et al.*, 2015, Park *et al.*, 2013, Fernandez-Funez, 2000, Tufi *et al.*, 2014, Kaltenbach *et al.*, 2007, Pandey *et al.*, 2011, Buff *et al.*, 2007, Saja *et al.*, 2010).

1.8.2 *Drosophila* nervous system

Drosophila nervous system (NS) can be divided into 3 distinct systems, defined by their developmental stage: embryonic, larval and adult stages. Each one of these systems provides different layers of information with regard to mechanisms of specific biological processes involved in neurodegeneration.

1.8.2.1 Larvae neuromuscular junction

Whilst, the embryonic CNS is very useful for the study of cell fate decisions and axon path-finding (Nichols, 2006), the larval NS provides a great tool for the study of synapses, and more specifically, the NMJ.
The larva is divided into two symmetrical segments each containing 36 motor-neurons innervating 30 individual body-wall muscles (Nichols, 2006, Johansen *et al.*, 1989, Keshishian *et al.*, 1996). The larva has a stereotyped connectivity that follows similar

arborisation patterns for specific muscles across all abdominal segments. This allows a relatively easy tracking and visualisation of individual NMJs to characterise their morphological as well as their electrophysiological properties with regards to synaptic transmission (Menon *et al.*, 2013).

Motor neurons in *Drosophila*, in contrast to mammals, are glutamatergic and their synapses are very similar to those in the vertebrate CNS, providing an excellent model for mammalian brain synapses (Johansen *et al.*, 1989, Keshishian *et al.*, 1996). Glutamatergic larval NMJ are characterized by postsynaptic density scaffolding complexes that are very similar to mammalian ones. Larval synapses use ionotropic glutamate receptors (GluRs) that are homologous to AMPA-type GluRs in the mammalian brain (Menon *et al.*, 2013, Nichols, 2006). Moreover, many of the vertebrate synaptic proteome have orthologs in *Drosophila*. Such proteins include Neurexin (Tabuchi *et al.*, 2002), Neuroligin (Banovic *et al.*, 2010, Sun *et al.*, 2011), PSD-95 (Lahey *et al.*, 1994) and Phosphodiesterase 4 (PDE-4) (Chen *et al.*, 1986, Davis *et al.*, 1989). Importantly, many pathways have been shown to be conserved across larval NMJ and mammalian synapses (Nichols, 2006). Studies carried out by our laboratory showed that the disruption of ubiquitination pathways in mouse models of SMA was also translatable to these lower organisms by showing the rescue of the NMJ phenotype in both mice and *Drosophila* using the same compound (Wishart *et al.*, 2014).

Furthermore, studies of the synapses of larval NMJ have been very important for the elucidation of the mechanisms underlying presynaptic signalling including plasticity and synaptic vesicle machinery (Zhang, 2003, Yoshihara *et al.*, 2004, Prokop *et al.*, 2006, Nichols, 2006).

1.8.2.2 The *Drosophila* compound eye

Despite the considerable morphological and structural differences between *Drosophila* and the mammalian eye, they are believed to have a common evolutionary ancestor which may explain why most molecular pathways underlying eye formation are conserved between human and flies (Arendt *et al.*, 2004). Some of these pathways include cell fate determination, programmed cell death, and axon guidance (Hanson, 2001, Kumar *et al.*, 2001).

The visual system of the adult fly develops from the larval imaginal eye/antenna discs forming a compound eye (Dickson *et al.*, 1993). Each eye is composed by around 750 facets (called ommatidium) which are clusters of differentiated eye cells. As illustrated in Fig. 1.6, each ommatidium is an assembly of 14 cells grouped in columns: 8 photoreceptor cells (R cells), 4 cone cells and 2 primary pigment cells (Cagan *et al.*, 1989, Ready *et al.*, 1976). The *Drosophila* visual system consists of the retina, lamina, medulla, lobula, and lobula plate (Heisenberg *et al.*, 1984). Each optic lobe is formed by 60,000 to 70,000 neurons on each side of the brain and their pattern of nerves and synaptic connectivity have been well characterized (Prokop *et al.*, 2006). The axons from a single ommatidium travel in a bundle from the retina to the optical ganglia of the brain in a precise retinotopic map (Meinertzhagen, 1989). Every R1-R6 photoreceptor terminal establishs around 50 presynaptic sites that arrange in tetrads into L1, L2, L3 or amacrine cells, while each cell from lamina L1 or L2 forms synapses with photoreceptor terminals of its lamina module or cartridge (Meinertzhagen *et al.*, 2001) (Fig 1.6).

Because of the very well established organized architecture of the *Drosophila* compound eye, it is easy to detect abnormalities in its structure. When a mutation or a protein produces a toxic effect, the number of ommatidium that are damaged is proportional to the degree of severity of the degenerative effect (Thomas *et al.*, 1999). For this reason, the eye has been an accepted system for the study of neurodegenerative diseases and are used to carry out genetic and pharmacological modifier screens (Bilen *et al.*, 2005, Sanhueza *et al.*, 2015, Fernandez-Funez, 2000, Park *et al.*, 2013, Nichols, 2006, Kaltenbach *et al.*, 2007).

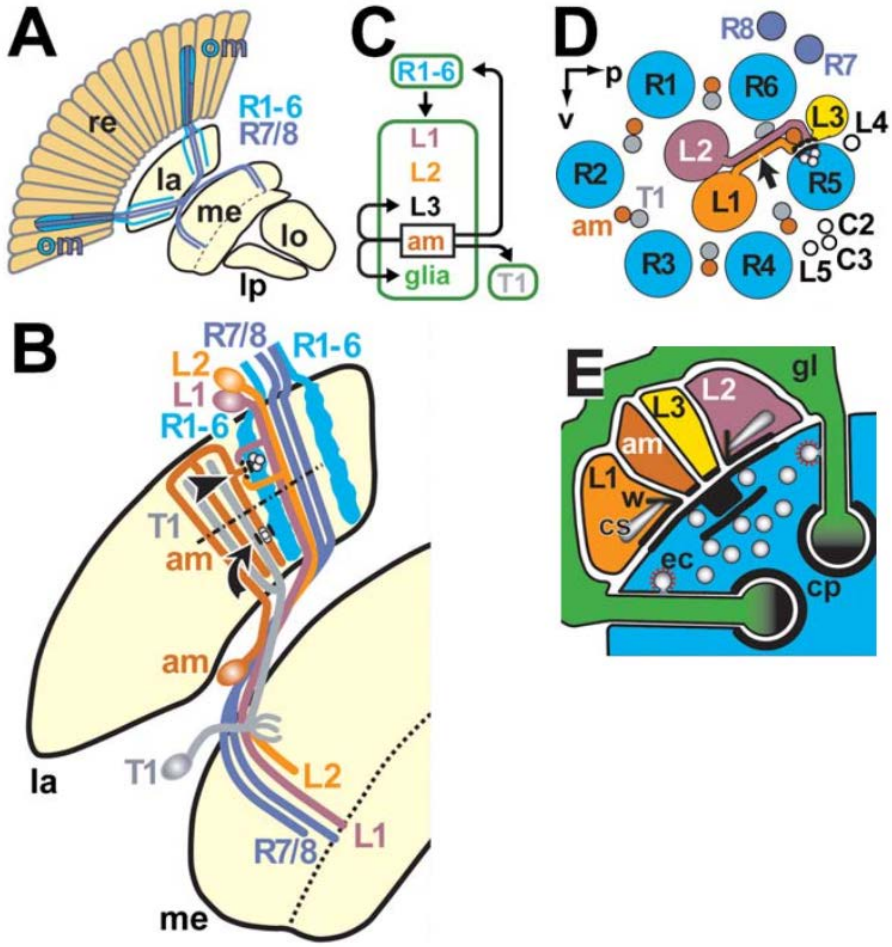

Fig. 1.6. Synaptic connections in the lamina. **A.** The retina (re) is composed 750 ommatidia (om) each containing eight photoreceptor neurons (R1–R8) which project onto the two outermost optic neuropiles of the brain, lamina (la) and medulla (me); central to these lie the lobula (lo) and lobula plate (lp). R7 and R8 terminate in the medulla, R1–R6 of each ommatidium sort into adjacent cartridges in the lamina. **B**. R1–R6 terminals are joined by projections of interneurons, the cell bodies of which lie in the surrounding cortex; L1 (pink) and L2 (orange) cells, a T1 (grey) and an amacrine cell (am, brown). **C**. Wiring diagram of synaptic microcircuits (green box) and including the most numerously represented synaptic circuits **D.** Cross-sectioned cartridge showing its conserved spatial organisation; each column comprises a ring of 6 photoreceptor terminals (each from a different ommatidium) surrounding L1 and L2 at the centre, separated by the paired neurites of amacrine (am) and T1 cells, and other interneurons (open circles: L3-L5, C2, C3). **E**. Schematic of the synaptic tetrad in C showing a presynaptic T-bar ribbon of the photoreceptor terminal, postsynaptic cisternae (cs) anchored via whiskers (w) in spines of lamina cells L1 and L2, and capitate projections (Khan *et al.*, 2014) from surrounding epithelial glia (gl) that penetrate the photoreceptor terminal, sites of vesicle endocytosis (ec). Figure adapted from Fig. 3 in (Prokop *et al.*, 2006).

1.8.3 NCL *Drosophila* models

Drosophila models are used to encode homologs of some of the most common NCL-causing genes in humans. These include the lysosomal enzymes Ppt1/CLN1 (75% similarity) (Glaser *et al.*, 2003) and cathepsin D/CLN10 (65% similarity) (Myllykangas *et al.*, 2005), the endo-lysosomal transmembrane proteins, CLN3 (60% similarity) (Tuxworth *et al.*, 2009) and CLN7/ MFSD8 (56% similarity) (Muzaffar *et al.*, 2008) and the synaptic vesicle protein cysteine string protein (CSP/DNAJC5 or CLN4, 56% similarity). NCL fly orthologs display very similar expression patterns to those seen in mammals. It has been shown that the expression of tagged forms of Ppt1, Cln3 and Cln7 are also localized in the lysosome (Bannan *et al.*, 2008, Tuxworth *et al.*, 2009, Mohammed *et al.*, 2017). Moreover, Ppt1 was shown to have the same enzymatic activity as the human protein (Glaser *et al.*, 2003). Since these proteins are conserved from humans to more simple organisms, it is likely that they perform essential core functions in the *Drosophila* CNS similar to their role in humans.

Thus, targeting *Drosophila* NCL orthologs could provide good animal models to study mechanisms underlying NCL. Both LOF and GOF models have been generated for NCL-related ortholog genes and some of them recapitulate key hallmarks of the human disease.
Mutations in Ppt1 lead to loss of enzymatic activity and show an accumulation of autofluorescent storage material with a 30% shorter lifespan in flies, which is not caused by neuronal cell loss (Hickey *et al.*, 2006). However, studies in the developmental stages of the fruit fly showed that a disruption of embryonic neural development of Ppt1 mutants, with defects in cell fate organization and axon guidance, which triggered defects in both CNS and PNS (Chu-LaGraff *et al.*, 2010). Later studies by Aby *et al.* showed the importance of Ppt1 function in the stability of synapse at the larval NMJ. In this report investigators showed electrophysiological and synaptic exo/endocytosis abnormalities. They also showed larval locomotion defects consistent with perturbations in the synaptic function (Aby *et al.*, 2013).

Loss-of-function models have also been generated for Cln3 disease (Tuxworth *et al.*, 2011). *Cln3* mutant flies have a shorter lifespan and are hypersensitive to oxidative stress (Tuxworth *et al.*, 2011). Furthermore, the Cln3 protein has been described to have a role in synaptic morphology at the larval NMJ. Non-published studies by Tuxworth and colleagues suggests that synapses from flies lacking Cln3 fail to mature appropriately and have alterations in bouton size (Bond *et al.*, 2013, Faller *et al.*, 2015). The recent development of CRISPR genome editing techniques is contributing to more detailed characterization studies of NCL-

related protein localization by generating knock-in tagged constructs. A recent study by Mohammed *et al.* using this technology, has indicated that Cln3 protein is highly enriched in glial cells, microvilli, glia, lysosomes and mitochondria, which may explain its previously identified role in oxidative stress (Tuxworth *et al.*, 2011, Mohammed *et al.*, 2017).

Both Ppt1 and Cln3 expression levels seem to be extremely important for the stability of the nervous system in *Drosophila*. The targeted overexpression of Ppt1 and Cln3 by means of the UAS/GAL4 system results in a severe neurodegeneration of the adult compound eye (Korey *et al.*, 2003, Tuxworth *et al.*, 2009). This pathology is thought to be caused by an increase of activity in Cln3 and Ppt1 since the overexpression (OE) of a truncated version of the Cln3 or Ppt1 does not cause degeneration. Cln3 OE was shown to have an impact on Notch and Jnk signaling pathways and interestingly, the OE of human CLN3 caused a very similar neurodegenerative phenotype in the eye (Tuxworth *et al.*, 2009). Therefore, we can interpret that the phenotypes caused by an overexpression of NCL-related genes may be disrupting similar pathways as those found in the loss of function flies of the same respective proteins.

The OE models of both Ppt1 and Cln3 have provided excellent tools for the study of genetic modifiers in large-scale screenings which have provided insight into the pathomechanisms of Ppt1 and Cln3 (Buff *et al.*, 2007, Saja *et al.*, 2010, Tuxworth *et al.*, 2011). A GOF modifier screen by Buff and colleagues identified a set of suppressors and enhancer genes that were involved in synaptic development, morphology and vesicle recycling as well as to endo-lysosomal trafficking (Buff *et al.*, 2007). Later, a LOF genetic modifier screen carried out in the same laboratory, also indicated that the synaptic and cellular trafficking pathways may be related to Ppt1 interactors (Saja *et al.*, 2010). GOF modifier screen in Cln3-OE flies indicated the link between the modifier genes of the Cln3-induced phenotype and stress-related pathways. These findings supported the role of Cln3 in the oxidative stress response suggested by experiments carried out in Cln3 LOF fly that showed to be hypersensitive to oxidative stress (Tuxworth *et al.*, 2011).

1.9 Experimental aims

Given the lack of effective therapeutic approaches targeting neurodegenerative diseases, there is a need for the understanding of molecular pathways underlying these conditions. Synapses are an early pathological target preceding somatic pathological changes in many of these conditions. Therefore, understanding the mechanisms regulating synaptic stability may help the elucidation of pathways modulating degeneration in the whole nervous system.

Using well-characterized murine models of NCL, a monogenetic childhood neurodegenerative disease, we carried out a data-driven target discovery approach. This involved a spatio-temporal proteomic study followed by *in vivo* phenotypic assessment in *Drosophila* models. In this study I aimed:

1. **To characterise the molecular changes correlating to synaptic vulnerability across brain areas at an early stage of disease progression in Cln3-null mice (Chapter 3).** In the NCLs as well as in many other neurodegenerative diseases, not all brain regions are affected equally. In Chapter 3, we take into account the region-specific pattern of synaptic vulnerability to identify molecular correlates. Individual protein candidates and pathways identified here have the potential to be modulators of synaptic stability.
2. **To characterise the regional molecular changes correlating to synaptic vulnerability throughout disease progression in Ppt1-deficient mice (Chapter 4).** Here we wanted to characterise and identify protein candidates and pathways changes correlating to the spatio-temporal pattern of synaptic vulnerability. Moreover, datasets from Chapter 3 were overlapped to those in Chapter 4 in order to identify conserved perturbations across the two mice models. Therefore these conserved proteins represent potential modulators of disease progression in both conditions. A subset of these candidates were also examined in *post mortem* patient brain samples to assess their relevance to the human disease.

3. ***In vivo* phenotypic assessment of protein candidates in *Drosophila melanogaster* models (Chapter 5).** After studying different fruit fly disease models, the modulatory effects of each candidate was assessed for their ability to modulate Cln3-induced neurodegenerative phenotype in the *Drosophila* nervous system *in vivo*. Candidates identified in Chapter 3&4 with the potential to modulate disease

progression were targeted genetically and/or pharmacologically in *Drosophila* disease and wild-type backgrounds.

4. **To identify molecular biomarkers of neurodegeneration correlating to disease progression in peripherally accessible tissues (Chapter 6).** The identification of molecular factors providing a read-out of the progression of neurodegeneration are essential to assess the effectiveness of new therapies in preclinical and clinical trials. Then, the molecular changes happening throughput the time-course of disease progression in Ppt1-deficient mice muscle samples were analysed. We identified a set of proteins changes which correlate to disease progression in a predictable manner in muscle and blood, some of which were also changed in *Cln3*$^{-/-}$ mice muscle and human *post mortem* brain samples from NCL patients.

Chapter 2

General materials and methods

2.1 Animals and tissues

2.1.1 Mice

Ethics statement: All animal experiments were performed under license by the UK Home Office (project license numbers 70/6567 and 70/7364). All the mice tissues were harvested alongside ongoing experiments in Prof Jonathan Cooper laboratory at Institute of Psychiatry, Psychology & Neuroscience, King's College London.

2.1.1.1 *Cln3*$^{-/-}$ mice

Cln3$^{-/-}$ and control (+/+, WT) mice were used in Chapters 3 and 6. *Cln3*$^{-/-}$ (Mitchison *et al.*, 1999) were bred on a *C57BL/6* background for at least 10 generations which is generally considered sufficient to be congenic on this strain background. Littermates resulting from heterozygous crosses were used in this study. *Cln3*$^{-/-}$ mice were genotyped as described in the reference (Mitchison *et al.*, 1999). Five *Cln3*$^{-/-}$ and five wild-type control mice (WT) at 6.5 months and 12-13 months of age were used for immunohistochemistry experiments. Four *Cln3*$^{-/-}$ and four control mice (WT) at 12-13 months were used for the proteomics and biochemical experiments. Numbers of animals required for experiments were based on experience and data in the Wishart laboratory, refining and reducing from numbers derived through power calculations.

2.1.1.2 *Ppt1*$^{-/-}$ mice

Ppt1$^{-/-}$ mice were used in Chapters 4 and 6. The Ppt1-deficient mice (*Ppt1*$^{-/-}$) used in this study were originally created through a targeted disruption strategy which eliminates the last exon in the coding sequence of Ppt1 (Gupta *et al.*, 2001). These mice were subsequently

backcrossed for 10 generations with *C57BL/6* control mice (Gupta *et al.*, 2001). *C57BL/6* congenic *Ppt1*$^{-/-}$ mice and age-matched *C57BL/6* control mice were bred and housed in the animal facility at the Institute of Psychiatry, Psychology & Neuroscience, King's College London.

2.1.2 Humans

Human *post mortem* cortical samples were used to validate *Cln3*$^{-/-}$ and *Ppt1*$^{-/-}$ proteomic data from Chapter 3 & 4. Samples were obtained from the Human Brain and Spinal Fluid Resource Center, Los Angeles and from The MRC London Neurodegenerative Disease Brain Bank, Institute of Psychiatry, Psychology & Neuroscience, King's College London. Samples were obtained at routine autopsy with fully informed written consent by the families. Study protocols for the use of this human material were approved by the Ethical Research Committees of the Institute of Psychiatry under the approval numbers 223/00 and 181/02. Anonymised details relating to samples are described in Table 2.1.

Table 2.1. Post mortem NCL and control patient sample details

Samples	Age	Sex	Brain Area
Control 1	2	F	Parietal Cortex
Control 2	16	F	Parietal Cortex
Control 3	20	M	Parietal Cortex
Control 4	22	M	Parietal Cortex
Control 5	25	M	Parietal Cortex
INCL 1	unknown	unknown	Frontal Cortex
INCL 2	unknown	unknown	Frontal Cortex
JNCL 1	23	M	Parietal Cortex
JNCL 2	unknown	unknown	Motor Cortex
JNCL 2.1	unknown	unknown	Frontal Cortex

F= female M= male

2.1.3 *Drosophila*

Drosophila melanogaster was used in Chapter 5 as a model organism to study the role of identified candidates from Chapters 3&4 in modulating the stability of the nervous system *in vivo*. During the second year of my PhD Dr. Giusy Pennetta hosted me in her laboratory (Centre of Integrative Physiology, University of Edinburgh) to learn *Drosophila*-related tecniques to use during my project. Dr Mario Sanhueza and Dr Giusy Pennetta advised and trained me in the *Drosophila* experiments carried out in Chapter 5. Additionally, during a

collaborative visit to OHSU (Portland, Oregon) I was able to observe advanced larval dissection techniques in the laboratory of Dr Mary Logan. More information regarding *Drosophila* stocks and specific experiments can be found in Chapter 5.

2.2 Antibodies

2.2.1 Primary antibodies

Table 2.2 Primary antibodies

Target	Species	Supplier	Cat. number	IHC	WB
ROCK2	Rabbit	Abcam	71598		1:1000
ROCK2	Rabbit	Abcam	125025		1:1000
HIBCH	Rabbit	Abcam	101672	1:500	1:1000
HIBCH	Rabbit	Proteintech	4603-1-AP		1:1000
HADHA	Rabbit	Abcam	54477		1:1000
β-catenin	Mouse	BD bioscience	610153		1:1000
SNCA	Rabbit	Santa Cuz	7011-R		1:500
Calretinin	Rabbit	Abcam	14689		1:1000
H2Ax	Rabbit	Abcam	20669		1:1000
Synaptobrevin	Mouse	Abcam	11104		1:1000
ANXA5	Rabbit	Abcam	14196		1:500
Calreticulin	Rabbit	Thermo	PA3-900		1:1000
UchL1	Mouse	Novus Biologicals	NB300676		1:5000
P4HB	Rabbit	Abcam	137110		1:2000
NDUFS3	Mouse	Abcam	110246		1:2000
Ubiquitin	Mouse	Milipore	MAB1510		1:100
Uba1	Mouse	Abcam	24623		1:5000
Syp	Mouse	Upstate		1:100	
Syp	Mouse	Abcam	8049		1:500
DBN1	Rabbit	Thermo	PA1-20222		1:1000
HRP	Rabbit	Jackson ImmunoResearch	323-005-021	1:500	
Dlg	Mouse	DSHB		1:500	
PSD-95	Rabbit	Abcam	18258	1:1000	1:1000
CS	Rabbit	OriGene	TA310356		1:1000
CFL1	Rabbit	Abcam	42824		1 µg/mL
SYN1	Rabbit	Abcam	64581		1:1000
SPTB2	Rabbit	Santa Cruz	9660		1:1000

2.2.2 Secondary antibodies

Table 2.3 Secondary antibodies

Target	Species	Supplier	Cat. number	IHC	WB
anti-rabbit IgG (H+L) 800CW	Goat	LI-COR Biosciences	926-32211		1:5000
anti-rabbit IRDye 680 RD	Goat	LI-COR Biosciences	926-68071		1:5000
anti-mouse IRDye 680 RD	Donkey	LI-COR Biosciences	926-68072		1:5000
Alexa anti-rabbit	Goat	Jackson immunoresearch	111-545-003	1:500	
Anti-mouse Cy3	Goat	Jackson immunoresearch	115-165-146	1:500	
Bioltynilated anti-rabbit IgG	Goat	Vector Laboratories	BA100	1:1000	

2.3 Immunohistochemistry

2.3.1 Mouse brain

During the first year of my PhD I spent one month in Prof Jonathan Copper's laboratory in Kings College London (KCL), learning his well-established tissue sectioning, processing, immunostaining and quantification techniques for brain samples. IHC in brain tissue sections was used at the beginning of Chapter 3.

Five *Cln3*$^{-/-}$ and five wild-type control mice (WT) at 6.5 months and 12-13 months of age were terminated and brains rapidly removed and immersed for fixation in 4% paraformaldehyde (pH 7.4). After cryoprotection in a solution containing 30% sucrose, 0.05% sodium azide and 50 mmol/L Tris-buffered saline (TBS), frozen coronal sections of 40 µm were cut with Microm HM430 Sliding Microtome (*Microm international*, Walldorf, Denmark) as previously described in (Bible *et al.*, 2004). The IHC protocol used allows quantitative and qualitative comparisons between animal tissues as previously described in (Bible *et al.*, 2012, Tegelberg *et al.*, 2012). Briefly, endogenous peroxidase activity was quenched by immersion of floating sections in 1% H_2O_2 in TBS, followed by blocking non-specific protein binding sites in 15% normal goat serum (NGS) (*Vector laboratories*). The primary antibody Synaptophysin (1:100; Upstate) was incubated overnight at 4°C followed

by incubation with the biotinylated secondary antibody incubated for 2 hours (goat anti-rabbit IgG 1:1000, *Vector Laboratories*). After that, sections were incubated for 2 hours in avidin biotinylated peroxidase-complex incubation (Vectastain® Elite® ABC kit, *Vector laboratories*). Visualization was carried out with 3,3'-diaminobenzidine tetra-hydrochloride (DAB) reaction catalysed by H_2O_2 (*Sigma*). Finally, stained sections were mounted onto Super-frost plus slides and air-dried overnight at room temperature, cleared in xylene and coverslipped with DPX.

2.3.2 *Drosophila* larvae neuromuscular junctions

Drosophila were used in Chapter 5. To study the synaptic morphology in *Drosophila*, wandering third instar larvae were dissected and processed as previously described in (Pennetta *et al.*, 2002). Dissected larval NMJs (fillet preparation) were fixed in Bouin's fixative (15:5:1 mixture of saturated picric acid, 37% formaldehyde and glacial acetic acid) for 10 min, washed extensively in PBT (PBS +0,1% TritonX-100), blocked in 10% normal goat serum in PBT for 2 hours. Next, *Drosophila* tissues were incubated with the primary antibody overnight at 4°C. Primary antibodies were rabbit anti-HRP antibodies (1:500, *Jackson ImmunoResearch Laboratories*) and mouse anti-Dlg monoclonal antibody (1:500, *Developmental Studies Hybridoma*). On the following day, larval tissues were respectively washed for 2 hours with PBT and incubated in secondary antibodies for 2 more hours. Secondary antibodies were alexa anti-rabbit and anti-mouse Cy3 (1:500, *Jackson ImmunoResearch Laboratories*). After secondary antibody incubation, larvae NMJ were washed again in PBT 2 hours and mounted in vectashield mounting media on superfrost slides. Once slides were dried, they were imaged using conventional fluorescence and confocal microscopy (see section 2.9 Imaging).

2.4 Synaptosome preparation

Mouse tissue dissections and synaptosome preparation for initial iTRAQ and label free proteomics was carried out by Dr. Thomas Wishart before the start of my PhD. Brains from each corresponding genotype were harvested and briefly chilled in ice cold ACSF (125mM NaCl, 26mM NaHCO3, 25mM glucose, 2.5mM KCl, 1.25mM NaH2PO4, 1mM CaCl2, 4mM MgCl2) before regional microdissection. Thalamus, cortex (predominantly pre-/frontal) and hippocampus were microdissected bilaterally (Kielar *et al.*, 2009, Wishart *et al.*, 2014,

Wishart *et al.*, 2010) and immediately processed for "crude" synaptosome production as previously described (Wishart *et al.*, 2010, Wishart *et al.*, 2014, Wishart *et al.*, 2007). Briefly, microdissected bilateral thalami, cortex and hippocampi were homogenised in an ice-cold isotonic sucrose solution (0.32 M sucrose, 1 mM EDTA, 5 mM Tris-HCl, pH 7.4). The homogenate was centrifuged in a continuously chilled (4 ºC) fixed-angle rotor at 900g for 10 min and the supernatant (S1) was collected. The pellet (P1) was resuspended in sucrose solution and centrifuged again at 900g for 10 min in an effort to free any "trapped" synaptosomes and thus increase the yield. The resulting pellet (P1') containing 'non-synaptic' material (synapse depleted) i.e. white matter tracts, nuclei, microglia etc. was immediately frozen and stored for later use. The resulting supernatant (S1') was combined with S1 and centrifuged in a continuously chilled (4 ºC) fixed angle rotor at 20,000g for 20 min. The supernatant (S2) was discarded and the pellet (P2) containing synaptosomes was then kept and stored at -80ºC for future protein extraction.

For *post mortem* cortical human samples, a portion of the total sample was obtained from frozen tissue (stored at -80 °C) and transferred into an eppendorf tube containing cold isotonic sucrose solution. The procedure was followed as described above. Protein extracts from synaptic and "non-synaptic" fractions were blotted for synaptic and nuclear markers to validate the enrichment of both fractions (Fig 3.11, Chapter 3).

2.5 Protein extraction

Resuspended brain homogenate, synaptosomes, muscle or blood were homogenised in each corresponding buffer (iTRAQ/label-free/RIPA) depending on the purpose of the extraction (iTRAQ/label-free proteomics or QWB) and 1% protease inhibitor. Unless otherwise stated, samples were spun at 20,000g for 20 minutes at 4°C and the supernatant was aspirated and collected as extracted sample. Pellets and extracted samples were stored at -80°C for subsequent examination. Extracted samples concentration was determined using a BCA assay (*Thermo*).

2.6 Proteomics

Although proteomic analysis was carried out as as specified below I was able to spend a week at the Dundee "Fingerprints" proteomic facility. In order that I should better understand the sample handling and processing workflows and the subsequent limitations in terms of analysis and data interpretation. This visit was under the supervision of Douglas Lamont and Amy Tavendale. Processed mice synaptosomes samples through the FASP and label free proteomic workflow. Additionally, I attended a two-day course specifically arranged by Non-Linear Dynamics for the training of the Wishart lab and "Fingerprints" staff in the use of *Progenesis LC MS-MS* software for label free data handling.

2.6.1 ITRAQ

Isobaric tags for relative and absolute quantitation (iTRAQ) proteomics was used in Chapters 3 & 6. ITRAQ was carried out by Dr. Heidi Fuller (Keele University) in a similar way to other studies (Fuller *et al.*, 2010). Four *Cln3*$^{-/-}$ and four control mice (WT) at 12-13 months were used for the proteomics and biochemical experiments. Protein extracts from thalamic, hippocampal, cortical synaptosomes and muscle were prepared for iTRAQ proteomics.

Sample preparation for mass spectrometry analysis*:* Reduction, alkylation and digestion steps were performed using the reagents and according to the recommendations in the iTRAQ labelling kit (*AB Sciex*). The extracts were diluted with 50mM TEAB so that the urea concentration was less than 1M, before the addition of trypsin and overnight incubation at 37°C. The digests were then dried down in a vacuum centrifuge and iTRAQ labelling was carried out according to the instructions in the iTRAQ labelling kit. Each tag was incubated with 85µg of total protein (as determined by a Bradford protein assay).

iTRAQ-labelled peptides were pooled and made up to a total volume of 2.4mL in SCX buffer A (10mM phosphate, pH3 in 20% acetonitrile (*Romil, UK*). The pooled peptides (2.4mL) were then separated by strong cation-exchange chromatography (SCX) using a polysulfoethyl A column, 300A, 5uM (PolyLC) at a flow rate of 400ul/minute. Following sample injection, the column was washed at with SCX buffer A until the baseline returned. The gradient was run as follows: 0-50% SCX buffer B (10mM phosphate, 1M NaCl, pH3 in 20% acetonitrile) over 25 minutes followed by a ramp up from 50% to 100% SCX buffer B

over 5 minutes. The column was then washed in 100% SCX buffer B for 5 minutes before equilibrating for 10 minutes with SCX buffer A. Fractions were collected (400ul) during the elution period and dried down completely in a vacuum centrifuge.

Protein identification and quantification by mass spectrometry: The iTRAQ tryptic peptide fractions were each resuspended in 35µl of RP buffer A (2% acetonitrile, 0.05% trifluoroacetic acid (TFA) in water (Sigma Chromasolv plus). Prior to mass spectrometry analysis, fractions were first separated by liquid chromatography (Dionex Ultimate 3000) on a Pepmap C18 column, 200µm x 15cm (*LC Packings*) at a flow rate of 3µl/minute. Fractions were injected by full-loop injection (20µl) and the order of loading was randomized to minimise effects from carry-over. The eluants used were: A. 0.05% TFA in 2% acetonitrile in water and B. 0.05% TFA in 90% acetonitrile in water. The gradient was run as follows: 10 minutes isocratic elution pre-run at 100% A, followed by a linear gradient from 0-30% B over 100 minutes, followed by another linear gradient from 30%-60% over 35minutes. The column was then washed in 100% B for a further 10 minutes, before a final equilibration step in 100% A for 10 minutes. During the elution gradient, sample was spotted at 10 second intervals using a Probot (*LC Packings*) with α-cyano-4-hydroxycinnamic acid (CHCA) at 3mg/ml (70% MeCN, 0.1% TFA) at a flow rate of 1.2µl/min.

Both MS and MS/MS analysis was performed on the fractionated peptides using an Applied Biosystems 4800 MALDI TOF/TOF mass spectrometer. The mass spectrometer was operated under control of 4000 Series Explorer v3.5.2 software (*Applied Biosystems*). A total of 1000 shots per MS spectrum (no stop conditions) and 2500 shots per MS/MS spectrum (no stop conditions) were acquired. The following MS/MS acquisition settings were used: 2KV operating mode with CID on and precursor mass window resolution set to 300.00 (FWHM). Peak lists of MS and MS/MS spectra were generated using 4000 Series Explorer v3.5.2 software and the following parameters were used after selective labelling of monoisotopic mass peaks: MS peak lists: S/N threshold 10, Savitzky Golay smoothing ((3 points across peak (FWHM)), no baseline correction, MS/MS peak lists: S/N threshold 14; smoothing algorithm: Savitzky Golay, smoothing (7 points across peak (FWHM)).

An automated database search was run using GPS Explorer v3.6 (*AB Sciex*). MASCOT was used as the search engine to search the NCBI non-redundant database using the following search parameters: precursor ion mass tolerance of 150ppm, MS/MS fragment ion mass

tolerance of 0.3Da, iTRAQ fragment ion mass tolerance of 0.2Da, the taxonomy was selected as rodents, oxidation of methionine residues were allowed as variable modifications and N-term (iTRAQ), lysine (iTRAQ) and MMTS modification of cysteine residues were set as fixed modifications. Quantification of the iTRAQ peptides was performed using the GPS Explorer v3.6 software. The identification criterion was at least 2 peptides by MS/MS with the most stringent search settings (peptide rank 1 and total ion score confidence intervals of at least 95%). iTRAQ Ratios were normalized using the following formula: iTRAQ Ratio = Ratio / (median iTRAQ Ratio of all found pairs) that was applied in GPS Explorer software.

2.6.2 Label-free

Label free proteomics was used in Chapters 4 & 6 to study the molecular changes happening throughout the time-course of disease progression in *Ppt1*$^{-/-}$ mice vs. controls. Label free proteomics was carried out on synaptosome preparations from thalamus and cortex (Chapter 4) and in limb muscle protein extractions (Chapter 6) as represented in Fig. 2.1. Each individual sample group was run in 3 replicates by Dr. Abdel Atrih (Proteomics Fingerprint facility, University of Dundee), before the start of my PhD. This experiment was carried out similarly to now published studies (Aghamaleky Sarvestany *et al.*, 2014, Mutsaers *et al.*, 2013).

FASP processing of samples: An equivalent of 1.5 mg of proteins from each sample pool were reduced with 20 mM DTT and samples are then processed using FASP protocol (Wisniewski *et al.*, 2009) with some modifications. After removal of SDS with 8 M urea, filters were washed 3 times with 100 mM Tris-HCL pH 8 then another 3 times with 100 mM triethyl ammonium bicarbonate (TEAB). Proteins on the filters were then digested twice at 30ºC with trypsin (2x6.25 µg), first overnight and then for another 6h in a final volume of 200 µl. Resulting peptides were desalted using C18 solid phase extraction cartridge (*Empore, Agilent technologies*) and dried prior to LC-MS analysis.

LC-MS analysis: Analysis of peptides was performed on an LTQ Velos-Pro orbitrap (*Thermo Scientific*) mass spectrometer coupled with a Dionex Ultimate 3000 RS (*Thermo Scientific*). LC buffers were the following: buffer A (2% acetonitrile and 0.1% formic acid in Milli-Q water (v/v)) and buffer B (80% acetonitrile and 0.08% formic acid in Milli-Q water (v/v). Samples were resuspended in 50 µL 1% formic acid and aliquots of 3.5 µL of each sample was loaded at 5 µL/min onto a trap column (100 µm × 2 cm, PepMap nanoViper C18 column, 5

μm, 100 Å, *Thermo Scientific*) equilibrated in 98% buffer A. The trap column was washed for 3 min at the same flow rate and then the trap column was switched in-line with a *Thermo Scientific*, resolving C18 column (75 μm × 50 cm, PepMap RSLC C18 column, 2 μm, 100 Å). The peptides were eluted from the column at a constant flow rate of 300 nl/min with a linear gradient from 98% buffer A to 40% buffer B in 90 min, and then to 98% buffer B by 92 min. The column was then washed with 98% buffer B for 10 min and re-equilibrated in 98% buffer A for 25 min. Each of the 8 samples were run in triplicate using *LTQ-Orbitap Velos* in data dependent mode. A scan cycle comprised MS1 scan (m/z range from 335-1800) in the velos orbitrap followed by 15 sequential dependant MS2 scans (the threshold value was set at 5000 and the minimum injection time was set at 200 ms) in LTQ with collision induced dissociation. The resolution of the Orbitrap Velos was set at to 60,000. To ensure mass accuracy, the mass spectrometer was calibrated on the first day that the runs are started.

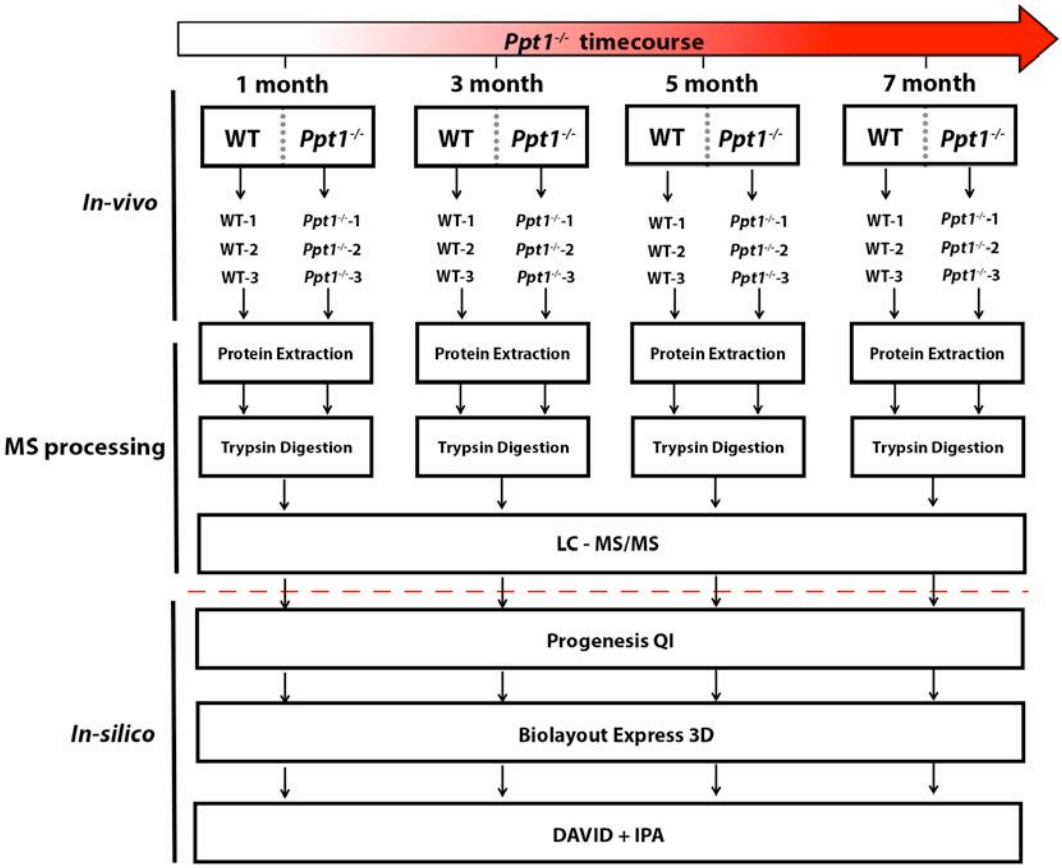

Fig. 2.1. Experiment design workflow of all the label-free proteomics datasets. Protein extracts from thalamic and cortical synaptic fractions (Chapter 4) and muscle (Chapter 6) were processed following the "*In vivo*", "MS processing" and "*In silico*" steps represented here.

2.7 Quantitative fluorescent western blotting (QWB)

QWB was used to validate the results from the proteomic and bioinformatics comparative analyses in mice and human tissue in Chapters 3, 4 & 6. Samples were denatured in NuPage® LDS Sample buffer 4X (*Invitrogen*, UK) at 98ºC and 10-50 µg of protein loaded and run on 4-12% Bis-Tris gel (*Invitrogen*). Accuracy of loading and protein estimation was confirmed by total protein analysis of Instant Blue (*Expedeon*) stained gels [as previously described (Eaton *et al.*, 2013)]. Protein transfer to a polyvinylidene fluoride (PDVF) membrane was carried out using the I-Blot® transfer system (Invitrogen, UK). Membranes were incubated with Odyssey blocking buffer (Li-Cor) prior to incubation with primary antibodies directed against the protein of interest, overnight at 4ºC (Table 2.2). Secondary antibodies were applied for 90 minutes at room temperature prior to washing with PBS (Table 2.3). Visualisation and quantification was carried out with the LI-COR Odyssey® scanner and Image Studio software (*LI-COR Biosciences*). Blots (and gels) were imaged using an Odyssey Infrared Imaging System. Scan resolution of the instrument ranges from 21 to 339 µm, and in this study blots (and gels) were imaged at 169 µm. Quantification was performed on single channels with the analysis software provided as previously described (Wishart *et al.*, 2014, Eaton *et al.*, 2013, McGorum *et al.*, 2015).

2.8 Bioinformatics

2.8.1 *Progenesis*

Progenesis was used to analyse the Ppt1 label free time-course proteomics data from Chapter 4 & 6. At the beginning of my PhD I attended a personalized course given by Martin Wells about the use of *Progenesis* to analyse our proteomics datasets. Raw label-free proteomic data from each brain area/muscle was imported into *Progenesis LCMS* for differential analysis and identification of peptides followed by quantification of relative ion abundance of peptides and corresponding proteins. Following alignment of all MS data, preliminary filtering of peptides (only those with power > 0.8, fold-change > 2, p value < 0.05). Furthermore, we only exported those ion peptides with stronger signals (which have a rank of at least 3). Peptide information was then exported from *Progenesis* for subsequent identification of individual peptide sequences using mouse database via *Mascot Search Engine (V2.3.2).* Enzyme specificity was set to that of trypsin, allowing for cleavage N-

terminal to proline residues and between aspartic acid and proline residues. Other parameters used were as follows. (i) Variable modifications: methionine oxidation, methionine dioxidation, protein N- acetylation, gln, pyro-glu. (ii) Fixed modifications: cysteine carbamidomethylation. (iii) MS/MS tolerance: FTMS- 10 ppm, ITMS- 0.6 Da. (iv) Minimum peptide length: 6. (v) Maximum missed cleavages: 2. (vi) False discovery rate: 1%. A cutoff score of >34 was used based on Mascot probability threshold of 0.05 that the observed hit is a random event. As an indication of identification certainty, the false discovery rate for peptide matches above identity threshold was set at 1%.

Mascot-generated data were then reimported into *Progenesis* for subsequent protein expression comparison and filtering. PCA was generated in order to confirm the correct distribution of the data as well as the reproducibility of technical replicates. Next, each time-point (1, 3, 5 and 7 months) was analysed as an independent 2-way comparison (*Ppt1*$^{-/-}$ vs. WT). Further filtering was applied to each individual time-point (ie. >2 unique peptides, p-value<0.05 and >1.2 or >2 Fold-change) in order to examine the changes occurring in each individual time-point.

2.8.2 *DAVID*

The *Database for Annotation, Visualization and Integrated Discovery* (*DAVID*) software (available at http://david.abcc.ncifcrf.gov) provides a relatively comprehensive set of functional annotation tools for large data set interpretation (Huang *et al.*, 2009b, Huang *et al.*, 2009a). One the one hand, *DAVID* was used to obtain an indication of the level of sample enrichment afforded through the process of synaptosome production inputting un-filtered mass spectrometry data as previously used in (Amorim *et al.*, 2017). On the other hand, it was also used to characterize the functions associated to the protein clusters from *BioLayout* (see below). *DAVID* was used in Chapters 3&4.

2.8.3 *BioLayout Express*

BioLayout software was used for the analysis of synaptic proteomic data in order to correlate their expression profile to the differentially vulnerable synaptic population across brain regions (Chapter 3) or time-points (Chapter 4) (Theocharidis *et al.*, 2009, Enright *et al.*, 2002). *BioLayout* was also used to track proteins through disease progression in Chapter 6 in order to identify muscle biomarkers in *Ppt1*$^{-/-}$ mice. *BioLayout* incorporates a complex

pattern recognition algorithm which groups protein data based only on expression profile. It allows the visualization and graphing of expression trends of co-expressed proteins to allow better characterization and understanding of large complex datasets (Theocharidis *et al.*, 2009). This software was developed by Prof Tom Freeman's research group at the Roslin Institute (The University of Edinburgh) and further information on the use of this program and free access can be found here: http://www.biolayout.org. *BioLayout* generates a three dimensional representation of the data in where each sphere represents an individual protein and its colour and proximity to its neighbour indicates the similarity in protein expression. Clusters (groupings of proteins delineated by colour) can be further analysed for cell type or functional association with other *in silico* tools such as *DAVID* enrichment tool (see above).
I was trained by Dr. Tom Freeman on the application of *BioLayout* and the interpretation of its outputs at a course run within the Roslin Institute.

2.8.4 *Ingenuity Pathway Analysis (IPA)*

IPA application (*Ingenuity Systems*) is used to obtain further insight into potential cellular pathways that may be perturbed in our proteomic datasets. *IPA* was used, as previously described (Wishart *et al.*, 2010, Wishart *et al.*, 2014, Wishart *et al.*, 2007, Wishart *et al.*, 2012). *IPA* dynamically generates networks of gene, protein, small molecule, drug, and disease associations on the basis of "hand-curated" data held in a proprietary database. More than 90% of the information in this database is "expert-curated" and is drawn from the full text of peer reviewed journals. Less than 10% of interactions have been identified by techniques such as natural language processing.
Canonical pathways function was used for the identification of known pathways within this dataset. IPA contains a library of biological pathways published in the literature that are ranked by significance of the association between the dataset and the canonical pathway. The significance is defined by two parameters: (1) the ratio of the number of proteins from the dataset that map on the pathway divided by the total number of genes within the canonical pathway and, (2) a P value calculated using Fischer's exact test that determines if the probability of association between proteins in the dataset and in the pathway are due to chance. Prediction activation scores (z-score) is a statistical measure of the match between an expected relationship direction and the observed protein expression. Positive z-score indicates activation (orange) and negative z-score indicate inhibition (blue) (Savli *et al.*, 2008). 1.2 Fold-change threshold filter was applied in *IPA* to each dataset analysed and only

experimentally observed interactions were selected for each analysis. Further information on the computational methods implemented in IPA can be obtained from *Ingenuity Systems*. Available at http://www.ingenuity.com/.
To learn to use *IPA*, I attended an 2-day advanced course in London during the first year of my PhD.

2.9 Imaging

Mouse brain Immunohistochemistry: Micrographs were taken with Leica DMRB x5/0.12 objective and AxioCam HRC Zeiss from the following brain regions: 1. The thalamic nuclei ventral posterior medial/ventral posterior lateral thalamic nucleus (VPM/VPL) and the dorsal lateral geniculate nucleus (LGNd); 2. Their respective cortical projections in the primary somatosensory cortex (S1BF) and primary visual cortex (V1) respectively, and 3; the hippocampal stratum radiatum and stratum oriens (See Fig 1A). Immunoreactivity measurements were carried out using a thresholding image analysis in *ImageJ* (National Institute of Health, Bethesda, MD), USA), as previously described (Pontikis *et al.*, 2004, Pontikis *et al.*, 2005, Bible *et al.*, 2004). Thirty non-overlapping images (x40) were taken, on three consecutive sections, through the brain areas described above. All parameters including lamp intensity, video camera setup and calibration were kept constant throughout image capturing.

***Drosophila* NMJ:** Dr Anisha Kubasik-Thayil and Dr Giusy Pennetta assisted in taking *Drosophila* NMJ confocal micrographs. Images were captured using a laser scanning confocal microscope (Nikon A1R) with 60X objective lens (Plan APO OIL NA=1.4) . Size of the images are set to 1024 x 1024 pixels (with pixel size 200nm) and z step size 500nm. Frame rate of the acquisition was 0.5 frames per second.

***Drosophila* eye images:** For the HIBCH and HADHA experiments fruit fly eye images were photographed with a Nikon D5100 camera attached to a SZX9 Nikon stereomicroscope. For the the rest of experiments, eye images were taken with an AxioCam ERc 5s Rev.2 attached to a Zeiss Stemi 305 trino stereomicroscope. Images were analyzed with *ImageJ* software (National Institute of Health, Bethesda, MD, USA) as previously described in (Sanhueza *et al.*, 2015).

2.10 Data collection and statistical analyses

All the data including proteomics raw data was exported/recorded and stored in Excel spreadsheets. QWB data was analysed using Image studio software as per manufacture guidelines and as previously described (Eaton *et al.*, 2013, McGorum *et al.*, 2015, Wishart *et al.*, 2014). Data was graphed and statistical comparisons for IHC thresholding, QWB protein intensity and *Drosophila* eye surface area quantification were carried out using *GraphPad Prism* as previously described (Wishart *et al.*, 2010, Sanhueza *et al.*, 2015). For QWB and IHC, Student T test was applied.

For *Drosophila* eye quantifications when comparing more than 3 samples a one-way ANOVA was carried out, followed by Tukey's multiple comparison test as a post-hoc when a significant difference was found in the ANOVA. When comparing 2 samples Student T test was applied. P values <0.05 were considered to be statistically significant for all analyses (*P<0.05; **P<0.01; ***P<0.001; ns (not significant) >0.05).

Statistical analysis of proteomic data was automatically carried out by *MASCOT* and *Progenesis*. P & Benjamini values to determine enrichment were automatically calculated by *DAVID* software (see above and http://david.abcc.ncifcrf.gov). P values/Fishers exact tests and z-scores for pathway and networking analysis were automatically determined by *IPA* (see above and http://www.ingenuity.com/).

Heatmaps representing the differentially expressed proteins across brain regions and/or time-points were produced using "*R*" (http://www.R-project.org) (R Development Core Team, 2008).

BioLayout display was generated using pearson correlation and Marckov clustering algorithm (van Dongen, 2000, Enright *et al.*, 2002).

Chapter 3

Characterisation of differentially vulnerable synaptic populations at an early disease stage using *Cln3*$^{-/-}$ mice as a model

3.1 Introduction

Our understanding of the reasons why specific synaptic populations are so vulnerable to such a broad range of neurodegenerative stimuli and the mechanisms that govern their stability, remains in its infancy (Wishart *et al.*, 2006, Wishart *et al.*, 2012, DeKosky *et al.*, 1990, Selkoe, 2002, Forno, 1996, Kielar *et al.*, 2009, Virmani *et al.*, 2005, Partanen *et al.*, 2008, Koch *et al.*, 2011, Cooper, 2010) (See Chapter 1. General Introduction). Some attempts have been made in order to shed light into the mechanisms regulating synaptic degeneration.

Our lab has been developing novel workflows based on identifying potential regulators of synaptic and neuronal stability using high-throughput proteomics on rodent models. Candidates identified in these screens are then tested in lower order organisms such as *Drosophila* and Zebrafish to study their role in modulating neuronal stability *in-vivo* (Wishart *et al.*, 2014, Wishart *et al.*, 2012, Fuller *et al.*, 2016). Studies using iTRAQ proteomics in synapses isolated from an injury-induced degeneration mouse model, found 13 individual proteins whose missexpression was able to modulate axonal-degeneration *in-vivo* (Wishart *et al.*, 2012). Later studies also by Wishart el al., attempted to do a similar study, but in this case, using mouse models of SMA. Proteomics carried out in isolated

synapses from SMA mouse model followed by *in silico* analyses, identified the dysruption of ubiquitination pathways. Targeting such pathways they were capable of rescuing not only the synaptic phenotype, but also the whole neuromuscular system in *Drosophila* and mouse models of SMA (Wishart *et al.*, 2014). Moreover, by tracking these molecular cascades further upstream, they we able to identify molecular modifiers capable of affecting disease progression in every organ system examined (Powis *et al.*, 2016).

In this project, we wanted to elucidate molecular regulatos of brain synapses and shed light into the reasons why the distal compartments of neurons are so vulnerable to a broad range of neurodegenerative stimuli. Moreover, we wanted to consider the differential vulnerability across brain areas (See Chapter 1. General Introduction). In order to do so we used a *Cln3*$^{-/-}$ mice model of juvenile NCL, (Mitchison *et al.*, 1999). Although neuronal loss is widespread by the end of the disease (Mitchison *et al.*, 1999, Kuhl *et al.*, 2013), there is a differential vulnerability across brain regions and their resident cell types/subcellular compartments. This differential degenerative progression follows the same pattern in the vast majority of NCL mouse models: during pre-symptomatic stages there is an early selectivity for relay neurons within the thalamic nuclei followed by the corresponding cortical areas (Pontikis *et al.*, 2005, Kielar *et al.*, 2007, Partanen *et al.*, 2008, Mitchison *et al.*, 1999, Kuhl *et al.*, 2013, Pontikis *et al.*, 2004)(Weimer JM, 2006 #81), as well as GABAergic hippocampal interneurons and Purkinje neurons (Mitchison *et al.*, 1999, Pontikis *et al.*, 2004). For more information, see General Introduction (Chapter 1).

Therefore, mouse models of CLN3 disease represent a useful tool to study the molecular pathways underlying differential vulnerability across brain areas. In this chapter, we aimed to define the molecular regulators of both synaptic stability and vulnerability using *Cln3*$^{-/-}$ mice (Mitchison *et al.*, 1999). We initially characterized differential patterns of synaptic pathology in *Cln3*$^{-/-}$ mice (Mitchison *et al.*, 1999) of two different time-points. This enabled the subsequent application of high-throughput proteomics followed by a combination of *in silico* tools in order to map the molecular fingerprint of differentially vulnerable biochemically-isolated synaptic populations. We identified multiple cascades correlating with synaptic vulnerability and described valine degradation and rho signalling as two promising pathways to target in subsequent *in vivo* studies (Chapter 5). Finally, we identified regulators of synaptic vulnerability and degeneration in the context of NCL, which are also likely conserved in their expression across other neurodegenerative conditions, where synapses are

an early pathological target (Wishart *et al.*, 2012). These results therefore open a window for further investigation into common molecular therapeutic targets and strategies for novel interventions across a range of neurodegenerative conditions during early disease stage.

3.2 Materials and methods

3.2.1 Animals and tissue harvesting

Cln3 null mice (*Cln3*$^{-/-}$) and *C57BL/6* littermates (WT) (Mitchison *et al.*, 1999) were used in this Chapter for IHC, proteomics and QWB analyses. Human *post mortem* cortical tissue was used for synaptosome production and subsequent QWB examination. Please refer to General materials and methods (Chapter 2) for more details.

3.2.2 Immunohictochemistry (IHC)

IHC using synaptophysin primary antibody (Syp) was performed with the objective to confirm the expected vulnerability pattern across distinct synaptic populations in *Cln3*$^{-/-}$ mice. Details of the methodology are described in General materials and methods (Chapter 2).

3.2.3 Synaptosome production

Once we confirmed the pathological pattern of synaptic vulnerability across brain areas in the *Cln3*$^{-/-}$ mice, we wanted to examine the proteomic composition of synapses in these differentially vulnerable brain areas (cortex, hippocampus and thalamus) and in cortical *post mortem* JNCL patients. To do so, synaptic enriched fractions were produced. Brains were harvested from six *Cln3*$^{-/-}$ and wild-type (WT) control mice at 13 months old and *post mortem* human cortical samples were processed for synaptosome production as previously described (Wishart *et al.*, 2007, Wishart *et al.*, 2014, Wishart *et al.*, 2012) . Please refer to General materials and methods (Chapter 2) for more details.

3.2.4 Protein extraction

For iTRAQ proteomics, crude synaptosomes were resuspended and homogenised in 4 volumes (w/v) of 6M Urea, 2M thiourea, 2% CHAPS, 0.5% SDS and 5% protease inhibitor cocktail (Roche) using a pellet pestle (50 strokes with the pestle, left on ice for 10mins, followed by another 50 strokes with the pestle). The extracts were sonicated briefly and left

on ice for 10 minutes, followed by centrifugation at 13,000 x g for 10 minutes at 4°C to pellet any insoluble material. For mass spectrometry analysis, an aliquot of extracted proteins from each mouse (n=6) and each brain region was pooled and precipitated in 6 volumes of ice cold acetone overnight at -20°C. The remaining extracts were stored (un-pooled) at -80°C for quantitative Western blotting validation (QWB). The acetone precipitates were pelleted by centrifugation at 13,000 x g for 10 minutes at 4°C and the supernatant was carefully remove and discarded. The pellets were resuspended in 6M Urea in 50mM TEAB. The protein concentration in each sample was determined using a Bradford protein assay.

Human synaptosomes were extracted in SDT lysis buffer containing 100 mM Tris-HCl (pH 7.6), 4% (W/V) Sodium dodecyl sulphate and 1% protease inhibitor cocktail (Roche). Please refer to General materials and methods (Chapter 2) for more details.

3.2.5 iTRAQ proteomics

Protein extracts from synaptosomes produced from *Cln3*$^{-/-}$ and wild-type (WT) controls mice at 13 months (cortex, hippocampi and thalamus) were processed for iTRAQ proteomics by Dr. Heidi Fuller (Keele University). Please refer to General materials and methods (Chapter 2) for iTRAQ methodology.

3.2.6 Quantitative fluorescent western blotting (QWB)

15 μg of protein was loaded for all the QWB within this chapter, except for the detection of ROCK2 in human synaptosome samples were gels were loaded with 50 μg of protein. QWB methodology and antibodies used can be found in the General materials and methods section (Chapter 2).

3.2.7 *In silico* analyses

Our collaborator Dr. Heidi Fuller provided raw iTRAQ proteomic data for its analyses. I utilized a combination of bioinformatics tools each one for a different purpose and used the identified pattern of synaptic pathology established by IHC, as a guide to analyzing and interpreting the data.

3.2.7.1 *Ingenuity pathway analyses (IPA)*

IPA was used at two different stages of the proteomic analyses. Firstly, it was used to investigate which canonical pathways were disrupted across cortex-hippocampus-thalamic synapses (following the described vulnerability pattern). To do so, common proteins which were identified by more than 2 peptides across the three brain areas (709 proteins) where inputed for comparative analyses. Secondly, *IPA* was used to analyse the thalamic synaptic dataset in more detail to further characterize the most vulnerable synaptic population. Please refer to General materials and methods (Chapter 2) for more details.

3.2.7.2 *BioLayout Express*

BioLayout was used to further define the proteins which pattern of expression correlated to synaptic vulnerability accross cortical, hippocampal and thalamic synaptic populations. Please refer to General materials and methods (Chapter 2) for more details.

3.2.7.3 *DAVID*

DAVID was used to investigate the basic biological functions of proteins showing expression pattern correlating to synaptic vulnerability (clusters identified using *BioLayout*, see above) and as a quality control to analyse the level of enrichment of synaptic terms from thalamic synaptic enriched fractions. Please refer to General materials and methods (Chapter 2) for more details.

3.3 Results

3.3.1 Quantitative immunohistochemistry identifies differential rates of synaptic pathology between brain regions in *Cln3*$^{-/-}$ mice

Although the spatio-temporal pattern of neuron loss in *Cln3*$^{-/-}$ mice has already been studied (Pontikis *et al.*, 2004, Kuhl *et al.*, 2013), little is known about the progression of synaptic pathology across differentially vulnerable brain regions. Studies in other NCLs using *Ppt1*$^{-/-}$, *Cln6*$^{-/-}$ or *CtsD*$^{-/-}$ mice have revealed progressive synaptic loss starting in the thalamus and following later in corresponding cortical areas (Partanen *et al.*, 2008, Kielar C, 2009). Hippocampal structures seem to be also affected early, although to a lesser extent than seen in the thalamus (Kuhl *et al.*, 2013).

To investigate whether a similar pattern of synaptic pathology might be present in *Cln3*$^{-/-}$ mice we studied the expression of the presynaptic marker synaptophysin (Syp; as previously described in (Kielar *et al.*, 2009)) in three brain regions that exhibit different degrees of neuronal vulnerability (Fig. 3.1) using quantitative immunohistochemistry at 6.5 and 13 months (as guided by Prof. Jonathan Cooper; see methods – Fig. 3.2 and Fig. 3.3). The three brain regions studied were: 1. Thalamus – ventral posteromedial/ventral posterolateral nuclei (VPM/VPL) and lateral geniculate nucleus (LGNd); 2. The corresponding cortical target regions in the primary somatosensory barrel field (S1BF) and primary visual areas (V1) respectively, and 3; Hippocampus- stratum radiatum and stratum oriens (Fig. 3.1).

At 6.5 months no significant changes in Syp expression were detected between *Cln3*$^{-/-}$ and control mice in any of the brain regions studied (Fig. 3.2). However, by 13 months, some differences between genotypes were apparent (Fig. 3.3). Similar to mouse models of other NCLs, thalamic nuclei demonstrated greater synaptic loss at 13 months as indicated by the lower Syp immunoreactivity to synaptophysin in *Cln3*$^{-/-}$ vs. controls. Hippocampal structures were also affected, although as predicted, the difference in Syp immunoreactivity between genotypes in both hippocampal subfields was much less than in thalamic nuclei. In contrast, cortical regions such as S1BF and V1 (corresponding to the thalamic nuclei VPM/VPL and LGNd) showed no statistical differences between genotypes in Syp immunoreactivity at 13 months (Fig. 3.3).

Thus, the synaptic pathology followed a similar pattern to that previously reported in mouse models of other forms of NCL (Partanen *et al.*, 2008, Kielar *et al.*, 2009), with the thalamus being the most affected region, followed by the hippocampus, whereas cortical synapses were still unaffected at this stage of disease. We would categorize these synaptic alterations as being mild at 13 months, as the synaptic loss quantified here is less than 10% (9.57% relative to controls).

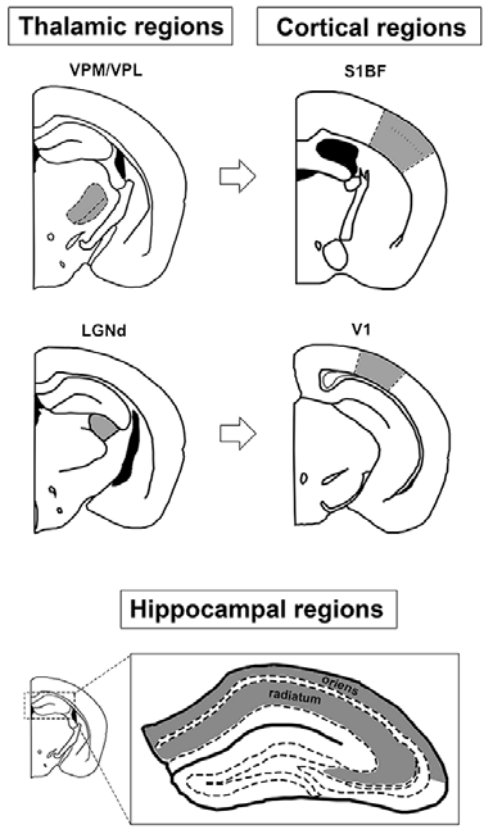

Fig. 3.1. Brain region schematic. Brain areas measured are shown in grey. Thalamic regions includes the ventral posterior medial/ventral posterior lateral thalamic nucleus (VPM/VPL) (up left) and the dorsal lateral geniculate nucleus (LGNd) (down left); their respective cortical projections in the primary somatosensory cortex (S1BF) (up left) and primary visual cortex (V1) respectively (down left); hippocampal regions measured were the stratum radiatum and stratum oriens from CA1-3 (bottom).

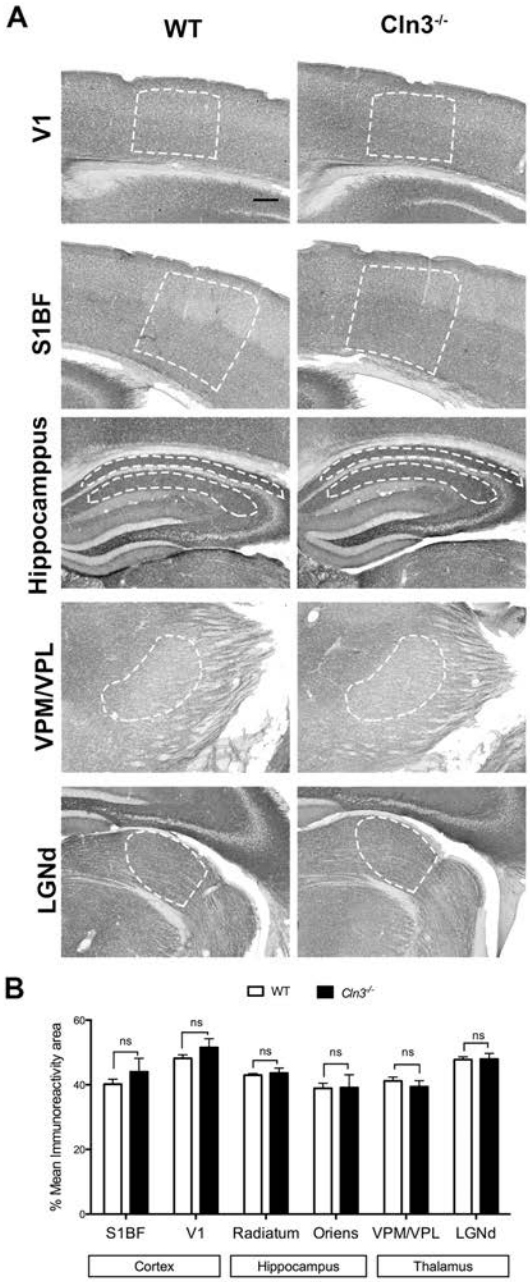

***Fig. 3.2. Pre-synaptic immunostaining detects no pathological change at 6.5 months across brain regions in* Cln3$^{-/-}$.** **A**. Representative photomicrographs of coronal sections of thalamic regions includes the ventral posterior medial/ventral posterior lateral thalamic nucleus (VPM/VPL) and the dorsal lateral geniculate nucleus (LGNd); their respective cortical projections in the primary somatosensory cortex (S1BF) and primary visual cortex (V1) respectively; hippocampal stratum radiatum and stratum oriens from CA1-3 immunostained with synaptophysin and a histogram showing its corresponding quantification based on are of Syp immunoreactivity a at 6.5 months in control and *Cln3*$^{-/-}$ mice. **B**. Histogram indicating measurements of immunoreactivity area for the corresponding brain regions at 6.5 months in WT controls and *Cln3*$^{-/-}$ mice. No significant changes were detected in any of the brain regions measured. Mean ± SEM; ns P>0.05. Student T test, 5 mice per each genotype and time-point were used, Scale bar in panel A = 200 um.

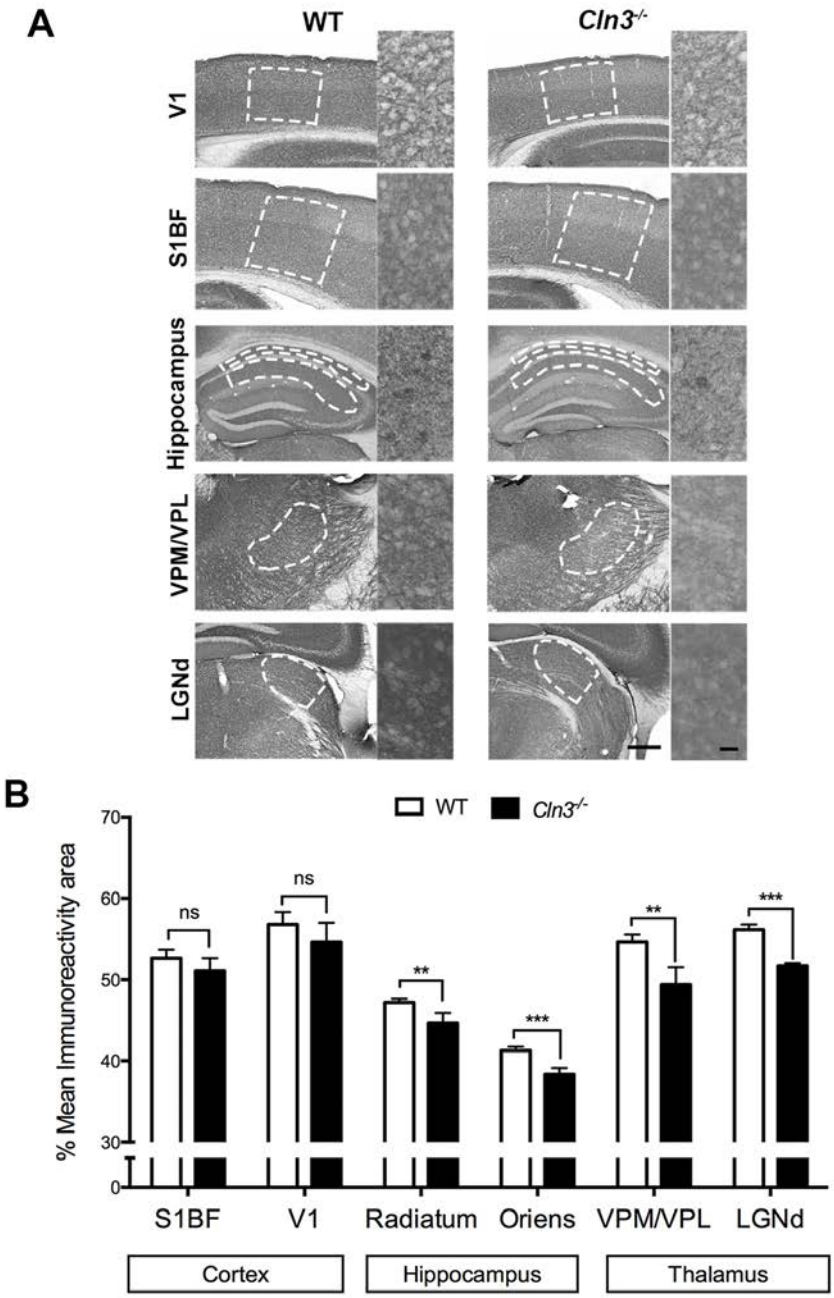

***Fig. 3.3. Spatio-temporal synaptic loss study in* Cln3$^{-/-}$ *detected differentially vulnerable synaptic populations across brain regions.* A&B.** Representative photomicrographs of coronal sections of the same brain regions immunostained with synaptophysin and bar chart showing its corresponding quantification based on the area of immunoreactivity at 13 month old in control and *Cln3*$^{-/-}$ mice. Syp immunoreactivity was lower in thalamic regions (VPM/VPL and LGNd) in the *Cln3*$^{-/-}$ mice when compared to controls indicating a major synaptic loss starting in the thalamus. Hippocampal stratum oriens and stratum radiatum also showed reduced Syp immunostaining, although the difference between genotypes was smaller. Cortical regions did not show difference in immunoreactivity for synaptophysin indicating that no synaptic loss is happening in these cortical areas at 13 months. Mean ± SEM; *P<0.05; **P<0.01; ***P<0.001; ns P>0.05. Student T test, 5 mice per each genotype and time-point were used, Scale bar= 200 um.

3.3.2 Comparative molecular profiling reveals proteomic perturbations that correlate with the extent of synaptic vulnerability

Despite advances in the characterization of the mammalian synaptic proteome, little is known about how these proteins interact and the molecular mechanisms that govern synaptic vulnerability. After confirming the synaptic vulnerability pattern across three distinct brain regions, we wanted to examine if the onset of synaptic pathology correlated with distinct molecular alterations in the synaptic proteome. To address this, we examined biochemically isolated synapse enriched fractions (synaptosomes) produced from microdissected brain regions from *Cln3*$^{-/-}$ mice and controls at 13 months of age where we characterise the pre-synaptic pathology as thalamus>hippocampus>cortex.

After synaptosome production and protein extraction, iTRAQ proteomics was carried out as detailed in Fig. 3.4 in collaboration with Dr Heidi Fuller (Keele University).

1536 total proteins were identified in hippocampus and thalamic samples whereas 2068 were detected in cortex. We then pre-filtered the proteins by those which were identified by at least 2 peptides and therefore are more likely to be reliable identifications. 914 proteins passed that filter in hippocampus and thalamus and 1295 in cortex. *DAVID* enrichment analysis was applied to the unfiltered thalamic data to confirm that the starting material was suitably enriched for synaptic proteins (Table 3.1).

Table 3.1. DAVID analysis of proteomic data confirms synaptic protein enrichment

Term	Fold Enrichment	P-Value	Benjamini
Clathrin coat of coated pit	20.5	9.30E-02	2.70E-01
Synaptic vesicle membrane	9.7	3.70E-02	1.50E-01
Synaptic vesicle	8.2	1.30E-05	1.20E-04
Dendritic spine	6.8	7.00E-02	2.20E-01
Presynaptic membrane	6.6	7.50E-02	2.30E-01
Axon	5.2	3.40E-04	2.50E-03
Mitochondrial inner membrane	5.2	7.10E-11	1.90E-08
Synaptosome	4.7	2.20E-02	9.50E-02
Synapse	4.1	2.20E-07	4.30E-06

Almost 40% of our pre-filtered thalamic proteome was altered when compared to control littermates. In contrast, only 20% and 17.6% of the synaptic proteome was altered in the cortex and hippocampus relative to controls respectively. The number of protein alterations also correlates with pre-synaptic pathology being more apparent in thalamic areas at this "moderate" stage of disease progression.

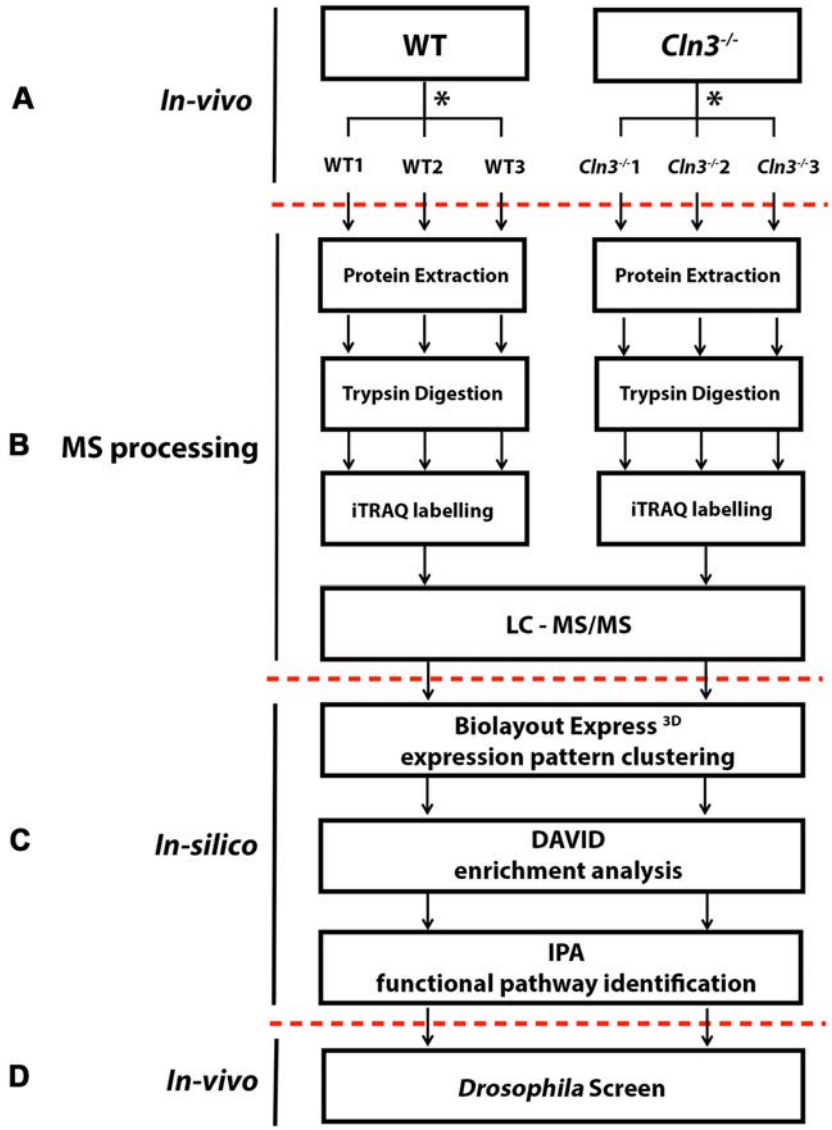

Fig. 3.4. Experimental design workflow. Experiments are divided into *in vivo* (animal models), MS processing and *in-silico* where the different bioinformatics tools are detailed. A & B were replicated for the three brain regions of interest: cortex, hippocampus, and thalamus.

Next, these pre-filtered proteins from the three pre-synaptic populations were aligned to look for overlapping proteins. 709 proteins were identified in all three brain regions and these were taken forward for comparative analysis (Fig. 3.5).

In order to gain a broad and unbiased overview for the types of processes that may be represented by the protein alterations detected in all three synaptic populations, we used *Ingenuity pathway analysis* (*IPA*) (see 3.2 Materials and methods – Fig. 3.5). Interestingly, we identified multiple canonical pathways which *IPA* designated as perturbed in a strikingly

progressive manner, consistent with the degree of synatic pathology outlined above i.e. –log P value = higher in thalamus>hippocampus>cortex (Fig. 3.5B). An example cascade, is the valine degradation pathway, where increasing number of disrupted proteins correlate to synaptic pathology across brain areas (Fig. 3.6). This analysis therefore indicates that in general, alterations in specific molecular cascades were increasing with pre-synaptic pathology, further confirming the differential vulnerability pattern previously identified by IHC. Thus, the synaptic vulnerability pattern described here appears consistent at both the morphological and molecular level.

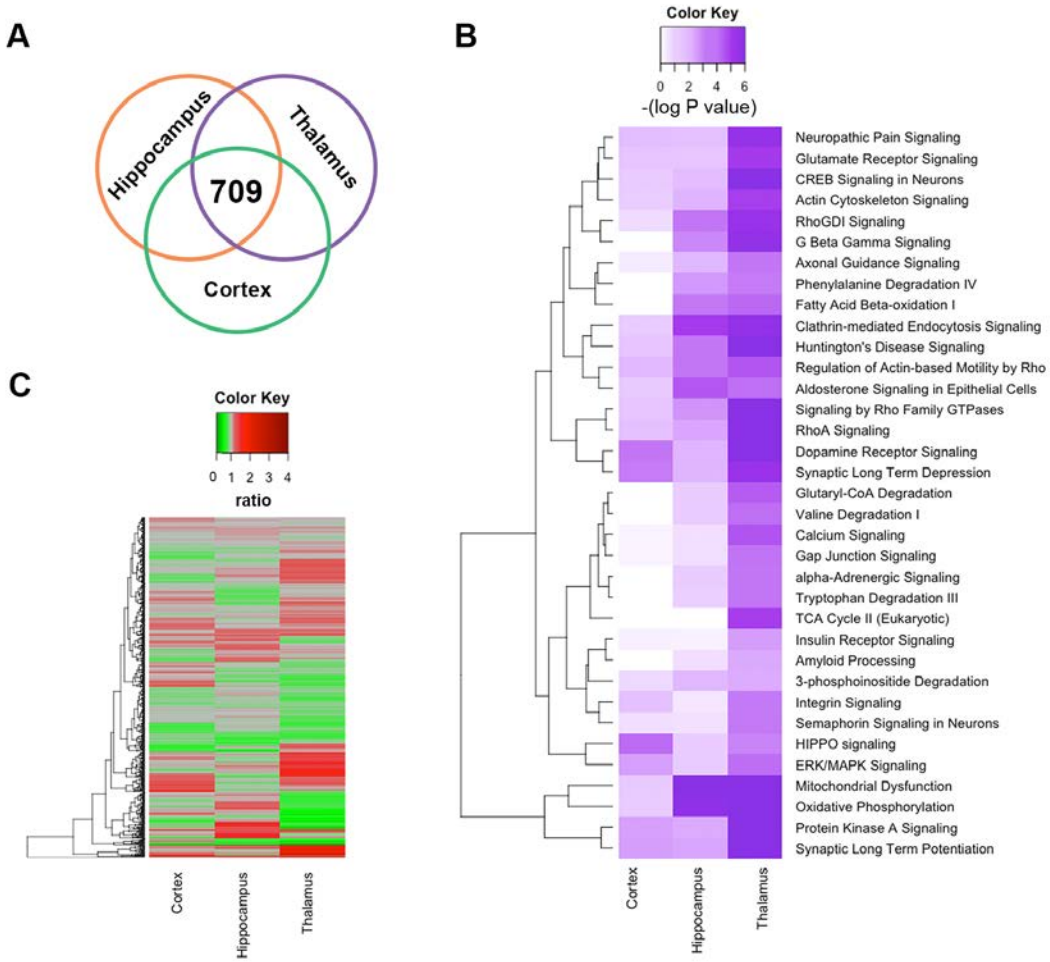

Fig. 3.5. Molecular changes correlate with the synaptic vulnerability characterized across brain areas. **A.** Venn diagram and heat map show the 709 common proteins identified and overlapped in cortical, hippocampus and thalamic synaptic proteomic datasets. **B.** Heat map representing the significance (-log P value) of the canonical pathways identified in *IPA* across cortex, hippocampus and thalamus datasets. It is observed a progressive increase in significance correlating to the synaptic vulnerability pattern described previously. **C.** Heat map showing the 709 common proteins identified and overlapping in cortical, hippocampus and thalamic synaptic proteomic datasets.

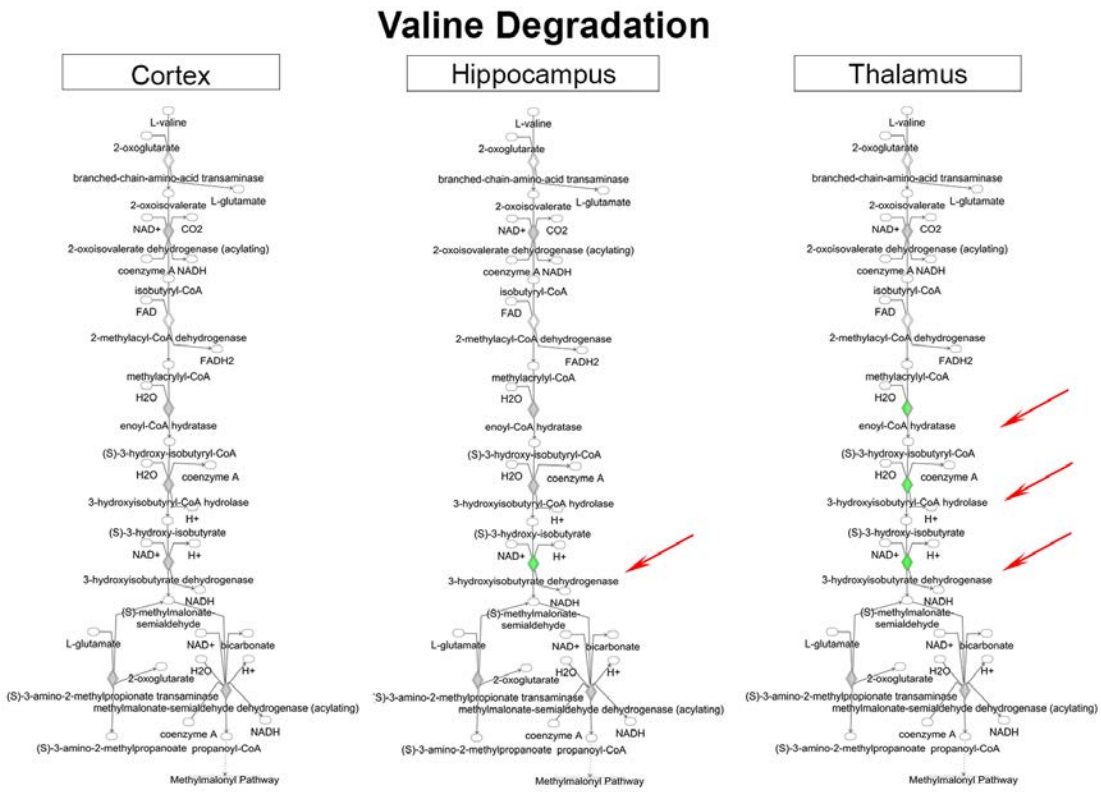

Fig. 3.6. Representation of the valine degradation pathway in cortex, hippocampus and thalamus using IPA. The amount of differentially expressed proteins between *Cln3*$^{-/-}$ and controls correlates with the disease vulnerability status of synapses across brain regions. Red arrows highlight proteins whose expression is disrupted by more than 20%. green = downregulated >20%, grey= change by <20%.

Whilst canonical cascade analysis is an interesting tool to use at the outset, multiple members of the same cascade do not necessarily need to change in the same manner, and whilst the trend of the majority of canonical cascades seen in Fig. 3.5B are consistent with the regional pathology reported, the individual protein alterations are far more complex (as seen in the heatmap in Fig. 3.5C). Thus, to better understand and visualize the different molecular expression trends occurring across the three datasets, individual proteins were tracked using *BioLayout Express* (see Methods). Simplistically, *BioLayout* is a complex pattern recognition software which generates a visual representation of the data based on protein abundance (Theocharidis *et al.*, 2009). In this case the software interrogates a regional expression profile generated by arranging the individual proteomic sets in order of increasing pre-synaptic pathology/vulnerability (cortex<hippocampus<thalamus). The outcome of this is that

proteins were found to cluster into 14 different groups according to similarities in their relative expression across these three regions (Fig. 3.7A) (Enright *et al.*, 2002). Of interest to us were Clusters 3 (70 proteins), 4 (68 proteins), 6 (51 proteins) and 7 (50 proteins). These clusters comprise proteins whose expression can be grouped (or clustered) together as having either a gradual upregulation or downregulation, therefore correlating (directly or inversely with) with synaptic vulnerability (Fig. 3.7 Appendix I-Tables A1-A4). Next, we applied an enrichment analysis to these distinct clusters in order to determine if each expression trend could be associated with a specific biological or functional category (using the *DAVID* software tool – see methods & Fig. 3.7B). Unexpectedly, clusters with proteins that were increasingly upregulated in vulnerable regions were enriched for structural associated candidates like cytoskeletal-related proteins, and specific biological functions such as endocytosis (Cluster 4&7). Perhaps more surprisingly, clusters whose protein expression decreased with increasing vulnerability were related to specific mitochondrial functions (Clusters 3&6) (Fig. 3.7). Thus, comparative proteomic profiling of differentially vulnerable synaptic populations revealed that significant alterations to the synaptic proteome correlated with the degree of pathology seen at these relatively moderate disease stages.

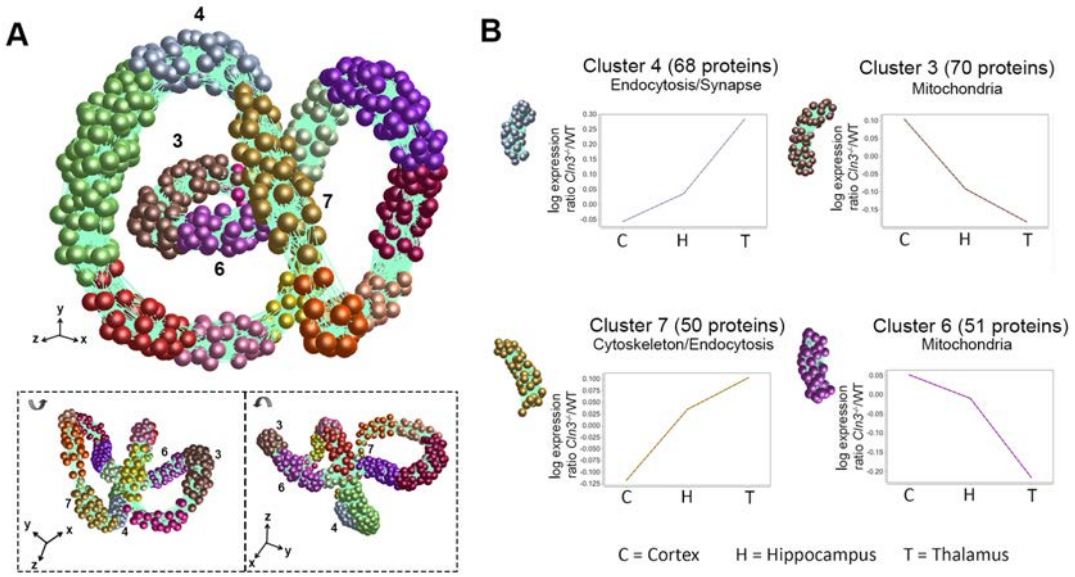

Fig. 3.7. Differentially vulnerable synaptic population molecular profiling. **A.** *BioLayout* clustering 3D representation of proteomic expression data across differentially vulnerable synaptic populations orientated at 3 different angles. Each sphere represents a single protein and the edge represents how similar their expression trend is towards the other proteins in the dataset. The closer the spheres are the more similar expression trend they have. The colours represent the different clusters of co-expressed proteins. **B.** Expression profile means in log scale

(*Cln3*$^{-/-}$/WT) of co-expressed proteins in clusters 3, 4, 6 and 7 (Appendix I-Tables A1-A4) and its main biological function/subcellular compartment identified by *DAVID* enrichment analysis. Clusters highlighted show steady up or downregulation across cortex (C), hippocampus (H) and thalamic (T) regions correlating with the vulnerability status of synapses.

3.3.3 *In silico* analysis highlights alterations in valine catabolic and ROCK2 signalling cascades in vulnerable thalamic synapses

After confirming that the synaptic proteome changes in a manner consistent with the differential vulnerability to disease in *Cln3*$^{-/-}$ mice, we next sought to tease out the potential molecular regulators of stability from our complex proteomic datasets. To do this, we focused our analyses on the thalamus, because synapses here were perturbed to a much greater extent than those in the hippocampus or cortex. In the thalamus dataset, 1536 total proteins were identified following iTRAQ processing. As described above, we applied filtering criteria based on the number of peptides (more than 2 unique peptides), those changed >20% (1.2 fold-change) and those which were mapped by *Ingenuity Pathway Analysis* (*IPA*) software. A total of 374 proteins met these criteria (Fig. 3.8A and Appendix I-Tables A5&A6).

To confirm the veracity of the filtered data before proceeding to *IPA* analysis, we carried out quantitative fluorescent Western blotting (QWB). Proteins for validation were chosen by a combination of their previous implication in neurodegeneration processes, and on their magnitude of change (Wishart *et al.*, 2014, Mutsaers *et al.*, 2013, Wishart *et al.*, 2012, McGorum *et al.*, 2015). For example, beta-catenin and alpha-synuclein are good representatives of validated large changes; HIBCH and ROCK2 are representative of validated moderate changes, and calretinin is a good example of an unchanged protein from the data set (Fig. 3.8B-G).

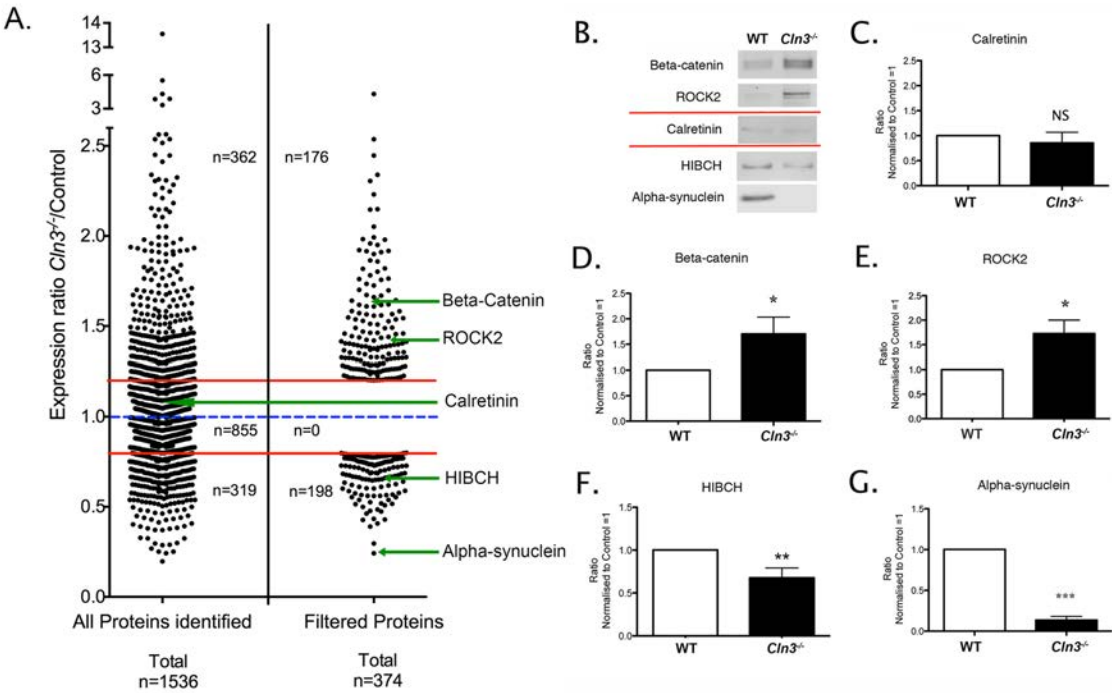

Fig. 3.8. Synaptic thalamic proteome filtering and validation. **A.** Dot plot demonstrating the process of proteomic data filtering. Each data point represents an individual protein identified using iTRAQ proteomic technique. LHS 1536 proteins were identified across all thalamic samples. Following filtering (see Methods) a molecular fingerprint for thalamic synaptic alterations comprising 374 candidate proteins was produced. **B**. Representative bands for two upregulated, two downregulated and one unchanged protein candidate verifying the proteomic data of in *Cln3*$^{-/-}$ mice at 13 months of age. **C – G**. Quantification and statistical analysis of the magnitude of alteration in *Cln3*$^{-/-}$ thalamic synaptic fractions. All the selected candidate proteins were altered as indicated by this iTRAQ analysis. Mean ± SEM; *P<0.05; ***P<0.001; T Student test, n= 6 mice per each genotype.

Higher order functional clustering highlights similarities with other neurodegenerative conditions

Once we confirmed the quality of the data by enrichment analysis and QWB, we wanted to elucidate which molecular pathways and biological networks were disrupted in "affected" thalamic synapses. In order to do this, *IPA* analysis was carried out.

We input the total pre-filtered thalamic data into *IPA* (those filtered by >2 peptides only) and applied the 1.2 fold-change cut-off in the software. Of the three-hundred and seventy-four proteins recognised by *IPA*, 68.3% have previously been reported in the literature as being associated with neurological disease (Fig. 3.9A). The majority of the diseases and disorders which fall under the category of "neurological disease" have synaptic pathology as an early event (Wishart *et al.*, 2006). Interestingly, the main molecular and cellular functions

identified in *IPA* were "molecular transport" and "cellular assembly and organization". These functional categories are consistent with the comparative analysis of differentially vulnerable synaptic populations carried out above (see Fig. 3.7), where clusters showing increases in protein expression from the levels detected in the comparatively spared cortical synapses through to higher levels again in the more vulnerable thalamic populations highlighted cytoskeletal protein alterations.

Molecular cascade tracking identified potentially conserved regulators of vulnerability The "Canonical pathways" function in *IPA* uses an algorithm to interrogate a library of known generalized biological pathways that represent common properties of a particular signaling module or pathway, which are ranked according to their relevance to the dataset analyzed (Savli *et al.*, 2008) (see Chapter 2, General materials and methods). In this analysis, mitochondrial dysfunction was the most significant canonical pathway identified. The contribution of synaptic mitochondria in neurodegeneration has been highlighted in recent years (Gillingwater *et al.*, 2013), and mitochondrial abnormalities have also been related to CLN3 disease and other NCLs (Luiro *et al.*, 2006, Kang *et al.*, 2013, Kolikova *et al.*, 2011, Jolly *et al.*, 2002), and therefore our data is consistent with these previous findings. However, in this study we wanted to consider pathways that have not been related to the NCLs before that could have been overlooked previously. Within the top canonical pathways identified with *IPA*, we could also detect perturbations in ROCK signalling and valine degradation pathways (Fig. 3.7B&C). Examining these pathways, proteins such as ROCK2 and HIBCH were differentially expressed key "hub" components. Their expression tracked in clusters 4 and 6 respectively correlating to the vulnerability status of synapses in the *Cln3*$^{-/-}$ mice (see above, Fig. 3.7 and Fig. 3.9). Moreover, we have previously identified ROCK2 and HIBCH as showing similar expression alterations in synapses following cortico-striatal lesion injury, and also having the potential to alter neurodegeneration in an injury specific context (Wishart *et al.*, 2012). Collectively these findings suggest that there may be a common molecular cascade underlying synaptic degeneration in a range of neurodegenerative contexts ranging from injury through to genetic causes. ROCK2 signaling and valine degradation pathways and specifically proteins such as ROCK2 and HIBCH, represent potentially novel regulators of synaptic stability in an NCL disease context, which have not been investigated yet. Therefore, we next sought to determine if such candidates have the ability to moderate NCL disease progression *in vivo*.

A

Category	Name	Molecules	p-value
Diseases and Disorders	Neurological Disease	194	1.12E-03 - 5.41E-28
	Skeletal and Muscular Disorders	97	9.51E-04 - 2.28E-21
	Psychological Disorders	140	1.08E-03 - 1.48E-20
	Hereditary Disorder	105	9.51E-04 - 3.78E-17
	Organismal Injury and Abnormalities	346	1.15E-03 - 3.78E-17
Molecular and Cellular Functions	Molecular Transport	150	1.17E-03 - 2.74E-24
	Cellular Assembly and Organization	151	1.12E-03 - 6.19E-24
	Cellular Function and Maintenance	172	1.12E-03 - 6.19E-24
	Cell-To-Cell Signaling and Interaction	115	1.19E-03 - 1.34E-23
	Cell Morphology	149	1.10E-03 - 1.18E-17

B

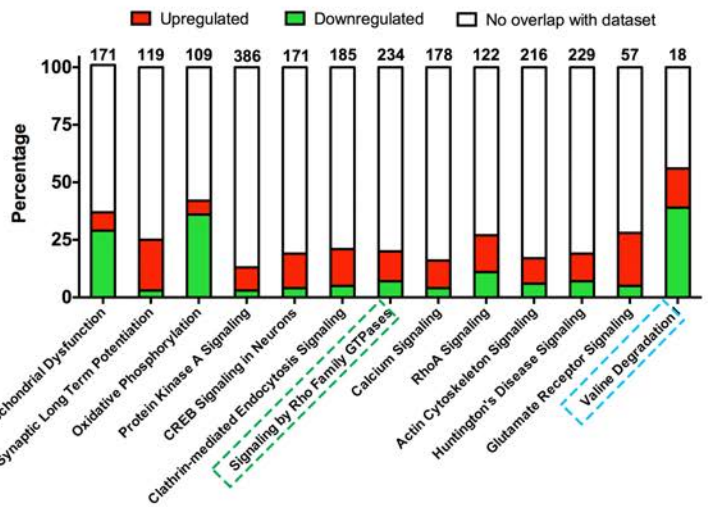

C

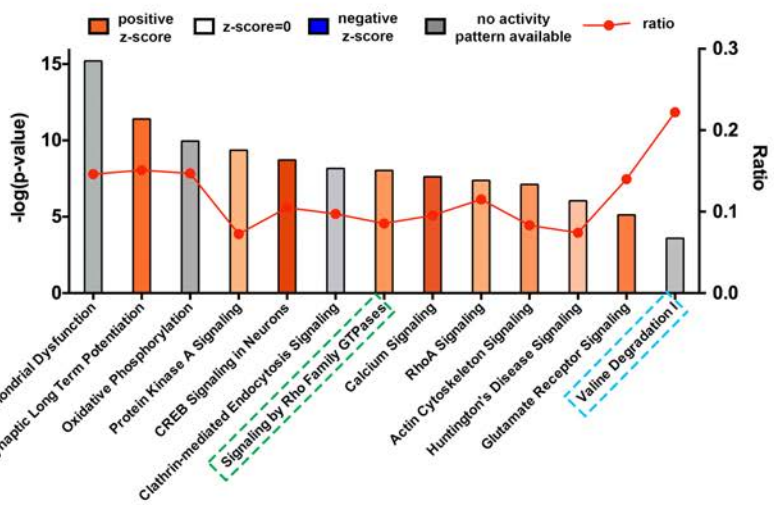

D

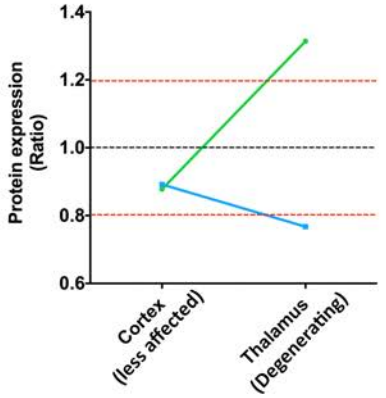

E

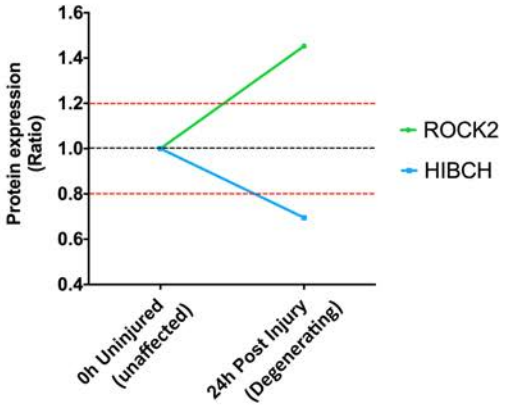

Fig. 3.9. IPA analysis of the thalamic synaptic proteome. **A**. Table of top 5 "diseases and disorders" and "molecular and cellular functions". **B-C.** Canonical pathways bar chart of representative pathways showing, **B**. The percentage of upregulated and downregulated proteins within each pathway. Numbers on the top indicate the total number of proteins within the canonical pathway. **C.** Significance of the association between the dataset and the canonical pathway (–log(p-value) and ratio) and z-score prediction of activation/inhibition (see Methods). Pathways highlighted in green and blue are associated to ROCK2 and HIBCH, respectively. **D.** HIBCH and ROCK2 protein expression ratio across cortex ("spared') and thalamic ("degenerating") synapses In these moderately affected *Cln3*$^{-/-}$ mice (*Cln3*$^{-/-}$/WT). **E**. HIBCH and ROCK2 protein expression is conserved in models of injury, following similar pattern of expression 24 hours post-injury when synapses start to degenerate (Wishart *et al.*, 2012).

Valine catabolic cascade is disrupted in* Cln3$^{-/-}$ *mice and it is relevant to the human disease

HIBCH is a 3-hydroxyisobutyryl-CoA hydrolase protein that fulfils a core function within the valine degradation cascade (Loupatty *et al.*, 2007). Mutations in *HIBCH* cause a progressive infantile neurodegeneration in humans, characterized by hypotonia, motor delay and neurological regression (Loupatty *et al.*, 2007, Brown *et al.*, 1982, Ferdinandusse *et al.*, 2013). Moreover, manipulation of HIBCH has been suggested to modulate injury-induced axonal degeneration (Wishart *et al.*, 2012). However, despite this apparently restricted function, very little is known about its role (if any) in synaptic compartments or its binding/interaction partners (see Fig. 3.10A).

Using QWB techniques we confirmed that HIBCH protein was less abundant in thalamic synaptosome extracts relative to wild type controls. Interestingly, HIBCH protein levels trended towards a slight up-regulation of HIBCH in "non-synaptic" compartments. Whilst not statistically significant, this non-synaptic increase may indicate a redistribution or altered trafficking of this protein in response to *Cln3* deficiency (Fig. 3.10B).

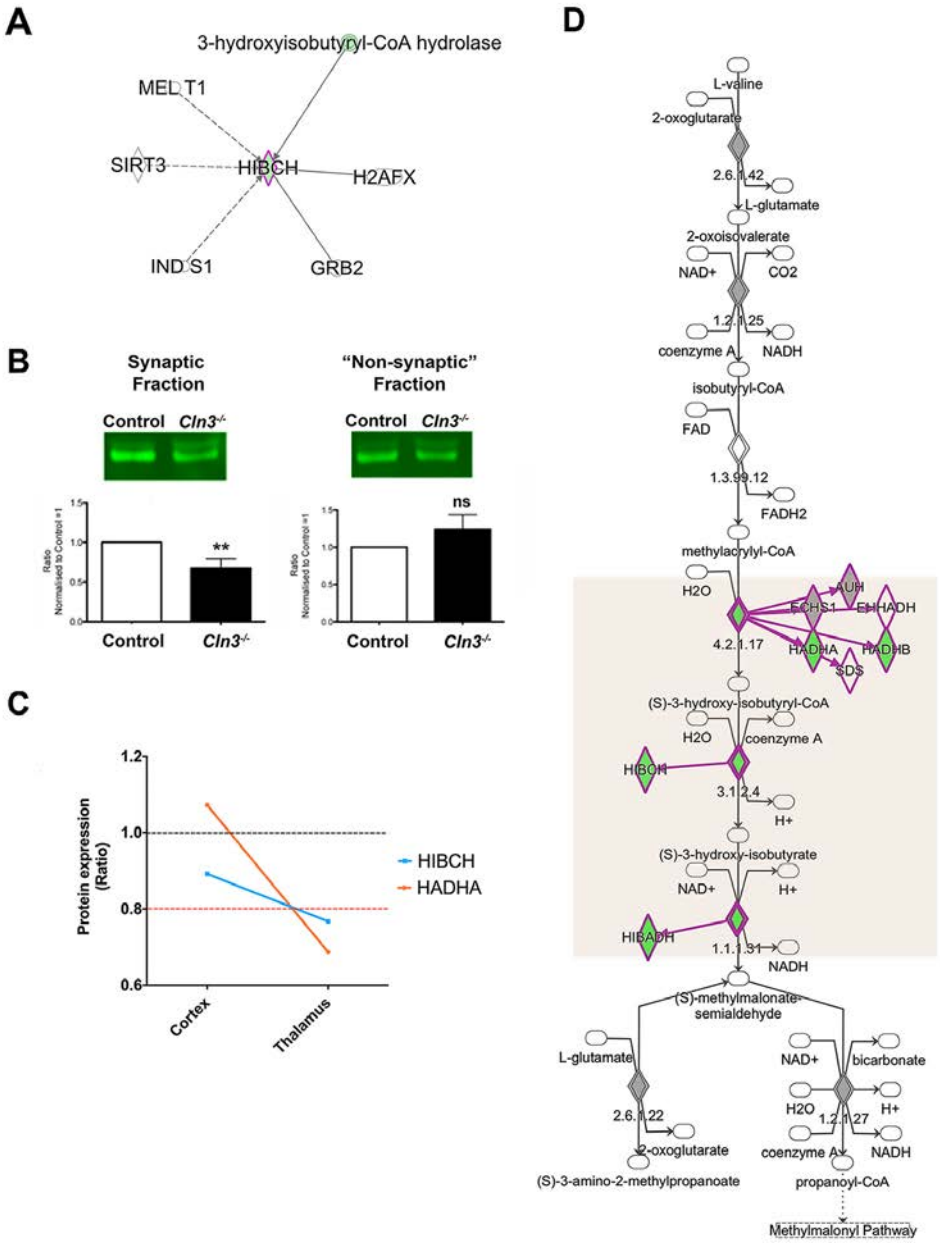

Fig. 3.10. HIBCH downregulation in thalamic synapses impacts in valine catabolism pathway. **A**. HIBCH proteome interactome represented by *IPA*. Only 6 genes/proteins are known to interact with HIBCH. **B**. QWB bands and quantification of HIBCH in synaptic and "non synaptic" fractions of *Cln3*$^{-/-}$ and control mice in thalamic protein extracts showing a downregulation in synapses and upregulation in non-synaptic parts Mean ± SEM; **P<0.01, ns P>0.05 (Student T test). **C.** HIBCH and HADHA are co-expressed and their expression trend correlates to the vulnerability status of synapses: unchanged in cortex ("spared") and downregulated in thalamus ("degenerating"). **D.** Valine degradation pathway represented with *IPA*. The first protein which expression is perturbed in the degradation process of valine is HADHA; upstream of HIBCH. **A&D**. Colored nodes illustrate proteins present in the thalamic dataset in *Cln3*$^{-/-}$ with respect to WT. Nodes in grey represent proteins changed <20%, down-/up-regulated proteins by >20% are represented in green and red respectively. Orange box highlights the steps that are disrupted in the valine degradation cascade.

Examination of human *post mortem* samples from patients with JNCL and controls was carried out in order to determine the relevance of our findings to the human condition. Synaptosomes were isolated from cortical brain areas from 5 controls and 3 JNCL patients (see methods). In order to confirm that the synaptosomes were indeed enriched for synaptic proteins and depleted from nuclear material, I carried out western blots using a synaptic and nuclear markers in both synaptic and non-synaptic fractions from the control human samples. Results show that whilst the nuclear marker H2Ax was clearly enriched in the non-synaptic fractions (Fig. 3.11A), synaptobrevin (synaptic marker) was more abundant in the synaptic enriched fractions (Fig. 3.11B). Moreover, to confirm that there was no obvious abnormalities in proteome composition in the synaptic fraction from controls and patients, total protein staining using instant blue was performed (Eaton *et al.*, 2013). The even banding pattern and equal loading of samples indicated the well-preserved protein content in the samples and therefore they were ready to be used for the detection of our protein candidates (Fig. 3.11C).

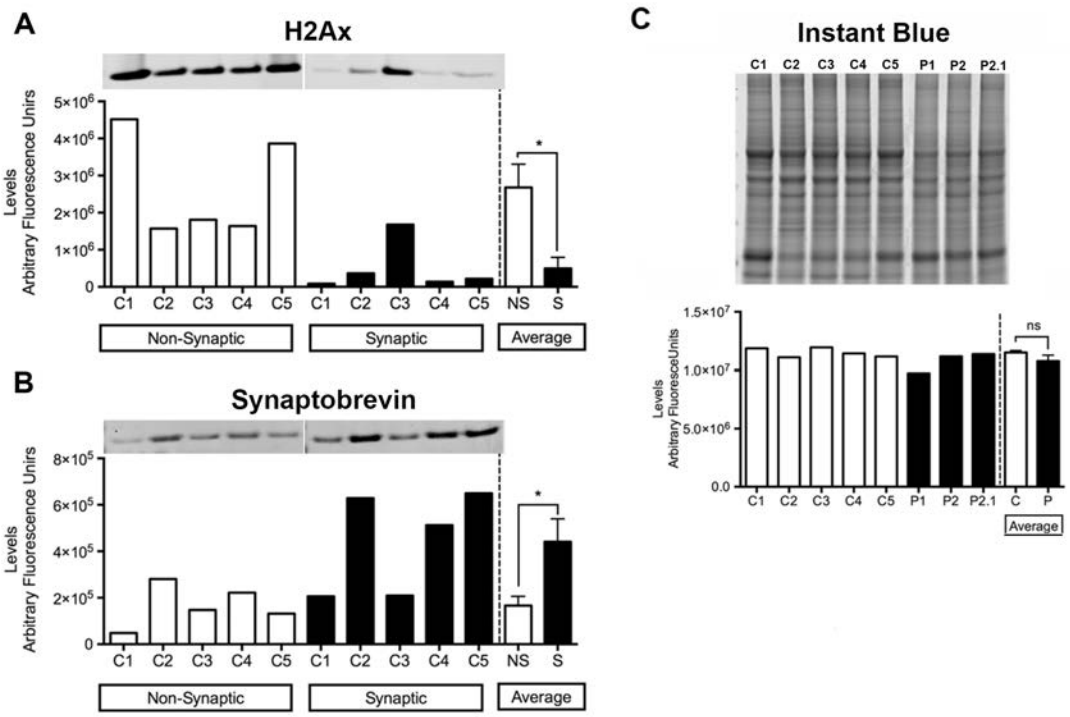

Fig. 3.11. QWB validation of fractionation of post mortem brain samples from JNCL patients and controls. **A&B.** QWB bands and corresponding quantification of protein histone H2Ax (nuclear marker) and synaptobrevin (synaptic vesicle marker) respectively. **C.** Instant blue staining of total protein as a loading control and validation of integrity of the protein content within synaptic isolates. The banding pattern and quantification showed no obvious protein degradation of the samples. C=Controls, P=Patient. Mean ± SEM; *P<0.05; ns P>0.05; Student T test.

The examination of human *post mortem* synaptic fractions showed that HIBCH protein levels were significantly reduced also in JNCL patients (Fig. 3.12), strengthening the relevance of our proteomic results in mouse models to the human disease.

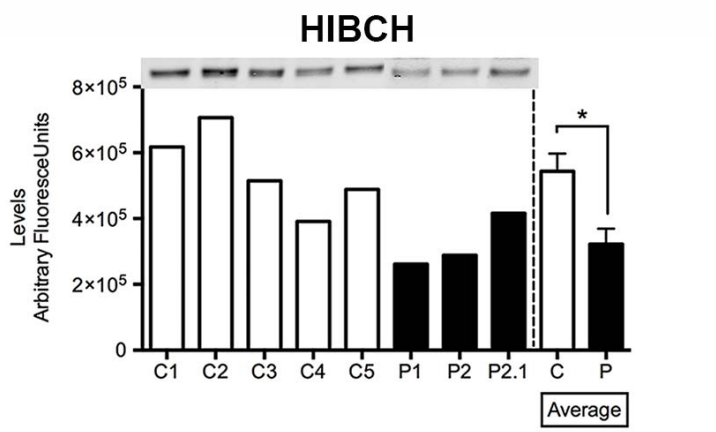

Fig. 3.12. HIBCH QWB bands and quantification of cortical synaptosomes isolated from post mortem human JNCL patients (P) and controls (C) showing its downregulation also at end stages in human disease. Mean ± SEM; *P<0.05; Student T test.

From comparing synaptic vulnerability (Fig. 3.7), HIBCH belonged to Cluster 6 (gradual downregulation profile) and was co-expressed with other mitochondria-related proteins (Fig. 3.7B) including Hydroxyacyl-CoA Dehydrogenase/3-Ketoacyl-CoA Thiolase/Enoyl-CoA Hydratase (Trifunctional Protein), Alpha Subunit (HADHA), which also fulfils an enzymatic role within the valine degradation pathway (Fig. 3.10C). HADHA sits upstream of HIBCH in the valine catabolism cascade (Fig. 3.10D) and catalyzes the final three steps of mitochondrial long chain fatty acid β-oxidation (Kamijo *et al.*, 1994). HADHA codes for the α subunit of the mitochondrial trifunctional protein (αMTP), and its deficiency causes a metabolic disease that presents with Reye-like syndrome, with cardiomyopathy, neuromyopathy and sudden death in infancy (Ibdah *et al.*, 2001). More recent reports have indicated that HADHA deficiency results in a pigmentary retinopathy leading to vision loss (Fletcher *et al.*, 2012).

Given the important role of these two proteins in the valine catabolism cascade, we included HIBCH and HADHA in our list of candidates for our *in vivo* experiments in order to assess their influence on synaptic and neuronal stability in an NCL-disease specific context (Chapter 5).

Increased ROCK2 expression is conserved across a range of diseases

ROCK cascades were also identified as being perturbed in degenerating thalamic synapses and they were predicted to be activated when compared to wildtype controls (Fig. 3.9 B&C). ROCK2 is a *Rho*-kinase belonging to a family of serine/threonine kinases, of which isoform 2 is the most predominant in the brain (Riento *et al.*, 2003). ROCK2 directly interacts with, and is activated by, Rho GTPases. These are the central mediators of actin reorganization (Riento *et al.*, 2003), which are reported to have a key role in synaptic plasticity and long term potentiation (LTP) (Zhou *et al.*, 2009). Activation of ROCK2 has been implicated in several adult-onset neurodegenerative conditions where synaptic pathology is present, such as HD, AD, ataxia, and in Purkinje cell degeneration (Deyts *et al.*, 2009, Herskowitz *et al.*, 2011, Zhou *et al.*, 2003, Blaise *et al.*, 2012, Wishart *et al.*, 2012). Moreover, ROCK2 has been shown to influence childhood neurodegenerative conditions such as SMA, where pharmacological inhibition partially recued symptoms and increases lifespan in an SMA mouse model (Bowerman *et al.*, 2012, Coque *et al.*, 2014). ROCK2 also was reported to influence axonal degeneration following injury (Wishart *et al.*, 2012). Taken together with our current data, this is consistent with a model whereby upregulation/activation of ROCK2 signalling correspons to increased neuronal vulnerability or degeneration in multiple infantile- and late-onset neurodegenerative conditions.

The ROCK2 interactome (displayed in Fig. 3.13A) illustrates its reported interactions with other gene/proteins, many of which were also altered in *Cln3*$^{-/-}$ thalamic synaptic extracts (coloured symbols represent proteins from this dataset: green – downregulated; red – upregulated; grey- identified but not crossing threshold). In the *Cln3*$^{-/-}$ thalamus, QWB confirmed that ROCK2 was upregulated by 53.7% in the synaptic fractions, and by 27.7% in the corresponding "non synaptic" *Cln3*$^{-/-}$ isolates, relative to controls (Fig. 3.13B), suggesting a more synaptically-focussed response to altered CLN3 expression. Our *in silico* analysis added support for this model by highlighting specific sub-cascades under multiple pathways related to ROCK2 such as "Signalling by Rho Family GTPases" and "Rho A signalling" (Fig. 3.9B&C). These cascades regulate actin dynamics and cytoskeletal organization (as shown in Fig. 3.13C&D) and can impact synaptic structure and affect synaptic transmission. Thus, the conserved increased expression of ROCK2 in *Cln3*$^{-/-}$ mice, and in other related conditions, is highly suggestive of an important contribution to synaptic vulnerability.

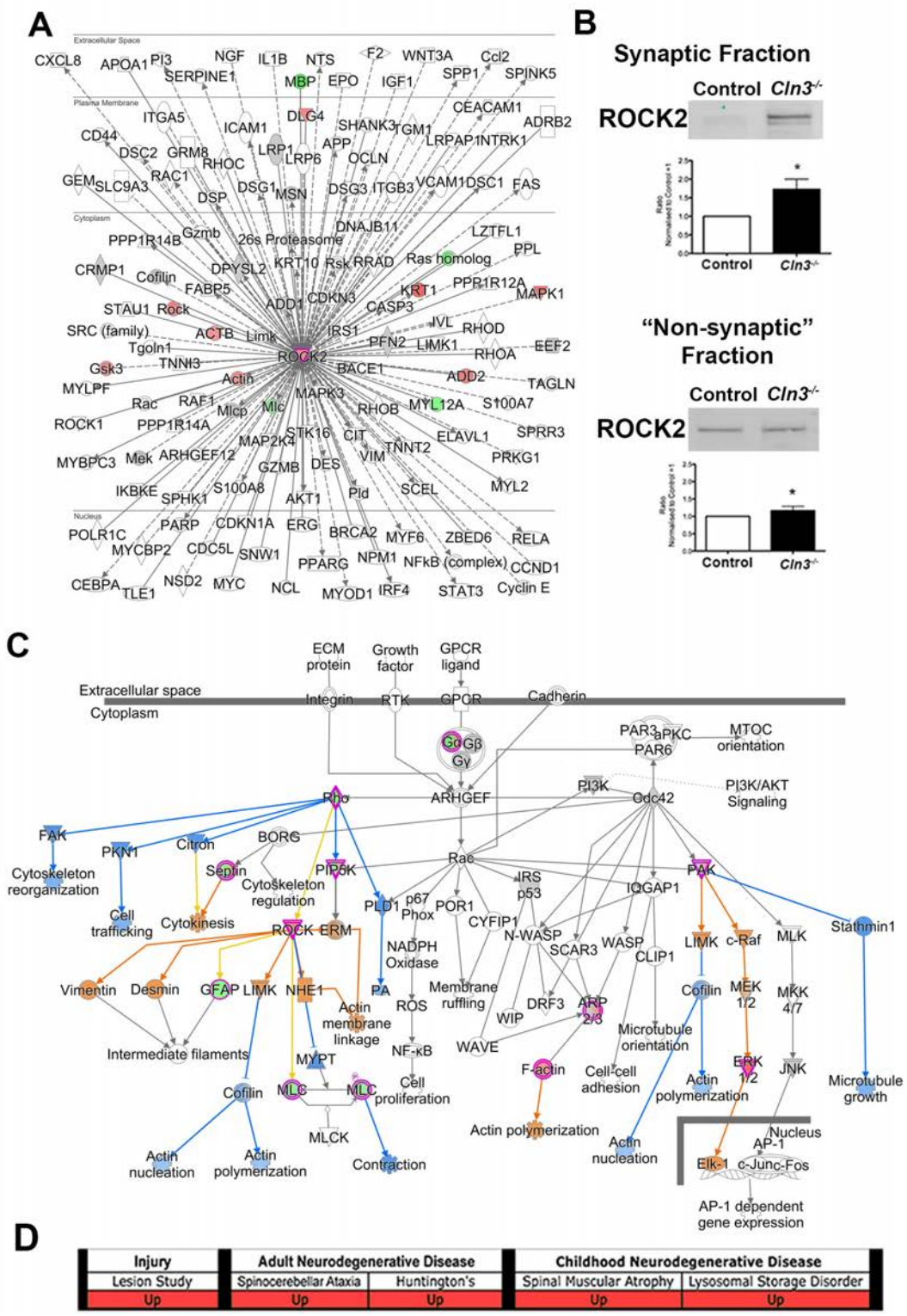

Fig. 3.13. ROCK2 upregulation is a synaptic specific change conserved across a range of neurodegenerative conditions including NCL. **A.** ROCK2 protein/gene interactome represented with *IPA* showing that some of the interactor partners of ROCK2 are also altered in thalamic synaptosome. **B.** QWB bands and quantification of control and *Cln3*$^{-/-}$ synaptic and "non synaptic" fraction. Upregulation of ROCK2 is higher in synapses than in the non-synaptic

fraction indicating a potential synaptic specific response Mean ± SEM; *P<0.05 (Student T test). **C. "**Signaling by Rho family GTPases" canonical pathway represented by *IPA* with the prediction activation tool (MAP). Upregulation/activation of ROCK2 impacts in actin nucleation and polymerization that may disrupt actin dynamics in the synapse. **A&C.** Coloured nodes illustrate proteins present in the thalamic dataset in $Cln3^{-/-}$ with respect WT. Nodes in grey represent proteins changed <20%, down-/up-regulated proteins by >20% are represented in green and red respectively, orange indicates predicted activation and blue; predicted inhibition. **D.** ROCK2 upregulation at early stage of disease is a converved event across animal models of injury, two adult-onset neurodegenerative diseases (Huntington and Spinocerebelar ataxia) (Wishart *et al.*, 2012) and two childhood neurodegenerative conditions (SMA and the lysosomal storage disorders-NCLs).

Conversely, in *post mortem* human cortical synaptic extracts, ROCK2 was found to be downregulated in JNCL patients with respect to controls (Fig. 3.14). Nevertheless, the interpretation of the results from *post mortem* tissue is challenging as at end stage of the disease brain atrophy is much more pronounced, making it difficult to distinguish which molecular alterations are more likely to be causative, and which are a consequence of the ongoing degeneration taking place. ROCK2 upregulation could be a disease stage-specific change that contributes to the initiation of degenerative stimuli, and it is not necessarily globally upregulated throughout disease progression.

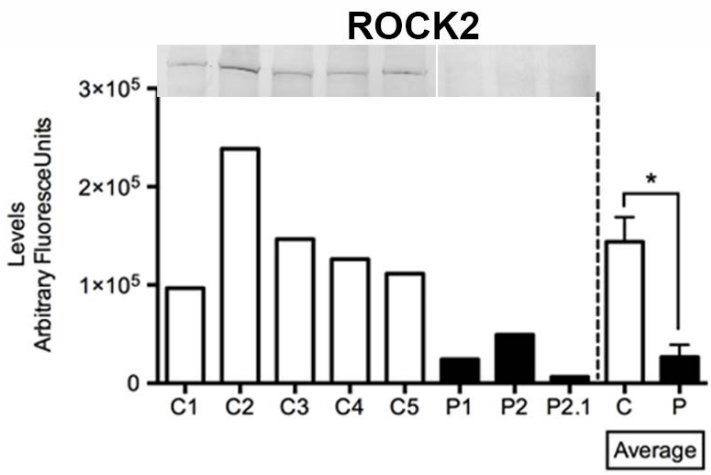

Fig. 3.14. QWB bands and quantification of ROCK2 in synaptic fractions showing downregulation of this protein at end stages of the disease. C=Controls, P=Patient. Mean ± SEM; *P<0.05; ns P>0.05; Student T test.

3.4 Discussion

In this chapter we have confirmed that *Cln3*$^{-/-}$ murine synapses follow the same differentially vulnerability pattern as other NCL subtypes including infantile NCL (CLN1/PPT1) and congenital NCL (CLN10/CTSD) (Partanen *et al.*, 2008, Kielar *et al.*, 2009). We show that, at 13 months of age in *Cln3*$^{-/-}$ mice the synaptic pathology is more pronounced in the thalamus (although still <10%), followed by hippocampal synaptic compartments, while cortical synaptic populations remain relatively unaffected (Fig. 3.3). iTRAQ proteomic and bioinformatics showed that differential synaptic pathology was also reflected at the molecular level, showing a progressive increase in the disruption of multiple canonical pathways correlating with our observations at the immunohistological level (Fig. 3.5B). Further analyses by means of a complex pattern recognition software identified alterations in the synaptic proteome (identified by iTRAQ analysis of "crude" synaptosomes) that correlated with the assigned vulnerability status of pre-synaptic populations in the *Cln3*$^{-/-}$ mice.
Pathway analysis highlighted perturbations in valine catabolism and *rho* signaling pathways, of proteins including HIBCH, HADHA and ROCK2 as key players, correlating with synaptic vulnerability. Furthermore, HIBCH and ROCK2 displayed a conserved direction of change in multiple neurodegenerative conditions, and we have previously demonstrated that they can alter axonal degeneration in an injury dependent context (Wishart *et al.*, 2012).

In humans, both HIBCH and HADHA deficiency cause infantile onset diseases with neurologic clinical scheme (Ferdinandusse *et al.*, 2013, Peters *et al.*, 2015, Stiles *et al.*, 2015). This may indicate that perturbations in valine catabolic pathways might be a shared event across multiple neurodegenerative conditions.

Interestingly, the upregulation of ROCK2 has been reported in a range of conditions by our laboratory and others (Wishart *et al.*, 2012, Deyts *et al.*, 2009, Herskowitz *et al.*, 2011, Blaise *et al.*, 2012). ROCK2 upregulation seemed to be a more synaptic-specific perturbation (at least at early stages) in the *Cln3*$^{-/-}$ mice and its magnitude of change tracked across differentially vulnerable brain regions (i.e. Thalamus>Hippocampus>Cortex). Its genetic and/or pharmacological downregulation has been shown to ameliorate the phenotype of several conditions including SMA, another relatively early onset neurodegenerative disease (Bowerman *et al.*, 2012, Coque *et al.*, 2014). However, in *post mortem* human cortical synaptic extracts from JNCL patients, and therefore, end-stage of disease progression,

ROCK2 was found to have opposite profile (Fig. 3.14). Further investigations will be needed in order to determine whether these differences in ROCK2 expression are a disease stage or a species difference. A study of the molecular alterations and pathways taking place throughout the time-course of disease progression in NCL would contribute to further understand the mechanisms underlying the initiation and progression of neurodegeneration.

In contrast, no lysosomal specific pathways were identified in our *in silico* analysis in synapses, indicating that loss of CLN3 may be impacting in other pathways beyond lysosomal function. This is supported by studies in which CLN3 was found to be expressed in other locations such as in synaptosomes (Luiro *et al.*, 2001), lipid rafts (Rakheja *et al.*, 2004, Persaud-Sawin *et al.*, 2004), Golgi (Persaud-Sawin *et al.*, 2004), mitochondria (Katz *et al.*, 1997), glia (Mohammed *et al.*, 2017) and endothelial cells (Phillips *et al.*, 2005, Katz *et al.*, 1997, Mohammed *et al.*, 2017, Tecedor *et al.*, 2013), where it may play other roles such as regulation of oxidative stress (Mohammed *et al.*, 2017, Tuxworth *et al.*, 2011) and glial function (Pontikis *et al.*, 2004, Pontikis *et al.*, 2005) or blood-brain barrier homeostasis (Tecedor *et al.*, 2013). For more information regarding localization and function of CLN3 see review (Phillips *et al.*, 2005). However, individual NCL and lysosomal-storage disorder-related proteins were identified, such as cathepsin D (Steinfeld *et al.*, 2006), prosaposin (O'Brien *et al.*, 1991, Tyynelä *et al.*, 1993) and acid ceramidase (Sugita *et al.*, 1972).

Overall, valine degradation and rock signaling pathways appear to be attractive pathways to further study in our *in vivo* experiments (Chaper 5). By targeting these specific cascades we might be able to elucidate regulatory pathways not only for NCL, but also in a wide range of more common neurodegenerative diseases to potentially halt or delay disease progression.

Chapter 4

Spatio-temporal analysis of differentially vulnerable synaptic populations in *Ppt1*$^{-/-}$ mice

4.1 Introduction

Following the characterization of the molecular changes happening at a static early time-point across three differentially vulnerable synaptic populations (Chapter 3), we next sought to build on this analysis by investigating such region-specific synaptic molecular fingerprints throughout the time-course of disease progression in NCLs.

As shown in Chapter 3, the synaptic upregulation of ROCK2 appears to be an early-specific change, as it was downregulated in *post mortem* human brain samples which are end stage by definition (Fig. 3.14). However, it is always possible that in such instances, the difference may be species specific, but the literature supports the notion of a dynamic neuronal proteome which changes in response to disease progression (Kielar *et al.*, 2009, Wishart *et al.*, 2014, Wishart *et al.*, 2012). Thus, we believe that a characterisation of the synaptic molecular changes throughout the time-course of disease progression, could provide a more complete picture of the mechanisms underpinning neurodegeneration.

Having demonstrated in Chapter 3 that using *Cln3*$^{-/-}$ mice and a combination of proteomics and bioinformatics analyses, we are able to identify potential protein regulators of synaptic stability, we sought to carry out more comprehensive and ambitious time-course analyses. However, the *Cln3*$^{-/-}$ model is not necessarily the most appropriate model for this type of temporal investigation. Reasons for this include (but are not limited to), the time-course length (approximately 23 months) (Pontikis *et al.*, 2004) and the increased potential for

molecular noise through protracted systemic chronic disease. Additionally, the morphological profiling of the *Cln3*$^{-/-}$ model is not as detailed in the later time-points as other shorter lived models. In contrast, *Ppt1*$^{-/-}$ mouse model of infantile NCL (INCL) has a shorter lifespan only reaching 8-8.5 months of age (Gupta *et al.*, 2001) and has been characterised in more detail at the pathological level (Kielar *et al.*, 2007, Kielar *et al.*, 2009) (Fig. 4.1). Given the more manageable time-span of disease progression and the extensive previous characterization of the *Ppt1*$^{-/-}$ model according to the degree of neuronal alterations, we identified four disease stages which from this point on will be referred to as pre-, early-, mid- and late symptomatic stages at 1, 3, 5 and 7 months of age respectively (Kielar *et al.*, 2007, Kielar *et al.*, 2009). Studies by Kielar *et al.* showed the temporal differential pathology across thalamus and cortex in the *Ppt1*$^{-/-}$ mice at both the neuronal (Kielar *et al.*, 2007) and the synaptic level (Kielar *et al.*, 2009). Such studies report thalamus as the first area of the brain to show synaptic pathology at 3 months. Cortical areas (corresponding to thalamic projections) did not show an equivalent degree of pathology until 5-month of age (Fig. 4.1.). Therefore, thalamic synapses are the most vulnerable (with pathological changes detectable at 3 months) followed by cortical synapses (with pathological changes detectable at 5 months) (Kielar *et al.*, 2009).

Importantly, after establishing the time-point in which the onset of synaptic pathology occurs in *Cln3*$^{-/-}$ model (Chapter 3), and after conversations with the pathologist Prof. Jonathan Cooper, we established for future comparisons that the 3 month early-symptomatic disease stage in *Ppt1*$^{-/-}$ could be considered to be equivalent to the 13 month disease stage in the *Cln3*$^{-/-}$ model for synaptic alterations (Kielar *et al.*, 2009) (Llavero Hurtado *et al.*, 2017).

In this project, we decided to focus on these two differentially vulnerable brain regions: thalamus and cortex. Therefore, similar to the approach from Chapter 3, we used this pathological characterization to design our analyses and map the molecular changes correlating with synaptic pathology. This type of temporal investigation also warranted a shift from iTRAQ to label-free proteomic techniques as it offers a higher protein coverage with less starting material (Craft *et al.*, 2013, Patel *et al.*, 2009, Bantscheff *et al.*, 2007), greater sample processing and data handling flexibility without the need and cost of multiple label incorporation (Xie *et al.*, 2011).

In this study, we carried out one of our most complex proteomic analyses consisting of 4 time-points (1, 3, 5 and 7 months), 2 conditions (*Ppt1*$^{-/-}$ and age-matched WT controls) and 2 differentially vulnerable synaptic populations (thalamus and cortex). Similar to Chapter 3, a combination of comparative (but in this case label-free) proteomics followed by bioinformatic analyses was utilised to identify the pathways and protein candidates which better correlate to the spatio-temporal synaptic vulnerability in *Ppt1*$^{-/-}$ mice, and are therefore more likely to be regulators of neurodegeneration.

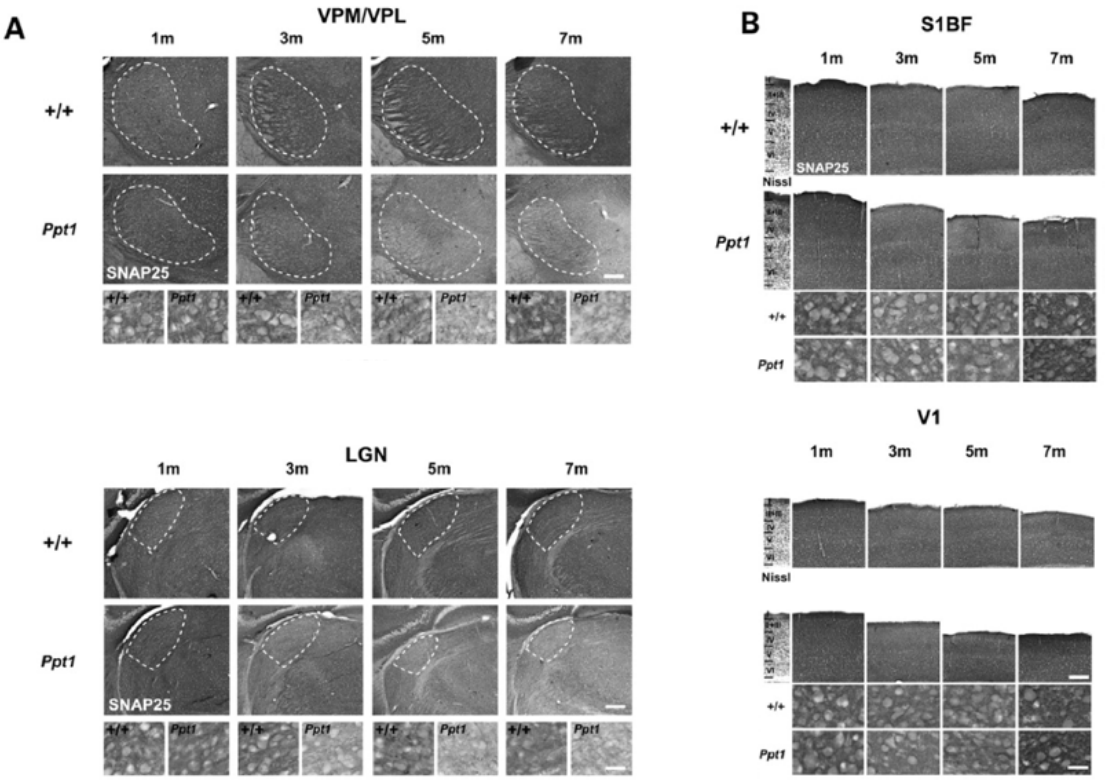

Fig. 4.1. Synaptic pathology in thalamus and cortex throughout disease progression in Ppt1$^{-/-}$ mice **A.** Changes in immunostaining for SNAP25 in VPM/VPL and LGNd thalamic nuclei of 1, 3, 5 and 7-month-old Ppt1$^{-/-}$ mice (Ppt1) and controls (+/+). Levels of SNAP 25 staining in both VPM/VPL and LGNd are very similar between Ppt1$^{-/-}$ and control mice at 1 month. However, levels of SNAP25 were markedly reduced in Ppt1$^{-/-}$ thalamus from 3 months of age and continued to decrease with increased age. The boundaries of thalamic nuclei are indicated by white dashed lines. **B.** SNAP25 immunoreactivity in the cortex was decreased by 3 months of age, but subsequently increased in intensity over time compared with age-matched control mice (+/+). Laminar boundaries are indicated by roman numerals on a Nissl-stained section through the same region of cortex. **A&B.** Representative images from experiments on >3 mice per genotype. Scale bar = 200 μm; 30 μm in higher magnification views. Figure adapted from Fig. 1 in (Kielar *et al.*, 2009).

4.2 Materials and methods

4.2.1 Animals and tissue harvesting

For the study of molecular changes happening throughout the time-course of disease progression, Ppt1-deficient mice (*Ppt1*$^{-/-}$) (Gupta *et al.*, 2001) and age-matched C57BL/6 control were terminated (WT) at 1, 3, 5 and 7 months of age. Human cortical *post mortem* samples were used to examine the relevance of specific protein candidates to the human disease. Please refer to General materials and methods (Chapter 2) for more details.

4.2.2 Synaptosome preparation

Both mice and human tissues were processed for synaptosome production. Mice tissue processing was carried out by Dr. Thomas Wishart and sent to The fingerprint proteomic facility (University of Dundee) for label free proteomics experiment. Mice were terminated and brains were rapidly removed and briefly chilled in ice cold ACSF (125mM NaCl, 26mM NaHCO3, 25mM glucose, 2.5mM KCl, 1.25mM NaH2PO4, 1mM CaCl2, 4mM MgCl2) before regional microdissection. Cortex (predominantly pre-/frontal) and thalamus were dissected bilaterally from four *Ppt1*$^{-/-}$ and four WT littermates at 1, 3, 5, and 7 months old and used for production of synaptosomes. Half of the synaptosomes were extracted for label-free proteomics processing and the other half was stored at -80 for later QWB.

Human *post mortem* cortical sample processing for synaptosome production was carried out for the analysis of human proteome. Please refer to General materials and methods (Chapter 2) for more details.

4.2.3 Protein extraction

For label-free proteomics (mice): Half of the synaptosomes from *Ppt1*$^{-/-}$ and WT controls at 1, 3, 5 and 7 months were resuspended and each corresponding genotype and time-point were pooled and massagrated using a pestle and morter in SDT lysis buffer containing 100 mM Tris-HCl (pH 7.6), 4% (W/V) Sodium dodecyl sulphate, 0.1 M D/L-dithiothreitol and 1% protease inhibitor cocktail (Wishart *et al.* 2014). Tissue underwent 7 rounds of homogenization and sonication. Next, samples were homogenized using the Gentle Macs dissociator (*Miltenyl Biotech Inc)* and M tubes (*Miltenyl Biotech Inc*). Please refer to General materials and methods (Chapter 2) for more details.

For QWB: the other half of synaptosomes from *Ppt1*$^{-/-}$ mice and corresponding WT controls and INCL, JNCL and control human synaptosomes were resuspended homogenized individually in SDT lysis buffer containing 100 mM Tris-HCl (pH 7.6), 4% (W/V) Sodium dodecyl sulphate and 1% protease inhibitor cocktail (Wishart *et al.* 2014) Please refer to General materials and methods (Chapter 2) for more details.

4.2.4 Label free proteomics

Time-course label free proteomics was carried out from thalamic and cortical synaptosomes. from *Ppt1*$^{-/-}$ and WT controls protein extracts (1, 3, 5 and 7 months), by Dr. Abdel Atrih (Fingerprints proteomics facility, University of Dundee). Please refer to General materials and methods (Chapter 2) for more details.

4.2.5 Quantitative fluorescent western blotting (QWB)

15 μg of protein was loaded for all the QWB within this chapter. QWB methodology and antibodies used can be found in the General materials and methods section (Chapter 2).

4.2.6 *In silico* proteomic analysis

4.2.6.1 *Progenesis*

Label-free proteomic thalamic and cortical synaptic raw data was imported into *Progenesis LCMS* for differential analysis and identification of peptides followed by quantification of relative ion abundance of peptides and corresponding proteins. Each individual brain area was analysed separately.

Thalamus: All the samples (*Ppt1*$^{-/-}$ and WT at 1, 3, 5 and 7 months) were aligned to the same sample reference to allow the identification of the same ion peptides across all the samples. This allows to obtain the same protein identifications throughout all the time-course. Reference sample WT-3B was automatically identified by *Progenesis* as the least different sample to all the others. Alignment scores were optimal, in between 96.8-98.9 % of overlap. Next, before the detection of ion peptides, a filtering step was applied based on 1. Retention times; in this case only the ions detected between 9-94 min were analysed as features outside this area are often not separated adequately for an optimal detection. Retention times were manually identified by looking at the 2-dimentional representation of each sample run. 2. Only peptides with maximum ion charge of 5 were considered. Peptides obtained after trypsin digestion rarely are long enough to contain more than 5 charges. And if there are,

they tend to not get detected due to its size. Therefore, by applying this filter we reduce computational time when analysing the experiment.

Cortex: Following the same criteria as stated above, all samples were aligned to the sample reference was Ppt1-1B. Alignment scores were also very good, in between 88.9—98.8 % overlap. Only peptides within the retention times between 9-93 min with less than 5 ion charges were considered for the analysis.

After pick picking, peptide data was then exported for each brain area and imported to MASCOT for protein ID assignment. Please refer to General materials and methods (Chapter 2) for more details.

Protein data generated in *MASCOT* was then imported back to *Progenesis* for further analysis. And an individual experiment from each time-point was carried out. An initial filtering of each individual time-point was applied to study the global changes taking place in each time-point (≥2 unique peptides, p-value<0.05 and >2 Fold-change). However, for the tracking of individual proteins across the 4 time-points, only proteins with ≥ 2 unique peptides were used. Excel spreadsheet with protein data was then exported for each time-point and brain area for further processing and analysis through different bioinformatics tools.

4.2.6.2 *DAVID*

The *Database for Annotation, Visualization and Integrated Discovery* (*DAVID*) software (available at http://david.abcc.ncifcrf.gov) was used to obtain an indication of the level of sample enrichment afforded through the process of synaptosome production inputting un-filtered mass spectrometry thalamic data and to characterize the functions associated to the protein clusters from *BioLayout* in both thalamic and cortical time-course datasets (see below). Please refer to General materials and methods (Chapter 2) for more details.

4.2.6.3 *BioLayout Express*

BioLayout was also used for clustering of proteins following similar expression trend in order to correlate their expression profile to the progression of the disease.

Clusters or group of clusters with similar expression trend were further analysed using *DAVID* (see above). Please refer to Generals materials and methods (Chapter 2) for more details.

4.2.6.4 *Ingenuity Pathway analysis (IPA)*

IPA was used for comparative analyses between thalamic and cortical synaptic proteomic time-course data. Please refer to General materials and methods (Chapter 2) for more details.

4.2.6.5 Data analysis and figure production

Protein candidates with "delayed" profile were identified using *Python* (*jupyter notebook and pandas package*) filtering by proteins changed in the same direction between 3 months in thalamus (3-T) & 5 months in thalamus (5-T) time-points and 5 months in cortex (5-C) & 7 months in cortex (7-C) time-points and which presented more than 1.2 fold-change in 3-T and 5-C (ie. Fig. 4.16 & 4.17). Please refer to General materials and methods (Chapter 2) for more details.

4.3 Results

4.3.1 Processing and analysis of thalamic proteomic data

Prior to this current work, *Ppt1*$^{-/-}$ (Gupta *et al.*, 2001) and age-matched C57BL/6 control (WT) were terminated and brains were rapidly removed. Thalamus and cortical brain areas were dissected bilaterally by Dr. Thomas Wishart and synaptosomes were produced for all the time-points and genotypes. Samples were processed for label free proteomics by the fingerprint facility in The university of Dundee. At the start of this project, the raw mass spectrometry (MS) data was then analysed (see 4.2 Materials and methods).

The thalamic synaptosomes MS were analysed first, because thalamus had been shown to be the most vulnerable area of the brain in the NCLs (see 4.1 Introduction). To process raw label-free MS data, we utilized *Progenesis* software. As explained in Chapter 2, *Progenesis* consists in a series of steps to convert the MS/MS data into a reliable lists of protein identifications and the respective fold-change between the different comparisons made. Unfortunately, at the time, *Progenesis* was not designed to process such complex time-course comparative analyses between two conditions (WT and *Ppt1*$^{-/-}$). For this reason, and after

assessing different experimental designs, it was decided that each time-point should be analysed separately (ie. *Ppt1*$^{-/-}$ vs. WT at 1 months, *Ppt1*$^{-/-}$ vs. WT at 3 months, etc). All the samples were aligned for the identification of the same peptides across all the samples (see 4.2 Materials and methods) In order to reduce the computational load, we filtered the peptides by the standard criteria where cutoffs where as follows: P value<0.05, fold-change>2 and power>0.8. Proteins were assigned to peptides using *MASCOT* database (see 4.2 Materials and methods). A total of 726 proteins were identified. As a quality control, Principal Component Analysis (PCA) was then generated by *Progenesis*. PCA shows a 2-dimentional representation of the distribution of the data that allows the detection of outliers as well as a means to visualize how well the samples group (Fig. 4.2A). As observed in Fig. 4.2A, each genotype and time-point cluster together, indicating that there are no outliers across each technical replicate for any of the groups. Also, the elliptical shape formed by each of the protein identifications (represented by its accession number in grey), indicates a normal distribution of the data. From Fig. 4.2A, it is evident that *Ppt1*$^{-/-}$ at 3 months is the most different group. This time-point group, correlates to the onset of synaptic pathology starting in the thalamus (Kielar *et al.*, 2009) (Fig. 4.1).

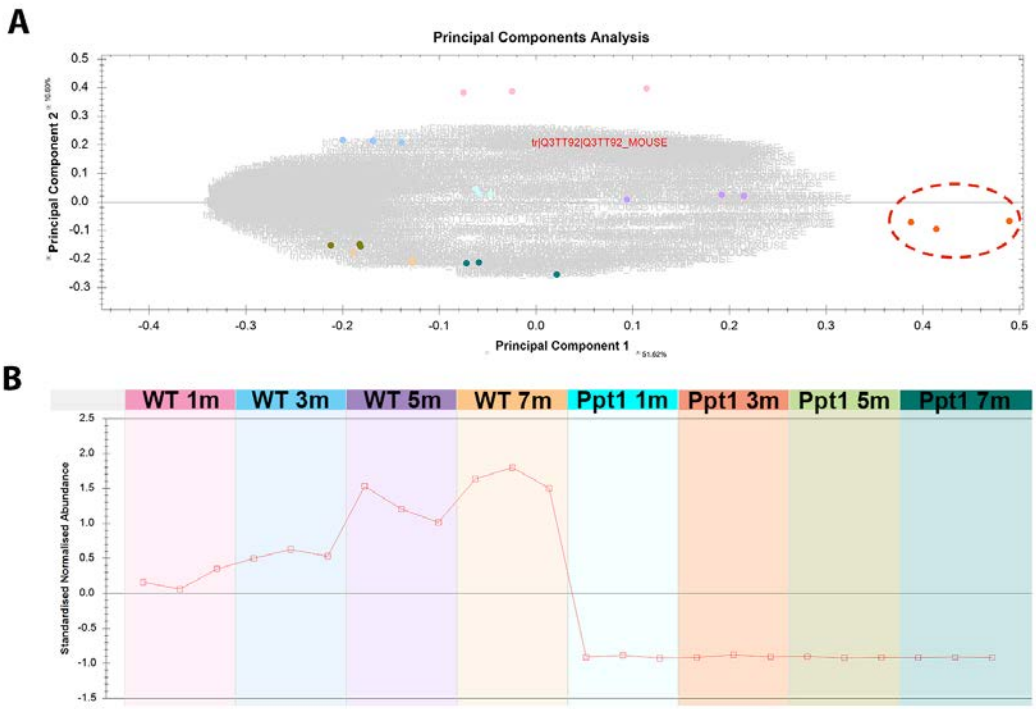

Fig. 4.2. Thalamus time-course quality control. **A.** PCA of all the thalamic samples generated in *Progenesis* indicating the presence of no outliers in the data, the optimal clustering of the different genotype-time-point groupings and the normal distribution of the data indicated by the elliptical gray shape of the protein identifications. Red oval indicates *Ppt1*$^{-/-}$ samples at 3 months are the most different when compared to the other groups. **B.** Standardized normalized abundance of Ppt1 protein

across the time-course and each technical replicate of WT control mice (left side 4xsections) and *Ppt1*$^{-/-}$ (right side 4xsections).

Furthermore, we detected Ppt1 protein to be consistently downregulated in *Ppt1*$^{-/-}$ samples across all the time-points and, very interestingly, showed a steady upregulation throughout the time-course in the WT controls (Fig. 4.2B). This finding supports the quality of the data. Importantly, previous studies reported that Ppt1 expression increases in the human embryonic brain from the beginning of cortical neurogenesis through cortical development indicating its potential implications for neuronal development (Heinonen *et al.*, 2000). However, no evidence was found yet regarding Ppt1 expression progressive increase through time-course postnatally.

Moreover, in order to assess the level of enrichment of the samples for synaptic terms, *DAVID* enrichment analysis was performed in the unfiltered thalamic proteome (726 proteins identified) (Amorim *et al.*, 2017). As shown in Table 4.1, synaptic terms were significantly enriched with fold-enrichments of 21.41-4.26. Therefore, we can be confident that we are working with synaptic enriched samples.

After standard quality control checks, we continued the analysis. A common analysis archive was used for the whole time-course and was reused as a new experiment for each time-point. Each time-point was processed independently in order to obtain the correct comparisons and statistical tests output (i.e. Fold-change between age-matched *Ppt1*$^{-/-}$ and WT and p-value (ANOVA)).

Table 4.1. DAVID enrichment analysis of unfiltered thalamic proteome

GO terms	Term	p-value	Fold Enrichment	Benjamini
GO:0033269	internode region of axon	6.31E-03	21.41	3.03E-02
GO:0048488	synaptic vesicle endocytosis	7.15E-05	12.15	1.39E-03
GO:0048489	synaptic vesicle transport	8.96E-09	10.06	3.52E-07
GO:0000149	SNARE binding	1.27E-04	6.74	2.68E-03
GO:0050804	regulation of synaptic transmission	3.31E-09	5.10	1.52E-07
GO:0007268	synaptic transmission	6.80E-15	4.92	1.66E-12
GO:0019226	transmission of nerve impulse	3.24E-15	4.41	8.86E-13
GO:0005739	mitochondrion	1.55E-46	4.26	3.19E-44

Global changes occurring at each time-point were examined through a stringent filtering criterion which emphasise the changes happening in each time-point between *Ppt1*$^{-/-}$ and WT. Selected proteins were identified by ≥2 unique peptides, p-value <0.05 and fold-change ≥2 (see Appendix I-Table A7 for information regarding proteins identified by ≥2 peptides). Out of the total 726 proteins identified across the 4 time-points, many did not pass the filtering criteria for each time-point (Fig. 4.3). The distribution of fold-change across the 4 time-points before and after filtering can be observed in Fig. 4.3A. Fig. 4.4B shows in more detail the differentially expressed proteins between WT (pink shaded) and *Ppt1*$^{-/-}$ (blue shaded) in each time-point. Importantly, and as predicted by the PCA (Fig. 4.2A), the time-point with more proteins differentially expressed was the 3 month time-point (146 proteins changed by at least 2 fold-change). It is also noticeable, that most of these proteins were downregulated at 3 months. Conversely, at the 5 month time-point, 98 proteins had at least a 2 fold-change and the major trend showed upregulation. Surprisingly at 7 months, where the atrophy and the pathological changes in these mice was very high, only 22 proteins were differentially expressed ≥2 fold-change, suggesting that the 3 and 5 month time-points (early and mid stages) are dynamically more active at the molecular level than end stages of the disease (Fig. 4.3B)

With these initial analyses, we could identify that the time-point with a higher number of differentially expressed proteins correlated to the onset of synaptic pathology (Kielar *et al.*, 2009), Fig. 4.1). The molecular pathology resembled the *Cln3*$^{-/-}$ brain-region proteomic analyses (Chapter 3), in which higher number of protein changes were occurring in thalamus in relation to less-vulnerable brain areas (hippocampus and cortex).

Further investigation was carried out to see if the highly changed proteins at 3 and 5 months were the same subset of the 726 proteins identified in total. After demonstrating that 3 months is a key time-point at both morphological and molecular level, the 146 proteins presenting at least 2 fold-change at 3 months were aligned to the other time-points to profile how these proteins were changing over time.

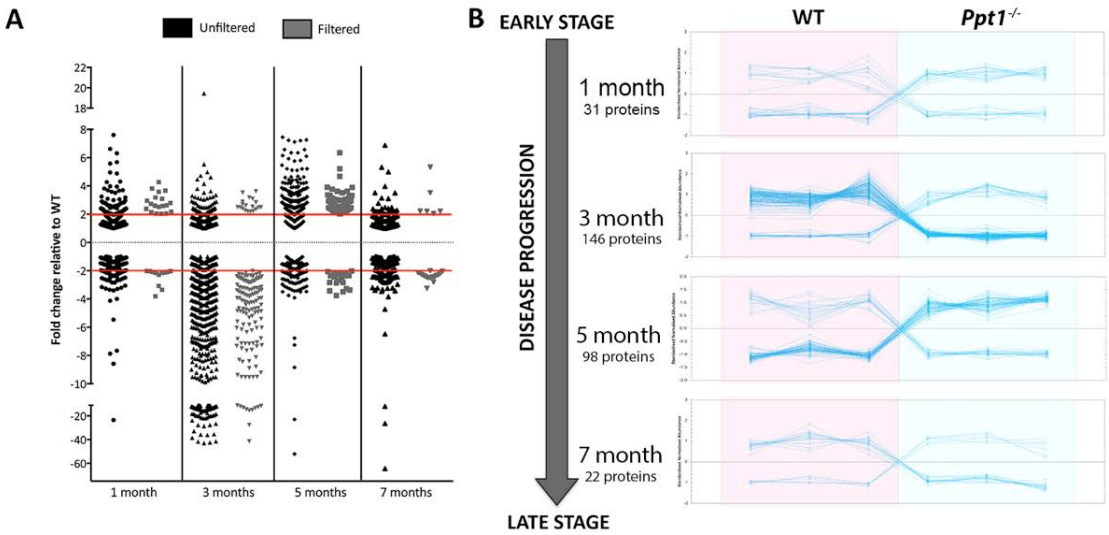

Fig. 4.3. Data filtering of thalamic proteomic data. **A.** Scatterplot representing the distribution of fold-changes of the 726 proteins identified in each time-point before (black dots) and after filtering (grey dots). **B.** Line graphs representing the standardized normalized abundance of the filtered proteins in each time-point in both WT (pink shaded background) and *Ppt1*$^{-/-}$ (blue shaded background). Each dot represents a technical replicate and each line the expression of an individual protein. The numbers of the protein that met the filtering criteria for each time-point are indicated to the left side of the plots.

Fig. 4.4A represents how these 146 proteins are changing throughout disease progression. The different line colours represent groups of proteins with similar expression trend that were manually identified (Fig. 4.4B). As represented by lines in red, most proteins showed a "down-up" trend between 3 and 5 months, indicating that most downregulated proteins at 3 months have indeed, the opposite change at 5 months. This trend was validated by QWB by looking at the most interesting 3 month time-point. At 3 months, synapses start to degenerate corresponding to a peak of differentially expressed proteins. As shown in Fig. 4.5, examples of up and downregulated proteins were validated based on the availability of antibodies and proteins which have been identified to be disrupted in other neurodegenerative diseases (Wishart *et al.*, 2014, Wishart *et al.*, 2012).

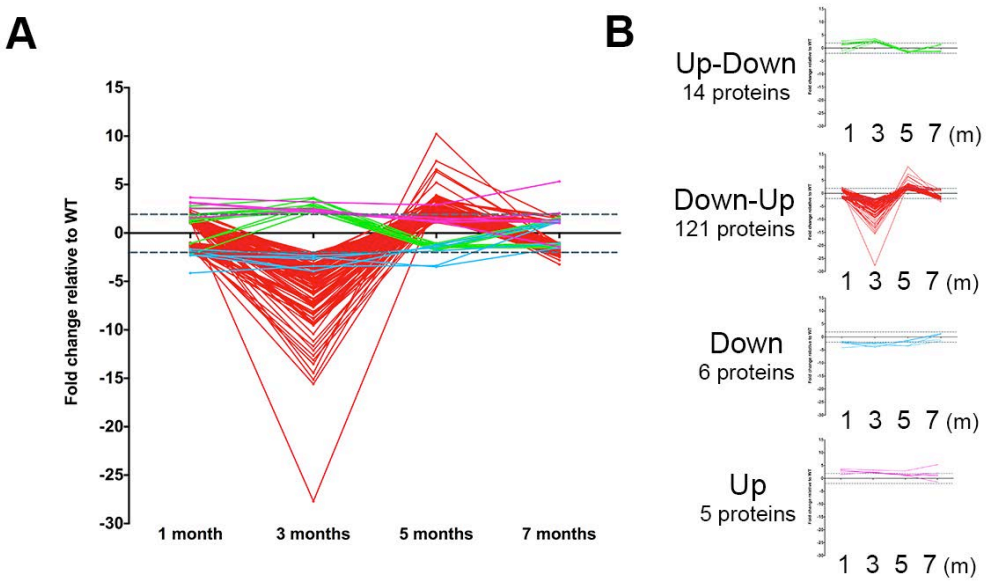

Fig. 4.4. Expression tracking of 3-month changed proteins throughout time-course of disease progression in thalamus. **A.** Line graph representing the fold-change expression of the 146 proteins that were changed ≥2 fold at 3 months across all the 4 time-points. **B.** Individual line-graph representation of protein subgroups presenting similar expression trends.

Due to the complexity of the molecular trends observed, *BioLayout Express* was used for further characterization. *BioLayout* recognizes the patterns of expression in more detail allowing the breakdown of the data into smaller lists (See Chapter 2. General materials and methods). For this analysis, all the proteins were identified by at least 2 unique peptides regardless of their magnitude of change (265 proteins). *BioLayout* identified 13 clusters of proteins which followed specific expression trends (Fig. 4.6). Afterwards, each cluster (or group of clusters following similar trends) was queried in *DAVID* in order to identify the biological pathways and GO terms associated with these proteins (Fig. 4.6).

DAVID enrichment analysis determined that clusters showing a down-up trend (Clusters 1, 2, 4 &5) were very enriched in mitochondrial proteins, including but not limited to oxidative phosphorylation (OXPHOS) and TCA cycle pathways. Proteins showing the opposite profile, up-down (Clusters 3, 8, 9, 12 and 6) were enriched for carbon metabolism, neuron development and synaptic terms.

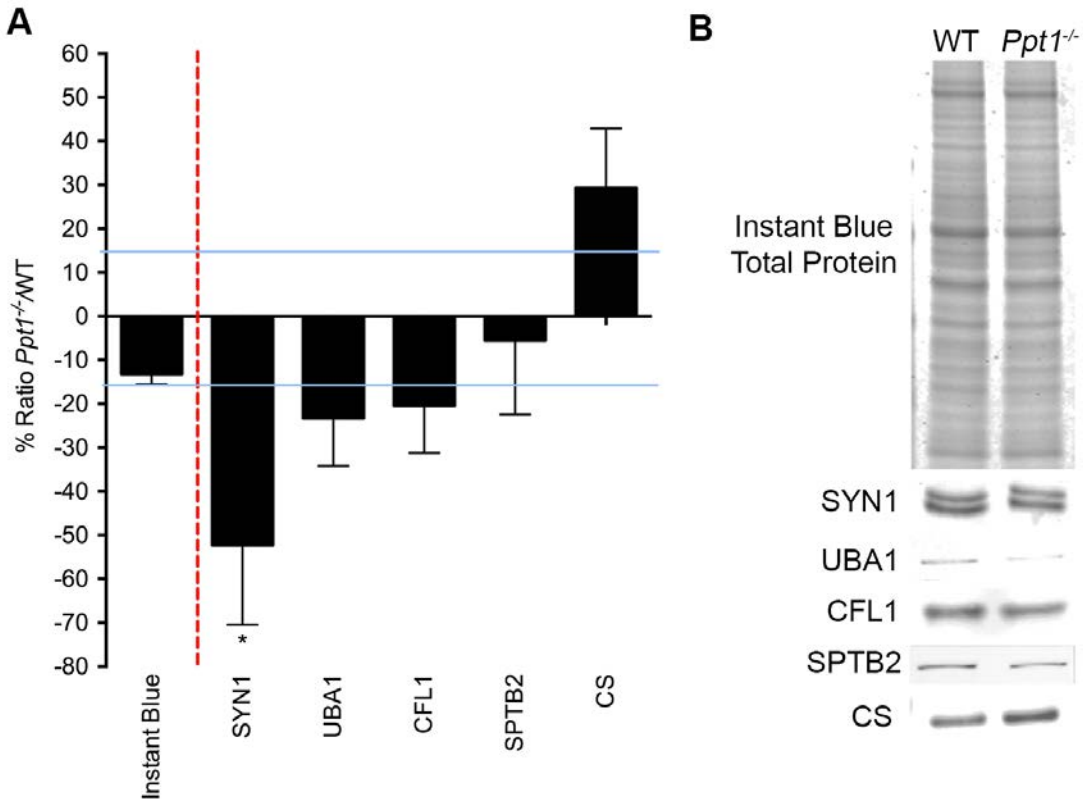

Fig. 4.5 QWB validation of thalamic proteomics. **A&B.** Bar chart showing the quantification as % ratio of *Ppt1*$^{-/-}$/WT and corresponding representative bands. Instant blue staining of total protein was used as a loading control. Mean ± SEM *P<0.05 (Student T test, N=3-4 mice per genotype).

Interestingly, similar results between differentially vulnerable synaptic population across brain areas were found in Chapter 3. In the *Cln3*$^{-/-}$ proteomic analyses, we showed that downregulated proteins correlating to synaptic vulnerability were enriched for mitochondrial proteins, whereas upregulated proteins were enriched for synaptic-related terms (Fig. 3.7).

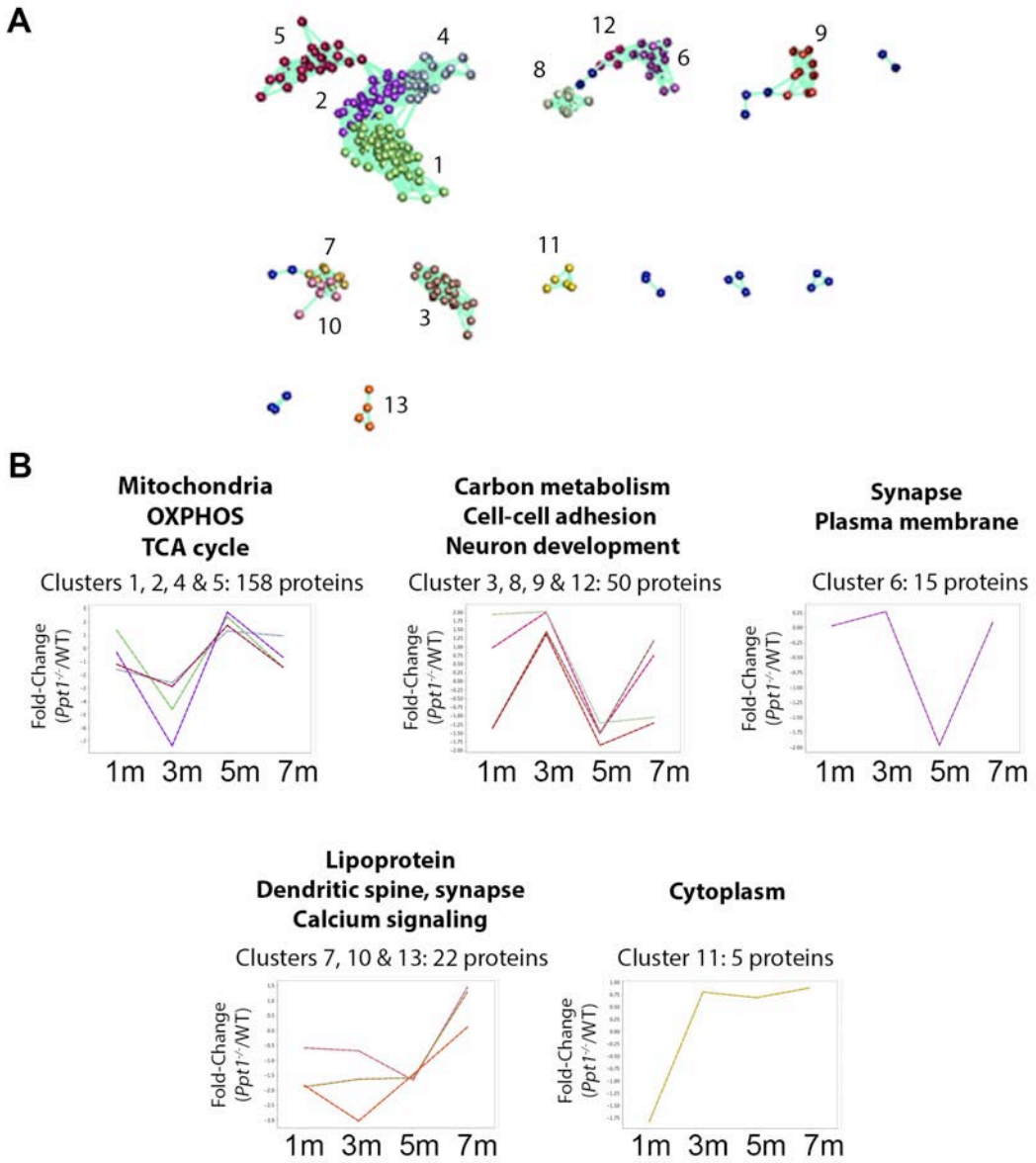

Fig. 4.6. Molecular profiling of protein changes through the time-course of disease progression in thalamic synaptosomes in* Ppt1$^{-/-}$ *mice. **A.** 3-dimentional representation of the proteomic data. Each sphere represents a protein (fold-change *Ppt1*$^{-/-}$/WT across 1, 3, 5 and 7 months). The colours and numbers represent clusters of proteins which display similar expression trend through the time-course. **B.** Line graphs of individual or group of clusters representing the mean expression trend of the proteins within each cluster (indicated by colour) and biological functions/organelles for which these proteins are enriched for, according to *DAVID* annotation analyses.

The work provided a more in-depth insight into the possible biological functions linked to each molecular trend happening throughout the time-course of disease progression. However, it was intriguing and unexpected that the pronounced downregulation at 3 months corresponds to a reversed upregulation at 5 months of many proteins related to mitochondrial function. Such unexpected results denote the complexity of the time-course analysed. Previous degenerative proteomics studies by our group had short time-scales (ie. SMA, 6 days; injury induced neurodegeneration, 2 days). Because of this, it is likely that the same population of synapses was being sampled across time-points. However, in the time-course analysed here, it is probable that the composition of the population of synapses at 5 months is very different compared to 3 months. Thus, by 5 months a larger proportion of degeneration-resistant synapses will be sampled whereas at 3 months there will be a combination of both (degenerating and "resistant") meaning that the data could be analysed in multiple ways. These questions are addressed in more detail later in the chapter.

4.3.2 Processing and analysis of cortical proteomic data

Following the in-depth characterization of the thalamic synaptosomes, the cortical data was characterized. *Progenesis* was used in exactly the same way as in the thalamus (see section 4.3.1). PCA was generated in order to detect any potential outlier and confirm that the genotype-time-point groups were clustered adequately. The normality of the data (statistically speaking) was also assessed by the elliptical shape of the distribution of the proteins identified (Fig. 4.7).

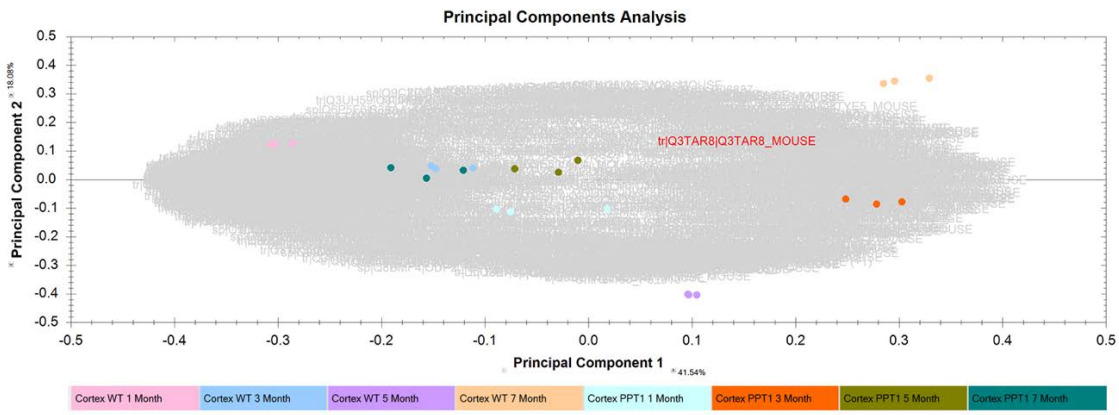

Fig. 4.7. Cortex time-course quality control. PCA of all the cortical samples generated in *Progenesis* indicating the presence of no outliers in the data, the optimal clustering of the different genotype-time-point groupings and the normal distribution of the data indicated by the elliptical gray shape of the protein identifications.

In order to get a general idea of the changes happening throughout the time-course of disease progression in the cortex, each time-point was filtered by the same criteria as the thalamus (≥2 unique peptides, p value <0.05 and fold-change ≥2, see Appendix I-Table A8 for information regarding proteins identified by ≥2 peptides). A total of 1326 proteins were identified across all the samples but only some met the filtering criteria for each time-point (Fig. 4.8). It is known in the literature that the synaptic pathology in the cortex starts at around 5 months of age (Kielar *et al.*, 2009). However, we identified 110 differentially expressed proteins already at 3 months. And similarly to protein changes in the thalamus at the same time-point, the main trend in protein changes is downregulation (Fig. 4.8B). Importantly, at 5 months of age (onset of synaptic pathology in cortex), we do see a downregulation trend followed by an upregulation trend at 7 months mirroring the 3 and 5 months in the thalamus.

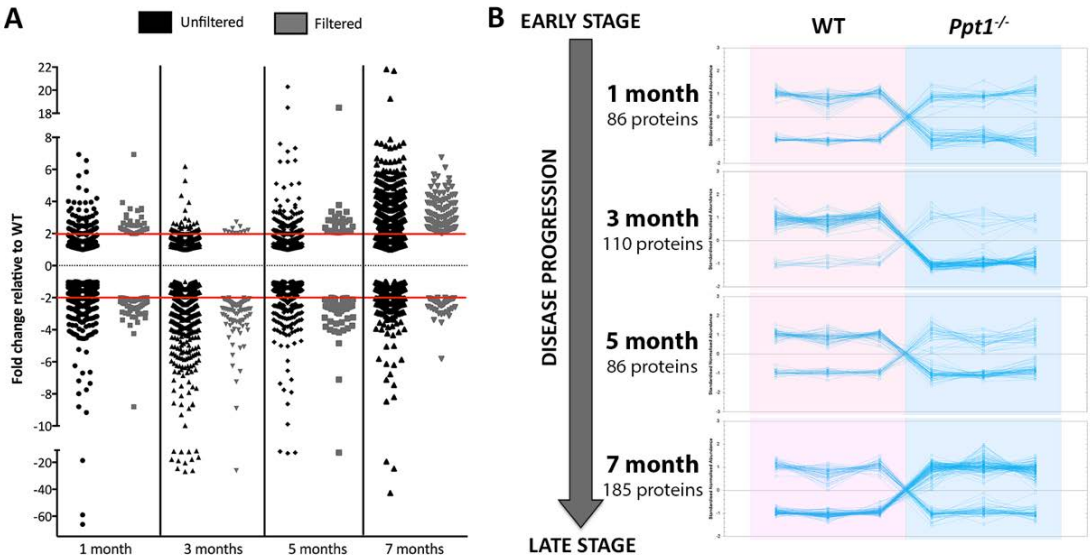

Fig. 4.8. Data filtering of cortical proteomic data. **A.** Scatterplot representing the distribution of fold-changes of the 1326 proteins identified in each time-point before filtering (black dots) and after filtering (grey dots). **B.** Line graphs representing the standardized normalized abundance of the filtered proteins in each time-point in both WT (pink shaded background) and *Ppt1*$^{-/-}$ (blue shaded background). Each dot is representing a technical replicate and each line the expression of an individual protein. The numbers of the protein that met the filtering criteria for each time-point are indicated to the left side of the plots.

Importantly, between the 146 proteins that were changed at 3 months in the thalamus and the 110 proteins that changed at 3 months in the cortex, there were only 25 proteins in common. This indicates, that even though there is a common downregulation at the same time-point in both synaptic populations, they are mostly different proteins. Therefore, it is unlikely that the same molecular processes are happening in both thalamic and cortical synapses at the same time-point.

To get a more in-depth insight into the biological functions disrupted throughout the time-course of disease progression in the cortex, *BioLayout* was used in the same manner as was done with the thalamic data. Proteins identified by ≥2 unique peptides, regardless their magnitude of change to study all the expression trends taking place were investigated. *BioLayout* identified 18 different clusters, which were grouped by similarity and were analysed using *DAVID* enrichment analysis. As seen in Fig. 4.9, more heterogeneous molecular trends were identified in the cortical data compared to the thalamic. In contrast to the thalamic data, a high number of proteins displayed a steady upregulation correlating to disease progression (264 proteins), which were related to mitochondria and synaptic terms (Fig. 4.9). Interestingly, proteins displaying an upregulation peak at 5 months (onset of synaptic degeneration in the cortex, clusters 6 &18), were associated to synaptic terms and neuronal development, similarly to the "up-down" clusters in thalamus. However, there was no clear correlation between "expression trend" and biological function. Instead, each biological function appeared to be linked to multiple expression profiles, demonstrating the great complexity of the cortical synaptic data.

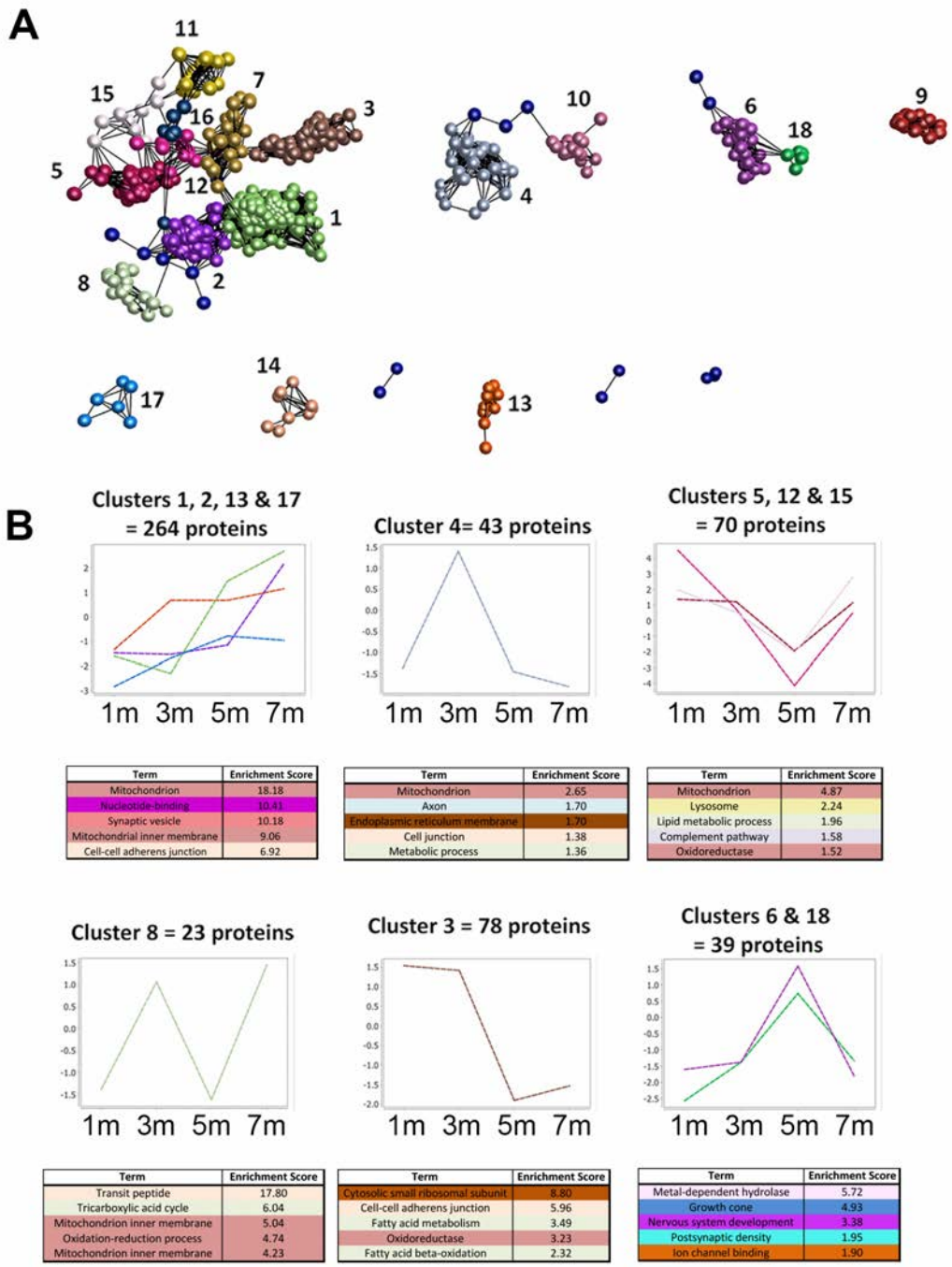

Fig. 4.9a. Molecular profiling of protein changes though the time-course of disease progression in cortical synaptosomes in* Ppt1$^{-/-}$ *mice. **A.** 3-dimentional representation of the proteomic data. Each sphere represents a protein (fold-change *Ppt1*$^{-/-}$/WT across 1, 3, 5 and 7 months). colours and numbers represent clusters of proteins which display similar expression trend through the time-course. **B.** Line graphs of individual or group of clusters representing the mean expression trend of the proteins within each cluster (indicated by the colour) and biological functions/organelles for which these proteins are enriched for, according to *DAVID* annotation analyses indicated by the table below each graph. Related functions were shaded with the same colour.

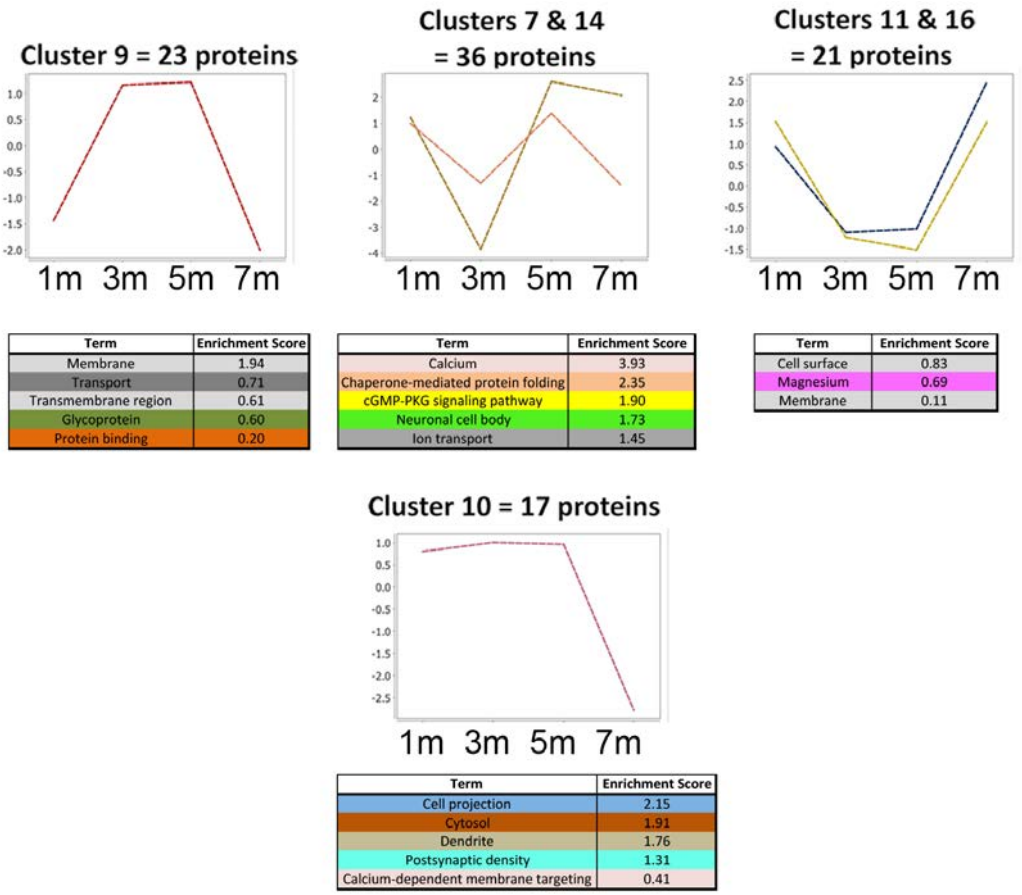

Term	Enrichment Score
Membrane	1.94
Transport	0.71
Transmembrane region	0.61
Glycoprotein	0.60
Protein binding	0.20

Term	Enrichment Score
Calcium	3.93
Chaperone-mediated protein folding	2.35
cGMP-PKG signaling pathway	1.90
Neuronal cell body	1.73
Ion transport	1.45

Term	Enrichment Score
Cell surface	0.83
Magnesium	0.69
Membrane	0.11

Term	Enrichment Score
Cell projection	2.15
Cytosol	1.91
Dendrite	1.76
Postsynaptic density	1.31
Calcium-dependent membrane targeting	0.41

Fig. 4.9b. Molecular profiling of protein changes though the time-course of disease progression in cortical synaptosomes in Ppt1$^{-/-}$ mice. Line graphs of individual or group of clusters representing the mean expression trend of the proteins within each cluster (indicated by the *colour*) and biological functions/organelles for which these proteins are enriched for, according to *DAVID* annotation analyses indicated by the table below each graph. Related functions were shaded with the same colour.

4.3.3 Thalamus and cortex comparative analysis

By looking at both thalamic and cortical data separately, the complexity of synaptic molecular protein changes happening throughout the time-course of degeneration is evident. The analysis helped us understand that the synaptic proteome dynamically changes from one time-point to another and is differentially constituted in each brain area. Moreover, we identified which pathways are perturbed in relation to WT controls. However, we do not know which changes are related to synaptic vulnerability and stability, which ones are compensatory responses to synaptic loss and which ones are simply consequences of

prolonged Ppt1 loss but are not related to synaptic loss at all [see General Introduction (Chapter 1, Fig. 1.3)]. Having demonstrated in Chapter 3 that analysing differentially vulnerable synaptic populations (same time-point, but different brain areas) can help refining and identifying which proteins are more likely to contribute to synaptic stability, we designed an experiment comparing thalamus and cortex to refine our list of candidates here.

A comparative analysis between thalamus and cortex was carried out, focusing on strategic time-points for each brain area, based on previous morphological studies (Kielar *et al.*, 2009). As shown in Fig. 4.10A, and as explained in the introduction of this chapter, the onset of synaptic pathology takes place at 3 months in thalamus and at 5 months in cortex. Synapses at such time-points in each area could be considered to have equivalent "vulnerability status" and therefore, those proteins modulating synaptic stability, would be expected to change in similar way in both brain areas at this equivalent disease stage (see 4.4. Discussion).

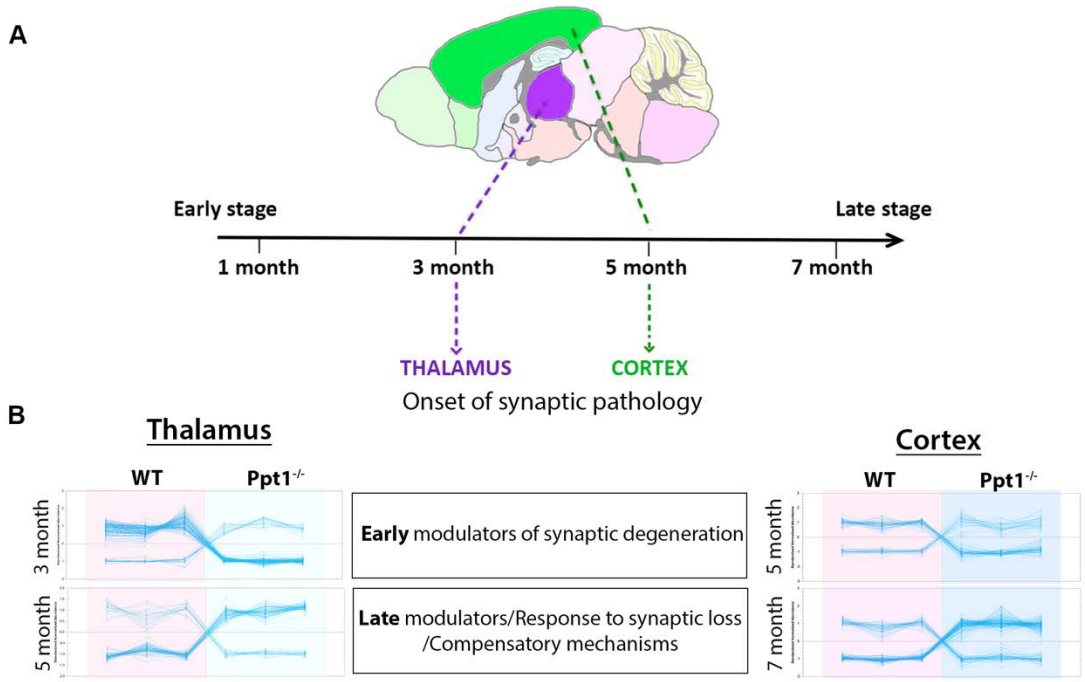

Fig. 4.10. Schematic and rationale used for comparative analysis of thalamic and cortical synaptic data. **A.** Sagital section of a mouse brain representation where each color represents a brain region. Thalamus in purple and cortex in green are the areas used in this study and 3 and 5 months are the time-points in which synaptic pathology starts for each brain area, respectively. **B.** Line graphs of filtered proteins for each of the time-points I am going to focus in each brain area.

Thus, the same would also be expected at 5 months in the thalamus and 7 months in the cortex. Changes happening at 3 months in the thalamus (3-T) and 5 months in the cortex (5-C) are therefore more likely to be early modulators of synaptic degeneration. However, 5 months in the thalamus (5-T) and 7 months in the cortex (7-C) are much more complex time-points. At such time-points, the population of synapses are very different to the ones at earlier stages. The population sampled at 5-T and 7-C are more likely to be a mixture of degenerating and resistant synapses. The changes expected at this mid/late stage time-point are more likely to be; 1. Late modulators; 2. Responses to the synaptic loss taking place or; 3. Compensatory mechanisms. Additionally, all time-points expected to change as a direct consequence of Ppt1 loss.

Comparative ingenuity pathway analysis of thalamic and cortical synapses

With this in mind, comparative analyses were carried out using *ingenuity pathway analysis (IPA)* to look for similarities between 3-T & 5-C and 5-T & 7-C. Similar changes at these strategic time-points, could be more likely to be related to synaptic stability.

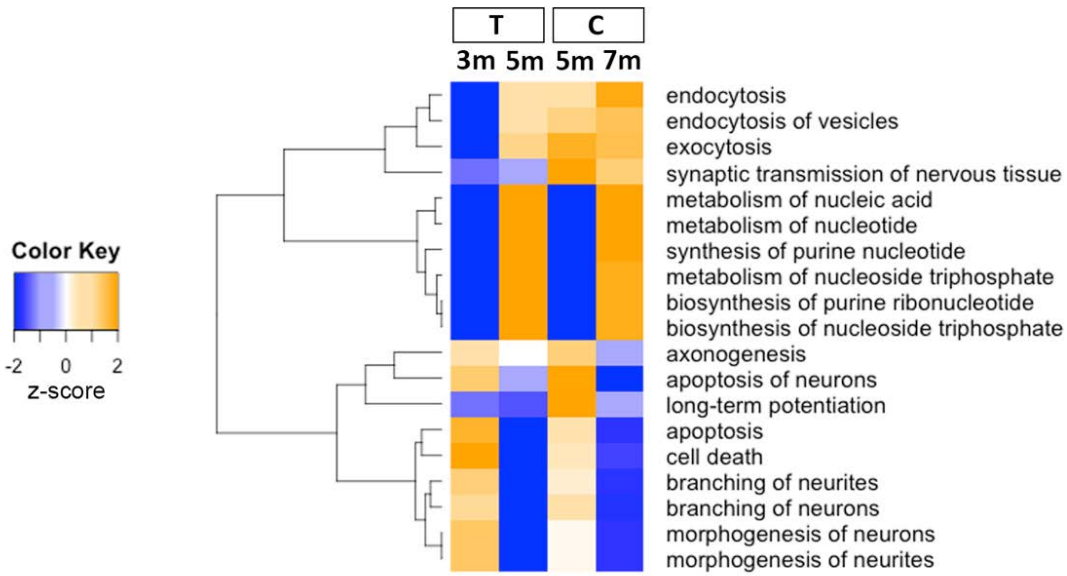

Fig. 4.11. Comparative analysis of biological functions perturbed in thalamic and cortical synapses at two equivalent stages. Heat-map representing the z-score measuring the level of activation/inhibition predicted by *IPA* of a specific biological function based on the proteomic data inputted.

When looking at the most significant "Diseases and biological functions" associated to each time-point and brain area, some specific functions which correlated to the comparative strategy were identified (Fig. 4.11). *IPA* predicts the level of activation/inhibition of specific functions/pathways given by a z-score based on the proteomic data inputted. The more negative the score (dark blue), the more inhibited a specific pathway or function is considered to be, whereas more active scores are indicated by a higher positive score (orange) (see Chapter 2. General materials and methods for more details). The heat-map in Fig. 4.11, highlights perturbations (activation/inhibition in relation to age-matched WT controls) correlating to the vulnerability status of synapses that are key for synaptic function such as endocytosis, metabolism of nucleotides, apoptotic pathways of morphogenesis of neurons.

Endocytosis was inhibited in 3-T but activated in all the other datasets. Nucleotide metabolism-related pathways were consistently inhibited at "early" time-points (3-T & 5-C) and activated at later time-points (5-T & 7-C). Conversely, an activation of cell-death pathways at 3-T & 5-C that was inhibited at 5-T & 7-C was identified which seems to indicate that at 5-T & 7-C there may be a strong neuroprotective response which fits with the initial hypothesis that at such a stage we could be sampling "resistant" synapses.

Next, proteins involved with this hypothetical neuroprotective response were examined. In Fig. 4.12 such proteins are highlighted in 4 different networks according to time-point and brain area. Such a response is predicted to be reflected in many proteins which may be involved in synaptic stability.

Looking at the upstream regulator analysis, a similar trend of activation/inhibitions across distinct synaptic populations was identified (Fig. 4.13). As we can see in the heat-map of Fig. 4.13, some proteins are predicted to be activated at 3-T & 5-C whereas they present an inhibited profile at 5-T and 7-C. The same happens in the opposite case where inhibition occurs when synapses start to degenerate but they appear activated at later stages of synaptic degeneration. Therefore, some of these proteins are likely to be upstream of the molecular pathways and biological functions described in Fig. 4.12, as they follow similar patterns of activation/inhibition.

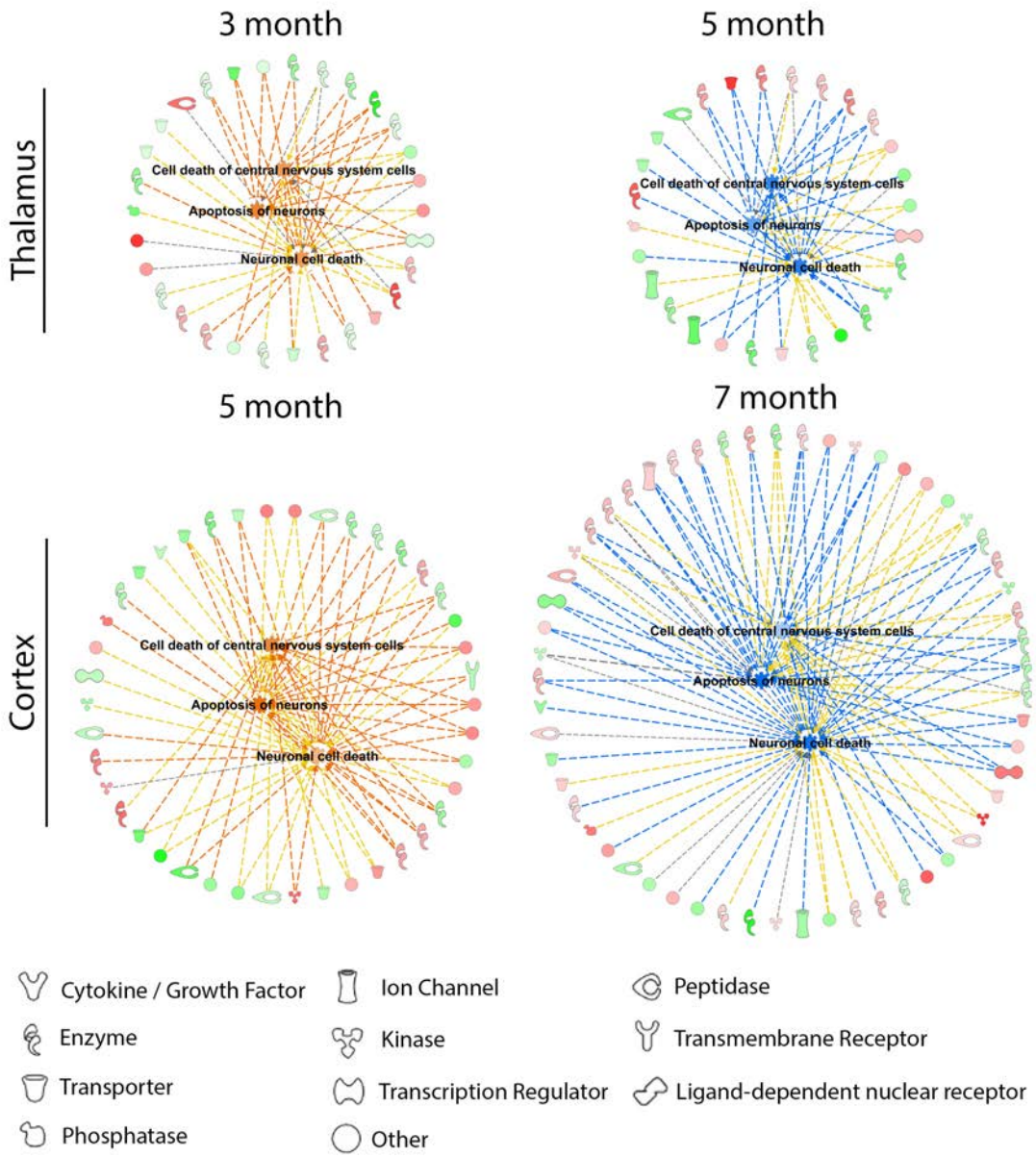

Fig. 4.12. Cell death-related protein networks generated in IPA in thalamus and cortex. Network representing which protein are related to "apoptosis of neurons", "cell death of central nervous system cells" and "neuronal cell death". Activation states of such networks are very similar at equivalent synaptic vulnerability status between thalamus and cortex (3-T & 5-C and 5-T and 7-C). Red=upregulated, green=downregulated, orange=predicted activation, blue=predicted inhibition.

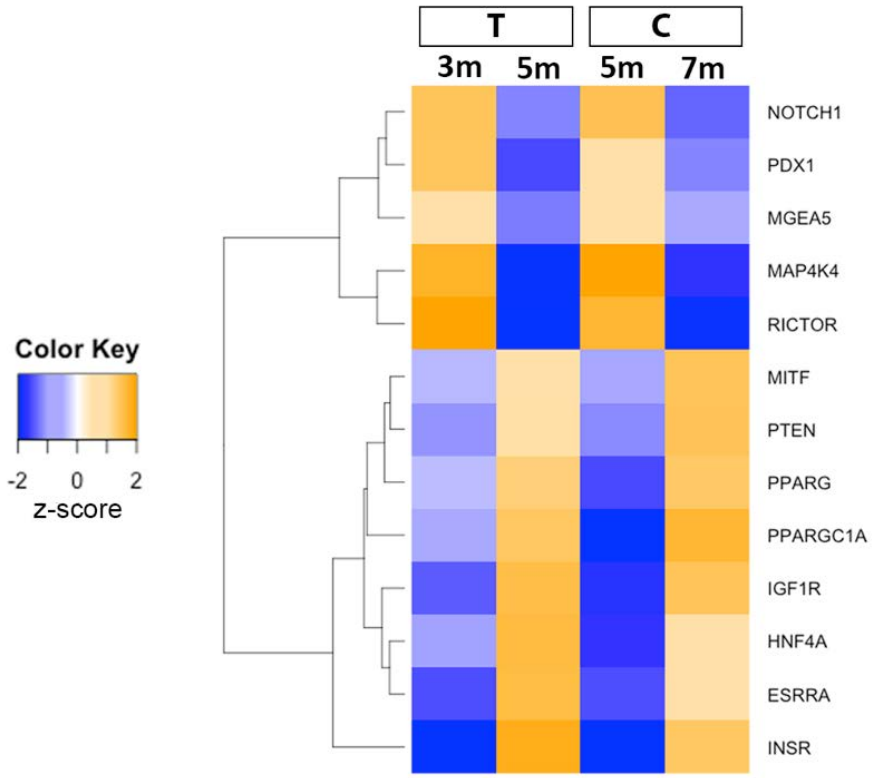

Fig. 4.13. Comparative analysis of predicted upstream regulators perturbed in thalamus and cortex at two equivalent stages. Heat-map representing the z-score measuring the level of activation/inhibition predicted by *IPA* of specific proteins, which are not in my datasets, but they are known to be upstream of the proteins in my dataset.

To confirm whether biological functions described in Fig. 4.11 and proteins in Fig. 4.13 were related, a regulatory network analysis was carried out in *IPA*. Such analysis highlighted that these elements were indeed significantly related through complex interaction networks. An example is shown in Fig. 4.14, where we find upstream regulator proteins such as ESRRA and INSR inhibited at 3-T and IGF1R, INSR, PPARGC1A and PTEN activated at 5 months. All these proteins are related to proteins identified in the proteomic data which, at the same time, relate to their biological functions. Some of these functions are cell survival and nucleotide metabolism which were stated earlier.

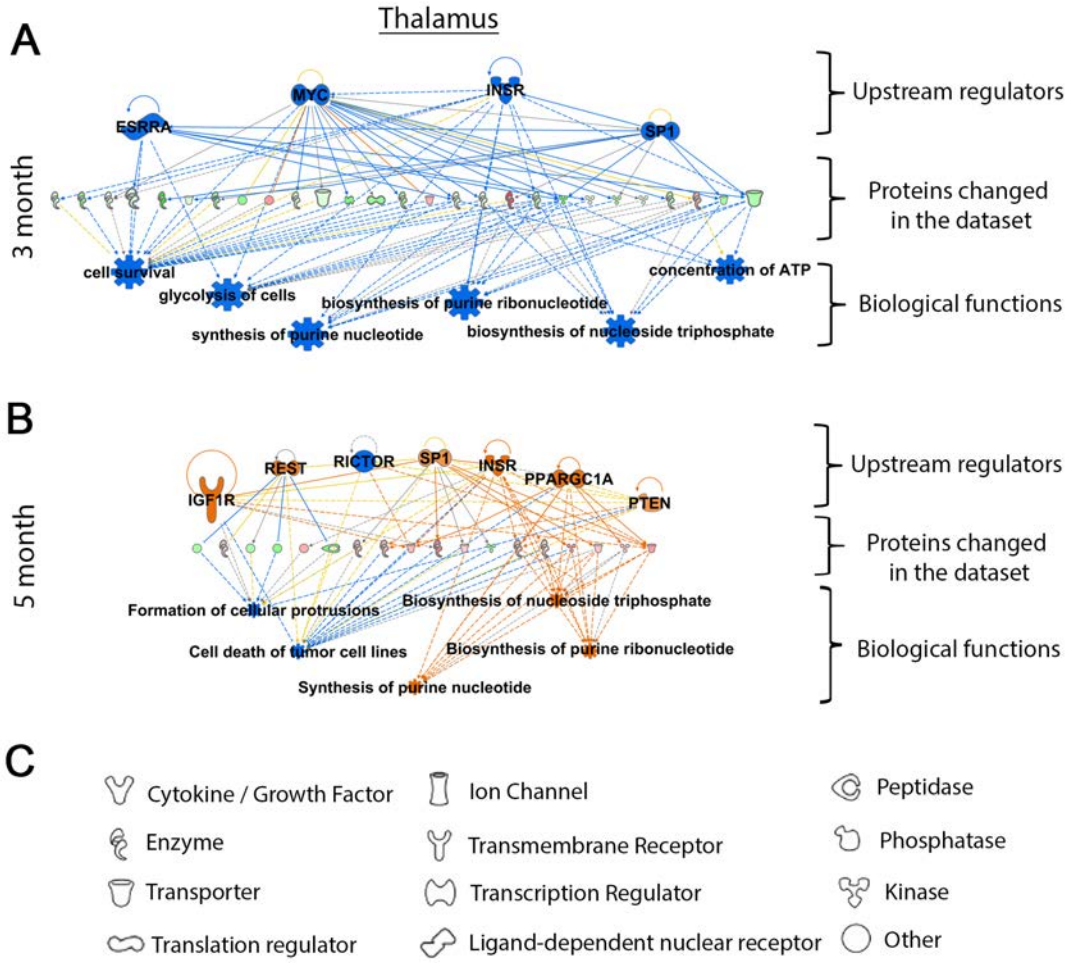

Fig. 4.14. Regulatory networks generated in IPA in thalamic synaptosomes at 3 (A) and 5 months (B). Network representing the interactions taking place between the predicted upstream regulators and the biological function identified which better correlated to the vulnerability status of synapses in thalamus and cortex. Upstream regulators are represented on the top of the network. In the middle there are the proteins within the thalamic dataset that sit downstream, and on the bottom layer are the biological function on which these proteins relate to. Red=upregulated, green=downregulated, orange=predicted activation, blue=predicted inhibition. **C.** Molecule shape legend.

The upstream regulators identified in Fig. 4.13 are therefore excellent candidates to target in *in vivo* experiments (Chapter 5), as their activation state correlates with the vulnerability status of synapses. These experiments are presented in Chapter 5, and allow determination of these candidates' ability to modulate the stability of neurons *in vivo*.

Identification of protein candidates with mirroring profiles between thalamus and cortex

After characterisation and comparisons between thalamic and cortical synapses at specific key time-points, it was of interest to identify specific proteins which were more likely to have a role in the stability of synapses. These proteins could then be added to the refined list of candidates from Chapter 3 (HIBCH, HADHA and ROCK2) and the 13 upstream regulators identified above (Fig. 4.13).

To do this, we took the overlapping proteins identified by ≥2 unique peptides in thalamic synapses (265 proteins) and cortical synapses (629 proteins) to look for common proteins across brain areas and be able to track specific candidates. 207 proteins were identified in both synaptic populations and were taken forward for further analysis (Fig. 4.15A).

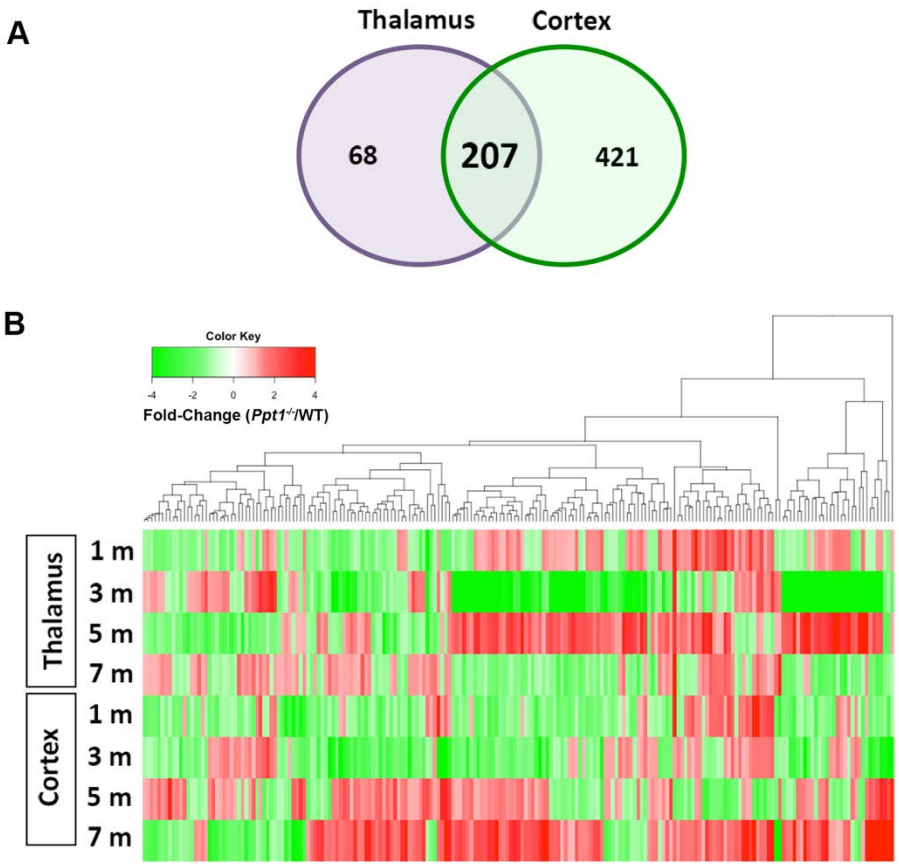

Fig. 4.15. Overlapping protein identifications between thalamic and cortical synaptosome proteomic data in* Ppt1$^{-/-}$ *mice. **A.** Venn diagram representing the overlapping proteins identified in thalamus and cortex identified ≥2 unique peptide. **B.** Heat-map representing how each overlapping protein changes throughout the time-course of disease progression and brain region.

Heat-map in Fig. 4.15B, indicates once again the level of complexity of these common 207 proteins identified and how they dynamically change across two brain regions throughout disease progression.

Again the focus was on the key time-points explained above (Fig. 4.10) to look for proteins whose expression profile is very similar at 3-T & 5-C and at 5-T & 7-C. The *Pandas* package of *Python* was used to filter my datasets. Using 1.2-fold cut-off for both up and downregulated proteins at 3-T & 5-C time-points, a total of 17 proteins were identified following the trends: 4 proteins followed the "up-down" trend in 3-T & 5-T and at 5-C & 7-C (Fig. 4.16) and 13 proteins the opposite profile, "down-up" trend in 3-T & 5-T and at 5-C & 7-C (Fig. 4.17).

Further investigations were done to see which pathways were related to these 17 proteins which displayed a delayed profile. These 17 proteins alone were analysed in *IPA*. Surprisingly, the top canonical pathway at early synaptic loss time-points for both thalamus and cortex was valine degradation (Table 4.2 & Fig. 4.18).

Interestingly, this is the same pathway identified to correlate to differentially vulnerable synaptic populations in the analysis of *Cln3*$^{-/-}$ (Chapter 3). And therefore, it seems relevant to both juvenile and infantile models of NCL. Although HIBCH was not detected in this proteomic study, enzymes such as HADHA, HIBADH or DLD were and showed the same trends as in the *Cln3*$^{-/-}$ analysis in the same brain region (thalamus) at equivalent disease stages (early). This time-course analysis provides more detail regarding the expression of these proteins with disease progression, and we can study how molecules in this pathway evolve with time. Looking at later time-points, we can detect that this pathway has the opposite profile than the one seen at early stages (Fig. 4.19).

Studying the different disrupted enzymes within the valine degradation pathway *in vivo* experiments (Chapter 5) could provide more insight into the role of this pathway, and each one of these enzymes in the stability of neurons.

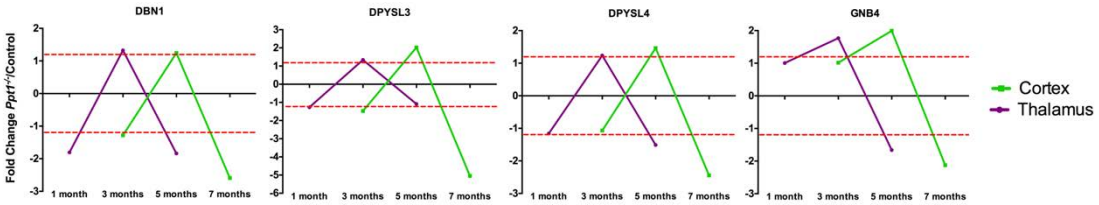

Fig. 4.16. Identified protein candidates with a "delayed up-down" profile between thalamus and cortex. Red dashed lines indicate 1.2-fold cut-off.

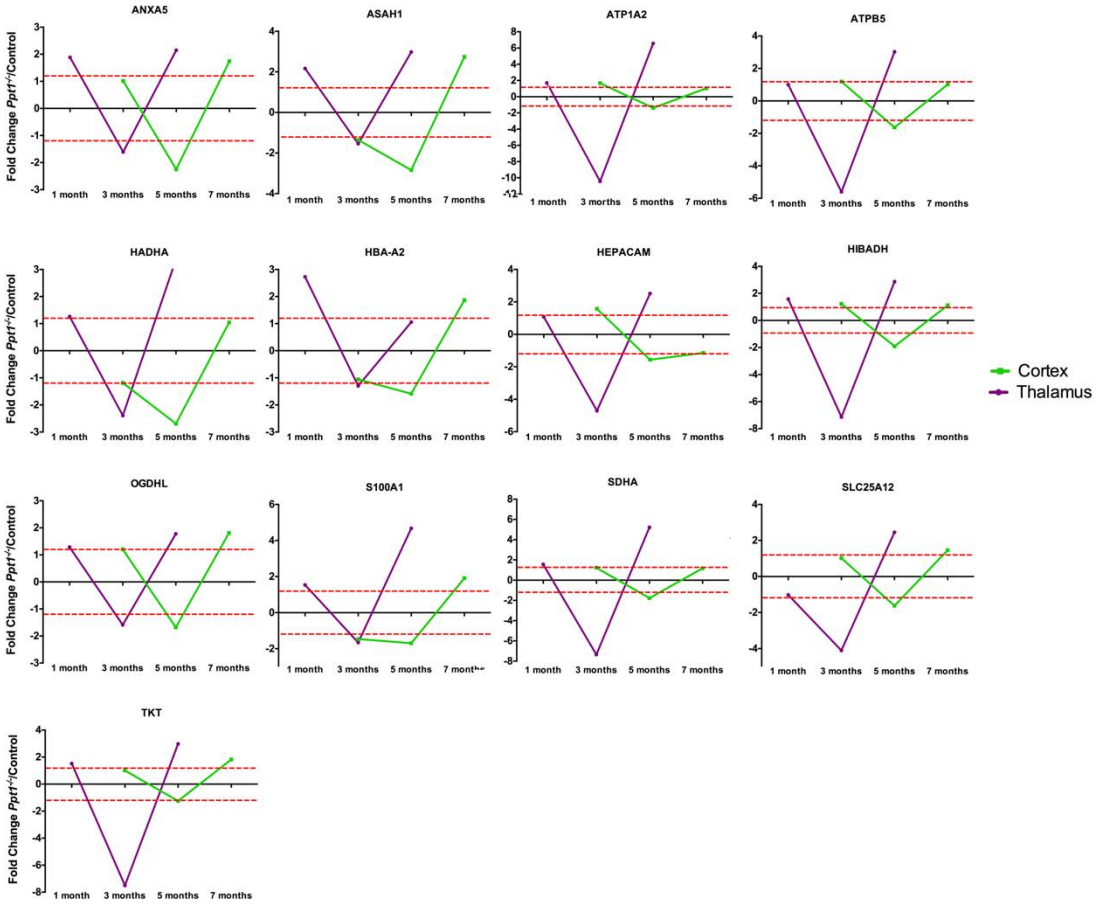

Fig. 4.17. Identified protein candidates with a "delayed down-up" profile between thalamus and cortex. Red dashed lines indicate 1.2-fold cut-off.

Table 4.2. Top canonical pathways identified in candidates with "delayed profile" between thalamic and cortical synaptosomes

Name	p-value	Overlap
Valine degradation I	8.17E-05	11.10%
TCA cycle II	1.35E-04	8.70%
Semaphorin signaling in neurons	7.25E-04	3.80%
Huntington's disease signaling	7.36E-04	1.20%
Oxidative phosphorylation	3.02E-03	1.80%

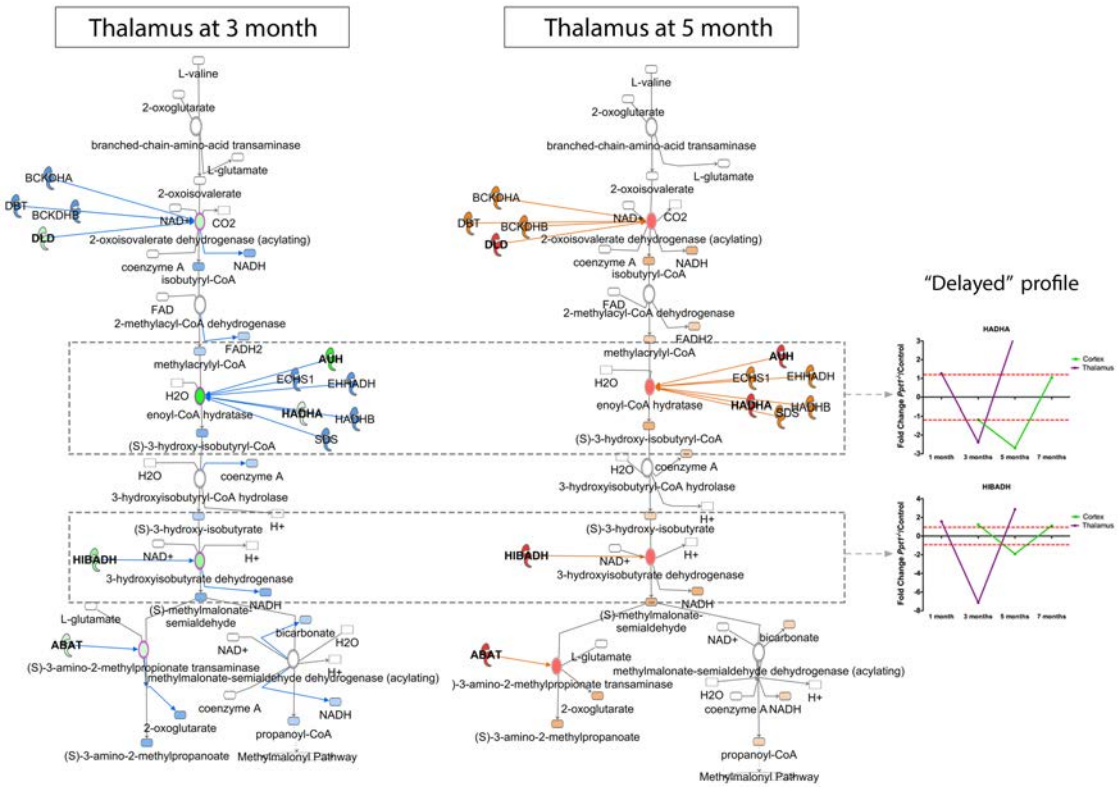

Fig. 4.18. Valine degradation cascade in the thalamus at 3 and 5 months. Top canonical pathway identified in relation to proteins with "delayed" profile between thalamic and cortical synapses. Two enzymes within this pathway, HADHA and HIBADH present downregulation at 3 months and upregulation at 5 months in thalamus and mirroring profiles can be seen in the cortex at 5 and 7 months. Red and names in bold=upregulated, green and names in bold=downregulated, orange=predicted activation, blue=predicted inhibition, white=not detected in the dataset and no prediction state.

4.3.4 *Ppt1*$^{-/-}$ and *Cln3*$^{-/-}$ comparative analysis

As pointed out above, another way to refine the list of candidates will be to look for conserved changes at equivalent disease stages in both *Ppt1*$^{-/-}$ and *Cln3*$^{-/-}$datasets. To do so, the most vulnerable synaptic population in the brain, the thalamus was focused on. This was compared to the equivalent disease stages of 3 months time-point in the *Ppt1*$^{-/-}$ mice and 13 months in the *Cln3*$^{-/-}$mice.

After finding the overlapping proteins between both datasets, 68 proteins were found to be identified in both mice models and from those, 31 presented a conserved up or downregulatation in the two mouse models (Table 4.3). Surprisingly, within this small list of 31 proteins there were 9 proteins (almost 30%) presenting a delayed profile (see above and Table 4.3). These candidates seem to correlate to the synaptic vulnerability status of synapses in *Ppt1*$^{-/-}$ and seem to be a conserved change at equivalent disease stage in *Cln3*$^{-/-}$. Therefore, these proteins seem to be very important in both mouse models of INCL and JNCL. But an important question is, are these candidates relevant to the human disease?

To answer this question, the QWB expression was examined for three examples of conserved changes between *Ppt1*$^{-/-}$ and *Cln3*$^{-/-}$ and "delayed" profile in *Ppt1*$^{-/-}$, in synaptosomes generated from *post mortem* cortical samples from patients with INCL and JNCL and healthy controls. These proteins were DBN1 (example of "up-down" profile) and HADHA and ANXA5 (examples of "down-up" profiles) (Fig. 4.19). The quality of the synaptic enriched fractions extracts of these samples were already examined and validated in Chapter 3 (see Fig. 3.11).

Next, the results were compared to the label free proteomics data and QWB of *Ppt1*$^{-/-}$ mice cortical synaptosomes at end stage (7 months) to be equivalent disease stage as the human samples (Fig. 4.19). Results indicated that these 3 candidates were changed in the same way in synaptosomes from *Ppt1*$^{-/-}$ mouse model (by label free proteomics and QWB) and in both INCL and JNCL indicating that these proteins are indeed relevant to the human condition in both infantile and juvenile forms, and ideal candidates to prioritize in future *in vivo* experiments (Chapter 5).

Table 4.3. Conserved proteins in Ppt1$^{-/-}$ and Cln3$^{-/-}$ at equivalent disease stage

Gene Symbol	Description	Fold-Change/WT		"Delayed" profile
		Ppt1$^{-/-}$	*Cln3*$^{-/-}$	
Upregulated				
NEFL	Nefl protein (Fragment)	1.808	1.229	
GPRIN1	G protein-regulated inducer of neurite outgrowth 1	1.542	1.899	
CACNG8	Voltage-dependent calcium channel gamma-8 subunit	1.332	1.764	
DBN1	Drebrin	1.326	1.82	✔
BSN	Protein bassoon	1.286	1.643	
SRCIN1	SRC kinase-signaling inhibitor 1	1.242	1.379	
DPYSL4	Dihydropyrimidinase-like 4	1.236	1.557	✔
Downregulated				
BIN1	Bin1 protein	-1.515	-1.275	
ASAH1	Acid ceramidase	-1.543	-1.786	✔
ANXA5	Annexin A5	-1.608	-1.944	✔
S100A1	Protein S100	-1.661	-2.308	
ATP5H	ATP synthase subunit d, mitochondrial (Fragment)	-2.239	-1.307	
HADHA	Trifunctional enzyme subunit alpha, mitochondrial	-2.392	-1.456	✔
PYGM	Glycogen phosphorylase, muscle form	-2.834	-1.928	
AHCYL2	Adenosylhomocysteinase	-3.277	-1.397	
NDUFA13	NADH dehydrogenase [ubiquinone] 1 alpha subcomplex subunit 13	-3.494	-1.206	
MYO18A	Myo18a protein	-4.144	-1.782	
ATP1A3	Sodium/potassium-transporting ATPase subunit α-3	-4.177	-1.298	
SACM1L	Phosphatidylinositide phosphatase SAC1	-4.749	-1.343	
PDHA1	Pyruvate dehydrogenase E1 alpha 1	-4.853	-1.299	
NDUFA9	NADH dehydrogenase [ubiquinone] 1 alpha subcomplex subunit 9, mitochondrial	-4.959	-1.231	
UQCRC2	Cytochrome b-c1 complex subunit 2, mitochondrial	-6.060	-1.226	
HIBADH	3-hydroxyisobutyrate dehydrogenase	-7.145	-1.504	✔
GLUD1	Glutamate dehydrogenase 1, mitochondrial	-7.148	-1.204	
SDHA	Succinate dehydrogenase [ubiquinone] flavoprotein subunit, mitochondrial	-7.356	-1.243	✔
TKT	Transketolase	-7.505	-1.547	✔
SLC32A1	Vasicular inhibitory amino acid transporter 10D	-8.797	-2.002	
SLC12A5	Solute carrier family 12 member 5	-9.531	-1.266	
ATP1A2	Sodium/potassium-transporting ATPase subunit α-2	-10.435	-1.497	✔
ATP5O	ATP synthase subunit O, mitochondrial	-11.183	-1.241	
HSPA5	Heat shock protein 5	-15.594	-1.227	

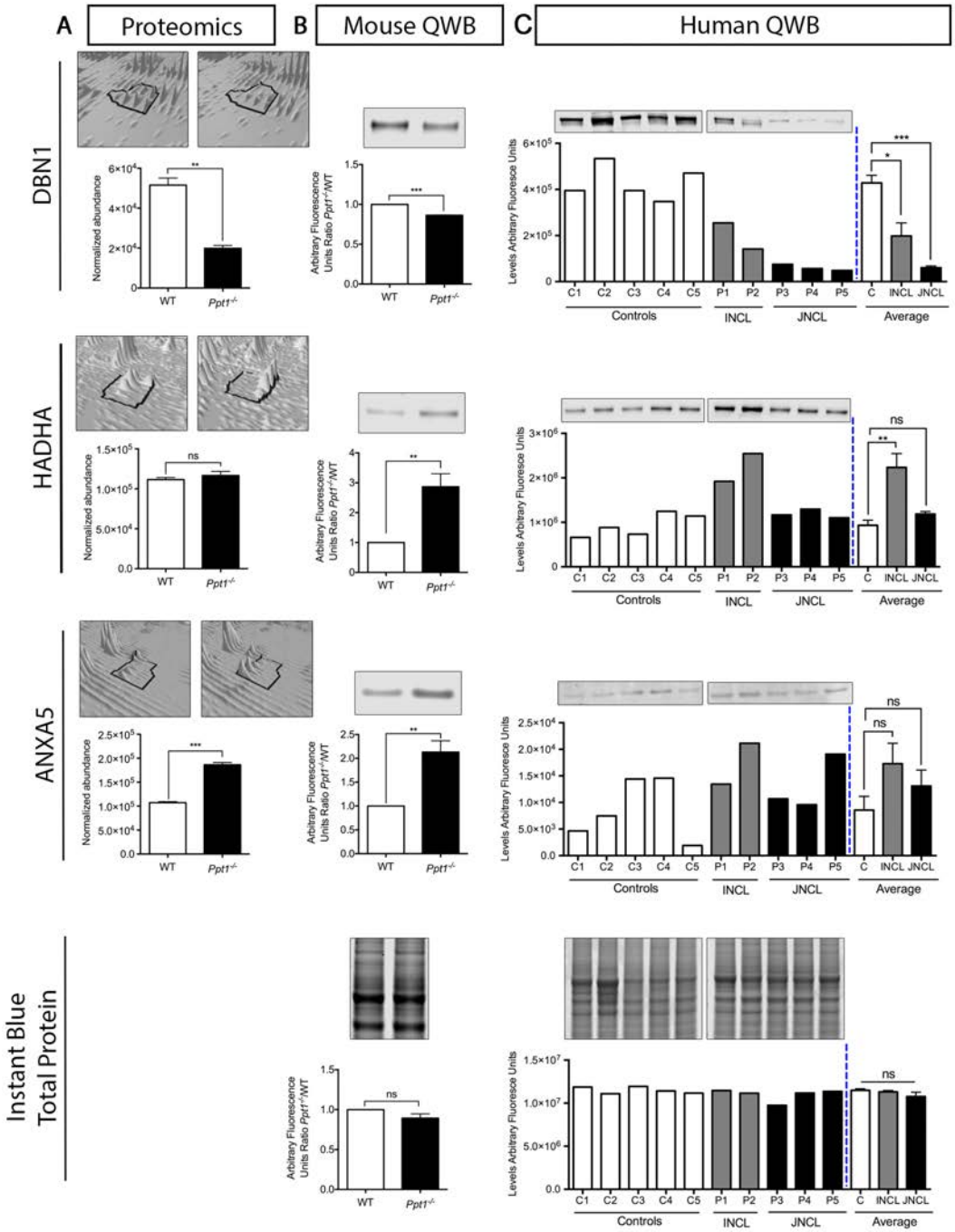

Fig. 4.19. Validation of proteomic data by QWB in mouse and human samples at end stage of the disease. **A&B.** DBN1, HADHA and ANXA5 expression quantification of cortical synaptosome extracts from *Ppt1*$^{-/-}$ mouse model through label free proteomics and QWB (with its corresponding representative bands) showing the same expression trend. **C.** QWB quantification and representative bands of the same proteins in *post mortem* cortical synaptic extracts of INCL and JNCL patients and controls showing the same trends as in the mouse in the same brain and disease stage. **B&C**. Instant blue total protein staining as loading control quantification and representative gel images for both mouse and human cortical synapstosome extracts showing even loading of the samples used (bottom). Mean ± SEM; * p-value<0.05, ** p -value<0.01, *** p-value<0.001, ns p-value>0.05 (Student T test).

4.4 Discussion

In this chapter, we pursued an understanding of the molecular changes taking place throughout the time-course of disease progression during the whole process of neurodegeneration. To do so, we carried out a complex spatio-temporal proteomic analysis of synaptic fractions with the aim to identify potential regulators of synaptic stability to take forward to *in vivo* experiments (Chapter 5). We investigated 4 distinct time-points (1, 3, 5 and 7 months), 2 conditions (*Ppt1*$^{-/-}$ and age-matched WT controls) and 2 differentially vulnerable synaptic populations (thalamus and cortex).

It was a challenging analysis at both a technical and analytical level. For this reason, I outline some of the caveats of the pipeline in the following sections.

Sampling of different synaptic populations across time-points

As pointed out above, in our laboratory we were accustomed to looking at molecular changes throughout shorter time-courses (Wishart *et al.*, 2012). This means that we were most likely to be sampling the same, or very similar, populations of synapses. In Wishart *et al.*, 2012, a study of the molecular changes in synapses after injury (injury-induced degeneration) was carried out. Synaptosomes were isolated at 0, 1 and 2 days post-injury (DPI). By 2 DPI, only around 10% of synapses were lost, therefore, the population of synapses were highly likely to not be that different from the ones at 0 and 1 DPI. In such a study, they were probably looking at the molecular changes happening throughout the same population of synapses. In contrast, in the time-course analysed here, even though we chose to study the most severe mouse model of NCL, we are extracting samples from a time period of 7 months. The level of synaptic loss at 7 months in the *Ppt1*$^{-/-}$ mice, is much higher than in the injury–induced degeneration mouse model, and therefore, very different populations of synapses are sampled at each time-point. That might be the explanation of why in thalamic synapses, there is a large shift in the level of expression of many proteins (from down to up) between 3 and 5 month time-points (Fig. 4.4), suggesting that we are sampling a very different population of synapses at 3 and 5 months respectively. Looking at the studies carried out by Kielar *et al.* in whole thalamic extracts, it was already detected by QWB that protein expression differ greatly between 3 and 5 months in several protein candidates (Kielar *et al.*, 2009). This molecular study carried out in the *Ppt1*$^{-/-}$ mice is in consensus with our results correlating with our time-course results. Bioinformatic analyses were also done using *IPA* at these two time-points highlighted. A strong activation of neuronal death pathways at 3

months as well as a detected inhibition of the same pathways at 5 months were predicted. This may indicate that at 3 months we are sampling mostly "degenerating synapses" whereas at 5 months, such synapses are gone and we are sampling synaptic populations which are resistant. Therefore, changes at 5 months might provide insight into potential neuroprotective pathways. Further studies addressing this specific point will be necessary to validate if synapses at 5 months are truly composed by a population of "resistant" synapses.

Differences between thalamic and cortical synapses

When examining cortical synaptic molecular changes, we identified similar profiles between 5 and 7 months to the ones between 3 and 5 months in the thalamus (which are morphologically equivalent time-points). However, we also detected a large number of changes at 3 months (where synapses are still intact in the cortex). Such proteins were not the same as the ones changed at 3 months in the thalamus and therefore, a distinct molecular fingerprint could be clearly detected across two differentially vulnerable synaptic populations. Importantly, we should also bear in mind that the vulnerability of cortical synapses was established by looking at only S1BF and V1 (which corresponded to VPM/VPL and LGNd thalamic nuclei) (Kielar *et al.*, 2009). However, the vulnerability status of synapses in other cortical regions such as the motor cortex, may be slightly different and since all the cortex was dissected and used for synaptosome production in this study, the other cortical areas not examined by IHC will be contributing to the overall molecular changes detected in the cortical synaptic proteomic data in this study. The larger heterogeneity of cortical synapses compared to thalamic synapses might be contributing to the larger variety of molecular profiles detected in cortex (10 different molecular trends, Fig. 4.9) compared to thalamus (5 different molecular trends, Fig. 4.6). Further IHC studies looking at the different cortical areas will help understand the exact contribution of each of the cortical synaptic populations to the overall molecular output.

Using morphological pathology to map molecular changes

To overcome sampling caveats, previously characterized morphological changes at different time-points are correlated to the molecular data. An examination of the molecular changes happening through disease progression in the thalamus (most vulnerable area) showed that 3 and 5 months are the two most "affected" time-points with very dynamic changes taking place. Afterwards, similar protein expression patterns mirroring the thalamic ones in the cortical samples with a 2 month delay in expression trend were looked for. This identified the

protein candidates without biasing the findings by other factors. Such biases include previous findings in the literature (which could hamper the identification of novel target) or the magnitude of change (which might be biologically irrelevant). In this way, 12 proteins were predicted to be upstream regulators and 17 proteins within the datasets that correlated with such a profile and that were further investigated in studies described in Chapter 5 using *in vivo* approaches.

These candidate identifications were based on the premise that equivalent morphological changes in two brain areas are accompanied by the same molecular changes. This may be true but there is the possibility that different synaptic populations/brain areas might degenerate in slightly different ways (especially very early on). Such subtle differences may not be detectable through IHC studies but omics studies could potentially see these differences. A specific protein change might be critical for a specific brain area at a specific time-point but might not be that relevant for another brain area. Such proteins will be overlooked in the approach used here. However, the use of the temporal morphological patterns described by IHC, increases confidence that only the major protein regulators of synaptic stability are detected.

Conserved molecular changes across NCL models

Interestingly, an *IPA* analysis of the 17 identified candidates with a "delayed" profile, detected "Valine degradation" as the top-canonical pathway most significantly disrupted. Valine degradation was already an implicated pathway in the previous chapter and was identified as important in *Cln3*$^{-/-}$ degenerating synapses. In the *Ppt1*$^{-/-}$ time-course two of the enzymes within this pathway (HADHA and HIBADH) had a characteristic "delayed profile" (Fig. 4.18).

Therefore, further studies were sought to identify conserved changes in the two mouse models at equivalent disease stages since this seemed most likely to detect regulators of synaptic stability. Comparing the molecular changes detected in thalamic synapses at 3 months in *Ppt1*$^{-/-}$ and 13 months in *Cln3*$^{-/-}$, similar expression trends were identified which were consistently linked to similar molecular functions (ie. upregulated proteins related to synaptic and vesicle functions whereas downregulated proteins were related to mitochondria). By tracking specific protein candidates in these two mice models to look for conserved changes, 31 proteins were identified with a similar up/down trend. Surprisingly, 9

out of 31 conserved proteins in *Ppt1*$^{-/-}$ and *Cln3*$^{-/-}$ also presented a "delayed" profile between thalamus and cortex in the *Ppt1*$^{-/-}$ time-course (Table 4.3).

Conserved molecular changes in* Ppt1$^{-/-}$ *&* Cln3$^{-/-}$ *mice and INCL & JNCL patients

A further analysis was done to investigate whether the changes detected in *Ppt1*$^{-/-}$ and *Cln3*$^{-/-}$ mice were also detectable in human *post mortem* INCL and JNCL patient samples. Only an end stage patient cortical tissue was available so, the study focused on the 7 month cortical samples in the *Ppt1*$^{-/-}$. Unfortunately, no end-stage Cln3 mice tissue was available for comparative analyses. Examination of three examples of the most promising candidates: DBN1, ANXA5 and HADHA ("delayed profile" in *Ppt1*$^{-/-}$ time-course and conserved changed between *Ppt1*$^{-/-}$ and *Cln3*$^{-/-}$), showed the same change seen in mice (by proteomics and QWB) and human (by QWB) (Fig. 4.19). We could then be more confident that at least these three candidates could be relevant to the human disease.

Overall, despite initial concerns regarding the difficulty of interpreting the proteomic data due to the differences in synaptic sampling, multiple different analyses utilising all available data such as morphologic (Kielar *et al.*, 2009), proteomics of *Ppt1*$^{-/-}$ (thalamus and cortex) and proteomics in *Cln3*$^{-/-}$ (Chapter 3) were combined to shortlist a final list of candidates by a consensus of evidences. With so many protein identifications and datasets it could have been easy to get lost in the noise. The workflow implemented here could be used as a protocol for analysing similar datasets with an unbiased knowledge-based experiment design. Such methodologies could increase the likelihood of identifying proteins which are more likely regulators of synaptic stability in an unbiased way but may be transferrable to other mechanistic studies. In order to determine if such candidates do indeed have a role in the stability of the nervous system, *in-vivo* experiments will be carried out in the following chapter.

Chapter 5

In vivo phenotypic assessment of protein candidates in *Drosophila melanogaster*

5.1 Introduction

This far in the project we have carried out in depth proteomic analysis of *Cln3*$^{-/-}$ and *Ppt1*$^{-/-}$ murine model synaptic populations (Chapters 3 & 4 respectivly), followed by in-depth *in silico* analyses. These distinct -omic experiments have enabled the development of specific workflows for the production and handling of data of increasing complexity. The outcome of which was the generation of a list of 33 protein candidates, identified in an unbiased manner, but centred around the correlation between their expression profile and synaptic vulnerability across brain regions and/or disease progression.

Up until this point in the workflow, the identification of such candidates can only suggest that they may play a role in the degenerative process. Next, we therefore wanted to determine the role, if any, of each candidate in modulating the stability of the nervous system *in vivo*. To do so we turn to the *Drosophila melanogaster* model system. As extensively covered in the General Introduction (Chapter 1, Section 1.8), the fruit fly is an excellent and commonly used organism for the study of neurodegenerative diseases. The availability of multiple genetic tools allows the manipulation of specific genes of interests in order to assess their role in modulating the stability in the different organ systems of the *Drosophila* (Martinez-Arias, 2008, Green, 2010, O'Kane, 2003, Mehregan *et al.*, 2016). During the second year of my PhD I was hosted in the laboratory of Dr Giusy Pennetta (Centre for integrative physiology,

University of Edinburgh) for a year, where I was trained in all of the techniques and experiments required for this analysis, and I subsequently used this training to set up the *Drosophila* screening facility in the Wishart Laboratory at the Roslin Institute.

As outlined in my general introduction (Chapter 1, Section 1.8.3), there are overexpression (OE) and loss of function (LOF) CLN3 and PPT1 *Drosophila* available, which could be used as tester lines for our *in vivo* experiments (Tuxworth *et al.*, 2011, Tuxworth *et al.*, 2009, Aby *et al.*, 2013, Hickey *et al.*, 2006, Buff *et al.*, 2007, Saja *et al.*, 2010). We initially aimed to use each corresponding CLN3 and PPT1 model and cross them with the misexpressed candidates identified in Chapters 3 & 4 respectively. In that way we could study their role as modulators of the nervous system in each disease condition. However, each one of the disease models, would require a detailed examination and characterization to reproduce the phenotypes described by other authors before its use in my modifier genetic screen. Therefore, due to time limitations, the high degree of molecular overlap in the pathways and cascades identified in chapter 3 & 4, and the convenience of the phenotypes in the CLN3 *Drosophila* models, we decided to focus on CLN3 for this chapter. Additionally, despite the effort of the NCL research community, very little is actually known about CLN3 function. Unlike PPT1 *Drosophila* models, no extensive modifier sceens have been carried out in the CLN3 fruit flies to date. Therefore, the results coming from the current genetic screen should prove valuable, not only in the context of the identification of regulators of neuronal stability, but also, to identify CLN3 interactors that might give clues about its wider function.

LOF CLN3 *Drosophila* have been generated by Tuxworth et al. (Tuxworth *et al.*, 2011). The LOF mutant fly ($Cln3^{\Delta MBI}$), was shown to be hypersensitive to oxidative stress, but authors did not note any obvious developmental or neurological defects (Tuxworth *et al.*, 2011). For this reason we decided to start looking at a CLN3 OE *Drosophila*, also generated by Tuxworth *et al.* (Tuxworth *et al.*, 2009). Using the UAS/GAL4 system (see Section 5.2.3), OE of CLN3 (*UAS-CLN3*) driven in the eye under the control of *GMR-GAL4*, presents with a noticeable degenerative eye phenotype indicated by glazing, reduction of surface area and loss of the regular shape of crystalline array of the compound eye including fusion of ommatidia and perturbations in somatosensory bristle patterns. Authors estimated that this model driving expression in the eye increased CLN3 level 2.86-fold (+0.42 SD) over basal CLN3 expression in the wing (Tuxworth *et al.*, 2009). Tuxworth and colleagues have added to the field by using this model to show that CLN3 interacts with Notch, inhibiting its

function at the protein level by regulating its processing and/or cleavage (Tuxworth *et al.*, 2009). Thus, such "simplified" i*n vivo* model systems can inform on the molecular processes taking pace in response to perturbations in a protein of interest.

First, we aimed to reproduce the phenotypes described in a CLN3 overexpression (OE) in the eye system (Tuxworth *et al.*, 2009), and investigate the presense or absence of a synaptic phenotype (in the neuromuscular junction (NMJ) in the larvae). Moreover, since the human CLN3 disease is caused by the LOF of CLN3 protein, we also wanted to investigate the effects of CLN3 LOF in *Drosophila* (eye and NMJ). Second of all, once we confirmed that the OE CLN3 driven in the eye would be a suitable tool for the genetic modifier screen, we studied the effects of the misexpression of identified candidates (from Chapter 3&4) on a CLN induced phenotype i.e. in the presence or absence of CLN3-induced degenerative eye (CLN3 OE & WT background respectively).

In this chapter we show that we can reproduce the phenotype described by Tuxworth *et al.* in a fly overexpressing CLN3 under the control of the *GMR-GAL4* driver. We also show that this model is a suitable tester line for the desired genetic modifier screen. Results of the genetic screen indicated that most of the candidates identified in proteomic studies in Chapter 3 & 4 are capable of modulating the stability of the nervous system *in vivo*. Thus confirming the veracity of the proteomic comparisons and the validity of the data filtering strategies used to generate the candidate lists. Interestingly, we show that some of the candidates are doing this in a CLN3-dependent manner. In contrast, other candidates are shown to be global regulators of the nervous system as their misexpression was capable of disrupting eye structure also in a WT background.

Overall, we demonstrated that protein candidates identified in an unbiased way from proteomic studies in synapses from murine neurodegenerative disease models can be targeted into lower order organisms such as *Drosophila* for the identification of regulators of neuronal stability (both in general and in a neurodegeneration specific context) *in vivo*. Candidates identified here warrant follow up as potential targets for the development of novel therapeutic interventions.

5.2 Materials and methods

5.2.1 *Drosophila* husbandry and maintenance

Stocks were maintained on standard cornmeal food at room temperature (RT) and flies were raised at specific temperatures according to the experiment. General stock information can be found in Table 5.1. *Drosophila* mouse orthologs for candidate proteins were identified using *Drosophila* RNAi Screening Center (*DRSC) Integrative Ortholog Prediction Tool* (*DIOPT*) (see below), and RNAi and OE lines were chosen from Flybase and obtained from Vienna *Drosophila* stock centre (VDSC) (Dietzl *et al.*, 2007), Bloomington *Drosophila* Stock Centre (BDSC) (Perkins *et al.*, 2015) and FlyORF (Bischof *et al.*, 2013) (see Table 5.2). All the RNAi and OE lines used in this study carry the *UAS* construct (ie. *CLN3-UAS-RNAi*) and therefore they will be expressed under the control of *GAL4* drivers (see section 5.2.3). However, all the RNAi lines utilized in this study will be referred as the "gene of interest" plus RNAi for short (ie. *CLN3-RNAi*).

5.2.2 *DIOPT*

Drosophila orthologs for mouse candidate proteins were identified using *DRSC Integrative Ortholog Prediction Tool* (*DIOPT*) as previously used in (Sanhueza *et al.*, 2015). This bioinformatic tool has been developed by the *Drosophila* RNAi screening center at the Harvard medical school (Hu *et al.*, 2011, Zoghbi *et al.*, 2000). It uses ten different algorithms to find ortholog matches for a specific gene. The number of positive results is represented by a score, the higher it is, the better the match. All the fly genes utilised in this study had a DIOPT score of at least 2 with proteins scoring less not being considered for these experiments as this indicates that the identification as an ortholog is only supported by one algorithm (Sanhueza *et al.*, 2015). *DIOPT* did not identify high rank orthologs for ASAH1, S100A1, HEPACAM and HBA-A2, therefore these candidates were not targeted *in vivo* in this chapter. Dpysl3 and Dpysl4 were shown to have the same ortholog in *Drosophila* (CRMP). More information regarding candidate misexpression lines purchased can be found in Table 5.2.

Table 5.1. **Drosophila** ***general stocks***

Line	Source	Description	Reference
Canton S	BDSC	Wild type line	N/A
UAS-CLN3	Richard Tuxworth	CLN3 overexpression	(Tuxworth *et al.*, 2009)
CLN3-RNAi/CyO	VDRC (v5322)	CLN3 RNAi line	(Dietzl *et al.*, 2007, Jones *et al.*, 2014)
GMR-GAL4;UAS-CLN3/CyOGFP	This study	Recombinant line	(Llavero Hurtado *et al.*, 2017)
CLN3-RNAi/CyOGFP	This study	CLN3 RNAi line with larvae balancer	N/A
D42-GAL4	BDSC	Motor neuron expression driver	(Parkes *et al.*, 1998)
elavC155-GAL4	BDSC	Pan-neuronal expression driver	(Yannoni *et al.*, 1997)
Bg57-GAL4	BDSC	Muscle expression driver	(Budnik *et al.*, 1996)
GMR-GAL4	BDSC	Eye expression driver	(Freeman, 1996)
Eyeless-GAL4	BDSC	Eye expression driver	(Tseng *et al.*, 2002)
L/CyOGFP	Giusy Pennetta	Larvae balancer	N/A

Table 5.2a **Drosophila *candidate stocks***

Candidate lines	Mouse Gene Symbol	Source	Genotype	Annotation symbol	Stock number	DIOPT score	Direction of change **
AnxB9-RNAi	Anxa5	V	w^{1118}; P{GD11750}v27493	CG5730	27493	2	Down
Atpalpha-OE	Atp1a2	F	M{UAS-Atpα.ORF}ZH-86Fb	CG5670	F001458	8	Down
ATPsynbeta RNAi TRiP	Atp5b	B	y^1 v^1; P{TRiP.JF02892}attP2	CG11154	28056	11	Down
Abp1-RNAi	Dbn1	V	w^{1118}; P{GD6858}v38331	CG10083	38331	9	Up
CRMP RNAi KK	Dpysl4/Dpysl3	V	P{KK108924}VIE-260B	CG1411	101510	7	Up
ERR RNAi KK	Esrra	V	P{KK108422}VIE-260B	CG7404	108349	8	Down*
Gbeta13F RNAi KK	Gnb4	V	P{KK102923}VIE-260B	CG10545	100011	10	Up
MTPαRNAi	Hadha	V	w^{1118}; P{GD11299}v21845	CG4389	v21845	10	Down
CG15093 RNAi TRiP	Hibadh	B	y^1 sc^* v^1; P{*TRiP*.HMC04926}attP40	CG15093	57736	11	Down
HibchRNAi	Hibch	V	w^{1118}; P{GD11513}v40570	CG5044	v40570	9	Down
Hnf4-OE	Hnf4a	F	M{UAS-Hnf4.ORF.3xHA.GW}ZH-86Fb	CG9310	F000144	9	Down*
InR-OE	Igf1r/InsR	B	y^1 w^{1118}; P{UAS-InR.Exel}2	CG18402	8262	8/6	Down*
msn RNAi KK	Map4k4	V	P{KK108948}VIE-260B	CG16973	101517	8	Up
Oga RNAi GD	Mgea5	V	w^{1118}; P{GD10644}v41822	CG5871	41822	11	Up*
Mitf RNAi KK	Mitf	V	P{KK113614}VIE-260B	CG43369	108519	8	Down*
Rel RNAi GD	Nfkb1	V	P{GD1199}v49414	CG11992	49414	6	Up*
N RNAi GD	Notch1	V	w^{1118}; P{GD144}v1112	CG3936	1112	10	Up*
Nc73EF RNAi KK	Ogdhl	V	P{KK100395}VIE-260B	CG11661	107713	10	Down

Table 5.2b **Drosophila *candidate stocks***

Candidate lines	Mouse Gene Symbol	Source	Genotype	Annotation symbol	Stock number	DIOPT score	Direction of change **
zen RNAi KK	Pdx1	V	P{KK113335}VIE-260B	CG1046	102915	2	Up*
Eip75B-OE	Pparg	F	M{UAS-Eip75B.ORF.3xHA.GW}ZH-86Fb	CG8127	F002207	3	Down*
Pten-OE	Pten	F	M{UAS-Pten.ORF.3xHA}ZH-86Fb	CG5671	F001033	11	Down*
Rictor RNAi TriP	Rictor	B	y^1 sc^* v^1; P{TRiP.GL00544}attP40	CG8002	36584	9	Up*
RokRNAi GD	Rock2	V	w^{1118}; P{GD1522}v3793	CG9774	v3793	9	Up
RokRNAi TRiP	Rock2	B	y^1 v^1; P{TRiP.JF03225}attP2	CG9774	28797	9	Up
SdhA RNAi KK	Sdha	V	P{KK101728}VIE-260B	CG17246	110440	11	Down
Aralar1 RNAi TRiP	Slc25a12	B	y^1 sc^* v^1; P{TRiP.HMC04105}attP40	CG2139	56884	11	Down
CG8036 RNAi KK	Tkt	V	P{KK101051}VIE-260B	CG8036	105633	10	Down

**Based on z-score prediction IPA tool*

***Based on KO/WT ratio from proteomic studies*

V: Vienna *Drosophila* stock centre (VDSC); B: Bloomington *Drosophila* Stock Centre (BDSC); F: FlyORF

5.2.3 UAS/GAL4 system

This is a widely used two-component system in *Drosophila* studies to direct the expression of a gene of interest in a tissue and time specific manner (Brand, 1993). One of the components expresses a yeast transcription factor called GAL4 which contains a P element vector for a specific cell type (promoter). The second component contains the Upstream Activating Sequence (Galione *et al.*, 2010) next to a specific gene of interest that will bind to GAL4 in a temperature dependent manner. Many tissue specific GAL4 drivers have been developed to target expression of genes in specific cell types including (but not limited to) pan-neuronal drivers (*elav^{C155}-GAL4*) (Yannoni *et al.*, 1997), motor-neuron drivers (*D42-GAL4*) (Sanyal, 2009, Parkes *et al.*, 1998, Gustafson *et al.*, 1996, Nitz *et al.*, 2002) and eye drivers (*GMR-GAL4*) (Freeman, 1996).

This approach provides a powerful system for experimentation ideal for the study of a phenotype when a gene is misexpressed in a spatio-temporal manner. The UAS/GAL4 system is widely used in modifier screens in a clean and efficient manner (St Johnston, 2002).

5.2.4 *Drosophila* phenotypic assessment

Drosophila were used as a model system to study the ability of the protein candidates identified through proteomics and bioinformatics analyses (Chapters 3 & 4), to modulate neuronal stability *in vivo*.

We first needed to characterize the phenotypes in different neuronal systems in NCL fly models in order to identify which system was the optimal for performing our candidate genetic screen. We studied the neuromuscular junction (NMJ) of musculature body wall in the third instar larvae and the adult eye in both OE and LOF of CLN3.

We utilized the well-characterized temperature-inducible UAS/GAL4 system (see above). For the phenotype characterisation experiments, 8-10 virgin females from each driver were crossed to 7-8 males (*UAS-CLN3* or *CLN3-RNAi*). Flies were raised at different temperatures to modulate the expression of the genes of interest including: 25, 27, 28 and 30ºC. As a control, crosses with the driver and a wild-type fly (Canton S (+/+)) were carried out in parallel for all the experiments.

5.2.4.1 Neuromuscular junction morphology

The synaptic phenotype was studied at the NMJ of the musculature body wall in the third instar larvae. To do so we studied the effects of CLN3 downregulation (*CLN3-RNAi*) and overexpression (*UAS-CLN3*) to the morphology of the NMJ. Homozygous *UAS-CLN3* fly was donated by Dr Richard Tuxworth. *RNAi-CLN3/CyO* line was obtained from Vienna *Drosophila* Resource Centre (VDRC) (Dietzl *et al.*, 2007, Jones *et al.*, 2014) and crossed to *L/CyOGFP* to generate a fly stock containing *CLN3-RNAi* over a larval balancer (*CLN3-RNAi/CyOGFP*) (see Table 5.2). *UAS-CLN3* and *CLN3-RNAi/CyOGFP* flies were crossed with a range of neuronal drivers including a motor-neuron driver (*D42-GAL4*) (Sanyal, 2009, Parkes *et al.*, 1998, Gustafson *et al.*, 1996, Nitz *et al.*, 2002), a pan-neuronal driver (*elav^{C155}-GAL4*) (Yannoni *et al.*, 1997) and to a post-synaptic/muscle driver (*Bg57-GAL4*) (Budnik *et al.*, 1996) (See Table 5.1).

In terms of the expression patterns of *GAL4* drivers, *D42-GAL4* expression is restricted to motor-neurons although it has also been found in some sensory neurons of the musculature body wall of the larvae (Sanyal, 2009). In contrast *elav^{C155}-GAL4* is expressed in all neurons in all developmental stages (Robinow *et al.,* 1988). Importantly, although *elav^{C155}-GAL4* tends to be used as an exclusive pan-neuronal by the research community, *elav* has also been described to be expressed in embryonic glial cells and in transiently proliferating progenitor cells (neuroblasts and glioblasts) (Berger *et al.,* 2007). Therefore, any effects triggered by either *UAS-CLN3* or *CLN3-RNAi* under the control of *elav^{C155}-GAL4* could not be uniquely attributed to the role of neurons. *BG57-GAL4* is expressed in all larval muscles, from mid first to third instar stage. Additionally, with *BG57*, *GAL4* expression is also observed in two sensory cell bodies in the body wall and in other mesodermally derived tissues, such as the gut. Importantly, no expression has been detected in ectodermal tissues, such as other areas of the CNS (Budnik *et al.,* 1996).

Crosses were left at room temperature for flies to mate and lay eggs. After 48 hours parents were removed and eggs were transferred to incubator/water bath and incubated at 25, 27, 28 and 30^{o} C. F1 third instar larvae were dissected and immunostained with pre- and post-synaptic markers as explained in IHC in General materials and methods (Chapter 2, Section 2.3.2). For *RNAi-CLN3/CyOGFP* crosses, only CyO+ flies were dissected which were distinguishable due to the absence of GFP expression, observable under fluorescent light.

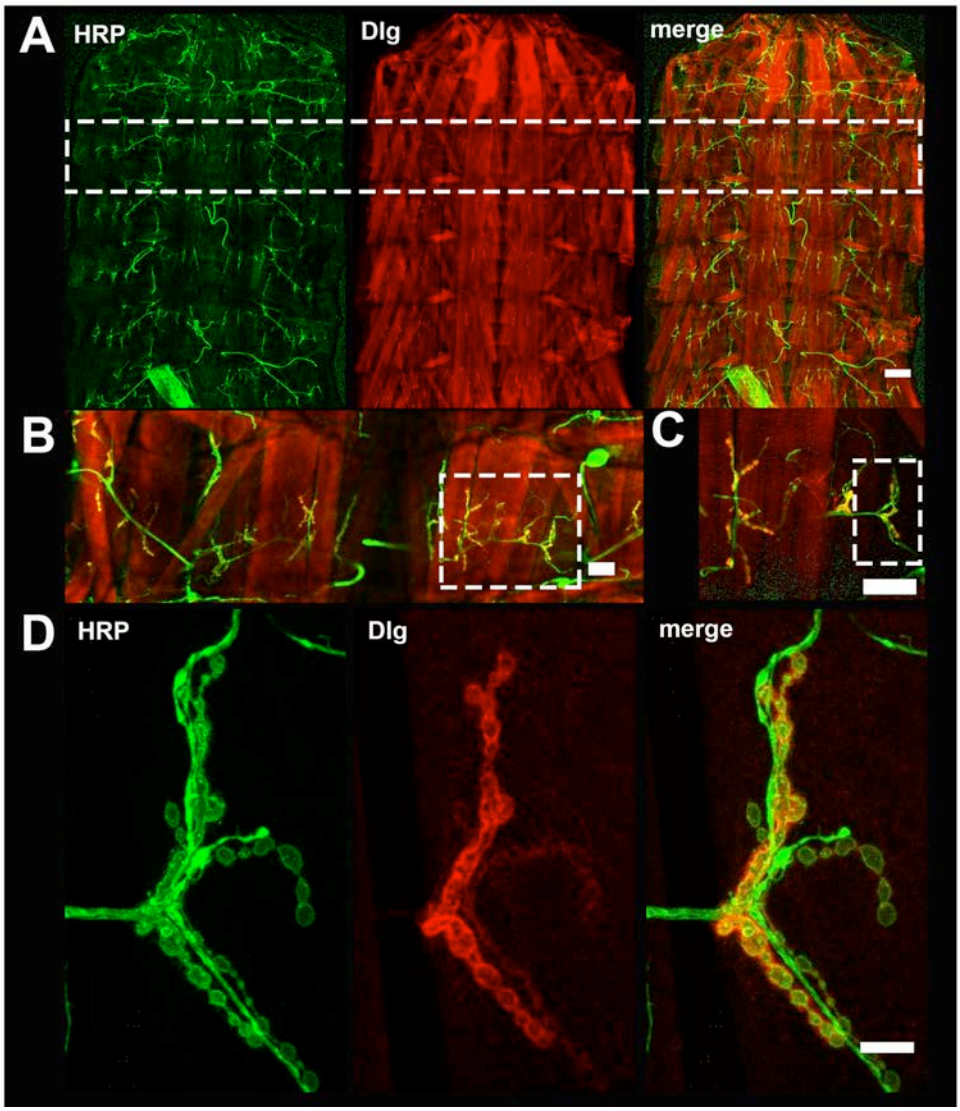

Fig. 5.1. Confocal imaging of NMJ in muscle 12/13 of WT* Drosophila *larvae fillet preparation stained with pre-synaptic (HRP) and post-synaptic markers (Dlg). **A**. 4x magnification micrographs of larvae filler preps with segment A3 highlighted with a white-dashed box. **B.** Micrograph of segment A3 of the same larva at 10x highlighting NMJs in muscles 6/7 &12/13 in a white-dashed box. **C.** Micrograph at 20x of NMJ 6/7 (left) & 12/13 (right). It is noticeable the tree-branching pattern of 6/7 NMJ whereas 12/13 (highlighted with white-dashed box) has a more defined triangular shape towards the distal side of the larvae. It is also obvious that the axon coming from the ventral side. **D.** High magnification (60x) micrographs of NMJ from muscle 12/13. WT (Canton S) NMJ displays an even beading of boutons with regular rounded shapes. Glutamatergic boutons (type I) are surrounded by Dlg staining whereas smaller boutons (type II and III) are not glutamatergic and do not express Dlg. Scale bars: 4x =200um, 10x & 20x= 50um., 60x=10um.

The same NMJ in muscle 12/13 within segment A3 was qualitatively characterized across all the genotypes in at least 8 larvae (See Fig. 5.1). This specific NMJ was chosen because: 1. It is relatively easy to find; and 2. It contains all bouton types (Menon *et al.*, 2013) and therefore can be used to determine whether a phenotype is bouton-specific. An initial characterization of the phenotype was performed through fluorescence imaging. If a phenotype was obvious we then proceeded to image the slides with confocal microscopy (see imaging section). Dr Giusy Pennetta confirmed all the NMJ phenotypes described in this thesis.

5.2.4.2 Eye structure

It has previously been described that overexpression of CLN3 in the eye triggers a degenerative phenotype in *Drosophila* using the *GMR-GAL4* eye driver (Tuxworth *et al.*, 2009) (See 5.1 Introduction). First of all, we investigated whether we could replicate this phenotype in our lab, and secondly, if we could obtain a similar phenotype by using a different eye driver (*Eyeless-GAL4*) (Tseng *et al.*, 2002). Additionally, we wanted to investigate if knocking-down CLN3 (*CLN3-RNAi*) also causes degeneration in the eye under the control of the same drivers (*GMR-GAL4* and *Eyeless-GAL4*).

Importantly, we needed to consider the expression pattern of both *GMR-GAL4* and *Eyeless-GAL4* drivers when interpreting results. *GMR* is found to be primarily expressed in the posterior region of the morphogenic furrow area, where ommatidia cells are starting to differentiate (Freeman, 1996). However, it has been recently found to be expressed also in specific neuronal cells in larval and pupal brain and the ventral ganglia as well as in the Bolwig's organ and the eye primodia in embryonic stages (Ray *et al.,* 2015). Studies by Li *et al.* also reported the expression of *GMR* in the wing and leg discs (Li *et al.,* 2012). Therefore, although flies are able to survive in the absence of eyes, due to the fact that *GMR* is also expressed in the CNS, some genes driven under the control of *GMR-GAL4* may cause lethality (Ray *et al.,* 2015). In contrast, *Eyeless-GAL4* driver, is a transgenic line based on the eyeless gene (*ey*). Ey is a key gene for the eye development in *Drosophila*. Driving the ectopic expression of *ey* is sufficient to induce eye formation in various tissues. *Ey* is expressed in the embryonic ventral nerve cord and in some areas of the brain. In larval stages, it is expressed in the eye imaginal disc and in third instar larvae its expression is restricted to undifferentiated cells located anterior to the morphogenic furrow (Halder *et al.,* 1995). Due

to these differences in expression patterns, the use of these two drivers allows the study of both LOF an OE of CLN3 at different stages of the developing eye.

Each eye driver was crossed with *UAS-CLN3* and *CLN3-RNAi* and were left to mate and lay eggs at room temperature. After 72 hours, the parents were removed and eggs were transferred and raised at different temperatures to study different degrees of overexpression/downregulation (ie. 25, 27 and 28ºC). F1 adults were counted and eyes examined for the identification of defects in eye structure which indicated neurodegeneration. Photographs of the eyes were taken for further examination and quantification (see Chapter 2 General materials and methods, Section 2.9). Eye surface area was quantified using *ImageJ* as previously described (Sanhueza *et al.*, 2015).

5.2.4.3 Genetic modifier screen

After assessing the different phenotypes triggered by both overexpression and knockdown of CLN3 in both NMJ and eye, we chose *UAS-CLN3* driven in the eye via *GMR-GAL4* as the system for performing a modifier screen. We then explored whether the misexpression of the identified candidates from Chapter 3 & 4 have the ability to modify CLN3-induced degeneration in the eye.

Because both driver and overexpression allele are in the second chromosome, we needed to build a recombinant fly with *GMR-GAL4* and *UAS-CLN3* to make sure that the candidate RNAi/OE construct is found on the same chromatid as the driver. To do so (taking the advice of Dr Mario Sanhueza – Pennetta Lab), a recombinant stock was established by conventional recombination methods to be used as a tester line for the modifier screen. According to the chromosomal position of CLN3, and using the web-based tool *Drosophila melanogaster Recombination Rate Calculator (RRC, Version 2*.3) (Comeron *et al.*, 2012, Fiston-Lavier *et al.*, 2010), recombination rates for CLN3 were predicted to be 0.14-0.70%. As shown in Fig. 5.2A, individual F1 *GMR-GAL4/UAS-CLN3* virgins were placed with 2-3 males which carried second chromosome balancers (*H16/CyOGFP)* into individual food vials. Resulting F2 offspring from each female virgin were then examined. Recombinant flies are then distinguishable by their phenotype - displaying CyO^- phenotype (curly wings) and the previously characterized CLN3-degenerative eye - as they will contain the eye driver (*GMR-GAL4*), the CLN3 overexpression construct (*UAS-CLN3*) and the CyO^- balancer (*CyO GFP*) (Fig. 5.2B).

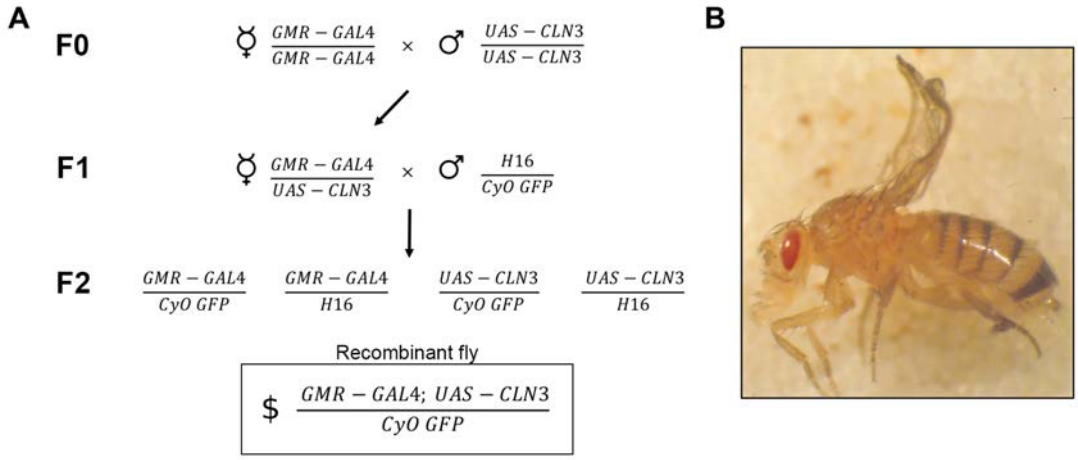

***Fig. 5.2 Generation of* GMR-GAL4 *and* UAS-CLN3 *recombinant* Drosophila *line.* A.** Mating scheme for the generation of recombinant tester fly line which requires two crosses: F0; regular eye driver (*GMR-GAL4*) x overexpression construct (*UAS-CLN3*) which will generate F1 flies *GMR-GAL4/UAS-CLN3*. Next, F1 individual female virgins will be crossed to males carrying a second chromosome balancer (H16/CyO GFP). With 0.14-0.70% probabilities, F2 will be expected to contain a fly carrying a recombinant construct over a CyOGFP balancer (*GMR-GAL4; UAS-CLN3/CyOGFP*). These flies are then amplified to keep as a stock ($) . **B.** Representative image of the recombinant fly obtained after 25 individual crosses. The small and rough CLN3-induced degenerative eye and the CyO^- phenotype in the wings (curly wings) are clear.

Once the recombinant flies are established (*GMR-GAL4;UAS-CLN3/CyO GFP),* these were used as a tester line to cross with misexpressed candidate lines (Table 5.2), as described in Fig. 5.3. 8-9 RNAi or OE candidate males were crossed to 10-12 virgin recombinant female. F1 progeny were sorted by genotype and flies carrying the recombinant and the misexpression candidate constructs (*GMR-GAL4;UAS-CLN3/Candidate-RNAi/OE)* were assessed for suppression or enhancement of the CLN3-derived small and rough eye phenotype (Fig. 5.3; right side). These flies are distinguishable by their regular wings (CyO^+). Flies carrying the *CyOGFP* balancer over a *Candidate-RNAi/OE* construct did not display any phenotype as they will be lacking the *GAL4* driver. Such flies are distinguished by their curly wings (CyO^-). These flies represent good internal controls, as any defects in eye structure or viability will indicate a problem within the experiment.

A control cross was carried out in parallel by crossing *GMR-GAL4;UAS-CLN3/CyO GFP* to a WT fly (+/+) (Fig. 5.3; left side). The control cross gave rise to F1 flies carrying the CyOGFP balancer over a WT allele (+/CyOGFP) which have curly wings (CyO^-). CyO^- have no

phenotype and are used as control flies. F1 flies containing the recombinant construct over a WT allele (*GMR-GAL4;UAS-CLN3/+)* have normal wings (*CyO*$^{+}$), and present a typical CLN3-induced degenerative eye. For this reason, they could be used as neurodegeneration model flies to compare against. All flies in the crosses of this sceen, were raised at 25 °C in a circadiarian light incubator.

To have a quantitative read out of the severity of the phenotypes obtained in our experiments the eye surface area was measured in *ImageJ* as previously described (Sanhueza *et al.*, 2015). Normalised surface areas of candidates identified in Chapter 4 were calculated as: (x- average eye surface area of CLN3 OE)/(average of eye surface area of the control - average eye surface area of CLN3 OE) x100.

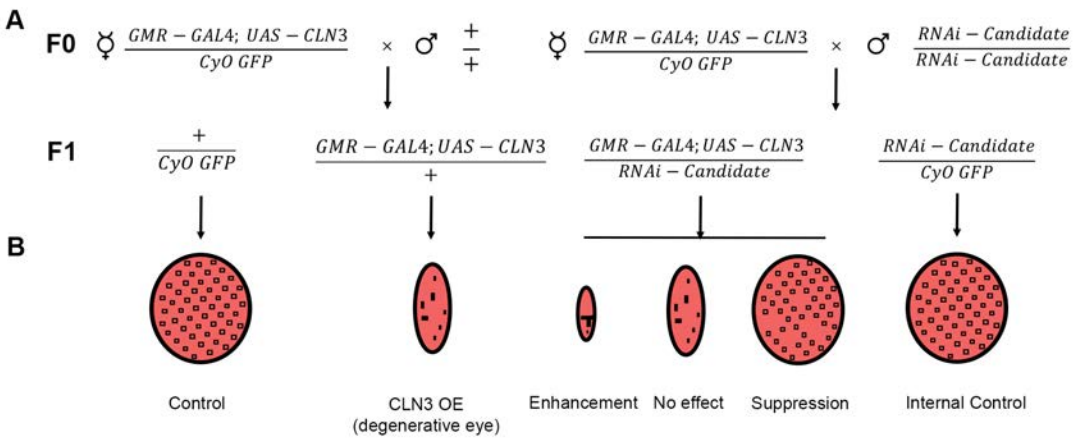

Fig. 5.3. Genetic modifier screen mating scheme. **A.** As indicated on the right; recombinant female virgins (*GMR-GAL4;UAS-CLN3/CyO GFP)* were crossed with misexpressed candidate lines (in this example RNAi homozygous in the second chromosome). In F1 50% of flies contain the misexpression construct and the CyO^{-} balancer (internal control, distinguishable by the curly wing phenotype). The other 50% will contain the recombinant allele *GMR-GAL4;UAS-CLN3* and the misexpression construct (*RNAi-Candidate*), which do not have curly wings (CyO^{+}). These flies are assessed for suppression or enhancement (or no effect) of the CLN3-induced phenotype. In parallel (indicated on the left), recombinant female virgins (*GMR-GAL4;UAS-CLN3/CyO GFP)* are crossed with a wild-type fly (Canton S) to generate control flies: GMR-GAL4;UAS-CLN3/+ (CLN3 OE control) and +/CyO GFP (WT phenotype control). **B**. Graphic representation of the resulting phenotypes in the adult *Drosophila* eye. Control and internal control will show no defects on the eye. CLN3 OE will show the previously characterized CLN3-induced degenerative eye. The fly containing the eye driver, CLN3 overexpression and candidate misexpressed construct will either have no effect (eye will be comparable to CLN3 OE) an enhancement of the phenotype (smaller eye and/or with more black puncta), or suppression of the phenotype (increased surface area and/or improvement of the compound structure of the eye).

5.2.4.4 Viability assay

To investigate the effect of CLN3 misexpression in the adult viability, we analysed the number of eclosed flies expressing *UAS-CLN3* or *CLN3-RNAi* under the control of different neuronal drivers: *GMR-GAL4*, *D42-GAL4*, *ElavC155-GAL4* and *Bg57-GAL4*.

For *UAS-CLN3* crosses viability was calculated as a percentage of the number of eclosed OE CLN3 flies/Number of eclosed control flies. A value of 100% is expected if the cross is non-toxic. A value lower than 100% indicates a toxic effect. For *CLN3-RNAi* crosses, the total number of eclosed flies for each F1 genotype was plotted so CyO^+ (containing *RNAi-CLN3*) expressing flies were compared to their CyO^- internal controls, as each of them are expected to be 50% of the total.

5.2.4.5 Fasudil drug assay

ROCK2 upregulation was found to correlate to synaptic vulnerability in Chapter 3. After a rescue was obtained when targeting ROCK2 genetically in *Drosophila* CLN3-induced degenerative eye phenotype (via ROCK2-*RNAi*), we wanted to investigate if we could also target ROCK2 upregulation pharmacologically. To do so we used the ROCK inhibitor Fasudil, Monohydrochloride Salt (*LC laboratories*, F-4660), which was previously used in mice models of SMA improving survival and skeletal muscle development (Bowerman *et al.*, 2012).

To establish the optimal dosage window *GMR-GAL4* x *UAS-CLN3* crosses were raised in regular food containing different concentrations of Fasudil as recommended in (0.1, 1 and 10 mM) (Pandey *et al.*, 2011). However, results were very variable between experiment and we thought there was difficulty mixing the drug with the pre-made food to an even consistency. Therefore, experiments were repeated using Nutri-Fly instant food (*Genesee Scientific*, 66-118) prepared and mixed in the laboratory. Results started to become more consistent and a therapeutic window dose was established to be between 1.4 and 5 mM (Fig. 5.4). The optimal dose established was 1.4 mM, in which a small but consistent improvement of the eye phenotype was observed. Therefore, three independent experiments were carried out with 1.5 mM of Fasudil to confirm the results. Eyes of the offspring were photographed and total surface area was measured with *ImageJ*. Suppression of the CLN3-degenerative eye were calculated from 3 independent experiments as "(x- average eye surface area of the CLN3 OE)/(average of eye surface area of the control - average eye surface area of CLN3 OE) x100" for each experiment.

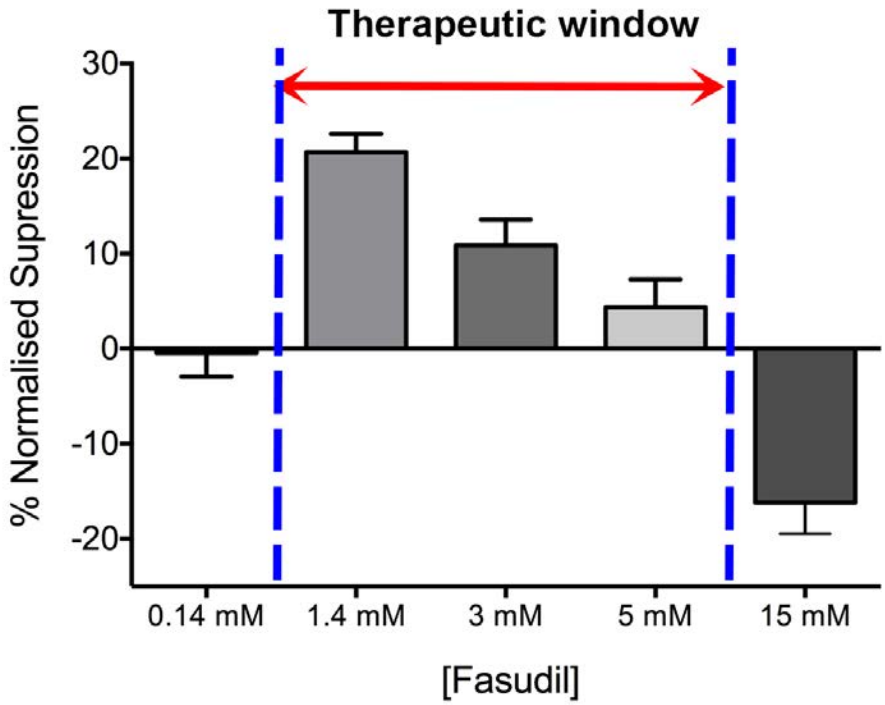

Fig. 5.4. Fasudil therapeutic window concentration is between 1.4 and 5 mM. Bar chart showing the normalised suppression effect of Fasudil in GMR-GAL4/UAS-CLN3 flies which were raised in food containing 0.14, 1.4, 3, 5 and 15 mM of Fasudil. 0.14 mM did not cause any effect in CLN3-induced phenotype, whereas 15 mM showed to enhance the eye phenotype by approximately 10 %. Mean ± SEM; N>20 flies per dosage.

5.3 Results

5.3.1 Characterization on CLN3 *Drosophila* models

First, we needed to characterize the phenotypes in different neuronal systems in CLN3 *Drosophila* models in order to identify which system was the optimal to perform our candidate genetic screen. We utilized the well-characterized temperature-inducible UAS/GAL4 system which allows the misexpression of a gene of interest in a spatio-temporal manner (Brand *et al.*, 1993, St Johnston, 2002) (see 5.2 Materials and methods).

5.3.1.1 CLN3 OE in the eye

There seemed to be a dosage window in which too much or too little CLN3 caused a disruption of the nervous system in *Drosophila* (Tuxworth *et al.*, 2009, Tuxworth *et al.*, 2011). The targeted overexpression of *CLN3* by means of the UAS/Gal4 system, using the *GMR-GAL4* driver (Freeman, 1996) was shown to cause severe neurodegeneration of the adult compound eye, which was indicated by fused ommatidia (glazing) and smaller eyes (See 5.1 Introduction) (Korey *et al.*, 2003, Tuxworth *et al.*, 2009).

First, we wanted to reproduce the phenotype described by Tuxworth *et al.*, and explore if we could utilize such a model as a tool to assess the role of our candidates *in vivo.* To do so, two eye drivers were used: *GMR-GAL4* (the same used by Tuxworth *et al.* and commonly used in genetic screens (Fernandez-Funez *et al.*, 2000) and *eyeless-GAL4* (Tseng *et al.*, 2002), also commonly used for genetic screens (Sanhueza *et al.*, 2015).

UAS-CLN3 flies (donated by R. Tuxworth) were crossed to the temperature inducible *GMR-GAL4* eye driver (see Table 5.1). Crosses were raised at 25, 27 and ≥28ºC in order to study the effects of CLN3 dosage in the eye. After eclosion, adults were examined under the stereomicroscope and eyes were photographed for total surface area quantification. At 25ºC, eye size was significantly smaller than control eyes, the structure of the compound eye was completely disrupted showing a glazing phenotype (fused ommatidia) and alteration of somatosensory interommatidial bristles, as previously described by Tuxworth *et al.* There was a detectable presence of black puncta in some flies, which indicates necrotic cell death. Very interestingly, the same crosses raised at 27ºC showed a more severe phenotype with an increase in lethality (Fig. 5.5). *GMR-GAL4 x UAS-CLN3* offspring raised at 28ºC proved to be 100% lethal at the pupa stage.

Conversely, *UAS-CLN3* driven with *eyeless-GAL4* did not cause any phenotype at 25 or 28° C. As mentioned in section 5.2.4.2, *Ey* is a key gene for the eye development in *Drosophila* and its expression is restricted to undifferentiated cells located anterior to the morphogenic furrow (Halder *et al.*, 1995). In contrast, *GMR-GAL4* driver (Freeman, 1996) is expressed in a different area than the *eyeless* gene. *GMR* is found to be primarily expressed in the posterior region of the morphogenic furrow area, where ommatidia cells are starting to differentiate (Freeman, 1996). Therefore, these results indicate that the role of CLN3 is likely to be more important to the the cells of the ommatidia when they are starting to differentiate and it might not play an essential role in previous steps of eye development in *Drosophila* (undifferentiated cells).

Importantly, here we show that we could successfully reproduce the already published phenotype in *Drosophila* eye using the same *GMR-GAL4* driver as the one reported by Tuxworth et al. Additionally, we established a way to quantify this phenotype by measuring the total surface area of the eye and demonstrated that the effects in the phenotype (eye and viability, Fig. 5.5) are CLN3-dose dependent.

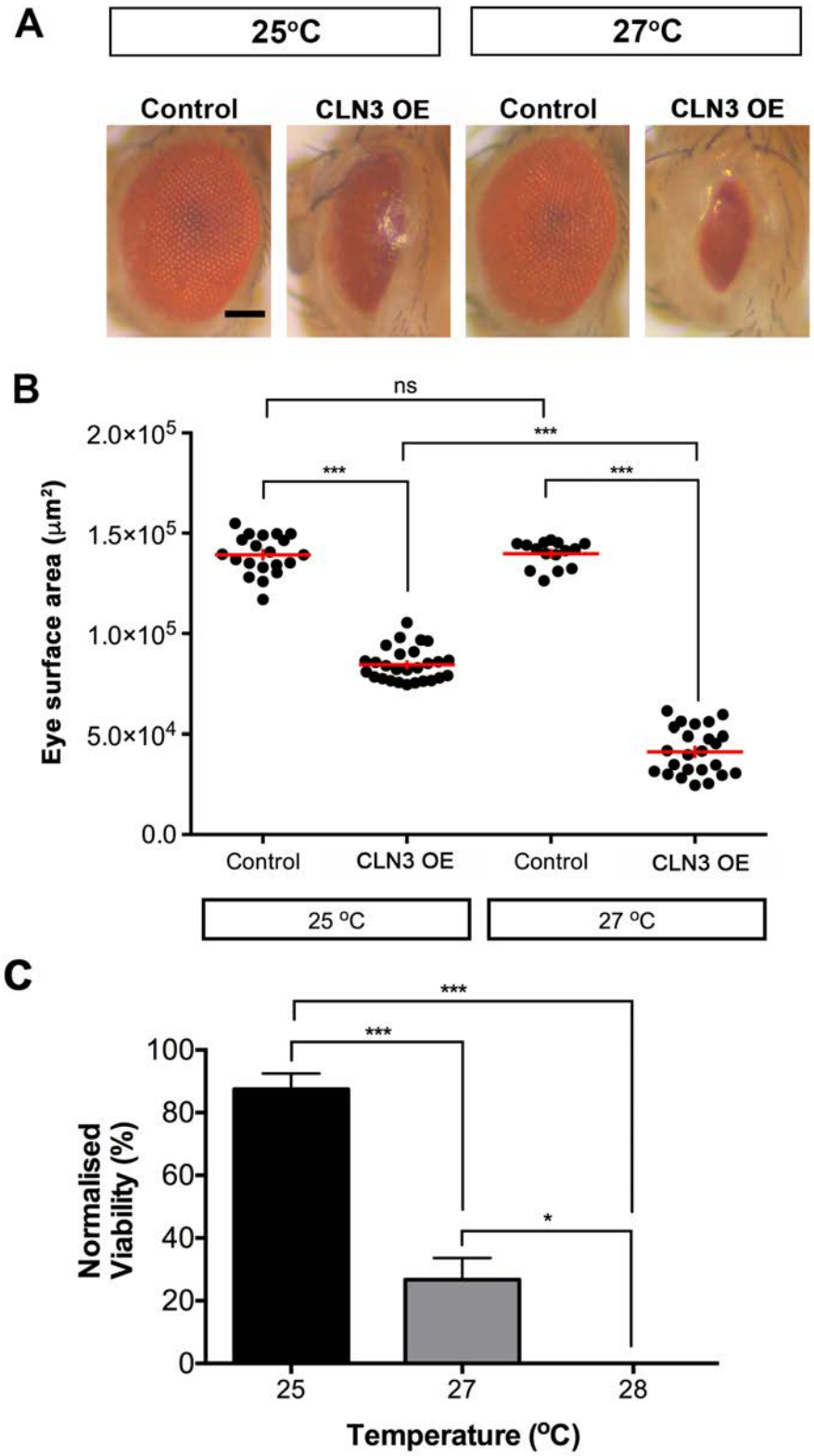

Fig. 5.5. CLN3-induced neurodegeneration in the eye is dose-dependent. **A.** Representative light microscope images of fruit fly eyes of control line (*GMR-GAL4/+)* and CLN3 OE line (*GMR-GAL4/UAS-CLN3)* at 25°C and 27°C. The higher the temperature the greater the expression of CLN3. **B.** Quantification of the eye surface area of these genotypes showing that the higher the dose of CLN3 gene, the greater the effect seen in the eye. **C.** Normalised viability to control cross

at 25, 27 and 28º C showing the progressive decrease in viability correlating to increase in CLN3 expression driven in the eye. One-way ANOVA with Tukey's multiple comparison post-hoc; * p-value<0.05, ** p -value<0.01, *** p-value<0.001, ns p-value>0.05. N=>20 (**B**), N=3 (**C**).

5.3.1.2 CLN3 OE in the NMJ

To date, no studies have been published regarding the effects of CLN3 OE at the synaptic level. Since, CLN3 OE causes neurodegeneration in the adult developing eye (see above), we also wanted to explore if CLN3 OE caused synaptic disruption in the neuromuscular junction of the musculature body wall in *Drosophila* larvae (see Chapter 1. General introduction, section 1.8.2.1 & 1.8.3).

To do so, we crossed *UAS-CLN3* to a motor-neuron driver (*D42-GAL4*) (Sanyal, 2009, Parkes *et al.*, 1998, Gustafson *et al.*, 1996, Nitz *et al.*, 2002), a pan-neuronal driver (*elav^{C155}-GAL4*) (Yannoni *et al.*, 1997) and to a post-synaptic/muscle driver (*Bg57-GAL4*) (Budnik *et al.*, 1996) (see Table 5.1 and 5.2 Materials and methods). Flies from these crosses were raised at 25, 27 and 28ºC, to assess the effects of CLN3 dose. To visualize larval NMJs, dissection of third instar larvae and fillet preparation was carried out followed by the use of primary and secondary antibodies labeling pre-synaptic neuron (HRP) and the post-synaptic side of glutamatergic boutons (Dlg) (see Chapter 2. General materials and methods; section 2.3.2).

Flies carrying *UAS-CLN3* under the control of a motor-neuron driver (*D42-GAL4*), presented a very severe phenotype at 27 ºC (Fig. 5.6A). They have a small number of boutons left and the remaining ones presented an abnormal shape. Axons were also affected, indicated by the lack of HRP (green) staining. Additionally, loss of Dlg (red) seemed proportional to the loss of its corresponding pre-synaptic side. At 25º C, abnormalities in the NMJ architecture were also detected although, as expected, they were milder than those at higher temperature.

Therefore, using a motor-neuron driver, we can also detect the dose-dependent effect of CLN3 protein on synaptic morphology and in terms of the viability.

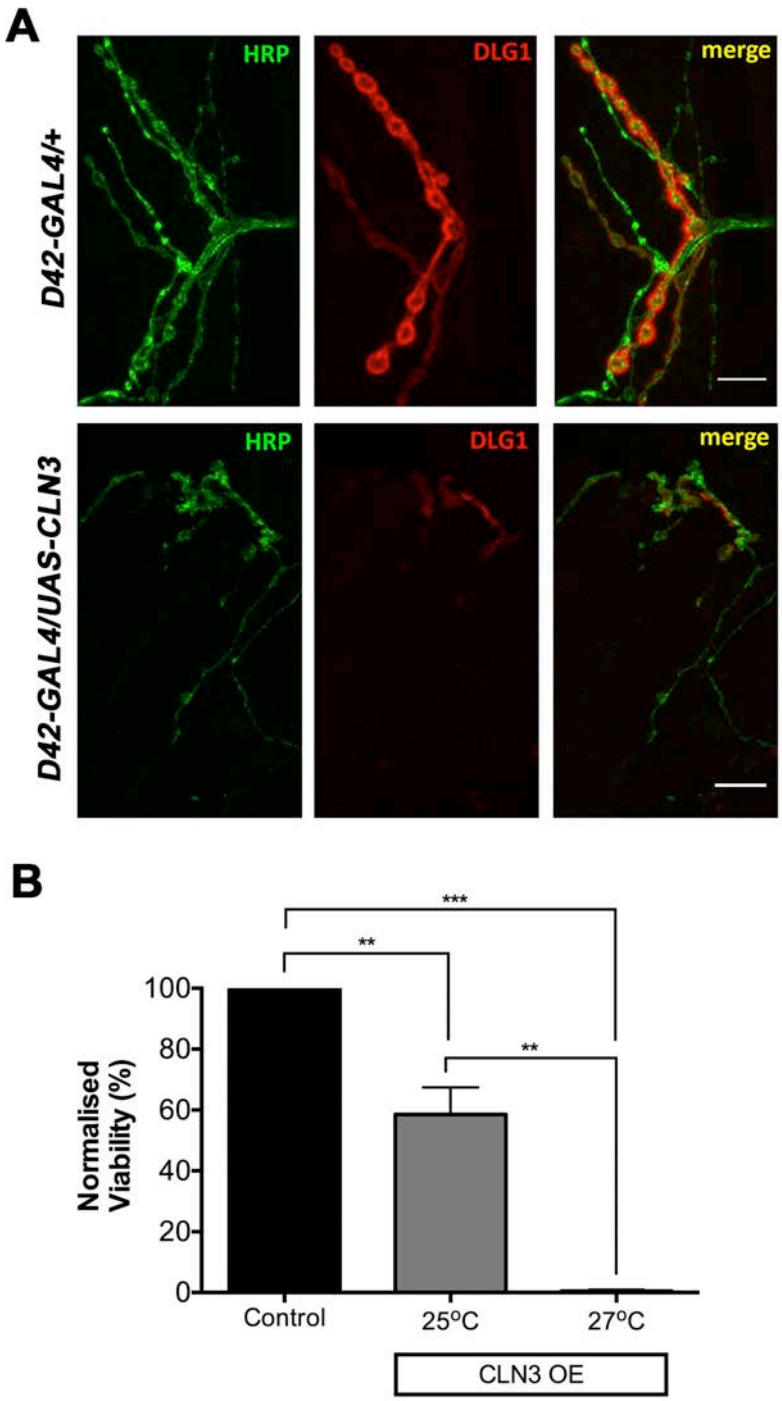

Fig. 5.6. Overexpression of CLN3 driven to the motor-neuron causes a dose-dependent disruption of the NMJ architecture in the third instar* Drosophila *larvae and a decreased viability of adult flies. **A.** Confocal micrographs NMJ of muscle 12/13 of control (*D42-GAL4/+)* and CLN3 OE *Drosophila* third instar larvae (*D42-GAL4/UAS-CLN3*) raised at 27º C. Larvae fillet preparations were stained with a neuronal (HRP, green) and post-synaptic glutamatergic markers (DLG1, red). The architecture of the OE NMJ larvae is severely disrupted with loss of axons, boutons at both pre- and post-synaptic level. **B.** Bar chart representing the normalised viability of the same crosses at 25 and 27º C showing that the dose-dependent effect of CLN3 OE was also

reflected in the surviving offspring. Mean ± SEM; One-way ANOVA with Tukey's multiple comparison post-hoc; ** p -value<0.01, *** p-value<0.001, N=2-3.

Some crosses were left in the incubator for a viability assay of eclosed adult flies. Flies raised at 25 ºC presented a viability of around 60%, whereas at 27º C viability was almost 0% and the *Drosophila* were dying between third instar and pupal stages (Fig. 5.6B).

In contrast, CLN3 OE under the control of a pan-neuronal driver (*elav^{C155}-GAL4*), caused 100% embryonic lethality at 27º C and above. Indicating, that CLN3 is needed for the stability of the PNS (consistent with the *D42-GAL4* experiment) as well as the CNS of the flies. CLN3 OE in both areas may have a synergistic toxic effect for the *Drosophila*, since CLN3 OE are driven only in the motor-neuron, allowing development of flies through larval stages. At 25º C, viability of adult flies was lower than with *D42-GAL4* (around 20%), but it was enough to allow the study of the phenotype of the NMJ in the third instar larvae (Fig. 5.7B). CLN3 OE driven with *elav^{C155}-GAL4* at 25º C, caused a disruption of the NMJ architecture with an absence of synaptic boutons (especially type Is). The phenotype caused was milder compared to the one caused when driven by *D42-GAL4* at 27º C and the axons were mostly unaffected. However, abnormalities in the boutons were still very obvious presenting irregular shapes and loss of parts of the boutons (Fig. 5.7A).

Importantly, here we demonstrate disruption of NMJ architecture caused by CLN3 OE using two independent neuronal drivers and highlight that it is consistently CLN3 dose-dependent.

Interestingly**,** CLN3 OE construct driven post-synaptically (muscle) at 25ºC caused a slightly different effect at the NMJ. There were detected abnormalities in synaptic bouton size, as indicated in Fig. 5.8. However, there seemed to also be an enlarged size of the boutons caused by the driver in the control cross, although to a lesser extent that in the *UAS-CLN3* flies. The dose-dependent effect was also detectable using a post-synaptic driver: the same cross raised at 28º C caused embryonic lethality, at 27º C flies died as larvae and, at 25 ºC flies died at pupa stages.

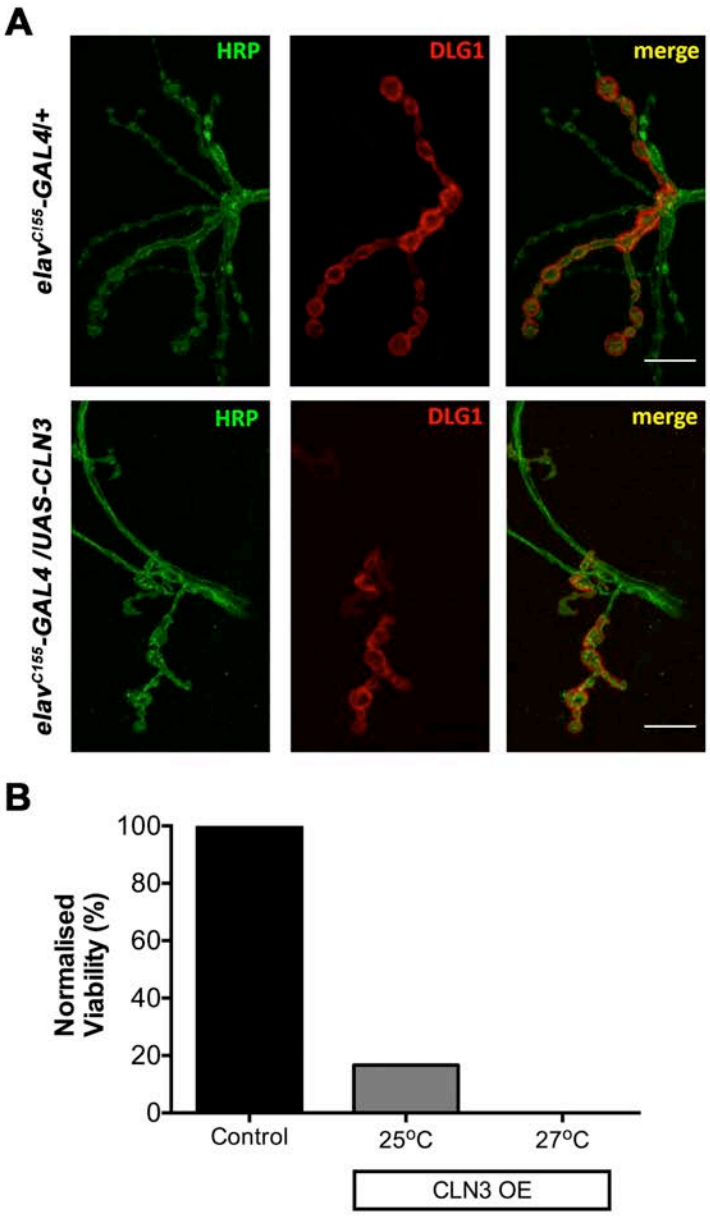

Fig. 5.7. Overexpression of CLN3 driven pan-neuronally causes a disruption of the NMJ architecture in the third instar* Drosophila *larvae and a dose-dependent decrease in viability of adult flies. **A.** Confocal micrographs NMJ of muscle 12/13 of control (*elav^{C155}-GAL4/+)* and CLN3 OE *Drosophila* third instar larvae (*elav^{C155}-GAL4/UAS-CLN3*) raised at 25ºC. Larvae fillet preparations were stained with a neuronal (HRP, green) and post-synaptic glutamatergic markers (DLG1, red). The architecture of the OE NMJ larvae is severely disrupted with a loss of boutons at both pre- and post-synaptic level. However, axons were not that severely affected. **B.** Bar chart representing the normalised viability of the same crosses at 25 and 27º C showing that the dose-dependent effect of CLN3 OE was also reflected in the surviving offspring.

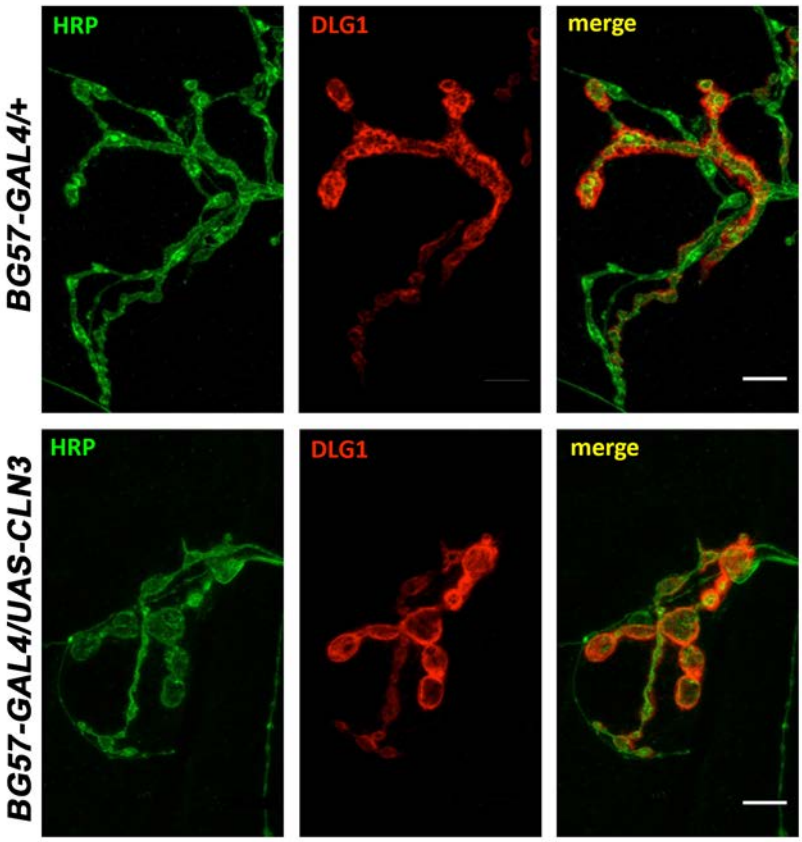

Fig. 5.8. Overexpression of CLN3 driven post-synaptically caused disruption of the NMJ architecture in the third instar* Drosophila *larvae and a dose-dependent decrease in the viability of adult flies. Confocal micrographs NMJ of muscle 12/13 of control (*Bg57-GAL4/+)* and CLN3 OE *Drosophila* third instar larvae (*Bg57-GAL4/UAS-CLN3*) raised at 25º C. Larvae fillet preparations were stained with a neuronal (HRP, green) and post-synaptic glutamatergic markers (DLG1, red). The bouton size of OE NMJ larvae were enlarged when compared to controls, although controls also seemed to have boutons of an irregular, larger size than normal.

As summarized on Table 5.3, OE of CLN3 caused a range of phenotypes depending on where and level of expression. CLN3 OE in both CNS and PNS caused severe effects in synaptic stability, causing embryonic lethality at 27º C and medium disruption of the synapse at 25 ºC. A specific motor-neuron driver, also severely affected the viability of *Drosophila*, and the surviving animals presented a complete disruption of NMJ architecture with almost no synaptic boutons left at 27º C. Following the CLN3 dose-dependent toxic effect, a mild disruption of NMJ morphology was also detected at lower temperatures (25 ºC). In contrast, using a post-synaptic driver (*Bg57-GAL4*), bouton sizes were larger whereas bouton number

seemed to be less affected. Nevertheless, there was also a detected increase in bouton size in the control animals, meaning a toxic effect caused by the driver might be contributing to the phenotype observed in the CLN3 OE animals.

Table 5.3 Summary of phenotypes observed in CLN3 OE driven in the synapse

Temperature (ºC)	***D42-GAL4* (Motor neuron)**	***Elav^{C155}-GAL4* (Pan-neuronal)**	***Bg57-GAL4* (Post-synapse)**
25	+Disruption of NMJ: decreased number of boutons	++Disruption of NMJ: decreased number of boutons	+Disruption of NMJ: larger boutons
27	+++Disruption of NMJ: decreased number of boutons. Pupal lethal	Embryonic lethal	Larval lethal
≥28	Embryonic lethal	Embryonic lethal	Embryonic lethal

+mild; ++medium; +++severe

5.3.1.3 CLN3 LOF in the NMJ

Unpublished studies by Tear laboratory [as stated in (Bond *et al.*, 2013, Faller *et al.*, 2015)] suggested that synapses in the NMJ of the larvae lacking CLN3 fail to mature appropriately and have alterations in bouton size. Therefore, since human CLN3 disease is caused by its LOF, we also wanted to investigate by means of the UAS/GAL4 system if a LOF could be suitable for genetic screening of our candidates.

Since, the *Bg57-GAL4* driver seemed to have a toxic effect on its own, we decided to focus only on the motor-neuron (*D42-GAL4*) and pan-neuronal drivers (*elav^{C155}-GAL4*) and crossed them with a *CLN3-RNAi* line (Table 5.1) to knock-down the expression of CLN3 at 25, 27 and 30º C.

Interestingly, decreasing the expression of CLN3 with both pan-neuronal and motor-neuron drivers caused a milder disruption of the synapse compared to CLN3 OE. *CLN3-RNAi* under

the control of *elav^{C155}-GAL4* at 27 ºC was qualitatively mild, with abnormalities in bouton number and shape and it was much more severe at 30º C (Fig. 5.4). Axons seemed not to be affected but there was a reduction in the number of boutons. Moreover, there was a loss of DLG staining in some of the boutons as indicated by the white arrows in Fig. 5.5A. Similar results were observed with *D42-GAL4* although to a lesser extent than with *elav^{C155}-GAL4* at the same temperatures. In terms of viability, the results of the assay were very variable due to CyO^- flies getting attached to the walls of the vials due to humidity issues in the water bath (used at 27 and 30º C for this experiment). At 25º C when using the *D42-GAL4* system, the incubator was used and eclosed adults counted suggesting a small but significant decrease in viability of the flies carryng the *CLN3-RNAi* construct (Fig.5.9B). Many experiments using the incubator (where humidity is better controlled) will be necessary in order to draw solid conclusions regarding the viability of *RNAi-CLN3* driven in the synapse.

Thus, in this section we confirm as previously reported (Faller *et al.*, 2015, Tuxworth *et al.*, 2011, Tuxworth *et al.*, 2009, Bond *et al.*, 2013), that either too much or too little expression of CLN3 disrupts nervous system stability in *Drosophila*.
We also show for the first time, that increasing CLN3 in the synapse leads to disruption of its general architecture and bouton morphology. We also confirm that lack of CLN3 in the synapse also produces perturbations in its morphology, consistent with unpublished observations stated in (Bond *et al.*, 2013, Faller *et al.*, 2015). However, the disruption is more severe when CLN3 is overexpressed.

Both CLN3 OE and *CLN3-RNAi* flies using either the *D42-GAL4* or the *elav^{C155}-GAL4* drivers, would have been excellent tools for the study of the role of my candidates in the larvae NMJ system. However, due to the fact that NMJ assay requires dissection, staining and posterior confocal imaging of the animals, we concluded that the more sensible assay protocol to perform candidate genetic screening as a first pass was the eye phenotype using the OE of CLN3 driven with *GMR-GAL4*. Misexpression of CLN3 driven in the NMJ would have be an excellent model for a secondary screen or a further characterization of the role of my candidates in the synapse *in vivo*, but this was beyond the time-scale and scope of this current work.

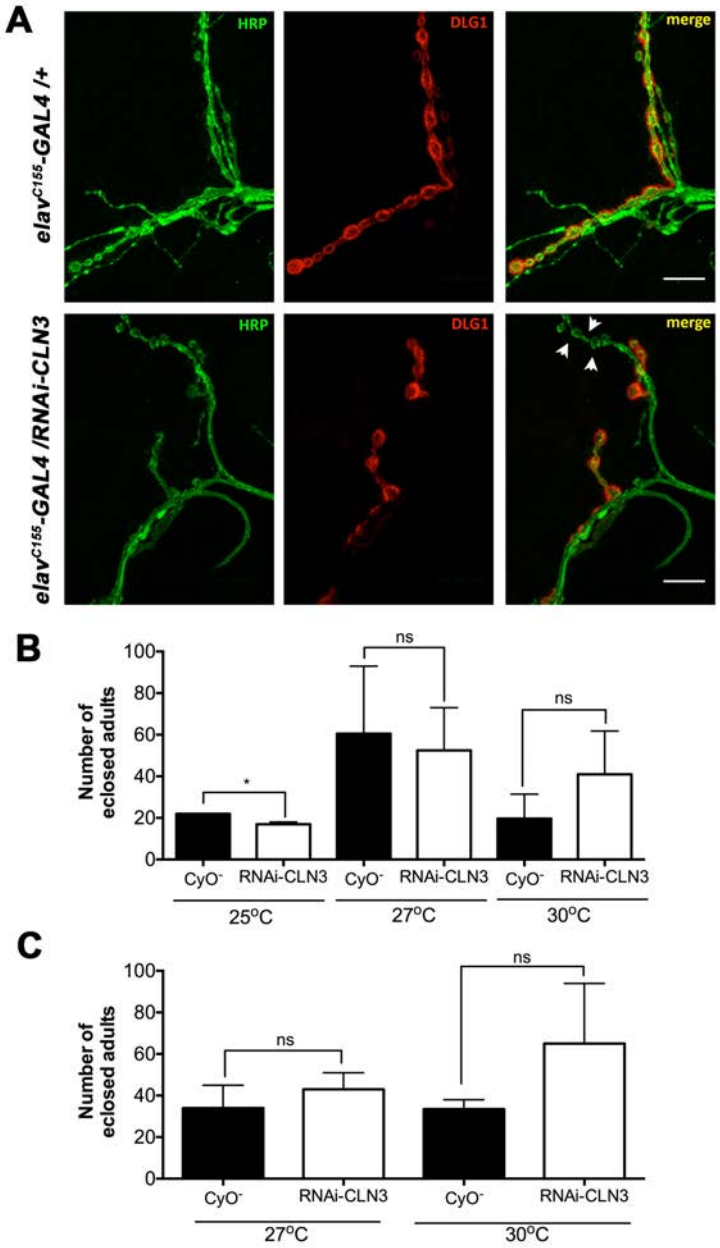

***Fig. 5.9. Knocking down CLN3 in the nervous system causes bouton loss in the NMJ of the third instar* Drosophila *larvae.* A.** Confocal micrographs of NMJ of muscle 12/13 of the control (*elav^{C155}-GAL4/+)* and CLN3 OE *Drosophila* third instar larvae (*elav^{C155}-GAL4/UAS-CLN3*) raised at 30° C. Larvae fillet preparations were stained with a neuronal (HRP, green) and post-synaptic glutamatergic markers (DLG1, red). There was a decrease in the number of boutons as well as a loss of DLG staining in some of the samples (white arrows). In contrast, axons did not seem affected by the loss of CLN3**.** The number of eclosed adult flies from RNAi-CLN3 driven with *D42-GAL4* and *elav^{C155}-GAL4* in bar charts **B&C** respectively. Mean ± SEM; * p-value<0.05, ns p-value>0.05 (Student T test).

5.3.2 Modifier screening in the eye

To summarise the sections within this chapter so far, we have decided to use a CLN3 overexpression system driven in the *Drosophila* eye to study the potential modulatory effects of my candidates (identified in Chapters 3&4) in a CLN3-induced degenerative model.

The use of the eye for modifier screens is very common in the study of neurodegenerative disease, and gross examination does not require dissection or staining (see Chapter 1. General Introduction, section 1.8.2.2). Here, we employed a system to quantify the degenerative phenotype in *Drosophila* by measuring the total surface area of the eye [as previously described in (Sanhueza *et al.*, 2015)]. This allowed a rapid, objective and unbiased quantitative assessment of the potential modulatory effects of candidate proteins on the CLN3-induced eye phenotype,

5.3.2.1 Generation on CLN3 recombinant stock

To begin with, we needed to generate an appropriate fly to use as a tester line for the study of my candidates on a "neurodegeneration" background. Since both *UAS-CLN3* and *GMR-GAL4* constructs are placed on the second chromosome, and many candidate lines carried out with an RNAi construct also found in the second chromosome, we needed to generate a recombinant fly carrying both *GMR-GAL4* and *UAS-CLN3* in the same allele, so they would inherit both drivers together in the offspring, leaving a "chromosomal space" for a potential *Candidate-RNAi/OE* construct (see 5.2 Materials and methods). As indicated in Fig. 5.2, a recombinant fly *(GMR-GAL4;UAS-CLN3/CyOGFP*) was obtained after 25 individual attempt crosses and was amplified to be used as a tester line (See 5.2 Materials and methods).

Before beginning the screen, some quality control was required to generate the new recombinant CLN3 OE fly. First, we wanted to confirm, that the degenerative eye phenotype was indeed caused by CLN3 OE. To do so, a double dosage experiment was carried out by generating flies carrying two *UAS-CLN3* constructs (*GMR-GAL4;UAS-CLN3/UAS-CLN3).* Both crosses raised at at 25 and 27º C caused 100% lethality of *GMR-GAL4;UAS-CLN3/UAS-CLN3* flies indicating again the dose-dependent toxicity of CLN3 protein (Fig. 5.10A).

Moreover, we carried out a second quality control experiment to confirm that any suppressor effects observed in the genetic screening were not due to the dilution effect of the GAL4 driver over two UAS constructs. To do this, we crossed the recombinant fly to *UAS-GFP* and to a WT fly line. F1 was sorted by CyO^+ and CyO^- for both GFP and control crosses, eyes were photographed and surface area was measured. We also measured the eyes of a WT

fly (Canton S, +/+) and compared that to our CyO$^-$ from the control cross to confirm that the CyO balancer was not affecting the eye phenotype. Results indicated on the one hand that the presence of an extra UAS construct under the control of *GMR-GAL4* driver did not produce any effect in the CLN3-dependent eye phenotype. On the other hand, it showed that a WT fly (+/+) and CyO$^-$ flies showed no difference in eye size (Fig. 5.10B).

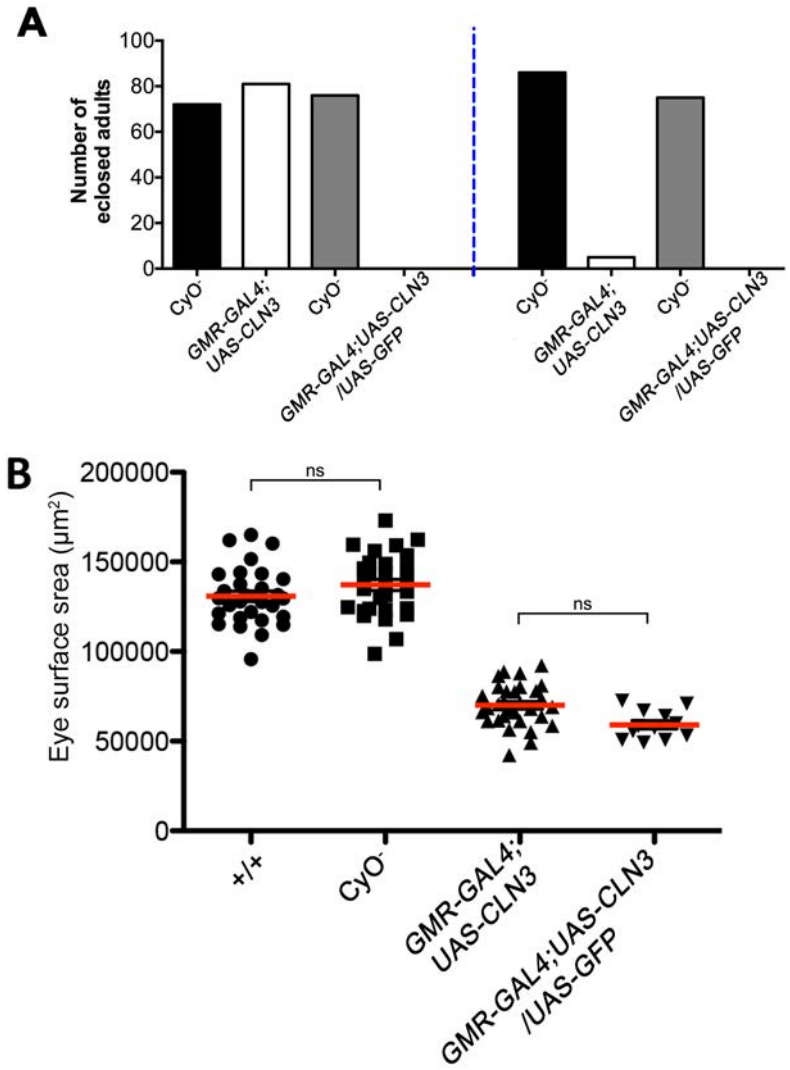

Fig. 5.10. Quality control of the CLN3 recombinant fly as a tester line. **A.** Bar chart indicating the number of eclosed flies from *GMR-GAL4;UAS-CLN3* crosses with *UAS-CLN3* and WT fly (+/+). Results showed that CLN3 (DD) double dosage was lethal at 25 and 27º C confirming the dose-dependent effects of CLN3 OE. **B.** Dot plot indicating the eye surface area of a WT fly (+/+), +/CyOGFP (CyO$^-$), *GMR-GAL4;UAS-CLN3*/+ and GMR-GAL4;UAS-CLN3/UAS-GFP. No significant difference was observed between +/+ and CyO$^-$ flies indicating no effects of the CyO balancer to the eye. No differences were either seen between *GMR-GAL4;UAS-CLN3*/+ and GMR-GAL4;UAS-CLN3/UAS-GFP indicating no dilution effects of the GAL4 driver. Mean ± SEM ns= p value>0.05 (Student T test) (N>15 flies per genotype).

We therefore concluded that our *GMR-GAL4;UAS-CLN3* recombinant fly is suitable for genetic modifier screening and that CyO^- flies resulting from *GMR-GAL4;UAS-CLN3* crossed to a WT fly (+/+) is equivalent to WT fly, and this was therefore used as a control fly during the genetic screen.

5.3.2.2 CLN3 regional candidates: Valine degradation and Rock2 signaling pathways

Once we confirmed that our *GMR-GAL4;UAS-CLN3* recombinant fly was suitable as a tester line, we proceeded to screen our protein candidates identified in Chapter 3 & 4 (Table 5.2). We started with examples of downregulated and upregulated candidates from Chapter 3 which sit in specific pathways related to valine degradation (HIBCH and HADHA) and ROCK2 signaling pathways (ROCK2) respectively (see Fig. 3.10 and 3.13 in Chapter 3).

Both HIBCH and HADHA were found to sit in the same metabolic pathway involved in the degradation of the valine amino acid. Both enzymes were downregulated in thalamic synapses (the most vulnerable brain area) whereas they were unchanged in cortical synapses (a less vulnerable area), and their expression profile therefore correlated to the pattern of synaptic vulnerability across brain areas as described in Chapter 3 (Fig. 3.3 & 3.5). Moreover, the valine degradation cascade itself was found to be progressively disrupted following the same vulnerability pattern across brain areas (Fig. 3.6).

Following the mating scheme described in Fig. 5.3, we crossed HIBCH and HADHA RNAi lines (Table 5.2) to the tester line. F1 was sorted by genotype and eyes were phenotypically assessed. Eyes were photographed and surface area was measured with *ImageJ*. Results indicated that knocking down both candidates in a CLN3 OE background enhanced the CLN3-induced degenerative phenotype. Eyes were visibly smaller for both HIBCH and HADHA RNAi crosses (Fig. 5.11). Interestingly, this correlated with the downregulation of both candidates observed in thalamic mouse synapses in $Cln3^{-/-}$ mice.

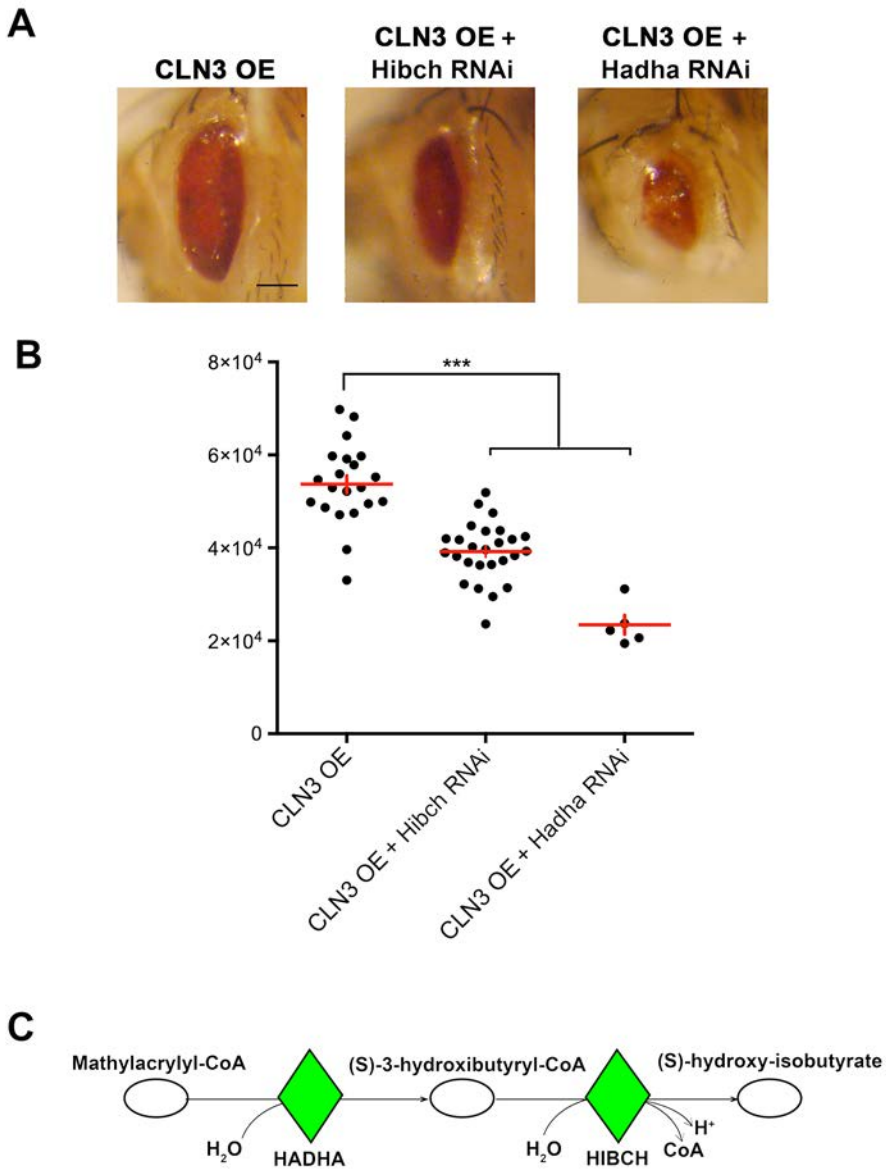

***Fig. 5.11. CLN3-induced degeneration is enhanced by the genetic downregulation of HIBCH and HADHA* in vivo. A.** Representative light microscope images of fruit fly eyes of the CLN3 OE (*GMR-GAL4;UAS-CLN3*), CLN3 OE with HIBCH-RNAi (*GMR-GAL4;UAS-CLN3/HIBCHRNA*i) and CLN3 OE with HADHA RNAi (*GMR-GAL4;UAS-CLN3/RNAiMTPα).* **B.** Quantification of the eye surface area of these genotypes. Scale bar=100um. Mean ± SEM ***P<0.001 (One-way ANOVA and Tukey's multiple comparison test as a post-hoc analysis). **C.** Schematic representation of the fourth and fifth steps of the valine catabolism cascade showing the enzymes HADHA and HIBCH catalyzing each step respectively. Downregulating both HADHA or HIBCH in the CLN3 fly enhanced the degenerative phenotype in the eye. Defects in HADHA enhanced the degenerative phenotype more than HIBCH downregulation, indicating that the further upstream the pathway is disrupted the greater the phenotypic effect.

Interestingly, the enhancement was more pronounced when knocking down HADHA, as indicated by a much smaller eye size and a more disrupted surface structure with a lack of pigmentation in some areas (Fig. 5.11). Interestingly, HADHA was shown to be upstream of HIBCH and was not changed in less vulnerable synaptic populations such as those of the hippocampal and cortical regions (See Chapter 3, Fig. 3.6). This indicates that both enzymes have the ability to modulate the CLN3-OE-induced degenerative eye and that the more upstream we disrupt the valine degradation pathway, the stronger the effect seen in the phenotype. Thus, proteins down regulated in vulnerable mammalian synapses, make a CLN3-OE induced phenotype worse when downregulated in *Drosophila in vivo*.

Conversely, the protein candidate ROCK2 was found to be upregulated in thalamic synapses, but not in cortical synapses, correlating again to the vulnerability pattern described (Fig. 3.13). As described in Chapter 3, ROCK2 has been reported (by our laboratory and others) to be upregulated in a wide range on neurodegenerative conditions (injury induced, adult-onset and childhood neurodegenerative conditions) (Fig. 3.1E). Therefore, ROCK2 might be a potential modulator of synaptic stability in a variety of conditions. To confirm if that was true, the same mating scheme was followed (Fig. 5.3). Two *ROCK2-RNAi* (GD and TRiP, see Table 5.2) lines were crossed to CLN3-OE tester line. Results indicated that both RNAi lines tested were able to suppress the CLN3-OE-induced degeneration in the eye. The TRiP line showed a 100% rescue and the eye surface structure was almost fully recovered (Fig. 5.12C-E). Thus, proteins up regulated in vulnerable mammalian synapses, alleviate a CLN3-OE induced phenotype when downregulated in *Drosophila in vivo*.

Due to the rescue obtained when targeting ROCK2 genetically and since there are multiple Rock inhibitors available, we decided to explore the possibility of targeting ROCK2 pharmacologically. Several ROCK inhibitors have been characterized, but their specificity for individual ROCK kinases is still unclear. Fasudil is a small molecule that non-specifically inhibits ROCK2. It was originally discovered as a blocker of cerebral vasospasm in animal models (Takayasu *et al.*, 1986). Importantly, fasudil has been demonstrated to be safe and effective in clinical trials of cerebral vasospasm, pulmonary hypertension, Raynaud phenomenon and cancer (Olson, 2008, Suzuki *et al.*, 2008, Masumoto *et al.*, 2002, Velat *et al.*, 2011, Bharadwaj *et al.*, 2005, Hinsenkamp *et al.*, 2016). Moreover, fasudil has previously been applied to murine models of SMA yeilding an improvement of the phenotype and lifespan of these mice (Bowerman *et al.*, 2012, Coque *et al.*, 2014). However, fasudil also targets other

kinases such as MAP4K4, PKC, PRKAA1 or PRKAA2 (Anastassiadis *et al.*, 2011), which are predicted to be activate using *IPA* in *Cln3*$^{-/-}$ thalamic synapses (Fig. 5.13). The activation of these kinases seem to have downstream consequences on biological functions relevant to NCL such as autophagy (Fig. 5.13A) or/and "Protein kinase A signalling" (Fig. 5.13B&C). Despite these caveats, given the success of the compound in mammalian systems (Bowerman *et al.*, 2012, Coque *et al.*, 2014, Hinsenkamp *et al.*, 2016), including humans (Masumoto *et al.*, 2002, Suzuki *et al.*, 2008), and the consistent conserved ROCK2 alterations across multiple-neurodegenerative paradigms, we decided to test Fasudil in CLN3 *Drosophila (GMR-GAL4/UAS-CLN3)*. The drug was added into the fly food in order to obtain 1.5 mM of fasudil, and the *Drosophila* were raised as normal (see 5.2 Materials and methods for therapeutic dosage window establishment). Pharmacological inhibition with fasudil caused a significant, albeit modest suppression of the CLN3-derived eye phenotype. Quantification of eye surface areas confirmed a 17% rescue of the CLN3 eye phenotype in the treated animals (Fig. 5.12E-F&I).

Thus, targeting of ROCK cascades with fasudil was sufficient to result in a beneficial effect on CLN3 induced phenotype *in vivo*.

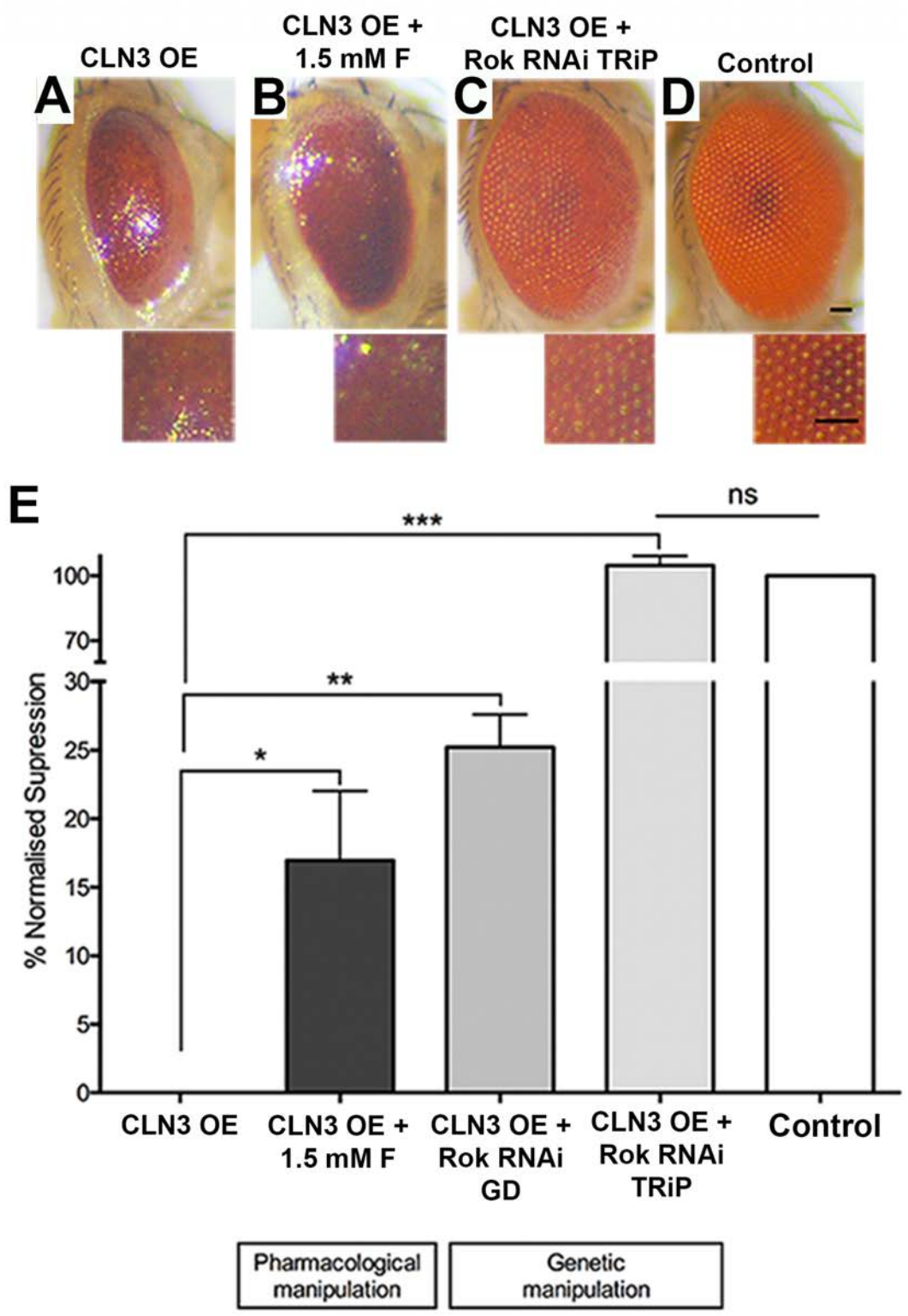

Fig. 5.12. CLN3-induced degeneration is suppressed by the downregulation of ROCK2 genetically and pharmacologically. **A-D.** Representative light microscope images of *Drosophila* eyes and corresponding 200x zoom of eye structure of **A.** CLN3 OE (*GMR-GAL4;UAS-CLN3*). **B.**

CLN3 OE + 1.5 mM Fasudil. **C.** CLN3 OE + Rok RNAi TRiP and **D.** Control fly (WT, Canton S). **E.** Bar chart representing the % of normalized suppression calculated from the average eye surface areas of three independent experiments as "(x- average eye surface area of the CLN3 OE)/(average of eye surface area of the control - average eye surface area of CLN3 OE) x100" for each of the three independent experiments. Scale bar=100um. Mean ± SEM N=3 ***P<0.001, *P<0.05 (One-way ANOVA and Tukey's multiple comparison test as a post-hoc analysis).

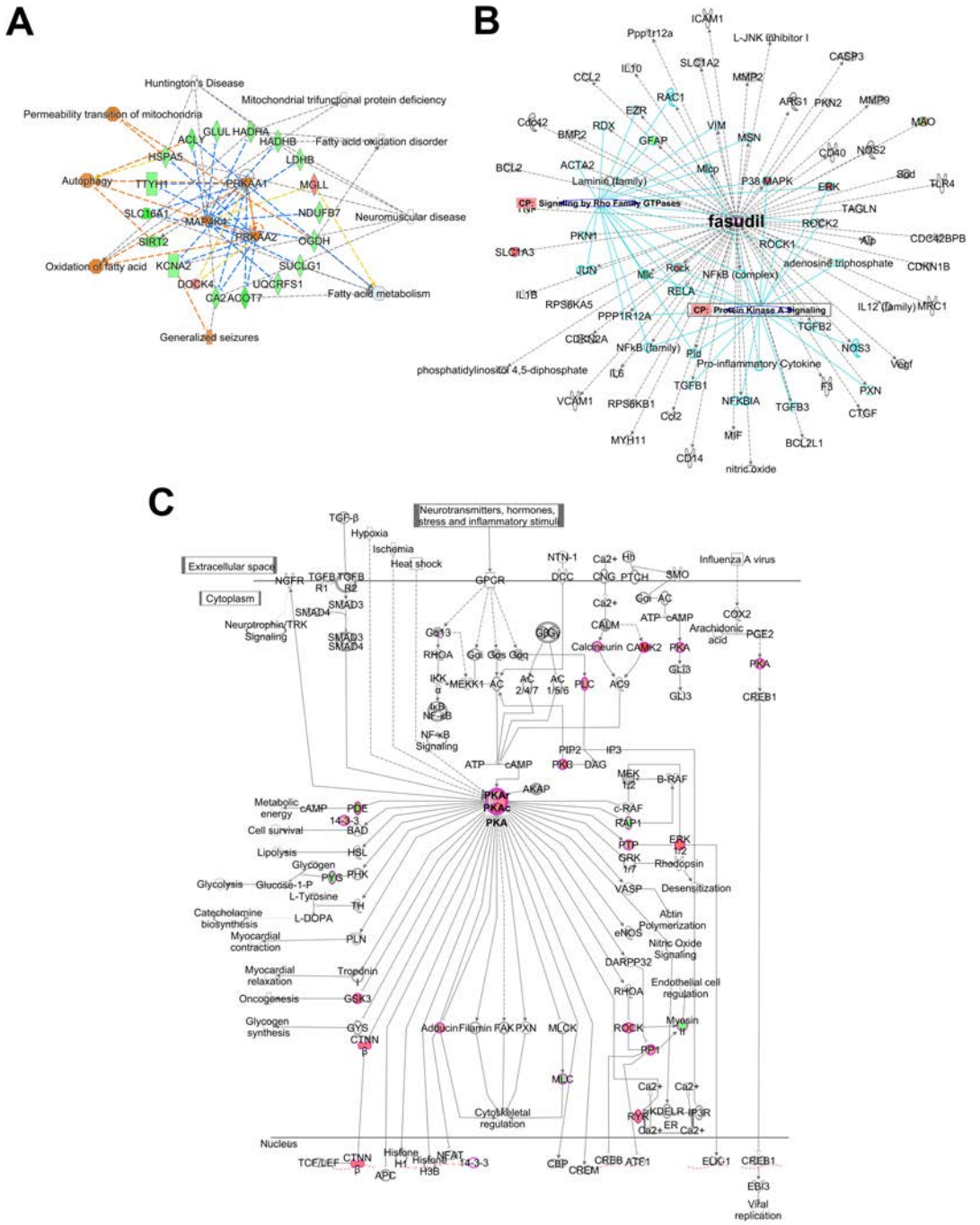

Fig. 5.13. Fasudil inhibition of ROCK2 and other kinases might contribute to the suppression of CLN3-OE induced degeneration. **A**. Network representation showing upstream regulator kinases predicted to be activated using *IPA* upstream regulator analysis that are targeted by Fasudil.

Activation of MAP4K4, PPKAA1 and PPKAA2 (center of the network) impacts on the disrupted expression of proteins such as HADHA, OGDH or SIRT2 (proteins in the thalamic dataset): proteins involved in mitochondria permeability, neuromuscular disease, or autophagy. **B.** The fasudil interactome highlights the interaction of fasudil with other proteins whose expressions are perturbed in thalamic degenerating synapses. Some of these proteins overlap with disrupted pathways such as "Signaling by Rho family GTPases" and "Protein Kinase A signaling"). **C.** "Protein kinase A signaling" pathway represented by *IPA*. Upregulation of PKAc (hub in this network), which is also a target of fasudil, impacts in the upregulation of some proteins such as ROCK2 or β-catenin. Orange = predicted activation, blue = predicted inhibition, red = upregulated >20% green = downregulated >20%.

So, the candidates identified in Chapter 3 (HIBCH, HADHA and ROCK2) are able tomodulate the CLN3-dependent phenotype in the eye. Next, we wanted to see if knocking down these candidates had an effect in a wild-type background. To do so *GMR-GAL4* driver were crossed to RNAi lines of HIBCH, HADHA and ROCK2. Crosses were raised at the same temperature as the modifier screen (25 ºC).

As shown in Fig. 5.14, knocking down these candidates had no effect on a wild-type background indicating that the effects in the phenotype observed in the CLN3 OE, are indeed CLN3-dependent.

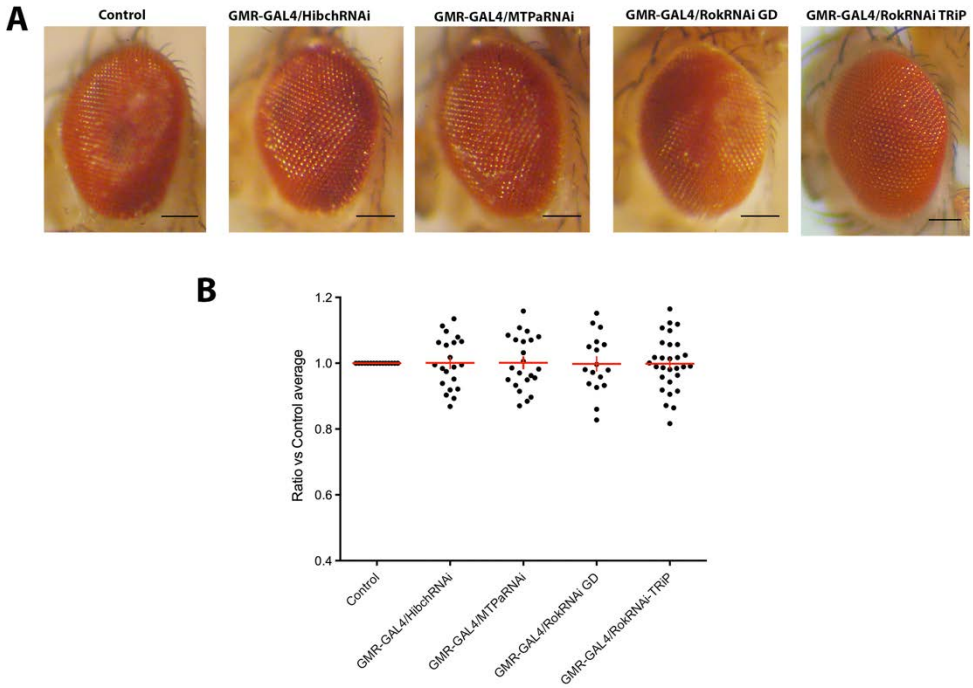

Fig. 5.14 Downregulation of candidates does not give any phenotype in the eye of a WT fly. **A**. Representative light microscope images of fruit fly eyes of control line, GMR-GAL4/UAS-CLN3, GMR-GAL4/HibchRNAi, GMR-GAL4/RNAiMTPα, GMR-GAL4/RokRNAi GD and GMR-GAL4/RokRNAi TRiP. **B**. Normalized quantification of the eye surface area of these genotypes showing no statistically significant change when compared to the control line. Scale bar=100um. Mean ± SEM (One-way ANOVA and Tukey's multiple comparison post-hoc analysis, N>20 flies per genotype.

5.3.2.3 Study of candidates identified in *Ppt1*$^{-/-}$ time-course analyses

As shown in the section above, the genetic and/or pharmacological screening using the CLN3 OE *Drosophila* eye system proved to be a robust system for the testing of modifiers when applied to candidates identified in our regional differential vulnerability -omic study (Chapter 3). Next, we proceeded to examine candidates identified in the much more complex -omic (spatio-temporal) study from Chapter 4. Candidates in Chapter 4 were identified based on their expression profile correlating to synaptic vulnerability between thalamus and cortex and throughout the time-course of disease progression. These candidates were divided into two subsets:

1. Those detected to be changed in the proteomic dataset (17 proteins); and

2; those predicted to be upstream regulators of the proteins in the dataset (13 proteins).

As explained in 5.2 Materials and methods, *DIOPT* tool was used to identify which *Drosophila* ortholog was more similar to the mouse protein candidates. Information about

Drosophila candidate lines purchased can be found in Table 5.2. ASAH1, S100A1, HEPACAM and HBA-A2 did not have high rank orthologs in *Drosophila* and therefore, were not tested in this experiment. For the rest of the candidates, RNAi lines were purchased except for downregulated candidates where overexpression lines were available.

We began by targeting proteins from subset 1. As shown before, misexpressed candidate lines were crossed to the recombinant fly (CLN3-OE background) and to *GMR-GAL4* driver (WT background). F1 CyO^{+} flies were then examined under the stereomicroscope, eyes were photographed and surface area was measured with *ImageJ*. Results indicated that 9 out of 11 lines tested, showed significant modifier effect in a CLN3-induced degenerative eye (Fig. 5.15A&B). Surprisingly, knocking down candidates that were upregulated at 3 months in thalamus (3-T) and 5 months in cortex (5-C) (Dbn1, Gnb4, Dpysl4, see Chapter 4 and Table 5.2), did not suppress the phenotype but enhanced it. Although knocking down Dpysl4 did not produced a significant effect in the eye surface area, there was an increased number of black puncta indicative of necrosis (highlighted by the white arrows in Fig. 5.15A). This suggests that the downregulation of Dpysl4 indeed has an effect on the CLN3-induced phenotype which is not detectable through eye surface area quantification, but it is visible through a qualitative examination. Conversely, knocking down Atp5b (which was downregulated at 3-T and 5-C, see Table 5.2), suppressed the CLN3-induced degenerative eye by 57.26% in size. Importantly, the compound structure of the eye was noticeably improved as well (Fig. 5.15A).

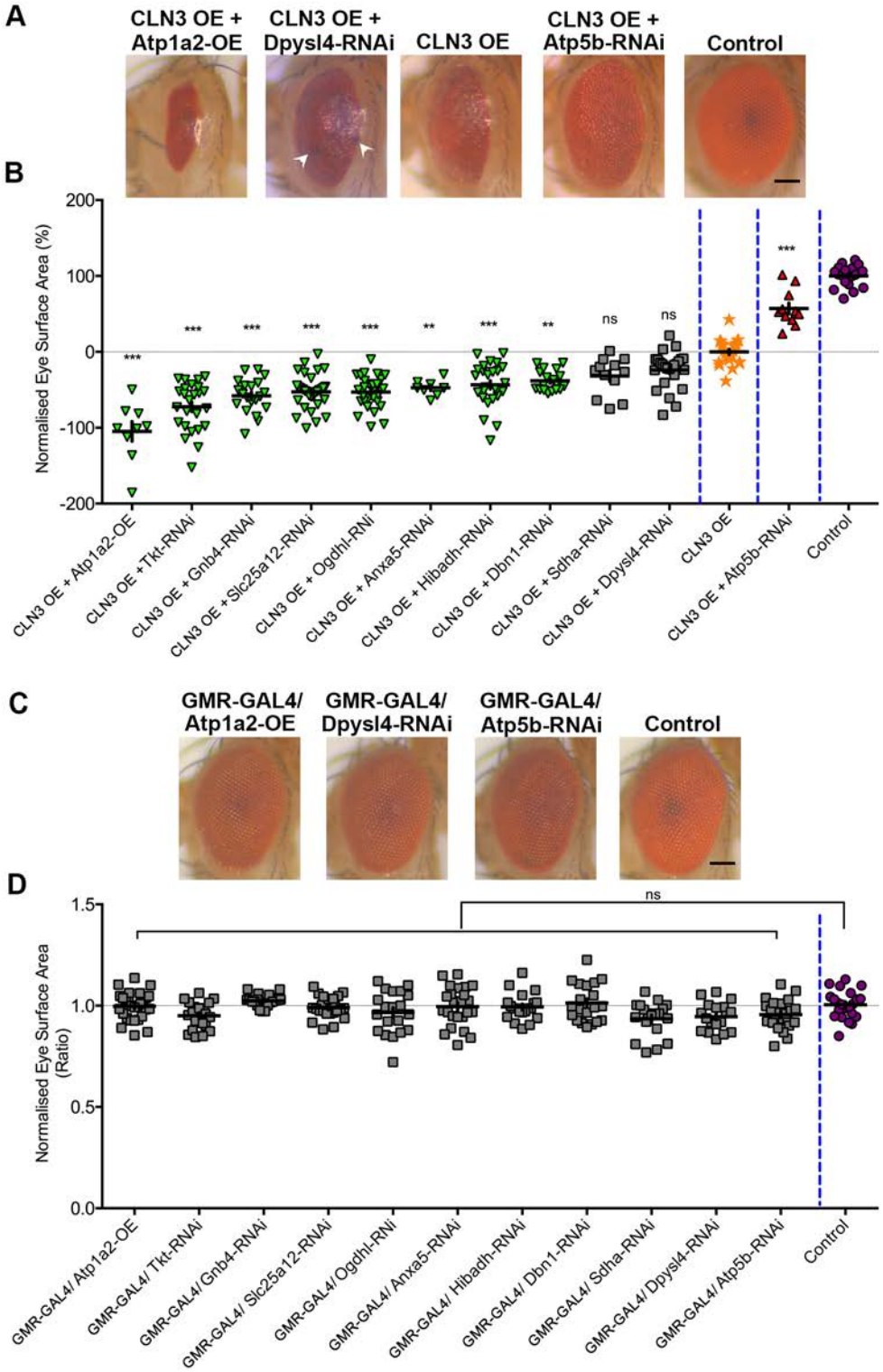

Fig. 5.15. Candidates identified in Ppt1$^{-/-}$ time-course dataset modulate eye morphology in CLN3-OE dependent manner. **A.** Representative light microscope images of *Drosophila* eyes of WT control (control, *GMR-GAL4;UAS-CLN3/+),* CLN3 OE control (CLN3 OE, *GMR-GAL4;UAS-CLN3*) and example candidates Atp1a2-OE (strongest enhancer), Dpysl4-RNAi (although eye size showed no difference to the CLN3 OE, there was a detected increased number of black puncta (white arrows), which indicate cell death) and Atp5b-RNAi (suppressor) in

CLN3-OE background. **B&D.** Dot plot quantification of the normalised eye surface area (%) of misexpressed candidates driven in the eye identified in Chapter 4 (subset 1) in CLN3-OE **(B**) and WT background (**D**). **C.** Representative light microscope images of *Drosophila* eyes of WT control (control, *GMR-GAL4/+*) and example candidates Atp1a2-OE, Dpysl4-RNAi and Atp5b-RNAi driven in the eye in a WT background. Mean ± SEM One-way ANOVA with Tukey's multiple comparison post-hoc analysis; ** p-value<0.01, *** p-value<0.001, ns p-value>0.05, N>15 flies per genotype.

In a manner similar to candidates from Chapter 3, the misexpression of these candidates on a wild-type background, did not cause any overt effect in the compound structure or size of the eye (Fig. 5.15C&D), indicating that the effects observed are again, CLN3-dependent.

Next, predicted upstream regulator candidates (subset 2) were targeted in both CLN3-OE and WT backgrounds. Ten out of twelve candidates again showed a range of effects in the CLN3-induced phenotype (Fig. 5.16A&B). The strongest enhancer was Pparg, which caused lethality at pupal stage. Similarly, to Dpysl4, Map4k4, did not show any effect to the surface area but showed necrosis (pointed out by the white arrows in Fig. 5.16A). Conversely, OE of InsR rescued the eye size until reaching equivalence to the control fly. However, compound eye structure still revealed the presence of fused ommatidium similar to the CLN3 OE fly and surface area showed an irregular elliptical shape.

In contrast to candidates tested from subset 1, some of the identified upstream regulators caused an effect in a WT background (Fig. 5.16C&D). Pparg overexpression caused lethality at pupal stage also in the WT fly. Surprisingly, Notch was shown to be lethal at pupal stages in a WT fly. However, as shown in Fig. 5.16A&B, although Notch was a very strong enhancer, it did not cause 100% lethality in CLN3-OE background. Interestingly, it has been reported that CLN3 inhibits Notch and that targeting delta protein, which is a ligand of Notch, enhances the CLN3 OE phenotype in the macrochaetae on the scutellum of the adult fly (Tuxworth *et al.*, 2009) (see 5.2 Introduction). Here we show that by knocking down Notch directly at the genetic level, also enhances the phenotype in the eye. However, at the same time, CLN3 OE seems to have a protective effect preventing lethality of Notch knock down effects. More experiments will be needed in order to clarify the regulatory effects seen when knocking down Notch in CLN3 OE or WT backgrounds.

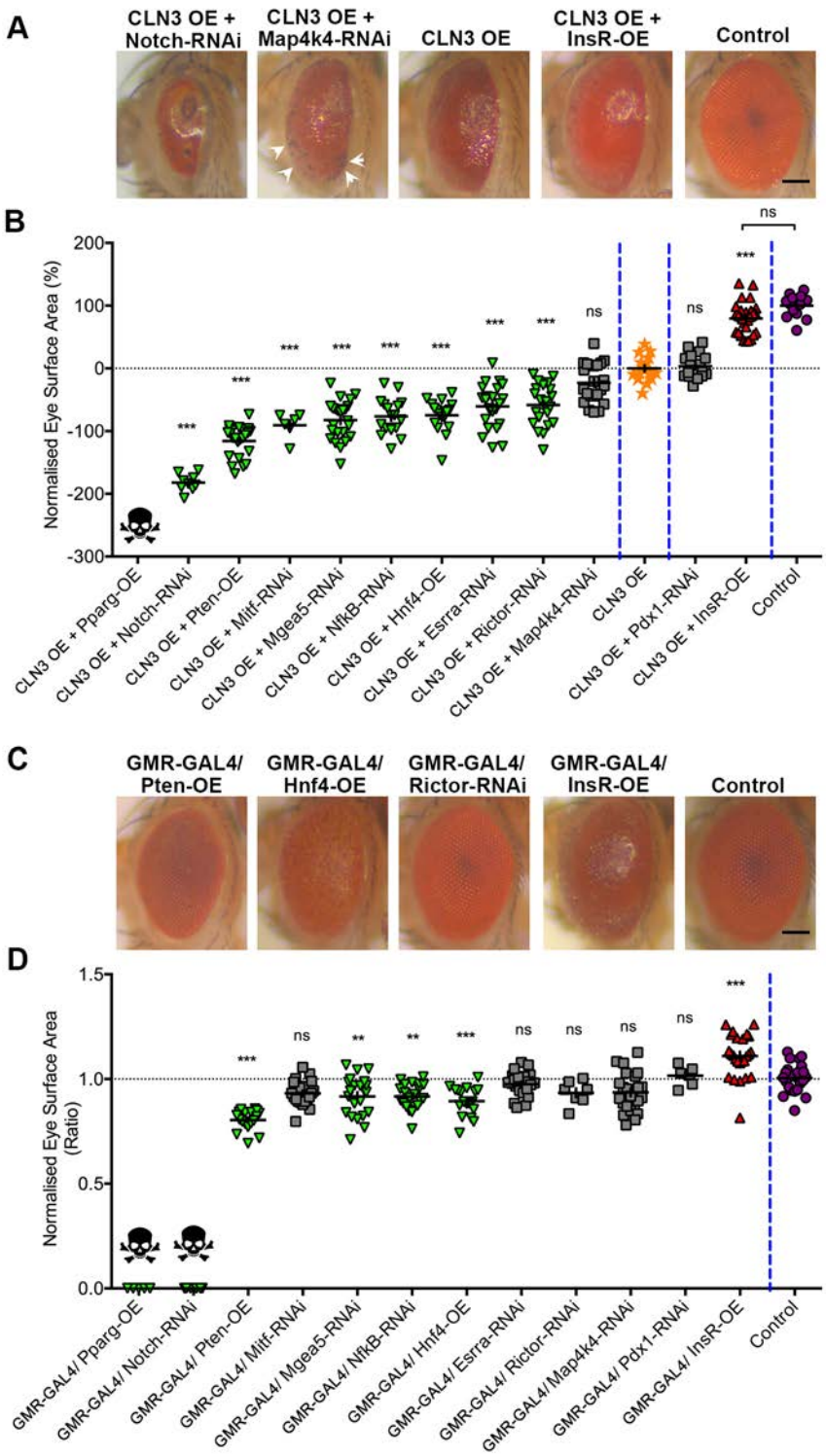

Fig. 5.16. Predicted upstream regulators modulate neurodegeneration in CLN3-OE and WT background. **A.** Representative light microscope images of *Drosophila* eyes of WT control (control, *GMR-GAL4;UAS-CLN3/+),* CLN3 OE control (CLN3 OE, *GMR-GAL4;UAS-CLN3*) and example candidates Notch-RNAi (strongest enhancer), Map4k4-RNAi (eye size showed no difference to CLN3 OE, however, there was detected an increasing number of black puncta-white arrows-, which indicate cell death) and InsR-OE (suppressor) in CLN3-OE background. **B&D.**

Dot plot quantification of the normalised eye surface area (%) of the upstream regulators driven in the eye identified in Chapter 4 in CLN3-OE **(B)** and WT background (**D**). **C.** Representative light microscope images of fruit fly eyes of WT control (control, *GMR-GAL4*/+) and example candidates Pten-OE, Hnf4-OE, Rictor-RNAi and InsR driven in the eye in a WT background. Mean ± SEM, One-way ANOVA with Tukey's multiple comparison post-hoc analysis; ** p-value<0.01, *** p-value<0.001, ns p-value>0.05, n>15 flies per genotype.

Other candidates such as Pten or Hnf4 also produced an effect in the *Drosophila* WT eye (Fig. 5.16C&D). OE of Pten under the control of *GMR-GAL4* resulted in a smaller eye, although the compound structure was not affected. In contrast, *Drosophila* overexpressing Hnf4, presented a small and rough eye with an abnormal bristle pattern and less fused ommatidia.

Interestingly, 12 out of 14 candidates whose expression was perturbed in proteomic analyses from Chapter 3 and Chapter 4 (subset 1) were identified as correlates with the vulnerability status of synapses, and were able to modulate neuronal stability in a CLN3-dependent manner. This was indicated by the absence of detectable phenotype when these candidates were misexpressed in a WT fly under the control of the same driver (*GMR-GAL4*). In contrast, most of the upstream regulators identified in Chapter 4, were also able to modulate neuronal stability in WT *Drosophila*, and therefore their effects were not CLN3 dependent. That is not that surprising, since these candidates were identified because they were potential master regulatory proteins impacting upon multiple cascades (see Chapter 4, Fig. 4.14). Thus, the effects of their misexpression is likely to regulate neuronal stability at a level upstream of CLN3 functional cascades.

Table 5.4. Summary of genetic modifier screen results

Mouse Gene Symbol	Mis-expression	Change in mouse proteomics**	Effect in CLN3-OE background		Effect in WT background	
			Enhancer/ Suppressor	Significance	Degeneration (Yes/No)	Significance
Anxa5	*RNAi*	Down	Enhancer	**	No	ns
Atp1a2	*OE*	Down	Enhancer	***	No	ns
Atp5b	*RNAi*	Down	Suppressor	***	No	ns
Dbn1	*RNAI*	Up	Enhancer	**	No	ns
Dpysl4/ Dpysl3	*RNAi*	Up	Enhancer	ns	No	ns
Esrra	*RNAi*	Down*	Enhancer	***	No	ns
Gnb4	*RNAi*	Up	Enhancer	***	No	ns
Hadha	*RNAi*	Down	Enhancer	***	No	ns
Hibadh	*RNAi*	Down	Enhancer	***	No	ns
Hibch	*RNAi*	Down	Enhancer	***	No	ns
Hnf4a	*OE*	Down*	Enhancer	***	Yes	***
Igf1r/ InsR	*OE*	Down*	Suppressor	***	Yes	***
Map4k4	*RNAi*	Up	Enhancer	ns	No	ns
Mgea5	*RNAi*	Up*	Enhancer	***	Yes	**
Mitf	*RNAi*	Down*	Enhancer	***	No	ns
Nfkb1	*RNAi*	Up*	Enhancer	***	Yes	**
Notch1	*RNAi*	Up*	Enhancer	***	Lethal	N/A
Ogdhl	*RNAi*	Down	Enhancer	***	No	ns
Pdx1	*RNAi*	Up*	No effect	ns	No	ns
Pparg	*OE*	Down*	Lethal	N/A	Lethal	N/A
Pten	*OE*	Down*	Enhancer	***	Yes	***
Rictor	*RNAi*	Up*	Enhancer	***	No	ns
Rock2	*RNAi GD*	Up	Suppressor	**	No	ns
Rock2	*RNAi TRiP*	Up	Suppressor	***	No	ns
Sdha	*RNAi*	Down	No effect	ns	No	ns
Slc25a12	*RNAi*	Down	Enhancer	***	No	ns
Tkt	*RNAi*	Down	Enhancer	***	No	ns

**Based on z-score prediction IPA tool*

***Based on KO/WT ratio from proteomic studies*

Significance was assessed with One-way ANOVA with Tukey's multiple comparison post-hoc analysis; ** p -value<0.01, *** p-value<0.001, ns p-value>0.05. in relation to CLN3 OE (neurodegenerative background) and Control WT (WT background).

5.4 Discussion

In this chapter, we evaluated multiple *Drosophila* body systems and CLN3 misexpression models for their potential as screening tools. Interestingly, we demonstrated that overexpression CLN3 at the synapse using three different neuronal drivers (a motor neuron, a pan-neuronal and post-synaptic driver) disrupts NMJ morphology affecting bouton number and size, as well as lethality of eclosed adult flies. Importantly, we replicated the degenerative-eye phenotype caused by CLN3 OE under the control of *GMR-GAL4* described by Tuxworth and colleagues (Tuxworth *et al.*, 2009). The generation of a *GMR-GAL4*; UAS-CLN3 fly allowed the screen of genetic modifiers of the CLN3-induced phenotype demonstrating that a subset of the identified candidates in Chapter 3&4 are indeed able to regulate CLN3 induced phenotype *in vivo*.

The* Drosophila *nervous system requires an optimal CLN3 dosage window for its stability

Importantly, our data is consistent with the previous reports suggesting that there is a CLN3 optimal dosage window for the proper stability of the nervous system and that either too much or too little of it disrupts neuronal homeostasis *in vivo* (Faller *et al.*, 2015, Tuxworth *et al.*, 2011, Tuxworth *et al.*, 2009). In this chapter, we detected a CLN3 dose-dependent effect under the control of all the neuronal drivers used for the characterisation of CLN3 OE phenotypes, supporting the previous statement regarding CLN3 optimal physiological dose. Furthermore, we know that in the human disease, CLN3 (and other NCL-related proteins) dose is crucial to the phenotype as heterozygous humans are not obviously affected. Dose is also crucial for the other monogenetic neurodegenerative diseases such TDP-43 linked ALS and frontotemporal dementia (FTD) where the mechanisms of the disease are not yet clearly defined as GOF or a LOF (Xu, 2012). Interestingly, in other monogenetic infantile neurological diseases such as Rett Syndrome a similar conundrum has been found. Rett syndrome is caused by the LOF of MeCP2 gene. However, when MeCP2 is overexpressed there are overlapping phenotypes including alterations in synaptic strength and number (Chao *et al.*, 2007), synaptic plasticity (Chahrour *et al.*, 2007, Collins *et al.*, 2004) and similar neurodevelopmental defects characterized by autism features, seizures, motor impairments, stereotyped behaviors, and intellectual disability (Chahrour *et al.*, 2007, Ramocki *et al.*, 2008). More recently it was reported that both GOF and LOF of MeCP2 cause very similar disfunction of hippocampal circuit (Lu *et al.*, 2016). This optimal dosage window, which

seems to be a common feature of some monogenetic neurodegenerative diseases, may give clues regarding the function of CLN3, which is still unclear.

Results of candidate genetic screen in* Drosophila *eye

In this chapter we demonstrated, that the unbiased identification of protein candidates based on their expression profile correlate to synaptic vulnerability throughout brain areas (Chapter 3) and/or disease progression (Chapter 4), is a robust approach for the identification of molecular modulators of neuronal stability. As summarized in Table 5.3, most of the candidates identified following such criteria, were indeed, able to modulate neuronal stability in a neurodegeneration context (CLN3 OE) in CLN3-dependent manner. Only a subset of the upstream regulators identified in the Ppt1 time-course analyses (Chapter 4) were demonstrated to be global regulators causing neurodegenerative phenotypes in a WT background under the control of the same driver (*GMR-GAL4*) (Fig. 5.17). Since candidates in subset 2 are known to be master regulators of complex mechanistic pathways, it is not surprising that their effects are shown to be global, as their misexpression is likely to impact a broad range of pathways. Such phenotypes in a WT background varied from candidate to candidate. For instance, some altered the size but the structure of the eye was less affected (Pten), whilst others altered both size and structure (Hnf4). It has been suggested that similar phenotypes between targeted genes may indicate higher enrichment of converging disrupted biological pathways (Oortveld *et al.*, 2013). Therefore, since most of the candidates tested were able to alter eye size in the CLN3 OE background, the misexpression of these candidates may be perturbing converging or overlapping pathways. In Fig. 5.18, published, known (direct and indirect) interactions between the candidates identified in Chapter 3&4 are highlighted, showing the complexity of these connections. It will take years of investigations to unravel such complex, potentially converging pathways and therefore, in this chapter I report on and discuss only a few corresponding pathways relevant to the potential candidate.

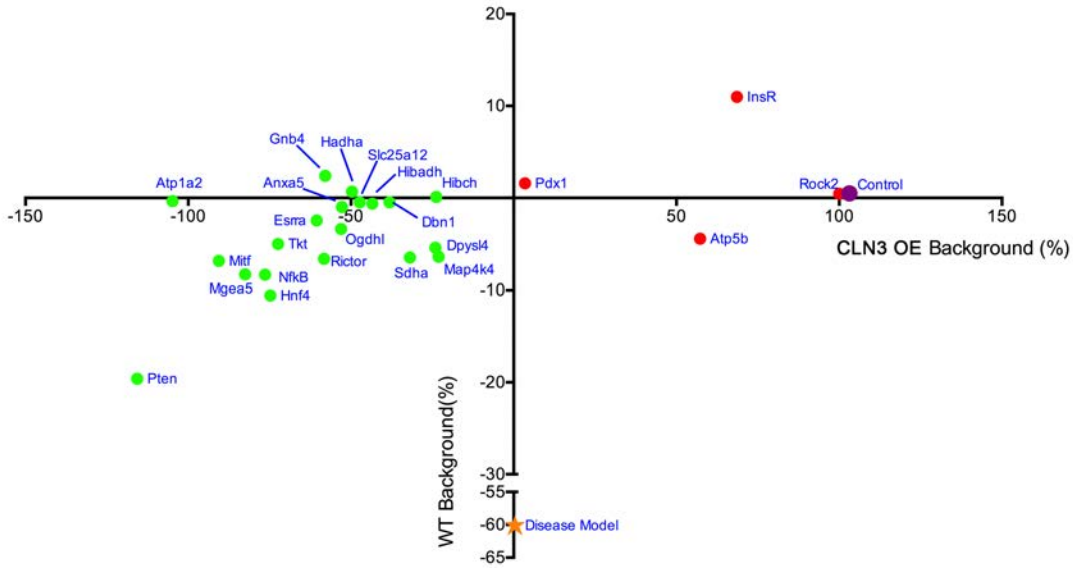

Fig. 5.17. Summary of candidate genetic screening in CLN3-induced degeneration in the eye. Two-axis plot expressing the correlation between eye size modification in CLN3 OE background (X axis) and WT background (Y axis) for all the candidates tested that were viable in both backgrounds tested. Each point represents the normalised eye size average of each candidate. Enhancers are coloured in green and suppressors in red, CLN3 OE in orange and control fly in purple. Pten was a candidate with strongest enhancing effects in CLN3 OE background and was also able to affect neuronal stability in WT background. Completely opposite to Pten, InR was shown to be a suppressor of the CLN3-derived eye and also increased eye size in WT background. Rock2 was the candidate which best rescued the CLN3-OE phenotype without affecting a WT fly. Most of the enhancers from subset 1, are very close to the x-axis which indicate no effects in WT *Drosophila* and therefore define them as CLN3-dependent modifiers.

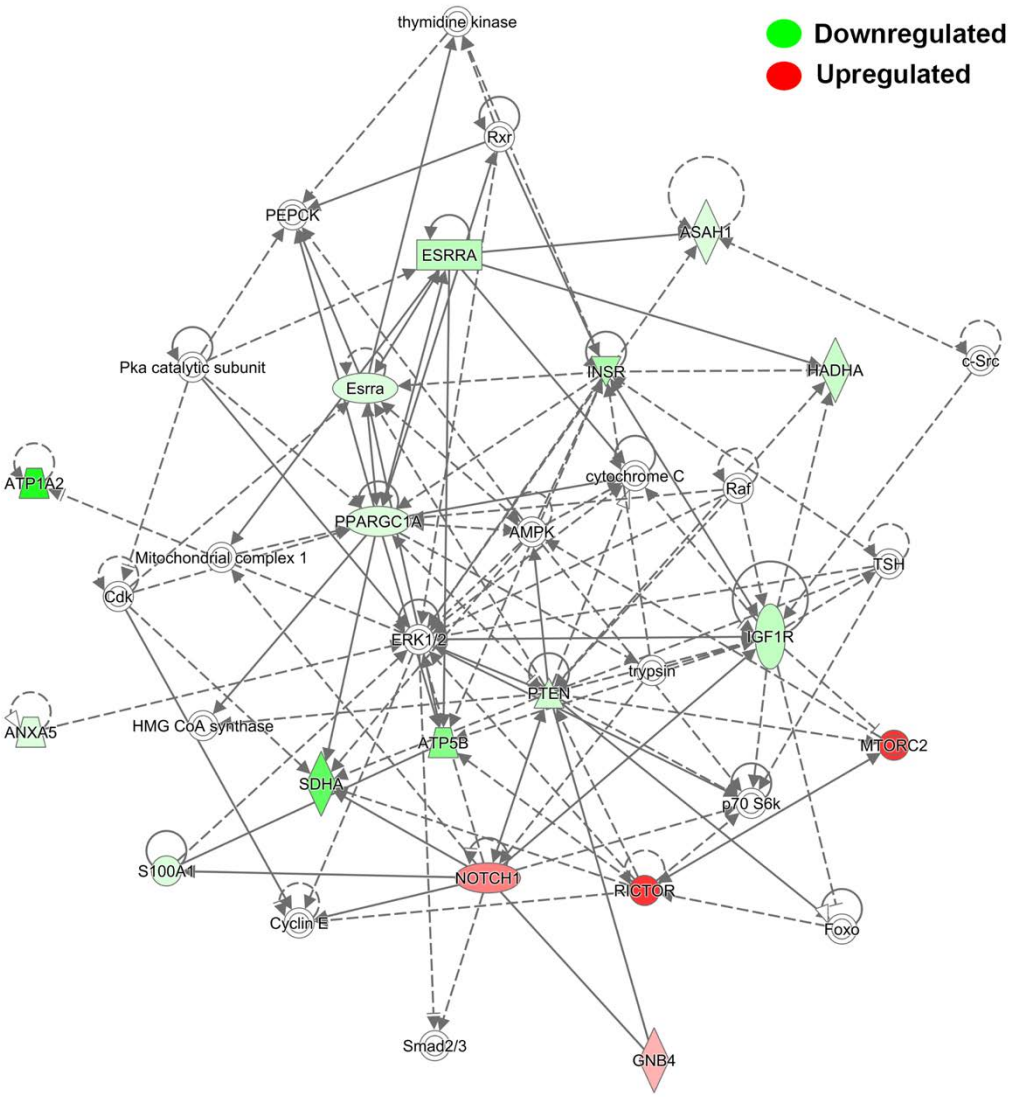

Fig. 5.18. Converging networks between candidates able to modulate neuronal stability in CLN3-induced neurodegeneration. The top network found using an *IPA* analysis of identified candidates. The network is involved in "Energy Production, Lipid Metabolism, Small Molecule Biochemistry" and incorporates 17 of the identified candidates. Upstream regulators were used as inputs in the analysis as either up/downregulated according to the *IPA* prediction tool. Dashed and solid lines indicate indirect and direct interactions respectively.

Valine degradation and ROCK2 signaling cascades

By influencing the valine catabolic cascade through genetic disruption of HIBCH and HADHA it was possible to alter the CLN3 degenerative phenotype in *Drosophila in vivo*. Moreover, the further upstream in the catabolic cascade we intervened, the greater the resulting effect on neurodegenerative phenotype. The valine catabolism cascade has remained enigmatic mainly because only a few defects in the pathway have been described

(Wanders *et al.*, 2012). In humans, both HIBCH and HADHA deficiency cause infantile onset diseases with neurological clinical scheme (Ferdinandusse *et al.*, 2013, Peters *et al.*, 2015, Stiles *et al.*, 2015). Crucially, this could indicate that perturbations in valine catabolic pathways might be a shared event across multiple neurodegenerative conditions and therefore targets identified here may be transferable to other diseases. Importantly, the role of branched-chain amino acids such as valine as a source of glutamate has recently been suggested (Yudkoff, 2017). Therefore, defects in valine metabolism defects may be impacting on glutamate pathways which can affect neurotransmission.

Interestingly, the upregulation of ROCK2 has been highlighted in a range of conditions by our laboratory and others (Wishart *et al.*, 2012, Deyts *et al.*, 2009, Herskowitz *et al.*, 2011, Blaise *et al.*, 2012). In this current study, I demonstrate for the first time that downregulation of ROCK2 also rescues the phenotype in a CLN3 model *in vivo,* when manipulated genetically, and to a lesser degree with available pharmacological agents (Fig. 5.12). Studies by others indicated that its genetic and/or pharmacological downregulation also ameliorated the phenotype of several conditions including SMA, another relatively early onset neurodegenerative disease (Bowerman *et al.*, 2012, Coque *et al.*, 2014). In general, ROCK2 appears to be an attractive target for the development of new therapeutic strategies, not only for NCL, but also in a wide range of more common neurodegenerative diseases to potentially delay or halt disease progression (see Chapter 4). There are currently multiple ROCK inhibitors with different degrees of specificity available (Anastassiadis *et al.*, 2011, Olson, 2008). However, in order to avoid off-target effects in future studies (see Fig. 5.13), it will be necessary to examine complex -omic derived interaction/cascade data to utilised a compound that targets ROCK2 more specifically (see Fig. 5.13).

Insulin-receptor signalling pathway and autophagy

Interestingly, overexpression of InR/Igf1r increased the size of eyes in both CLN3 OE and WT background. In neurodegeneration background (CLN3 OE) the rescue was noticeable only in size as the structure of the eye showed a similar glazing effect from fused ommatidia similar to the CLN3 OE. The insulin receptor signalling (IRS) pathway is very conserved from *Drosophila* to mammals (Yamaguchi *et al.*, 1995) and it has been extensively related in the regulation of cell growth (Brogiolo *et al.*, 2001, Gu *et al.*, 2014). Mutations in InR has been shown to affect nervous system development (Fernandez *et al.*, 1995, Dutriaux *et al.*,

2013), including synapse number and plasticity (Chiu *et al.*, 2008), neuronal pruning (Wong *et al.*, 2013) or axonal guidance of photoreceptors during visual system development (Song *et al.*, 2003). Insulin-related pathways alterations have been linked to a range of neurodegenerative diseases such as AD, HD or PD [reviewed in (Procaccini *et al.*, 2016)]. For instance, alterations in IGF1 signaling, contributed to progressive neuronal loss (Talbot *et al.*, 2012, Procaccini *et al.*, 2016) whereas the administration of insulin agonists (Bassil *et al.*, 2014), showed positive effects in models of neurodegeneration.
On the other hand, overexpression of Pten, which antagonizes InR signalling (Meléndez *et al.*, 2008), was shown to enhance the CLN3-derived phenotype but also had an effect in a WT eye, producing a decrease in eye surface area (Fig. 5.16). Therefore, the phenotypic effects observed using both InR-OE and PTEN-OE constructs, confirms that promoting the insulin-signaling pathway improves neuronal stability.

The IRS pathway has not been reported to be altered in the NCLs so far, however using IGF treatment as a neurotrophic factor, proved to partially restore interneuron number and brain hypertrophy in CLN8 mouse models (Cooper *et al.*, 1999). Since, in our data InR overexpression seemed to have an effect in both CLN3 OE and WT fly, it is unclear if there is an interaction between CLN3 and InR related pathyways. If CLN3 and the IRS pathway do interact, a possible connection could be autophagy. Autophagy has been a proposed neurodegenerative mechanism in CLN3 mouse models (Mitchison *et al.*, 2004), and Tuxworth *et al.* (Tuxworth *et al.*, 2009) already suggested that apoptosis was not a mechanism triggering cell death in the CLN3 OE *Drosophila* model. Therefore, since InR suppresses autophagy (Mohseni *et al.*, 2014), this negative regulation of autophagy by the InR-OE will be a plausible hypothesis by which InR-OE rescues the eye size in CLN3-degenerative eye.

Notch signaling pathway

Tuxworth *et al.* indicated that CLN3 blocks Notch signalling at the protein level (Tuxworth *et al.*, 2009) and that it may be mediating cell death in the CLN3 OE fly. Therefore, the enhancement of the phenotype when knocking down Notch was not surprising to find (Fig. 5.16). Paradoxically, knocking down notch caused 100% lethality of wild-type flies whereas it did not cause such high lethality in the CLN3 OE flies. A possible explanation for this, are the patterns of expression of the *GMR-GAL4* driver (Freeman, 1996). We know that *GMR-GAL4* had been recently found to be expressed also in embryo and larval stages CNS (Ray *et al.*,

2015), and therefore it might be driving CLN3-OE and Notch-RNAi in other organs during *Drosophila* development. Our results indicate that the downregulation of Notch without the presence of CLN3-OE (WT crosses) is lethal but not in the CLN3 OE fly. Therefore, CLN3-OE might be "protecting" the Notch-RNAi effects in embryo and larval tissues, suggesting that CLN3 may have different roles depending on the *Drosophila* stage/organ. Further experiments raising the flies at different temperatures only at specific developmental stages will be necessary in order to shed light on these intriguing results.

Nervertheless, our experiments clearly support the interaction between Notch and CLN3-related pathways leading to neurodegeneration, as previously reported (Tuxworth *et al.*, 2009). We show that by knocking down Notch genetically we are able to enhance the CLN3-OE-induced phenotype.

Knocking-down the ATP synthase subunit ß suppresses CLN3-OE--induced phenotype

An interesting suppressor found in this screen was the subunit ß of the ATP synthase (Atp5b), which forms the F1 (hydrophilic) portion of the complex V of the mitochondrial respiratory chain. Improvement of the eye surface area by almost 60% was accomplished by knocking down Atp5b expression via RNAi. Interestingly, the subunit C of the ATP synthase is the main storage protein which accumulates in most forms of NCL including CLN3, but not CLN1, CLN4 and CLN10 (Palmer *et al.*, 2013). Despite the efforts of the NCL research community, the mechanisms that explain why the subunit C accumulates in the lysosome in various forms of NCL is still to be clarified. Importantly, no other subunits have been found in the storage material composition, indicating that the subunit C may be following a specific turnover pathway (Fearnley *et al.*, 1990). Disregulation in ATP synthase activity has been reported in CLN3 and CLN2 patient fibroblasts (Das *et al.*, 1996), but also in CLN1 patients (Das *et al.*, 1999), indicating that these abnormalities are independent from the storage material composition of the different NCLs forms. More recently, other authors reported the interaction between Atp5b and Ppt1 protein (Lyly *et al.*, 2008, Scifo *et al.*, 2015). Interestingly, Lyly *et al.* showed that Ppt1-deficiency results in alterations in the amount of F1-ATP synthase on the plasma membrane, but not in mitochondria by immunohistochemistry studies (Lyly *et al.*, 2008). Recent reports are starting to highlight the extra-mitochondrial expression of F1-ATP in plasma membrane and lipid rafts where it may have unknown functions [reviewed in (Champagne *et al.*, 2006)]. Moreover, alterations were

also shown in Atp5b expression in whole thalamus extracts at symptomatic stages in *Ppt1*$^{\Delta ex4}$ mouse model by proteomic studies (Tikka *et al.*, 2016).

Altogether, our data is consistent with previous reports where abnormalities in ATP synthase, and more specifically, Atp5b is perturbed in CLN1 and CLN3 disease (Das *et al.*, 1996, Das *et al.*, 1999, Lyly *et al.*, 2008, Scifo *et al.*, 2015, Tikka *et al.*, 2016). However, it is not clear whether these abnormalities reside in the mitochondria and/or elsewhere (Lyly *et al.*, 2008). In our Ppt1 time-course proteomic study (Chapter 4), we showed that Atp5b was down at 3-T & 5-C and up in 5-T &7-C synapses indicating that it could be accumulating towards late stages of the disease. Knocking down Atp5b in *Drosophila* CLN3 OE model, partially rescues the CLN3-derived neurodegeneration of the external and internal structure of the eye. Thus, our *in vivo* results, suggests that a potential accumulation/upregulation of Atp5b may be contributing to the CLN3 degenerative phenotype.

Chapter 6

Proteomic profiling of peripherally accessible tissues identifies molecular pathology and putative biomarkers

6.1 Introduction

Investigations into the genetic underpinnings of the different NCL forms is leading to a growing number of gene repair and gene product replacement trials at the pre-clinical and clinical level including gene therapies and enzyme replacement trials respectively (Neverman *et al.*, 2015). Thus, methodologies for determining disease progression and the effectiveness of therapeutic intervention become critical in the clinical setting.

Behavioral and morphological markers are currently being developed and used in this context. For example, unified rating scales are currently being developed to quantify physical, behavioral and functional aspects for juvenile NCL (JNCL) (Adams *et al.*, 2006, Marshall *et al.*, 2005, Ragbeer *et al.*, 2016, Kwon *et al.*, 2011). Additionally, quantitative MR diffusion-weighted imaging has also been used to assess disease severity in late infantile NCL (LINCL) (Dyke *et al.*, 2007). Although these studies are contributing to the evaluation of neurological form and function in patients, the development of standardized scales are necessary for all the NCL forms. However, such behavioral scales may be subjective, not prove sensitive enough, be impractical at advanced stages of disease or fail to provide

sufficient information reflecting very subtle pathological alterations. Thus, an ideal biomarker would be a detectable objectively quantifiable molecular factor – alterations in which correlate to disease progression in a trackable and predictable manner for a specific form(s) of NCL (Biomarkers Definition Working Group, 2001) irrespective of a patients ability to perform behavioural tasks.

NCL pathology in extra-neuronal tissues in patients have been extensively characterized and proved to be valuable for diagnostic purposes, which include blood, skin and muscle samples (Goebel *et al.*, 1975, Rapola *et al.*, 1973, Licchetta *et al.*, 2015, Jadav *et al.*, 2014, Anderson *et al.*, 2013, Hersheson *et al.*, 2014). Therefore, we can also foresee molecular perturbances in such peripherally accessible tissues. Some studies in the NCLs have attempted to identify molecular biomarkers in cerebrospinal fluid (CSF) (Kay *et al.*, 2009). CSF can be a source of detectable molecular alterations likely to be a consequence of the ongoing neurodegeneration in the brain. However, sampling CSF is a very invasive method and can be very stressful, especially to small infants. Additionally, quantification of such factors from CSF is complicated by high levels of albumin. Other researchers have conducted preliminary examinations on more accessible tissues such as blood fractions including plasma (Hersrud *et al.*, 2016) and lymphocytes (Lebrun *et al.*, 2011) demonstrating that it is possible to find potential biomarkers in such tissues. Nonetheless, none of the studies to date have provided a correlation between potential biomarker expression data and the time-course of NCL disease progression.

We and others have demonstrated that perturbations in ubiquitously expressed genes resulting in a disorder with a predominantly neurological presentation (such as the NCLs or Spinal Muscular Atrophy (SMA), also result in molecular pathology which is detectable in non-neuronal tissues (Hersrud *et al.*, 2016, Lebrun *et al.*, 2011, Kielar *et al.*, 2009, Mutsaers *et al.*, 2013). Multiple platforms can be used for the discovery of molecular biomarkers including genomics, transcriptomics or metabolomics. However, most biomarkers used in clinical trials have their origin in proteomic studies due to the fact that most developed drugs target proteins (Guest *et al.*, 2013, Overington *et al.*, 2006). In fact, applying proteomic techniques in an unbiased manner to the analysis of muscle, our laboratory has previously identified novel protein-based biomarkers which track with disease progression, and report on therapeutic efficacy in SMA (Mutsaers *et al.*, 2013). Due to the disease causing mutation being expressed systemically, more extensive potential biomarker lists which are derived

from analysis of tissue samples with a complex molecular composition such as muscle as a starting point can then be scaled down into less complex but more easily accessible samples such as skin and blood (Mutsaers *et al.*, 2013)

Studies by our laboratory have previously detected perturbations in protein expression in muscle extracts at early time-points of disease progression in the *Ppt1*$^{-/-}$ mouse model using quantitative western blotting techniques (QWB) (Kielar *et al.*, 2009). Therefore, we are confident that by applying similar proteomic approaches as those used with brain derived isolates in Chapters 3 and 4, to peripherally accessible tissue such as muscle, we can identify multiple differentially expressed proteins, which after adequate filtering and processing could represent putative biomarkers for disease progression in the NCLs.

Thus, in this study we begin by confirming that molecular pathology is detectable even at early time-points preceding morphological alterations in *Cln3*$^{-/-}$mice. Interestingly, we show that the molecular signature identified in muscle may also report on perturbations in the CNS including specific canonical cascades. These pathways included mitochondrial function and ubiquitin proteasome system regulation which are detectable in both infantile and juvenile NCL patient samples. Secondly, label free proteomics throughout the time-course of disease progression in *Ppt1*$^{-/-}$ murine samples, followed by a complex filtering strategy, identified a list of 40 putative biomarkers whose expression correlates with disease progression in *Ppt1*$^{-/-}$. Additionally, a subset of these candidates also correlated with equivalent disease staging in *Cln3*$^{-/-}$and therefore could represent potential biomarkers for both infantile and juvenile NCL. Finally, I demonstrate that specific candidates identified in muscle (i.e. Ndufs3), report the same molecular trends at the same time-points in blood and are changed in NCL patients samples as predicted by murine time-course expression profiling.

6.2 Materials and methods

6.2.1 Animals and tissue harvesting

Hind limb muscle tissues from six *Cln3*$^{-/-}$ mice at 13 months and four *Ppt1*$^{-/-}$ at 1, 3, 5 and 7 months with each corresponding C57BL/6 age-matched control mice were dissected by Dr. Thomas Wishart and used for iTRAQ and label-free proteomics respectively (See Chapter 2. General materials and methods). Blood from four *Ppt1*$^{-/-}$ and C57BL/6 age-matched control at 3 and 7 months was collected by Dr Hemanth Navelgal from Prof. Jonathan Cooper's laboratory (KCL) and sent to the Roslin Institute for its processing. For QWB, *Cln3*$^{-/-}$ muscle extracts at 13 months and *Ppt1*$^{-/-}$ muscle and blood were used at 3, and 7 months.

Human cortical *post mortem* samples were used to examine the relevance of specific protein candidates to the human disease by QWB. Please refer to General materials and methods (Chapter 2) for more details.

6.2.2 Synaptosome preparation

Post mortem human patient and control frozen cortex were processed for synaptosome production as previously described (Wishart *et al.*, 2007, Wishart *et al.*, 2012). Please refer to General materials and methods (Chapter 2) for more details.

6.2.3 Protein extraction

For iTRAQ proteomics: Cln3$^{-/-}$ and WT controls hind limb muscles were homogenised in 4 volumes (w/v) of 6M Urea, 2M thiourea, 2% CHAPS, 0.5% SDS and 5% protease inhibitor cocktail (Roche) using a pellet pestle (50 strokes with the pestle, left on ice for 10mins, followed by another 50 strokes with the pestle). The extracts were sonicated briefly and left on ice for 10 minutes, followed by centrifugation at 13,000 x g for 10 minutes at 4°C to pellet any insoluble material. For mass spectrometry analysis, an aliquot of extracted proteins from each mouse (n=6) and each brain region was pooled and precipitated in 6 volumes of ice cold acetone overnight at -20°C. The remaining extracts were stored (un-pooled) at -80°C for quantitative Western blotting validation. The acetone precipitates were pelleted by centrifugation at 13,000 x g for 10 minutes at 4°C and the supernatant was carefully remove and discarded. The pellets were resuspended in 6M Urea in 50mM TEAB. The protein concentration in each sample was determined using a Bradford protein assay.

For label-free proteomics: a section from forelimb muscle (predominantly gastroctemius) from 4 *Ppt1*$^{-/-}$ and 4 WT controls at 1, 3, 5 and 7 months were cut. Each corresponding genotype and time-point were pooled and masserated using a pestle and morter in SDT lysis buffer containing 100 mM Tris-HCl (pH 7.6), 4% (W/V). Please refer to General materials and methods (Chapter 2) for more details.

For QWB: a section from hind limb muscle from 4 *Cln3*$^{-/-}$, 4 *Ppt1*$^{-/-}$ mice and corresponding WT controls (4 for each) were homogenized individually in RIPA buffer and 1% protease inhibitor cocktail (Roche) using the Gentle Macs dissociator (Miltenyl Biotech Inc) and M tubes (Miltenyl Biotech Inc 130-093-236).
Human patient and control brain homogenates and synaptosome fractions were homogenized in a solution containing 100mM Tris-HCl, 4% (w/v) SDS and 1% protease inhibitor cocktail (Roche). Please refer to General materials and methods (Chapter 2) for more details.

6.2.4 iTRAQ Proteomic processing

Cln3$^{-/-}$ and WT controls muscle extracts were processed for iTRAQ proteomics by Dr Heidi Fuller (Keele University). Please refer to General materials and methods (Chapter 2) for more details.

6.2.5 Label-free proteomic processing

Ppt1$^{-/-}$ and WT controls time-course muscle extracts (1, 3, 5 and 7 months) were processed for label-free proteomics by Abdel Atrih (Fingerprints proteomics facility, University of Dundee). Please refer to General materials and methods (Chapter 2) for more details.

6.2.6 Quantitative fluorescent western blotting (QWB)

15-60 μg of protein loaded for western blotting examination. Please refer to General materials and methods (Chapter 2) for more details.

6.2.7 *In silico* proteomic analysis

6.2.7.1 *Ingenuity Pathway analysis (IPA)*

IPA application (Ingenuity Systems) was used to obtain further insight into potential cellular pathways that may be perturbed in the iTRAQ proteomics data in *Cln3*$^{-/-}$ compared to control mice. Please refer to General materials and methods (Chapter 2) for more details.

6.2.7.2 *Progenesis*

Label-free proteomic raw data was imported into *Progenesis LCMS* for differential analysis and identification of peptides followed by quantification of relative ion abundance of peptides and corresponding proteins. Samples were processed similarly to section 4.2.6.1 in Chapter 4. Only features contained between 8.84-93 min retention times with a limit of 5 ion charges were considered in the analyses. For this analyses we applied all the standard peptide filters except fold change filter that was not applied. Muscle is supposed to not be severely affected at early stage of the disease and potential biomarkers might not be differentially expressed in th early time-points. Please refer to General materials and methods (Chapter 2) for more details.

6.2.7.3 *BioLayout Express*

BioLayout software was used firstly, to analyse *Ppt1*$^{-/-}$ and WT time-course proteomic samples to examine the similarity between sample groups. Data was clustered by sample type and each sphere represents an individual sample and the closer they are, the more similar the samples are (Fig. 6.4B). Secondly, *BioLayout* was also used for clustering by co-expressed proteins in order to correlate their expression profile to the progression of the disease. In this display each sphere represents an individual protein and its colour and proximity to its neighbour indicates the similarity in protein expression (Fig. 6.5A&B). Please refer to General material and methods (Chapter 2) for more details.

6.2.8 Data analysis and figure production

Please refer to General materials and methods (Chapter 2) for more details.

6.3 Results

6.3.1 iTRAQ proteomics identifies molecular pathology at early stages of *Cln3*$^{-/-}$ mice

To confirm that the causative mutation is affecting the molecular constituents of peripherally accessible tissue samples, we examined the proteome of limb muscle extracts of the *Cln3*$^{-/-}$ murine model of JNCL (relative to littermate controls) at 13 months old.

Using iTRAQ proteomics a total of 598 individual proteins were identified. After filtering of proteins which were identified by less than 2 peptides and those whose expression differed from controls by less than 20%, 106 proteins remained for further analyses (Fig. 6.1A, Appendix I- Table A9) (Wishart *et al.*, 2007, Wishart *et al.*, 2012). Distribution of filtered proteins can be seen in Fig. 6.1A&B.

Quantitative fluorescent western blotting (QWB) was used for the validation of the proteomic data confirming that proteins such Ndufs3, P4hb and Anxa5 (examples of sub-threshold upregulation, upregulation and downregulation respectively) followed the same trends indicated by the proteomic analysis (Fig. 6.1C&D). After determining the veracity of the proteomic data and finding that so many proteins were indeed differentially expressed in muscle tissue, we sought to determine if any specific pathways or processes are perturbed. This was assessed with *Ingenuity Pathway Analysis (IPA)* software (see methods).

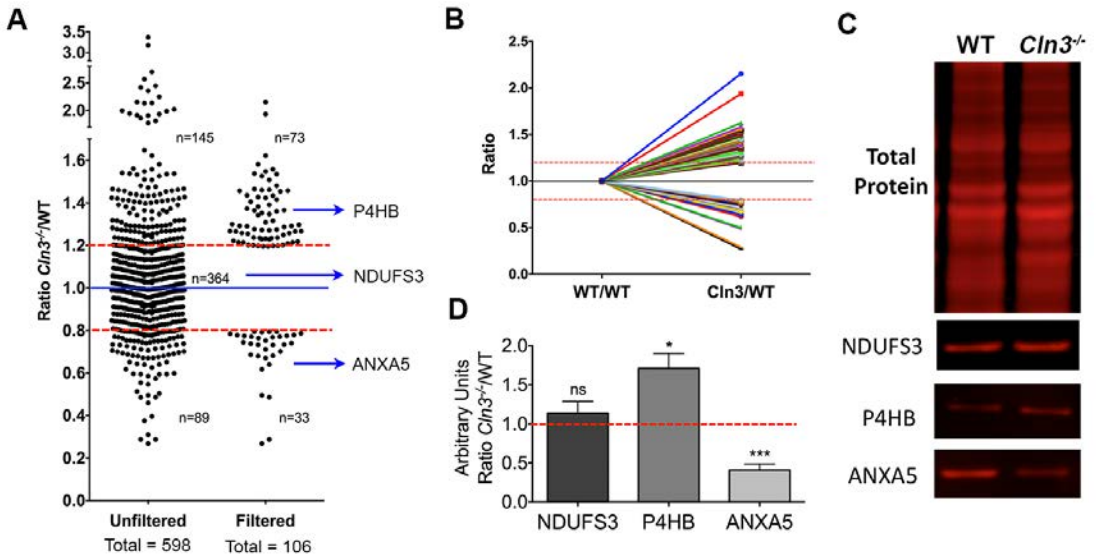

***Fig. 6.1. iTRAQ proteomics identified perturbations in muscle proteome from* Cln3$^{-/-}$ *mice compared to controls at 13 months.* A.** Scatterplot representing the unfiltered (LHS) and filtered

(RHS) identified proteins (>1.2 Fold-Change, identified by ≥2 peptides). **B.** Representation of filtered proteins showing 60 upegulated and 31 downreguated proteins. **C.** QWB representative bands of total protein instant blue staining, NDUFS3, P4HB and ANXA5 validating the iTRAQ proteomics. **D.** Corresponding quantification of arbitrary fluorescent unit ratio of NDUFS3, P4HB and ANXA5. Mean ± SEM; * p -value<0.05, *** p-value<0.001, ns p-value>0.05 (Student T test, n=3-4 mice per genotype).

IPA highlighted that the pathways which are likely to be the most affected by the alterations identified at this point are related to metabolic cascades associated with mitochondria such as "oxidative phosphorylation" and "TCA cycle". This is perhaps unsurprising given the role of the causative mutation being examined here. Interestingly, other pathways related to cell-junction and axonal guidance signaling were also altered suggesting either a potential perturbation in neuromuscular constituents or general machinery associated with neuronal formation and maintenance (Fig. 6.2A). Mitochondrial components have the potential to be useful biomarkers because of their presence in multiple cell types and the responsive nature of their biochemistry in relation the local envrironment (Raefsky *et al.*, 2017, Chen *et al.*, 2007) (Krasnianski *et al.*, 2005). Furthermore, mitochondrial dysfunction has been related to the pathogenesis of the NCLs as well as in other lysosomal storage disorders (de la Mata *et al.*, 2016) (Plotegher *et al.*, 2017). In the *Cln3*$^{-/-}$ murine muscle proteome, specific upregulation of enzymes within complexes I & II of the mitochondria respiratory chain were identified, along with a decrease in complexes IV and V. This indicates, that this is likely a mitochondrial intrinsic response rather than an error in sample processing (Fig. 6.2B). Moreover, the data suggests a predicted activation of cascades leading to the synthesis and metabolism of reactive oxygen species (ROS), in this case regulated by PPARG, which is associated with lysosomal biogenesis (Song *et al.*, 2011) (Fig. 6.2C&D).

Here we confirm that individual differentially expressed proteins can be detected in the muscle proteome even at early disease stages in *Cln3*$^{-/-}$ mice. This analysis also demonstrates that perturbations in mitochondrial pathways and processes are highly represented in these peripheral samples suggesting mitochondrial proteins may be a potential source of molecular biomarkers for NCL.

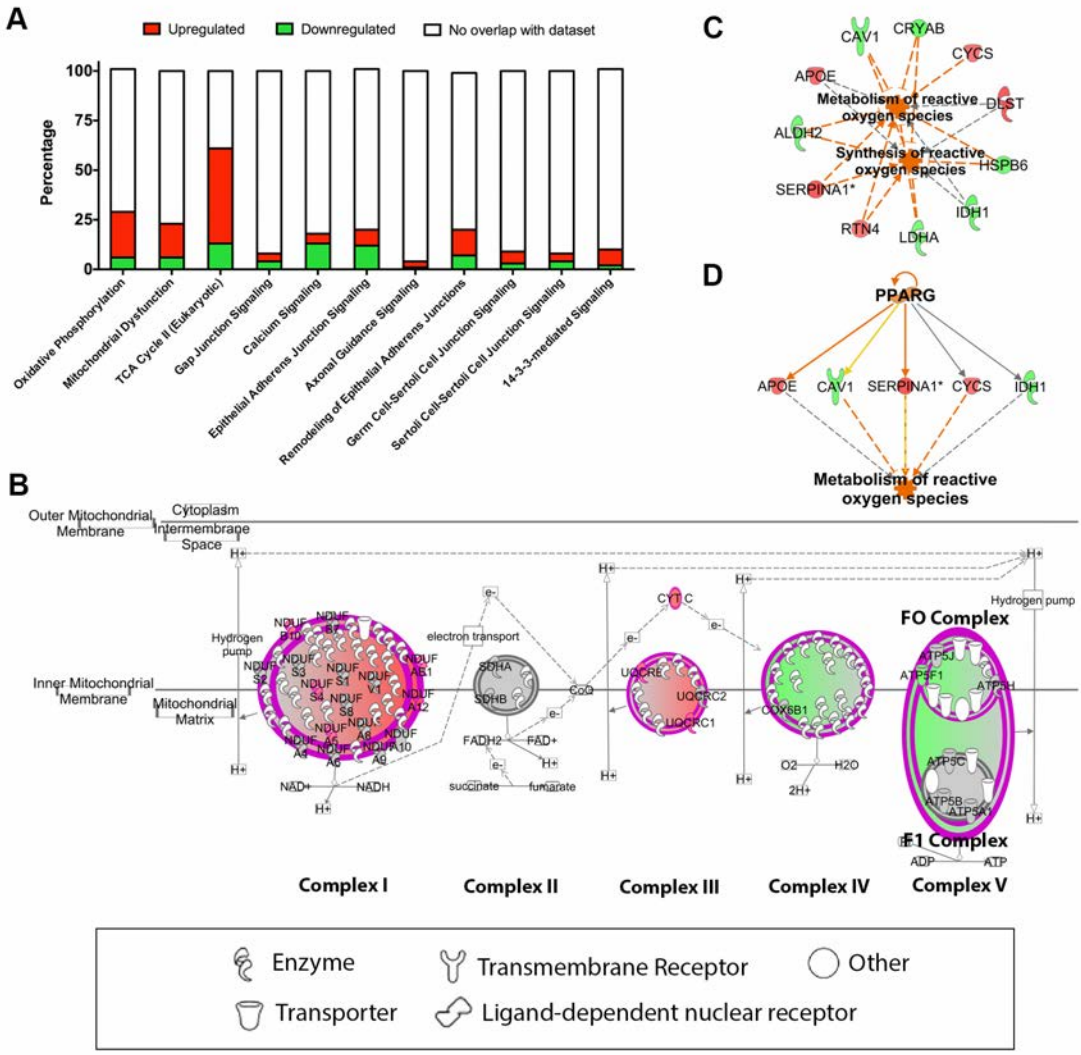

Fig. 6.2. IPA analysis reveals alterations in mitochondria-related pathways. **A.** Canonical pathway bar chart representing the most significant pathways linked to the *Cln3*$^{-/-}$ differentially expressed proteins identified by iTRAQ proteomics. **B.** Oxidative phosphorylation pathway representation showing the upregulation of enzymatic complexes I and II and the downregulation of complexes IV and V within the respiratory chain. **C.** *IPA* predicts the activation of the metabolism and synthesis of reactive oxygen species (ROS). **D.** PPARG is upstream of the proteins involved in the metabolism of ROS and it is predicted to be activated by *IPA*. Nodes in red, green, grey and white represent upregulated, downregulated, changed less than 20% and proteins not present in the analysed dataset respectively. Nodes in orange represent activation of predicted functions/molecules related to the proteins input in the analyses.

6.3.2 Proteomic analyses of *Cln3*$^{-/-}$ mouse muscle correctly predicts disruption of ubiquitination-related pathway perturbations in patient post mortem brain

Given that the disease causing protein is expressed in all tissues, it is likely that a subset of its potential of the resulting downstream cascades will be affected in many sample types. As this disease presents primarily as a neurological condition, we used *IPA* to determine if the 106 filtered detectable molecular perturbations in muscle isolates would cluster under any known neuronal designations. Interestingly, of the five "disease and disorder" top clusters identified by *IPA*, three have clear neuronal associations (Table 6.1). These included "neurological disease" (the most significant), psychological disorders and skeletal and muscular disorders. This suggests that (as suspected) many of the protein pathways downstream of Cln3 loss, whose manipulation results in a disease with a predominantly neurological presentation, are likely to be perturbed in other neurological conditions. Thus, these proteins also reside in other tissues such as muscle, but may have subtly different functional consequences in alternative biological systems (Table 6.1).

Table 6.1. Top Diseases and Disorders identified using IPA in* Cln3$^{-/-}$ *muscle extracts

Name	p-value	#Molecules
Neurological Disease	2.99E-03 - 1.26E-19	58
Organismal Injury and Abnormalities	3.09E-03 - 5.62E-18	90
Psychological Disorders	2.99E-03 - 5.62E-18	47
Skeletal and Muscular Disorders	2.99E-03 - 3.37E-15	56
Hereditary Disorder	2.99E-03 - 3.92E-15	51

Having determined that alterations reported in the literature as being primarily neuronal in association, are being detected in pre-symptomatic muscle, we next sought to assess if this data could be used to identify/predict biologically relevant alterations in brain samples from human patients. A closer examination of the *IPA* based clustering shows a predicted perturbation of ubiquitin as a potential master regulator of multiple alterations identified in the *Cln3*$^{-/-}$ muscle proteome (Fig. 6.3A). These candidates, which include mitochondrial proteins such as SOD1 and CS, are linked to ubiquitin through multiple molecular intermediate regulators. Some of these intermediate proteins, have previously been reported in relation to models of altered neuronal stability/vulnerability (i.e. Wlds) such as PTTG1 and SIRT (Gillingwater *et al.*, 2006) (Fig. 6.3A). Ubiquitin homeostasis has been associated in

the literature with adult-onset neurodegenerative diseases such as Alzheimer's, Parkinson's and Huntington's diseases (Zheng *et al.*, 2016). Interestingly, the disruption of ubiquitination pathways has also been implicated in other childhood neurodegenerative diseases (with a ubiquitously expressed causative monogenetic mutation) such as spinal muscular atrophy (SMA) (Wishart *et al.*, 2014) .In the case of SMA, studies targeting elements of the ubiquitin proteasome system were able to rescue the neuromuscular system (Wishart *et al.*, 2014) and provide systemic beneficial effects in animal models (Powis *et al.*, 2016). Perturbations in the UPS have also been reported in animal models of NCLs (Cao *et al.*, 2006, McCue *et al.*, 2015) and in a human subtype of infantile onset NCL caused by mutations in the *KCTD7* gene (Staropoli *et al.*, 2012).

In order to confirm that the identification of ubiquitin alteration was accurate as a predicted cascade in muscle, we began by showing with QWB that mono-ubiquitin was indeed downregulated in the *Cln3*$^{-/-}$ murine muscle extracts (Fig. 6.3B). To determine if the muscle proteome could be used to report on/or predict molecular pathology in human disease relevant tissue samples, we proceeded to examine different components of the UPS pathway by QWB in *post mortem* cortical extracts from JNCL and INCL patients. An antibody directed against ubiquitin protein was used for the detection of the different ubiquitin forms (Fig. 6.3C-F). As in the *Cln3*$^{-/-}$ mice, monomeric ubiquitin (mono-ubiquitin) was detected to be downregulated in both INCL and JNCL patients. However, an upregulation of tri – and multimeric ubiquitin (poli-ubiquitin) was also detected, suggesting a deregulation in ubiquitin homeostasis. To address this, we asked if other elements of the UPS are also altered. QWB of UchL1 and Uba1 showed differential expression in both juvenile and infantile patient samples (Fig. 6.3G-H), indicating disruption of the UPS pathway at end stage of disease in both INCL and JNCL. Interestingly, Uba1 and UchL1 alterations were also seen in SMA mouse models, although not to the same magnitude, which could be a consequence of the differential time-course and regional specific severity of each condition (Wishart *et al.*, 2014).

Thus we confirm that by examining molecular pathology in muscle samples we are able to predict pathway disruption in disease relevant *post mortem* human neural NCL tissue from infantile and juvenile pateints. Muscle may therefore be a source of potential molecular biomarkers for two of the most common NCL forms.

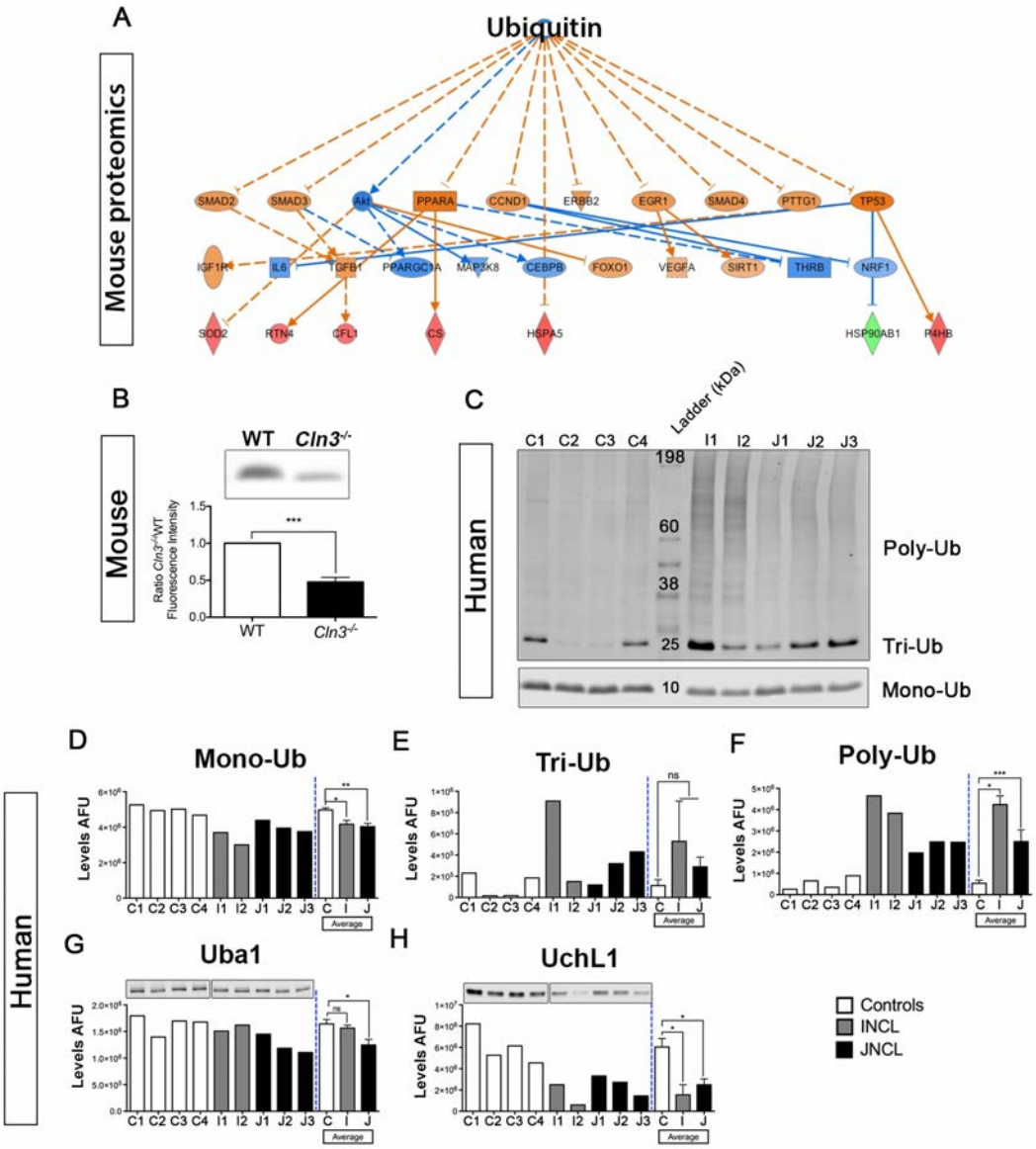

***Fig. 6.3.* Cln3$^{-/-}$ *mice muscle proteomics predicts perturbations in ubiquitin homeostasis confirmed by QWB in* post mortem *cortical extracts from INCL and JNCL patients.* A. Murine proteomics:** Mono-ubiquitin (Ubiquitin) is upstream some of the differentially expressed proteins in the *Cln3*$^{-/-}$ muscle proteome and it is predicted by IPA to be inhibited. Nodes in red, green, grey and white represent upregulated, downregulated, changed less than 20% and proteins not present in the analysed dataset, respectively. Nodes in orange and blue represent activation and inhibition respectively of predicted functions/molecules related to the proteins input in the analyses. **B. Murine muscle protein:** QWB representative bands and quantification bar chart of fluorescent intensity ratio of *Cln3*$^{-/-}$ vs. WT mice confirming the downregulation on ubiquitin predicted by *IPA*. **C-H. Human post mortem brain protein: C-F.** Poly-ubiquitin (Poly-Ub), Tri-ubiquitin (Tri-Ub) and mono-ubiquitin (Mono-Ub) representative bands of Controls (C), INCL (I) and JNCL (J) patient cortical samples and corresponding quantification bar chart of their arbitrary fluorescent units (AFU). Mono-ub was shown to be downregulated in both INCL and JNCL with respect controls whereas Tri and poli-ub showed to be upregulated. **G&H**. Fluorescence quantification bar chart and corresponding QWB bands of proteins acting in the

ubiquitin-proteasome system such as Uba1 and UchL1 showing a trend towards downregulation in both INCL and JNCL samples. Mean ± SEM; * p-value<0.05, ** p -value<0.01, *** p-value<0.001, ns p-value>0.05 (Student T test, Controls n=4, INCL n=2, JNCL n=3).

6.3.3 Label-free proteomics throughout the whole time-couse of disease identifies proteins whose expression profile correlates with progression

Having demonstrated (with iTRAQ proteomics of the *Cln3*$^{-/-}$ disease model) that muscle will likely prove to be a useful source of biomarkers, we next sought to identify and track molecular alterations taking place throughout the time-course of disease progression in a traceable and predictable manner (Biomarkers Definition Working Group, 2001).

However, the *Cln3*$^{-/-}$ model is not necessarily the most appropriate for this type of temporal investigation. Reasons for this include but are not limited to the time-course length (approximately 23 months) (Pontikis *et al.*, 2004) and increasing potential molecular noise through protracted systemic and chronic disease. Moreover, the morphological profiling of the the *Cln3*$^{-/-}$ model is not as detailed in the later time-points as other shorter lived models. *Ppt1*$^{-/-}$ murine models of Infantile (I)NCL and have a shorter lifespan only reaching 8-8.5 months of age (Gupta *et al.*, 2001) and have been characterised in more detail at the pathological level (Kielar *et al.*, 2007, Kielar *et al.*, 2009). We therefore carried out a proteomic analysis of limb muscle extracts from *Ppt1*$^{-/-}$ and WT control mice. Given the more manageable time-course of the disease and our characterization of the model according to the degree of neuronal alterations we identified four disease stages which from this point on will be referred to as pre-, early-, mid- and late symptomatic stages at 1, 3, 5 and 7 months of age respectively (Kielar *et al.*, 2007, Kielar *et al.*, 2009). For future reference the 3 month early-symptomatic disease stage in *Ppt1*$^{-/-}$ is equivalent to 13 months in the *Cln3*$^{-/-}$ model (Kielar *et al.*, 2009) and (Llavero Hurtado *et al.*, 2017) This type of temporal investigation also warrants a shift from iTRAQ to label-free proteomic techniques as it offers a higher protein coverage with less starting material (Craft *et al.*, 2013, Patel *et al.*, 2009, Bantscheff *et al.*, 2007), greater sample processing and data analysis flexibility without the need for multiple label incorporation (Xie *et al.*, 2011).

After protein extraction and label-free proteomic analysis, *Progenesis* software was used to process and analyse the raw proteomic data (see methods). A total of 985 proteins were identified. Standard filters were applied at the peptide (only p<0.05 and power>0.8) and

protein level (unique peptides >2) as previously described (Aghamaleky Sarvestany *et al.*, 2014) No fold-change filter was used at this level as we would expect to identify proteins which are not differentially expressed at all time points throughout the time course. After filtering, 427 proteins remain for further analysis. Principal component analysis (PCA) carried out in *Progenesis* illustrated a normal distribution of identified protein abundances with no clear outliers within each sample group (Fig. 6.4A). In order to further confirm the reproducibility of the proteomic replicates we used *BioLayout*. *BioLayout* is a complex pattern recognition software which can be used to cluster sample or proteins according to their molecular expression trend (Theocharidis *et al.*, 2009, Carpanini *et al.*, 2017, Enright *et al.*, 2002) (see methods). Confirming the PCA results, each replicate clustered together indicating consistency of the proteomic results (Fig. 6.4B).

As we presumed, multiple differentially expressed proteins were detected across the *Ppt1*$^{-/-}$ mice time-course when compared to WT control as shown in the heat-map in Fig. 6.4C. A higher number of upregulated proteins were detectable at early stages (1 & 3 months) with a shift towards the downregulation at end stage (5 & 7 months) (Fig. 6.4C&D).
However, the numbers shown only represent the proteins whose expression changes meet the filters at each time-point (Fig. 6.4D). Thus, in order to identify which of the 427 proteins were more likely to represent effective biomarkers, we next sought to track individual proteins throughout the time-course of disease progression in *Ppt1*$^{-/-}$ mice. To do so we turn again to *BioLayout* software, with the objective to identify proteins demonstrating a steady up or downregulation. Proteins showing a change of more than 20% at 7 months were input into *BioLayout* for molecular profiling clustering. A total of 40 individual proteins were clustered into specific up/downregulated clusters with a useful trend (Fig. 6.5, Table 2). Interesting examples of upregulated proteins are Cand2 and CtsD (Fig. 6.5C). CtsD shows no change at 1 month and progressively increases with disease progression until changing by more than 3 fold- by end-stage. Interesting examples of downregulated proteins are Ces1d and Clec3b. Ces1d is highly upregulated at 1 month (4.72 Fold-Change) but then quickly declines in abundance with disease progression. So in addition to correlating with neurodegenerative progression in the brain, Ces1d expression may also represent a useful biomarker for the early detection of infantile NCL.

Here we demonstrate that we are able to track individual proteins throughout the time-course of disease progression of NCL by combining label-free proteomic analysis with a

bioinformatic molecular profiling. We identify a list of 40 proteins whose changes track with the time course of disease progression in *Ppt1*$^{-/-}$ mice (Kielar *et al.*, 2009, Kielar *et al.*, 2007).

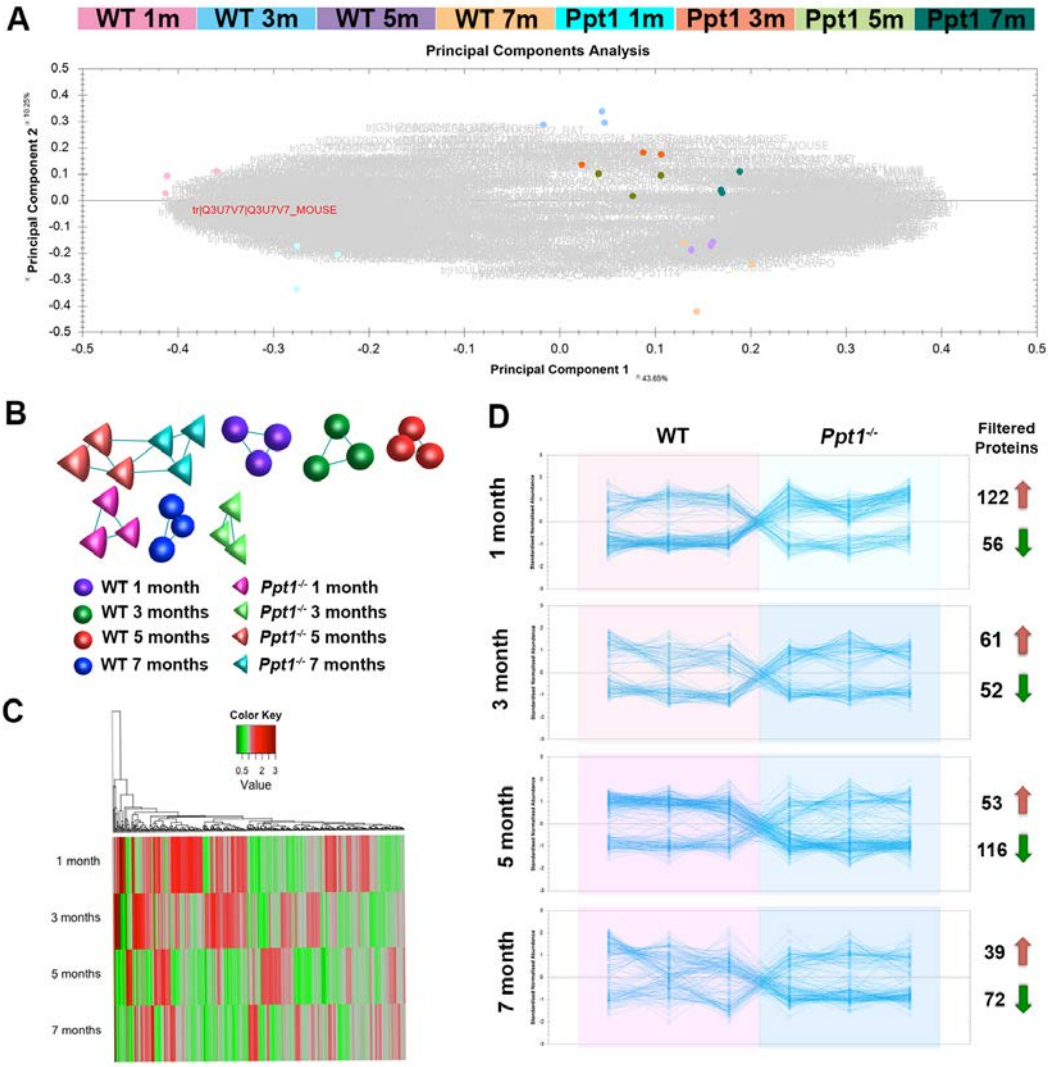

Fig. 6.4. Label-free proteomics reveals perturbations in muscle proteome throughout the time-course of disease progression in* Ppt1$^{-/-}$ *mice. **A.** Principal component analysis (PCA) generated in *Progenesis* based on protein abundance corresponding to each genotype and time-point. Proteins are represented by accession number (in grey) and followed a normal distribution (ellipse shape). PC1 represents the differences between genotypes (WT & *Ppt1*$^{-/-}$) and PC2 indicates the differences between technical replicates (technical error). All the technical replicates within each group clustered together indicating the absence of outliers in the analysis. **B.** *BioLayout* representation of the proteomic data clustered by sample similarity indicating, again, the clustering of technical replicates corresponding to the same genotype and time-point. Each sphere represents a sample and the closer they are, the more similar they are. **C.** Heat-map representing protein expression ratios of *Ppt1*$^{-/-}$ vs. WT showing the differentially expressed proteins identified across the 4 time-points. Red and green represents upregulated and downregulated proteins respectively. **D.** Proteins filtered by those identified by >2 peptides, >1.2 fold-change and p-value<0.05 are shown in 4 line graphs representing expression of individual

proteins (blue lines, 3 technical replicate per group) in WT (background in pink) and *Ppt1*$^{-/-}$ (background in blue) across time-course (1, 3, 5 and 7 months). The number of up/downregulated proteins is shown to the right of each graph. **C&D.** Note the higher number of upregulated proteins at 1 & 3 months and the shift towards downregulation at 5 & 7 months.

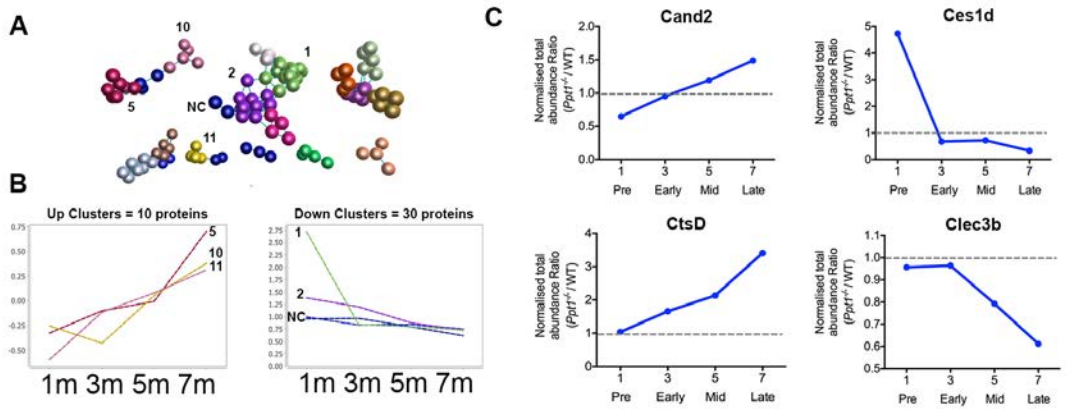

***Fig. 6.5.* BioLayout *clustering by protein expression trend allows the identification of 40 individual biomarker candidates whose expression correlates to disease progression in* Ppt1$^{-/-}$ *vs. WT*. **A.** *BioLayout* clustering 3D representation of proteomic expression data across the time-course of disease progression of *Ppt1*$^{-/-}$ vs. WT. Each sphere represents a single protein and the edge represents how similar their expression trend is towards the other proteins in the dataset. The closer the spheres are the more similar expression trend they have. The colours represent the different clusters of co-expressed proteins. **B.** Up and downregulated clusters identified with the Marckov clustering algorithm. 10 proteins showed a steady upregulation whereas 30 proteins were steady downregulated. Each dashed line is representing the average expression ratio in log scale of the proteins within each selected cluster. **C.** Line graphs showing the expression ratio *Ppt1*$^{-/-}$ vs. WT across time-course of example of individual protein candidates within the upregulated (Cand2 and CtsD) and downregulated clusters (Ces1d and Clec3b).

Table 6.2. Proteins identified by label-free proteomics showing steady up/downregulated profile throughout the time-course of disease progression in* Ppt1$^{-/-}$/*WT

		Ratio *Ppt1*$^{-/-}$/WT			
Gene Symbol	**Protein name**	**1 m**	**3 m**	**5 m**	**7 m**
ACAA2	3-ketoacyl-CoA thiolase, mitochondrial	1.74	0.87	0.81	0.81
ACADL	Long-chain specific acyl-CoA dehydrogenase, mit.	1.78	0.95	0.75	0.71
ACADV	Very long-chain specific acyl-CoA dehydrogenase, mitochondrial	1.49	0.96	0.78	0.83
APOA1	Apolipoprotein A-I	1.08	0.93	0.79	0.76
ATP5B	ATP synthase subunit b, mitochondrial	1.53	1.28	0.80	0.62
ATP5O	ATP synthase subunit O, mitochondrial	1.28	1.20	0.95	0.80
ATPA	ATP synthase subunit alpha, mitochondrial	1.21	1.14	0.88	0.75
CALR	Calreticulin	0.86	0.77	1.09	1.43
CAND2	Cullin-associated NEDD8-dissociated protein 2	0.65	0.95	1.19	1.49
CES1D	Carboxylesterase 1D	4.72	0.68	0.72	0.33
CILP2	Protein Cilp2	1.85	1.56	1.18	0.70
CLEC3B	C-type lectin domain family 3, member b	0.96	0.96	0.79	0.61
COL6A2	Collagen type VI alpha 2 subunit	1.48	1.07	0.80	0.76
COX5A	Cytochrome c oxidase subunit 5A, mitochondrial	1.48	1.38	0.87	0.64
CTSD	Cathepsin D	1.04	1.66	2.13	3.41
ETFDH	Electron transfer flavoprotein-ubiquinone oxidored., mit.	1.70	0.93	0.87	0.69
GBAS	Guanine nucleotide-binding protein G(s) subunit alpha	1.55	0.86	0.74	0.73
HADHA	Trifunctional enzyme subunit alpha, mit.	1.47	1.19	0.86	0.65
HADHB	Trifunctional enzyme subunit beta, mitochondrial	1.49	0.98	0.79	0.83
KRT84	Keratin, type II cuticular Hb4	0.16	0.32	0.42	0.48
LOC100909612	Protein LOC100909612	15.3	0.15	0.60	0.76
MTCH2	Mitochondrial carrier homolog 2	1.72	0.98	0.93	0.76
NDUFA10	NADH dehydrogenase 1 alpha subcomplex subunit 10, mitochondrial	1.37	1.16	0.81	0.81
NDUFA6	NADH dehydrogenase [ubiquinone] 1 α subcomplex subunit 6	1.36	1.12	0.83	0.79
NDUFA9	NADH dehydrogenase [ubiquinone] 1 α subcomplex subunit 9, mit.	1.26	1.14	0.91	0.79
NDUFS3	NADH dehydrogenase [ubiquinone] iron-sulfur protein 3, mit.	1.45	1.08	0.94	0.81
NEFH	MKIAA0845 protein (Fragment)	0.59	0.57	0.97	1.37
PDHX	Pdhx protein (Fragment)	1.50	0.81	0.80	0.81
PGK1	Phosphoglycerate kinase 1	0.79	0.67	0.95	1.39
PHB2	Prohibitin-2	1.39	1.10	0.99	0.75
PPIC	Peptidyl-prolyl cis-trans isomerase	0.60	1.06	1.12	1.49
PRDX5	Peroxiredoxin-6	1.47	0.99	0.77	0.81
RNH1	Ribonuclease H1	0.72	0.91	0.99	2.02
RPL4	60S ribosomal protein L4	0.78	1.07	1.24	1.33
S100A1	Protein S100-A1	1.46	1.29	0.70	0.57
SPTBN1	Protein Sptbn1	0.90	0.62	1.23	1.69
TKT	Transketolase	2.21	0.53	0.74	0.66
TNNC2	Troponin C, skeletal muscle	1.27	0.81	0.84	0.71
VIM	Vimentin	0.99	0.83	0.84	0.75

6.3.4 Ndufs3 and Calreticulin represent putative biomarkers for disease progression relevant to human NCL, and are detectable in muscle and blood samples in *Ppt1*$^{-/-}$ mice

To strengthen the confidence in the proteins identified thus far and their utility as putative biomarkers, we next wanted to identify those candidates whose expression is "conserved" at equivalent disease stages in both the infantile and juvenile forms of the disease. Interestingly, we could find 181 overlapping proteins in both *Cln3*$^{-/-}$ iTRAQ and *Ppt1*$^{-/-}$ label-free datasets (Fig. 6.6A). From these common proteins, 8 had a relatively steady in-/de-creasing profile in the *Ppt1*$^{-/-}$ time-course, and also presented similar fold-change at equivalent disease stage in *Cln3*$^{-/-}$ (Fig. 6.6B). This suggests that these 8 proteins may be putative biomarkers for both juvenile and infantile NCL.

Using QWB we then successfully validated the only example of an upregulated protein within the list, calreticulin (Calr) (Fig. 6.7A&E). Interestingly, calreticulin has also been shown to be a muscle and skin biomarker of disease progression in SMA with a very similar expression trend profile to that seen in the *Ppt1*$^{-/-}$ mice (Fig. 6.8) (Mutsaers *et al.*, 2013). We also validated an example of a downregulated protein, Ndufs3, which is an enzyme from the complex I mitochondrial respiratory chain and was also altered in the *Cln3*$^{-/-}$ proteomic data (Fig. 6.2B, Fig. 6.7B&D). Thus, we can demonstrate that proteins identified with a predictable trend in expression alteration correlating with disease progression in PPT1 and exhibiting similar expression alterations at equivalent disease stages in CLN3 are also detectable by western blotting.

Although muscle sampling yields a much more complex protein isolate of a greater yeild than CSF, it is very painful. A much less invasive method to obtain a sample is blood extraction. For this reason, we attempted to detect Calr and Ndufs3 in blood protein extracts from *Ppt1*$^{-/-}$ and WT controls. Here, we quantified Calr and Ndufs3 expression at early and late disease stages (3&7 months respectively) by QWB in order to determine if these proteins followed the same trend as in muscle. Our results confirm that both candidates followed the same trend as in muscle, with Calr was being upregulated and Ndufs3 downregulated as the disease progresses (Fig. 6.7). Moreover, the consistent strong upregulation of Ndufs3 at 1 month across different tissues could serve as a biomarker for the early detection of NCL.

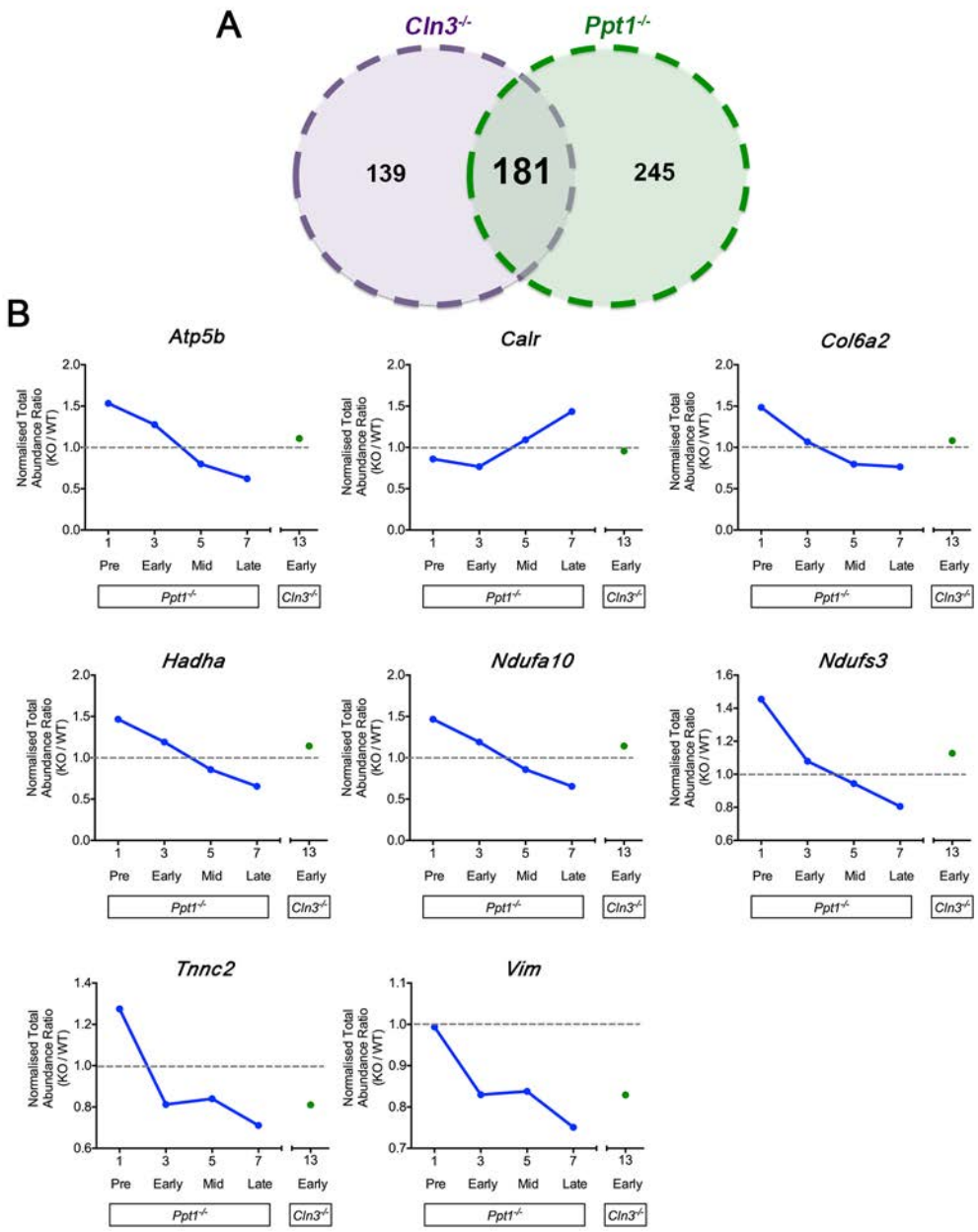

***Fig. 6.6. Eight identified biomarker candidates from the* Ppt1$^{-/-}$ *analyses have a conserved change in the* Cln3$^{-/-}$ *mice at equivalent disease stage.* **A.** Venn diagram showing 181 overlapping proteins identified in both iTRAQ *Cln3*$^{-/-}$ and *Ppt1*$^{-/-}$ label-free proteomics. **B.** Line graphs showing the expression ratio *Ppt1*$^{-/-}$ vs. WT across time-course of the 8 individual candidate biomarkers which expression correlates to disease progression in *Ppt1*$^{-/-}$ mice and is conserved between *Cln3*$^{-/-}$ (green) and *Ppt1*$^{-/-}$ (blue) at equivalent disease stage (13 months in *Cln3*$^{-/-}$ and 3 months in the *Ppt1*$^{-/-}$).

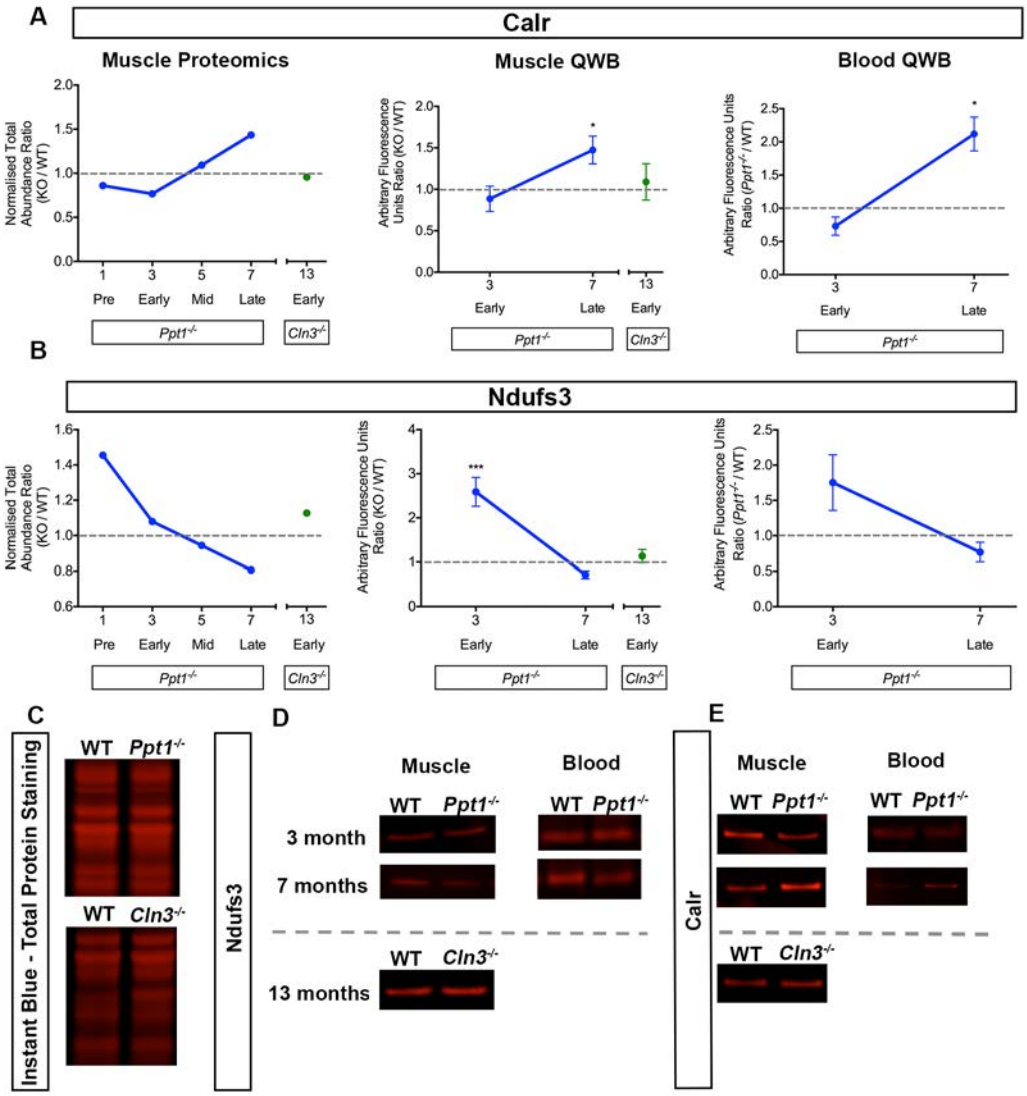

***Fig. 6.7. Calreticulin and Ndufs3 represent putative biomarkers of disease progression detectable in muscle and blood in* Ppt1$^{-/-}$ *mice.* A&B.** Line graphs representing calreticulin (Calr) and Ndufs3 expression ratio *Ppt1*$^{-/-}$ vs. WT across time-course in muscle proteomics, muscle QWB and blood QWB respectively. QWB in muscle validated the upregulation of Calr and downregulation of Ndufs3 throughout the time-course of disease progression in *Ppt1*$^{-/-}$mice. Expression ratio was also validated in *Cln3*$^{-/-}$ mice at 13 months. The same expression trends were detected in blood extracts at the same time-points in *Ppt1*$^{-/-}$mice. **C.** Instant blue total protein staining representative bands showing equal loading for both *Ppt1*$^{-/-}$ and *Cln3*$^{-/-}$ and corresponding WT controls. **D&E.** Representative QWB bands of Calr and Ndufs3 in muscle and blood in *Ppt1*$^{-/-}$ and WT mice at 3 and 7 months and in *Cln3*$^{-/-}$ and WT mice at 13 months. Mean ± SEM; * p-value<0.05, *** p-value<0.001 N=3 (Student T test).

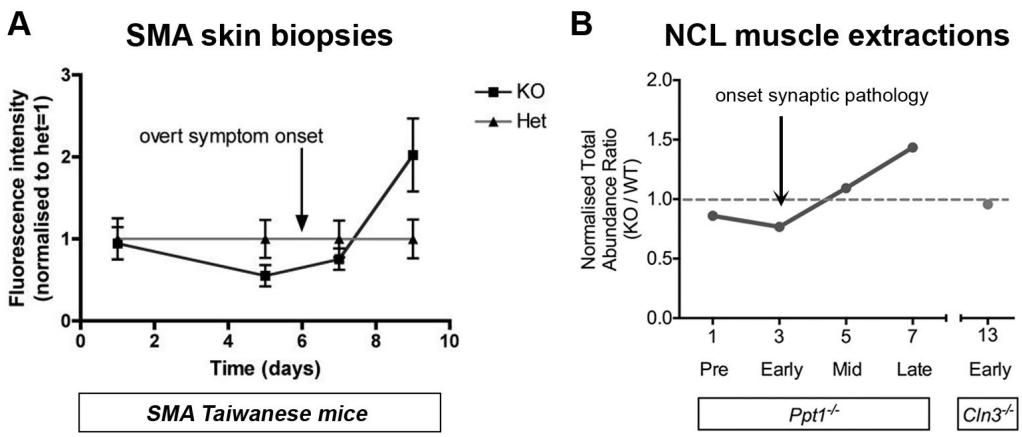

Fig. 6.8. Calreticulin and expression levels in SMA mice skin biopsies and NCL mice muscle extractions. **A&B.** In both mice models Calreticulin increases only after the onset of symptoms (in SMA) and synaptic pathology (in NCL). Therefore, calreticulin may be a potential conserved biomarker in two conditions where synapses are an early pathological target. Panel A is adapted from Fig. 4 in (Mutsaers *et al.*, 2013).

Finally, we wanted to determine if these changes identified and validated in muscle and blood from mouse models of NCL, are actually relevant to the molecular pathology occurring in brain in NCL patients. Being aware of the limitations of using *post-mortem* end stage samples, we proceeded to examine Calr and Ndufs3 by QWB. We can show that Ndufs3 had the same trend in cortical protein extracts from both INCL and JNCL patients as in the muscle and blood from mouse models at equivalent disease stage. Although Calr did not reach significance, Ndufs3 showed a deep consistent downregulation (Fig. 6.9).

Overall, we demonstrate that we can identify biomarkers of disease progression in *Ppt1*$^{-/-}$ mice, some of which may be conserved in both INCL and JNCL. Muscle is a rich source of peripherally accessible biomarkers, and we can identify differentially expressed proteins in blood that follow the same molecular expression trend as muscle. Finally, we confirm that changes detected in muscle and blood which correlate to the time-course of disease progression in *Cln3*$^{-/-}$ and *Ppt1*$^{-/-}$ are likely to be physiologically relevant to the human disease as they are also changed in the same direction in *post mortem* cortical protein extracts from JNCL and INCL patients.

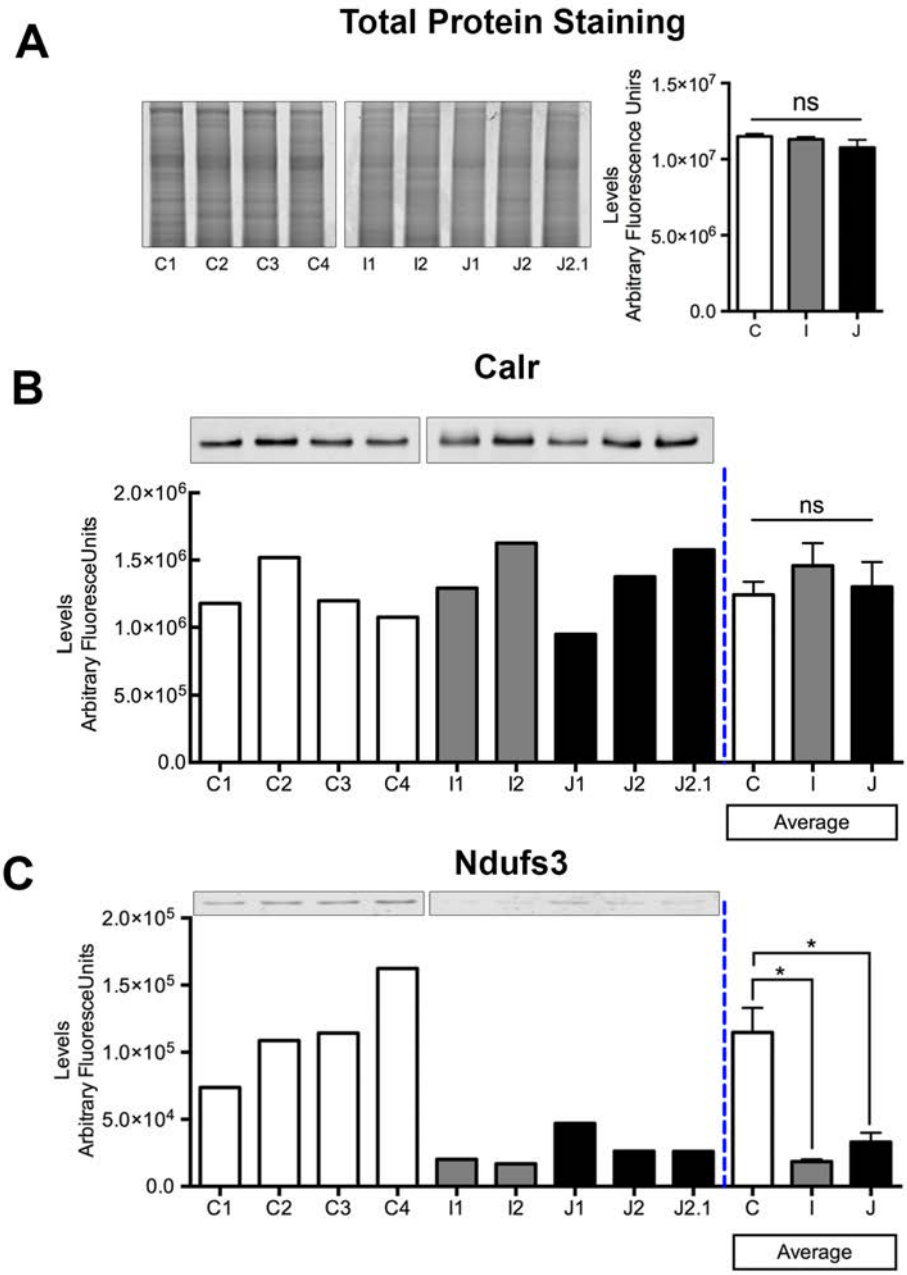

Fig. 6.9. Ndufs3 changes detected in muscle and blood from mice models are relevant to infantile and juvenile NCL in humans. **A.** Instant blue total protein staining scanned image and corresponding bar chart quantification of fluorescence abundance indicating equal loading across samples. **B&C.** Calreticulin (Calr) did not show a consistent or significant change in post mortem brain samples, but Ndufs3 shows the same expression trend in post mortem cortical extracts from INCL and JNCL patients compared to controls (C) as predicted from muscle and blood from *Ppt1*$^{-/-}$ and *Cln3*$^{-/-}$ murine models. Mean ± SEM; * p-value<0.05, ns p-value>0.05 (Student T test, Controls n=4, INCL n=2, JNCL n=3).

6.4 Discussion

In this chapter we demonstrate that muscle protein extracts are a rich source of biomarkers of disease progression in the NCLs mice models, predicting molecular perturbation at the neuronal level in humans. We are able to track individual protein candidates throughout the time-course of disease progression in mice models of NCL by means of state-of-the art label-free proteomics followed by bioinformatics analyses. We have identified calreticulin and Ndufs3 as putative biomarkers of disease progression in muscle and blood extracts in *Ppt1*$^{-/-}$ mice and demonstrated that Ndufs3 expression in human *post mortem* tissue from both INCL and JNCL patients follows the alterations predicted from analysis of murine peripheral samples.

iTRAQ proteomics carried out in muscle extracts from the *Cln3*$^{-/-}$ mouse model of JNCL at an early stage (13 months), identified multiple molecular perturbations related primarily to mitochondrial pathways (Fig. 6.1 & Fig. 6.2). Disrupted cascades predicted by the mice proteomics followed by *IPA* analysis were validated in *post mortem* cortical extracts from NCL patients highlighting the relevance of these changes to the human condition (Fig. 6.3). Therefore, we confirmed that muscle proteome is a potential source of biomarkers in the NCLs.

In order to track specific candidates throughout disease progression, a time-course proteomic study was carried out in *Ppt1*$^{-/-}$ mice model of INCL. Label-free proteomics followed by hierarchical clustering bioinformatic methods; identified 40 individual candidates with correlated to the disease progression of *Ppt1*$^{-/-}$ mice (Table 6.2) (Kielar *et al.*, 2009, Kielar *et al.*, 2007). From these 40 proteins, a subset of 8 candidates presented a conserved change between *Cln3*$^{-/-}$ and *Ppt1*$^{-/-}$ at equivalent disease stage (Fig. 6.6). This highlights the possibility of identifying common biomarkers across multiple NCL conditions but also specific ones for each form of NCL (Fig. 6.5).

Importantly, Calreticulin and Ndufs3 expression trend was conserved in blood samples at the same time-points in *Ppt1*$^{-/-}$ mice, suggesting that changes in specific proteins might be conserved across less invasive peripherally accessible tissues. Examination of *post mortem* cortical protein extracts from INCL and JNCL patients identified the same expression trend in Ndufs3 at the neuronal level, confirming the relevance of this candidate to human NCL.

Interestingly, previous studies in our laboratory detected Calreticulin to be also upregulated with disease progression in muscle and skin in SMA animal models and patients (Fig. 6.8) (Mutsaers *et al.*, 2013). Both SMA and NCL are neurodegenerative diseases of childhood where synapses are an early pathological target (Kielar *et al.*, 2009, Partanen *et al.*, 2008, Murray *et al.*, 2008, Wishart *et al.*, 2006). Some commonalities at the molecular level in neurons between these two conditions were already highlighted in this chapter such as the defects in ubiquitin homeostasis and some of the enzymes within the UPS (Fig. 6.3) (Wishart *et al.*, 2014). Therefore, common perturbations between NCL and SMA might be also occuring in muscle, suggesting the possibility to identify accessible biomarkers of disease progression in multiple conditions where some pathological events might be shared [ie. early synaptic loss (Wishart *et al.*, 2006)]. The discovery of common biomarkers across multiple neurodegenerative diseases could provide a more efficient way to develop new platforms for the detection of specific predictive alterations, or it can even allow us to repurpose tools available for existing reagents.

Nevertheless, due to the inter-species differences, a complete mapping of the molecular fingerprint of peripherally accessible tissues in humans will be required in order to determine the validity of candidates such as Calreticulin and Ndufs3 as peripherally accessible biomarkers for NCL patients. Moreover, it will be important to consider that blood and muscle proteomic composition is very different and further proteomic studies focused solely in blood would provide more insight for the discovery of specific blood biomarkers.

Altogether, this chapter offers a proof of concept that such techniques and such tissues are a reliable source of biomarkers in the mouse models of NCL. The exponential improvements in proteomic technologies combined with carefully planned experimental design (Fuller *et al.*, 2016), allows the reliable characterization of molecular changes taking place in complex protein extracts from multiple tissue types i.e. dried blood spots (Ozcan *et al.*, 2017), CSF (Heywood *et al.*, 2015), nerve (Catenaccio *et al.*, 2017, McGorum *et al.*, 2015), muscle (Mutsaers *et al.*, 2013) and even subcellular fractions (Wishart *et al.*, 2014, Graham *et al.*, 2017). Here we demonstrate, that using such technologies we can successfully track specific proteins through disease progression in animal models. Follow up for this particular line of research will now be limited by the availability of a range of patient and control samples to

more effectively enable the application of similar workflows and techniques to translate these finding into the clinics more efficiently.

Chapter 7

General discussion

7.1 Overview of results

In this project, we demonstrated that:

1 We can use proteomic technologies to underpin a data-driven target discovery approach. We mapped the molecular changes correlating to the synaptic vulnerability patterns across various brain regions and throughout the time-course of disease progression in two distinct neurodegenerative mouse models of NCL (*Ppt1*$^{-/-}$ and *Cln3*$^{-/-}$). The combination of multiple *in silico* tools allows interpretation and characterization of these molecular changes, and identifies specific pathways which are perturbed at different stages of disease progression.

2 We showed that some of these changes are conserved across both the *Ppt1*$^{-/-}$ and *Cln3*$^{-/-}$ mouse models as well as other neurodegenerative diseases where synapses are an early pathological target. Such candidates may therefore be conserved regulators across multiple conditions. Importantly, a subset of these candidates presented similar perturbations in *post mortem* infantile and juvenile NCL patient samples. This highlights the relevance of these findings to human disease.

3 Ultimately, we generated a list of protein candidates which were targeted using *Drosophila* models of NCL. We showed that many of these candidates do indeed have the ability to modulate neuronal stability *in vivo*.

4 We also combined the use of proteomics and *in silico* analysis for the discovery of putative biomarkers of disease progression, detectable in muscle and blood. Protein changes detected in peripherally accessible tissues were able to predict molecular changes at the neuronal level in NCL patient samples. A subset of these candidates presented similar alterations at equivalent disease stages in both *Ppt1*$^{-/-}$ and *Cln3*$^{-/-}$ mice, and therefore may prove to be common biomarkers in two forms of NCL.

Overall, we showed that refining experimental design to take into account regional vulnerability for tissue sampling, using state-of-the-art proteomics and *in silico* analyses in murine models of neurodegeneration, and combined with rapid phenotypic assessment in lower order animal organisms is a robust approach for the elucidation of regulators of neuronal stability *in vivo*.

7.2 The importance of target and biomarker discovery

In the past decade, there has been a dramatic decline in new entities approved by the Food and Drug Administration (FDA) (Munos, 2009), as a result, there are no effective disease modifying drugs available for any neurodegenerative disease. Target identification is a key step in the drug discovery pipeline, which generally occurs 10-15 years before a drug gets approval. The cost of drug development has also increased in the last few years, highlighting the importance and the need of target validation approaches during pre-clinical investigations. Along with drug target discovery, the importance of molecular biomarkers should not be overlooked. Biomarkers allow the monitoring of disease progression and are essential to the drug discovery pipeline. This is because they are also used to evaluate the efficacy of novel therapies in pre- and clinical trials (Paul *et al.*, 2010).

Importantly, it has been pointed out by many investigators that the activity of a single drug or target is unlikely to regulate the whole process of neurodegeneration (Prior *et al.*, 2014). Thus, omics approaches such as proteomic technologies combined with phenotypic assessment experiments as target validation, offer the possibility to shed light into the complex mechanistic pathways underlying neurodegeneration (see section 1.7).

The results outlined in this thesis support the notion that multiple cascades may be regulating neuronal stability. The identification of protein candidates, based on their expression profile correlating to synaptic pathology in mouse models of NCL (Chapter 3 &4), gave rise to interesting and promising results which were assessed in *Drosophila* models (Chapter 5). The misexpression of many of the identified candidates were able to regulate neuronal stability in a CLN3-dependent manner.

Moreover, the modifier effect observed by each one of the candidates yielded different phenotypes indicating that these proteins may participate in different pathways (See section 5.4) (Oortveld *et al.*, 2013).
Importantly, some of the changes detected in the mouse models were conserved in patients and are therefore relevant to the human disease. Further experiments would be needed in order to establish the cascade initiator and which pathway(s) is/are downstream, or whether or not candidate-related pathways converge to a common hub, triggering neuronal loss.

However, we should also consider that although *Drosophila* are excellent "simple" organisms and an attractive platform to do *in vivo* studies, further steps are needed to translate these results to patients. The use of human-derived neuronal cultures would be a valuable platform to validate genetically and pharmacologically some of our proposed targets such a ROCK2 or ATP5B, for which compounds exist (Vargas-Caballero *et al.*, 2016, Olson, 2008, Ivanes *et al.*, 2014). Large animal models also offer multiple advantages over rodents and interestingly, some neurodegenerative diseases naturally occur in these animals (Eaton *et al.*, 2017). This is the case for some of the NCLs, including the existence of; ovine (Palmer *et al.*, 2015), porcine (Cesta *et al.*, 2006) and dog models (Jolly *et al.*, 1997). Interestingly, Amorim *et al.,* reported that multiple protein perturbations were conserved across different model systems such as *Drosophila*, mice, and CLN5 sheep synaptic compartments (Amorim *et al.*, 2015). Therefore, ovine models of NCL represent valuable systems to bridge the gap between the findings highlighted here and patients.

Nonetheless, the results shown in this thesis give some clues regarding specific protein and pathways that may be involved in regulating the process of neurodegeneration.

7.3 Conserved modulators of neurodegeneration across multiple conditions

In this project, we aimed to identify novel regulators of synaptic stability. Thus, it is important to highlight that all of the protein candidates in this thesis were identified based solely on how their expression profiles correlated to synaptic vulnerability and/or disease progression. We therefore avoided biasing our candidate list with recurrent proteins popular in the neurodegenerative literature (i.e. Tau, APP, synuclein etc).

Nevertheless, when it came to unravelling the functions and pathways in which these proteins interact, many have shown to be perturbed in other neurodegenerative diseases. For instance, the valine degradation cascade was identified in two independent proteomic studies. The first one, carried out in *Cln3*$^{-/-}$ mice (Chapter 3), where there was shown to have a progressive disruption correlating to synaptic vulnerability across brain areas (Llavero Hurtado *et al.*, 2017). The second in the *Ppt1*$^{-/-}$ time-course study (Chapter 4), the valine degradation pathway was identified in *IPA* to be the top most significant pathway perturbed among all the candidates identified. Several enzymes catalyzing the catabolism of valine seem to be disrupted in both NCL mouse models. HIBCH and HADHA, two of the perturbed enzymes in the pathway, were also changed in the same direction in cortical synaptic fractions from *post mortem* NCL patients. Thus, these changes are relevant to the human disease. Knocking down these two enzymes in *Drosophila* enhanced the CLN3-OE-induced degenerative phenotype but did not cause any phenotypic change in a WT fly when knocking them down under the same conditions. This indicates that these two enzymes have the ability to change neuronal stability in a CLN3-dependent manner. Importantly, HADHA and HIBCH deficiencies have been reported to cause neurological disease in humans (Loupatty *et al.*, 2007, Ibdah *et al.*, 2001). Interestingly, mutations in HADHA cause retinopathy leading to vision loss (Fletcher *et al.*, 2012). Vision loss is generally the first symptom detected in CLN3 patients. Moreover, previous studies in our laboratory highlighted that HIBCH was also disrupted in synapses following injury in mice (Wishart *et al.*, 2012).

Taken together, there is strong evidence to indicate that enzymes within the valine degradation cascade are affected by CLN3 perturbations contributing to neurodegeneration. Importantly, metabolomic studies by Pears *et al.* in Cln6 sheep brain detected increased levels of valine at both early and late clinical stages, which correlate to our results in mice, suggesting a deficiency in the degradation of this amino acid (Pears *et al.*, 2007).

But why is disruption of valine degradation affecting neuronal stability? Some studies have indicated that branched-chain amino acids such as valine are important to maintain synthesis of the neurotransmitter, glutamate (Yudkoff, 2017). More specifically, Bak *et al.* showed that valine amino acid was needed for the synthesis of vesicular glutamate neurotransmitter during synaptic activity in cultured cerebellar neurons (Bak *et al.*, 2012). The correct homeostasis of amino acids in neurons and especially in synapses is crucial for synaptic function (see 1.5.3). Metabolomic studies have indicated a dysregulation of glutamate levels in mouse models in Cln3 (Pears *et al.*, 2005) and Cln6 sheep (Pears *et al.*,

2007), which have been related to excitotoxicity (Chattopadhyay *et al.*, 2002). Interestingly, it has also been reported that there are alterations in glutamate receptor function in both *Ppt1*$^{-/-}$ and *Cln3*$^{-/-}$ mutant mice (Finn *et al.*, 2012, Finn *et al.*, 2011).

We show that the knock-down of valine degradation enzymes enhances the CLN3-OE-induced phenotype in *Drosophila*. A plausible hypothesis of why this is happening may be a disruption in amino acid balance, and more specifically valine and glutamate perturbations. Importantly, this could to be conserved from lower model organisms (yeast) up to higher organisms such as *Drosophila*, through to mice and sheep.

Conversely, in this study we also detected the upregulation of ROCK2 in *Cln3*$^{-/-}$, correlating to synaptic vulnerability across brain areas (Chapter 3). By suppressing ROCK2 expression (genetic manipulation) or inhibiting its function (ROCK2 inhibitor compound), we showed a rescue of the CLN3-induced phenotype in *Drosophila*.

Upregulation of ROCK2 has been implicated in several adult-onset neurodegenerative conditions where synaptic pathology is present, such as HD, AD, ataxia, and in Purkinje cell degeneration (Deyts *et al.*, 2009, Herskowitz *et al.*, 2011, Zhou *et al.*, 2003, Blaise *et al.*, 2012, Wishart *et al.*, 2012). Moreover, pharmacological inhibition of ROCK2 partially rescued symptoms and increases lifespan in an SMA mouse model (Bowerman *et al.*, 2012, Coque *et al.*, 2014). ROCK2 also was reported to influence axonal degeneration following injury (Wishart *et al.*, 2012). Thus, ROCK2 is an attractive target for NCL but also for many other neurodegenerative diseases where synapses are an early pathological target (Llavero Hurtado *et al.*, 2017).

Importantly, more intriguing commonalities between NCL and SMA have been highlighted throughout this thesis. In Chapter 6, we aimed to identify molecular biomarkers in peripherally accessible tissues, which correlated to synaptic pathology/neuronal loss. Proteomics carried out at an early stage in *Cln3*$^{-/-}$ muscle extracts were followed by *in silico* analysis which helped identify mono-ubiquitin as a predicted master regulator, estimated to be inhibited/downregulated. After confirming mono-ubiquitin downregulation in mouse muscle tissue, by examining *post mortem* brain samples of NCL patients we identified the dysregulation of ubiquitin-related proteins including Uba1 and UchL1 proteins. Interestingly, Wishart *et at*. reported dysregulation of ubiquitin homeostasis and targeting

this pathway allowed the rescue of the neuromuscular system and the whole organism in animal models of the disease (Wishart *et al.*, 2014, Powis *et al.*, 2016). Therefore, it will be interesting to further investigate the role of this pathway in the NCLs as it also indicates that ubiquitin-related proteins may be common regulators of neuronal stability across multiple conditions (Zheng *et al.*, 2016).

Moreover, the unbiased study of molecular biomarkers correlating to disease progression, using a pattern recognition software, *Biolayout*, identified that calreticulin steadily increases with disease progression in muscle and blood extracts from *Ppt1*$^{-/-}$ mice. Surprisingly, calreticulin was reported by our laboratory to display a very similar expression profile in skin samples in SMA mouse models (Fig 6.8) (Mutsaers *et al.*, 2013). Therefore, conserved biomarkers may exist across multiple neurodegenerative disease sharing common aspects, such as early synaptic vulnerability. This will allow the utilization of the same methods for biomarker detection or perhaps they can even be used on already existing platforms.

Overall, the identification of common molecular regulators and biomarkers of neurodegeneration across multiple diseases will facilitate the development of therapeutic strategies to halt or delay the progression of all these conditions.

7.4 The NCLs as model of neurodegeneration

As highlighted in the previous section, we suggest that common mechanisms regulating the process of neurodegeneration and/or vulnerability of synapses may occur across a range of neurodegenerative conditions triggered by different genetic insults. In fact, other investigators already reported similarities between the NCLs and one of the most common adult-onset neurodegenerative diseases such as Parkinsons's disease. In the CLN3 disease, motor difficulties start with epilepsy and extrapyramidal/parkinsonian signs that include rigidity, hypokinesia and impaired balance, leading to complete immobility (Gardiner, 2002, Haltia, 2003, Nita *et al.*, 2016). This highlights the potential mechanistic connections between these two conditions.

We then should consider that most of the more common adult-onset neurodegenerative diseases such as Alzheimer's or Parkinson's disease have a very complex and poorly

understood (potentially multifactorial) aetiology for which the genetic insult triggering neuronal loss is not well understood. Therefore, the availability of animal models that fully replicate the disease in humans are limited (Escott-Price *et al.*, 2015, La Cognata *et al.*, 2017). In contrast, the NCLs are monogenetic diseases for which there are available many well-characterized mice models that more accurately replicate the human disease (Mitchison *et al.*, 1999, Pontikis *et al.*, 2004, Cotman *et al.*, 2002, Gupta *et al.*, 2001, Kielar *et al.*, 2007, Partanen *et al.*, 2008). In this project, we demonstrated that we can use the NCLs as a model to study a specific neurodegenerative process (i.e. synaptic loss) which is likely to be governed by mechanisms which may indeed be conserved across multiple conditions ranging from injury through to chronic neurodegenerative conditions (i.e. Huntington disease and spinocerebellar ataxia) and diseases of childhood (i.e. SMA & the NCLs) (Wishart *et al.*, 2012) (Llavero Hurtado *et al.*, 2017).

The connection between the NCLs and more common ageing-related diseases such as Alzheimer's will benefit academia, the pharmaceutical and biotechnology industries. This is because these shared common pathophysiological pathways will open up funding and investment opportunities for targeting "synaptopathies" such as the NCLs and Alzheimer's simultaneously.

7.5 Conclusions

In this work, we identified regulators of neuronal stability which may serve as drug targets for the development of novel therapies, not only for the NCLs, but also for other neurodegenerative conditions where synapses are an early pathological target. The workflows highlighted in this project should not be viewed as a mass screening "stamp collecting" exercise. Instead it should be clear that combining mammalian models with "–omic" screening of differentially vulnerable tissues with *in silico* candidate identification and *in vivo* phenotypic assessment in *Drosophila* is an efficient pipeline for elucidating the mechanistic cascades governing neurodegenerative processes. Ultimately, we have developed "target-rich" and data-driven pipelines for identifying factors which are capable of modulating neurodegeneration, and therefore may be therapeutically targetable.

References

Abbott, R. D., Ross, G. W., White, L. R., Nelson, J. S., Masaki, K. H., Tanner, C. M., Curb, J. D., Blanchette, P. L., Popper, J. S. & Petrovitch, H. 2002. Midlife adiposity and the future risk of Parkinson's disease. *Neurology,* 59**,** 1051-1057.

Aby, E., Gumps, K., Roth, A., Sigmon, S., Jenkins, S. E., Kim, J. J., Kramer, N. J., Parfitt, K. D. & Korey, C. A. 2013. Mutations in palmitoyl-protein thioesterase 1 alter exocytosis and endocytosis at synapses in *Drosophila* larvae. *Fly (Austin),* 7**,** 267-79.

Adams, H., Blieck, E. a. D., Md, J. W. M., Marshall, F. J., Kwon, J., Leon Dure Md, D. O. P., Rothberg, P. G., Ramirez-Montealegre, D. & Pearce, D. A. 2006. Standardized assessment of behavior and adaptive living skills in juvenile neuronal ceroid lipofuscinosis. *Dev Med Child Neuro,* 48**,** 259–264.

Aebersold, R. & Mann, M. 2016. Mass-spectrometric exploration of proteome structure and function. *Nature,* 537**,** 347-355.

Aghamaleky Sarvestany, A., Hunter, G., Tavendale, A., Lamont, D. J., Llavero Hurtado, M., Graham, L. C., Wishart, T. M. & Gillingwater, T. H. 2014. Label-free quantitative proteomic profiling identifies disruption of ubiquitin homeostasis as a key driver of Schwann cell defects in spinal muscular atrophy. *J Proteome Res,* 13**,** 4546-57.

Ahtiainen, L., Luiro, K., Kauppi, M., Tyynela, J., Kopra, O. & Jalanko, A. 2006. Palmitoyl protein thioesterase 1 (PPT1) deficiency causes endocytic defects connected to abnormal saposin processing. *Exp Cell Res,* 312**,** 1540-53.

Ahtiainen, L., Van Diggelen, O. P., Jalanko, A. & Kopra, O. 2003. Palmitoyl protein thioesterase 1 is targeted to the axons in neurons. *J Comp Neurol,* 455**,** 368-77.

Alberts, B. 1998. The Cell as a Collection of Protein Machines: Preparing the Next Generation of Molecular Biologists. *Cell,* 92**,** 291-294.

Amorim, I. S., Graham, L. C., Carter, R. N., Morton, N. M., Hammachi, F., Kunath, T., Pennetta, G., Carpanini, S. M., Manson, J. C., Lamont, D. J., Wishart, T. M. & Gillingwater, T. H. 2017. Sideroflexin 3 is an α-synuclein-dependent mitochondrial protein that regulates synaptic morphology. *Journal of Cell Science,* 130**,** 325-331.

Amorim, I. S., Mitchell, N. L., Palmer, D. N., Sawiak, S. J., Mason, R., Wishart, T. M. & Gillingwater, T. H. 2015. Molecular neuropathology of the synapse in sheep with CLN5 Batten disease. *Brain and Behavior,* 5**,** e00401-n/a.

Anastassiadis, T., Deacon, S. W., Devarajan, K., Ma, H. & Peterson, J. R. 2011. Comprehensive assay of kinase catalytic activity reveals features of kinase inhibitor selectivity. *Nat. Biotechnol.,* 29**,** 1039-45.

Anderson, G. W., Goebel, H. H. & Simonati, A. 2013. Human pathology in NCL. *Biochim Biophys Acta,* 1832**,** 1807-26.

Angel, T. E., Aryal, U. K., Hengel, S. M., Baker, E. S., Kelly, R. T., Robinson, E. W. & Smith, R. D. 2012. Mass spectrometry-based proteomics: existing capabilities and future directions. *Chemical Society Reviews,* 41**,** 3912-3928.

Arendt, D., Tessmar-Raible, K., Snyman, H., Dorresteijn, A. W. & Wittbrodt, J. 2004. Ciliary photoreceptors with a vertebrate-type opsin in an invertebrate brain. *Science,* 306**,** 869-871.

Au, C. E., Bell, A. W., Gilchrist, A., Hiding, J., Nilsson, T. & Bergeron, J. J. M. 2007. Organellar proteomics to create the cell map. *Current Opinion in Cell Biology,* 19**,** 376-385.

Autti, T., Hämäläinen, J., Aberg, L., Lauronen, L., Tyynelä, J. & Van Leemput, K. 2007. Thalami and corona radiata in juvenile NCL (CLN3): a voxel-based morphometric study. *Eur J Neurol.,* 14**,** 447-50.

Bak, L. K., Johansen, M. L., Schousboe, A. & Waagepetersen, H. S. 2012. Valine but not leucine or isoleucine supports neurotransmitter glutamate synthesis during synaptic activity in cultured cerebellar neurons. *Journal of Neuroscience Research,* 90**,** 1768-1775.

Bannan, B. A., Van Etten, J., Kohler, J. A., Tsoi, Y., Hansen, N. M., Sigmon, S., Fowler, E., Buff, H., Williams, T. S., Ault, J. G., Glaser, R. L. & Korey, C. A. 2008. The *Drosophila* protein palmitoylome: Characterizing palmitoyl-thioesterases and DHHC palmitoyl-transferases. *Fly,* 2**,** 198-214.

Banovic, D., Khorramshahi, O., Owald, D., Wichmann, C., Riedt, T., Fouquet, W., Tian, R., Sigrist, S. J. & Aberle, H. 2010. *Drosophila* Neuroligin 1 promotes growth and postsynaptic differentiation at glutamatergic neuromuscular junctions. *Neuron,* 66**,** 724-738.

Bantscheff, M., Schirle, M., Sweetman, G., Rick, J. & Kuster, B. 2007. Quantitative mass spectrometry in proteomics: a critical review. *Anal Bioanal Chem,* 389**,** 1017-31.

Bassil, F., Fernagut, P.-O., Bezard, E. & Meissner, W. G. 2014. Insulin, IGF-1 and GLP-1 signaling in neurodegenerative disorders: Targets for disease modification? *Progress in Neurobiology,* 118**,** 1-18.

Bayer, T. A. 2015. Proteinopathies, a core concept for understanding and ultimately treating degenerative disorders? *European Neuropsychopharmacology,* 25**,** 713-724.

Berger, C., Renner, S., Lüer, K. & Technau, G. M. 2007. The commonly used marker ELAV is transiently expressed in neuroblasts and glial cells in the *Drosophila* embryonic CNS. *Developmental Dynamics,* 236**,** 3562-3568.

Bertoni-Freddari, C., Fattoretti, P., Casoli, T., Spagna, C., Meier-Ruge, W. & Ulrich, J. 1993. Morphological plasticity of synaptic mitochondria during aging. *Brain Research,* 628**,** 193-200.

Bharadwaj, S., Thanawala, R., Bon, G., Falcioni, R. & Prasad, G. L. 2005. Resensitization of breast cancer cells to anoikis by tropomyosin-1: role of Rho kinase-dependent cytoskeleton and adhesion. *Oncogene,* 24**,** 8291-303.

Bible, E., Gupta, P., Hofmann, S. L. & Cooper, J. D. 2004. Regional and cellular neuropathology in the palmitoyl protein thioesterase-1 null mutant mouse model of infantile neuronal ceroid lipofuscinosis. *Neurobiol. Dis.,* 16**,** 346–359.

Bible, M., Lehesjoki, A. E., Jalanko, A., Cooper, J. D. & Kopra, O. 2012. Selective spatiotemporal patterns of glial activation and neuron loss in the sensory thalamocortical pathways of neuronal ceroid lipofuscinosis 8 mice. *Neurobiol. Dis.,* 47**,** 444-57.

Bilen, J. & Bonini, N. M. 2005. *Drosophila* as a model for human neurodegenerative disease. *Annu. Rev. Genet.,* 39:153–71.

Biomarkers Definition Working Group 2001. Biomarkers and surrogate endpoints: preferred definitions and conceptual framework. *Clin Pharmacol Ther,* 69**,** 89–95.

Bischof, J., Björklund, M., Furger, E., Schertel, C., Taipale, J. & Basler, K. 2013. A versatile platform for creating a comprehensive UAS-ORFeome library in *Drosophila*. *Development,* 140**,** 2434-2442.

Blaise, S., Kneib, M., Rousseau, A., Gambino, F., Chenard, M. P., Messadeq , N., Muckenstrum, M., Alpy, F., Tomasetto, C., Humeau, Y. & Rio, M. C. 2012. In vivo evidence that TRAF4 is required for central nervous system myelin homeostasis. *PLoS One,* 7**,** e30917.

Bond, M., Holthaus, S. M., Tammen, I., Tear, G. & Russell, C. 2013. Use of model organisms for the study of neuronal ceroid lipofuscinosis. *Biochim Biophys Acta,* 1832**,** 1842-65.

Bowerman, M., Murray, L. M., Boyer, J. G., Anderson, C. L. & Kothary, R. 2012. Fasudil improves survival and promotes skeletal muscle development in a mouse model of spinal muscular atrophy. *BMC Med,* 10**,** 24.

Braak, H. & Braak, E. 1995. Staging of Alzheimer's disease-related neurofibrillary changes. *Neurobiol Aging,* 16**,** 271–8.

Brand, A. & Perrimon, N. 1993. Targeted gene expression as a means of altering cell fates and generating dominant phenotypes. *Development,* 118**,** 401-415.

Brand, A. H. P., N. 1993. Targeted gene expression as a means of altering cell fates and generating dominant phenotypes. *Development,* 118 (2)**,** 401– 415.

Bras, J., Verloes, A., Schneider, S. A., Mole, S. E. & Guerreiro, R. J. 2012. Mutation of the parkinsonism gene ATP13A2 causes neuronal ceroid-lipofuscinosis. *Hum. Mol. Genet.,* 21**,** 2646–2650.

Brogiolo, W., Stocker, H., Ikeya, T., Rintelen, F., Fernandez, R. & Hafen, E. 2001. An evolutionarily conserved function of the *Drosophila* insulin receptor and insulin-like peptides in growth control. *Current Biology,* 11**,** 213-221.

Brown, D. F., Risser, R. C., Bigio, E. H., Tripp, P., Stiegler, A., Welch, E., Eagan, K. P., Hladik, C. L. & White, I. I. I. C. L. 1998. Neocortical synapse density and braak stage in the Lewy body variant of Alzheimer Disease: A Comparison with classic Alzheimer Disease and normal aging. *Journal of Neuropathology & Experimental Neurology,* 57**,** 955-960.

Brown, G. K., Hunt, S. M., Scholem, R., Fowler, K., Grimes, A., Mercer, J. F., Truscott, R. M., Cotton, R. G., Rogers, J. G. & Danks, D. M. 1982. b- hydroxyisobutyryl coenzyme A deacylase deficiency: a defect in valine metabolism associated with physical malformations. *Pediatrics,* 70**,** 532–538.

Brown, M. R., Sullivan, P. G. & Geddes, J. W. 2006. Synaptic mitochondria are more susceptible to ca2+overload than nonsynaptic mitochondria. *J Biol Chem* 281**,** 11658–68.

Budnik, V., Koh, Y.-H., Guan, B., Hartmann, B., Hough, C., Woods, D. & Gorczyca, M. 1996. Regulation of synapse structure and function by the *Drosophila* tumor suppressor gene *dlg*. *Neuron,* 17**,** 627-640.

Buff, H., Smith, A. C. & Korey, C. A. 2007. Genetic modifiers of *Drosophila* palmitoyl-protein thioesterase 1-induced degeneration. *Genetics,* 176**,** 209-20.

Cagan, R. L. & Ready, D. F. 1989. The emergence of order in the *Drosophila* pupal retina. *Developmental Biology,* 136**,** 346-362.

Camandola, S. & Mattson, M. P. 2017. Brain metabolism in health, aging, and neurodegeneration. *The EMBO Journal,* 36**,** 1474-1492.

Camp, L. A. & Hofmann, S. L. 1993. Purification and properties of a palmitoyl-protein thioesterase that cleaves palmitate from H-Ras. *J Biol Chem.,* 268**,** 22566-7.

Cao, Y., Espinola, J. A., Fossale, E., Massey, A. C., Cuervo, A. M., Macdonald, M. E. & Cotman, S. L. 2006. Autophagy is disrupted in a knock-in mouse model of juvenile neuronal ceroid lipofuscinosis. . *J. Biol. Chem.,* 281**,** 20483–20493.

Cao, Y., Staropoli, J. F., Biswas, S., Espinola, J. A., Macdonald, M. E., Lee, J. M. & Cotman, S. L. 2011. Distinct early molecular responses to mutations causing vLINCL and JNCL presage ATP synthase subunit C accumulation in cerebellar cells. *PLoS One.,* 6.

Carcel-Trullols, J., Kovacs, A. D. & Pearce, D. A. 2015. Cell biology of the NCL proteins: What they do and don't do. *Biochim Biophys Acta,* 1852**,** 2242-55.

Carpanini, S. M., Wishart, T. M., Gillingwater, T. H., Manson, J. C. & Summers, K. M. 2017. Analysis of gene expression in the nervous system identifies key genes and novel candidates for health and disease. *Neurogenetics*.

Catenaccio, A., Llavero Hurtado, M., Diaz, P., Lamont, D. J., Wishart, T. M. & Court, F. A. 2017. Molecular analysis of axonal-intrinsic and glial-associated co-regulation of axon degeneration. *Cell Death Dis.* 8(11):e3166.

Cesta, M. F., Mozzachio, K., Little, P. B., Olby, N. J., Sills, R. C. & Brown, T. T. 2006. Neuronal ceroid lipofuscinosis in a vietnamese pot-bellied pig (Sus scrofa). *Veterinary Pathology,* 43**,** 556-560.

Chahrour, M. & Zoghbi, H. Y. 2007. The Story of Rett Syndrome: From Clinic to Neurobiology. *Neuron,* 56**,** 422-437.

Chai, A. & Pennetta, G. 2015. Insights into ALS pathomechanisms: from flies to humans. *Fly (Austin),* 9**,** 91-8.

Champagne, E., Martinez, L. O., Collet, X. & Barbaras, R. 2006. Ecto-F1Fo ATP synthase/F1 ATPase: metabolic and immunological functions. *Current opinion in lipidology,* 17**,** 279-84.

Chan, D. C. 2006. Mitochondria: Dynamic Organelles in Disease, Aging, and Development. *Cell,* 125**,** 1241-1252.

Chan, Y. B., Miguel-Aliaga, I., Franks, C., Thomas, N., Trülzsch, B., Sattelle, D. B., Davies, K. E. & Van Den Heuvel, M. 2003. Neuromuscular defects in a *Drosophila* survival motor neuron gene mutant. *Human Molecular Genetics,* 12**,** 1367-1376.

Chang, H. C., Dimlich, D. N., Yokokura, T., Mukherjee, A., Kankel, M. W., Sen, A., Sridhar, V., Fulga, T. A., Hart, A. C., Van Vactor, D. & Artavanis-Tsakonas, S. 2008a. Modeling spinal muscular atrophy in *Drosophila*. *PLoS One,* 3**,** e3209.

Chang, M., Cooper, J. D., Sleat, D. E., Cheng, S. H., Dodge, J. C., Passini, M. A., Lobel, P. & Davidson, B. L. 2008b. Intraventricular enzyme replacement improves disease phenotypes in a mouse model of late infantile neuronal ceroid lipofuscinosis. *Mol Ther,* 16**,** 649-56.

Chao, H.-T., Zoghbi, H. Y. & Rosenmund, C. 2007. MeCP2 Controls excitatory synaptic strength by regulating glutamatergic synapse number. *Neuron,* 56**,** 58-65.

Chattopadhyay, S., Ito, M., Cooper, J. D., Brooks, A. I., Curran, T. M., Powers, J. M. & Pearce, D. A. 2002. An autoantibody inhibitory to glutamic acid decarboxylase in the neurodegenerative disorder Batten disease. *Hum Mol Genet.,* 11**,** 1421-31.

Chattopadhyay, S., Kingsley, E., Serour, A., Curran, T. M., Brooks, A. I. & Pearce, D. A. 2004. Altered gene expression in the eye of a mouse model for batten disease. *Invest Ophthalmol Vis Sci,* 45**,** 2893-905.

Chattopadhyay, S. & Pearce, D. A. 2000. Neural and extraneural expression of the neuronal ceroid lipofuscinoses genes CLN1, CLN2, and CLN3: functional implications for CLN3. *Mol Genet Metab,* 71**,** 207-11.

Chen, C. M., Wu, Y. R., Cheng, M. L., Liu, J. L., Lee, Y. M., Lee, P. W., Soong, B. W. & Chiu, D. T. 2007. Increased oxidative damage and mitochondrial abnormalities in the peripheral blood of Huntington's disease patients. *Biochem Biophys Res Commun,* 359**,** 335-40.

Chen, C. N., Denome, S. & Davis, R. L. 1986. Molecular analysis of cDNA clones and the corresponding genomic coding sequences of the *Drosophila* dunce+ gene, the structural gene for cAMP phosphodiesterase. *Proceedings of the National Academy of Sciences of the United States of America,* 83**,** 9313-9317.

Chiesa, R., Piccardo, P., Dossena, S., Nowoslawski, L., Roth, K. A., Ghetti, B. & Harris, D. A. 2005. Bax deletion prevents neuronal loss but not neurological symptoms in a transgenic model of inherited prion disease. *Proceedings of the National Academy of Sciences of the United States of America,* 102**,** 238-243.

Chiu, S.-L., Chen, C.-M. & Cline, H. T. 2008. Insulin receptor signaling regulates synapse number, dendritic plasticity and circuit function in vivo. *Neuron,* 58**,** 708-719.

Chu-Lagraff, Q., Blanchette, C., O'hern, P. & Denefrio, C. 2010. The Batten disease Palmitoyl Protein Thioesterase 1 gene regulates neural specification and axon connectivity during *Drosophila* embryonic development. *PLoS One,* 5**,** e14402.

Citri, A. & Malenka, R. C. 2007. Synaptic plasticity: multiple forms, functions, and mechanisms. *Neuropsychopharmacology,* 33**,** 18.

Coleman, M. 2005. Axon degeneration mechanisms: commonality amid diversity. *Nat Rev Neurosci 2005;6:889Y98,* 6**,** 889-898

Coleman, P., Federoff, H. & Kurlan, R. 2004. A focus on the synapse for neuroprotection in Alzheimer disease and other dementias. *Neurology,* 63**,** 1155-1162.

Collins, A. L., Levenson, J. M., Vilaythong, A. P., Richman, R., Armstrong, D. L., Noebels, J. L., David Sweatt, J. & Zoghbi, H. Y. 2004. Mild overexpression of MeCP2 causes a progressive neurological disorder in mice. *Human Molecular Genetics,* 13**,** 2679-2689.

Collins, S. R., Kemmeren, P., Zhao, X.-C., Greenblatt, J. F., Spencer, F., Holstege, F. C. P., Weissman, J. S. & Krogan, N. J. 2007. Toward a comprehensive atlas of the physical interactome of Saccharomyces cerevisiae. *Molecular & Cellular Proteomics,* 6**,** 439-450.

Comeron, J. M., Ratnappan, R. & Bailin, S. 2012. The many landscapes of recombination in *Drosophila melanogaste*r. *PLoS Genet,* 8**,** e1002905.

Cooper, D. J., Zunino, G., Bixby, J. L. & Lemmon, V. P. 2017. Phenotypic screening with primary neurons to identify drug targets for regeneration and degeneration. *Mol Cell Neurosci,* 80**,** 161-169.

Cooper, J. D. 2003. Progress towards understanding the neurobiology of Batten disease or neuronal ceroid lipofuscinosis. *Curr Opin Neurol,* 16**,** 121-8.

Cooper, J. D. 2010. The neuronal ceroid lipofuscinoses: the same, but different? *Biochem Soc Trans,* 38**,** 1448-52.

Cooper, J. D., Lange, J., Trigt, L. V., Brooks, H., Parviainen, L., Dihanich, S., Anderson, G. & Williams, B. P. 2016. The nature Of glial dysfunction and its impact upon neurons varies between forms f NCL. The 15th international conference on neuronal ceroid lipofuscinosis (batten disease)**,** O13 abstract.

Cooper, J. D., Messer, A., Feng, A. K., Chua-Couzens, J. & Mobley, W. C. 1999. Apparent loss and hypertrophy of interneurons in a mouse model of neuronal ceroid lipofuscinosis: evidence

for partial response to insulin-like growth factor-1 treatment. *The Journal of Neuroscience,* 19**,** 2556-2567.

Cooper, J. D., Russell, C. & Mitchison, H. M. 2006. Progress towards understanding disease mechanisms in small vertebrate models of neuronal ceroid lipofuscinosis. *Biochim Biophys Acta,* 1762**,** 873-89.

Cooper, J. D., Tarczyluk, M. A. & Nelvagal, H. R. 2015. Towards a new understanding of NCL pathogenesis. *Biochim Biophys Acta,* 1852**,** 2256-61.

Coque, E., Raoul, C. & Bowerman, M. 2014. ROCK inhibition as a therapy for spinal muscular atrophy: understanding the repercussions on multiple cellular targets. *Front Neurosci,* 8**,** 271.

Corbett, A. & Ballard, C. 2012. New and emerging treatments for Alzheimer's disease. *Expert Opinion on Emerging Drugs,* 17**,** 147-156.

Cotman, S. L., Vrbanac, V., Lebel, L. A., Lee, R. L., Johnson, K. A., Donahue, L. R., Teed, A. M., Antonellis, K., Bronson, R. T., Lerner, T. J. & Macdonald, M. E. 2002. Cln3(Deltaex7/8) knock-in mice with the common JNCL mutation exhibit progressive neurologic disease that begins before birth. *Hum Mol Genet.,* 11**,** 2709-21.

Couteaux, R. & Pecot-Dechavassine, M. 1970. L'Ouverture des vesicules synaptiques au niveau des 'zones actives.' *Septieme Congres International de Microscopie Electronique (Grenoble, France)***,** 709–710.

Craft, G. E., Chen, A. & Nairn, A. C. 2013. Recent advances in quantitative neuroproteomics. *Methods,* 61**,** 186–218.

D.E. Sleat, R. J. D., H. Lackland, C.G. Liu, I. Sohar, R.K. Pullarkat, P. Lobel 1997. Association of mutations in a lysosomal protein with classical late-infantile neuronal ceroid lipofuscinosis. *Science,* 277**,** 1802–1805.

Das, A. M., Jolly, R. D. & Kohlschütter, A. 1999. Anomalies of mitochondrial ATP synthase regulation in four different types of neuronal ceroid lipofuscinosis. *Molecular Genetics and Metabolism,* 66**,** 349–355.

Das, A. M. & Kohlschütter, A. 1996. Decreased activity of the mitochondrial ATP-synthase in fibroblasts from children with late-infantile and juvenile neuronal ceroid lipofuscinosis. *Journal of Inherited Metabolic Disease,* 19**,** 130-132.

Davies, P. & Maloney, A. J. F. 1976. Selective loss of central cholinergic neurons in alzheimer's disease. *The Lancet,* 308**,** 1403.

Davies, S. W., Turmaine, M., Cozens, B. A., Difiglia, M., Sharp, A. H. & Ross, C. A. 1997. Formation of neuronal intranuclear inclusions underlies the neurological dysfunction in mice transgenic for the HD mutation. *Cell,* 90(3)**,** 537–548.

Davis, R. L., Takayasu, H., Eberwine, M. & Myres, J. 1989. Cloning and characterization of mammalian homologs of the *Drosophila* dunce+ gene. *Proceedings of the National Academy of Sciences of the United States of America,* 86**,** 3604-3608.

Dawson, J. C. & Carragher, N. O. 2014. Quantitative phenotypic and pathway profiling guides rational drug combination strategies. *Front Pharmacol,* 5**,** 118.

De La Mata, M., Cotán, D., Villanueva-Paz, M., De Lavera, I., Álvarez-Córdoba, M., Luzón-Hidalgo, R., Suárez-Rivero, J., Tiscornia, G. & Oropesa-Ávila, M. 2016. Mitochondrial Dysfunction in Lysosomal Storage Disorders. *Diseases,* 4**,** 31.

Dekosky, S. T. & Scheff, S. W. 1990. Synapse loss in frontal cortex biopsies in Alzheimer's disease: correlation with cognitive severity. *Ann Neurol.,* 27**,** 457-64.

Deyts, C., Galan-Rodriguez, B., Martin, E., Bouveyron, N., Roze, E., Charvin, D., Caboche, J. & Bétuing, S. 2009. Dopamine D2 receptor stimulation potentiates PolyQ-Huntingtin-induced mouse striatal neuron dysfunctions via Rho/ROCK-II activation. *PLoS One,* 4**,** e8287.

Dickson, B. & Hafen, E. 1993. Genetic dissection of eye development in *Drosophila*. In C. Bate, & A. Martinez-Arias (Eds.), The Development of *Drosophila melanogaster New York: Cold Spring Harbor Laboratory Press.***,** 1327–1362.

Dietzl, G., Chen, D., Schnorrer, F., Su, K.-C., Barinova, Y., Fellner, M., Gasser, B., Kinsey, K., Oppel, S., Scheiblauer, S., Couto, A., Marra, V., Keleman, K. & Dickson, B. J. 2007. A genome-wide transgenic RNAi library for conditional gene inactivation in *Drosophila*. *Nature,* 448**,** 151.

Difiglia, M., Sapp, E., Chase, K. O., Davies, S. W., Bates, G. P. & Vonsattel, J. P. 1997. Aggregation of huntingtin in neuronal intranuclear inclusions and dystrophic neurites in brain. . *Science,* 277**,** 1990–1993.

Dimauro, S. & Schon, E. A. 2008. Mitochondrial disorders in the nervous system. *Annual Review of Neuroscience,* 31**,** 91-123.

Dutriaux, A., Godart, A., Brachet, A. & Silber, J. 2013. The insulin receptor is required for the development of the *Drosophila* peripheral nervous system. *PLoS ONE,* 8**,** e71857.

Dyke, J. P., Voss, H. U., Sondhi, D., Hackett, N. R., Worgall, S., Heier, L. A., Kosofsky, B. E., Ulug, A. M., Shungu, D. C., Mao, X., Crystal, R. G. & Ballon, D. 2007. Assessing disease severity in late infantile neuronal ceroid lipofuscinosis using quantitative MR diffusion-weighted imaging. *AJNR Am J Neuroradiol,* 28**,** 1232-6.

Eaton, S. L., Roche, S. L., Llavero Hurtado, M., Oldknow, K. J., Farquharson, C., Gillingwater, T. H. & Wishart, T. M. 2013. Total protein analysis as a reliable loading control for quantitative fluorescent Western blotting. *PLoS One,* 8**,** e72457.

Eaton, S. L. & Wishart, T. M. 2017. Bridging the gap: large animal models in neurodegenerative research. *Mammalian Genome,* 28**,** 324-337.

Eden, E., Navon, R., Steinfeld, I., Lipson, D. & Yakhini, Z. 2009. GOrilla: a tool for discovery and visualization of enriched GO terms in ranked gene lists. *BMC Bioinformatics,* 10**,** 48.

Ehlers, M. D. 2003. Activity level controls postsynaptic composition and signaling via the ubiquitin-proteasome system. *Nat Neurosci,* 6**,** 231-42.

Elias, M. F., Beiser, A., Wolf, P. A., Au, R., White, R. F. & D'agostino, R. B. 2000. The preclinical phase of alzheimer disease: A 22-year prospective study of the framingham cohort. *Archives of Neurology,* 57**,** 808-813.

Eliason, S. L., Stein, C. S., Mao, Q., Tecedor, L., Ding, S. L., Gaines, D. M. & Davidson, B. L. 2007. A knock-in reporter model of Batten disease. *J Neurosci,* 27**,** 9826-34.

Ellis, R. J. 2001. Macromolecular crowding: obvious but underappreciated. *Trends in Biochemical Sciences,* 26**,** 597-604.

Ellis, R. J. 2006. Molecular chaperones: assisting assembly in addition to folding. *Trends in Biochemical Sciences,* 31**,** 395-401.

Enright, A. J., Van Dongen, S. & Ouzounis, C. A. 2002. An efficient algorithm for large-scale detection of protein families. *Nucleic Acids Res,* 30**,** 1575–1584.

Escott-Price, V., Sims, R., Bannister, C., Harold, D., Vronskaya, M., Majounie, E., Badarinarayan, N., Gerad/Perades, Consortia, I., Morgan, K., Passmore, P., Holmes, C., Powell, J., Brayne, C., Gill, M., Mead, S., Goate, A., Cruchaga, C., Lambert, J.-C., Van Duijn, C., Maier, W., Ramirez, A., Holmans, P., Jones, L., Hardy, J., Seshadri, S., Schellenberg, G. D., Amouyel, P. & Williams, J. 2015. Common polygenic variation enhances risk prediction for Alzheimer's disease. *Brain,* 138**,** 3673-3684.

Faller, K. M., Gutierrez-Quintana, R., Mohammed, A., Rahim, A. A., Tuxworth, R. I., Wager, K. & Bond, M. 2015. The neuronal ceroid lipofuscinoses: Opportunities from model systems. *Biochim Biophys Acta,* 1852**,** 2267-78.

Fearnley, I. M., Walker, J. E., Martinus, R. D., Jolly, R. D., Kirkland, K. B., Shaw, G. J. & Palmer, D. N. 1990. The sequence of the major protein stored in ovine ceroid lipofuscinosis is identical with that of the dicyclohexylcarbodiimide-reactive proteolipid of mitochondrial ATP synthase. *Biochemical Journal,* 268**,** 751-758.

Feiguin, F., Godena, V. K., Romano, G., D'ambrogio, A., Klima, R. & Baralle, F. E. 2009. Depletion of TDP-43 affects *Drosophila* motoneurons terminal synapsis and locomotive behavior. *FEBS Letters,* 583**,** 1586-1592.

Ferdinandusse, S., Waterham, H. R., Heales, S. J., Brown, G. K., Hargreaves, I. P., Taanman, J. W., Gunny, R., Abulhoul, L., Wanders, R. J., Clayton, P. T., Leonard, J. V. & Rahman, S. 2013. HIBCH mutations can cause Leigh-like disease with combined deficiency of multiple mitochondrial respiratory chain enzymes and pyruvate dehydrogenase. *Orphanet J Rare Dis.,* 8**,** 188.

Fernandez, R., Tabarini, D., Azpiazu, N., Frasch, M. & Schlessinger, J. 1995. The *Drosophila* insulin receptor homolog: a gene essential for embryonic development encodes two receptor isoforms with different signaling potential. *The EMBO Journal,* 14**,** 3373-3384.

Fernández-Chacón, R., Wölfel, M., Nishimune, H., Tabares, L., Schmitz, F., Castellano-Muñoz, M., Rosenmund, C., Montesinos, M. L., Sanes, J. R., Schneggenburger, R. & Südhof, T. C. 2004. The synaptic vesicle protein CSPα prevents presynaptic degeneration. *Neuron,* 42**,** 237-251.

Fernandez-Funez, P., Nino-Rosales, M. L., De Gouyon, B., She, W.-C., Luchak, J. M., Martinez, P., Turiegano, E., Benito, J., Capovilla, M., Skinner, P. J., Mccall, A., Canal, I., Orr, H. T., Zoghbi, H. Y. & Botas, J. 2000. Identification of genes that modify ataxin-1-induced neurodegeneration. *Nature,* 408**,** 101-106.

Ferrer, I., López-Gonzalez, I., Carmona, M., Dalfó, E., Pujol, A. & Martínez, A. 2012. Neurochemistry and the non-motor aspects of PD. *Neurobiol Dis.,* 46**,** 508-26.

Fiesel, F. C., Voigt, A., Weber, S. S., Van Den Haute, C., Waldenmaier, A., Görner, K., Walter, M., Anderson, M. L., Kern, J. V., Rasse, T. M., Schmidt, T., Springer, W., Kirchner, R., Bonin, M., Neumann, M., Baekelandt, V., Alunni-Fabbroni, M., Schulz, J. B. & Kahle, P. J. 2010. Knockdown of transactive response DNA-binding protein (TDP-43) downregulates histone deacetylase 6. *The EMBO Journal,* 29**,** 209-221.

Finn, R., Kovács, A. D. & Pearce, D. A. 2011. Altered sensitivity of cerebellar granule cells to glutamate receptor overactivation in the Cln3Δex7/8-knock-in mouse model of juvenile neuronal ceroid lipofuscinosis. *Neurochemistry International,* 58**,** 648-655.

Finn, R., Kovács, A. D. & Pearce, D. A. 2012. Altered glutamate receptor function in the cerebellum of the Ppt1−/− mouse, a murine model of infantile neuronal ceroid lipofuscinosis. *Journal of Neuroscience Research,* 90**,** 367-375.

Fiston-Lavier, A. S., Singh, N. D., Lipatov, M. & Petrov, D. A. 2010. *Drosophila melanogaster* recombination rate calculator. *Gene,* 463**,** 18-20.

Fletcher, A. L., Pennesi, M. E., Harding, C. O., Weleber, R. G. & Gillingham, M. B. 2012. Observations regarding retinopathy in mitochondrial trifunctional protein deficiencies. *Mol Genet Metab.,* 106**,** 18-24.

Forno, L. S. 1996. Neuropathology of Parkinson disease. *J. Neuropathol. Exp. Neurol,* 55**,** 259–272.

Forrest, S., Chai, A., Sanhueza, M., Marescotti, M., Parry, K., Georgiev, A., Sahota, V., Mendez-Castro, R. & Pennetta, G. 2013. Increased levels of phosphoinositides cause neurodegeneration in a *Drosophila* model of amyotrophic lateral sclerosis. *Hum Mol Genet,* 22**,** 2689-704.

Fossale, E., Wolf, P., Espinola, J. A., Lubicz-Nawrocka, T., Teed, A. M., Gao, H., Rigamonti, D., Cattaneo, E., Macdonald, M. E. & Cotman, S. L. 2004. Membrane trafficking and mitochondrial abnormalities precede subunit c deposition in a cerebellar cell model of juvenile neuronal ceroid lipofuscinosis. *BMC Neurosci,* 5**,** 57.

Freeman, M. R. 1996. Reiterative use of the EGF receptor triggers differentiation of all cell types in the *Drosophila* eye. *Cell,* 87**,** 651-660.

Fuller, H. R., Graham, L. C., Llavero Hurtado, M. & Wishart, T. M. 2016. Understanding the molecular consequences of inherited muscular dystrophies: advancements through proteomic experimentation. *Expert Review of Proteomics,* 13**,** 659-671.

Fuller, H. R., Man, N. T., Lam Le, T., Shamanin, V. A., Androphy, E. J. & Morris, G. E. 2010. Valproate and bone loss: iTRAQ proteomics show that valproate reduces collagens and osteonectin in SMA cells. *J Proteome Res.,* 9**,** 4228-33.

Galione, A. 2015. A primer of NAADP-mediated Ca2+ signalling: From sea urchin eggs to mammalian cells. *Cell Calcium,* 58**,** 27-47.

Galione, A., Morgan, Anthony j., Arredouani, A., Davis, Lianne c., Rietdorf, K., Ruas, M. & Parrington, J. 2010. NAADP as an intracellular messenger regulating lysosomal calcium-release channels. *Biochemical Society Transactions,* 38**,** 1424-1431.

Gandal, M. J., Leppa, V., Won, H., Parikshak, N. N. & Geschwind, D. H. 2016. The road to precision psychiatry: translating genetics into disease mechanisms. *Nat Neurosci,* 19**,** 1397-1407.

Gao, H., Boustany, R. M., Espinola, J. A., Cotman, S. L., Srinidhi, L., Antonellis, K. A., Gillis, T., Qin, X., Liu, S., Donahue, L. R., Bronson, R. T., Faust, J. R., Stout, D., Haines, J. L., Lerner, T. J. & Macdonald, M. E. 2002. Mutations in a novel CLN6-encoded transmembrane protein cause variant neuronal ceroid lipofuscinosis in man and mouse. *Am J Hum Genet,* 70**,** 324-35.

Gardiner, R. M. 2002. Clinical features and molecular genetic basis of the neuronal ceroid lipofuscinoses. *Adv Neurol,* 89**,** 211-5.

Gillingwater, T. H., Ingham, C. A., Parry, K. E., Wright, A. K., Haley, J. E., Wishart, T. M., Arbuthnott, G. W. & Ribchester, R. R. 2006. Delayed synaptic degeneration in the CNS of Wlds mice after cortical lesion. *Brain,* 129**,** 1546-56.

Gillingwater, T. H. & Ribchester, R. R. 2001. Compartmental neurodegeneration and synaptic plasticity in the Wld s mutant mouse. *Journal of Physiology,* 534**,** 627–639.

Gillingwater, T. H., Thomson, D., Mack, T. G. A., Soffin, E. M., Mattison, R. J., Coleman, M. P. & Ribchester, R. R. 2002. Age-dependent synapse withdrawal at axotomised neuromuscular junctions in Wlds mutant and Ube4b/Nmnat transgenic mice. *The Journal of Physiology,* 543**,** 739-755.

Gillingwater, T. H. & Wishart, T. M. 2013. Mechanisms underlying synaptic vulnerability and degeneration in neurodegenerative disease. *Neuropathol Appl Neurobiol,* 39**,** 320-34.

Gilman, C. P., Chan, S. L., Guo, Z., Zhu, X., Greig, N. & Mattson, M. P. 2003. p53 is present in synapses where it mediates mitochondrial dysfunction and synaptic degeneration in response to DNA damage, and oxidative and excitotoxic insults. *NeuroMolecular Medicine,* 3**,** 159-172.

Glaser, R. L., Hickey, A. J., Chotkowski, H. L. & Chu-Lagraff, Q. 2003. Characterization of *Drosophila* palmitoyl-protein thioesterase 1. *Gene,* 312**,** 271-279.

Glenner, G. G. W., C. W. 1984. Alzheimer's disease: initial report of the purification and characterization of a novel cerebrovascular amyloid protein. *Biochem. Biophys. Res. Commun,* 120**,** 885–890.

Goebel, H. H. 1995. The neuronal ceroid-lipofuscinoses. *J. Child. Neurol,* 10**,** 424–437.

Goebel, H. H., Zeman, W. & Pilz, H. 1975. Significance of muscle biopsies in neuronal ceroid-lipofuscinoses. *J Neurol Neurosurg Psychiatry,* 38**,** 985-93.

Golabek, A. A., Kida, E., Walus, M., Kaczmarski, W., Michalewski, M. & Wisniewski, K. E. 2000. CLN3 protein regulates lysosomal pH and alters intracellular processing of Alzheimer's amyloid-beta protein precursor and cathepsin D in human cells. *Mol Genet Metab,* 70**,** 203-13.

Graham, L. C., Eaton, S. L., Brunton, P. J., Atrih, A., Smith, C., Lamont, D. J., Gillingwater, T. H., Pennetta, G., Skehel, P. & Wishart, T. M. 2017. Proteomic profiling of neuronal mitochondria reveals modulators of synaptic architecture. *Molecular Neurodegeneration,* 12**,** 77.

Greaves, J. & Chamberlain, L. H. 2007. Palmitoylation-dependent protein sorting. *J Cell Biol,* 176**,** 249-54.

Green, M. M. 2010. 2010: A century of *Drosophila* genetics through the prism of the white gene. *Genetics,* 184**,** 3-7.

Griffey, M., Bible, E., Vogler, C., Levy, B., Gupta, P., Cooper, J. & Sands, M. S. 2004. Adeno-associated virus 2-mediated gene therapy decreases autofluorescent storage material and increases brain mass in a murine model of infantile neuronal ceroid lipofuscinosis. *Neurobiol Dis,* 16**,** 360-9.

Griffey, M. A., Wozniak, D., Wong, M., Bible, E., Johnson, K., Rothman, S. M., Wentz, A. E., Cooper, J. D. & Sands, M. S. 2006. CNS-directed AAV2-mediated gene therapy ameliorates functional deficits in a murine model of infantile neuronal ceroid lipofuscinosis. *Mol Ther,* 13**,** 538-47.

Grundke-Iqbal, I., Iqbal, K., Quinlan, M., Tung, Y. C., Zaidi, M. S. & Wisniewski, H. M. 1986. Microtubule-associated protein tau. A component of Alzheimer paired helical filaments. *J Biol Chem.,* 261**,** 6084-9.

Gu, T., Zhao, T. & Hewes, R. S. 2014. Insulin signaling regulates neurite growth during metamorphic neuronal remodeling. *Biol Open,* 3**,** 81-93.

Guarneri, R., Russo, D., Cascio, C., D'agostino, S., Galizzi, G., Bigini, P., Mennini, T. & Guarneri, P. 2004. Retinal oxidation, apoptosis and age- and sex-differences in the mnd mutant mouse, a model of neuronal ceroid lipofuscinosis. *Brain Research,* 1014**,** 209-220.

Guest, P. C., Gottschalk, M. G. & Bahn, S. 2013. Proteomics: improving biomarker translation to modern medicine? *Genome Med,* 5**,** 17.

Guidetti, P., Charles, V., Chen, E.-Y., Reddy, P. H., Kordower, J. H., Whetsell, W. O., Schwarcz, R. & Tagle, D. A. 2001. Early degenerative changes in transgenic mice expressing mutant huntingtin involve dendritic abnormalities but no impairment of mitochondrial energy production. *Experimental Neurology,* 169**,** 340-350.

Gupta, P., Soyombo, A. A., Atashband, A., Wisniewski, K. E., Shelton, J. M., Richardson, J. A., Hammer, R. E. & Hofmann, S. L. 2001. Disruption of PPT1 or PPT2 causes neuronal ceroid lipofuscinosis in knockout mice. *Proc. Natl Acad. Sci. USA,* 98**,** 13566–13571.

Gustafson, K. & Boulianne, G. L. 1996. Distinct expression patterns detected within individual tissues by the GAL4 enhancer trap technique. *Genome,* 39**,** 174-182.

Gustavsson, A., Svensson, M., Jacobi, F., Allgulander, C., Alonso, J., Beghi, E., Dodel, R., Ekman, M., Faravelli, C., Fratiglioni, L., Gannon, B., Jones, D. H., Jennum, P., Jordanova, A., Jönsson, L., Karampampa, K., Knapp, M., Kobelt, G., Kurth, T., Lieb, R., Linde, M., Ljungcrantz, C., Maercker, A., Melin, B., Moscarelli, M., Musayev, A., Norwood, F., Preisig, M., Pugliatti, M., Rehm, J., Salvador-Carulla, L., Schlehofer, B., Simon, R., Steinhausen, H.-C., Stovner, L. J., Vallat, J.-M., Den Bergh, P. V., Van Os, J., Vos, P., Xu, W., Wittchen, H.-U., Jönsson, B. & Olesen, J. 2011. Cost of disorders of the brain in Europe 2010. *European Neuropsychopharmacology,* 21**,** 718-779.

Gylys, K. H., Fein, J. A., Wiley, D. J. & Cole, G. M. 2004. Rapid annexin-V labeling in synaptosomes. *Neurochemistry International,* 44**,** 125-131.

Haass, C. & Selkoe, D. J. 2007. Soluble protein oligomers in neurodegeneration: lessons from the Alzheimer's amyloid beta-peptide. *Nat Rev Mol Cell Biol,* 8.

Halder, G., Callaerts, P. & Gehring, W. 1995. Induction of ectopic eyes by targeted expression of the eyeless gene in *Drosophila*. *Science,* 267**,** 1788-1792.

Haltia, M. 2003. The neuronal ceroid-lipofuscinoses. *J Neuropathol Exp Neurol.,* 62**,** 1-13.

Hamilton, G. & Gillingwater, T. H. 2013. Spinal muscular atrophy: going beyond the motor neuron. *Trends Mol Med.,* 19**,** 40-50.

Hanson, I. M. 2001. Mammalian homologues of the *Drosophila* eye specification genes. *Seminars in Cell & Developmental Biology,* 12**,** 475-484.

Harris, Julia j., Jolivet, R. & Attwell, D. 2012. Synaptic energy use and supply. *Neuron,* 75**,** 762-777.

Hassing, L. B., Dahl, A. K., Thorvaldsson, V., Berg, S., Gatz, M., Pedersen, N. L. & Johansson, B. 2009. Overweight in midlife and risk of dementia: a 40-year follow-up study. *Int J Obes,* 33**,** 893-898.

Hay, M., Thomas, D. W., Craighead, J. L., Economides, C. & Rosenthal, J. 2014. Clinical development success rates for investigational drugs. *Nat Biotech,* 32**,** 40-51.

Heinonen, O., Salonen, T., Jalanko, A., Peltonen, L. & Copp, A. 2000. CLN-1 and CLN-5, genes for infantile and variant late infantile neuronal ceroid lipofuscinoses, are expressed in the embryonic human brain. *J Comp Neurol. ,* 426**,** 406-12.

Heisenberg, M. & Wolf, R. 1984. Vision in *Drosophila*. *Berlin: Springer- Verlag.*

Herrmann, P., Druckrey-Fiskaaen, C., Kouznetsova, E., Heinitz, K., Bigl, M., Cotman, S. L. & Schliebs, R. 2008. Developmental impairments of select neurotransmitter systems in brains of Cln3Δex7/8 knock-in mice, an animal model of juvenile neuronal ceroid lipofuscinosis. *Journal of Neuroscience Research,* 86**,** 1857-1870.

Hersheson , J., Burke, D., Clayton, R., Anderson, G., Ts, J., Mills, P., Wood, N. W., Gissen, P., Clayton, P. T., Fearnley, J., Mole, S. E. & Houlden, H. 2014. Cathepsin D deficiency causes juvenile-onset ataxia and distinctive muscle pathology. *Neurology,* 83**,** 1873–1875.

Hershko, A. & Ciechanover, A. 1998. The ubiquitin system. *Annual Review of Biochemistry,* 67**,** 425-479.

Herskowitz, J. H., Seyfried, N. T., Gearing, M., Kahn, R. A., Peng, J., Levey, A. I. & Lah, J. J. 2011. Rho kinase II phosphorylation of the lipoprotein receptor LR11/SORLA alters amyloid-beta production. *J Biol Chem,* 286**,** 6117-27.

Hersrud, S. L., Geraets, R. D., Weber, K. L., Chan, C. H. & Pearce, D. A. 2016. Plasma biomarkers for neuronal ceroid lipofuscinosis. *FEBS J,* 283**,** 459-71.

Heywood, W. E., Galimberti, D., Bliss, E., Sirka, E., Paterson, R. W., Magdalinou, N. K., Carecchio, M., Reid, E., Heslegrave, A., Fenoglio, C., Scarpini, E., Schott, J. M., Fox, N. C., Hardy, J., Bhatia, K., Heales, S., Sebire, N. J., Zetterberg, H. & Mills, K. 2015. Identification of novel CSF biomarkers for neurodegeneration and their validation by a high-throughput multiplexed targeted proteomic assay. *Mol Neurodegener,* 10**,** 64.

Hickey, A. J., Chotkowski, H. L., Singh, N., Ault, J. G., Korey, C. A., Macdonald, M. E. & Glaser, R. L. 2006. Palmitoyl-protein thioesterase 1 deficiency in *Drosophila melanogaster* causes accumulation of abnormal storage material and reduced life span. *Genetics,* 172**,** 2379-90.

Hinsenkamp, I., Schulz, S., Roscher, M., Suhr, A. M., Meyer, B., Munteanu, B., Fuchser, J., Schoenberg, S. O., Ebert, M. P., WäNgler, B., Hopf, C. & Burgermeister, E. 2016. Inhibition of rho-associated kinase 1/2 attenuates tumor growth in murine gastric cancer. *Neoplasia,* 18**,** 500-11.

Hirth, F. 2010. *Drosophila* melanogaster in the study of human neurodegeneration. *CNS & Neurological Disorders - Drug Targets,* 9**,** 504-523.

Hobert, J. A. & Dawson, G. 2007. A novel role of the Batten disease gene CLN3: association with BMP synthesis. *Biochem Biophys Res Commun,* 358**,** 111-6.

Holopainen, J. M., Saarikoski, J., Kinnunen, P. K. & Järvelä, I. 2001. Elevated lysosomal pH in neuronal ceroid lipofuscinoses (NCLs). *Eur J Biochem.,* 268**,** 5851-6.

Hoyer, S. 1982a. The abnormally aged brain. Its blood flow and oxidative metabolism. A review — Part II. *Archives of Gerontology and Geriatrics,* 1**,** 195-207.

Hoyer, S. 1982b. The young-adult and normally aged brain its blood flow and oxidative metabolism. A review - part I. *Archives of Gerontology and Geriatrics,* 1**,** 101-116.

Hu, J., Lu, J. Y., Wong, A. M., Hynan, L. S., Birnbaum, S. G., Yilmaz, D. S., Streit, B. M., Lenartowicz, E. M., Thompson, T. C., Cooper, J. D. & Hofmann, S. L. 2012. Intravenous high-dose enzyme replacement therapy with recombinant palmitoyl-protein thioesterase reduces visceral lysosomal storage and modestly prolongs survival in a preclinical mouse model of infantile neuronal ceroid lipofuscinosis. *Mol Genet Metab,* 107**,** 213-21.

Hu, Y., Flockhart, I., Vinayagam, A., Bergwitz, C., Berger, B., Perrimon, N. & Mohr, S. E. 2011. An integrative approach to ortholog prediction for disease-focused and other functional studies. *BMC Bioinformatics* 12:357.

Huang, D. W., Sherman, B. T. & Lempicki, R. A. 2009a. Bioinformatics enrichment tools: paths toward the comprehensive functional analysis of large gene lists. *Nucleic Acids Res.,* 37**,** 1-13.

Huang, D. W., Sherman, B. T. & Lempicki, R. A. 2009b. Systematic and integrative analysis of large gene lists using DAVID Bioinformatics Resources. *Nature Protoc.,* 4**,** 44-57.

Ibdah, J. A., Paul, H., Zhao, Y., Binford, S., Salleng, K., Cline, M., Matern, D., Bennett, M. J., Rinaldo, P. & Strauss, A. 2001. Lack of mitochondrial trifunctional protein in mice causes neonatal hypoglycemia and sudden death. *J Clin Invest.,* 107**,** 1403-9.

Imlach, Wendy l., Beck, Erin s., Choi, Ben j., Lotti, F., Pellizzoni, L. & Mccabe, Brian d. 2012. SMN is required for sensory-motor circuit function in *Drosophila*. *Cell,* 151**,** 427-439.

Itoh, K., Nakamura, K., Iijima, M. & Sesaki, H. 2013. Mitochondrial dynamics in neurodegeneration. *Trends in cell biology,* 23**,** 64-71.

Ivanes, F., Faccenda, D., Gatliff, J., Ahmed, A. A., Cocco, S., Cheng, C. H. K., Allan, E., Russell, C., Duchen, M. R. & Campanella, M. 2014. The compound BTB06584 is an IF1-dependent selective inhibitor of the mitochondrial F1Fo-ATPase. *British Journal of Pharmacology,* 171**,** 4193-4206.

Jackson, G. R., Salecker, I., Dong, X., Yao, X., Arnheim, N., Faber, P. W., Macdonald, M. E. & Zipursky, S. L. 1998. Polyglutamine-expanded human Huntingtin transgenes induce degeneration of *Drosophila* photoreceptor neurons. *Neuron,* 21**,** 633-642.

Jadav, R. H., Sinha, S., Yasha, T. C., Aravinda, H., Gayathri, N., Rao, S., Bindu, P. S. & Satishchandra, P. 2014. Clinical, electrophysiological, imaging, and ultrastructural description in 68 patients with neuronal ceroid lipofuscinoses and its subtypes. *Pediatr Neurol,* 50**,** 85-95.

Jalanko, A., Vesa, J., Manninen, T., Von Schantz, C., Minye, H., Fabritius, A. L., Salonen, T., Rapola, J., Gentile, M., Kopra, O. & Peltonen, L. 2005. Mice with Ppt1Deltaex4 mutation replicate the INCL phenotype and show an inflammation-associated loss of interneurons. *Neurobiol Dis,* 18**,** 226-41.

Järvelä, I., Autt, I. T., Lamminranta, S., Aberg, L., Raininko, R. & Santavuori, P. 1997. Clinical and magnetic resonance imaging findings in Batten disease: analysis of the major mutation (1.02-kb deletion). *Ann Neurol.,* 42**,** 799-802.

Järvelä I, S. M., Rantamäki T, Olkkonen Vm, Carpén O, Peltonen L, Jalanko 1998. Biosynthesis and intracellular targeting of the CLN3 protein defective in Batten disease. *Hum Mol Genet.,* 7**,** 85-90.

Jensen, L. J., Kuhn, M., Stark, M., Chaffron, S., Creevey, C., Muller, J., Doerks, T., Julien, P., Roth, A., Simonovic, M., Bork, P. & Von Mering, C. 2009. STRING 8—a global view on proteins and their functional interactions in 630 organisms. *Nucleic Acids Research,* 37**,** D412-D416.

Johansen, J., Halpern, M., Johansen, K. & Keshishian, H. 1989. Stereotypic morphology of glutamatergic synapses on identified muscle cells of *Drosophila* larvae. *The Journal of Neuroscience,* 9**,** 710-725.

Jolly, R. D., Brown, S., Das, A. M. & Walkley, S. U. 2002. Mitochondrial dysfunction in the neuronal ceroid-lipofuscinoses (Batten disease). *Neurochemistry International,* 40 565–57.

Jolly, R. D. & Walkley, S. U. 1997. Lysosomal storage diseases of animals: an essay in comparative pathology. *Veterinary Pathology,* 34**,** 527-548.

Jones, J. P., Nicholas, H. J. & Ramsey, R. B. 1975. Rate of sterol formation by rat brain glia and neurons in vitro and in vivo. *Journal of Neurochemistry,* 24**,** 123-126.

Jones, M. A., Amr, S., Ferebee, A., Huynh, P., Rosenfeld, J. A., Miles, M. F., Davies, A. G., Korey, C. A., Warrick, J. M., Shiang, R., Elsea, S. H., Girirajan, S. & Grotewiel, M. 2014. Genetic studies in *Drosophila* and humans support a model for the concerted function of CISD2, PPT1 and CLN3 in disease. *Biology Open,* 3**,** 342-352.

K.R. Smith, J. D., S. Franceschetti, S. Carpenter, L. Canafoglia, M. Morbin, G. Rossi, D. Pareyson, S.E. Mole, J.F. Staropoli, K.B. Sims, J. Lewis, W.L. Lin, D.W. Dickson, H.H. Dahl, M. Bahlo, S.F. Berkovi 2012. Strikingly different clinicopathological phenotypes determined by progranulin-mutation dosage. *Am. J. Hum. Genet.,* 90**,** 1102–1107.

Kaltenbach, L. S., Romero, E., Becklin, R. R., Chettier, R., Bell, R., Phansalkar, A., Strand, A., Torcassi, C., Savage, J., Hurlburt, A., Cha, G. H., Ukani, L., Chepanoske, C. L., Zhen, Y., Sahasrabudhe, S., Olson, J., Kurschner, C., Ellerby, L. M., Peltier, J. M., Botas, J. & Hughes, R. E. 2007. Huntingtin interacting proteins are genetic modifiers of neurodegeneration. *PLoS Genet,* 3**,** e82.

Kamijo, T., Aoyama, T., Komiyama, A. & Hashimoto, T. 1994. Structural analysis of cDNAs for subunits of human mitochondrial fatty acid β-oxidation trifunctional protein. *Biochem. Biophys. Res. Commun.,* 199**,** 818–825.

Kang, S., Seo, J. H., Heo, T. H. & Kim, S. J. 2013. Batten disease is linked to altered expression of mitochondria-related metabolic molecules. *Neurochem Int,* 62**,** 931-5.

Kariya, S., Park, G.-H., Maeno-Hikichi, Y., Leykekhman, O., Lutz, C., Arkovitz, M. S., Landmesser, L. T. & Monani, U. R. 2008. Reduced SMN protein impairs maturation of the neuromuscular junctions in mouse models of spinal muscular atrophy. *Human Molecular Genetics,* 17**,** 2552-2569.

Katz, M. L., Gao, C. L., Prabhakaram, M., Shibuya, H., Liu, P. C. & Johnson, G. S. 1997. Immunochemical localization of the Batten disease (CLN3) protein in retina. *Investigative Ophthalmology & Visual Science,* 38**,** 2375-2386.

Katz, M. L., Shibuya, H., Liu, P. C., Kaur, S., Gao, C. & Johnson, G. S. 1999. A mouse gene knockout model for juvenile ceroid-lipofuscinosis (Batten disease). *J Neurosci Res.,* 57**,** 551-6.

Kawas, C. H., Corrada, M. M., Brookmeyer, R., Morrison, A., Resnick, S. M., Zonderman, A. B. & Arenberg, D. 2003. Visual memory predicts Alzheimer's disease more than a decade before diagnosis. *Neurology,* 60**,** 1089-1093.

Kay, G. W., Verbeek, M. M., Furlong, J. M., Willemsen, M. A. & Palmer, D. N. 2009. Neuropeptide changes and neuroactive amino acids in CSF from humans and sheep with neuronal ceroid lipofuscinoses (NCLs, Batten disease). *Neurochem Int,* 55**,** 783-8.

Keshishian, H., Broadie, K., Chiba, A. & Bate, M. 1996. The drosophila neuromuscular junction- a model system for studying synaptic development and function. *Annu Rev Neurosci.,* 19**,** 545-75.

Khan, U., Liu, L., Provenzano, F., Berman, D., Profaci, C., Sloan, R., Mayeux, R., Duff, K. & Small, S. 2014. Molecular drivers and cortical spread of lateral entorhinal cortex dysfunction in preclinical Alzheimer's disease. *Nat Neurosci. ,* 17**,** 304–11.

Khurana, V., Tardiff, D. F., Chung, C. Y. & Lindquist, S. 2015. Toward stem cell-based phenotypic screens for neurodegenerative diseases. *Nat Rev Neurol,* 11**,** 339-50.

Kielar, C., Maddox, L., Bible, E., Pontikis, C. C., Macauley, S. L., Griffey, M. A., Wong, M., Sands, M. S. & Cooper, J. D. 2007. Successive neuron loss in the thalamus and cortex in a mouse model of infantile neuronal ceroid lipofuscinosis. *Neurobiol Dis,* 25**,** 150-62.

Kielar, C., Wishart, T. M., Palmer, D. A., Dihanich, S., Wong, A. M., Macauley, S. L., Chan, C., Sands, M. S., Pearce, D. A., Cooper, J. D. & Gillingwater, T. H. 2009. Molecular correlates of axonal and synaptic pathology in mouse models of Batten disease. *Hum Mol Genet,* 18**,** 4066-80.

Kielar C, W. T., Palmer a, Dihanich S, Wong Am, Macauley Sl, Chan Ch, Sands Ms, Pearce Da, Cooper Jd, Gillingwater Th 2009. Molecular correlates of axonal and synaptic pathology in mouse models of Batten disease. *Hum Mol Genet,* 1;18(21)**,** 4066- 80.

Kim, S.-J., Zhang, Z., Saha, A., Sarkar, C., Zhao, Z., Xu, Y. & Mukherjee, A. B. 2010. Omega-3 and omega-6 fatty acids suppress ER- and oxidative stress in cultured neurons and neuronal progenitor cells from mice lacking PPT1. *Neuroscience Letters,* 479**,** 292-296.

Kim, S. H., Shi, Y., Hanson, K. A., Williams, L. M., Sakasai, R., Bowler, M. J. & Tibbetts, R. S. 2008a. Potentiation of ALS-associated TDP-43 aggregation by the proteasome-targeting factor, Ubiquilin 1. *J Biol Chem,* 284.

Kim, S. J., Zhang, Z., Lee, Y. C. & Mukherjee, A. B. 2006. Palmitoyl-protein thioesterase-1 deficiency leads to the activation of caspase-9 and contributes to rapid neurodegeneration in INCL. *Hum Mol Genet,* 15**,** 1580-6.

Kim, S. J., Zhang, Z., Sarkar, C., Tsai, P. C., Lee, Y. C., Dye, L. & Mukherjee, A. B. 2008b. Palmitoyl protein thioesterase-1 deficiency impairs synaptic vesicle recycling at nerve terminals, contributing to neuropathology in humans and mice. *J Clin Invest,* 118**,** 3075-86.

Kitzmuller, C., Haines, R. L., Codlin, S., Cutler, D. F. & Mole, S. E. 2008. A function retained by the common mutant CLN3 protein is responsible for the late onset of juvenile neuronal ceroid lipofuscinosis. *Hum Mol Genet,* 17**,** 303-12.

Kivipelto, M., Ngandu, T., Fratiglioni, L. & Et Al. 2005. Obesity and vascular risk factors at midlife and the risk of dementia and alzheimer disease. *Archives of Neurology,* 62**,** 1556-1560.

Klapstein, G. J., Fisher, R. S., Zanjani, H., Cepeda, C., Jokel, E. S., Chesselet, M.-F. & Levine, M. S. 2001. Electrophysiological and morphological changes in striatal spiny neurons in R6/2 Huntington's Disease transgenic mice. *Journal of Neurophysiology,* 86**,** 2667-2677.

Koch, S., Molchanova, S. M., Wright , A. K., Edwards, A., Cooper, J. D., Taira, T., Gillingwater, T. H. & Tyynelä, J. J. 2011. Morphologic and functional correlates of synaptic pathology in the cathepsin D knockout mouse model of congenital neuronal ceroid lipofuscinosis. *Neuropathol Exp Neurol,* 70**,** 1089–96.

Kocher, T. & Superti-Furga, G. 2007. Mass spectrometry-based functional proteomics: from molecular machines to protein networks. *Nat Meth,* 4**,** 807-815.

Koester, H. J. & Johnston, D. 2005. Target cell-dependent normalization of transmitter release at neocortical synapses. *Science,* 308**,** 863-866.

Kohler, R. E. 1994. Lords of the Fly: Drosophila genetics and the experimental life. *Univ. Chicago Press, Chicago, Illinois,* 15.

Koike, M., Shibata, M., Waguri, S., Yoshimura, K., Tanida, I., Kominami, E., Gotow, T., Peters, C., Von Figura, K., Mizushima, N., Saftig, P. & Uchiyama, Y. 2005. Participation of autophagy in storage of lysosomes in neurons from mouse models of neuronal ceroid-lipofuscinoses (Batten Disease). *The American Journal of Pathology,* 167**,** 1713-1728.

Kolikova, J., Afzalov, R., Surin, A., Lehesjoki, A. E. & Khiroug, L. 2011. Deficient mitochondrial Ca(2+) buffering in the Cln8(mnd) mouse model of neuronal ceroid lipofuscinosis. *Cell Calcium,* 50**,** 491-501.

Kollmann, K., Uusi-Rauva, K., Scifo, E., Tyynela, J., Jalanko, A. & Braulke, T. 2013. Cell biology and function of neuronal ceroid lipofuscinosis-related proteins. *Biochim Biophys Acta,* 1832**,** 1866-81.

Konsolaki, M. 2013. Fruitful research: drug target discovery for neurodegenerative diseases in *Drosophila*. *Expert Opinion on Drug Discovery,* 8**,** 1503-1513.

Korey, C. A. & Macdonald, M. E. 2003. An over-expression system for characterizing Ppt1 function in *Drosophila*. *BMC Neurosci.,* 20**,** 30.

Kousi, M., Lehesjoki, A.-E. & Mole, S. E. 2012. Update of the mutation spectrum and clinical correlations of over 360 mutations in eight genes that underlie the neuronal ceroid lipofuscinoses. *Hum. Mutat.,* 33**,** 42–63.

Kraemer, B. C., Schuck, T., Wheeler, J. M., Robinson, L. C., Trojanowski, J. Q., Lee, V. M. & Schellenberg, G. D. 2010. Loss of murine TDP-43 disrupts motor function and plays an essential role in embryogenesis. *Acta Neuropathol,* 119.

Krasnianski, A., Deschauer, M., Neudecker, S., Gellerich, F. N., Müller, T., Schoser, B. G., Krasnianski, M. & Zierz, S. 2005. Mitochondrial changes in skeletal muscle in amyotrophic lateral sclerosis and other neurogenic atrophies. *Brain,* 128**,** 1870-1876.

Kuhl, T. G., Dihanich, S., Wong, A. M. & Cooper, J. D. 2013. Regional brain atrophy in mouse models of neuronal ceroid lipofuscinosis: a new rostrocaudal perspective. *J Child Neurol,* 28**,** 1117-22.

Kumar, J. P. & Moses, K. 2001. Expression of evolutionarily conserved eye specification genes during *Drosophila* embryogenesis. *Development Genes and Evolution,* 211**,** 406-414.

Kuronen, M., Lehesjoki, A. E., Jalanko, A., Cooper, J. D. & Kopra, O. 2012. Selective spatiotemporal patterns of glial activation and neuron loss in the sensory thalamocortical pathways of neuronal ceroid lipofuscinosis 8 mice. *Neurobiol Dis,* 47**,** 444-57.

Kwon, J. M., H. Adams, Rothberg, P. G., Augustine, E. F., Marshall, F. J., Deblieck, E. A., Vierhile, A., Beck, C. A., Newhouse, N. J., Cialone, J., Levy, E., Ramirez-Montealegre, D., Mink, J. W., Dure, L. S., Rose, K. R. & Mink, J. W. 2011. Quantifying physical decline in juvenile neuronal ceroid lipofuscinosis (Batten disease). *Neurology,* 77**,** 1801-7.

La Cognata, V., Morello, G., D'agata, V. & Cavallaro, S. 2017. Copy number variability in Parkinson's disease: assembling the puzzle through a systems biology approach. *Human Genetics,* 136**,** 13-37.

Lahey, T., Gorczyca, M., Jia, X.-X. & Budnik, V. 1994. The *Drosophila* tumor suppressor gene dlg is required for normal synaptic bouton structure. *Neuron,* 13**,** 823-835.

Lai, J. C. K., Walsh, J. M., Dennis, S. C. & Clark, J. B. 1977. Synaptic and non-synaptic mitochondria from rat brain: isolation and characterization. *Journal of Neurochemistry,* 28**,** 625-631.

Lebrun, A. H., Moll-Khosrawi, P., Pohl, S., Makrypidi, G., Storch, S., Kilian, D., Streichert, T., Otto, B., Mole, S. E., Ullrich, K., Cotman, S., Kohlschutter, A., Braulke, T. & Schulz, A. 2011. Analysis of potential biomarkers and modifier genes affecting the clinical course of CLN3 disease. *Mol Med,* 17**,** 1253-61.

Lee, S. H., Kim, K.-R., Ryu, S.-Y., Son, S., Hong, H. S., Mook-Jung, I., Lee, S.-H. & Ho, W.-K. 2012. Impaired short-term plasticity in mossy fiber synapses caused by mitochondrial dysfunction of dentate granule cells is the earliest synaptic deficit in a mouse model of Alzheimer's Disease. *The Journal of Neuroscience,* 32**,** 5953-5963.

Lee, W.-C. M., Yoshihara, M. & Littleton, J. T. 2004. Cytoplasmic aggregates trap polyglutamine-containing proteins and block axonal transport in a *Drosophila* model of Huntington's disease. *Proceedings of the National Academy of Sciences of the United States of America,* 101**,** 3224-3229.

Lehtovirta, M., Kyttälä, A., Eskelinen, E. L., Hess, M., Heinonen, O. & Jalanko, A. 2001. Palmitoyl protein thioesterase (PPT) localizes into synaptosomes and synaptic vesicles in neurons: implications for infantile neuronal ceroid lipofuscinosis (INCL). *Hum Mol Genet.,* 10**,** 69-75.

Levin, S. W., Baker, E. H., Zein, W. M., Zhang, Z., Quezado, Z. M., Miao, N., Gropman, A., Griffin, K. J., Bianconi, S., Chandra, G., Khan, O. I., Caruso, R. C., Liu, A. & Mukherjee, A. B. 2014. Oral cysteamine bitartrate and N-acetylcysteine for patients with infantile neuronal ceroid lipofuscinosis: a pilot study,. *The Lancet Neurology,* 13**,** 777–787.

Lewandowski, N. M., Bordelon, Y., Brickman, A. M., Angulo, S., Khan, U., Muraskin, J., Griffith, E. Y., Wasserman, P., Menalled, L., Vonsattel, J. P., Marder, K., Small, S. A. & Moreno, H. 2013. Regional vulnerability in Huntington's disease: fMRI-guided molecular analysis in patients and a mouse model of disease. *Neurobiol Dis,* 52**,** 84-93.

Li, J.-Y., Plomann, M. & Brundin, P. 2003. Huntington's disease: a synaptopathy? *Trends in Molecular Medicine,* 9**,** 414-420.

Li, W. Z., Li, S. L., Zheng, H. Y., Zhang, S. P. & Xue, L. 2012. A broad expression profile of the GMR-GAL4 driver in *Drosophila melanogaster*. *Genet Mol Res.,* 11**,** 1997-2002.

Licchetta, L., Bisulli, F., Fietz, M., Valentino, M. L., Morbin, M., Mostacci, B., Oliver, K. L., Berkovic, S. F. & Tinuper, P. 2015. A novel mutation af Cln3 associated with delayed-classic juvenile ceroid lipofuscinois and autophagic vacuolar myopathy. *Eur J Med Genet,* 58**,** 540-4.

Lima, S. Q. & Miesenböck, G. 2005. Remote control of behavior through genetically targeted photostimulation of neurons. *Cell,* 121**,** 141-152.

Ling, K. K. Y., Lin, M.-Y., Zingg, B., Feng, Z. & Ko, C.-P. 2010. Synaptic defects in the spinal and neuromuscular circuitry in a mouse model of spinal muscular atrophy. *PLOS ONE,* 5**,** e15457.

Lipton, A. M., Cullum, C., Satumtira, S. & Et Al. 2001. Contribution of asymmetric synapse loss to lateralizing clinical deficits in frontotemporal dementias. *Archives of Neurology,* 58**,** 1233-1239.

Llavero Hurtado, M., Fuller, H. R., Wong, A. M. S., Eaton, S. L., Gillingwater, T. H., Pennetta, G., Cooper, J. D. & Wishart, T. M. 2017. Proteomic mapping of differentially vulnerable pre-synaptic populations identifies regulators of neuronal stability in vivo. *Scientific Reports,* 7**,** 12412.

Loupatty, F. J., Clayton, P. T., Ruiter, J. P., Ofman, R., Ijlst, L., Brown, G. K., Thorburn, D. R., Harris, R. A., Duran, M., Desousa, C., Krywawych, S., Heales, S. J. & Wanders, R. J. 2007. Mutations in the gene encoding 3-hydroxyisobutyryl-CoA hydrolase results in progressive infantile neurodegeneration. *Am J Hum Genet,* 80**,** 195-9.

Lu, H., Ash, R. T., He, L., Kee, S. E., Wang, W., Yu, D., Hao, S., Meng, X., Ure, K., Ito-Ishida, A., Tang, B., Sun, Y., Ji, D., Tang, J., Arenkiel, B. R., Smirnakis, S. M. & Zoghbi, H. Y. 2016. Loss and Gain of MeCP2 Cause similar hippocampal circuit dysfunction that is rescued by deep brain stimulation in a rett syndrome mouse model. *Neuron,* 91**,** 739-47.

Lu, J. Y., Nelvagal, H. R., Wang, L., Birnbaum, S. G., Cooper, J. D. & Hofmann, S. L. 2015. Intrathecal enzyme replacement therapy improves motor function and survival in a preclinical mouse model of infantile neuronal ceroid lipofuscinosis. *Mol Genet Metab,* 116**,** 98-105.

Lu, Y., Ferris, J. & Gao, F.-B. 2009. Frontotemporal dementia and amyotrophic lateral sclerosis-associated disease protein TDP-43 promotes dendritic branching. *Molecular Brain,* 2**,** 30.

Luiro, K., Kopra, O., Blom, T., Gentile, M., Mitchison, H. M., Hovatta, I., Tornquist, K. & Jalanko, A. 2006. Batten disease (JNCL) is linked to disturbances in mitochondrial, cytoskeletal, and synaptic compartments. *J Neurosci Res,* 84**,** 1124-38.

Luiro, K., Kopra, O., Lehtovirta, M. & Jalanko, A. 2001. CLN3 protein is targeted to neuronal synapses but excluded from synaptic vesicles: new clues to Batten disease. . *Hum Mol Genet.,* 10**,** 2123-31.

Luiro, K., Yliannala, K., Ahtiainen, L., Maunu, H., Jarvela, I., Kyttala, A. & Jalanko, A. 2004. Interconnections of CLN3, Hook1 and Rab proteins link Batten disease to defects in the endocytic pathway. *Hum Mol Genet,* 13**,** 3017-27.

Ly, C. V. & Verstreken, P. 2006. Mitochondria at the synapse. *The Neuroscientist,* 12**,** 291-299.

Lyly, A., Marjavaara, S. K., Kyttala, A., Uusi-Rauva, K., Luiro, K., Kopra, O., Martinez, L. O., Tanhuanpaa, K., Kalkkinen, N., Suomalainen, A., Jauhiainen, M. & Jalanko, A. 2008. Deficiency of the INCL protein Ppt1 results in changes in ectopic F1-ATP synthase and altered cholesterol metabolism. *Hum Mol Genet,* 17**,** 1406-17.

Macauley, S. L., Pekny, M. & Sands, M. S. 2011. The role of attenuated astrocyte activation in infantile neuronal ceroid lipofuscinosis. *J Neurosci,* 31**,** 15575-85.

Macauley, S. L., Roberts, M. S., Wong, A. M., Mcsloy, F., Reddy, A. S., Cooper, J. D. & Sands, M. S. 2012. Synergistic effects of central nervous system-directed gene therapy and bone marrow transplantation in the murine model of infantile neuronal ceroid lipofuscinosis. *Ann Neurol,* 71**,** 797-804.

Macauley, S. L., Wozniak, D. F., Kielar, C., Tan, Y., Cooper, J. D. & Sands, M. S. 2009. Cerebellar pathology and motor deficits in the palmitoyl protein thioesterase 1-deficient mouse. *Exp Neurol,* 217**,** 124-35.

March, P. A., Wurzelmann, S. & Walkley, S. U. 1995. Morphological alterations in neocortical and cerebellar GABAergic neurons in a canine model of juvenile Batten disease. *Am J Med Genet.,* 57**,** 204-12.

Marchetti, S. & Schellens, J. H. M. 2007. The impact of FDA and EMEA guidelines on drug development in relation to Phase 0 trials. *Br J Cancer,* 97**,** 577-581.

Margraf, L., Boriack, R., Routheut, A., Cuppen, I., Alhilali, L., Bennett, C. & Bennett, M. 1999. Tissue expression and subcellular localization of CLN3, the Batten disease protein. *Mol Genet Metab. 1999 Apr;66(4):,* 66**,** 283-9.

Marshall, F. J., De Blieck, E. A., Mink, J. W., Dure, L. S., Adams, H., Messing, S., Rothberg, P. G., Levy, E., Mcdonough, T., Deyoung, J., Wang, M., Ramirez-Montealegre, D., Kwon, J. M. & Pearce, D. A. 2005. A clinical rating scale for Batten disease: reliable and relevant for clinical trials. *Neurology,* 65**,** 275-9.

Martinez-Arias, A. 2008. *Drosophila melanogaster* and the development of biology in the 20th century. *Methods Mol Biol.,* 420**,** 1-25.

Maselli, R. A., Wollman, R. L., Leung, C., Distad, B., Palombi, S., Richman, D. P., Salazar-Grueso, E. F. & Roos, R. P. 1993. Neuromuscular transmission in amyotrophic lateral sclerosis. *Muscle & Nerve,* 16**,** 1193-1203.

Masumoto, A., Mohri, M., Shimokawa, H., Urakami, L., Usui, M. & Takeshita, A. 2002. Suppression of coronary artery spasm by the Rho-kinase inhibitor fasudil in patients with vasospastic angina. *Circulation,* 105**,** 1545-7.

Mattson, M. P. 2000. Apoptotic and anti-apoptotic synaptic signaling mechanisms. *Brain Pathology,* 10**,** 300-312.

Mattson, M. P., Keller, J. N. & Begley, J. G. 1998. Evidence for synaptic apoptosis. *Experimental Neurology,* 153**,** 35-48.

Mccue, H. V., Chen, X., Barclay, J. W., Morgan, A. & Burgoyne, R. D. 2015. Expression profile of a Caenorhabditis elegans model of adult neuronal ceroid lipofuscinosis reveals down regulation of ubiquitin E3 ligase components. *Sci Rep. 2015 Sep 23;5:14392. doi: 10.1038/srep14392.,* 5.

Mcgorum, B. C., Pirie, R. S., Eaton, S. L., Keen, J. A., Cumyn, E. M., Arnott, D. M., Chen, W., Lamont, D. J., Graham, L. C., Llavero Hurtado, M., Pemberton, A. & Wishart, T. M. 2015. Proteomic profiling of cranial (superior) cervical ganglia reveals beta-amyloid and ubiquitin proteasome system perturbations in an equine multiple system neuropathy. *Mol Cell Proteomics,* 14**,** 3072-86.

Meek, P. D., Mckeithan, K. & Schumock, G. T. 1998. Economic considerations in Alzheimer's disease. *Pharmacotherapy.,* 2 Pt 2**,** 68-73; discussion 79-82.

Mehregan, H., Najmabadi, H. & Kahrizi, K. 2016. Genetic studies in intellectual disability and behavioral impairment. *Arch Iran Med.,* 19**,** 363-75.

Meinertzhagen, I. A. 1989. Fly photoreceptor synapses: Their development, evolution, and plasticity. *Journal of Neurobiology,* 20**,** 276-294.

Meinertzhagen, I. A. & Sorra, K. E. 2001. Synaptic organization in the fly's optic lamina: few cells, many synapses and divergent microcircuits. *Prog Brain Res,* 131.

Meissner, W. G., Frasier, M., Gasser, T., Goetz, C. G., Lozano, A., Piccini, P., Obeso, J. A., Rascol, O., Schapira, A., Voon, V., Weiner, D. M., Tison, F. & Bezard, E. 2011. Priorities in Parkinson's disease research. *Nat Rev Drug Discov,* 10**,** 377-393.

Meléndez, A. & Neufeld, T. P. 2008. The cell biology of autophagy in metazoans: a developing story. *Development,* 135**,** 2347-2360.

Meng, Y., Sohar, I., Wang, L., Sleat, D. E. & Lobel, P. 2012. Systemic administration of tripeptidyl peptidase I in a mouse model of late infantile neuronal ceroid lipofuscinosis: effect of glycan modification. *PLoS One,* 7**,** e40509.

Menon, K. P., Carrillo, R. A. & Zinn, K. 2013. Development and plasticity of the *Drosophila* larval neuromuscular junction. *Wiley Interdiscip Rev Dev Biol,* 2**,** 647-70.

Mentis, G. Z., Blivis, D., Liu, W., Drobac, E., Crowder, M. E., Kong, L., Alvarez, F. J., Sumner, C. J. & O'donovan, M. J. 2011. Early functional impairment of sensory-motor connectivity in a mouse model of Spinal Muscular Atrophy. *Neuron,* 69**,** 453-467.

Miller, R. A. & Spellman, D. S. 2014. Mass spectrometry-based biomarkers in drug development. *Adv Exp Med Biol,* 806**,** 341-59.

Minna Savukoski, Tuomas Klockars, Ville Holmberg, Pirkko Santavuori, Eric S. Lander & Peltonen, L. 2008. CLN5, a novel gene encoding a putative transmembrane protein mutated in Finnish variant late infantile neuronal ceroid lipofuscinosis. *Nature Genetics,* 19**,** 286 - 288.

Mitchison, H. M., Bernard, D. J. & Greene, N. 1999. Targeted disruption of the Cln3 gene provides a mouse model for Batten disease. The Batten Mouse Model Consortium. *Neurobiol Dis.,* 6**,** 321-334.

Mitchison, H. M., Lim, M. J. & Cooper, J. D. 2004. Selectivity and types of cell death in the Neuronal Ceroid Lipofuscinoses (NCLs). *Brain Pathol.,* 14**,** 86-96.

Mizushima, N., Levine, B., Cuervo, A. M. & Klionsky, D. J. 2008. Autophagy fights disease through cellular self-digestion. *Nature,* 451**,** 1069–107.

Mohammed, A., O'hare, M. B., Warley, A., Tear, G. & Tuxworth, R. I. 2017. in vivo localization of the neuronal ceroid lipofuscinosis proteins, CLN3 and CLN7, at endogenous expression levels. *Neurobiol Dis,* 103**,** 123-132.

Mohseni, N., Mcmillan, S. C., Chaudhary, R., Mok, J. & Reed, B. H. 2014. Autophagy promotes caspase-dependent cell death during *Drosophila* development. *Autophagy,* 5**,** 329-338.

Mole, S., Williams, R. & Goebel, H. H. 2011. The neuronal ceroid lipofuscinoses (Batten disease). *2nd ed. Oxford: Oxford University Press*.

Mole, S. E., Williams, R. E. & Goebel, H. H. 2005. Correlations between genotype, ultrastructural morphology and clinical phenotype in the neuronal ceroid lipofuscinoses. *Neurogenetics,* 6**,** 107 – 126.

Monastirioti, M. 1999. Biogenic amine systems in the fruit fly *Drosophila melanogaster*. *Microsc Res Tech.,* 45**,** 106-21.

Moreno-Gonzalez I, S. C. 2011. Misfolded protein aggregates: mechanisms, structures and potential for disease transmission. *Semin Cell Dev Biol,* (5):482-7.

Morgan, J. P., Magee, H., Wong, A., Nelson, T., Koch, B., Cooper, J. D. & Weimer, J. M. 2013. A murine model of variant late infantile ceroid lipofuscinosis recapitulates behavioral and pathological phenotypes of human disease. *PLoS One,* 8**,** e78694.

Munos, B. 2009. Lessons from 60 years of pharmaceutical innovation. *Nat Rev Drug Discov,* 8**,** 959-968.

Murray, L. M., Comley, L. H., Thomson, D., Parkinson, N. & Talbot, K. 2008. Selective vulnerability of motor neurons and dissociation of pre- and post- synaptic pathology at the neuromuscular junction in mouse models of spinal muscular atrophy. *Hum Mol Genet,* 17**,** 949–62.

Mutsaers, C. A., Lamont, D. J., Hunter, G., Wishart, T. M. & Gillingwater, T. H. 2013. Label-free proteomics identifies Calreticulin and GRP75/Mortalin as peripherally accessible protein biomarkers for spinal muscular atrophy. *Genome Med,* 5**,** 95.

Muzaffar, N. E. & Pearce, D. A. 2008. Analysis of NCL Proteins from an evolutionary standpoint. *Current Genomics,* 9**,** 115-136.

Myllykangas, L., Tyynelä, J., Page-Mccaw, A., Rubin, G. M., Haltia, M. J. & Feany, M. B. 2005. Cathepsin D-deficient *Drosophila* recapitulate the key features of neuronal ceroid lipofuscinoses. *Neurobiology of Disease,* 19**,** 194-199.

Neefjes, J. & Van Der Kant, R. 2014. Stuck in traffic: an emerging theme in diseases of the nervous system. *Trends in Neurosciences,* 37**,** 66-76.

Neverman, N. J., Best, H. L., Hofmann, S. L. & Hughes, S. M. 2015. Experimental therapies in the neuronal ceroid lipofuscinoses. *Biochim Biophys Acta,* 1852**,** 2292-300.

Nichols, C. D. 2006. *Drosophila melanogaster* neurobiology, neuropharmacology, and how the fly can inform central nervous system drug discovery. *Pharmacol Ther,* 112**,** 677-700.

Nita, D. A., Mole, S. E. & Minassian, B. A. 2016. Neuronal ceroid lipofuscinoses. *Epileptic Disord,* 18**,** 73-88.

Nitz, D. A., Van Swinderen, B., Tononi, G. & Greenspan, R. J. 2002. Electrophysiological correlates of rest and activity in *Drosophila melanogaster*. *Current Biology,* 12**,** 1934-1940.

Nosková, L., Stránecký, V., Hartmannová, H., Přistoupilová, A., Barešová, V., Ivánek, R., Hůlková, H., Jahnová, H., Van der zee, J., Staropoli, John f., Sims, Katherine b., Tyynelä, J., Van broeckhoven, C., Nijssen, Peter c. G., Mole, Sara e., Elleder, M. & Kmoch, S. 2011. Mutations in DNAJC5, encoding cysteine-string protein alpha, cause autosomal-dominant

adult-onset neuronal ceroid lipofuscinosis. *The American Journal of Human Genetics,* 89**,** 241-252.

O'brien, J. S. & Kishimoto, Y. 1991. Saposin proteins: structure, function, and role in human lysosomal storage disorders. *FASEB J.* 5**,** 301-8.

O'kane, C. J. 2003. Modelling human diseases in *Drosophila* and *Caenorhabditis*. *Seminars in Cell & Developmental Biology* 14**,** 3–10.

Olson, M. F. 2008. Applications for ROCK kinase inhibition. *Curr Opin Cell Biol,* 20**,** 242-8.

Oortveld, M. a. W., Keerthikumar, S., Oti, M., Nijhof, B., Fernandes, A. C., Kochinke, K., Castells-Nobau, A., Van Engelen, E., Ellenkamp, T., Eshuis, L., Galy, A., Van Bokhoven, H., Habermann, B., Brunner, H. G., Zweier, C., Verstreken, P., Huynen, M. A. & Schenck, A. 2013. Human intellectual disability genes form conserved functional modules in *Drosophila*. *PLOS Genetics,* 9**,** e1003911.

Oswald, M. J., Palmer, D. N., Kay, G. W., Shemilt, S. J., Rezaie, P. & Cooper, J. D. 2005. Glial activation spreads from specific cerebral foci and precedes neurodegeneration in presymptomatic ovine neuronal ceroid lipofuscinosis (CLN6). *Neurobiol Dis.,* 20**,** 49-63.

Outeiro, T. F. & Giorgini, F. 2006. Yeast as a drug discovery platform in Huntington's and Parkinson's diseases. *Biotechnology Journal,* 1**,** 258-269.

Overington, J. P., Al-Lazikan, I. B. & Hopkins, A. L. 2006. How many drug targets are there? . *Nat Rev Drug Discov* 5**,** 993-996.

Ozcan, S., Cooper, J. D., Lago, S. G., Kenny, D., Rustogi, N., Stocki, P. & Bahn, S. 2017. Towards reproducible MRM based biomarker discovery using dried blood spots. *Sci Rep,* 7**,** 45178.

Padamsey, Z., Mcguinness, L., Bardo, S. J., Reinhart, M., Tong, R., Hedegaard, A., Hart, M. L. & Emptage, N. J. 2017. Activity-dependent exocytosis of lysosomes regulates the structural plasticity of dendritic spines. *Neuron,* 93**,** 132-146.

Palmer, D. N., Barry, L. A., Tyynelä, J. & Cooper, J. D. 2013. NCL mechanisms. *Biochim Biophys Acta.,* 1832**,** 1882-93. Review.

Palmer, D. N., Fearnley, I. M., Medd, S. M., Walker, J. E., Martinus, R. D., Bayliss, S. L., Hall, N. A., Lake, B. D., Wolfe, L. S. & Jolly, R. D. 1989. Lysosomal storage of the DCCD reactive proteolipid subunit of mitochondrial ATP synthase in human and ovine ceroid lipofuscinoses. *Advances in experimental medicine and biology,* 266**,** 211-22; discussion 223.

Palmer, D. N., Neverman, N. J., Chen, J. Z., Chang, C.-T., Houweling, P. J., Barry, L. A., Tammen, I., Hughes, S. M. & Mitchell, N. L. 2015. Recent studies of ovine neuronal ceroid lipofuscinoses from BARN, the Batten Animal Research Network. *Biochimica et Biophysica Acta (BBA) - Molecular Basis of Disease,* 1852**,** 2279-2286.

Pandey, U. B. & Nichols, C. D. 2011. Human disease models in *Drosophila melanogaster* and the role of the fly in therapeutic drug discovery. *Pharmacol Rev,* 63**,** 411-36.

Pangalos, M. N., Schechter, L. E. & Hurko, O. 2007. Drug development for CNS disorders: strategies for balancing risk and reducing attrition. *Nat Rev Drug Discov,* 6**,** 521-532.

Park, J., Al-Ramahi, I., Tan, Q., Mollema, N., Diaz-Garcia, J. R., Gallego-Flores, T., Lu, H. C., Lagalwar, S., Duvick, L., Kang, H., Lee, Y., Jafar-Nejad, P., Sayegh, L. S., Richman, R., Liu, X., Gao, Y., Shaw, C. A., Arthur, J. S., Orr, H. T., Westbrook, T. F., Botas, J. & Zoghbi, H. Y. 2013. RAS-MAPK-MSK1 pathway modulates ataxin 1 protein levels and toxicity in SCA1. *Nature,* 498**,** 325-31.

Parkes, T. L., Elia, A. J., Dickinson, D., Hilliker, A. J., Phillips, J. P. & Boulianne, G. L. 1998. Extension of *Drosophila* lifespan by overexpression of human SOD1 in motorneurons. *Nat Genet,* 19**,** 171-174.

Parson, S. H., Ribchester, R. R., Davie, N., Gandhi, N. P., Malik, R. Q., Gillingwater, T. H. & Thomson, D. 2004. Axotomy-dependent and independent synapse elimination in organ cultures of Wlds mutant mouse skeletal muscle. *J Neurosci Res.,* 76**,** 64-75.

Partanen, S., Haapanen, A., Kielar, C., Pontikis, C., Alexander, N., Inkinen, T., Saftig, P., Gillingwater, T. H., Cooper, J. D. & Tyynela, J. 2008. Synaptic changes in the thalamocortical system of cathepsin D-deficient mice: a model of human congenital neuronal ceroid-lipofuscinosis. *J. Neuropathol. Exp. Neurol.,* 67**,** 16–29.

Parviainen, L., Dihanich, S., Anderson, G. W., Wong, A. M., Brooks, H. R., Abeti, R., Rezaie, P., Lalli, G., Pope, S., Heales, S. J., Mitchison, H. M., Williams, B. P. & Cooper, J. D. 2017. Glial cells

are functionally impaired in juvenile neuronal ceroid lipofuscinosis and detrimental to neurons. *Acta Neuropathol Commun,* 5**,** 74.

Passini, M. A., Dodge, J. C., Bu, J., Yang, W., Zhao, Q., Sondhi, D., Hackett, N. R., Kaminsky, S. M., Mao, Q., Shihabuddin, L. S., Cheng, S. H., Sleat, D. E., Stewart, G. R., Davidson, B. L., Lobel, P. & Crystal, R. G. 2006. Intracranial delivery of CLN2 reduces brain pathology in a mouse model of classical late infantile neuronal ceroid lipofuscinosis. *J Neurosci,* 26**,** 1334-42.

Patel, V. J., Thalassinos, K., Slade, S. E., Connolly, J. B., Crombie, A., Murrell, J. C. & Scrivens, J. H. 2009. A Comparison of labeling and label-free mass spectrometry-based proteomics approaches. *J. Proteome Res.,* 8**,** 3752–3759.

Paul, S. M., Mytelka, D. S., Dunwiddie, C. T., Persinger, C. C., Munos, B. H., Lindborg, S. R. & Schacht, A. L. 2010. How to improve R&D productivity: the pharmaceutical industry's grand challenge. *Nat Rev Drug Discov,* 9**,** 203-214.

Pearce, D. A., Nosel, S. A. & Sherman, F. 1999. Studies of pH regulation by Btn1p, the yeast homolog of human Cln3p. *Mol Genet Metab.,* 66**,** 320-3.

Pears, M. R., Cooper, J. D., Mitchison, H. M., Mortishire-Smith, R. J., Pearce, D. A. & Griffin, J. L. 2005. High resolution 1H NMR-based metabolomics indicates a neurotransmitter cycling deficit in cerebral tissue from a mouse model of Batten disease. *J Biol Chem,* 280**,** 42508-14.

Pears, M. R., Salek, R. M., Palmer, D. N., Kay, G. W., Mortishire-Smith, R. J. & Griffin, J. L. 2007. Metabolomic investigation of CLN6 neuronal ceroid lipofuscinosis in affected South Hampshire sheep. *Journal of Neuroscience Research,* 85**,** 3494-3504.

Pennetta, G., Hiesinger, P. R., Fabian-Fine, R., Meinertzhagen, I. A. & Bellen, H. J. 2002. *Drosophila* VAP-33A Directs bouton formation at neuromuscular junctions in a dosage-dependent manner. *Neuron,* 35**,** 291-306.

Perkins, L. A., Holderbaum, L., Tao, R., Hu, Y., Sopko, R., Mccall, K., Yang-Zhou, D., Flockhart, I., Binari, R., Shim, H.-S., Miller, A., Housden, A., Foos, M., Randkelv, S., Kelley, C., Namgyal, P., Villalta, C., Liu, L.-P., Jiang, X., Huan-Huan, Q., Wang, X., Fujiyama, A., Toyoda, A., Ayers, K., Blum, A., Czech, B., Neumuller, R., Yan, D., Cavallaro, A., Hibbard, K., Hall, D., Cooley, L., Hannon, G. J., Lehmann, R., Parks, A., Mohr, S. E., Ueda, R., Kondo, S., Ni, J.-Q. & Perrimon, N. 2015. The Transgenic RNAi Project at Harvard Medical School: resources and validation. *Genetics,* 201**,** 843-852.

Persaud-Sawin, D.-A., Mcnamara, J. O., Rylova, S., Vandongen, A. & Boustany, R.-M. N. 2004. A galactosylceramide binding domain is involved in trafficking of CLN3 from Golgi to rafts via recycling endosomes. *Pediatr Res,* 56**,** 449-463.

Peters, H., Ferdinandusse, S., Ruiter, J. P., Wanders, R. J., Boneh, A. & Pitt, J. 2015. Metabolite studies in HIBCH and ECHS1 defects: implications for screening. *Mol Genet Metab,* 115**,** 168-73.

Phillips, S. N., Benedict, J. W., Weimer, J. M. & Pearce, D. A. 2005. CLN3, the protein associated with batten disease: structure, function and localization. *J Neurosci Res,* 79**,** 573-83.

Picconi, B., Piccoli, G. & Calabresi, P. 2012. Synaptic dysfunction in Parkinson's Disease. *In:* Kreutz, M. R. & Sala, C. (eds.) *Synaptic Plasticity: Dynamics, Development and Disease.* Vienna: Springer Vienna.

Plotegher, N. & Duchen, M. R. 2017. Mitochondrial dysfunction and neurodegeneration in Lysosomal Storage Disorders. *Trends Mol Med,* 23**,** 116-134.

Pontikis, C. C., Cella, C. V., Parihar, N., Lim, M. J., Chakrabarti, S., Mitchison, H. M., Mobley, W. C., Rezaie, P., Pearce, D. A. & Cooper, J. D. 2004. Late onset neurodegeneration in the Cln3-/- mouse model of juvenile neuronal ceroid lipofuscinosis is preceded by low level glial activation. *Brain Res,* 1023**,** 231-42.

Pontikis, C. C., Cotman, S. L., Macdonald, M. E. & Cooper, J. D. 2005. Thalamocortical neuron loss and localized astrocytosis in the Cln3Deltaex7/8 knock-in mouse model of Batten disease. *Neurobiol Dis.,* 20**,** 823-36.

Powis, R. A., Karyka, E., Boyd, P., Come, J., Jones, R. A., Zheng, Y., Szunyogova, E., Groen, E. J., Hunter, G., Thomson, D., Wishart, T. M., Becker, C. G., Parson, S. H., Martinat, C., Azzouz, M. & Gillingwater, T. H. 2016. Systemic restoration of UBA1 ameliorates disease in spinal muscular atrophy. *JCI Insight,* 1**,** e87908.

Prescott, G. R., Gorleku, O. A., Greaves, J. & Chamberlain, L. H. 2009. Palmitoylation of the synaptic vesicle fusion machinery. *Journal of Neurochemistry,* 110**,** 1135-1149.

Prior, M., Chiruta, C., Currais, A., Goldberg, J., Ramsey, J., Dargusch, R., Maher, P. A. & Schubert, D. 2014. Back to the future with phenotypic screening. *ACS Chem Neurosci,* 5**,** 503-13.

Procaccini, C., Santopaolo, M., Faicchia, D., Colamatteo, A., Formisano, L., De Candia, P., Galgani, M., De Rosa, V. & Matarese, G. 2016. Role of metabolism in neurodegenerative disorders. *Metabolism - Clinical and Experimental,* 65**,** 1376-1390.

Prokop, A. & Meinertzhagen, I. A. 2006. Development and structure of synaptic contacts in *Drosophila*. *Seminars in Cell & Developmental Biology,* 17**,** 20-30.

Prusothman, Y. & Yann, G. 2017. The use of the zebrafish model to aid in drug discovery and target validation. *Current Topics in Medicinal Chemistry,* 17**,** 2041-2055.

Puranam, K., Guo, W., Qian, W., Nikbakht, K. & Boustany, R. 1999. CLN3 defines a novel antiapoptotic pathway operative in neurodegeneration and mediated by ceramide. *Mol Genet Metab.,* 66**,** 294-308.

Purves, P., Augustine, G. J., Fitzpatrick, D., Hall, W. C., Lamantia, A.-S., Mcnamara, J. O. & Williams, S. M. 2004. Neuroscience. *Sunderland, MA, Sinauer Associates Inc.*

R Development Core Team 2008. R: A language and environment for statistical computing. R Foundation for Statistical Computing. *R Foundation for Statistical Computing, Vienna, Austria.* .

Raefsky, S. M. & Mattson, M. P. 2017. Adaptive responses of neuronal mitochondria to bioenergetic challenges: Roles in neuroplasticity and disease resistance. *Free Radic Biol Med,* 102**,** 203-216.

Ragbeer, S. N., Augustine, E. F., Mink, J. W., Thatcher, A. R., Vierhile, A. E. & Adams, H. R. 2016. Remote assessment of cognitive function in Juvenile Neuronal Ceroid Lipofuscinosis (Batten disease): A pilot study of feasibility and reliability. *J Child Neurol,* 31**,** 481-7.

Rajendra, T. K., Gonsalvez, G. B., Walker, M. P., Shpargel, K. B., Salz, H. K. & Matera, A. G. 2007. A *Drosophila melanogaster* model of spinal muscular atrophy reveals a function for SMN in striated muscle. *The Journal of Cell Biology,* 176**,** 831-841.

Rakheja, D., Narayan, S. B., Pastor, J. V. & Bennett, M. J. 2004. CLN3P, the Batten disease protein, localizes to membrane lipid rafts (detergent-resistant membranes). *Biochemical and Biophysical Research Communications,* 317**,** 988-991.

Ramadan, H., Al-Din, A. S., Ismail, A., Balen, F., Varma, A., Twomey, A., Watts, R., Jackson, M., Anderson, G., Green, E. & Mole, S. E. 2007. Adult neuronal ceroid lipofuscinosis caused by deficiency in palmitoyl protein thioesterase 1. *Neurology,* 68**,** 387-8.

Ramocki, M. B. & Zoghbi, H. Y. 2008. Failure of neuronal homeostasis results in common neuropsychiatric phenotypes. *Nature,* 455**,** 912-918.

Ramsey, R. B., Jones, J. P. & Nicholas, H. J. 1972. The biosynthesis of cholesterol and other sterols by brain tissue. *Journal of Neurochemistry,* 19**,** 931-936.

Ransohoff, R. M. 2016. How neuroinflammation contributes to neurodegeneration. *Science,* 353**,** 777-83.

Rapola, J. & Haltia, M. 1973. Cytoplasmatic inclusions in the vermiform appendix and skeletal muscle in two types of so-calledneuronal ceroid-lipofuscinosis. *96,* 96**,** 833-40.

Ray, M. & Lakhotia, S. C. 2015. The commonly used eye-specific sev-GAL4 and GMR-GAL4 drivers in *Drosophila melanogaster* are expressed in tissues other than eyes also. *J. Genet.,* 94**,** 407–416.

Ready, D. F., Hanson, T. E. & Benzer, S. 1976. Development of the *Drosophila* retina, a neurocrystalline lattice. *Developmental Biology,* 53**,** 217-240.

Reddy, P. H. & Shirendeb, U. P. 2012. Mutant huntingtin, abnormal mitochondrial dynamics, defective axonal transport of mitochondria, and selective synaptic degeneration in Huntington's disease. *Biochimica et Biophysica Acta (BBA) - Molecular Basis of Disease,* 1822**,** 101-110.

Reiter, L. T., Potocki, L., Chien, S., Gribskov, M. & Bier, E. 2001. A systematic analysis of human disease-associated gene sequences in *Drosophila melanogaster. Genome Res,* 11**,** 1114–25.

Riento, K. & Ridley, A. J. 2003. Rocks: multifunctional kinases in cell behaviour. *Nat Rev Mol Cell Biol,* 4**,** 446–456.

Rishton, G. M. 2008. Natural products as a robust source of new drugs and drug leads: past successes and present day issues. *American Journal of Cardiology,* 101**,** S43-S49.

Robberecht, W. & Philips, T. 2013. The changing scene of amyotrophic lateral sclerosis. *Nat Rev Neurosci,* 14**,** 248-264.

Robinow, S. & White, K. 1988. The locus elav of *Drosophila melanogaster* is expressed in neurons at all developmental stages. *Developmental Biology,* 126**,** 294-303.

Rossetto, O., Pirazzini, M. & Montecucco, C. 2014. Botulinum neurotoxins: genetic, structural and mechanistic insights. *Nature Reviews Microbiology,* 12**,** 535.

Rozas, J. L., Gómez-Sánchez, L., Tomás-Zapico, C., Lucas, J. J. & Fernández-Chacón, R. 2011. Increased neurotransmitter release at the neuromuscular junction in a mouse model of polyglutamine disease. *The Journal of Neuroscience,* 31**,** 1106-1113.

Rubin, G. M., Yandell, M. D., Wortman, J. R., Gabor , G. L., Miklos, Nelson, C. R., Hariharan, I. K., Fortini, M. E., Li, P. W., Apweiler, R., Fleischmann, W., Cherry, J. M., Henikoff, S., Skupski, M. P., Misra, S., Ashburner, M., Birney, E., Boguski, M. S., Brody, T., Brokstein, P., Celniker, S. E., Chervitz, S. A., Coates, D., Cravchik, A., Gabrielian, A., Galle, R. F., Gelbart, W. M., George, R. A., Goldstein, L. S. B., Gong, F., Guan, P., Harris, N. L., Hay, B. A., Hoskins, R. A., Li, J., Li, Z., Hynes, R. O., Jones, S. J. M., Kuehl, P. M., Lemaitre, B., Littleton, J. T., Morrison, D. K., Mungall, C., O'farrell, P. H., Pickeral, O. K., Shue, C., Vosshall, L. B., Zhang, J., Zhao, Q., Zheng, X. H., Zhong, F., Zhong, W., Gibbs, R., Venter, J. C., Adams, M. D. & Lewis, S. 2000. Comparative genomics of the eukaryotes. *Science,* 287**,** 2204-2215.

Saja, S., Buff, H., Smith, A. C., Williams, T. S. & Korey, C. A. 2010. Identifying cellular pathways modulated by *Drosophila* palmitoyl-protein thioesterase 1 function. *Neurobiology of Disease,* 40**,** 135-145.

Sanhueza, M., Chai, A., Smith, C., Mccray, B. A., Simpson, T. I., Taylor, J. P. & Pennetta, G. 2015. Network analyses reveal novel aspects of ALS pathogenesis. *PLoS Genet,* 11**,** e1005107.

Sanhueza, M., Zechini, L., Gillespie, T. & Pennetta, G. 2014. Gain-of-function mutations in the ALS8 causative gene VAPB have detrimental effects on neurons and muscles. *Biology Open,* 3**,** 59-71.

Santavuori, P. 1998. Neuronal ceroid-lipofuscinoses in childhood. *Brain Dev.,* 10**,** 80-83.

Santavuori, P., Haltia, M. & Rapola, J. 1973. Infantile type so-called neuronal ceroid lipofuscinosis. *Dev. Med. Child Neurol.,* 16**,** 644–653.

Santavuori, P., Vanhanen, S. L. & Autti, T. 2001. Clinical and neuroradiological diagnostic aspects of neuronal ceroid lipofuscinoses disorders. *Eur J Paediatr Neurol.,* 5**,** 157-61.

Sanyal, S. 2009. Genomic mapping and expression patterns of C380, OK6 and D42 enhancer trap lines in the larval nervous system of *Drosophila*. *Gene Expression Patterns,* 9**,** 371-380.

Sarkar, C., Chandra, G., Peng, S., Zhang, Z., Liu, A. & Mukherjee, A. B. 2013. Neuroprotection and lifespan extension in Ppt1(-/-) mice by NtBuHA: therapeutic implications for INCL. *Nat Neurosci,* 16**,** 1608-17.

Sasaki, S. & Iwata, M. 1999. Ultrastructural change of synapses of Betz cells in patients with amyotrophic lateral sclerosis. *Neuroscience Letters,* 268**,** 29-32.

Sasaki, S. & Maruyama, S. 1994. Synapse loss in anterior horn neurons in amyotrophic lateral sclerosis. *Acta Neuropathologica,* 88**,** 222-227.

Savino, R., Paduano, S., Preiano, M. & Terracciano, R. 2012. The proteomics big challenge for biomarkers and new drug-targets discovery. *Int J Mol Sci,* 13**,** 13926-48.

Savli, H., Szendröi, A., Romics, I. & Nagy, B. 2008. Gene network and canonical pathway analysis in prostate cancer: a microarray study. *Exp Mol Med.,* 40**,** 176-85.

Scheibye-Knudsen, M., Fang, E. F., Croteau, D. L., Wilson, D. M. & Bohr, V. A. 2015. Protecting the mitochondrial powerhouse. *Trends in Cell Biology,* 25**,** 158-170.

Schmitz, F., Tabares, L., Khimich, D., Strenzke, N., De La Villa-Polo, P., Castellano-Muñoz, M., Bulankina, A., Moser, T., Fernández-Chacón, R. & Südhof, T. C. 2006. CSPα-deficiency causes massive and rapid photoreceptor degeneration. *Proceedings of the National Academy of Sciences of the United States of America,* 103**,** 2926-2931.

Scifo, E., Szwajda, A., Soliymani, R., Pezzini, F., Bianchi, M., Dapkunas, A., Debski, J., Uusi-Rauva, K., Dadlez, M., Gingras, A. C., Tyynela, J., Simonati, A., Jalanko, A., Baumann, M. H. & Lalowski, M. 2015. Proteomic analysis of the palmitoyl protein thioesterase 1 interactome in SH-SY5Y human neuroblastoma cells. *J Proteomics,* 123**,** 42-53.

Seehafer, S. S., Ramirez-Montealegre, D., Wong, A. M., Chan, C. H., Castaneda, J., Horak, M., Ahmadi, S. M., Lim, M. J., Cooper, J. D. & Pearce, D. A. 2011. Immunosuppression alters disease severity in juvenile Batten disease mice. *J Neuroimmunol,* 230**,** 169-72.

Selkoe, D. J. 2002. Alzheimer's disease is a synaptic failure. *Science,* 298**,** 789–791.

Settembre, C., Fraldi, A., Medina, D. L. & Ballabio, A. 2013. Signals from the lysosome: a control centre for cellular clearance and energy metabolism. *Nat Rev Mol Cell Biol,* 14**,** 283-96.

Shacka, J. J. 2012. Mouse models of neuronal ceroid lipofuscinoses: useful pre-clinical tools to delineate disease pathophysiology and validate therapeutics. *Brain Res Bull,* 88**,** 43-57.

Sharma, M., Burre, J. & Sudhof, T. C. 2011. CSP[alpha] promotes SNARE-complex assembly by chaperoning SNAP-25 during synaptic activity. *Nat Cell Biol,* 13**,** 30-39.

Shen, D.-N., Zhang, L.-H., Wei, E.-Q. & Yang, Y. 2015. Autophagy in synaptic development, function, and pathology. *Neuroscience Bulletin,* 31**,** 416-426.

Sheng, Z.-H. 2014. Mitochondrial trafficking and anchoring in neurons: New insight and implications. *The Journal of Cell Biology,* 204**,** 1087-1098.

Shyng, C., Nelvagal, H. R., Dearborn, J. T., Tyynelä, J., Schmidt, R. E., Sands, M. S. & Cooper, J. D. 2017. Synergistic effects of treating the spinal cord and brain in CLN1 disease. *Proceedings of the National Academy of Sciences,* 114**,** E5920-E5929.

Sieradzan, K. A. & Mann, D. M. A. 2001. The selective vulnerability of nerve cells in Huntington's disease. *Neuropathology and Applied Neurobiology,* 27**,** 1-21.

Siintola, E., Partanen, S., Stromme, P., Haapanen, A., Haltia, M., Maehlen, J., Lehesjoki, A.E., Tyynela, J. 2006. Cathepsin D deficiency underlies congenital human neuronal ceroid-lipofuscinosis. *Brain,* 129**,** 1438–1445.

Siintola, E., Topcu, M., Aula, N., Lohi, H., Minassian, B. A., Paterson, A. D., Liu, X. Q., Wilson, C., Lahtinen, U., Anttonen, A. K. & Lehesjoki, A. E. 2007. The novel neuronal ceroid lipofuscinosis gene MFSD8 encodes a putative lysosomal transporter. *Am J Hum Genet,* 81**,** 136-46.

Sleat, D. E., Gedvilaite, E., Zhang, Y., Lobel, P. & Xing, J. 2016. Analysis of large-scale whole exome sequencing data to determine the prevalence of genetically-distinct forms of neuronal ceroid lipofuscinosis. *Gene,* 593**,** 284-91.

Smith, K. R., Dahl, H.-H. M., Canafoglia, L., Andermann, E., Damiano, J., Morbin, M., Bruni, A. C., Giaccone, G., Cossette, P., Saftig, P., Grötzinger, J., Schwake, M., Andermann, F., Staropoli, J. F., Sims, K. B., Mole, S. E., Franceschetti, S., Alexander, N. A., Cooper, J. D., Chapman, H. A., Carpenter, S., Berkovic, S. F. & Bahlo, M. 2013. Cathepsin F mutations cause Type B Kufs disease, an adult-onset neuronal ceroid lipofuscinosis. *Human Molecular Genetics,* 22**,** 1417-1423.

Song, J., Wu, L., Chen, Z., Kohanski, R. A. & Pick, L. 2003. Axons guided by insulin receptor in *Drosophila* visual system. *Science,* 300**,** 502-505.

Song, M., Kim, Y. J. & Ryu, J. C. 2011. Phospholipidosis induced by PPARgamma signaling in human bronchial epithelial (BEAS-2B) cells exposed to amiodarone. *Toxicol Sci,* 120**,** 98-108.

Soto, C. 2003. Unfolding the role of protein misfolding in neurodegenerative diseases. *Nature Reviews Neuroscience,* 4**,** 49-60.

Spillantini, M. G. 1997. α-Synuclein in Lewy bodies. *Nature Reviews Neuroscience,* 388**,** 839–840

St Johnston, D. 2002. The art and design of genetic screens: *Drosophila* melanogaster. *Nat Rev Genet,* 3**,** 176-88.

Staropoli, J. F., Karaa, A., Lim, E. T., Kirby, A., Elbalalesy, N., Romansky, S. G., Leydiker, K. B., Coppel, S. H., Barone, R., Xin, W., Macdonald, M. E., Abdenur, J. E., Daly, M. J., Sims, K. B. & Cotman, S. L. 2012. A homozygous mutation in KCTD7 links neuronal ceroid lipofuscinosis to the ubiquitin-proteasome system. *Am J Hum Genet,* 91**,** 202-8.

Steffan, J. S., Bodai, L., Pallos, J., Poelman, M., Mccampbell, A., Apostol, B. L., Kazantsev, A., Schmidt, E., Zhu, Y.-Z., Greenwald, M., Kurokawa, R., Housman, D. E., Jackson, G. R., Marsh, J. L. & Thompson, L. M. 2001. Histone deacetylase inhibitors arrest polyglutamine-dependent neurodegeneration in *Drosophila*. *Nature,* 413**,** 739-743.

Steinfeld, R., Reinhardt, K., Schreiber, K., Hillebrand, M., Kraetzner, R., Brück, W., Saftig, P. & Gärtner, J. 2006. Cathepsin D deficiency is associated with a human neurodegenerative disorder. *The American Journal of Human Genetics,* 78**,** 988-998.

Stiles, A. R., Ferdinandusse, S., Besse, A., Appadurai, V., Leydiker, K. B., Cambray-Forker, E. J., Bonnen, P. E. & Abdenur, J. E. 2015. Successful diagnosis of HIBCH deficiency from exome sequencing and positive retrospective analysis of newborn screening cards in two siblings presenting with Leigh's disease. *Mol Genet Metab,* 115**,** 161-7.

Sudhof, T. C. 2004. The synaptic vesicle cycle. *Annu Rev Neurosci,* 27**,** 509-47.

Sudhof, T. C. 2012. The presynaptic active zone. *Neuron,* 75**,** 11-25.

Sugita, M., Dulaney, J. T. & Moser, H. W. 1972. Ceramidase deficiency in Farber's Disease (Lipogranulomatosis). *Science,* 178**,** 1100-1102.

Sun, M., Xing, G., Yuan, L., Gan, G., Knight, D., With, S. I., He, C., Han, J., Zeng, X., Fang, M., Boulianne, G. L. & Xie, W. 2011. Neuroligin 2 is required for synapse development and function at the *Drosophila* neuromuscular junction. *The Journal of Neuroscience,* 31**,** 687-699.

Surmeier, D. J., Obeso, J. A. & Halliday, G. M. 2017. Selective neuronal vulnerability in Parkinson disease. *Nat Rev Neurosci,* 18**,** 101-113.

Susanna Ranta, Yonghui Zhang, Barbara Ross, Liina Lonka, Elina Takkunen, Anne Messer, Julie Sharp, Ruth Wheeler, Kenro Kusumi, Sara Mole, Wencheng Liu, Marcelo Bento Soares, Maria De Fatima Bonaldo, Aune Hirvasniemi, Albert De La Chapelle, Gilliam, T. C. & Lehesjoki, A.-E. 1999. The neuronal ceroid lipofuscinoses in human EPMR and mnd mutant mice are associated with mutations in CLN8. *Nat Genet.,* 23**,** 233-6.

Suzuki, Y., Shibuya, M., Satoh, S., Sugiyama, H., Seto, M. & Takakura, K. 2008. Safety and efficacy of fasudil monotherapy and fasudil-ozagrel combination therapy in patients with subarachnoid hemorrhage: sub-analysis of the post-marketing surveillance study. *Neurol Med Chir (Tokyo),* 48**,** 241-8.

Swinney, D. C. & Anthony, J. 2011. How were new medicines discovered? *Nat Rev Drug Discov,* 10**,** 507-519.

Tabuchi, K. & Südhof, T. C. 2002. Structure and evolution of Neurexin genes: Insight into the mechanism of alternative splicing. *Genomics,* 79**,** 849-859.

Takayasu, M., Suzuki, Y., Shibuya, M., Asano, T., Kanamori, M., Okada, T., Kageyama, N. & Hidaka, H. 1986. The effects of HA compound calcium antagonists on delayed cerebral vasospasm in dogs. *Journal of Neurosurgery,* 65**,** 80-85.

Talbot, K., Wang, H.-Y., Kazi, H., Han, L.-Y., Bakshi, K. P., Stucky, A., Fuino, R. L., Kawaguchi, K. R., Samoyedny, A. J., Wilson, R. S., Arvanitakis, Z., Schneider, J. A., Wolf, B. A., Bennett, D. A., Trojanowski, J. Q. & Arnold, S. E. 2012. Demonstrated brain insulin resistance in Alzheimer's disease patients is associated with IGF-1 resistance, IRS-1 dysregulation, and cognitive decline. *The Journal of Clinical Investigation,* 122.

Tammen, I., Houweling, P. J., Frugier, T., Mitchell, N. L., Kay, G. W., Cavanagh, J. A., Cook, R. W., Raadsma, H. W. & Palmer, D. N. 2006. A missense mutation (c.184C>T) in ovine CLN6 causes neuronal ceroid lipofuscinosis in Merino sheep whereas affected South Hampshire sheep have reduced levels of CLN6 mRNA. *Biochim Biophys Acta,* 1762**,** 898-905.

Tecedor, L., Stein, C. S., Schultz, M. L., Farwanah, H., Sandhoff, K. & Davidson, B. L. 2013. CLN3 loss disturbs membrane microdomain properties and protein transport in brain endothelial cells. *The Journal of Neuroscience,* 33**,** 18065-18079.

Tedford, N. C., Hall, A. B., Graham, J. R., Murphy, C. E., Gordon, N. F. & Radding, J. A. 2009. Quantitative analysis of cell signaling and drug action via mass spectrometry-based systems level phosphoproteomics. *Proteomics,* 9**,** 1469-1487.

Tegelberg, S., Kopra, O., Joensuu, T., Cooper, J. D. & Lehesjoki, A. E. 2012. Early microglial activation precedes neuronal loss in the brain of the cstb−/− mouse model of progressive myoclonus epilepsy, EPM1. *J. Neuropathol. Exp. Neurol,* 71**,** 40-53.

Terry, R. D., Masliah, E., Salmon, D. P., Butters, N., Deteresa, R., Hill, R., Hansen, L. A. & Katzman, R. 1991. Physical basis of cognitive alterations in alzheimer's disease: Synapse loss is the major correlate of cognitive impairment. *Annals of Neurology,* 30**,** 572-580.

The International Batten Disease Consortium 1995. Isolation of a novel gene underlying Batten disease, CLN3. *Cell,* 82**,** 949-57.

Thelen, M., Damme, M., Schweizer, M., Hagel, C., Wong, A. M., Cooper, J. D., Braulke, T. & Galliciotti, G. 2012. Disruption of the autophagy-lysosome pathway is involved in

neuropathology of the nclf mouse model of neuronal ceroid lipofuscinosis. *PLoS One,* 7**,** e35493.

Theocharidis, A., Van Dongen, S., Enright, A. J. & Freeman, T. C. 2009. Network visualization and analysis of gene expression data using BioLayout Express(3D). *Nat. Protoc.,* 4**,** 1535-50.

Thomas, B. J. & Wassarman, D. A. 1999. A fly's eye view of biology. *Trends in Genetics,* 15**,** 184-190.

Tikka, S., Monogioudi, E., Gotsopoulos, A., Soliymani, R., Pezzini, F., Scifo, E., Uusi-Rauva, K., Tyynela, J., Baumann, M., Jalanko, A., Simonati, A. & Lalowski, M. 2016. Proteomic profiling in the brain of CLN1 disease model reveals affected functional modules. *Neuromolecular Med,* 18**,** 109-33.

Tseng, A.-S. K. & Hariharan, I. K. 2002. An overexpression screen in *Drosophila* for genes that restrict growth or cell-cycle progression in the developing eye. *Genetics,* 162**,** 229-243.

Tufi, R., Gandhi, S., De Castro, I. P., Lehmann, S., Angelova, P. R., Dinsdale, D., Deas, E., Plun-Favreau, H., Nicotera, P., Abramov, A. Y., Willis, A. E., Mallucci, G. R., Loh, S. H. Y. & Martins, L. M. 2014. Enhancing nucleotide metabolism protects against mitochondrial dysfunction and neurodegeneration in a PINK1 model of Parkinson's disease. *Nat Cell Biol,* 16**,** 157-166.

Tuxworth, R. I., Chen, H., Vivancos, V., Carvajal, N., Huang, X. & Tear, G. 2011. The Batten disease gene CLN3 is required for the response to oxidative stress. *Hum Mol Genet,* 20**,** 2037-47.

Tuxworth, R. I., Vivancos, V., O'hare, M. B. & Tear, G. 2009. Interactions between the juvenile Batten disease gene, CLN3, and the Notch and JNK signalling pathways. *Hum Mol Genet,* 18**,** 667-78.

Tyynelä, J., Palmer, D. N., Baumann, M. & Haltia, M. 1993. Storage of saposins A and D in infantile neuronal ceroid-lipofuscinosis. *FEBS Letters,* 330**,** 8-12.

Uvebrant, P. & Hagberg, B. 1997. Neuronal ceroid lipofuscinoses in Scandinavia. Epidemiology and clinical pictures. *Neuropediatrics,* 28**,** 6-8.

Uylings, H. B. M. & De Brabander, J. M. 2002. Neuronal Changes in Normal Human Aging and Alzheimer's Disease. *Brain and Cognition,* 49**,** 268-276.

Van Diggelen, O. P., Keulemans, J. L., Kleijer, W. J., Thobois, S., Tilikete, C. & Voznyi, Y. V. 2001. Pre- and postnatal enzyme analysis for infantile, late infantile and adult neuronal ceroid lipofuscinosis (CLN1 and CLN2). *Eur J Paediatr Neurol.,* 5**,** 189-92.

Van Dongen, S. 2000. Graph Clustering by Flow Simulation. *PhD thesis, University of Utrecht*.

Vanhanen, S. L., Puranen, J., Autti, T., Raininko, R., Liewendahl, K., Nikkinen, P., Santavuori, P., Suominen, P., Vuori, K. & Häkkinen, A. M. 2004. Neuroradiological findings (MRS, MRI, SPECT) in infantile neuronal ceroid-lipofuscinosis (infantile CLN1) at different stages of the disease. *Neuropediatrics,* 35**,** 27-35.

Vanhauwaert, R. & Verstreken, P. 2015. Flies with Parkinson's disease. *Exp Neurol,* 274**,** 42-51.

Vargas-Caballero, M., Willaime-Morawek, S., Gomez-Nicola, D., Perry, V. H., Bulters, D. & Mudher, A. 2016. The use of human neurons for novel drug discovery in dementia research. *Expert Opin Drug Discov,* 11**,** 355-67.

Velat, G. J., Kimball, M. M., Mocco, J. D. & Hoh, B. L. 2011. Vasospasm after aneurysmal subarachnoid hemorrhage: review of randomized controlled trials and meta-analyses in the literature. *World Neurosurg.,* 6**,** 446-54.

Venken, K. J. & Bellen, H. J. 2005. Emerging technologies for gene manipulation in *Drosophila* melanogaster. *Nat. Rev. Genet,* 6**,** 167–78.

Verhoog, M. B., Goriounova, N. A., Obermayer, J., Stroeder, J., Hjorth, J. J. J., Testa-Silva, G., Baayen, J. C., De Kock, C. P. J., Meredith, R. M. & Mansvelder, H. D. 2013. Mechanisms underlying the rules for associative plasticity at adult human neocortical synapses. *The Journal of Neuroscience,* 33**,** 17197-17208.

Vesa, J., Hellsten, E., Verkruyse, L. A., Camp, L. A., Rapola, J., Santavuori, P., Hofmann, S. L. & Peltonen, L. 1995. Mutations in the palmitoyl protein thioesterase gene causing infantile neuronal ceroid lipofuscinosis. *Nature,* 376**,** 584–587.

Virmani, T., Gupta, P., Liu, X., Kavalali, E. T. & Hofmann, S. L. 2005. Progressively reduced synaptic vesicle pool size in cultured neurons derived from neuronal ceroid lipofuscinosis-1 knockout mice. *Neurobiol. Dis,* 20**,** 314–323.

Vrba, R., Gaitonde, M. K. & Richter, D. 1962. The conversion of glucose carbon into protein in the brain and other organs of the rat. *Journal of Neurochemistry,* 9**,** 465-475.

Wanders, R. J. A., Duran, M. & Loupatty, F. J. 2012. Enzymology of the branched-chain amino acid oxidation disorders: the valine pathway. *Journal of Inherited Metabolic Disease,* 35**,** 5-12.

Wang, H., Alvarez, S. & Hicks, L. M. 2012. Comprehensive comparison of iTRAQ and label-free LC-based quantitative proteomics approaches using two Chlamydomonas reinhardtii strains of interest for biofuels engineering. *J Proteome Res,* 11**,** 487-501.

Wang, X., Michaelis, M. & Michaelis, E. 2010. Functional genomics of brain aging and Alzheimers disease: focus on selective neuronal vulnerability. *Curr Genomics,* 11**,** 618–33.

Wang, Y.-C., Lauwers, E. & Verstreken, P. 2017. Presynaptic protein homeostasis and neuronal function. *Current Opinion in Genetics & Development,* 44**,** 38-46.

Warde-Farley, D., Donaldson, S. L., Comes, O., Zuberi, K., Badrawi, R., Chao, P., Franz, M., Grouios, C., Kazi, F., Lopes, C. T., Maitland, A., Mostafavi, S., Montojo, J., Shao, Q., Wright, G., Bader, G. D. & Morris, Q. 2010. The GeneMANIA prediction server: biological network integration for gene prioritization and predicting gene function. *Nucleic Acids Research,* 38**,** W214-W220.

Watson, M. R., Lagow, R. D., Xu, K., Zhang, B. & Bonini, N. M. 2008. A *Drosophila* model for amyotrophic lateral sclerosis reveals motor neuron damage by human SOD1. *J Biol Chem,* 283**,** 24972-81.

Wheeler, R. B., Sharp, J. D., Schultz, R. A., Joslin, J. M., Williams, R. E. & Mole, S. E. 2002. The gene mutated in variant late-infantile neuronal ceroid lipofuscinosis (CLN6) and in nclf mutant mice encodes a novel predicted transmembrane protein. *Am J Hum Genet,* 70**,** 537-42.

Wishart, T. M., Huang, J. P., Murray, L. M., Lamont, D. J., Mutsaers, C. A., Ross, J., Geldsetzer, P., Ansorge, O., Talbot, K., Parson, S. H. & Gillingwater, T. H. 2010. SMN deficiency disrupts brain development in a mouse model of severe spinal muscular atrophy. *Hum Mol Genet,* 19**,** 4216-28.

Wishart, T. M., Mutsaers, C. A., Riessland, M., Reimer, M. M., Hunter, G., Hannam, M. L., Eaton, S. L., Fuller, H. R., Roche, S. L., Somers, E., Morse, R., Young, P. J., Lamont, D. J., Hammerschmidt, M., Joshi, A., Hohenstein, P., Morris, G. E., Parson, S. H., Skehel, P. A., Becker, T., Robinson, I. M., Becker, C. G., Wirth, B. & Gillingwater, T. H. 2014. Dysregulation of ubiquitin homeostasis and beta-catenin signaling promote spinal muscular atrophy. *J Clin Invest,* 124**,** 1821-34.

Wishart, T. M., Parson, S. H. & Gillingwater, T. H. 2006. Synaptic vulnerability in neurodegenerative disease. *J Neuropathol Exp Neurol.,* 65**,** 733-9.

Wishart, T. M., Paterson, J. M., Short, D. M., Meredith, S., Robertson, K. A., Sutherland, C., Cousin, M. A., Dutia, M. B. & Gillingwater, T. H. 2007. Differential proteomics analysis of synaptic proteins identifies potential cellular targets and protein mediators of synaptic neuroprotection conferred by the slow Wallerian degeneration (Wlds) gene. *Mol Cell Proteomics,* 6**,** 1318-30.

Wishart, T. M., Rooney, T. M., Lamont, D. J., Wright, A. K., Morton, A. J., Jackson, M., Freeman, M. R. & Gillingwater, T. H. 2012. Combining comparative proteomics and molecular genetics uncovers regulators of synaptic and axonal stability and degeneration in vivo. *PLoS Genet,* 8**,** e1002936.

Wisniewski, J. R., Zougman, A., Nagaraj, N. & Mann, M. 2009. Universal sample preparation method for proteome analysis. *Nat Meth,* 6**,** 359-362.

Wong, E. & Cuervo, A. M. 2010. Autophagy gone awry in neurodegenerative diseases. *Nat Neurosci,* 13**,** 805-811.

Wong, J. J. L., Li, S., Lim, E. K. H., Wang, Y., Wang, C., Zhang, H., Kirilly, D., Wu, C., Liou, Y.-C., Wang, H. & Yu, F. 2013. A cullin1-based SCF E3 Ubiquitin ligase targets the inr/pi3k/tor pathway to regulate neuronal pruning. *PLOS Biology,* 11**,** e1001657.

Xie, F., Liu, T., Qian, W. J., Petyuk, V. A. & Smith, R. D. 2011. Liquid chromatography-mass spectrometry-based quantitative proteomics. *J Biol Chem,* 286**,** 25443-9.

Xu, W. L., Atti, A. R., Gatz, M., Pedersen, N. L., Johansson, B. & Fratiglioni, L. 2011. Midlife overweight and obesity increase late-life dementia risk: A population-based twin study. *Neurology,* 76**,** 1568-1574.

Xu, Z.-S. 2012. Does a loss of TDP-43 function cause neurodegeneration? *Molecular Neurodegeneration,* 7**,** 27.

Yamaguchi, T., Fernandez, R. & Roth, R. A. 1995. Comparison of the signaling abilities of the *drosophila* and human insulin receptors in mammalian cells. *Biochemistry,* 34**,** 4962-4968.

Yan, S.-K., Liu, R.-H., Jin, H.-Z., Liu, X.-R., Ye, J., Shan, L. & Zhang, W.-D. 2015. "Omics" in pharmaceutical research: overview, applications, challenges, and future perspectives. *Chinese Journal of Natural Medicines,* 13**,** 3-21.

Yannoni, Y. M. & White, K. 1997. Association of the neuron-specific RNA binding domain-containing protein ELAV with the coiled body in *Drosophila* neurons. *Chromosoma. ,* 105**,** 332-41.

Yoshihara, M. & Montana, E. S. 2004. The Synaptotagmins: calcium sensors for vesicular trafficking. *The Neuroscientist,* 10**,** 566-574.

Yuan, J., Lipinski, M. & Degterev, A. 2003. Diversity in the mechanisms of neuronal cell death. *Neuron,* 40**,** 401–413.

Yudkoff, M. 2017. Interactions in the metabolism of glutamate and the branched-chain amino acids and ketoacids in the CNS. *Neurochemical Research,* 42**,** 10-18.

Zang, D. W., Lopes, E. C. & Cheema, S. S. 2005. Loss of synaptophysin-positive boutons on lumbar motor neurons innervating the medial gastrocnemius muscle of the SOD1G93A G1H transgenic mouse model of ALS. *Journal of Neuroscience Research,* 79**,** 694-699.

Zhang, B. 2003. Genetic and molecular analysis of synaptic vesicle recycling in *Drosophila*. *J Neurocytol.,* 32**,** 567-89.

Zhang, M., Luo, G., Zhou, Y., Wang, S. & Zhong, Z. 2014. Phenotypic screens targeting neurodegenerative diseases. *J Biomol Screen,* 19**,** 1-16.

Zheng, Q., Huang, T., Zhang, L., Zhou, Y., Luo, H., Xu, H. & Wang, X. 2016. Dysregulation of ubiquitin-proteasome system in neurodegenerative diseases. *Front Aging Neurosci,* 8**,** 303.

Zhou, L., Miller, B. L., Mcdaniel, C. H., Kelly, L., Kim, O. J. & Miller, C. A. 1998. Frontotemporal dementia: Neuropil spheroids and presynaptic terminal degeneration. *Annals of Neurology,* 44**,** 99-109.

Zhou, Y., Su, Y., Li, B., Liu, F., Ryder, J. W., Wu, X., Gonzalez-Dewhitt, P. A., Gelfanova, V., Hale, J. E., May, P. C., Paul, S. M. & Ni, B. 2003. Nonsteroidal anti-inflammatory drugs can lower amyloidogenic AB42 by inhibiting Rho. *Science,* 302**,** 1215-17.

Zhou, Z., Meng, Y., Asrar, S., Todorovski, Z. & Jia, Z. 2009. A critical role of Rho-kinase ROCK2 in the regulation of spine and synaptic function. *Neuropharmacology,* 56**,** 81-9.

Zoghbi, H. Y. & Orr, H. T. 2000. Glutamine repeats and neurodegeneration. *Annu. Rev. Neurosci.,* 23**,** 217-247.

Appendix. Data tables

Table A1. BioLayout analysis of cortical, hippocampal and thalamic samples in **Cln3$^{-/-}$**: *Cluster 3 (Chapter 3)*			Ratio Cln3/WT		
ID	**Gene Symbol**	**Description**	**Cortex**	**Hippocampus**	**Thalamus**
91130		neural cell adhesion molecule - mouse (fragments)	1.160	1.039	1.036
200022	TMEM154	transmembrane protein 154	1.438	1.123	1.095
347839	CCT3	chaperonin containing TCP1 subunit 3	1.261	0.944	0.726
400269	ALDH6A1	aldehyde dehydrogenase 6 family member A1	1.085	1.012	0.950
417489	Pcmt1	protein-L-isoaspartate (D-aspartate) O-methyltransferase 1	1.079	0.740	0.687
790470	PA2G4	proliferation-associated 2G4	1.160	0.989	0.934
1170970	MYL12A	myosin light chain 12A	1.064	0.904	0.742
1769577	TWF1	twinfilin actin binding protein 1	1.133	0.798	0.553
1902905	HSPA4L	heat shock protein family A (Hsp70) member 4 like	0.922	0.824	0.759
2078522	DLD	dihydrolipoamide dehydrogenase	1.132	1.061	1.049
3318958	OR2AG1	olfactory receptor family 2 subfamily AG member 1 (gene/pseudogene)(OR2AG1)	1.236	0.940	0.760
3329498	HNRNPA2B1	heterogeneous nuclear ribonucleoprotein A2/B1	1.415	1.314	1.311
3766201	SUCLA2	succinate-CoA ligase ADP-forming beta subunit	1.013	0.935	0.917
6671549	PRDX6	peroxiredoxin 6	1.038	0.957	0.890
6679439	PPIA	peptidylprolyl isomerase A	1.050	0.941	0.939
6681069	CSRP1	cysteine and glycine rich protein 1	1.054	0.834	0.683
6681079	CTSB	cathepsin B	0.815	0.735	0.720
6746357	PRDX5	peroxiredoxin 5	1.130	0.967	0.821
6754976	PRDX1	peroxiredoxin 1	0.971	0.794	0.768
6981600	STX1B	syntaxin 1B	1.047	0.911	0.816
8393866	OAT	ornithine aminotransferase	1.132	1.005	0.864
9483736	SUCLG1	succinate-CoA ligase alpha subunit	1.044	0.842	0.782
9489054		G protein Gi2 alpha, partial	1.055	0.960	0.900
11693172	CALR	calreticulin	0.950	0.909	0.865
12805413	ECHS1	enoyl-CoA hydratase, short chain 1	1.190	0.971	0.849
12833936	CYB5B	cytochrome b5 type B	1.162	0.969	0.765
13385558	NDUFB8	NADH:ubiquinone oxidoreductase subunit B8	0.983	0.796	0.774

13385968	TPPP3	tubulin polymerization promoting protein family member 3	1.031	0.751	0.651
13543186	NDUFA9	NADH:ubiquinone oxidoreductase subunit A9	1.132	0.913	0.813
13592051	RPL5	ribosomal protein L5	0.937	0.926	0.916
14193690	GFAP	glial fibrillary acidic protein	1.555	1.027	0.798
15029655	BPNT1	3'(2'), 5'-bisphosphate nucleotidase 1	1.005	0.851	0.840
15042971	HAPLN2	hyaluronan and proteoglycan link protein 2	0.884	0.538	0.427
16307381	DNM2	dynamin 2	0.909	0.793	0.753
16758748	DNAH10	dynein axonemal heavy chain 10(DNAH10)	1.011	0.875	0.773
16930823	PROSC	proline synthetase cotranscribed homolog (bacterial)	1.229	0.862	0.849
18152793	PDHB	pyruvate dehydrogenase (lipoamide) beta	1.112	1.004	0.982
18700024	IDH3B	isocitrate dehydrogenase 3 (NAD(+)) beta	1.041	0.877	0.815
21314826	NDUFB4	NADH:ubiquinone oxidoreductase subunit B4	1.097	0.882	0.800
26328615	ETFA	electron transfer flavoprotein alpha subunit	0.934	0.846	0.755
26329027	PCYOX1	prenylcysteine oxidase 1	1.250	0.899	0.750
26329893	GPD2	glycerol-3-phosphate dehydrogenase 2	1.102	1.043	1.029
26337977	NDUFA10	NADH:ubiquinone oxidoreductase subunit A10	1.070	0.924	0.846
26342124	Nefm	neurofilament, medium polypeptide	1.828	1.016	1.061
26347027	HIBADH	3-hydroxyisobutyrate dehydrogenase	1.171	0.794	0.665
26348195	ENDOD1	endonuclease domain containing 1	1.065	0.926	0.783
26352474	TWF2	twinfilin actin binding protein 2	1.024	0.892	0.874
26352986	NDUFB5	NADH:ubiquinone oxidoreductase subunit B5	1.091	0.941	0.903
26361821	ARPC2	actin related protein 2/3 complex subunit 2	1.181	1.071	1.066
27465523	KCNA1	potassium voltage-gated channel subfamily A member 1	0.930	0.834	0.790
28200903	PLXNA4	plexin A4	1.281	1.095	0.912
29420429	AKAP12	A-kinase anchoring protein 12	1.364	0.981	0.861
29789148	NDUFB9	NADH:ubiquinone oxidoreductase subunit B9	0.968	0.623	0.565
31543797	SYT2	synaptotagmin 2	0.968	0.843	0.768
31982273	HSD17B4	hydroxysteroid 17-beta dehydrogenase 4	0.877	0.830	0.789
31982332	GLUL	glutamate-ammonia ligase	1.079	0.916	0.749
33469051	TPPP	tubulin polymerization promoting protein	1.065	0.998	0.964
33667095	VAT1L	vesicle amine transport 1-like	1.286	1.057	0.896
34610235	RTN4	reticulon 4	1.123	0.992	0.882
39204499	NEFL	neurofilament, light polypeptide	2.090	1.289	1.229
51773592	IDH3G	isocitrate dehydrogenase 3 (NAD(+)) gamma	1.150	0.937	0.924
56541260	RPL10	ribosomal protein L10	1.645	0.918	0.850
57164091	UQCRHL	ubiquinol-cytochrome c reductase hinge protein like	1.214	0.964	0.791

57164133	NDUFC2	NADH:ubiquinone oxidoreductase subunit C2	1.006	0.893	0.877
78214312	ATP5F1	ATP synthase, H+ transporting, mitochondrial Fo complex subunit B1	1.088	0.995	0.941
126723393	ENO3	enolase 3	1.098	0.930	0.875
188035915	ALDH7A1	aldehyde dehydrogenase 7 family member A1	0.979	0.920	0.914
226694171	PLS3	plastin 3(Pls3)	1.000	0.910	0.855
312032384	DPP6	dipeptidyl peptidase like 6	1.069	0.940	0.871

Table A2. BioLayout analysis of cortical, hippocampal and thalamic samples in* Cln3$^{-/-}$: *Cluster 4 (Chapter3)			**Ratio Cln3/WT**		
ID	**Gene Symbol**	**Description**	**Cortex**	**Hippocampus**	**Thalamus**
49868	ACTB	actin beta	1.044	1.060	1.210
203276	CLTA	clathrin light chain A	0.919	1.038	1.264
206440	EEF1A2	eukaryotic translation elongation factor 1 alpha 2	0.997	1.012	1.067
288120	PRKACB	protein kinase cAMP-activated catalytic subunit beta	0.905	1.095	1.470
1001011	HSPH1	heat shock protein family H (Hsp110) member 1	0.868	0.943	1.135
1167982	ABCB7	ATP binding cassette subfamily B member 7	0.817	1.015	1.268
1527199	USP9X	ubiquitin specific peptidase 9, X-linked	0.701	0.756	1.149
1809320	AP2S1	adaptor related protein complex 2 sigma 1 subunit	1.106	1.145	1.327
2769587	MAP6	microtubule associated protein 6	0.999	1.038	1.215
3171934	MAP6	microtubule associated protein 6	1.025	1.076	1.191
4506005	PPP1CB	protein phosphatase 1 catalytic subunit beta	0.704	0.862	1.175
4584820	PPP3CA	protein phosphatase 3 catalytic subunit alpha	1.131	1.173	1.321
5901688	GPRIN1	G protein regulated inducer of neurite outgrowth 1	1.168	1.278	1.899
6636119	ACTN4	actinin alpha 4	1.106	1.187	1.582
6671561	AP2A1	adaptor related protein complex 2 alpha 1 subunit	0.836	0.940	1.127
6679593	RAB3A	RAB3A, member RAS oncogene family	0.952	0.964	1.102
6729920		Chain A, Mu2 Adaptin Subunit (Ap50) Of Ap2 Adaptor (Second Domain), Complexed With Egfr Internaliza	0.937	1.032	1.250
6754240	HPCA	hippocalcin	0.842	1.065	1.566
6755080	PRKCG	protein kinase C gamma	1.032	1.238	1.915
7305485	SH3GL1	SH3 domain containing GRB2 like 1, endophilin A2	1.011	1.223	1.698
7670399	MAP2K1	mitogen-activated protein kinase kinase 1	0.904	0.989	1.161
7949055	HPCAL1	hippocalcin like 1	1.106	1.188	1.618
8393496	GSK3A	glycogen synthase kinase 3 alpha	1.007	1.072	1.263
9790285	VPS29	VPS29, retromer complex component	0.826	1.014	1.548
11177910	HSPA2	heat shock protein family A (Hsp70) member 2	0.899	0.985	1.194
11528518	SV2A	synaptic vesicle glycoprotein 2A	0.828	0.990	1.196

12408324	CPLX1	complexin 1	0.954	1.012	1.096
12835802	ACTR3	ARP3 actin related protein 3 homolog	0.955	1.082	1.661
13470090	RAB3C	RAB3C, member RAS oncogene family	0.942	0.979	1.234
14250186	AP1B1	adaptor related protein complex 1 beta 1 subunit	0.983	0.995	1.046
14719578		Chain E, Crystal Structure Of The Catalytic Subunit Of Camp- Dependent Protein Kinase Complexed Wit	0.971	1.048	1.250
16758726	SLC17A7	solute carrier family 17 member 7	0.896	1.176	4.311
16758742	CAP2	CAP, adenylate cyclase-associated protein, 2 (yeast)	0.994	1.095	1.346
17105370	ATP6V1B2	ATPase H+ transporting V1 subunit B2	0.990	1.101	1.544
19424194	RAB3C	RAB3C, member RAS oncogene family	0.925	0.976	1.260
19526936	LANCL2	LanC like 2	0.968	1.091	1.922
20138800		RecName: Full=Intersectin-1; AltName: Full=EH and SH3 domains protein 1	0.843	1.006	1.284
20141804		RecName: Full=Catenin delta-2; AltName: Full=Neural plakophilin-related ARM-repeat protein; Short=N	0.926	0.986	1.307
21594625	PGM2L1	phosphoglucomutase 2 like 1	0.829	0.870	1.183
26329629	NCALD	neurocalcin delta	0.921	1.099	1.526
26337253	SLC2A3	solute carrier family 2 member 3	1.042	1.073	1.369
26355647	NAPG	NSF attachment protein gamma	0.940	0.966	1.091
26667199	CAMK2G	calcium/calmodulin dependent protein kinase II gamma	1.046	1.248	1.917
27372319	PCLO	piccolo presynaptic cytomatrix protein	0.951	1.018	1.168
27574127		Chain A, High Resolution Structure Of A Truncated Neuronal Snare Complex	1.132	1.277	1.897
28972065	CKAP5	cytoskeleton associated protein 5	0.780	0.901	1.259
31560792	SH3GL2	SH3 domain containing GRB2 like 2, endophilin A1	1.013	1.146	1.351
31791059	ALCAM	activated leukocyte cell adhesion molecule	0.935	0.975	1.275
37360508	SRCIN1	SRC kinase signaling inhibitor 1	0.943	1.025	1.379
38454230	ATP6V1E1	ATPase H+ transporting V1 subunit E1	0.951	1.030	1.250
39104547	SH3GLB2	SH3 domain containing GRB2 like endophilin B2	0.927	0.996	1.143
41018346	SYNJ1	synaptojanin 1	0.905	1.017	1.158
47059104	ATP6V1G2	ATPase H+ transporting V1 subunit G2	0.860	0.966	1.283
47605990	ROCK2	Rho associated coiled-coil containing protein kinase 2	0.878	1.013	1.314
50510671	DMXL2	Dmx like 2	0.980	1.013	1.074
52345394	ACTR3B	ARP3 actin related protein 3 homolog B	0.930	1.083	2.051
54291704	PACS1	phosphofurin acidic cluster sorting protein 1	1.028	1.036	1.056
56205559	Myh10	myosin, heavy polypeptide 10, non-muscle [Mus musculus]	0.944	0.994	1.072
60360046	TRIM2	tripartite motif containing 2	0.865	0.893	1.113
71061466	ENSA	endosulfine alpha	0.927	0.936	1.038

77416393	CLASP2	cytoplasmic linker associated protein 2	0.920	0.943	1.014
78711838	Ap2b1	adaptor-related protein complex 2, beta 1 subunit	1.006	1.090	1.210
114520592	MAP6	microtubule associated protein 6	1.016	1.068	1.287
117647240	MADD	MAP kinase activating death domain	0.987	1.006	1.227
158749626	SCAMP1	secretory carrier membrane protein 1	0.922	1.000	1.122
161086898	CACNA2D1	calcium voltage-gated channel auxiliary subunit alpha2delta 1	1.038	1.147	1.440
164565391	CNKSR2	connector enhancer of kinase suppressor of Ras 2	0.942	1.104	1.420
347360906	ACTB	actin, cytoplasmic 1	1.024	1.055	1.230

Table A3. BioLayout analysis of cortical, hippocampal and thalamic samples in* Cln3$^{-/-}$: *Cluster 6 (Chapter 3)			**Ratio Cln3/WT**		
ID	**Gene Symbol**	**Description**	**Cortex**	**Hippocampus**	**Thalamus**
57657	PDHA1	pyruvate dehydrogenase (lipoamide) alpha 1	1.049	0.946	0.770
114400	ATP1B2	ATPase Na+/K+ transporting subunit beta 2	0.882	0.823	0.719
198884	LTA4H	leukotriene A4 hydrolase	1.027	0.974	0.832
226486	RAB1B	rab1B protein	1.004	0.961	0.900
832851		manganese superoxide dismutase	0.917	0.911	0.876
930145	SPTAN1	spectrin alpha, non-erythrocytic 1	1.106	1.068	1.007
1730559	PYGB	phosphorylase, glycogen; brain	1.124	1.013	0.767
1747304	Nptn	neuroplastin	1.055	1.047	0.974
1942391		Chain A, G Protein Heterotrimer Mutant Gi_alpha_1(G203a) Beta_1 Gamma_2 With Gdp Bound	1.064	1.062	1.040
2118463		GTP-binding protein MEL - mouse	1.142	1.018	0.862
4506713	RPS27A	ribosomal protein S27a	1.172	1.052	0.855
6671664	CANX	calnexin	0.964	0.938	0.898
6680027	GLUD1	glutamate dehydrogenase 1	1.099	0.986	0.831
6680748	ATP5A1	ATP synthase, H+ transporting, mitochondrial F1 complex, alpha subunit 1, cardiac muscle	0.993	0.952	0.867
6753498	COX4IL	cytochrome c oxidase subunit 4 isoform 1, mitochondrial precursor	0.975	0.966	0.920
6753992	GJA1	gap junction protein alpha 1	1.186	1.070	0.852
6754974	PACSIN1	protein kinase C and casein kinase substrate in neurons 1	0.998	0.980	0.916
7949005	ATP5J	ATP synthase, H+ transporting, mitochondrial Fo complex subunit F6	0.998	0.982	0.899
12833077	CYC1	cytochrome c1	1.139	1.070	0.854
12839092	ASRGL1	asparaginase like 1	1.164	1.131	0.904
13385854	PPID	peptidylprolyl isomerase D	1.024	0.997	0.898
14714615	HSP90B1	heat shock protein 90 beta family member 1	1.011	0.943	0.809

15030102	SDHA	succinate dehydrogenase complex flavoprotein subunit A	1.053	1.024	0.805
16758642	DARS	aspartyl-tRNA synthetase	0.966	0.873	0.688
19527228	CISD1	CDGSH iron sulfur domain 1	1.020	1.010	0.974
20070420	C21orf33/LOC102724023	chromosome 21 open reading frame 33	1.047	1.029	0.990
20072543	FBXO2	F-box protein 2	1.175	1.042	0.654
21312520	QDPR	quinoid dihydropteridine reductase	1.230	1.118	0.650
23271467	ALDH1L1	aldehyde dehydrogenase 1 family member L1	1.020	0.984	0.814
26328021	ME3	malic enzyme 3	1.162	1.090	0.830
26336659	Ank2	ankyrin 2, brain	1.151	1.012	0.711
26344409	Nptn	neuroplastin	1.032	1.026	0.966
26346450	UQCRC2	ubiquinol-cytochrome c reductase core protein II	1.018	0.965	0.816
26354805	SFXN3	sideroflexin 3	1.165	1.095	1.000
27369581	SLC25A12	solute carrier family 25 member 12	0.970	0.949	0.852
27503563	MAP4	microtubule associated protein 4	1.037	0.993	0.683
28893409	ENPP6	ectonucleotide pyrophosphatase/phosphodiesterase 6	1.174	1.048	0.477
29293809	ACLY	ATP citrate lyase	1.093	0.891	0.561
31981515	RPL7	ribosomal protein L7	1.033	0.962	0.848
33859482	EEF2	eukaryotic translation elongation factor 2	1.012	0.992	0.962
54037163	GANAB	glucosidase II alpha subunit	0.899	0.869	0.791
54887356	HADHA	hydroxyacyl-CoA dehydrogenase/3-ketoacyl-CoA thiolase/enoyl-CoA hydratase (trifunctional protein), alpha subunit	1.072	0.995	0.687
59808764	NIPSNAP1	nipsnap homolog 1 (C. elegans)	0.950	0.854	0.621
60360580	OGDH	oxoglutarate dehydrogenase	0.983	0.927	0.804
61556993	HIBCH	3-hydroxyisobutyryl-CoA hydrolase	0.892	0.839	0.767
83921618	EZR	ezrin	1.012	1.009	0.999
89001109	GNA13	G protein subunit alpha 13	0.959	0.916	0.724
125987842	MYO18A	myosin XVIIIA	1.067	1.026	0.561
162138936	HAPLN1	hyaluronan and proteoglycan link protein 1	1.150	0.963	0.611
228480241	MTX2	metaxin 2	1.056	0.995	0.863
254587947	PTPA	protein phosphatase 2 phosphatase activator	1.376	1.324	0.735

Table A4. BioLayout analysis of cortical, hippocampal and thalamic samples in* Cln3$^{-/-}$*: Cluster 7 (Chapter 3)			**Ratio Cln3/WT**		
ID	**Gene Symbol**	**Description**	**Cortex**	**Hippocampus**	**Thalamus**
53754	PABPC1	poly(A) binding protein cytoplasmic 1	0.900	0.954	0.976

192912	MAPT	microtubule associated protein tau	0.663	1.001	1.256
199023	MAP2	microtubule associated protein 2	0.995	1.046	1.092
464506	PC	pyruvate carboxylase	0.888	0.933	0.952
557967	PSAP	prosaposin	0.766	1.052	1.246
557967	PSAP	prosaposin	0.803	1.052	1.246
817984	NCAM1	neural cell adhesion molecule 1	1.107	1.169	1.180
1054878	ATP2B4	ATPase plasma membrane Ca2+ transporting 4	0.939	1.008	1.066
1346311		RecName: Full=Hypoxanthine-guanine phosphoribosyltransferase; Short=HGPRT; Short=HGPRTase	1.028	1.061	1.078
1517864	PEBP1	phosphatidylethanolamine binding protein 1	1.050	1.146	1.168
1708161	HTT	huntingtin	0.839	1.032	1.196
1840399	SYT3	synaptotagmin 3	0.992	1.076	1.092
2062607	KIF5B	kinesin family member 5B	0.870	1.039	1.073
3046247		aldose reductase [Mus musculus]	0.920	1.010	1.016
3955098	ATP6V1C1	ATPase H+ transporting V1 subunit C1	0.841	1.026	1.143
4506025	PPP3R1	protein phosphatase 3 regulatory subunit B, alpha	0.984	1.090	1.186
4507729	TUBB2A	tubulin beta 2A class IIa	0.961	1.072	1.128
4507789	UBE2L3	ubiquitin conjugating enzyme E2 L3	0.814	0.966	1.043
6693834	SRCIN1	SRC kinase signaling inhibitor 1	0.890	1.114	1.200
7106439	TUBB	tubulin beta class I	0.907	1.028	1.062
7657031	NT5C	5', 3'-nucleotidase, cytosolic	0.917	1.140	1.264
8394027	PPP2R1A	protein phosphatase 2 scaffold subunit Aalpha	0.813	1.111	1.211
9790219	DSTN	destrin, actin depolymerizing factor	0.841	1.116	1.204
12844989	PGAM1	phosphoglycerate mutase 1	0.934	1.022	1.074
12851187	TUBB4A	tubulin beta 4A class IVa	0.915	0.973	0.995
13542680	TUBB4B	tubulin beta 4B class IVb	0.893	1.029	1.081
17865351	VCP	valosin containing protein	0.961	1.042	1.093
20072952	AUH	AU RNA binding protein/enoyl-CoA hydratase	0.868	0.943	1.033
21165514	LETM1	leucine zipper and EF-hand containing transmembrane protein 1	0.816	0.951	0.991
21311871	Nebl	nebulette	0.857	1.058	1.139
21746161	TUBB2B	tubulin beta 2B class IIb	0.956	1.057	1.159
24817674	UBE2V2	ubiquitin conjugating enzyme E2 V2	0.847	0.921	0.945
26327655	MAOB	monoamine oxidase B	1.080	1.150	1.229
26345590	EEF1A1	eukaryotic translation elongation factor 1 alpha 1	0.909	1.026	1.102
26353710	RPS8	ribosomal protein S8	0.823	0.849	0.865
26353870	PPP2R1A	protein phosphatase 2 scaffold subunit Aalpha	0.813	1.111	1.211

27754056	TUBB6	tubulin beta 6 class V	0.930	1.043	1.115
34996495	RPN2	ribophorin II	0.885	1.034	1.052
37812499	OPA1	OPA1, mitochondrial dynamin like GTPase	0.879	0.954	1.022
38259194	DNAJC6	DnaJ heat shock protein family (Hsp40) member C6	0.777	0.996	1.073
41281852	AMPH	amphiphysin	0.882	1.105	1.292
45598372	BASP1	brain abundant membrane attached signal protein 1	0.972	1.061	1.113
56744242	AP1G1	adaptor related protein complex 1 gamma 1 subunit	0.887	1.182	1.491
57164143	ACTR2	ARP2 actin related protein 2 homolog	0.983	1.033	1.087
57527421	Sh3glb2	SH3 domain-containing GRB2-like endophilin B2	1.018	1.278	1.403
81867523	LRP1	LDL receptor related protein 1	0.812	0.932	0.978
112807195	Cox5b	cytochrome c oxidase subunit Vb	0.852	0.908	0.920
148491097	DYNC1H1	dynein cytoplasmic 1 heavy chain 1	0.863	0.954	0.981
157787064	GRM2	glutamate metabotropic receptor 2	0.817	0.992	1.018
172072590	NCDN	neurochondrin	0.727	1.078	1.140

Table A5.* Cln3$^{-/-}$ *thalamic filtered proteins upregulated more than 20% (Chapter 3)

Entrez Gene Name	ID	Gene Symbol	Fold Change Cln3/Control	Standard Deviation	Best Ion Score	iTRAQ Peptides
solute carrier family 17 (vesicular glutamate transporter), member 7	16758726	SLC17A7	4.311	10.117	85.29	5
calcium/calmodulin-dependent protein kinase II alpha	39104626	CAMK2A	2.537	0.841	130.09	14
actinin, alpha 1	61097906	ACTN1	2.447	1.829	80.05	9
CaM kinase-like vesicle-associated	21704242	CAMKV	2.340	1.716	112.93	10
ankyrin repeat and sterile alpha motif domain containing 1B	31088914	ANKS1B	2.305	4.244	52.48	4
inositol-trisphosphate 3-kinase A	124808	ITPKA	2.231	2.298	99.10	2
glutamate receptor, metabotropic 5	8393490	GRM5	2.149	1.194	55.86	2
lectin, galactoside-binding-like	26349211	LGALSL	2.146	2.737	54.71	2
ARP3 actin-related protein 3 homolog B (yeast)	52345394	ACTR3B	2.051	1.069	66.33	4
calcium/calmodulin-dependent protein kinase II delta	26667180	CAMK2D	1.992	0.993	130.09	6
syntaxin 1A (brain)	220777	STX1A	1.983	0.737	101.88	10
synaptic vesicle glycoprotein 2B	27261824	SV2B	1.979	0.945	77.38	8
Dmx-like 2	26327915	DMXL2	1.959	0.397	73.26	3
seryl-tRNA synthetase 2, mitochondrial	228008415	SARS2	1.950	1.089	44.17	2
LanC lantibiotic synthetase component C-like 2 (bacterial)	19526936	LANCL2	1.922	0.586	99.94	4
calcium/calmodulin-dependent protein kinase II gamma	26667199	CAMK2G	1.917	0.988	130.09	5
protein kinase C, gamma	6755080	PRKCG	1.915	0.038	51.04	2

crystallin, mu	7710012	CRYM	1.911	0.379	73.61	4
G protein regulated inducer of neurite outgrowth 1	5901688	GPRIN1	1.899	4.100	60.52	3
synaptic Ras GTPase activating protein 1	2935448	SYNGAP1	1.864	1.271	74.69	9
synaptotagmin VII	41281824	SYT7	1.858	1.339	54.01	4
drebrin 1	19909851	DBN1	1.820	1.783	60.28	5
keratin 1, type II	81891716	KRT1	1.818	0.413	66.06	2
phospholipase C, eta 2	30354507	PLCH2	1.802	0.392	67.98	2
histone cluster 2, H4a	51311	HIST2H4A	1.781	0.231	65.47	4
calcium channel, voltage-dependent, gamma subunit 8	21687018	CACNG8	1.764	0.708	62.10	2
KIAA1211-like	12842691	KIAA1211L	1.761	1.117	62.50	2
solute carrier family 1 (glial high affinity glutamate transporter), member 3	232176	SLC1A3	1.757	0.955	113.68	5
glutamate receptor, ionotropic, AMPA 2	22096313	GRIA2	1.734	1.478	102.27	11
Rho GTPase activating protein 1	13879250	ARHGAP1	1.727	0.674	44.90	2
glycoprotein M6B	30316333	GPM6B	1.725	0.471	62.72	6
NCK-associated protein 1	28395023	NCKAP1	1.701	0.575	79.30	8
SH3-domain GRB2-like 1	7305485	SH3GL1	1.698	0.462	61.56	3
catenin (cadherin-associated protein), delta 2	20177853	CTNND2	1.673	2.479	54.59	4
mitogen-activated protein kinase 1	6754632	MAPK1	1.669	0.381	86.05	4
ARP3 actin-related protein 3 homolog (yeast)	12835802	ACTR3	1.661	0.875	58.56	8
bassoon presynaptic cytomatrix protein	3413810	BSN	1.643	0.637	118.55	15
thioredoxin-related transmembrane protein 2	56090369	TMX2	1.641	2.331	39.21	2
PHD finger protein 24	27369996	PHF24	1.621	0.379	59.41	2
hippocalcin-like 1	7949055	HPCAL1	1.618	0.657	68.83	5
synaptotagmin I	148356226	SYT1	1.617	0.780	110.97	16
complexin 2	5729783	CPLX2	1.609	0.154	72.91	3
CDP-diacylglycerol synthase (phosphatidate cytidylyltransferase) 2	37589410	CDS2	1.608	0.767	57.79	2
lymphocyte antigen 6 complex, locus H	6754586	LY6H	1.583	0.216	58.43	3
actinin, alpha 4	6636119	ACTN4	1.582	1.060	61.66	6
catenin (cadherin-associated protein), alpha 2	475010	CTNNA2	1.571	0.350	146.07	3
hippocalcin	6754240	HPCA	1.566	0.855	100.20	4
thymosin beta 10	207318	TMSB10/TMSB4X	1.565	0.157	88.25	3
flotillin 1	158636004	FLOT1	1.559	0.501	77.71	4
dihydropyrimidinase-like 4	3122044	DPYSL4	1.557	0.177	70.41	3
VPS29 retromer complex component	9790285	VPS29	1.548	1.581	48.18	3
ATPase, H+ transporting, lysosomal 56/58kDa, V1 subunit B2	17105370	ATP6V1B2	1.544	0.595	68.59	8
catenin (cadherin-associated protein), beta 1, 88kDa	6671684	CTNNB1	1.537	0.411	73.57	7

epsin 1	16923990	EPN1	1.537	0.253	87.72	2
flotillin 2	13929186	FLOT2	1.529	0.720	111.15	5
neurocalcin delta	26329629	NCALD	1.526	0.636	67.10	5
synapsin II	77404242	SYN2	1.512	0.654	102.12	11
calcium/calmodulin-dependent protein kinase ID	79750129	CAMK1D	1.508	0.984	54.11	2
adaptor-related protein complex 1, gamma 1 subunit	56744242	AP1G1	1.491	0.230	43.55	2
actin related protein 2/3 complex, subunit 3, 21kDa	9790141	ARPC3	1.490	0.033	62.78	3
calcium/calmodulin-dependent protein kinase II beta	125287	CAMK2B	1.488	0.827	130.09	9
protein kinase, cAMP-dependent, catalytic, beta	288120	PRKACB	1.470	0.479	54.31	2
glutaminase	121447	GLS	1.463	0.571	85.77	8
clathrin, light chain B	12844891	CLTB	1.462	0.548	96.68	3
cytochrome b5 reductase 3	19745150	Cyb5r3	1.459	0.263	85.50	3
adducin 2 (beta)	26325436	ADD2	1.458	0.511	60.35	4
dynein, cytoplasmic 1, light intermediate chain 1	22122795	DYNC1LI1	1.455	1.295	37.64	3
CD47 molecule	6754382	CD47	1.444	0.183	84.63	3
calcium channel, voltage-dependent, alpha 2/delta subunit 1	161086898	CACNA2D1	1.440	0.319	69.46	5
mitochondrial carrier 1	6453809	MTCH1	1.437	0.854	49.64	2
mercaptopyruvate sulfurtransferase	90110410	MPST	1.435	0.477	36.88	2
reticulon 1	31982561	RTN1	1.424	0.341	87.99	9
connector enhancer of kinase suppressor of Ras 2	164565391	CNKSR2	1.420	0.126	65.51	2
protein kinase, cAMP-dependent, regulatory, type II, beta	45598396	PRKAR2B	1.415	0.454	130.95	6
septin 9	164698479	SEPT9	1.414	0.457	53.32	3
potassium channel, calcium activated large conductance subfamily M alpha, member 1	1305547	KCNMA1	1.404	0.042	73.55	2
early endosome antigen 1	26337923	EEA1	1.404	0.394	86.60	3
SH3-domain GRB2-like endophilin B2	57527421	Sh3glb2	1.403	0.093	47.88	2
prosaposin	298231229	PSAP	1.399	0.129	85.31	5
synapsin I	160707903	SYN1	1.398	0.491	133.06	19
signal-regulatory protein alpha	110626109	SIRPA	1.397	0.137	104.74	4
copine IV	12852219	CPNE4	1.393	0.270	47.62	3
ubiquitin specific peptidase 5 (isopeptidase T)	7305619	USP5	1.391	0.284	78.84	6
chromosome 14 open reading frame 2	21312554	C14orf2	1.389	0.053	54.78	2
receptor accessory protein 2	54261730	REEP2	1.388	0.498	44.75	2
discs, large homolog 4 (Drosophila)	9665227	DLG4	1.387	0.392	97.64	5
internexin neuronal intermediate filament protein, alpha	148539957	INA	1.387	0.346	79.73	10
glycoprotein M6A	19483938	GPM6A	1.385	0.624	84.99	5
phospholipase C-like 2	28972610	PLCL2	1.379	0.396	37.81	2

SRC kinase signaling inhibitor 1	37360508	SRCIN1	1.379	0.838	53.91	4
WD repeat domain 1	29144967	WDR1	1.375	0.316	51.49	3
solute carrier family 2 (facilitated glucose transporter), member 3	26337253	SLC2A3	1.369	0.295	82.36	5
NADH dehydrogenase (ubiquinone) complex I, assembly factor 2	188035926	NDUFAF2	1.368	1.334	55.23	3
TBC1 domain family, member 10B	15076925	TBC1D10B	1.367	0.081	58.14	2
solute carrier family 25 (mitochondrial carrier: glutamate), member 22	21311845	SLC25A22	1.366	0.581	73.57	4
phosphoenolpyruvate carboxykinase 2 (mitochondrial)	28077029	PCK2	1.358	0.111	62.45	2
monoglyceride lipase	6754690	MGLL	1.355	0.760	57.26	2
guanine nucleotide binding protein (G protein), alpha 11 (Gq class)	6754004	GNA11	1.353	0.091	62.01	2
plectin	40849920	PLEC	1.353	0.326	96.64	6
SH3-domain GRB2-like 2	31560792	SH3GL2	1.351	0.389	112.49	12
CAP, adenylate cyclase-associated protein, 2 (yeast)	16758742	CAP2	1.346	0.392	79.68	3
L1 cell adhesion molecule	115558	L1CAM	1.344	0.212	56.44	3
cytoplasmic FMR1 interacting protein 2	34784177	CYFIP2	1.328	0.665	108.76	8
spectrin, beta, non-erythrocytic 2	55926127	SPTBN2	1.328	0.507	94.30	23
dedicator of cytokinesis 4	62543571	DOCK4	1.328	0.061	36.76	2
adaptor-related protein complex 2, sigma 1 subunit	1809320	AP2S1	1.327	0.273	79.59	2
thioredoxin-related transmembrane protein 3	37360566	TMX3	1.327	0.154	79.98	2
heterogeneous nuclear ribonucleoprotein A3	157277969	Hnrnpa3	1.325	0.252	49.13	2
adaptor-related protein complex 2, alpha 2 subunit	49880	AP2A2	1.323	0.376	74.55	11
ryanodine receptor 2 (cardiac)	11321166	RYR2	1.323	1.025	47.66	3
septin 6	293597553	SEPT6	1.323	0.352	126.73	6
protein phosphatase 1, regulatory subunit 7	57634526	PPP1R7	1.322	0.387	82.05	2
protein phosphatase 3, catalytic subunit, alpha isozyme	4584820	PPP3CA	1.321	0.498	76.23	8
BR serine/threonine kinase 1	47013801	BRSK1	1.319	0.130	44.87	2
neurotrimin	31982044	NTM	1.314	0.148	81.05	3
Rho-associated, coiled-coil containing protein kinase 2	47605990	ROCK2	1.314	0.194	66.68	2
threonyl-tRNA synthetase	27229277	TARS	1.312	0.006	71.89	2
heterogeneous nuclear ribonucleoprotein A2/B1	3329498	HNRNPA2B1	1.311	0.189	81.03	6
actin related protein 2/3 complex, subunit 4, 20kDa	12857620	ARPC4	1.295	0.076	50.11	2
amphiphysin	41281852	AMPH	1.292	0.944	136.98	14
septin 11	57634518	SEPT11	1.292	0.424	82.12	6
ATP synthase, H+ transporting, mitochondrial Fo complex, subunit G	31980744	ATP5L	1.291	0.205	64.34	2
ankyrin 3, node of Ranvier (ankyrin G)	25121946	ANK3	1.290	1.209	50.58	4
microtubule-associated protein 6	114520592	MAP6	1.287	0.443	90.89	13

phosphodiesterase 2A, cGMP-stimulated	56606121	PDE2A	1.286	0.155	51.50	2
LIM and SH3 protein 1	6754508	LASP1	1.284	0.083	47.54	2
tyrosine 3-monooxygenase/tryptophan 5-monooxygenase activation protein, zeta	6756041	YWHAZ	1.283	0.399	152.20	27
ATPase, H+ transporting, lysosomal 13kDa, V1 subunit G2	47059104	ATP6V1G2	1.283	0.577	76.84	3
glutamate receptor, ionotropic, N-methyl D-aspartate 2A	3915771	GRIN2A	1.280	0.206	48.49	2
Thy-1 cell surface antigen	6678347	THY1	1.277	0.269	84.78	9
tyrosine 3-monooxygenase/tryptophan 5-monooxygenase activation protein, eta	1526541	YWHAH	1.276	0.321	77.24	11
activated leukocyte cell adhesion molecule	31791059	ALCAM	1.275	0.240	57.47	4
protein kinase, cAMP-dependent, regulatory, type I, beta	6016420	PRKAR1B	1.269	0.423	45.75	2
ATP-binding cassette, sub-family B (MDR/TAP), member 7	1167982	ABCB7	1.268	0.344	60.05	2
secretory carrier membrane protein 5	13929020	SCAMP5	1.267	0.235	91.66	3
eukaryotic translation initiation factor 4 gamma, 3	29126896	EIF4G3	1.266	0.420	46.33	2
NSFL1 (p97) cofactor (p47)	41017503	NSFL1C	1.266	0.260	61.96	3
calcium channel, voltage-dependent, gamma subunit 3	21687008	CACNG3	1.265	0.002	52.18	2
clathrin, light chain A	203276	CLTA	1.264	0.770	54.73	6
5', 3'-nucleotidase, cytosolic	7657031	NT5C	1.264	0.062	60.79	3
glycogen synthase kinase 3 alpha	8393496	GSK3A	1.263	0.325	51.75	3
protein phosphatase 1, regulatory subunit 9B	22535257	PPP1R9B	1.261	0.001	77.27	2
doublecortin	59797481	DCX	1.261	0.457	56.06	2
RAB3C, member RAS oncogene family	19424194	RAB3C	1.260	0.323	70.93	5
cytoskeleton associated protein 5	28972065	CKAP5	1.259	0.202	58.02	5
cystatin C	192912	CST3	1.256	0.175	82.15	3
SH3-domain GRB2-like (endophilin) interacting protein 1	26335469	SGIP1	1.251	0.072	92.35	2
coactosin-like F-actin binding protein 1	19482160	COTL1	1.250	0.347	71.02	3
WW domain binding protein 2	20376818	WBP2	1.250	0.054	110.95	2
ATPase, H+ transporting, lysosomal 31kDa, V1 subunit E1	38454230	ATP6V1E1	1.250	0.260	114.67	12
p21 protein (Cdc42/Rac)-activated kinase 3	304307785	PAK3	1.248	0.445	70.00	2
guanine nucleotide binding protein (G protein), alpha activating activity polypeptide O	164607137	GNAO1	1.245	0.304	112.24	24
coronin, actin binding protein, 2B	38541878	CORO2B	1.237	0.123	66.10	2
monoamine oxidase B	26327655	MAOB	1.229	0.014	56.95	2
neurofilament, light polypeptide	39204499	NEFL	1.229	0.226	62.03	8
MAP-kinase activating death domain	117647240	MADD	1.227	0.580	37.08	2
ATPase, Ca++ transporting, cardiac muscle, slow twitch 2	6806903	ATP2A2	1.224	0.297	125.07	8
calbindin 1, 28kDa	6753242	CALB1	1.222	0.114	49.47	2
ATPase, H+ transporting, lysosomal V0 subunit a1	340007377	ATP6V0A1	1.221	0.417	88.60	13

neuroplastin	9507073	NPTN	1.216	0.800	104.78	8
secernin 1	38044104	SCRN1	1.216	0.339	69.09	5
phosphatidylinositol-5-phosphate 4-kinase, type II, gamma	81882183	PIP4K2C	1.216	0.343	80.01	3
huntingtin interacting protein 1 related	12718814	HIP1R	1.212	0.054	70.49	2
actin, beta-like 2	30425250	ACTBL2	1.212	0.141	87.32	14
protein phosphatase 2, regulatory subunit A, alpha	26353870	PPP2R1A	1.211	0.222	72.75	6
actin, beta	49868	ACTB	1.210	0.392	115.47	33
G protein-coupled receptor 158	52350563	GPR158	1.210	0.167	51.25	2
adaptor-related protein complex 2, beta 1 subunit	78711838	Ap2b1	1.210	0.431	124.94	24
phosphofructokinase, platelet	8489537	PFKP	1.209	0.436	79.09	5
importin 5	12057236	IPO5	1.209	0.625	61.49	3
esterase D	13937355	ESD	1.205	0.440	66.89	2
cortactin	2996044	CTTN	1.204	0.241	83.75	5
destrin (actin depolymerizing factor)	9790219	DSTN	1.204	0.007	47.54	2
UBX domain protein 6	16741117	UBXN6	1.204	0.098	53.48	2
biphenyl hydrolase-like (serine hydrolase)	21624609	BPHL	1.204	0.105	77.95	2
3-hydroxybutyrate dehydrogenase, type 1	20071589	BDH1	1.202	0.046	61.59	2

Table A6.* Cln3$^{-/-}$ *thalamic filtered proteins downregulated more than 20% (Chapter 3)

Entrez Gene Name	ID	Gene Symbol	Fold Change Cln3/Control	Standard Deviation	Best Ion Score	iTRAQ Peptides
talin 2	26325762	TLN2	-1.201	0.101	84.01	2
leukotriene A4 hydrolase	198884	LTA4H	-1.202	0.129	78.46	3
microtubule-associated protein, RP/EB family, member 1	78097100	MAPRE1	-1.202	0.208	70.97	4
glutamate dehydrogenase 1	6680027	GLUD1	-1.204	0.316	92.27	18
acetyl-CoA acetyltransferase 1	21450129	ACAT1	-1.205	0.374	100.64	4
ADP-ribosylation factor-like 3	12083661	ARL3	-1.206	0.030	37.03	2
NADH dehydrogenase (ubiquinone) 1 alpha subcomplex, 13	12963633	NDUFA13	-1.206	0.109	85.23	5
malic enzyme 3, NADP(+)-dependent, mitochondrial	26328021	ME3	-1.206	0.197	58.25	3
COP9 signalosome subunit 6	33563284	COPS6	-1.206	0.185	41.73	2
Rho GDP dissociation inhibitor (GDI) alpha	26344461	ARHGDIA	-1.207	0.353	75.31	5
pyrophosphatase (inorganic) 1	26353394	PPA1	-1.207	0.173	51.29	2
transferrin	17046471	TF	-1.208	0.064	42.72	2
neuronal calcium sensor 1	26347817	NCS1	-1.211	0.168	58.70	2
creatine kinase, mitochondrial 1B	6753428	CKMT1A/CKMT1B	-1.212	0.358	90.27	7

NADH dehydrogenase (ubiquinone) flavoprotein 2, 24kDa	12850902	NDUFV2	-1.212	0.167	53.16	5
solute carrier family 25 (mitochondrial carrier; adenine nucleotide translocator), member 5	32189350	SLC25A5	-1.212	0.207	88.94	22
ATPase, Na+/K+ transporting, beta 1 polypeptide	6753138	ATP1B1	-1.213	0.187	88.36	19
glucose-6-phosphate dehydrogenase	6996917	G6PD	-1.213	0.054	83.94	3
peptidylglycine alpha-amidating monooxygenase	1711199	PAM	-1.214	0.322	39.82	2
protein kinase C and casein kinase substrate in neurons 2	22256944	PACSIN2	-1.215	0.112	52.98	3
Tu translation elongation factor, mitochondrial	254911131	TUFM	-1.216	0.272	74.07	7
transaldolase 1	12002054	TALDO1	-1.217	0.080	87.82	2
glutamate decarboxylase 2 (pancreatic islets and brain, 65kDa)	2558495	GAD2	-1.218	0.130	75.16	3
peroxiredoxin 5	6746357	PRDX5	-1.218	0.208	101.70	9
glutathione S-transferase, mu 6	2275019	Gstm6	-1.220	0.288	62.60	4
dynein, cytoplasmic 1, light intermediate chain 2	2618478	DYNC1LI2	-1.223	0.089	108.96	2
phosphatidylinositol-5-phosphate 4-kinase, type II, beta	33563294	PIP4K2B	-1.224	0.192	109.32	2
syntaxin 1B	6981600	STX1B	-1.225	0.269	90.79	24
ubiquinol-cytochrome c reductase core protein II	26346450	UQCRC2	-1.226	0.267	146.53	8
heat shock 70kDa protein 5 (glucose-regulated protein, 78kDa)	12835845	HSPA5	-1.227	0.783	103.16	15
isocitrate dehydrogenase 3 (NAD+) beta	18700024	IDH3B	-1.228	0.342	121.42	11
aldehyde dehydrogenase 1 family, member L1	23271467	ALDH1L1	-1.229	0.101	63.73	2
heat shock protein 90kDa alpha (cytosolic), class B member 1	51859516	HSP90AB1	-1.229	0.350	93.20	19
glutamic-oxaloacetic transaminase 2, mitochondrial	2690302	GOT2	-1.230	0.171	86.03	16
NADH dehydrogenase (ubiquinone) 1 alpha subcomplex, 9, 39kDa	13543186	NDUFA9	-1.231	0.274	95.46	9
RAP1B, member of RAS oncogene family	7661678	RAP1B	-1.234	0.192	78.27	3
mechanistic target of rapamycin (serine/threonine kinase)	8132058	MTOR	-1.234	0.093	53.90	2
electron-transfer-flavoprotein, beta polypeptide	12832367	ETFB	-1.234	0.410	40.89	2
phosphoserine aminotransferase 1	26354941	PSAT1	-1.234	0.060	60.75	3
septin 4	6755120	SEPT4	-1.235	0.014	54.40	2
heat shock protein 90kDa beta (Grp94), member 1	14714615	HSP90B1	-1.236	0.221	74.95	8
lactate dehydrogenase B	6678674	LDHB	-1.237	0.195	120.96	15
dynactin 1	2104495	DCTN1	-1.238	0.307	96.43	7
neurocan	40789268	NCAN	-1.239	0.713	72.94	3
ATP synthase, H+ transporting, mitochondrial F1 complex, O subunit	20070412	ATP5O	-1.241	0.336	53.65	7
succinate dehydrogenase complex, subunit A, flavoprotein	15030102	SDHA	-1.243	0.406	75.18	11

(Fp)						
immunoglobulin superfamily, member 8	32189434	IGSF8	-1.243	0.385	84.16	5
junction plakoglobin	41529837	JUP	-1.243	0.419	42.60	2
oxoglutarate (alpha-ketoglutarate) dehydrogenase (lipoamide)	60360580	OGDH	-1.244	0.212	88.55	17
tumor protein D52	6678407	TPD52	-1.246	0.058	71.62	2
NADH dehydrogenase (ubiquinone) 1 beta subcomplex, 4, 15kDa	21314826	NDUFB4	-1.250	0.226	49.80	3
synaptogyrin 3	4731936	SYNGR3	-1.252	0.108	41.91	2
glial fibrillary acidic protein	14193690	GFAP	-1.253	0.049	69.47	3
leucine aminopeptidase 3	58865398	LAP3	-1.255	0.091	66.21	3
adenylate kinase 4	6753022	AK4	-1.257	0.120	45.85	2
proline dehydrogenase (oxidase) 1	6649587	LOC102724788/PRODH	-1.259	0.185	43.28	2
malic enzyme 1, NADP(+)-dependent, cytosolic	266504	ME1	-1.262	0.108	93.04	2
pyruvate kinase, muscle	16757994	PKM	-1.263	0.274	112.60	22
glucosidase, alpha; neutral AB	54037163	GANAB	-1.264	0.439	73.93	4
ubiquinol-cytochrome c reductase hinge protein like	57164091	UQCRHL	-1.265	0.187	49.02	4
potassium channel, voltage gated shaker related subfamily A, member 1	27465523	KCNA1	-1.266	0.263	58.35	4
solute carrier family 12 (potassium/chloride transporter), member 5	28972652	SLC12A5	-1.266	0.245	79.92	11
hydroxysteroid (17-beta) dehydrogenase 4	31982273	HSD17B4	-1.268	0.331	41.33	2
NADH dehydrogenase (ubiquinone) Fe-S protein 3, 30kDa (NADH-coenzyme Q reductase)	12832533	NDUFS3	-1.269	0.471	63.68	4
ATPase, Na+/K+ transporting, alpha 1 polypeptide	21450277	ATP1A1	-1.270	0.346	167.03	43
translocase of inner mitochondrial membrane 44 homolog (yeast)	2351410	TIMM44	-1.271	0.057	52.26	2
bridging integrator 1	6753050	BIN1	-1.275	0.290	79.10	7
succinate-CoA ligase, alpha subunit	9483736	SUCLG1	-1.278	0.203	129.75	7
endonuclease domain containing 1	26348195	ENDOD1	-1.278	0.057	49.81	2
sorbin and SH3 domain containing 1	39104628	SORBS1	-1.280	0.001	44.02	2
NADH dehydrogenase (ubiquinone) 1 beta subcomplex, 7, 18kDa	13385322	NDUFB7	-1.281	0.115	56.32	3
potassium channel, voltage gated shaker related subfamily A, member 2	25742772	KCNA2	-1.284	0.164	58.35	3
chaperonin containing TCP1, subunit 7 (eta)	26346713	CCT7	-1.284	0.189	53.07	3
caldesmon 1	21704156	Cald1	-1.287	0.096	62.86	2
myosin, heavy chain 9, non-muscle	47847498	MYH9	-1.289	0.196	52.50	5

serine/threonine kinase receptor associated protein	58865512	STRAP	-1.290	0.387	51.35	3
NADH dehydrogenase (ubiquinone) 1 beta subcomplex, 8, 19kDa	13385558	NDUFB8	-1.291	0.271	76.19	4
ATPase, Na+/K+ transporting, alpha 3 polypeptide	6978547	ATP1A3	-1.298	0.262	167.03	72
exocyst complex component 4	213688367	EXOC4	-1.298	0.164	88.39	3
pyruvate dehydrogenase (lipoamide) alpha 1	57657	PDHA1	-1.299	0.114	55.65	4
peroxiredoxin 1	6754976	PRDX1	-1.301	0.340	76.38	13
acyl-CoA dehydrogenase, long chain	31982520	ACADL	-1.301	0.232	42.87	2
glutathione peroxidase 4	90903233	GPX4	-1.301	0.006	44.27	2
synaptotagmin II	31543797	SYT2	-1.302	0.512	110.97	7
phosphorylase, glycogen; brain	1730559	PYGB	-1.303	0.254	104.93	14
3-hydroxyisobutyryl-CoA hydrolase	61556993	HIBCH	-1.303	0.321	74.67	2
ubiquinol-cytochrome c reductase, Rieske iron-sulfur polypeptide 1	13385168	UQCRFS1	-1.307	0.152	98.69	4
ATP synthase, H+ transporting, mitochondrial Fo complex, subunit d	21313679	ATP5H	-1.307	0.363	106.89	9
palmitoyl-protein thioesterase 1	121674797	PPT1	-1.307	0.030	47.63	2
cytochrome b5 type B (outer mitochondrial membrane)	12833936	CYB5B	-1.308	0.283	47.18	2
pyridoxal (pyridoxine, vitamin B6) kinase	26348803	PDXK	-1.310	0.238	66.09	3
heat shock 70kDa protein 4-like	1902905	HSPA4L	-1.318	0.166	77.96	5
COP9 signalosome subunit 2	4759264	COPS2	-1.325	0.070	57.75	2
electron-transfer-flavoprotein, alpha polypeptide	26328615	ETFA	-1.325	0.252	146.80	3
dynamin 2	16307381	DNM2	-1.329	0.326	42.26	2
ARP1 actin-related protein 1 homolog A, centractin alpha (yeast)	5031569	ACTR1A	-1.331	0.435	72.62	4
B-cell receptor-associated protein 31	12841984	BCAP31	-1.331	0.125	85.73	5
prenylcysteine oxidase 1	26329027	PCYOX1	-1.332	0.215	85.96	3
tweety family member 1	47496738	TTYH1	-1.332	0.037	62.23	2
microtubule-associated protein 1A	6272692	MAP1A	-1.335	0.292	64.80	5
glutamate-ammonia ligase	31982332	GLUL	-1.335	0.177	79.93	14
ribophorin I	26325850	RPN1	-1.340	0.022	63.95	2
cell adhesion molecule 4	23346547	CADM4	-1.341	0.178	64.74	3
SAC1 suppressor of actin mutations 1-like (yeast)	28972437	SACM1L	-1.343	0.156	45.82	3
myosin, light chain 12A, regulatory, non-sarcomeric	1170970	MYL12A	-1.348	0.456	40.51	3
creatine kinase, brain	10946574	CKB	-1.351	0.275	121.95	22
malate dehydrogenase 1, NAD (soluble)	254540027	MDH1	-1.352	0.297	114.28	9
solute carrier family 6 (neurotransmitter transporter), member 11	27370360	SLC6A11	-1.357	0.055	81.33	5

monoamine oxidase A	20810093	MAOA	-1.358	0.132	56.77	2
leucine rich repeat containing 7	16924000	LRRC7	-1.359	0.020	41.72	2
N-myc downstream regulated 1	118150658	NDRG1	-1.359	0.201	107.99	5
protein phosphatase 2A activator, regulatory subunit 4	254587947	PPP2R4	-1.360	0.015	55.32	2
proteasome 26S subunit, non-ATPase 12	12841273	PSMD12	-1.370	0.033	78.98	2
hydroxyacyl-CoA dehydrogenase/3-ketoacyl-CoA thiolase/enoyl-CoA hydratase (trifunctional protein), beta subunit	26350301	HADHB	-1.370	0.496	46.09	2
hemoglobin, beta	31982300	HBB	-1.372	0.205	89.15	9
semaphorin 7A, GPI membrane anchor (John Milton Hagen blood group)	3523117	SEMA7A	-1.373	0.075	86.69	2
peroxiredoxin 3	11968132	PRDX3	-1.375	0.045	40.64	2
chaperonin containing TCP1, subunit 3 (gamma)	347839	CCT3	-1.378	0.124	80.66	2
guanine nucleotide binding protein (G protein), alpha 13	89001109	GNA13	-1.382	0.213	75.64	5
chaperonin containing TCP1, subunit 5 (epsilon)	37359776	CCT5	-1.388	0.928	74.83	5
cathepsin B	6681079	CTSB	-1.389	0.001	66.16	2
ATPase, Na+/K+ transporting, beta 2 polypeptide	114400	ATP1B2	-1.391	0.180	78.58	6
adenosylhomocysteinase-like 2	342307099	AHCYL2	-1.397	0.317	90.27	4
ankyrin 2, brain	26336659	Ank2	-1.407	0.817	66.78	6
AHA1, activator of heat shock 90kDa protein ATPase homolog 1 (yeast)	26345022	AHSA1	-1.415	0.269	56.52	4
acyl-CoA synthetase long-chain family member 6	75992915	ACSL6	-1.423	0.164	59.40	6
hemoglobin, alpha 1	145301549	HBA1/HBA2	-1.431	0.175	105.53	8
BTB (POZ) domain containing 17	58037273	BTBD17	-1.432	0.080	74.35	2
glyoxalase I	19354350	GLO1	-1.450	0.273	80.57	2
aspartyl-tRNA synthetase	16758642	DARS	-1.453	0.236	103.35	2
ribosomal protein S15	40287237	RPS15	-1.454	0.026	49.83	2
protein-L-isoaspartate (D-aspartate) O-methyltransferase 1	417489	Pcmt1	-1.456	0.106	59.88	2
hydroxyacyl-CoA dehydrogenase/3-ketoacyl-CoA thiolase/enoyl-CoA hydratase (trifunctional protein), alpha subunit	54887356	HADHA	-1.456	0.298	95.64	6
fatty acid amide hydrolase	226443015	FAAH	-1.457	0.011	37.86	2
cysteine and glycine-rich protein 1	6681069	CSRP1	-1.465	0.208	92.69	6
microtubule-associated protein 4	27503563	MAP4	-1.465	0.560	70.70	4
hydroxysteroid (17-beta) dehydrogenase 12	9789991	HSD17B12	-1.476	0.195	56.78	2
potassium channel, voltage gated subfamily A regulatory beta subunit 2	8393646	KCNAB2	-1.480	0.127	63.66	5
v-ral simian leukemia viral oncogene homolog A (ras	12851417	RALA	-1.482	0.084	64.11	3

related)						
carbonic anhydrase II	157951596	CA2	-1.491	0.182	72.37	7
ATPase, Na+/K+ transporting, alpha 2 polypeptide	37360088	ATP1A2	-1.497	0.252	167.03	53
aspartoacylase	12842492	ASPA	-1.501	0.001	86.83	2
ADP-ribosylarginine hydrolase	6680658	ADPRH	-1.502	0.092	73.54	2
3-hydroxyisobutyrate dehydrogenase	26347027	HIBADH	-1.504	0.047	78.63	2
RAB21, member RAS oncogene family	51948448	RAB21	-1.509	0.224	68.61	3
adenosylhomocysteinase-like 1	21361647	AHCYL1	-1.513	0.163	90.27	7
synuclein, gamma (breast cancer-specific protein 1)	122066261	SNCG	-1.526	0.165	72.29	2
F-box protein 2	20072543	FBXO2	-1.529	0.208	80.52	4
acyl-CoA synthetase bubblegum family member 1	16716465	ACSBG1	-1.532	0.432	84.72	5
CD9 molecule	6680894	CD9	-1.536	0.108	65.77	2
tubulin polymerization-promoting protein family member 3	13385968	TPPP3	-1.537	0.038	80.73	2
quinoid dihydropteridine reductase	21312520	QDPR	-1.538	0.044	67.69	3
transketolase	11066098	TKT	-1.547	0.273	83.80	7
ATP synthase, H+ transporting, mitochondrial Fo complex, subunit F2	10181184	ATP5J2	-1.562	0.071	67.34	3
cytochrome c oxidase III	34538604	MT-CO3	-1.570	0.024	92.03	2
ATPase, Ca++ transporting, plasma membrane 3	56699478	ATP2B3	-1.577	0.333	146.05	10
nicalin	12859602	NCLN	-1.598	0.122	89.99	2
nipsnap homolog 1 (C. elegans)	59808764	NIPSNAP1	-1.610	0.181	61.94	2
translocase of inner mitochondrial membrane 13 homolog (yeast)	7305581	TIMM13	-1.617	0.078	63.72	2
guanine nucleotide binding protein (G protein), alpha z polypeptide	6980966	GNAZ	-1.637	0.209	58.23	2
hyaluronan and proteoglycan link protein 1	162138936	HAPLN1	-1.638	0.095	64.47	6
up-regulated during skeletal muscle growth 5 homolog (mouse)	77404294	USMG5	-1.657	0.053	57.18	2
sirtuin 2	170650632	SIRT2	-1.662	0.210	73.05	10
glycerol-3-phosphate dehydrogenase 1 (soluble)	13543176	GPD1	-1.665	0.217	72.10	4
ras homolog family member G	9625037	RHOG	-1.699	0.211	63.39	3
solute carrier family 12 (sodium/potassium/chloride transporter), member 2	13929130	SLC12A2	-1.703	0.033	60.92	3
nucleobindin 1	12841873	NUCB1	-1.734	0.165	56.87	2
gamma-aminobutyric acid (GABA) A receptor, alpha 1	6753936	GABRA1	-1.739	0.176	53.81	3
versican	21431624	VCAN	-1.761	0.155	79.33	3
annexin A6	31981302	ANXA6	-1.767	0.183	95.36	4
NADH dehydrogenase (ubiquinone) 1 beta subcomplex, 9,	29789148	NDUFB9	-1.771	0.180	51.11	3

22kDa						
myosin XVIIIA	125987842	MYO18A	-1.782	0.357	50.22	4
ATP citrate lyase	29293809	ACLY	-1.783	0.350	52.19	3
N-acylsphingosine amidohydrolase (acid ceramidase) 1	9790019	ASAH1	-1.786	0.072	43.31	3
RAB33B, member RAS oncogene family	8394133	RAB33B	-1.806	0.314	69.46	2
twinfilin actin binding protein 1	1769577	TWF1	-1.807	0.447	59.25	3
2',3'-cyclic nucleotide 3' phosphodiesterase	2160434	CNP	-1.856	0.199	116.30	40
S100 calcium binding protein B	6981498	S100B	-1.856	0.112	105.92	2
hyaluronan and proteoglycan link protein 4	30349291	HAPLN4	-1.859	0.085	48.61	2
proteolipid protein 1	200425	PLP1	-1.901	0.239	99.93	22
claudin 11	6679186	CLDN11	-1.925	0.053	95.27	2
phosphorylase, glycogen, muscle	6755256	PYGM	-1.928	0.182	101.55	11
myosin ID	56799396	MYO1D	-1.935	0.287	62.80	4
annexin A5	13277612	ANXA5	-1.944	0.079	72.81	6
secretory carrier membrane protein 3	2232237	SCAMP3	-1.968	0.181	63.63	2
solute carrier family 32 (GABA vesicular transporter), member 1	26665359	SLC32A1	-2.002	0.219	121.41	5
myelin associated glycoprotein	8393742	MAG	-2.063	0.105	71.70	4
ectonucleotide pyrophosphatase/phosphodiesterase 6	28893409	ENPP6	-2.095	0.059	65.23	4
acyl-CoA thioesterase 7	14587839	ACOT7	-2.110	0.246	64.59	3
myelin basic protein	69885032	MBP	-2.163	0.171	101.64	23
S100 calcium binding protein A1	12856441	S100A1	-2.308	0.172	63.05	2
myelin oligodendrocyte glycoprotein	399589	MOG	-2.330	0.041	105.68	5
hyaluronan and proteoglycan link protein 2	15042971	HAPLN2	-2.343	0.091	52.69	2
glycolipid transfer protein	6959684	GLTP	-2.452	0.074	62.92	2
ATPase, Na+/K+ transporting, beta 3 polypeptide	6680744	ATP1B3	-2.565	0.237	52.43	2
solute carrier family 16 (monocarboxylate transporter), member 1	26353846	SLC16A1	-3.344	0.050	100.49	2
ermin, ERM-like protein	26346945	ERMN	-3.381	0.134	76.64	2
synuclein, alpha (non A4 component of amyloid precursor)	6678047	SNCA	-4.133	1.947	96.88	6

Table A7. Proteins identified by ≥ 2 peptide in Ppt1$^{-/-}$ *thalamic synaptosomes (Chapter 4)*			Fold change *Ppt1*$^{-/-}$/WT			
ID	**Gene Symbol**	**Entrez Gene Name**	**1 m**	**3 m**	**5 m**	**7 m**
P61922	ABAT	4-aminobutyrate aminotransferase	1.15	-3.22	2.59	-1.47
Q61282	Acan	aggrecan	3.08	2.17	1.18	-1.43
Q99KI0	ACO2	aconitase 2	1.41	-2.42	2.21	-1.59
Q3TSB7	ACTG1	actin gamma 1	-3.35	-1.37	-1.17	-1.13
A1BN54	ACTN1	actinin alpha 1	-1.48	-1.73	-1.22	-1.08
E9PY16	ADAP1	ArfGAP with dual PH domains 1	-1.38	-1.68	-1.14	-1.16
P84309	ADCY5	adenylate cyclase 5	1.67	1.19	-1.88	-1.24
Q3TF14	AHCY	Adenosylhomocysteinase	1.48	-2.21	1.66	-1.07
H3BKT5	AHCYL2	adenosylhomocysteinase like 2	-1.58	-3.28	1.90	1.28
Q9R0Y5	AK1	adenylate kinase 1	-1.28	-2.45	1.83	1.19
D3YVF0	AKAP5	A-kinase anchoring protein 5	-2.31	-2.47	-3.49	-1.52
P07724	ALB	albumin	2.03	1.27	1.22	1.83
Q8R0Y6	ALDH1L1	aldehyde dehydrogenase 1 family member L1	1.20	3.52	-1.54	-1.05
Q5FWB7	ALDOA	aldolase, fructose-bisphosphate A	-2.28	1.51	-1.17	1.02
P05063	ALDOC	aldolase, fructose-bisphosphate C	1.04	2.70	-1.57	1.19
C6EQG9	AMPH	ASL1/Amph fusion protein	1.29	-1.25	-1.09	-1.26
Q8C8R3-2	Ank2	ankyrin 2, brain	-1.86	-1.23	-1.09	1.13
P48036	ANXA5	annexin A5	1.88	-1.61	2.15	1.74
P17426	AP2A1	adaptor related protein complex 2 alpha 1 subunit	-2.04	-4.24	1.37	1.15
H3BKM0	Ap2b1	adaptor-related protein complex 2, beta 1 subunit	-1.07	-3.35	1.43	1.09
Q3TH69	AP2M1	adaptor related protein complex 2 mu 1 subunit	-2.02	1.04	-1.31	1.35
Q8BSL7	Arf2	ADP-ribosylation factor 2	-1.26	-4.24	1.66	-1.20
Q3TGS9	ARFGAP1	ADP ribosylation factor GTPase activating protein 1	-1.18	1.44	-1.91	-1.15
Q8R5J9	ARL6IP5	ADP ribosylation factor like GTPase 6 interacting protein 5	1.31	-4.84	2.49	-1.60
H7BWZ3	ARPC3	actin related protein 2/3 complex subunit 3	-1.66	-4.68	1.40	-1.27
Q7TPD9	ARPC4	actin related protein 2/3 complex subunit 4	-1.97	-1.94	1.35	1.28
Q3TWT5	ASAH1	N-acylsphingosine amidohydrolase 1	2.17	-1.54	2.97	1.31
Q3TXF9	ATP1A1	ATPase Na+/K+ transporting subunit alpha 1	-1.07	1.24	-1.58	1.90
D3YYN7	ATP1A2	ATPase Na+/K+ transporting subunit alpha 2	1.71	-10.44	6.56	-1.18
Q6PIC6	ATP1A3	ATPase Na+/K+ transporting subunit alpha 3	1.03	-4.18	3.43	-1.73
J3KMM5	ATP2A2	Sarcoplasmic/endoplasmic reticulum calcium ATPase 2	-1.45	-4.87	1.73	-1.31
G5E829	ATP2B1	ATPase plasma membrane Ca2+ transporting 1	-1.27	-1.06	-1.49	1.09
Q3UHH0	ATP2B2	ATPase plasma membrane Ca2+ transporting 2	1.09	1.20	-1.82	1.19
D3Z6F5	ATP5A1	ATP synthase, H+ transporting, mitochondrial F1 complex, alpha subunit 1, cardiac muscle	1.35	-2.73	2.18	-1.45
P56480	ATP5B	ATP synthase, H+ transporting, mitochondrial F1 complex, beta polypeptide	1.00	-5.61	3.03	-1.55
B1ASE2	ATP5H	ATP synthase, H+ transporting, mitochondrial Fo complex subunit D	-1.01	-2.24	1.08	-1.03

Q3TF25	ATP5O	ATP synthase, H+ transporting, mitochondrial F1 complex, O subunit	1.20	-11.18	2.66	-1.46
K3W4T3	ATP6V0A1	ATPase H+ transporting V0 subunit a1	-1.20	-3.24	1.51	-1.75
P51863	ATP6V0D1	ATPase H+ transporting V0 subunit d1	1.03	-12.14	2.80	-1.99
P50516	ATP6V1A	ATPase H+ transporting V1 subunit A	-1.07	-5.32	1.86	-1.53
P62814	ATP6V1B2	ATPase H+ transporting V1 subunit B2	-1.11	-3.71	2.41	-1.07
Q3TG21	ATP6V1C1	ATPase H+ transporting V1 subunit C1	-1.83	-3.95	-1.26	1.33
Q8BVE3	ATP6V1H	ATPase H+ transporting V1 subunit H	1.06	-4.93	1.70	-1.46
Q9JLZ3	AUH	AU RNA binding methylglutaconyl-CoA hydratase	1.26	-27.70	3.23	-3.24
B1AZ46	BAIAP2	BAI1 associated protein 2	-1.20	-1.01	-2.52	-1.09
Q91XV3	BASP1	brain abundant membrane attached signal protein 1	-4.13	-3.40	-3.37	1.22
Q61361	BCAN	brevican	2.37	-2.69	2.71	-1.10
A2AVX1	BCAS1	breast carcinoma amplified sequence 1	1.72	2.88	-1.06	1.48
Q80XN0	BDH1	3-hydroxybutyrate dehydrogenase 1	1.05	-1.08	1.30	1.24
Q6P1B9	BIN1	bridging integrator 1	-1.04	-1.51	1.21	-1.11
O88737	BSN	bassoon presynaptic cytomatrix protein	-1.25	1.29	-3.43	-1.14
Q9DB72	BTBD17	BTB domain containing 17	1.36	2.18	-1.52	-1.54
P00920	CA2	carbonic anhydrase 2	1.54	1.43	-1.11	1.00
F7CZ64	CACNG8	calcium voltage-gated channel auxiliary subunit gamma 8	-1.91	1.33	-2.38	-1.28
Q80TN1	CAMK2A	calcium/calmodulin dependent protein kinase II alpha	-1.45	-1.17	-2.26	-1.30
Q5SVI0	CAMK2B	calcium/calmodulin dependent protein kinase II beta	1.01	-3.62	1.46	-1.64
Q3UHL1	CAMKV	CaM kinase like vesicle associated	-2.08	-1.15	-2.87	-1.33
P80316	CCT5	chaperonin containing TCP1 subunit 5	-1.14	-7.27	2.18	-1.82
Q8BS79	CDH13	cadherin 13	-1.25	1.22	-2.35	-1.64
F8WGL3	CFL1	cofilin 1	1.02	-5.06	2.55	-1.25
Q04447	CKB	creatine kinase B	-1.06	-3.96	1.68	-1.68
F7DCH5	CLASP2	cytoplasmic linker associated protein 2	-1.05	-2.37	1.48	-1.63
Q60771	CLDN11	claudin 11	1.91	2.84	-1.52	1.13
Q5SXR6	CLTC	clathrin heavy chain	1.27	-4.24	2.91	-1.09
Q3TYL9	CNP	2',3'-cyclic nucleotide 3' phosphodiesterase	3.81	-1.02	1.72	-1.19
Q5M8N0	CNRIP1	cannabinoid receptor interacting protein 1	-1.17	-13.12	1.81	-2.46
P12960	CNTN1	contactin 1	-1.67	-2.75	1.20	1.19
Q3U1N0	CORO1A	coronin 1A	-1.10	-1.99	-1.19	-1.48
B2L0P0	COX2	Cytochrome c oxidase subunit 2	-1.34	-2.51	1.71	-1.42
A2RSV8	COX4I1	cytochrome c oxidase subunit 4I1	-1.07	2.53	-1.73	1.09
P36552	CPOX	coproporphyrinogen oxidase	-1.06	-1.94	1.46	-1.19
Q3TXY0	CRMP1	collapsin response mediator protein 1	-1.22	-1.30	-1.09	-1.06
Q52L78	CRYAB	crystallin alpha B	1.49	1.06	-1.12	1.32
Q3UPX0	CRYM	crystallin mu	-1.29	-1.14	-2.32	-1.22
Q0QEL9	CS	citrate synthase	1.38	2.61	-1.70	1.21
Q71M36-2	CSPG5	chondroitin sulfate proteoglycan 5	-1.51	1.13	-1.71	1.12
G3UZG6	CYB5R1	cytochrome b5 reductase 1	1.18	-1.24	1.57	-1.09
Q3TRK3	DBN1	drebrin 1	-1.80	1.33	-1.84	1.04

Q3UGP0	DCLK1	doublecortin like kinase 1	-1.32	1.01	-1.38	1.04
G3UZR0	DDAH2	dimethylarginine dimethylaminohydrolase 2	1.03	1.31	1.33	1.76
Q3TQX5	DDX3X	DEAD-box helicase 3, X-linked	1.71	-3.23	3.31	-1.32
Q8BMF4	DLAT	dihydrolipoamide S-acetyltransferase	1.14	1.45	-1.26	-1.14
Q3TIE8	DLD	dihydrolipoamide dehydrogenase	1.40	-4.67	2.39	-2.19
B0V2P5	DMXL2	Dmx like 2	-1.16	-1.26	1.06	1.05
P39053	DNM1	dynamin 1	1.28	-7.33	2.20	-2.34
Q3TT92	DPYSL3	dihydropyrimidinase like 3	-1.27	1.34	-1.09	1.05
Q3TMU8	DPYSL4	dihydropyrimidinase like 4	-1.16	1.24	-1.51	1.07
Q9EQF6	DPYSL5	dihydropyrimidinase like 5	-1.34	-1.29	1.03	-1.08
Q9JHU4	DYNC1H1	dynein cytoplasmic 1 heavy chain 1	1.71	-3.83	2.58	-1.47
P62631	EEF1A2	eukaryotic translation elongation factor 1 alpha 2	-1.07	-4.88	3.05	-2.19
Q3TJZ1	EEF2	eukaryotic translation elongation factor 2	1.07	-8.90	3.62	1.08
Q5FW97	ENO1	Enolase 1, alpha non-neuron	-1.22	1.67	-1.38	1.30
Q3UJ20	ENO2	enolase 2	1.26	-1.58	2.28	-1.09
A2AUK5	EPB41L1	erythrocyte membrane protein band 4.1 like 1	-1.76	1.11	-1.41	1.41
D0VYV6	EPB41L3	erythrocyte membrane protein band 4.1 like 3	-1.01	-7.66	2.56	-1.64
Q5NDA4	FABP7	fatty acid binding protein 7	-1.36	1.70	1.02	1.90
P97807	FH	fumarate hydratase	-1.05	-8.32	3.77	-1.60
Q9CQ92	FIS1	fission, mitochondrial 1	1.36	-3.15	2.35	-1.77
P26883	FKBP1A	FK506 binding protein 1A	-1.21	1.35	-1.66	1.27
Q61553	FSCN1	fascin actin-bundling protein 1	-1.09	-1.72	1.03	1.01
P48318	GAD1	glutamate decarboxylase 1	-1.55	-2.81	1.80	-1.04
P06837	GAP43	growth associated protein 43	-1.39	1.28	-1.78	-1.01
M0QWZ0	GAPDH	Uncharacterized protein	-1.97	-3.36	1.29	1.08
Q3U0C4	GDA	guanine deaminase	-1.62	-1.83	-1.38	1.11
Q3TSQ7	GLUD1	glutamate dehydrogenase 1	-1.01	-7.15	3.91	-1.11
P15105	GLUL	glutamate-ammonia ligase	-2.21	2.21	-1.82	1.12
G3UWG1	GM10108	MCG115977	-1.43	-4.98	2.19	-1.24
P18872	GNAO1	G protein subunit alpha o1	-1.03	-2.77	1.36	-1.12
D3YZX3	GNB2	G protein subunit beta 2	-1.00	-13.54	7.44	1.36
Q3THF3	GNB4	G protein subunit beta 4	1.01	1.77	-1.66	1.88
P05201	GOT1	glutamic-oxaloacetic transaminase 1	1.27	-9.51	2.27	-2.30
A2AQR0	GPD2	glycerol-3-phosphate dehydrogenase 2	1.61	-15.14	6.35	-1.10
P06745	GPI	glucose-6-phosphate isomerase	1.08	-5.82	2.13	-1.07
P35802	GPM6A	glycoprotein M6A	-1.15	-1.30	-2.83	1.25
A2AEG6	GPM6B	glycoprotein M6B	1.21	-1.06	-3.27	1.21
Q3UNH4	GPRIN1	G protein regulated inducer of neurite outgrowth 1	-1.65	1.54	-2.44	-1.00
Q9WVL0	GSTZ1	glutathione S-transferase zeta 1	1.22	1.06	1.42	-1.03
Q8BMS1	HADHA	hydroxyacyl-CoA dehydrogenase/3-ketoacyl-CoA thiolase/enoyl-CoA hydratase (trifunctional protein), alpha subunit	1.26	-2.39	3.36	1.50
Q9QUP5	HAPLN1	hyaluronan and proteoglycan link protein 1	1.27	-1.14	1.30	-1.17
Q3U890	HARS	histidyl-tRNA synthetase	2.14	-2.58	3.51	-1.11
Q8BPF4	HBA1/HBA2	hemoglobin subunit alpha 2	2.73	-1.30	1.05	1.80
D0U281	HBBT1	Beta-globin	2.62	-1.17	1.11	1.71
B2RSY3	HEPACAM	hepatic and glial cell adhesion molecule	1.08	-4.71	2.52	1.12
A0ZNJ2	HIBADH	3-hydroxyisobutyrate dehydrogenase	1.57	-7.15	2.86	-2.50

G3UVV4	HK1	hexokinase 1	1.38	-2.02	1.55	-1.27
Q3UJ70	HMGCS1	3-hydroxy-3-methylglutaryl-CoA synthase 1	-1.04	1.65	-1.41	-1.07
B2RRY8	HPCAL4	hippocalcin like 4	-1.59	-1.90	-1.52	-1.03
Q3UIF3	HSP90AA1	heat shock protein 90 alpha family class A member 1	-1.36	1.53	-1.13	1.41
Q3TI47	HSPA5	heat shock protein family A (Hsp70) member 5	-1.39	-15.59	3.89	-1.56
Q3TEK2	HSPA8	heat shock protein family A (Hsp70) member 8	-1.98	-1.05	1.10	-1.15
P63038	HSPD1	heat shock protein family D (Hsp60) member 1	-1.21	-1.20	1.47	1.14
Q5HZJ8	IDH1	isocitrate dehydrogenase (NADP(+)) 1, cytosolic	-1.95	-2.35	1.27	1.09
Q9D6R2	IDH3A	isocitrate dehydrogenase 3 (NAD(+)) alpha	-1.32	-1.03	-1.34	-1.56
G3UYZ1	IGSF8	immunoglobulin superfamily member 8	1.89	1.22	-1.35	-1.55
Q3UMG4	INA	internexin neuronal intermediate filament protein alpha	1.87	2.50	-1.51	-1.29
P85094	ISOC2	isochorismatase domain containing 2	1.68	-1.49	2.21	-1.06
Q8C7Z5	KCNJ10	potassium voltage-gated channel subfamily J member 10	-1.15	1.19	-1.53	-1.47
G3X9J4	KIAA1468	KIAA1468	-1.10	1.16	-1.27	1.26
A2AFG7	L1CAM	L1 cell adhesion molecule	-1.21	1.12	-1.29	1.01
Q3TCI7	LDHA	lactate dehydrogenase A	-1.50	-1.85	1.20	1.10
Q9Z2I0	LETM1	leucine zipper and EF-hand containing transmembrane protein 1	1.37	-5.21	2.80	-1.89
Q6PB66	LRPPRC	leucine rich pentatricopeptide repeat containing	1.21	-3.77	2.63	-1.36
P20917	MAG	myelin associated glycoprotein	1.96	1.00	1.85	1.18
B2RQQ5	MAP1B	microtubule associated protein 1B	1.45	-5.42	1.67	-2.50
Q3U4H0	MAPRE1	microtubule associated protein RP/EB family member 1	-1.11	1.64	-1.30	1.41
P26645	Marcks	myristoylated alanine rich protein kinase C substrate	-1.46	-1.02	-1.54	1.32
P28667	MARCKSL1	MARCKS like 1	-1.09	1.42	1.04	3.51
F6RT34	MBP	myelin basic protein	2.96	1.70	-1.01	-1.39
P14152	MDH1	malate dehydrogenase 1	-1.57	-1.45	1.50	1.39
P08249	MDH2	malate dehydrogenase 2	1.34	-1.12	1.35	-1.48
Q3UY21	MOG	myelin oligodendrocyte glycoprotein	1.73	1.30	-1.70	-1.12
Q3UH59	MYH10	myosin heavy chain 10	1.18	-1.73	1.27	1.17
B2RRE2	MYO18A	myosin XVIIIA	1.58	-4.14	2.94	-1.60
D3YZ62	MYO5A	myosin VA	1.40	-9.54	2.87	-2.36
Q9DB05	NAPA	NSF attachment protein alpha	1.14	-4.42	1.56	-1.34
D3YVA2	NCALD	neurocalcin delta	-2.28	-2.69	-1.49	1.08
P13595	NCAM1	neural cell adhesion molecule 1	-1.58	-1.02	-1.73	1.25
O35136	NCAM2	neural cell adhesion molecule 2	-1.92	-1.58	-1.53	1.51
Q9Z0E0	NCDN	neurochondrin	-1.18	-8.41	2.93	-1.18
Q9QYG0	NDRG2	NDRG family member 2	1.05	-7.61	2.25	-1.20
Q99LC3	NDUFA10	NADH:ubiquinone oxidoreductase subunit A10	1.68	-4.66	2.65	-1.76
G5E814	NDUFA11	NADH:ubiquinone oxidoreductase subunit A11	1.06	-1.89	2.13	-1.24
Q9ERS2	NDUFA13	NADH:ubiquinone oxidoreductase subunit A13	-1.44	-3.49	2.52	1.07
Q9DC69	NDUFA9	NADH:ubiquinone oxidoreductase subunit A9	1.11	-4.96	2.54	-1.40
D3YUK4	NDUFB10	NADH:ubiquinone oxidoreductase subunit B10	1.29	-9.22	3.08	-1.94

Q3UIQ2	NDUFS1	NADH:ubiquinone oxidoreductase core subunit S1	-1.21	-4.42	2.32	-1.98
F6RJ83	NDUFS2	NADH dehydrogenase [ubiquinone] iron-sulfur protein 2, mitochondrial (Fragment)	1.83	-14.46	10.24	-2.01
D3YW32	NDUFS6	NADH dehydrogenase [ubiquinone] iron-sulfur protein 6, mitochondrial	1.29	-1.57	1.80	1.05
D3YUM1	NDUFV1	NADH:ubiquinone oxidoreductase core subunit V1	1.07	-6.23	1.82	-2.44
Q80TQ3	NEFH	neurofilament heavy	2.79	3.62	-1.23	-1.13
Q05DD2	NEFL	neurofilament light	1.83	1.81	-1.35	-1.26
P08553	Nefm	neurofilament, medium polypeptide	2.60	2.46	-1.31	-1.46
A0A4W9	NEGR1	neuronal growth regulator 1	-1.31	1.44	-1.87	-1.03
Q3U536	NPM1	nucleophosmin	2.03	-1.33	1.84	1.45
P97300	Nptn	neuroplastin	-1.38	1.07	-2.84	-1.01
P46460	NSF	N-ethylmaleimide sensitive factor, vesicle fusing ATPase	-1.17	-12.66	2.04	-2.04
Q8VCE6	NT5M	5',3'-nucleotidase, mitochondrial	1.19	-2.56	2.15	-1.58
Q8BRD3	NUCB1	nucleobindin 1	1.15	1.07	1.83	-1.13
Q60597-3	OGDH	oxoglutarate dehydrogenase	1.24	-2.55	2.10	-1.40
B2RXT3	OGDHL	oxoglutarate dehydrogenase-like	1.29	-1.59	1.78	-1.08
E0CXD1	OPA1	OPA1, mitochondrial dynamin like GTPase	1.43	-2.51	2.35	-1.16
Q3UJQ9	OXCT1	3-oxoacid CoA-transferase 1	-1.24	1.14	1.10	1.14
Q4KMM3	OXR1	oxidation resistance 1	-1.47	1.20	-2.02	1.13
Q3TBF1	PADI2	peptidyl arginine deiminase 2	3.67	3.18	2.88	5.32
Q8BP54	PC	pyruvate carboxylase	1.19	-4.31	2.10	-1.33
Q7TPG1	PDE10A	phosphodiesterase 10A	2.04	-1.17	-1.08	1.13
Q3UFJ3	PDHA1	pyruvate dehydrogenase (lipoamide) alpha 1	1.10	-4.85	2.23	-2.46
Q9D051	PDHB	pyruvate dehydrogenase (lipoamide) beta	-1.60	-1.57	-1.40	1.12
Q8C605	PFKP	phosphofructokinase, platelet	-1.31	-3.17	1.90	1.23
Q3U7Z6	PGAM1	phosphoglycerate mutase 1	-1.25	-1.27	-1.57	-1.34
A1A4A7	PGAM5	PGAM family member 5, mitochondrial serine/threonine protein phosphatase	-1.08	1.30	-1.31	-1.19
P09411	PGK1	phosphoglycerate kinase 1	-1.31	-7.18	1.70	-1.93
Q3V235	PHB2	prohibitin 2	-1.05	-7.16	2.23	-1.70
P52480-2	PKM	pyruvate kinase, muscle	-1.55	-11.70	3.62	-1.13
Q2M4J2	PLCB1	phospholipase C beta 1	1.04	-6.35	2.01	-1.38
Q9DBG5	PLIN3	perilipin 3	1.92	-3.56	1.61	-1.01
Q5DTP6	PLPPR3	phospholipid phosphatase related 3	-1.56	1.24	-1.54	-1.23
Q3U7K1	Ppp1cc	protein phosphatase 1, catalytic subunit, gamma isoform	1.79	-9.40	2.50	-2.00
Q3UM45	PPP1R7	protein phosphatase 1 regulatory subunit 7	1.29	-1.14	-1.28	1.10
Q7TMX2	PPP2R1A	protein phosphatase 2 scaffold subunit Aalpha	-1.14	-3.73	1.93	-1.02
B2RRX2	PPP3CA	protein phosphatase 3 catalytic subunit alpha	-1.01	-9.51	1.48	-1.70
P31324	PRKAR2B	protein kinase cAMP-dependent type II regulatory subunit beta	-1.18	-1.03	-1.59	-1.29
P68404	PRKCB	protein kinase C beta	-1.36	-1.19	-1.11	1.60
Q3UN66	PRKCG	protein kinase C gamma	-1.11	-1.16	-2.05	1.65
B2RUD7	PSAP	prosaposin	3.58	-1.04	3.01	2.22
Q3UWT6	PSMA2	proteasome subunit alpha 2	1.13	-6.16	3.12	-1.31
Q9WUB3	PYGM	glycogen phosphorylase, muscle associated	1.66	-2.83	2.10	-1.41
D3YWR7	QDPR	quinoid dihydropteridine reductase	2.51	2.49	1.11	1.38

Q0PD66	RAB1B	RAB1B, member RAS oncogene family	-2.08	-1.71	1.32	1.51
Q0PD63	RAB3A	RAB3A, member RAS oncogene family	-1.91	-3.35	1.71	-1.32
C5H0E9	RAP1A	RAP1A, member of RAS oncogene family	1.14	-5.68	2.45	-1.09
Q80ZJ1	RAP2A	RAP2A, member of RAS oncogene family	-1.19	-3.67	1.32	-1.09
P52760	RIDA	reactive intermediate imine deaminase A homolog	1.55	2.34	1.24	2.04
A2ACG7	RPN2	ribophorin II	1.34	-6.79	2.94	-1.70
Q9CTF6	RRAS2	related RAS viral (r-ras) oncogene homolog 2	1.44	1.23	1.09	1.35
A3QM89	RTN1	reticulon 1	-1.81	-3.25	1.14	1.15
Q99P72	RTN4	reticulon 4	-2.16	-1.58	1.22	2.21
Q9D3M4	S100A1	S100 calcium binding protein A1	1.53	-1.66	4.68	2.20
Q9EP69	SACM1L	SAC1 suppressor of actin mutations 1 like (yeast)	1.25	-4.75	2.85	-1.29
Q8K2B3	SDHA	succinate dehydrogenase complex flavoprotein subunit A	1.56	-7.36	5.21	-2.29
Q8BK60	SERPINB1	serpin family B member 1	4.27	1.43	1.07	-1.05
Q8VD37	SGIP1	SH3 domain GRB2 like endophilin interacting protein 1	1.38	-1.24	-1.46	-1.44
Q91VW3	SH3BGRL3	SH3 domain binding glutamate rich protein like 3	-1.17	-1.66	1.24	-1.06
E0CYM8	SIRPA	signal regulatory protein alpha	1.04	-5.82	1.18	-1.51
Q91V14	SLC12A5	solute carrier family 12 member 5	1.38	-9.53	2.61	-2.14
Q3TXX4	SLC17A7	solute carrier family 17 member 7	-1.20	-1.60	-2.18	-1.47
A2APL5	SLC1A2	solute carrier family 1 member 2	-1.34	-3.56	1.33	-1.01
Q8C3T7	SLC1A3	solute carrier family 1 member 3	-1.56	-1.41	-1.30	1.78
Q5SX53	SLC25A11	solute carrier family 25 member 11	-1.22	-3.22	2.43	-1.39
Q8BH59	SLC25A12	solute carrier family 25 member 12	-1.02	-4.10	2.45	-1.63
Q3THU8	SLC25A3	solute carrier family 25 member 3	1.60	-4.77	2.42	-1.47
P51881	SLC25A5	solute carrier family 25 member 5	-1.29	-6.03	1.72	-1.19
Q3TPL8	SLC2A3	solute carrier family 2 member 3	-1.28	-1.38	1.07	-1.26
Q49S98	SLC32A1	solute carrier family 32 member 1	-1.99	-8.80	2.28	-1.58
A2AMH3	SLC44A1	solute carrier family 44 member 1	2.57	-1.08	1.01	1.41
B2RQX9	SLC6A5	solute carrier family 6 member 5	3.18	2.25	1.55	1.02
Q6ZPY3	SLC8A2	MKIAA1087 protein (Fragment)	-1.11	-1.06	-2.19	1.02
P60879	SNAP25	synaptosome associated protein 25	1.01	-1.25	-1.32	1.99
O55042	SNCA	synuclein alpha	-1.15	-1.01	-2.20	-1.11
P08228	SOD1	superoxide dismutase 1	-1.11	3.09	-1.59	1.64
A3KGU5	SPTAN1	spectrin alpha, non-erythrocytic 1	-1.27	-8.12	1.28	-1.19
Q62261	SPTBN1	spectrin beta, non-erythrocytic 1	-1.02	-2.11	1.25	-1.45
B1AQX9	SRCIN1	SRC kinase signaling inhibitor 1	-1.36	1.24	-2.36	1.27
Q9QZX7	SRR	serine racemase	-1.43	-1.21	-2.27	1.03
Q5D0A4	STX1A	syntaxin 1A	-1.67	-2.33	-1.85	-1.09
P61264	STX1B	syntaxin 1B	1.22	1.66	-1.41	1.10
O08599	STXBP1	syntaxin binding protein 1	1.20	-1.17	-1.02	-1.61
Q8BG39	SV2B	synaptic vesicle glycoprotein 2B	-1.37	-1.55	-2.69	-1.25
O88935	SYN1	synapsin I	-1.30	-2.84	1.49	-2.39
Q64332	SYN2	synapsin II	-1.49	-8.46	2.00	-1.66
J3QQ18	SYNGAP1	synaptic Ras GTPase activating protein 1	-1.64	-1.06	-3.75	-1.28
Q3TPT3	SYT1	synaptotagmin 1	1.13	-1.98	1.16	-1.06
P11983	TCP1	t-complex 1	-1.04	-2.60	1.91	-1.25
Q8C872	TFRC	transferrin receptor	-1.60	1.07	-1.28	1.17
P40142	TKT	transketolase	1.52	-7.51	2.97	-2.81
Q9D1D4	TMED10	transmembrane p24 trafficking	1.16	-2.68	2.54	-1.43

		protein 10				
Q8BYI9	TNR	tenascin R	1.36	-2.26	1.68	-1.25
Q3UQD0	TOMM40	translocase of outer mitochondrial membrane 40	1.08	-2.27	1.81	-1.30
Q3URG1	TPPP	tubulin polymerization promoting protein	1.37	-1.88	1.13	-1.32
P68368	TUBA4A	tubulin alpha 4a	1.24	1.47	-1.15	1.12
P99024	TUBB	tubulin beta class I	-1.69	-7.08	3.55	1.02
B2RSN3	TUBB2B	tubulin beta 2B class IIb	-1.34	1.03	1.04	1.29
Q9D6F9	TUBB4A	tubulin beta 4A class IVa	1.53	-9.54	3.68	-1.02
B9EHN0	UBA1	ubiquitin like modifier activating enzyme 1	1.19	-1.90	2.27	1.38
Q3TCH2	UCHL1	ubiquitin C-terminal hydrolase L1	-1.09	2.47	-2.07	1.26
Q3THM1	UQCRC1	ubiquinol-cytochrome c reductase core protein I	-1.33	-6.84	2.08	-1.94
Q9DB77	UQCRC2	ubiquinol-cytochrome c reductase core protein II	1.02	-6.06	2.45	-1.98
Q80TB8	VAT1L	vesicle amine transport 1 like	-1.26	-3.94	1.82	-1.66
G3XA35	VCAN	versican	1.10	1.30	-1.14	1.31
Q8BNF8	VCP	valosin containing protein	-2.22	-3.94	-1.21	1.28
Q3TJ43	VPS35	VPS35, retromer complex component	-1.74	-3.40	3.32	1.71
B2L107	VSNL1	visinin like 1	-1.84	1.53	1.43	1.25
Q5SS40	YWHAE	tyrosine 3-monooxygenase/tryptophan 5-monooxygenase activation protein epsilon	-1.50	1.64	-1.98	1.03
P68510	YWHAH	tyrosine 3-monooxygenase/tryptophan 5-monooxygenase activation protein eta	1.23	-3.61	1.67	1.07
A3KML3	YWHAQ	tyrosine 3-monooxygenase/tryptophan 5-monooxygenase activation protein theta	1.10	2.38	-2.77	1.22

Table A8. Proteins identified by ≥ 2 peptide in* Ppt1$^{-/-}$ *cortical synaptosomes (Chapter 4)

			Fold change *Ppt1*$^{-/-}$/WT			
ID	**Gene Symbol**	**Entrez Gene Name**	**1m**	**3m**	**5m**	**7m**
Q3V1S0	ABAT	4-aminobutyrate aminotransferase	-1.53	-1.87	1.04	2.86
Q99LR1	ABHD12	abhydrolase domain containing 12	-1.07	1.68	-1.74	-1.38
Q8R2Y0	ABHD6	abhydrolase domain containing 6	-2.55	-1.70	-1.31	2.32
H3BJZ9	ACAA1	acetyl-CoA acyltransferase 1	1.05	1.18	-2.50	-2.19
Q8BWT1	ACAA2	acetyl-CoA acyltransferase 2	1.15	1.13	-2.60	-1.23
Q9D7B6	ACAD8	acyl-CoA dehydrogenase family member 8	-1.37	1.33	-2.08	-2.05
P51174	ACADL	acyl-CoA dehydrogenase, long chain	1.45	1.02	-2.48	1.17
Q07417	ACADS	acyl-CoA dehydrogenase, C-2 to C-3 short chain	1.23	1.21	-2.73	-1.46
Q7TMY2	ACADSB	acyl-CoA dehydrogenase, short/branched chain	1.05	1.22	-4.10	-1.70
P50544	ACADVL	acyl-CoA dehydrogenase, very long chain	-1.07	-1.07	-2.16	-1.24
Q3TQP7	ACAT1	acetyl-CoA acetyltransferase 1	-1.74	1.24	-1.16	-1.55
Q3TED3	ACLY	ATP citrate lyase	-1.06	-1.14	-1.32	1.91
Q99KI0	ACO2	aconitase 2	-1.67	-1.33	-1.06	2.52
Q4VA32	ACOT13	acyl-CoA thioesterase 13	1.60	1.86	-1.81	1.62
Q6P2K2	ACOT2	acyl-CoA thioesterase 2	1.53	1.01	-2.03	1.10
Q8VCW8	ACSF2	acyl-CoA synthetase family member 2	1.49	1.02	-3.29	-1.06

Q5F2C5	ACSL6	acyl-CoA synthetase long-chain family member 6	-1.23	-1.09	-1.60	1.57
A1BN54	ACTN1	actinin alpha 1	-1.76	-2.05	-1.97	1.19
Q3ULT2	ACTN4	actinin alpha 4	-1.23	-1.15	1.44	-1.45
Q8R5C5	ACTR1B	ARP1 actin-related protein 1 homolog B, centractin beta	-2.06	-2.59	1.02	1.91
Q3TGE1	ACTR3	ARP3 actin related protein 3 homolog	-1.43	-1.79	1.36	1.30
D3YUP9	ADAM22	ADAM metallopeptidase domain 22	-1.37	-1.48	1.03	3.24
E9PY16	ADAP1	ArfGAP with dual PH domains 1	-2.53	-2.71	2.11	2.26
E9Q706	ADCY9	adenylate cyclase 9	-1.93	-1.63	-1.16	3.19
F8WGR0	ADD1	adducin 1	-1.85	-2.21	1.04	2.48
J3QN31	ADSSL1	adenylosuccinate synthase like 1	1.51	-1.25	-1.52	3.89
Q91VJ9	AGPAT1	1-acylglycerol-3-phosphate O-acyltransferase 1	-1.01	1.34	-1.31	-1.37
Q80SW1	AHCYL1	adenosylhomocysteinase like 1	-1.20	-1.61	-1.17	1.63
Q9R0Y5	AK1	adenylate kinase 1	-2.46	-2.49	1.41	3.50
Q9WTP7	AK3	adenylate kinase 3	1.11	1.34	-2.11	1.05
P07724	ALB	albumin	1.91	-1.34	-1.72	1.60
P24549	ALDH1A1	aldehyde dehydrogenase 1 family member A1	-1.20	-2.44	-1.40	1.94
Q9CZS1	ALDH1B1	aldehyde dehydrogenase 1 family member B1	-3.26	-1.60	1.21	-1.71
Q8R0Y6	ALDH1L1	aldehyde dehydrogenase 1 family member L1	1.50	1.60	-1.76	-1.10
Q3TVM2	ALDH2	aldehyde dehydrogenase 2 family (mitochondrial)	-1.03	1.19	-2.01	1.19
B2RS41	ALDH5A1	aldehyde dehydrogenase 5 family member A1	-1.57	1.07	-1.69	1.31
Q9EQ20	ALDH6A1	aldehyde dehydrogenase 6 family member A1	1.42	1.29	-1.92	1.16
Q9DBF1	ALDH7A1	aldehyde dehydrogenase 7 family member A1	1.91	1.24	-1.85	-1.13
Q5FWB7	ALDOA	aldolase, fructose-bisphosphate A	-1.15	-1.52	1.43	2.15
P05063	ALDOC	aldolase, fructose-bisphosphate C	1.58	1.35	-1.38	-1.10
Q9DBE8	ALG2	ALG2, alpha-1,3/1,6-mannosyltransferase	-1.38	-1.21	-1.15	1.66
C6EQG9	Amph	ASL1/Amph fusion protein	-1.27	-2.16	1.50	2.93
Q8C8R3	Ank2	ankyrin 2, brain	-1.31	-1.05	1.23	-1.20
P48036	ANXA5	annexin A5	2.50	1.01	-2.25	1.74
Q3TJ49	ANXA7	annexin A7	2.24	1.64	-1.06	1.44
Q3TVN4	AP1B1	adaptor related protein complex 1 beta 1 subunit	-1.07	-1.45	1.04	1.91
P17426	AP2A1	adaptor related protein complex 2 alpha 1 subunit	-1.11	-2.91	2.07	2.00
Q3U7X9	AP2A2	adaptor related protein complex 2 alpha 2 subunit	-1.40	-2.15	1.37	2.52
Q5SWR1	Ap2b1	adaptor-related protein complex 2, beta 1 subunit	-1.21	-2.71	1.71	2.93
Q3TH69	AP2M1	adaptor related protein complex 2 mu 1 subunit	1.88	-4.50	3.35	3.91
Q9JME5	AP3B2	adaptor related protein complex 3 beta 2 subunit	-1.23	-1.64	1.65	1.36
Q3TXU4	APOE	apolipoprotein E	3.44	1.06	-2.13	1.07
B1AV14	APOOL	apolipoprotein O like	-1.37	1.41	-2.16	1.35
Q3TGS9	ARFGAP1	ADP ribosylation factor GTPase activating protein 1	-1.21	1.60	1.15	-1.87
Q8R5J9	ARL6IP5	ADP ribosylation factor like GTPase 6 interacting protein 5	-2.53	-2.11	1.46	3.01
Q9CQW2	ARL8B	ADP ribosylation factor like GTPase 8B	-2.80	-5.06	3.78	22.35

Q9R0Q6	ARPC1A	actin related protein 2/3 complex subunit 1A	-1.77	-1.45	1.54	1.62
H7BWZ3	ARPC3	actin related protein 2/3 complex subunit 3	1.04	-1.40	1.93	1.30
Q3U646	ASAH1	N-acylsphingosine amidohydrolase 1	1.17	-1.35	-2.84	2.74
Q3UHD7	ASTN1	astrotactin 1	-3.00	-1.68	1.05	-1.38
Q8BH66	ATL1	atlastin GTPase 1	-1.94	-1.75	1.40	1.25
Q3TXF9	ATP1A1	ATPase Na+/K+ transporting subunit alpha 1	-1.46	-1.51	-1.37	1.30
D3YYN7	ATP1A2	ATPase Na+/K+ transporting subunit alpha 2	1.60	1.67	-1.39	1.03
Q6PIC6	ATP1A3	ATPase Na+/K+ transporting subunit alpha 3	1.06	-1.49	1.94	1.71
Q3UR55	ATP1B2	ATPase Na+/K+ transporting subunit beta 2	1.57	1.72	-1.47	-1.13
J3KMM5	Atp2a2	Sarcoplasmic/endoplasmic reticulum calcium ATPase 2	-1.39	-3.22	1.47	1.83
G5E829	ATP2B1	ATPase plasma membrane Ca2+ transporting 1	-1.85	-2.26	1.39	2.05
Q0VF54	ATP2B3	ATPase plasma membrane Ca2+ transporting 3	1.11	-1.65	1.80	2.45
D1FNM8	ATP2B4	ATPase plasma membrane Ca2+ transporting 4	-1.14	1.18	1.53	1.03
D3Z6F5	ATP5A1	ATP synthase, H+ transporting, mitochondrial F1 complex, alpha subunit 1, cardiac muscle	-1.75	-1.22	-1.20	1.83
P56480	ATP5B	ATP synthase, H+ transporting, mitochondrial F1 complex, beta polypeptide	-1.57	1.19	-1.64	1.02
A2AKU9	ATP5C1	ATP synthase, H+ transporting, mitochondrial F1 complex, gamma polypeptide 1	-1.61	1.36	1.01	1.84
Q3TJD4	ATP5F1	ATP synthase, H+ transporting, mitochondrial Fo complex subunit B1	-1.80	-1.83	-1.07	3.78
Q9CPQ8	ATP5L	ATP synthase, H+ transporting, mitochondrial Fo complex subunit G	-1.89	-1.32	-1.94	1.49
Q3TF25	ATP5O	ATP synthase, H+ transporting, mitochondrial F1 complex, O subunit	-2.38	-1.75	-1.25	1.74
K3W4T3	ATP6V0A1	ATPase H+ transporting V0 subunit a1	-1.44	-1.51	1.71	2.41
A3KML5	ATP6V0C	ATPase H+ transporting V0 subunit c	1.21	-1.49	1.35	2.61
P51863	ATP6V0D1	ATPase H+ transporting V0 subunit d1	-1.49	-2.21	2.09	3.60
P50516	ATP6V1A	ATPase H+ transporting V1 subunit A	-1.39	-1.67	1.20	1.76
P62814	ATP6V1B2	ATPase H+ transporting V1 subunit B2	-1.27	-1.47	1.35	2.22
Q3TG21	ATP6V1C1	ATPase H+ transporting V1 subunit C1	-1.30	-1.89	1.41	2.32
P50518	ATP6V1E1	ATPase H+ transporting V1 subunit E1	-1.09	-2.11	1.79	2.87
Q5HZY7	ATP6V1G1	ATPase H+ transporting V1 subunit G1	-1.06	1.16	-1.75	-1.66
B0V2H4	ATP6V1G2	ATPase H+ transporting V1 subunit G2	-1.55	-1.39	1.03	-1.26
Q8BVE3	ATP6V1H	ATPase H+ transporting V1 subunit H	-1.31	-1.42	1.69	1.69
Q91XV3	BASP1	brain abundant membrane attached signal protein 1	1.56	-1.04	2.43	-1.15
Q61361	BCAN	brevican	2.27	1.04	-1.19	1.67

Q80YN3	BCAS1	breast carcinoma amplified sequence 1	-1.08	2.72	-1.33	-3.14
Q3TNR7	BCL2L13	BCL2 like 13	-1.67	1.03	-1.25	-1.67
Q80XN0	BDH1	3-hydroxybutyrate dehydrogenase 1	-3.40	-1.26	-1.34	-2.98
Q6P1B9	BIN1	bridging integrator 1	-1.22	-1.19	-1.02	2.87
O88737-2	BSN	bassoon presynaptic cytomatrix protein	-1.03	2.13	-1.18	-1.74
Q3TXB1	C1QA	complement C1q A chain	6.93	1.46	-4.05	1.68
Q3U6I5	C1QB	complement C1q B chain	10.93	1.72	-4.85	1.60
Q9D172	C21orf33/LOC102724023	chromosome 21 open reading frame 33	-1.32	-1.06	-1.43	1.52
Q3U590	C2CD2L	C2CD2 like	1.01	1.66	1.00	-2.09
B2RWX2	C4A/C4B	complement C4B (Chido blood group)	10.70	1.13	-12.87	1.04
P00920	CA2	carbonic anhydrase 2	2.66	1.64	-1.59	3.46
P28651	CA8	carbonic anhydrase 8	-1.20	-8.91	2.17	-1.72
Q14BH8	CACNA2D1	calcium voltage-gated channel auxiliary subunit alpha2delta 1	-1.07	1.19	1.26	-1.65
Q9Z1L5	CACNA2D3	calcium voltage-gated channel auxiliary subunit alpha2delta 3	-3.20	-1.39	-1.37	-2.26
F7CZ64	CACNG8	calcium voltage-gated channel auxiliary subunit gamma 8	-1.14	1.38	1.11	-2.04
G3UZM4	CADM2	cell adhesion molecule 2	-3.02	-3.79	1.45	4.98
K4DI58	CADM3	cell adhesion molecule 3	1.14	-1.01	1.53	1.59
J3QJW3	CADPS	calcium dependent secretion activator	-1.63	-6.26	2.16	7.88
Q8C5H2	CALB1	calbindin 1	-1.06	-2.92	2.06	1.04
Q8CCS7	CALB2	calbindin 2	1.29	-1.92	2.21	-1.75
P62204	Calm1	Calmodulin	-3.01	-1.89	-1.30	-1.45
B2MWM9	CALR	calreticulin	1.02	-1.01	1.07	-1.86
F8WHB5	CAMK2A	calcium/calmodulin dependent protein kinase II alpha	-2.63	-6.27	2.46	10.11
Q3TY93	CAMK2B	calcium/calmodulin dependent protein kinase II beta	-1.52	-1.67	1.55	1.54
Q6PHZ2	CAMK2D	calcium/calmodulin dependent protein kinase II delta	-1.70	-2.41	1.92	2.70
Q8BGR3	CAMK4	calcium/calmodulin dependent protein kinase IV	-1.68	-1.65	1.36	-1.42
Q3UHL1	CAMKV	CaM kinase like vesicle associated	-1.05	1.10	1.26	-1.84
Q6ZQ38	CAND1	cullin associated and neddylation dissociated 1	-1.46	-2.45	1.10	2.66
Q3TXE5	CANX	calnexin	1.12	-2.70	1.63	2.29
Q3U3A8	CAPN2	calpain 2	2.28	1.10	-1.21	2.29
D3YW48	CAPNS1	calpain small subunit 1	1.33	-1.40	-1.36	1.40
Q3UBZ3	CAPZA2	capping actin protein of muscle Z-line alpha subunit 2	-1.58	1.26	1.29	-1.55
Q6P9K8	CASKIN1	CASK interacting protein 1	-1.02	1.77	-1.26	-2.21
Q0VBU4	CCDC47	coiled-coil domain containing 47	-1.20	1.17	-1.22	-2.13
Q3U0I3	CCT3	chaperonin containing TCP1 subunit 3	-1.19	-1.35	-1.15	1.26
P80316	CCT5	chaperonin containing TCP1 subunit 5	-2.17	-2.79	-1.09	1.54
Q3TIJ7	CCT7	chaperonin containing TCP1 subunit 7	-1.99	-1.32	1.01	1.29
Q3UKQ2	CCT8	chaperonin containing TCP1 subunit 8	1.17	1.14	1.01	-1.19
Q61735-2	CD47	CD47 molecule	-1.46	-1.51	1.16	1.39
Q3UWG5	CD81	CD81 molecule	1.02	-1.32	-1.75	1.27
Q8CE18	CDH13	cadherin 13	-1.74	1.29	1.42	-3.39
Q4VAA2	CDV3	CDV3 homolog	1.43	2.09	1.15	-1.58

Q9JKC6	CEND1	cell cycle exit and neuronal differentiation 1	1.42	-2.00	2.74	1.78
Q9R1K9	CETN2	centrin 2	-2.12	-3.65	2.36	3.89
Q8BMK4	CKAP4	cytoskeleton associated protein 4	-1.59	1.15	-1.07	-2.68
Q04447	CKB	creatine kinase B	-1.08	-1.68	1.01	2.25
B0R0E9	CKMT1A/CKMT1B	creatine kinase, mitochondrial 1B	-1.99	-1.17	-3.54	-1.51
F7DCH5	CLASP2	cytoplasmic linker associated protein 2	-1.63	1.16	-1.00	-1.54
Q60771	CLDN11	claudin 11	2.73	1.90	-1.36	3.61
Q9QYB1	CLIC4	chloride intracellular channel 4	1.10	-1.05	-1.60	1.10
Q5SXR6	CLTC	clathrin heavy chain	-1.27	-2.28	1.42	2.95
Q06890	CLU	clusterin	1.85	1.47	-2.53	-1.74
Q9DBP5	CMPK1	cytidine/uridine monophosphate kinase 1	-1.84	-2.76	2.09	3.26
Q9DAW9	CNN3	calponin 3	2.51	1.52	-3.81	-1.47
Q3TYL9	CNP	2',3'-cyclic nucleotide 3' phosphodiesterase	1.35	1.34	1.20	2.07
P12960	CNTN1	contactin 1	-1.01	1.58	1.08	-1.60
O54991	CNTNAP1	contactin associated protein 1	-1.03	1.19	1.06	1.93
Q9DBL7	COASY	Coenzyme A synthase	-3.73	-2.90	-7.12	-2.63
Q8CIE6	COPA	coatomer protein complex subunit alpha	1.34	1.17	-1.83	-2.25
Q3UQL2	COPS3	COP9 signalosome subunit 3	-1.26	-2.39	1.19	2.30
Q3U1N0	CORO1A	coronin 1A	-1.82	-1.43	1.96	1.61
Q3TEU8	CORO1C	coronin 1C	-2.52	-1.90	1.29	1.65
B2L0P0	COX2	Cytochrome c oxidase subunit 2	-2.13	-2.51	-1.48	2.70
P56391	COX6B1	cytochrome c oxidase subunit 6B1	-1.83	-1.69	-1.11	2.08
Q00493	CPE	carboxypeptidase E	1.22	1.43	-1.24	-2.01
Q3UN71	CPNE6	copine 6	1.44	1.34	1.21	-2.21
Q6P1J1	CRMP1	collapsin response mediator protein 1	-1.79	-1.22	1.34	-1.70
Q52L78	CRYAB	crystallin alpha B	3.57	1.59	-2.11	6.12
Q3UPX0	CRYM	crystallin mu	1.15	-1.38	1.82	-1.31
Q3UYY0	CRYZ	crystallin zeta	2.52	2.07	-1.58	-1.08
Q9CZU6	CS	citrate synthase	-1.11	2.05	-2.14	-1.66
Q71M36-2	CSPG5	chondroitin sulfate proteoglycan 5	-1.05	-1.38	-1.05	-1.52
Q4FJX4	CSRP1	cysteine and glycine rich protein 1	1.60	1.69	-1.94	1.26
O88712	CTBP1	C-terminal binding protein 1	-2.60	-2.38	1.28	4.72
Q61301-3	CTNNA2	catenin alpha 2	-2.12	-1.48	-1.07	-1.41
Q3UZT7	CTNNB1	catenin beta 1	-2.88	-1.03	-1.70	-2.49
B7ZNF6	CTNND2	catenin delta 2	-1.37	1.35	-1.09	-2.09
Q3TVS6	CTSB	cathepsin B	1.04	-1.48	-1.42	3.02
Q3TWD0	CTSD	cathepsin D	1.49	1.31	-3.48	1.11
Q8BNA5	CTTN	cortactin	1.11	-1.36	1.66	-1.44
B9EJA2	CTTNBP2	cortactin binding protein 2	-1.47	-1.19	1.38	-1.82
Q6ZQ84	CUL3	cullin 3	1.06	-5.15	1.99	3.87
Q3TH64	CYB5B	cytochrome b5 type B	-1.68	-3.16	-1.19	2.40
Q9D0M3	CYC1	cytochrome c1	-1.08	1.14	-1.22	2.90
Q3US73	CYP46A1	cytochrome P450 family 46 subfamily A member 1	1.67	2.09	1.76	1.15
Q548W7	DBI	diazepam binding inhibitor, acyl-CoA binding protein	1.85	1.07	-1.56	-1.50
Q9QXS6	DBN1	drebrin 1	-1.75	-1.28	1.24	-2.59
A3KN70	DCLK1	doublecortin like kinase 1	-1.84	-1.02	1.16	-2.26
D3YX34	DCTN1	dynactin subunit 1	-1.31	-2.46	1.49	4.92
D3YU15	DDAH1	dimethylarginine dimethylaminohydrolase 1	1.39	1.09	-1.54	1.07
Q3TQX5	DDX3X	DEAD-box helicase 3, X-linked	1.06	1.21	-1.21	-1.42
Q4FJK0	DECR1	2,4-dienoyl-CoA reductase 1	1.62	1.20	-3.92	-1.03

Q3TVU9	DHRS1	dehydrogenase/reductase 1	1.88	1.76	-4.01	-1.82
Q3UWU7	DIRAS2	DIRAS family GTPase 2	-1.84	-2.09	1.66	1.88
Q8BMF4	DLAT	dihydrolipoamide S-acetyltransferase	-1.11	1.11	-1.80	2.16
O08749	DLD	dihydrolipoamide dehydrogenase	-1.62	-1.76	1.17	4.16
Q62108	DLG4	discs large MAGUK scaffold protein 4	-1.56	-2.44	1.51	2.09
Q9D2G2	DLST	dihydrolipoamide S-succinyltransferase	-1.08	1.36	-2.51	1.05
B0V2P5	DMXL2	Dmx like 2	-2.36	-1.50	-1.06	-1.22
G3X8S5	DNAJB6	DnaJ heat shock protein family (Hsp40) member B6	2.25	-3.03	2.91	3.32
P39053	DNM1	dynamin 1	-1.67	-2.41	2.42	7.67
Q8K1M6	DNM1L	dynamin 1 like	-2.02	-2.40	1.30	2.66
Q8BZ98	DNM3	dynamin 3	-1.41	-1.95	1.13	2.63
D3Z5I7	DPP10	dipeptidyl peptidase like 10	-1.67	-2.51	2.09	4.92
Q3TY19	DPP6	dipeptidyl peptidase like 6	-1.04	-1.20	1.56	1.00
O08553	DPYSL2	dihydropyrimidinase like 2	-1.15	-2.30	1.92	6.56
Q3TT92	DPYSL3	dihydropyrimidinase like 3	-3.74	-1.47	2.02	-5.05
Q3TMU8	DPYSL4	dihydropyrimidinase like 4	-1.72	-1.07	1.46	-2.45
Q9EQF6	DPYSL5	dihydropyrimidinase like 5	-3.53	-2.10	2.81	-3.56
Q9JHU4	DYNC1H1	dynein cytoplasmic 1 heavy chain 1	-1.21	-1.70	1.31	2.04
Q3TWG5	DYNC1LI1	dynein cytoplasmic 1 light intermediate chain 1	-1.34	-4.23	2.17	3.60
O35459	ECH1	enoyl-CoA hydratase 1	1.10	-1.01	-3.75	1.43
Q9DBN7	ECI1	enoyl-CoA delta isomerase 1	1.74	1.17	-2.69	1.31
Q3TCD4	ECI2	enoyl-CoA delta isomerase 2	1.08	1.04	-2.59	-1.53
Q8BL66	EEA1	early endosome antigen 1	-1.74	1.55	-1.36	-2.91
D3YZ68	EEF1A1	eukaryotic translation elongation factor 1 alpha 1	-1.90	-6.36	1.68	4.27
P62631	EEF1A2	eukaryotic translation elongation factor 1 alpha 2	-1.50	-1.60	1.56	2.31
O70251	EEF1B2	eukaryotic translation elongation factor 1 beta 2	-1.40	-1.38	1.14	1.21
Q80T06	EEF1D	eukaryotic translation elongation factor 1 delta	1.23	1.21	-1.41	-2.07
Q4FZK2	EEF1G	eukaryotic translation elongation factor 1 gamma	-1.11	-1.06	1.04	-1.43
Q3TJZ1	EEF2	eukaryotic translation elongation factor 2	-1.27	-2.20	1.28	2.33
Q8BTU6	EIF4A2	eukaryotic translation initiation factor 4A2	-1.13	-1.18	1.15	-1.09
Q3TDD8	EIF4B	eukaryotic translation initiation factor 4B	-1.12	1.56	1.09	-1.93
Q3TG58	EIF4H	eukaryotic translation initiation factor 4H	-1.90	1.12	-1.46	-1.03
Q5FW97	Eno1	Enolase 1, alpha non-neuron	-1.44	-1.67	1.12	2.03
Q3UJ20	ENO2	enolase 2	-1.53	-3.22	1.68	4.73
D3YU63	ENPP6	ectonucleotide pyrophosphatase/phosphodiesterase 6	-1.13	-1.89	-1.16	1.55
Q3T9U8	ENTPD2	ectonucleoside triphosphate diphosphohydrolase 2	1.46	1.58	-2.13	-1.18
A2AUK5	EPB41L1	erythrocyte membrane protein band 4.1 like 1	-1.00	-1.20	1.34	-1.56
B6ZHC5	EPB41L2	erythrocyte membrane protein band 4.1 like 2	1.37	1.25	-1.68	-1.37
D0VYV6	EPB41L3	erythrocyte membrane protein band 4.1 like 3	-1.36	-2.86	1.88	4.58
Q3UQ71	EPHX2	epoxide hydrolase 2	3.17	1.27	-1.43	1.23
Q80VP1	EPN1	epsin 1	-1.34	-3.00	2.07	4.43
Q8BFZ9	ERLIN2	ER lipid raft associated 2	1.34	1.54	-1.34	-1.76
Q5EBJ4	ERMN	ermin	2.00	1.74	-1.60	2.11

Q3URM4	ERP44	endoplasmic reticulum protein 44	-2.90	-1.15	-1.22	-2.06
H3BJL6	ESD	esterase D	-1.21	1.01	-1.12	-1.24
Q99LC5	ETFA	electron transfer flavoprotein alpha subunit	-1.26	-1.71	-2.12	1.06
Q9DCW4	ETFB	electron transfer flavoprotein beta subunit	1.07	1.03	-1.77	-1.01
Q3TCP5	EZR	ezrin	1.07	1.10	-2.10	-1.04
Q3UUF0	FAAH	fatty acid amide hydrolase	-1.86	-2.06	1.39	1.83
Q5NDA4	FABP7	fatty acid binding protein 7	-1.93	-1.33	-1.58	-10.81
Q8C729	FAM126B	family with sequence similarity 126 member B	-1.49	-1.78	1.07	2.51
Q921M7	FAM49B	family with sequence similarity 49 member B	-1.26	-1.59	1.15	1.37
F8VPU2	FARP1	FERM, ARH/RhoGEF and pleckstrin domain protein 1	1.77	1.62	-1.75	-1.86
Q3UHT6	FASN	fatty acid synthase	-1.76	-2.10	-1.22	1.86
A2RT62	FBXL16	F-box and leucine rich repeat protein 16	-1.17	-1.35	1.30	-1.42
Q3USR5	FBXO2	F-box protein 2	1.06	-1.82	1.02	2.81
P97807	FH	fumarate hydratase	-2.69	-2.77	-1.42	4.41
Q540I4	FLOT1	flotillin 1	1.04	1.62	-1.47	-1.47
Q61553	FSCN1	fascin actin-bundling protein 1	-2.13	-1.96	1.63	1.55
Q7TPM6	FSD1	fibronectin type III and SPRY domain containing 1	-1.33	-1.73	1.06	1.16
Q3USY4	Fus	fused in sarcoma	-1.88	-2.46	-1.12	1.78
Q3UVW2	GABRG2	gamma-aminobutyric acid type A receptor gamma2 subunit	-1.91	-1.32	1.64	1.69
M0QWZ0	GADPH	Uncharacterized protein	-1.26	-1.61	-1.22	1.71
A1A4T2	GANAB	glucosidase II alpha subunit	1.15	-2.83	1.82	2.06
P06837	GAP43	growth associated protein 43	-1.47	1.15	2.17	-2.78
D3YU09	GDA	guanine deaminase	-1.47	-1.29	-1.05	-1.31
A2A5H8	GDAP1L1	ganglioside induced differentiation associated protein 1 like 1	-1.66	-1.63	1.15	1.26
P50396	GDI1	GDP dissociation inhibitor 1	-1.49	-2.31	1.26	1.73
P03995	GFAP	glial fibrillary acidic protein	4.86	1.58	-7.90	-1.19
Q7TMQ1	GJA1	gap junction protein alpha 1	2.99	1.83	-2.98	-1.10
F8WHM5	GLG1	golgi glycoprotein 1	-1.66	1.02	1.49	-1.10
Q9CPV4	GLOD4	glyoxalase domain containing 4	1.14	-1.45	-1.04	2.82
D3Z7P3	GLS	glutaminase	-1.71	-1.45	-1.07	1.55
P26443	GLUD1	glutamate dehydrogenase 1	1.38	1.12	-1.98	1.12
P15105	GLUL	glutamate-ammonia ligase	1.47	1.61	-1.46	-1.12
G3UWG1	Gm10108	MCG115977	-1.78	-1.98	1.06	2.42
G3X9L6	Gm10250	ATP synthase, H+ transporting, mitochondrial F0 complex, subunit d pseudogene	-1.74	-1.70	1.02	2.23
B2RTM0	Gm11275	Histone H4	-1.14	1.01	-1.22	4.12
E9PZF0	Gm20390	Nucleoside diphosphate kinase	1.34	-3.61	2.44	1.82
E9Q035	Gm20425	Protein Gm20425	1.46	-1.00	-2.22	-1.46
Q3UE40	GNA13	G protein subunit alpha 13	1.51	1.97	-1.26	1.34
P08752	GNAI2	G protein subunit alpha i2	1.45	1.64	-1.52	-1.22
P18872	GNAO1	G protein subunit alpha o1	-2.64	-2.71	1.03	2.50
Q6R0H7	GNAS	GNAS complex locus	-1.47	-1.02	1.56	2.39
Q3TQ70	GNB1	G protein subunit beta 1	1.06	1.23	-1.28	-1.29
D3YZX3	GNB2	G protein subunit beta 2	1.03	-1.68	1.63	3.57
Q3THF3	GNB4	G protein subunit beta 4	-1.91	1.02	2.00	-2.13
Q9DAS9	GNG12	G protein subunit gamma 12	1.96	1.69	-1.33	1.15
Q3UGN1	GNG7	G protein subunit gamma 7	2.16	-2.19	2.84	2.11
P05201	GOT1	glutamic-oxaloacetic transaminase 1	-1.56	-3.74	3.23	11.31
P05202	GOT2	glutamic-oxaloacetic transaminase 2	-1.34	-1.11	-1.13	2.44

E0CXN5	GPD1	glycerol-3-phosphate dehydrogenase 1	-1.07	-1.29	1.09	2.36
A2AQR0	GPD2	glycerol-3-phosphate dehydrogenase 2	-2.06	-1.95	-1.86	1.11
A0JNY3	GPHN	gephyrin	-1.03	-2.04	2.83	-1.19
P06745	GPI	glucose-6-phosphate isomerase	-1.17	-1.82	1.24	2.33
P35802	GPM6A	glycoprotein M6A	-1.06	-1.76	2.68	1.64
A2AEG6	GPM6B	glycoprotein M6B	-1.56	1.10	1.27	-1.79
Q3UNH4	GPRIN1	G protein regulated inducer of neurite outgrowth 1	-1.18	1.57	1.34	-2.45
Q4LG64	GRIA2	glutamate ionotropic receptor AMPA type subunit 2	-1.78	-3.44	1.11	1.80
G3X9V4	GRIN2B	glutamate ionotropic receptor NMDA type subunit 2B	-2.30	-3.23	-1.19	1.16
Q3TGJ9	GSN	gelsolin	1.91	1.14	-2.93	-1.37
E9PVM7	GSTM3	glutathione S-transferase mu 3	-1.02	-1.48	1.70	2.61
P10649	GSTM5	glutathione S-transferase mu 5	2.12	1.36	-1.29	1.77
P19157	GSTP1	glutathione S-transferase pi 1	1.57	1.11	-1.16	2.45
Q61425	HADH	hydroxyacyl-CoA dehydrogenase	1.04	1.04	-1.84	1.10
Q8BMS1	HADHA	hydroxyacyl-CoA dehydrogenase/3-ketoacyl-CoA thiolase/enoyl-CoA hydratase (trifunctional protein), alpha subunit	-1.07	-1.19	-2.69	1.05
Q99JY0	HADHB	hydroxyacyl-CoA dehydrogenase/3-ketoacyl-CoA thiolase/enoyl-CoA hydratase (trifunctional protein), beta subunit	1.32	1.21	-2.43	-1.30
Q9QUP5	HAPLN1	hyaluronan and proteoglycan link protein 1	1.84	1.28	-1.86	1.61
Q8BPF4	HBA1/HBA2	hemoglobin subunit alpha 2	1.96	-1.06	-1.59	1.87
D0U281	Hbbt1	Beta-globin	2.05	-1.14	-1.90	2.24
Q3UGR5	HDHD2	haloacid dehalogenase like hydrolase domain containing 2	-1.25	-1.91	1.14	2.65
Q3U4Z7	HDLBP	high density lipoprotein binding protein	1.28	1.41	-1.82	-2.50
B2RSY3	HEPACAM	hepatic and glial cell adhesion molecule	1.59	1.57	-1.56	-1.14
Q3TXR9	HEXB	hexosaminidase subunit beta	1.26	1.30	-4.17	-1.26
A0ZNJ2	HIBADH	3-hydroxyisobutyrate dehydrogenase	1.26	1.22	-1.91	1.11
A0JLV3	HIST1H2BL	histone cluster 1 H2B family member l	-1.41	1.17	1.21	4.15
G3UVV4	HK1	hexokinase 1	-1.46	-1.52	-1.20	2.47
B7ZP22	HNRNPA2B1	heterogeneous nuclear ribonucleoprotein A2/B1	-1.31	-1.80	1.42	1.70
Q9Z2Y3	HOMER1	homer scaffolding protein 1	-1.17	-1.96	1.80	1.30
P62748	HPCAL1	hippocalcin like 1	1.62	-1.47	1.71	1.25
B2RRY8	HPCAL4	hippocalcin like 4	-1.91	-2.84	1.23	-1.10
C0H5X4	HRAS	HRas proto-oncogene, GTPase	-3.05	-3.44	-1.16	2.30
A2AFQ2	HSD17B10	hydroxysteroid 17-beta dehydrogenase 10	-1.05	1.56	-2.47	-1.69
Q3TT11	HSD17B4	hydroxysteroid 17-beta dehydrogenase 4	1.05	1.48	-1.46	-1.67
Q3UIF3	HSP90AA1	heat shock protein 90 alpha family class A member 1	-1.05	-2.19	2.39	2.94
Q80YC2	HSP90AB1	heat shock protein 90 alpha family class B member 1	-1.78	-3.48	1.41	3.18
Q3UAD6	HSP90B1	heat shock protein 90 beta family member 1	-1.04	-1.40	1.04	-1.54
Q8K0U4	HSPA12A	heat shock protein family A (Hsp70)	-1.71	-2.16	1.72	2.57

		member 12A				
Q3U2G2	HSPA4	heat shock protein family A (Hsp70) member 4	-1.34	-1.63	1.22	1.78
E0CY23	HSPA4L	heat shock protein family A (Hsp70) member 4 like	-1.23	-1.46	1.25	2.75
Q3TI47	HSPA5	heat shock protein family A (Hsp70) member 5	-1.04	1.32	-1.61	-2.16
Q3KQJ4	HSPA8	heat shock protein family A (Hsp70) member 8	1.23	-5.04	3.21	1.99
P38647	HSPA9	heat shock protein family A (Hsp70) member 9	-1.27	1.25	-1.76	-1.04
P63038	HSPD1	heat shock protein family D (Hsp60) member 1	-1.63	-1.44	-1.38	1.62
Q8C6H1	HSPH1	heat shock protein family H (Hsp110) member 1	-1.94	-2.42	1.19	2.63
Q8R2M5	IARS2	isoleucyl-tRNA synthetase 2, mitochondrial	-1.20	-1.33	-1.35	2.20
Q2KHL7	ICAM5	intercellular adhesion molecule 5	-1.08	-1.54	1.64	-1.69
P54071	IDH2	isocitrate dehydrogenase (NADP(+)) 2, mitochondrial	1.32	1.11	-2.04	1.09
Q9D6R2	IDH3A	isocitrate dehydrogenase 3 (NAD(+)) alpha	-1.53	-1.12	-1.25	1.72
Q91VA7	IDH3B	isocitrate dehydrogenase 3 (NAD(+)) beta	-1.34	-1.00	-1.24	1.93
Q3TGZ3	IDH3G	isocitrate dehydrogenase 3 (NAD(+)) gamma	-1.71	-1.66	-1.61	1.25
G3UYZ1	IGSF8	immunoglobulin superfamily member 8	1.59	1.71	-1.06	1.89
Q3TEY5	IMMT	inner membrane mitochondrial protein	-1.35	1.07	-1.46	1.54
B2RY90	ISOC2	isochorismatase domain containing 2	-1.28	-2.72	-2.13	3.88
M0QWA7	ITGB2	integrin subunit beta 2	2.54	1.62	-1.74	1.21
P11881	ITPR1	inositol 1,4,5-trisphosphate receptor type 1	1.06	-1.87	1.06	1.19
E0CXZ9	KCNAB2	potassium voltage-gated channel subfamily A regulatory beta subunit 2	-1.26	1.02	-1.29	1.55
G3X9J4	KIAA1468	KIAA1468	-2.70	-3.57	1.11	1.46
Q61768	KIF5B	kinesin family member 5B	-1.63	-1.56	-1.35	-1.31
Q3TFE8	KPNB1	karyopherin subunit beta 1	-1.60	-2.79	1.21	1.93
Q61765	KRT31	keratin 31	-4.24	-1.49	1.22	1.19
Q61595-12	Ktn1	kinectin 1	-1.99	-1.26	-1.73	-1.82
A2AFG7	L1CAM	L1 cell adhesion molecule	-2.05	-1.18	1.10	-2.16
Q3TA96	LAMP1	lysosomal associated membrane protein 1	1.76	1.44	-1.69	1.28
Q9CPY7	LAP3	leucine aminopeptidase 3	1.79	1.46	-1.69	1.12
D3Z7F0	LDHB	lactate dehydrogenase B	-1.10	-1.85	1.39	2.84
Q9Z2I0	LETM1	leucine zipper and EF-hand containing transmembrane protein 1	-2.32	-1.32	1.49	3.96
P16045	LGALS1	galectin 1	2.78	1.18	-3.62	-1.20
Q9JIA1	LGI1	leucine rich glioma inactivated 1	1.15	1.61	1.64	2.14
Q9D1T0	LINGO1	leucine rich repeat and Ig domain containing 1	-1.70	-1.27	1.76	1.13
Q9WU79	LOC102724788/PRODH	proline dehydrogenase 1	1.07	-1.25	-2.49	-1.11
Q3V2D0	LONP1	lon peptidase 1, mitochondrial	-1.48	1.14	-1.65	1.05
Q91ZX7	LRP1	LDL receptor related protein 1	1.16	1.35	-1.62	1.23
Q6PB66	LRPPRC	leucine rich pentatricopeptide repeat containing	-1.89	-1.17	-1.33	-1.18
B9EHV0	LRRC7	leucine rich repeat containing 7	-2.64	-1.86	-1.31	-1.58
Q9WTL7	LYPLA2	lysophospholipase II	-1.19	-2.29	1.55	4.97

Q3ZB60	MAG	myelin associated glycoprotein	1.36	1.33	1.31	1.52
A2ARP8	MAP1A	microtubule associated protein 1A	1.53	-1.12	1.36	-1.01
B2RQQ5	MAP1B	microtubule associated protein 1B	1.10	1.02	1.64	-1.20
P20357	MAP2	microtubule associated protein 2	1.23	-1.29	1.29	-1.12
Q3TMJ8	MAP2K1	mitogen-activated protein kinase kinase 1	-1.48	-2.27	-1.21	1.68
E9QPW8	Map4	Microtubule-associated protein	-1.35	-1.80	-1.83	1.32
Q7TSJ2	MAP6	microtubule associated protein 6	1.36	2.18	-1.14	-1.24
Q3U4H0	MAPRE1	microtubule associated protein RP/EB family member 1	-1.04	1.32	-1.06	-3.04
Q2UZW7	MAPRE3	microtubule associated protein RP/EB family member 3	1.14	1.97	-1.14	-2.07
P10637-3	MAPT	microtubule associated protein tau	-1.17	-1.16	1.93	-1.26
E0CZH6	MARC2	mitochondrial amidoxime reducing component 2	-1.17	-1.39	-1.61	1.63
P26645	Marcks	myristoylated alanine rich protein kinase C substrate	-1.09	-1.68	3.37	-1.24
P28667	MARCKSL1	MARCKS like 1	-2.95	-1.19	1.79	-10.60
F6RT34	MBP	myelin basic protein	1.76	1.44	1.11	2.75
P14152	MDH1	malate dehydrogenase 1	-1.35	-2.14	1.59	3.33
P08249	MDH2	malate dehydrogenase 2	-1.37	1.46	-1.68	1.19
Q3TQP6	ME1	malic enzyme 1	-1.63	-3.97	-1.16	1.28
Q8BMF3	ME3	malic enzyme 3	-1.87	-1.35	-1.18	1.68
D3YYS6	MGLL	monoglyceride lipase	-1.78	-2.36	-1.65	2.29
Q8VHK5	MLC1	megalencephalic leukoencephalopathy with subcortical cysts 1	1.62	1.46	-1.86	-1.72
Q3UY21	MOG	myelin oligodendrocyte glycoprotein	2.18	1.11	1.07	4.21
Q9CQX8	MRPS36	mitochondrial ribosomal protein S36	-1.86	1.75	-1.83	-1.15
P26041	MSN	moesin	1.51	1.17	-2.71	-1.08
Q3USP9	Mt3	metallothionein 3	1.89	1.51	-1.84	-1.23
A2AFW6	MTCH2	mitochondrial carrier 2	-1.85	-1.02	1.02	-1.09
Q3UH59	MYH10	myosin heavy chain 10	-1.43	-1.74	2.75	1.08
Q8VDD5	MYH9	myosin heavy chain 9	-1.93	-3.90	1.12	3.12
E9Q405	MYO18A	myosin XVIIIA	-2.01	1.29	-1.08	-1.16
D3YZ62	MYO5A	myosin VA	-1.33	-1.07	1.41	2.11
E9Q174	MYO6	myosin VI	1.74	1.75	-2.40	-1.13
Q9DB05	NAPA	NSF attachment protein alpha	-1.53	-1.57	-1.55	1.03
P28663	NAPB	NSF attachment protein beta	-1.25	-2.55	1.29	2.86
D3YVA2	NCALD	neurocalcin delta	1.02	-4.28	1.88	1.57
P13595	NCAM1	neural cell adhesion molecule 1	-1.62	-1.06	1.56	-1.89
O35136	NCAM2	neural cell adhesion molecule 2	1.13	-1.33	1.60	-1.54
Q9Z0E0	NCDN	neurochondrin	-1.06	-1.48	1.57	1.19
Q8BLF1	NCEH1	neutral cholesterol ester hydrolase 1	-1.89	-1.10	-1.61	1.08
A1L0U6	NCKAP1	NCK associated protein 1	-1.21	-2.30	-1.10	1.84
Q3TGR3	NCL	nucleolin	1.40	-1.47	-1.19	1.23
B2L0N7	ND1	NADH dehydrogenase subunit 1	-1.09	-5.60	2.14	6.75
Q3TD08	NDRG1	N-myc downstream regulated 1	2.11	1.64	-1.55	1.61
Q9QYG0-2	NDRG2	NDRG family member 2	-1.57	-4.12	1.13	2.68
Q9QYF9	NDRG3	NDRG family member 3	-1.60	-1.48	1.27	1.71
Q99LC3	NDUFA10	NADH:ubiquinone oxidoreductase subunit A10	-1.92	-2.19	1.36	2.95
Q5M9K5	NDUFA12	NADH:ubiquinone oxidoreductase subunit A12	-1.41	-1.06	-1.65	1.50
Q9CQZ5	NDUFA6	NADH:ubiquinone oxidoreductase subunit A6	-1.05	-1.32	-1.64	1.94
Q9DCJ5	NDUFA8	NADH:ubiquinone oxidoreductase subunit A8	-1.62	-1.56	1.32	2.87
Q9DC69	NDUFA9	NADH:ubiquinone oxidoreductase	-1.50	-1.47	-1.25	2.09

		subunit A9				
Q9DCS9	NDUFB10	NADH:ubiquinone oxidoreductase subunit B10	-1.50	1.32	-1.34	1.18
Q3UIQ2	NDUFS1	NADH:ubiquinone oxidoreductase core subunit S1	-1.77	-1.84	-1.75	1.40
Q9DCT2	NDUFS3	NADH:ubiquinone oxidoreductase core subunit S3	-1.76	-1.61	-1.07	2.67
P52503	NDUFS6	NADH:ubiquinone oxidoreductase subunit S6	1.34	2.44	-1.96	-2.98
D3YUM1	NDUFV1	NADH:ubiquinone oxidoreductase core subunit V1	-1.63	-1.18	-1.49	1.51
Q9D6J6	NDUFV2	NADH:ubiquinone oxidoreductase core subunit V2	-1.20	1.09	-1.36	1.24
P08551	NEFL	neurofilament light	-1.78	-1.06	1.34	-1.97
Q810U3	NFASC	neurofascin	1.68	1.97	-1.33	1.49
Q3UJC3	NMT1	N-myristoyltransferase 1	1.34	-2.10	1.23	1.89
Q8C550	NOL3	nucleolar protein 3	1.62	1.05	-1.76	-1.13
Q6GQT9	NOMO1 (includes others)	NODAL modulator 1	-1.30	1.56	-1.44	-2.26
F6QYF8	NPEPPS	aminopeptidase puromycin sensitive	-1.48	-1.15	1.00	2.32
Q3U536	NPM1	nucleophosmin	-1.11	-2.05	1.06	-1.15
H3BIX4	Nptn	neuroplastin	-1.89	-1.55	-1.47	-1.33
Q3UH37	NPTXR	neuronal pentraxin receptor	1.14	1.15	-1.10	-2.73
Q810U4-2	NRCAM	neuronal cell adhesion molecule	1.33	1.40	-1.42	-1.78
P46460	NSF	N-ethylmaleimide sensitive factor, vesicle fusing ATPase	-1.11	-1.03	1.23	1.78
Q3UHE3	NTRK2	neurotrophic receptor tyrosine kinase 2	-1.06	1.41	-1.30	-1.48
Q3TG75	OAT	ornithine aminotransferase	1.42	1.38	-2.26	-1.19
Q9D8W7	OCIAD2	OCIA domain containing 2	-1.53	2.32	-1.78	-1.68
Q60597	OGDH	oxoglutarate dehydrogenase	-1.69	-1.11	-1.33	1.60
B2RXT3	OGDHL	oxoglutarate dehydrogenase-like	-1.23	1.20	-1.68	1.81
H7BX01	OPA1	OPA1, mitochondrial dynamin like GTPase	-1.95	-1.47	-1.40	1.44
D3Z7I9	OSBPL1A	oxysterol binding protein like 1A	-1.33	-1.86	1.72	3.15
D3YWF6	Otub1	OTU domain, ubiquitin aldehyde binding 1	-1.67	-2.53	2.73	1.26
Q3U9P7	OXCT1	3-oxoacid CoA-transferase 1	-2.63	1.08	-1.50	-2.07
Q4KMM3	OXR1	oxidation resistance 1	-1.57	-1.86	-1.02	1.39
Q8BZV8	P2RY12	purinergic receptor P2Y12	-3.22	-1.30	1.43	-1.22
Q3TF72	P4HB	prolyl 4-hydroxylase subunit beta	-1.47	-2.33	-2.09	-1.15
Q3TYF2	PACSIN1	protein kinase C and casein kinase substrate in neurons 1	-1.77	-1.49	-1.34	2.06
Q08642	PADI2	peptidyl arginine deiminase 2	3.55	1.18	-2.02	1.82
Q3TRX4	PALM	paralemmin	-1.16	1.01	1.75	-1.53
Q3T9S7	PC	pyruvate carboxylase	-1.25	-1.05	-1.48	1.96
A0PJE6	PCCB	propionyl-CoA carboxylase beta subunit	-1.63	-1.03	-1.64	-1.12
Q9QYX7	PCLO	piccolo presynaptic cytomatrix protein	-1.73	-2.28	1.05	1.53
Q9QXV0	PCSK1N	proprotein convertase subtilisin/kexin type 1 inhibitor	1.39	2.21	1.66	-1.74
Q3UFJ3	PDHA1	pyruvate dehydrogenase (lipoamide) alpha 1	-2.01	-1.10	-1.32	2.12
Q9D051	PDHB	pyruvate dehydrogenase (lipoamide) beta	-1.43	-1.30	-1.23	2.25
Q8BKZ9	PDHX	pyruvate dehydrogenase complex component X	-1.74	2.02	-1.54	-2.34
P27773	PDIA3	protein disulfide isomerase family A	-1.13	1.46	-1.48	-1.91

		member 3				
Q3THH1	PDIA6	protein disulfide isomerase family A member 6	-1.26	-3.73	1.84	1.37
Q8BFP9	PDK1	pyruvate dehydrogenase kinase 1	-1.18	1.55	-1.95	-1.05
D3YYH0	PEX5L	peroxisomal biogenesis factor 5 like	1.35	-1.18	-1.58	1.11
P12382	PFKL	phosphofructokinase, liver type	-1.14	-4.01	1.67	4.30
Q99K08	PFKM	phosphofructokinase, muscle	-1.04	-1.90	1.50	1.96
Q8C605	PFKP	phosphofructokinase, platelet	-1.22	-1.92	1.03	1.96
Q3U7Z6	PGAM1	phosphoglycerate mutase 1	-1.04	1.11	1.03	1.31
A1A4A7	PGAM5	PGAM family member 5, mitochondrial serine/threonine protein phosphatase	-2.21	1.19	1.01	-2.80
A2CEK3	PGM1	phosphoglucomutase 1	1.15	-1.23	-1.05	2.01
Q8CAA7	PGM2L1	phosphoglucomutase 2 like 1	-1.96	-1.70	1.26	1.77
Q5SQG5	PHB	prohibitin	-1.01	1.53	-1.31	-1.09
Q3V235	PHB2	prohibitin 2	-1.64	-1.15	-1.19	1.71
Q61753	PHGDH	phosphoglycerate dehydrogenase	1.69	1.31	-1.27	-1.10
Q6DIC7	PI4KA	phosphatidylinositol 4-kinase alpha	-1.71	-3.11	1.82	4.52
J3QPW1	PITPNA	phosphatidylinositol transfer protein alpha	-1.03	-2.77	1.99	1.41
Q2M4J2	PLCB1	phospholipase C beta 1	-1.73	-1.61	1.31	2.38
O35405	PLD3	phospholipase D family member 3	-1.71	-2.03	-1.07	1.75
Q9DBG5	PLIN3	perilipin 3	-1.53	-3.52	-2.70	1.53
Q3UYM8	PLP1	proteolipid protein 1	2.00	1.40	1.23	3.68
Q7TME0	PLPPR4	phospholipid phosphatase related 4	-1.56	1.37	-1.06	-5.81
Q3TYF5	PPP1CA	protein phosphatase 1 catalytic subunit alpha	-2.38	-4.02	1.95	5.57
Q60829	PPP1R1B	protein phosphatase 1 regulatory inhibitor subunit 1B	1.20	-1.40	-1.03	-1.29
Q3TDD9	PPP1R21	protein phosphatase 1 regulatory subunit 21	-1.04	1.44	-1.62	-1.94
Q6R891	PPP1R9B	protein phosphatase 1 regulatory subunit 9B	-1.43	-1.40	1.40	-1.34
Q8BN07	PPP2CB	protein phosphatase 2 catalytic subunit beta	-2.22	-3.41	1.07	4.05
Q7TMX2	PPP2R1A	protein phosphatase 2 scaffold subunit Aalpha	-1.52	-4.97	1.31	3.00
Q3UZJ4	PPP2R5E	protein phosphatase 2 regulatory subunit B'epsilon	-1.21	1.09	-1.13	-1.42
B2RRX2	PPP3CA	protein phosphatase 3 catalytic subunit alpha	-1.86	-3.38	2.17	5.15
Q63810	PPP3R1	protein phosphatase 3 regulatory subunit B, alpha	1.10	-2.66	2.08	2.17
B1AXW5	PRDX1	peroxiredoxin 1	1.71	1.45	-1.75	-1.08
P20108	PRDX3	peroxiredoxin 3	-1.40	-1.77	-1.09	2.64
H3BJQ7	PRDX5	peroxiredoxin 5	-1.43	-1.53	-1.31	2.21
Q6GT24	PRDX6	peroxiredoxin 6	3.02	1.25	-2.59	1.26
Q8K1M3	PRKAR2A	protein kinase cAMP-dependent type II regulatory subunit alpha	-1.72	-2.42	1.21	2.26
P31324	PRKAR2B	protein kinase cAMP-dependent type II regulatory subunit beta	-1.58	-1.10	1.62	-1.47
P16054	PRKCE	protein kinase C epsilon	1.25	1.84	1.10	-1.97
Q2NKI4	PRKCG	protein kinase C gamma	1.49	1.28	1.15	-1.98
B2RUD7	PSAP	prosaposin	1.14	1.27	-2.54	1.17
Q3ULZ3	PSAT1	phosphoserine aminotransferase 1	1.54	1.37	-1.53	1.23
Q3UWT6	PSMA2	proteasome subunit alpha 2	-2.25	-2.85	1.08	2.49
Q8BWM0	PTGES2	prostaglandin E synthase 2	-1.69	-1.33	-1.76	1.93
Q9D0J8	Ptms	parathymosin	1.47	1.11	-1.18	-1.65
P42669	PURA	purine rich element binding protein A	1.10	-1.71	1.10	1.57

O35295	PURB	purine rich element binding protein B	-1.07	-1.27	1.54	-1.08
Q3TFQ8	PYGB	glycogen phosphorylase B	1.79	1.22	-1.18	1.53
Q9WUB3	PYGM	glycogen phosphorylase, muscle associated	-1.35	-1.39	1.68	2.92
D3YWR7	QDPR	quinoid dihydropteridine reductase	2.09	1.64	-1.78	1.89
A2AL34	RAB14	RAB14, member RAS oncogene family	-1.16	-1.66	1.28	2.33
Q3TU36	RAP1GDS1	Rap1 GTPase-GDP dissociation stimulator 1	-1.90	-2.69	1.53	2.53
Q9Z268	RASAL1	RAS protein activator like 1	-1.43	-1.38	1.59	1.39
Q8CHX7	RFTN2	raftlin family member 2	1.37	1.96	-1.46	-1.23
Q4VAE6	RHOA	ras homolog family member A	-1.68	-2.14	1.53	2.60
Q3UDZ1	RHOG	ras homolog family member G	1.51	1.66	-1.82	1.35
P52760	RIDA	reactive intermediate imine deaminase A homolog	3.93	1.62	-2.75	1.35
Q3UM23	RNH1	ribonuclease/angiogenin inhibitor 1	1.60	1.50	-1.74	-1.37
P47708	RPH3A	rabphilin 3A	-1.69	-1.80	1.26	1.79
Q3TIQ2	RPL12	ribosomal protein L12	1.35	1.32	-1.42	-1.82
D3YX54	Rpl13-ps3	60S ribosomal protein L13	1.56	1.63	-1.38	-1.99
Q3T9U9	RPL3	ribosomal protein L3	1.26	-1.02	-1.10	-1.28
Q3TK73	RPL7	ribosomal protein L7	1.68	1.47	-1.28	-1.58
Q3U900	RPN1	ribophorin I	-1.09	-1.10	-1.06	-1.98
A2ACG7	RPN2	ribophorin II	-2.17	-1.93	1.02	2.38
Q3U9P0	RPS10	ribosomal protein S10	1.69	-1.36	1.05	1.20
Q3UJS5	RPS14	ribosomal protein S14	1.53	1.42	-1.01	-1.61
Q5M9M4	RPS15A	ribosomal protein S15a	1.85	1.18	-1.42	-1.49
Q3TW65	RPS18	ribosomal protein S18	1.81	1.23	-1.32	-1.57
Q5M9P3	RPS19	ribosomal protein S19	2.30	1.61	-1.04	-1.29
D3YVC1	RPS2	ribosomal protein S2	1.67	1.46	-1.54	-1.82
Q8C1L7	RPS21	ribosomal protein S21	2.00	1.28	-1.33	-1.62
D3YV43	RPS3	ribosomal protein S3	1.52	1.29	-1.06	-1.63
Q3UXQ6	RPS4Y1	ribosomal protein S4, Y-linked 1	1.61	1.13	-1.26	-1.66
Q91V55	RPS5	ribosomal protein S5	1.60	1.57	-1.49	-2.00
Q3TL53	RPS6	ribosomal protein S6	1.74	1.25	-1.59	-1.90
Q6ZWN5	RPS9	ribosomal protein S9	1.80	2.02	-1.37	-1.99
Q9CTF6	RRAS2	related RAS viral (r-ras) oncogene homolog 2	-2.96	-2.35	1.94	-2.43
A3QM89	RTN1	reticulon 1	1.24	-3.15	2.36	1.79
Q9ES97	RTN3	reticulon 3	1.14	1.14	1.61	-1.17
Q99P72	RTN4	reticulon 4	-1.49	-2.47	1.33	1.69
Q9D394	RUFY3	RUN and FYVE domain containing 3	-1.15	1.55	-1.07	-1.68
Q9D3M4	S100A1	S100 calcium binding protein A1	1.91	-1.46	-1.70	1.91
Q9EP69	SACM1L	SAC1 suppressor of actin mutations 1 like (yeast)	-1.08	1.48	-1.32	-2.07
Q8R127	SCCPDH	saccharopine dehydrogenase (putative)	-1.46	1.92	1.43	5.44
Q9CZC8	SCRN1	secernin 1	-1.31	-2.04	1.98	-1.40
Q8K2B3	SDHA	succinate dehydrogenase complex flavoprotein subunit A	-2.12	1.23	-1.77	1.17
Q0QEZ4	SDHB	succinate dehydrogenase complex iron sulfur subunit B	-1.53	-1.33	-1.08	1.63
Q3UZ06	SEC22B	SEC22 homolog B, vesicle trafficking protein (gene/pseudogene)	-1.59	-1.34	-1.06	1.77
Q8C1E4	SEC23A	Sec23 homolog A, coat complex II component	-2.12	-2.40	1.71	5.25
G3X972	SEC24C	SEC24 homolog C, COPII coat complex component	-1.32	1.30	1.17	-1.32
Q8C1B7	SEPT11	septin 11	-1.05	1.54	-1.74	-1.25
P42208	SEPT2	septin 2	1.38	1.27	-2.21	-1.55

B7ZNM7	SEPT5	septin 5	-1.22	1.14	1.27	2.31
Q5DTS3	SEPT7	septin 7	-1.15	-1.14	1.08	2.27
B1AQY9	SEPT8	septin 8	1.52	1.90	-1.14	1.19
Q3UEI6	SERBP1	SERPINE1 mRNA binding protein 1	2.05	1.70	-1.16	-1.55
Q91V61	SFXN3	sideroflexin 3	-1.58	-1.63	1.04	1.73
Q8BRQ9	SFXN5	sideroflexin 5	1.02	1.05	-2.17	-1.32
Q8VD37	SGIP1	SH3 domain GRB2 like endophilin interacting protein 1	-1.74	-1.71	1.11	1.70
Q3TJB4	SH3GL1	SH3 domain containing GRB2 like 1, endophilin A2	-8.80	-6.60	1.72	3.30
A2ALV1	SH3GL2	SH3 domain containing GRB2 like 2, endophilin A1	1.15	1.10	1.19	1.56
A2AWI7	SH3GLB2	SH3 domain containing GRB2 like, endophilin B2	-2.26	-3.05	1.29	2.45
Q3UJK6	SIRT2	sirtuin 2	-1.08	1.00	-1.34	1.49
E9QM38	SLC12A2	solute carrier family 12 member 2	1.02	1.44	-1.17	1.50
Q91V14	SLC12A5	solute carrier family 12 member 5	-1.27	-1.43	1.45	3.09
Q3TXX4	SLC17A7	solute carrier family 17 member 7	-1.36	-3.51	3.05	5.68
Q8C3T7	SLC1A3	solute carrier family 1 member 3	-1.07	-4.37	-2.27	1.82
Q3US35	SLC1A4	solute carrier family 1 member 4	2.04	-1.27	-1.58	1.14
Q8BH59	SLC25A12	solute carrier family 25 member 12	-1.47	1.02	-1.62	1.46
Q9DB41	SLC25A18	solute carrier family 25 member 18	1.75	1.23	-3.23	-1.31
Q9D6M3	SLC25A22	solute carrier family 25 member 22	-1.66	1.42	-1.50	-2.42
Q3THU8	SLC25A3	solute carrier family 25 member 3	-1.02	1.06	-1.09	2.17
Q8BVI9	SLC25A4	solute carrier family 25 member 4	-1.65	-1.22	-1.63	1.32
P51881	SLC25A5	solute carrier family 25 member 5	-1.21	-1.69	1.06	2.75
Q3TPL8	SLC2A3	solute carrier family 2 member 3	-1.27	1.24	1.16	1.68
Q49S98	SLC32A1	solute carrier family 32 member 1	-1.15	1.27	1.70	-1.11
G3UWA6	SLC3A2	solute carrier family 3 member 2	-1.44	-1.63	1.17	1.71
A2AMH3	SLC44A1	solute carrier family 44 member 1	1.96	1.96	-1.76	1.63
B1AWV9	SLC4A10	solute carrier family 4 member 10	1.18	-1.78	2.23	2.89
E9Q8N8	SLC4A4	solute carrier family 4 member 4	-1.03	-1.92	1.19	1.04
P60879	SNAP25	synaptosome associated protein 25	-1.63	1.42	-1.15	-2.08
Q8R570	SNAP47	synaptosome associated protein 47	-1.14	1.23	-1.00	-1.71
Q3UI39	SNAP91	synaptosome associated protein 91	-1.20	-2.42	1.69	2.44
O55042	SNCA	synuclein alpha	-1.12	1.42	1.02	-1.72
Q3TRW3	SND1	staphylococcal nuclease and tudor domain containing 1	-1.15	1.31	-1.46	-2.47
P08228	SOD1	superoxide dismutase 1	2.63	1.69	1.16	-1.42
A3KGU5	SPTAN1	spectrin alpha, non-erythrocytic 1	-1.19	-2.18	1.69	1.38
Q62261	SPTBN1	spectrin beta, non-erythrocytic 1	-1.28	-1.14	1.29	-1.10
Q3UGZ4	SPTBN2	spectrin beta, non-erythrocytic 2	-2.60	-1.94	-1.20	-1.38
B1AQX9	SRCIN1	SRC kinase signaling inhibitor 1	-1.37	1.58	1.11	-2.08
Q8C2H3	STMN1	stathmin 1	1.79	1.35	1.21	-1.13
Q99JB2	STOML2	stomatin like 2	-1.73	1.60	-1.76	-2.27
Q5D0A4	STX1A	syntaxin 1A	-1.14	-1.64	1.32	2.32
P61264	STX1B	syntaxin 1B	3.49	-7.25	1.35	1.84
O08599	STXBP1	syntaxin binding protein 1	-1.29	-1.69	1.65	3.48
Q3U6C7	SUCLA2	succinate-CoA ligase ADP-forming beta subunit	1.13	1.50	-1.31	1.79
Q9WUM5	SUCLG1	succinate-CoA ligase alpha subunit	-2.00	1.20	-1.74	1.28
Q9CX34	SUGT1	SGT1 homolog, MIS12 kinetochore complex assembly cochaperone	1.05	1.06	-1.45	-1.39
Q8BG39	SV2B	synaptic vesicle glycoprotein 2B	-1.14	-2.62	1.86	3.04
O88935	SYN1	synapsin I	-1.11	1.18	1.36	1.50
Q64332	SYN2	synapsin II	1.32	1.57	1.14	-1.49
J3QQ18	SYNGAP1	synaptic Ras GTPase activating protein 1	-1.85	-1.61	1.21	1.96
D3Z656	SYNJ1	synaptojanin 1	-1.37	-1.47	-1.01	-1.01

D3Z7R4	SYT1	synaptotagmin 1	-1.14	-26.10	18.49	4.34
Q3TPT3	SYT1	synaptotagmin 1	-1.39	-1.88	1.54	2.92
Q5DTI3	SYT2	synaptotagmin 2	-1.13	1.04	1.13	2.21
Q0D2K7	SYT7	synaptotagmin 7	-2.00	-1.73	1.19	1.20
Q9WVA4	TAGLN2	transgelin 2	1.35	-1.22	-4.21	-1.31
Q9R1Q8	TAGLN3	transgelin 3	1.06	1.14	-1.72	1.14
Q8CCT4	TCEAL5	transcription elongation factor A like 5	1.24	1.32	1.14	-2.01
P11983	TCP1	t-complex 1	-1.40	1.18	1.25	-2.11
Q8C872	TFRC	transferrin receptor	-2.04	-1.67	1.98	-1.88
Q9D880	TIMM50	translocase of inner mitochondrial membrane 50	-1.67	-1.84	-1.08	2.09
P40142	TKT	transketolase	1.01	1.00	-1.25	1.82
Q68FD6	TLN2	talin 2	-1.17	1.29	-1.04	-1.62
Q9D1D4	TMED10	transmembrane p24 trafficking protein 10	-1.54	-1.84	1.38	3.18
Q6ZWX2	Tmsb4x (includes others)	thymosin, beta 4, X chromosome	1.23	1.24	1.21	-2.63
Q8BYI9	TNR	tenascin R	1.43	-1.14	-1.21	1.59
Q3TSX8	TOMM70	translocase of outer mitochondrial membrane 70	-1.59	-1.30	-1.85	1.02
H7BXC3	TPI1	triosephosphate isomerase 1	-1.28	-2.01	2.12	3.86
Q545Y3	Tpm1	tropomyosin 1, alpha	1.63	-1.02	-1.89	1.22
Q3TW28	TPP2	tripeptidyl peptidase 2	-1.29	-1.02	1.54	-1.52
Q3URG1	TPPP	tubulin polymerization promoting protein	-1.19	-1.81	1.55	4.51
Q0KL02	TRIO	trio Rho guanine nucleotide exchange factor	-1.92	-2.10	1.46	1.07
P52196	TST	thiosulfate sulfurtransferase	1.68	-1.15	-3.25	1.03
P68368	TUBA4A	tubulin alpha 4a	1.51	1.03	1.28	3.48
P99024	TUBB	tubulin beta class I	-1.54	-3.97	1.44	3.74
B2RSN3	TUBB2B	tubulin beta 2B class IIb	-2.41	-1.60	1.74	-3.84
Q9ERD7	TUBB3	tubulin beta 3 class III	-1.77	-1.81	-1.50	1.45
Q9D6F9	TUBB4A	tubulin beta 4A class IVa	1.57	-1.06	-1.05	1.92
Q8BFR5	TUFM	Tu translation elongation factor, mitochondrial	-1.64	-1.35	-1.10	2.11
B9EHN0	UBA1	ubiquitin like modifier activating enzyme 1	-2.05	-1.69	1.08	1.96
Q8BJ53	Ubap2l	ubiquitin-associated protein 2-like	1.66	1.20	-1.47	-2.03
Q3TCH2	UCHL1	ubiquitin C-terminal hydrolase L1	-1.24	-1.73	1.12	1.65
Q3U548	UGP2	UDP-glucose pyrophosphorylase 2	1.08	-1.11	-1.30	1.58
Q9D855	UQCRB	ubiquinol-cytochrome c reductase binding protein	-1.30	-1.22	-1.05	2.12
Q3THM1	UQCRC1	ubiquinol-cytochrome c reductase core protein I	-1.55	-1.24	-1.56	2.21
Q9DB77	UQCRC2	ubiquinol-cytochrome c reductase core protein II	-2.02	1.09	-1.34	1.07
Q9CR68	UQCRFS1	ubiquinol-cytochrome c reductase, Rieske iron-sulfur polypeptide 1	-1.20	1.17	-1.87	1.21
Q3U4W8	USP5	ubiquitin specific peptidase 5	-1.46	-3.06	1.68	4.40
Q4FE56	USP9X	ubiquitin specific peptidase 9, X-linked	-1.40	-1.55	1.40	-1.06
B0QZN5	VAMP2	vesicle associated membrane protein 2	-1.00	-1.15	1.55	-1.49
G3UY93	VARS	valyl-tRNA synthetase	1.10	1.51	-1.57	-2.37
Q3TXD3	VAT1	vesicle amine transport 1	1.70	1.43	-1.90	-1.30
Q80TB8	VAT1L	vesicle amine transport 1 like	-1.07	1.17	1.23	-2.57
G3XA35	VCAN	versican	2.36	1.58	-2.69	1.75
Q8BNF8	VCP	valosin containing protein	-1.66	-3.41	1.47	1.62

F2Z471	VDAC1	voltage dependent anion channel 1	-1.40	-1.06	-1.28	1.46
J3QMG3	VDAC3	voltage dependent anion channel 3	-1.40	1.41	-1.03	-1.43
Q0VGU4	VGF	VGF nerve growth factor inducible	1.44	1.52	-1.49	-2.26
Q3TJ43	VPS35	VPS35, retromer complex component	1.01	1.22	-1.13	-1.50
Q4W4C9	VSNL1	visinin like 1	1.16	-3.02	2.62	3.22
Q8CGF6	WDR47	WD repeat domain 47	-1.20	1.17	1.38	-1.54
Q920I9	WDR7	WD repeat domain 7	-1.92	-2.75	1.70	1.28
A2A5N2	YWHAB	tyrosine 3-monooxygenase/tryptophan 5-monooxygenase activation protein beta	-2.09	-3.10	1.82	5.08
Q5SS40	YWHAE	tyrosine 3-monooxygenase/tryptophan 5-monooxygenase activation protein epsilon	1.14	-1.10	-1.14	1.45
P68510	YWHAH	tyrosine 3-monooxygenase/tryptophan 5-monooxygenase activation protein eta	-1.35	-1.79	1.40	1.05
A3KML3	YWHAQ	tyrosine 3-monooxygenase/tryptophan 5-monooxygenase activation protein theta	-1.19	-1.58	-1.05	1.17

Table A9 Proteins identified by ≥ 2 peptides and with a change >20% in Cln3$^{-/-}$ muscle (Chapter 6)

Protein Name	Gene Symbol	Accession Number	Best Ion Score	Ratio (Cln3/WT)	Standard Deviation	Peptides
hypothetical protein LOC66273 isoform 2	AAMDC	40254393	36.69	2.15	0.58	2
transthyretin	TTR	7305599	88.12	1.94	0.33	6
hemopexin	HPX	1881768	89.40	1.62	0.35	27
NADH dehydrogenase [ubiquinone] 1 alpha subcomplex subunit 12	NDUFA12	47117166	35.57	1.58	0.49	2
alpha-1-antitrypsin 1-3	SERPINA1C	6678083	115.46	1.56	0.35	12
dihydrolipoyllysine-residue succinyltransferase component of 2-oxoglutarate dehydrogenase complex	DLST	21313536	55.77	1.55	0.65	3
citrate lyase beta subunit	CLYBL	19073015	76.41	1.54	0.81	3
fatty acid-binding protein, heart	FABP3	6753810	103.10	1.54	0.29	7
Long-chain specific acyl-CoA dehydrogenase, mitochondrial	ACADL	32130423	77.55	1.53	0.48	3
Hydroxyacyl glutathione hydrolase	HAGH	13435786	67.98	1.51	0.44	3
myoglobin	MB	21359820	157.45	1.48	0.50	3
collagen alpha-1(VI) chain precursor	COL6A1	6753484	78.49	1.47	0.21	6
Me1 protein	ME1	13096987	56.07	1.46	0.37	4
phosphatidylethanolamine binding protein	PEBP1	1517864	69.12	1.46	0.11	44
cofilin-2	CFL2	6671746	72.97	1.46	0.34	10
brain protein 44	BRP44	21312594	80.01	1.46	0.19	3
ubiquitin-like modifier-activating enzyme 1 isoform 1	UBA1	6678483	49.73	1.45	0.13	9
unnamed protein product	SYNM	26343513	82.33	1.44	0.03	2
Serpina1d protein	SERPINA1D	18256880	74.93	1.44	0.35	4
alpha-1-antitrypsin 1-4 precursor	SERPINA1D	6678085	74.93	1.43	0.28	10
alpha-1 antitrypsin precursor	SERPINA1B	309079	115.46	1.42	0.24	44
biglycan	BGN	348962	48.27	1.42	0.42	58

histidine triad nucleotide-binding protein 1	HINT1	33468857	87.78	1.41	0.71	3
unnamed protein product	HSPA5	12835845	56.83	1.39	0.22	5
apolipoprotein A-I precursor - mouse	APOE	109571	72.11	1.38	0.17	114
Heat shock protein 2	HSPB2	39850111	76.34	1.37	0.53	2
type VI collagen alpha 3 subunit	COL6A3	3236370	75.36	1.37	0.04	13
protein disulfide-isomerase precursor	P4HB	42415475	76.05	1.37	0.54	2
cytochrome b-c1 complex subunit 1, mitochondrial precursor	UQCRC1	46593021	132.46	1.36	0.49	2
unnamed protein product	TUBB6	12853521	105.62	1.35	0.53	4
tubulin beta-2B chain	TUBB2B	21746161	105.62	1.35	0.41	3
cytochrome b-c1 complex subunit 6, mitochondrial	UQCRH	21539599	112.29	1.34	0.43	3
cytochrome b-c1 complex subunit 7	UQCRB	13385726	64.76	1.32	0.36	4
pyruvate dehydrogenase E1 component subunit beta, mitochondrial precursor	PDHB	18152793	94.57	1.31	0.15	4
creatine kinase S-type, mitochondrial precursor	CKMT2	38259206	125.99	1.30	0.25	2
isocitrate dehydrogenase 3 (NAD+), gamma	IDH3G	51773592	144.48	1.30	0.20	2
histone H2B type 1-C/E/F/G/I	HIST1H2BC	4504257	63.18	1.29	0.59	16
stretch-responsive fibronectin protein type 3	CMYA5	45774102	86.22	1.29	0.40	2
cytochrome c, somatic	CYCS	6681095	112.54	1.29	0.44	8
unnamed protein product	DCI	12836323	77.43	1.29	0.51	4
Lectin, galactose binding, soluble 1	LGALS1	12805209	125.67	1.28	0.26	5
skeletal muscle calsequestrin	CASQ1	2618621	153.89	1.28	0.52	24
phosphate carrier protein, mitochondrial precursor	SLC25A3	19526818	84.37	1.27	0.37	3
reticulon-4 isoform C	RTN4	13195648	114.10	1.27	0.19	5
S-adenosylhomocysteine hydrolase	AHCY	56541076	40.63	1.27	0.00	2
isocitrate dehydrogenase	IDH2	1236984	140.97	1.27	0.42	33
Tubulin, beta 2C	TUBB2C	13542680	110.42	1.27	0.35	3
unnamed protein product	EEF2	26324898	63.58	1.27	0.97	3

calpastatin type II	CAST	11603006	70.39	1.26	0.22	5
NADH-ubiquinone oxidoreductase 18 kDa IP subunit	NDUFS4	4836509	59.78	1.26	0.14	14
unnamed protein product	NDUFA5	12844779	64.30	1.26	0.05	4
tubulin beta-3 chain	TUBB3	12963615	99.07	1.25	0.41	4
heat shock protein 65	HSPD1	51455	62.32	1.24	0.14	254
manganese superoxide dismutase	SOD2	832851	106.34	1.24	0.38	24
unnamed protein product	RPS2	12835827	40.94	1.24	0.19	5
unnamed protein product	CFL1	12861068	72.97	1.24	0.06	4
unnamed protein product	SUCLG1	12836764	101.38	1.23	0.14	6
Trim72 protein	TRIM72	45500997	77.98	1.23	0.05	2
Acyl-Coenzyme A dehydrogenase, medium chain	ACADM	15488707	61.84	1.23	0.27	3
citrate synthase, mitochondrial precursor	CS	13385942	114.82	1.22	0.21	4
tubulin beta-5 chain	TUBB5	7106439	99.07	1.22	0.29	7
myelin basic protein isoform 1	MBP	69885032	82.32	1.21	0.03	2
acyl carrier protein, mitochondrial precursor	NDUFAB1	27754007	101.75	1.21	0.09	2
NADH dehydrogenase (ubiquinone] 1 beta subcomplex subunit 10	NDUFB10	58037109	54.70	1.21	0.11	2
isocitrate dehydrogenase 3, beta subunit	IDH3B	18700024	73.44	1.21	0.07	3
ES1 protein homolog, mitochondrial precursor	D10JHU81E	20070420	88.12	1.20	0.52	3
unnamed protein product	MYOM3	26329053	66.75	1.20	0.27	3
Acetyl-Coenzyme A acyltransferase 2 (mitochondrial 3-oxoacyl-Coenzyme A thiolase)	ACAA2	20810027	114.58	1.20	0.34	3
synemin isoform M	SYNM	41687955	82.33	1.20	0.27	2
mlrq-like protein	NDUFA4	1401252	78.69	1.20	0.27	70
heterogeneous nuclear ribonucleoprotein A3 isoform c	HNRNPA3	157277969	136.04	1.20	0.19	2
synaptophysin-like protein 2	SYPL2	6678874	212.22	1.20	0.15	8
cytochrome c oxidase subunit 6C	COX6C	16716343	66.56	1.20	0.34	3
unnamed protein product	ATL2	26332771	44.79	0.80	0.03	2

eukaryotic initiation factor 4A-II isoform c	EIF4A2	176866061	69.57	0.80	0.19	2
myosin heavy chain	MYH4	199980	64.49	0.79	0.24	95
ubiquitin-40S ribosomal protein S27a precursor	RPS27A	13195690	57.89	0.79	0.13	5
ATP synthase subunit b, mitochondrial precursor	ATP5F1	78214312	39.68	0.79	0.20	2
aldehyde dehydrogenase AHD-M1	ALDH2	560645	62.31	0.79	0.05	31
Chain E, Crystal Structure Of The Catalytic Subunit Of Camp- Dependent Protein Kinase Complexed Wit	PRKACA	14719578	84.67	0.78	0.10	3
dystrophin	DMD	6681203	69.54	0.78	0.09	8
alcohol dehydrogenase-B2	ADH5	191722	85.80	0.78	0.10	55
Chain A, Adipocyte Lipid Binding Protein Complexed With 1-Anilino-8-Naphthalene Sulfonate	FABP4	5822455	92.82	0.78	0.11	12
myosin light chain 6B	MYL6B	26986555	58.97	0.77	0.01	2
polymerase I and transcript release factor	PTRF	6679567	50.29	0.77	0.13	8
unnamed protein product	CAV1	26330776	130.09	0.77	0.05	2
myozenin-2	MYOZ2	10946916	61.94	0.76	0.01	6
60S ribosomal protein L17 isoform a	RPL17	4506617	67.15	0.75	0.12	13
cAMP-dependent protein kinase type II-alpha regulatory subunit	PRKAR2A	22550094	64.03	0.75	0.01	3
26S proteasome non-ATPase regulatory subunit 2	PSMD2	19882201	57.10	0.74	0.03	3
Isocitrate dehydrogenase 1 (NADP+), soluble	IDH1	57242927	60.86	0.74	0.02	2
mKIAA1248 protein	NDRG2	50510857	54.32	0.73	0.11	2
cytochrome b5	CYB5	13385268	181.78	0.73	0.07	4
alpha-crystallin B chain	CRYAB	6753530	75.77	0.73	0.16	7
epidermal keratin 10	KRT10	7638398	44.93	0.71	0.21	5
calnexin precursor	CANX	6671664	44.28	0.70	0.24	11
unnamed protein product	EIF4A1	50815	74.90	0.69	0.04	286
GTP-binding nuclear protein Ran	RAN	5453555	78.64	0.68	0.01	17
Anxa5 protein	ANXA5	13277612	89.32	0.68	0.10	4

Voltage-dependent L-type calcium channel subunit alpha-1S	CACNA1S	60391852	63.39	0.67	0.19	2
carbonic anhydrase 3	CAR3	31982861	111.53	0.64	0.14	2
troponin I, slow skeletal muscle	TNNI1	10946862	73.19	0.62	0.19	5
unnamed protein product	KRT1	12859782	73.21	0.50	0.11	5
Troponin T, slow skeletal muscle	TNNT1	66773945	101.48	0.49	0.15	2
parvalbumin alpha	PVALB	31980767	113.92	0.29	0.26	2
immunoglobulin kappa chain V-region (V-J)	KV5A8	197166	64.03	0.27	0.04	96